# Electronic Raman scattering in high-temperature superconductors

Von der Fakultät für Physik der Universität Stuttgart
zur Erlangung der Würde eines
Doktors der Naturwissenschaften (Dr. rer. nat.)
zu genehmigende Abhandlung

vorgelegt von

Thomas Strohm

aus Stuttgart

Hauptberichter: Prof. Dr. M. Cardona
Mitberichter: Prof. Dr. A. Muramatsu

Tag der Einreichung: 31. Mai 1999
Tag der Prüfung: 30. August 1999

MAX-PLANCK-INSTITUT FÜR FESTKÖRPERFORSCHUNG
STUTTGART
1999

*Scientific knowledge is a body of statements of varying degrees of certainty—some most uncertain, some nearly sure, none absolutely certain.*

R. P. Feynman

*Mathematiker sind eine Art Franzosen. Redet man zu ihnen, so übersetzen sie es in ihre Sprache und dann ist es alsobald ganz etwas anderes.*

J. W. von Goethe, *Maximen und Reflexionen*

*In mathematics you don't understand things. You just get used to them.*

Johann von Neumann

…descubrieron treinta o cuarenta molinos de viento que hay en el campo, y así como don Quijote los vió, dijo a su escudero:

—La aventura va guiando nuestras cosas mejor de lo que acertáramos a desear; porque ves allí, amigo Sancho Panza, dónde se descubren treinta, o poco más, desaforados gigantes, con quien pienso hacer batalla y quitarles a todos las vidas, con cuyos despojos comenzaremos a enriquecer, que ésta es buena guerra, y es gran servicio de Dios quitar tan mala simiente de sobre la faz de la tierra.

—¿Qué gigantes? —dijo Sancho Panza.

—Aquellos que allí ves —respondió su amo— de los brazos largos que los suelen tener algunos de casi dos lenguas.

—Mire vuestra merced —respondió Sancho— que aquellos que allí se parecen no son gigantes, sino molinos de viento, y lo que en ellos parecen brazos son las aspas, que, volteadas del viento, hacen andar la piedra del molino.

—Bien parece —respondió don Quijote— que no estás cursado en esto de las aventuras: ellos son gigantes; y si tienes miedo, quítate de ahí y ponte en oración en el espacio que yo voy a entrar con ellos en fiera y desigual batalla.

Miguel de Cervantes, *Don Quijote de la Mancha I,* Cap. VIII

# Zusammenfassung

## Geschichtlicher Überblick

In der Geschichte der Physik hat die Verfügbarkeit neuer Technologien sehr oft die Entdeckung neuer physikalischer Phänomene zur Folge gehabt. Als Kammerlingh Onnes im Jahre 1911 an der Universität zu Leiden den supraleitenden Zustand festen Quecksilbers entdeckte, war dies möglich geworden, weil er 3 Jahre zuvor erfolgreich Helium verflüssigte. Flüssiges Helium war der Schlüssel zum Erreichen von Temperaturen welche im Bereich von wenigen Kelvin liegen. Solche sind notwendig, um die kritische Temperatur $T_c$, welche den Phasenübergang zum supraleitenden Zustand markiert, zu unterschreiten.

Für die theoretischen Physiker begann die Suche nach einer Theorie des neuen Zustandes. Der supraleitende Zustand ist durch zwei grundlegende Eigenschaften charakterisierbar: den Meissner-Ochsenfeld-Effekt (d.h. das Verdrängen des magnetischen Flusses aus dem Inneren eines Supraleiters) und dem vollständigen Verschwinden des elektrischen Gleichstromwiderstandes. Ein erster Schritt war gemacht, als 1935 F. und H. London die grundlegenden elektrodynamischen Eigenschaften des supraleitenden Zustandes mittels der zwei London-Gleichungen im Rahmen der klassischen makroskopischen Elektrodynamik erklärten.

Zwei weitere wichtige Eigenschaften des supraleitenden Zustandes führten noch näher an ein theoretisches Verständnis. Daunt und Mendelssohn entdeckten das Verschwinden thermoelektrischer Effekte und Corak *et al.* zeigten, daß für Temperaturen, die wesentlich unterhalb von $T_c$ liegen, die elektronische spezifische Wärme eine exponentielle Abhängigkeit von der Temperatur aufweist. Diese zwei Effekte legten die Existenz einer Energielücke $\Delta$ zwischen dem Grundzustand des Systemes und seinem Anregungsspektrum nahe. Im Jahre 1950 kam ein weiterer Meilenstein dazu: der Vorschlag von Fröhlich, daß die Elektron-Gitter-Wechselwirkung von ausschlaggebender Bedeutung für die Erklärung der Supraleitung sein sollte. Die Entdeckung des Isotopeneffektes (d.h. der Tatsache, daß die kritische Temperatur $T_c$ proportional dem Inversen der Quadratwurzel der Isotopenmasse, also zu $M^{-1/2}$ ist) kurze Zeit später zeigte, daß Fröhlich mit seiner Vermutung richtig lag.

Der endgültige Durchbruch war jedoch die Formulierung der Theorie der Supraleitung (BCS-Theorie) durch Bardeen, Cooper und Schrieffer im Jahre 1956. Sie zeigten, daß der Grundzustand (Fermisee) eines Elektronengases bezüglich einer schwachen attraktiven Wechselwirkung zwischen Elektronen instabil ist. Solch eine anziehende Wechselwirkung zieht die Bildung von Cooperpaaren nach sich, das heißt von Paaren aus Elektronen mit entgegengesetztem Gitterimpuls und Spin. Die räumliche Ausdehnung solcher Paare ist durch die Pippardsche Kohärenzlänge $\xi_0$ gegeben. Die Theorie sagt in der Tat eine Energielücke $2\Delta = 3.528\, T_c$ im Anregungsspektrum des supraleitenden Zustandes voraus und erklärt die meisten physikalischen Eigenschaften des supraleitenden Zustandes.

Die BCS-Theorie ist eine Theorie der schwachen Kopplung, sie ist nur anwendbar falls die anziehende Wechselwirkung zwischen den Elektronen schwach ist. Zwar wird der supraleitende Zustand der Elementsupraleiter Al, In und Zn ziemlich gut von der BCS-Theorie beschrieben, die Eigenschaften von Pb und Hg weichen mit $2\Delta = 4.3\,T_c$ und $2\Delta = 4.6\,T_c$ jedoch beträchtlich von der Vorhersage der BCS-Theorie ab. Diese Abweichung ist hauptsächlich eine Folge einer groben Näherung bei der Beschreibung der Elektron-Elektron-Wechselwirkung in der BCS-Theorie. Die anziehende Wechselwirkung ist eine Konsequenz des Austausches von virtuellen Phononen und basiert auf Fröhlichs Elektron-Gitter-Wechselwirkung. Dieser Tatsache wird in der Eliashberg-Theorie Rechnung getragen. Dort wird die Wechselwirkung mittels der Funktion $\alpha^2 F(\omega)$, welche die durch die Elektron-Phonon-Kopplungsstärke gewichtete phononische Zustandsdichte darstellt, beschrieben. Die Vorhersagen der Eliashberg-Theorie für Pb und Hg bezüglich des Quotienten $2\Delta/k_B T_c$ decken sich mit den experimentell ermittelten Werten.

Die friedliche Zeit der Übereinstimmung zwischen Theorie und Experiment fand mit der Entdeckung der Schweren-Fermion-Supraleiter, welche nicht im Rahmen der Eliashberg-Theorie beschrieben werden können, ein jähes Ende. Beispiele für solche Systeme sind $\mathrm{CeCu_2Si_2}$ ($T_c = 0.7\,\mathrm{K}$) und $\mathrm{UPt_3}$ ($T_c = 1.5\,\mathrm{K}$); Schwere-Fermion-Systeme enthalten stets Ionen mit $f$-Elektronen. Die spezifische Wärme dieser Materialien liegt Größenordnungen über jener von typischen Metallen, was auf die Existenz von Ladungsträgern mit einer Masse, die viel größer als die freie Elektronenmasse ist, hinweist. Die spezifische Wärme dieser Systeme scheint bei tiefen Temperaturen einem Potenzgesetz zu folgen. Solch eine Eigenschaft könnte von einer Lückenfunktion (d.h. einer $\boldsymbol{k}$-abhängige Lücke $\Delta_{\boldsymbol{k}}$) herrühren, die auf einigen Punkten (oder Linien) auf der Fermifläche verschwindet. Die sehr niedrigen kritischen Temperaturen der Schweren-Fermion-Supraleiter sind jedoch für das Experiment sehr problematisch. Möglicherweise sind diese Materialien aus diesem Grunde fast in Vergessenheit geraten.

Dies war die Situation, als 1986 Bednorz und Müller am IBM Forschungslabor in Zürich die epochemachende Entdeckung der Hochtemperatursupraleitung in keramischem $\mathrm{La_{2-x}Ba_xCuO_4}$ unterhalb einer kritischen Temperatur von etwa 35 K gelang. Schon sehr bald nach diesem außergewöhnlichen Ereignis wurde die Hochtemperatursupraleitung auch in $\mathrm{YBa_2Cu_3O_7}$ unterhalb von $T_c \approx 92\,\mathrm{K}$ und in vielen anderen in ähnlicher Art und Weise auf Schichten aus CuO-Ebenen basierenden Materialien nachgewiesen.

Die Tatsache, daß die kritische Temperatur von vielen Hochtemperatursupraleitern höher als die Siedetemperatur von Stickstoff ist, öffnet den Weg zur technischen Anwendung der Supraleitung, denn flüssiger Stickstoff ist preiswert und leicht handhabbar. Klare Nachteile für eine technische Anwendung sind jedoch die im Vergleich zu Metallen sehr kleine Ladungsträgerdichte, die ausgeprägte Anisotropie der elektronischen Eigenschaften (aufgrund der Schichtstruktur) und die kleine Kohärenzlänge, welche ein kleines kritisches Feld $H_{\mathrm{c},1}$ mit sich bringt.

Es gibt keine Zweifel, daß die Supraleitfähigkeit der Hochtemperatursupraleiter auf Cooperpaaren mit einem verschwindenden Gesamtkristallimpuls (das gemessene Flußquant ist $hc/2e$) und die sich im Spinsingulettzustand befinden (dies kann aus den Messungen der Knight-Verschiebung gefolgert werden), basiert. Soweit sind die Hochtemperatursupraleiter mit der BCS-Beschreibung konsistent.

Zwei andere Typen von Beobachtungen können jedoch nicht mittels einer isotropen Theorie wie der BCS-Theorie erklärt werden. Dies sind Experimente, die sich direkte Folgerungen aus der räumlichen Symmetrie der Lückenfunktion zunutze machen. Ein gutes Beispiel sind die Messungen des in SQUID-Ringen (welche aus zwei Stücken gegeneinander verdrehter Supraleiter bestehen) eingefangenen magnetischen Flusses. Desweiteren Experimente, in welchen die Zustandsdichte der Quasiteilchenanregungen (oder einer darauf basierenden Größe) gemessen wird. Photoelektronenemission, Infrarotabsorption und Ramanstreuung decken die Existenz von Quasiteilchenanregungen für beliebig kleine Anregungsenergien auf. Daraus folgt das Verschwinden der Lückenfunktion in gewissen Gebieten auf der Fermifläche. Ergebnisse aus Messungen der spezifischen Wärme deuten ebenfalls in diese Richtung. Sie zeigen eine lineare Abhängigkeit der (elektronischen) spezifischen Wärme von der Temperatur bei niedrigen Temperaturen. Messungen der Eindringtiefe sprechen ebenso für die Behauptung, daß die Lückenfunktion Knoten besitzt.

Dieses Bild der Phänomene der Hochtemperatursupraleitung ist jedoch weit davon entfernt, umfassend zu sein. Hochtemperatursupraleiter besitzen ein ausgesprochen kompliziertes Phasendiagramm. Sie glänzen mit weiteren Schwierigkeiten, zum Beispiel ihrem Normalzustand, der nicht innerhalb eines einfachen Fermiflüssigkeitsmodells beschrieben werden kann.

## Experimentelle Ergebnisse der Ramanstreuung an Hochtemperatursupraleitern

Das typische Experiment zur Ramanstreuung besteht darin, einen monochromen Laserstrahl auf eine in einem Kryostaten bei der Temperatur kondensierenden Heliums gehaltene Probe zu fokussieren. Man beobachtet dann natürlich elastisch gestreutes Licht, das jedoch bei der Ramanstreuung nicht interessiert. Vielmehr wird das *inelastisch* gestreute Licht ausgewertet. Das gestreute Licht wird mit optischen Mitteln gesammelt und in ein Spektrometer geleitet. Das so entstehende Spektrum wird dann mittels einer CCD-Kamera detektiert. Bei den Spektren trägt man die Intensität des inelastisch gestreuten Laserlichtes (die *Ramanintensität*) über der *Ramanverschiebung*, das ist (beim Stokes-Prozeß) die Energie, die bei der inelastischen Streuung auf die Probe übertragen wurde, auf. Die Energieskala von Ramanspektren reicht typischerweise bis knapp in den eV-Bereich, mit einer Auflösung von einigen wenigen Zehntel meV. Das typische Spektrum von Hochtemperatursupraleitern im supraleitenden Zustand zeigt ein breites Kontinuum, auf dem einige Peaks sitzen. Die meisten dieser Peaks sind relativ scharf und werden deshalb diskreten Anregungen, welche im vorliegenden Fall $\Gamma$-Punkt-Phononen sind, zugeordnet. Diese Phononen lassen sich vom Ramanspektrum mittels eines wohldefinierten Verfahrens subtrahieren, und der Rest, das *elektronische Kontinuum*, wird üblicherweise als von elektronischen Anregungen verursacht angesehen. Das elektronische Kontinuum ist eine Konsequenz *elektronischer Ramanstreuung*.

Beim Experiment benutzt man Laserlicht, das sich in einem definierten Polarisationszustand befindet. Außerdem wird das inelastisch gestreute Licht durch einen Polarisationsfilter geschickt, bevor es dem Spektrometer zugeleitet wird. Durch die Änderung der Wahl der Polarisationsrichtungen kann man dann mehrere unabhängige Spektren messen.

Gewisse Eigenschaften des elektronischen Kontinuums sieht man nur in ganz bestimmten Polarisationskonfigurationen. Dies ist ebenso der Fall für die Phononen. Die Polarisationsabhängigkeit der Spektren definiert dann auch den Raman-Tensor. Der *Raman-Tensor* ist ein Tensor zweiter Stufe, welcher nach Kontraktion mit den Polarisationsvektoren des einfallenden und des gestreuten Lichtes und darauffolgendem Quadrieren proportional zur Ramanintensität wird.

Die Kristallstruktur der untersuchten Hochtemperatursupraleiter besitzt zum großen Teil eine "'schwach" orthorhombisch (Punktgruppe $D_{2h}$) gestörte tetragonale (Punktgruppe $D_{4h}$) Symmetrie. Dies erlaubt, den Raman-Tensor in eine Summe von Tensoren zu zerlegen, von denen jeder nach einer bestimmten irreduziblen Darstellung der Punktgruppe transformiert. Im Falle tetragonaler Symmetrie sind einige solche die total symmetrische $A_{1g}$-Darstellung sowie die $B_{1g}$- und die $B_{2g}$-Darstellung.

## Die Theorie der Ramanstreuung

Die Formulierung der Theorie zur elektronischen Ramanstreuung geht von einem System von nichtwechselwirkenden Elektronen (genaugenommen handelt es sich um Bloch-Elektronen) aus, welche an das elektromagnetische Feld gekoppelt werden. Dies liefert zwei Kopplungsterme von denen einer, $H_{\boldsymbol{Ap}}$, proportional zum Produkt aus dem Impulsoperator der Elektronen und dem Vektorpotential des elektromagnetischen Feldes ist. Der Zweite, $H_{\boldsymbol{A}^2}$, ist proportional zum Quadrat des Vektorpotentiales.

Um die Übergangsrate zur Beschreibung der Ramanstreuung zu ermitteln, müssen Randbedingungen formuliert werden. Ramanstreuung ist inelastische Lichtstreuung. Im Experiment wird zeitlich und räumlich kohärentes Laserlicht benutzt. Dieses fällt auf die zu untersuchende Probe ein und bewirkt dort Anregungen. Sind das elektronische Anregungen, so handelt es sich um Elektron-Loch-Paare mit verschwindendem Kristallimpuls. Die Anregungen erzeugen wieder Licht, welches als elastisch oder inelastisch gestreutes dann im Detektor nachgewiesen wird. Zwischen dem einfallenden und dem gestreuten Licht besteht eine Korrelation, bei Ramanstreuung handelt es sich daher nicht um Lichtabsorption gefolgt von Lichtemission.

In der Praxis werden wir die Ramanstreuung daher als Wahrscheinlichkeit für *einen* Übergang auffassen. Der Anfangszustand $|i\rangle$ ist gegeben durch das elektromagnetische Feld, in dem eine einzige Mode durch $n$ Photonen besetzt ist, und dem elektronischen System der Probe, welches sich im Grundzustand befindet. Die elektromagnetische Mode nennen wir L-Mode; sie entspricht dem einfallenden Laserlicht. Alle anderen Moden des elektromagnetischen Feldes sind unbesetzt. Der Streuprozeß führt dann zu einem Endzustand $|f\rangle$, in welchem die L-Mode nur noch mit $n-1$ Photonen besetzt ist und eine weitere Mode, die S-Mode, ein Photon enthält. Diese Mode entspricht der ebenen Welle, die auf den Detektor trifft. Das elektronische System ist im Endzustand angeregt. Wir werden annehmen, daß es sich um eine Elektron-Loch-Anregung handelt.

Der Hamilton-Operator $H_0$ des ungekoppelten Systems von Elektronen und Photonen alleine induziert natürlich noch keinen Übergang von $|i\rangle$ nach $|f\rangle$, da es sich um Eigenzustände von $H_0$ handelt. Die Kopplungsterme $H_{\boldsymbol{Ap}}$ und $H_{\boldsymbol{A}^2}$ jedoch bewirken Ramanstreuung. Die Tatsache, daß sich Anfangs- und Endzustand nur um jeweils ein Photon in der L-Mode und der S-Mode unterscheiden, bedeutet, daß der Operator $H_{\boldsymbol{Ap}}$ nur in gerader

Ordnung der Störungstheorie zum Raman-Prozeß beiträgt. Wir werden Renormierungseffekte der Elektronen aufgrund von Photonen nicht berücksichtigen, und gelangen so zu dem Schluß, daß $H_{\boldsymbol{Ap}}$ lediglich in zweiter Ordnung der Störungstheorie interessant ist. Eine ähnliche Überlegung führt dann zu der Feststellung, daß der relevante Beitrag des Operators $H_{\boldsymbol{Ap}}$ zur gesuchten Übergangswahrscheinlichkeit aus der Störungstheorie erster Ordnung herrührt.

Es ist natürlich umständlich, eine Übergangswahrscheinlichkeit durch zwei verschiedene Operatoren, die überdies in unterschiedlicher Ordnung der Störungstheorie ihren Beitrag liefern, zu beschreiben. Aus diesem Grunde faßt man die Operatoren zu einem einzigen Störoperator, dem Raman-Operator $H_{\text{Raman}}$ zusammen. Dieser wird so gewählt, daß er die relevanten Übergänge in Störungstheorie erster Ordnung beschreibt.

Schreibt man die den L- und S-Moden entsprechenden ebenen Wellen als ein Produkt aus einem Polarisationsvektor und einer skalaren Welle, so wird klar, daß sich die Freiheit der Wahl der Polarisation der einfallenden sowie der gestreuten Welle in der Theorie darin widerspiegelt, daß der Raman-Operator ein Tensor zweiter Stufe ist. Die Übergangswahrscheinlichkeit, welche vermöge der goldenen Regel quadratisch im Raman-Operator ist, wird dadurch ein zu einem Tensoren vierter Stufe.

Der Raman-Operator beschreibt die Erzeugung eines Elektron-Loch-Paares zusammen mit der Streuung eines Photons. Er ist deswegen proportional zum Produkt eines Erzeugungs- und eines Vernichtungsoperators für Elektronen zum einen, und für Photonen zum anderen. Bei der Berechnung der Übergangswahrscheinlichkeit separieren die elektronischen von den photonischen Anteilen, so daß die interessante Größe letztendlich eine Eigenschaft des elektronischen Systemes ist. Berechnet man die Wahrscheinlichkeit eines in Störungstheorie erster Ordnung durch einen Dichteoperator verursachten Übergangs zwischen zwei Zuständen, so sieht man, daß diese durch die Dichte-Dichte-Fluktuationen gegeben ist. Mittels des Fluktuations-Dissipations-Theoremes kann man diese Größe auf eine Suszeptibilität zurückführen, welche in diesem Falle mit der longitudinalen dielektrischen Funktion in Zusammenhang steht. Ganz ähnlich verhält es sich bei der Ramanstreuung. Die Fluktuationen des Raman-Operators beschreiben die Ramanstreuung. Und das Fluktuations-Dissipations-Theorem schafft eine Beziehung zwischen diesen und dem Imaginärteil einer Suszeptibilität, der *Raman-Suszeptibilität*. Wir werden im folgenden sehen, daß der Raman-Operator unter bestimmten Einschränkungen der inversen effektiven Masse der Ladungsträger – einem Tensor – entspricht. Aus diesem Grunde spricht man im Falle der Fluktuationen des Raman-Operators auch oft von den *Massenfluktuationen* (genauer den Fluktuationen der inversen effektiven Masse).

Die Tatsache, daß ein Teil des Raman-Operators ein Resultat aus der zweiten Ordnung der Störungstheorie ist, verleiht dem Raman-Operator einen Resonanznenner. Ist die Energie des einfallenden Lichtes sehr ähnlich derjenigen der Anregung im elektronischen System, wird die Übergangswahrscheinlichkeit verstärkt. Unter bestimmten Umständen aber kann man die im Resonanznenner auftretende Laserfrequenz gegen die restlichen Terme vernachlässigen. Dadurch nimmt der Ausdruck für den *Ramanvertex* eine Form an, wie sie auch der Tensor der inversen effektiven Masse (als Funktion von $\boldsymbol{k}$) nach Anwendung des Theorems der effektiven Masse hat. Wir identifizieren also innerhalb obengenannter Annahmen den Ramanvertex mit dem Tensor der inversen effektiven Masse. Die Prüfung der Anwendbarkeit dieser *Näherung der effektiven Masse* ist nicht trivial und muß von Fall zu

Fall untersucht werden.

Wir gelangen also zu dem vorläufigen Schluß, daß die Intensität der elektronischen Ramanstreuung proportional zum Imaginärteil der Raman-Suszeptibilität ist. Die Raman-Suszeptibilität ist im einfachen Modell nichtwechselwirkender Elektronen durch die Behandlung des Raman-Operators in Störungstheorie erster Ordnung gegeben.

Natürlich ist das oben benutzte theoretische Modell der nichtwechselwirkenden Elektronen der Komplexität des vorliegenden Problemes nicht angemessen. Insbesondere zwei Effekte, die von der Wechselwirkung zweier Elektronen herrühren, haben wir in Betracht zu ziehen. Dies ist zum ersten die *elektronische Abschirmung*. Entsteht durch eine Anregung ein Loch, so entspricht dies einer positiven Ladung, welche durch die Verschiebung negativer Ladungen abgeschirmt wird. Und zum zweiten den Effekt, der zur Existenz von Cooper-Paaren im supraleitenden Zustand führt (oder, alternativ, die ungewöhnlichen Eigenschaften des Normalzustandes nach sich zieht). Beide Effekte sind Vielteilcheneffekte und entsprechend kompliziert in der mathematischen Handhabung. Wir werden zur weiteren Entwicklung der Theorie deshalb den Formalismus der Greenschen Funktionen und zur Veranschaulichung Feynman-Diagramme heranziehen. Die Raman-Suszeptibilität wird in diesem Rahmen durch eine Elektron-Loch-Schleife gegeben, deren beide Vertices dem Ramanvertex entsprechen. Die Renormierung von Suszeptibilitäten durch elektronische Abschirmung geschieht wie üblich im Rahmen der Random Phase Approximation (RPA). In diesem Zusammenhang wirkt es sich positiv aus, daß im relevanten Grenzfall $\boldsymbol{q} \rightarrow 0$ die Inverse der Coulomb-Wechselwirkung verschwindet. Man kann dann eine sehr kompakte Formel für die durch elektronische Abschirmung renormierte Raman-Suszeptibilität angeben.

Die Änderungen, die es uns dann erlauben, die Suszeptibilität auch für den Fall der supraleitenden Phase zu berechnen, beschränken sich auf die Elektron-Loch-Schleife selbst. In der BCS-Theorie wird gezeigt, daß eine Elektronenflüssigkeit, die sich in der supraleitenden Phase befindet, durch eine Flüssigkeit aus Quasiteilchen (den sogenannten Bogolonen) beschrieben werden kann. Das Energiespektrum der Bogolonen besitzt eine Lücke direkt über dem Grundzustand. Zur Modifikation der Schleife haben wir die Greensche Funktion der Elektronen durch die der Quasiteilchen zu ersetzen. Aufgrund der Tatsache, daß der Ramanvertex nur vom Kristallimpuls, nicht jedoch von der Frequenz abhängt, kann die Frequenzintegration, die bei der Auswertung einer Quasiteilchen-Schleife auftritt, ohne detaillierte Kenntnis des Vertex durchgeführt werden. Die Integration führt dann auf die *Tsuneto-Funktion*. Diese Funktion hängt von der Frequenz und der Quasiteilchendispersion ab, letztere ist wiederum eine Funktion der Dispersion der Elektronen und der Lückenfunktion.

# Problemstellung

An dieser Stelle angekommen, ist die Theorie nun auszuwerten. Die Arbeiten, die schon vor der unseren vorhanden waren, fallen in zwei Gruppen. Die erste beinhaltet einige Arbeiten von Devereaux *et al.* Deren Rechnungen bauen auf einer einfachen zweidimensionalen Modellbandstruktur mit einem elektronischen Band auf. Die $\boldsymbol{k}$-Abhängigkeit des Ramanvertex wird durch die ersten Terme einer Entwicklung in Fermiflächenharmonische dargestellt. Die zur Berechnung der Suszeptibilitäten notwendige Integration über die Brillouinzone (BZ) wird durch eine Integration über die Fermifläche (FF) angenähert. Es ist klar, daß bei dieser Vorgehensweise spezifische Eigenschaften der Bandstruktur der Hochtemperatursupraleiter (die ja in den Ramanvertex eingehen) unberücksichtigt bleiben müssen. Ein Problem dieser Methode ist nicht nur der fehlende Bezug zu einer realistischen Bandstruktur. Ebenso ist der Fehler, der bei der Näherung der BZ-Integration durch eine FF-Integration entsteht, nur sehr schlecht abschätzbar.

Ein Ergebnis der Arbeiten von Devereaux *et al.* betrifft die Lage der Peaks im Ramanspektrum, welche der supraleitenden Lücke zugeordnet werden (den sog. Paarbrechungspeaks). Messungen zeigten, daß der Peak im $A_{1g}$-Spektrum bei einer beträchtlich niedrigeren Ramanverschiebung angesiedelt ist als der Peak im $B_{1g}$-Spektrum. Das Verhältnis der Positionen beläuft sich fast auf einen Faktor Zwei. Für tetragonale Systeme sagt die Theorie der elektronischen Ramanstreuung voraus, daß Effekte der elektronischen Abschirmung nur in der total symmetrischen $A_{1g}$-Komponente des Spektrums vorhanden sind. Unter bestimmten Umständen wird durch den Effekt der *Überabschirmung* der Peak im $A_{1g}$-Spektrum hin zu niedrigeren Werten der Ramanverschiebung verschoben. Mittels einer einfachen Modellrechnung konnten Devereaux *et al.* ein experimentell ermitteltes Spektrum fitten. Später stellte sich jedoch heraus, daß die dem Fit zugrunde liegende Rechnung mit einem Fehler behaftet war. Dennoch erscheint die elektronische Abschirmung als eine Möglichkeit, die unterschiedliche Lage des Peaks im $A_{1g}$- und im $B_{1g}$-Spektrum zu erklären.

Ein weiterer Versuch zur Erklärung der Position der Ramanpeaks wurde von Krantz *et al.* unternommen. In deren Arbeit wurde der Ramanvertex aus der elektronischen Bandstruktur (über die Näherung der effektiven Masse) und einem Ansatz für die Lückenfunktion ermittelt. Die elektronische Bandstruktur wurde mittels der Linear-Muffin-Tin-Orbital-Methode (LMTO-Methode) in der Näherung der atomaren Kugeln (ASA) basierend auf der Dichtefunktionaltheorie und der Näherung der lokalen Dichte (LDA) berechnet. Die Rechnungen waren zweidimensional und die Integrationen auf die Fermifläche beschränkt. Es wurden zum Teil auch bandabhängige Lückenfunktionen benutzt, und für $YBa_2Cu_3O_7$ (Y-123) gezeigt, daß man durch bestimmte unterschiedliche Lückenfunktionen für das Band mit gerader und für jenes mit ungerader Symmetrie erreichen kann, daß die Peaks im $A_{1g}$- sowie im $B_{1g}$-Spektrum an verschiedene Positionen fallen. In der Arbeit von Krantz *et al.* wurde die elektronische Abschirmung jedoch nicht ganz korrekt berücksichtigt.

# Ergebnisse

Ein Teil der vorliegenden Arbeit war also daraufhin ausgerichtet, einige Probleme, die nach den oben beschriebenen Arbeiten noch geblieben sind, auszuräumen. Dazu wurde das theoretische Modell so angesetzt, daß die offensichtlichen Einschränkungen der beiden Arbeiten umgangen wurden. Wir benutzten also ebenfalls eine mittels der LMTO-Methode gewonnene elektronische Bandstruktur (die untersuchten Systeme waren Y-123 und $YBa_2Cu_4O_8$ (Y-124)), beschränkten uns dabei aber nicht auf zwei Dimensionen, sondern führten die Rechnung in drei Dimensionen durch. Weiterhin wurde die elektronische Abschirmung nach der Theorie korrekt berücksichtigt. Als Lückenfunktion wurde die $d_{x^2-y^2}$-Welle $\Delta_{\boldsymbol{k}} = \Delta_0 \cos\varphi_{\boldsymbol{k}}$ gewählt. Die Integrationen wurden außerdem über die gesamte Brillouinzone ausgedehnt. Weiterhin haben wir auch Fermiflächenintegrationen durchgeführt, um die Anwendbarkeit dieser Näherung durch Vergleich der Ergebnisse mit denjenigen aus der BZ-Integration zu überprüfen. Dabei ist eine Bemerkung angebracht: Die mittels der LMTO-Methode berechnete elektronische Bandstruktur von Y-123 weist eine van Hove-

Singularität etwa 25 meV unterhalb der Fermienergie auf. Diese befindet sich am Rande der Brillouinzone, fern von der Fermifläche. Dadurch ist zu erwarten, daß die Singularität keinen Einfluß auf die aus der FF-Integration erlangte Ramanintensität hat. Die mit der van Hove-Singularität verbundene hohe Zustandsdichte etwa 25 meV unterhalb der Fermienergie sollte sich jedoch in der durch eine BZ-Integration berechneten Ramanintensität widerspiegeln. Das tut sie in der Tat.

In der Arbeit wurde Wert darauf gelegt, nicht nur die Form der elektronischen Ramanspektren, sondern auch die *absoluten Werte der Ramanintensität* zu reproduzieren. Solch ein Unterfangen wurde für Hochtemperatursupraleiter nie zuvor durchgeführt. Man muß dazu zum einen große Sorgfalt bei der Messung walten lassen, außerdem ist eine geeignete Eichung der Meßapparatur unumgänglich. Desweiteren ist auch allen Vorfaktoren bei der Berechnung der Ramanintensität korrekt Rechnung zu tragen. Als Ergebnis erhielten wir bis auf einen Faktor Zwei eine zufriedenstellende Übereinstimmung der theoretisch bestimmten mit den experimentell ermittelten Ramanintensitäten. Dies ist ein wichtiger Hinweis darauf, daß die elektronische Ramanstreuung an Hochtemperatursupraleitern tatsächlich von Massenfluktuationen verursacht wird (das bedeutet auch, daß für eine konstante Masse keine Streuung stattfindet).

Ein weiteres überraschendes Ergebnis der Rechnungen betrifft die Position des von der Paarbrechnung herrührenden Peaks im $A_{1g}$- sowie im $B_{1g}$-Spektrum. Er befindet sich fast genau an *derselben Position*. Dies steht im krassen Widerspruch zu den experimentell ermittelten Daten und ebenso zu Ergebnissen aus den Arbeiten von Devereaux *et al.* Der Befund hat zur Aufdeckung des Fehlers in einer Modellrechnung letzterer Autoren geführt. In unserer Arbeit haben wir die Möglichkeit erwähnt, daß nur der Peak im elektronischen $A_{1g}$-Spektrum von der Paarbrechung herrührt, und der Peak im $B_{1g}$-Spektrum eventuell einen magnetischen Ursprung hat.

# Das Niederenergiespektrum

Ein Thema, das auch schon von Devereaux *et al.* aufgegriffen wurde, ist das Verhalten der Ramanintensität bei niedrigen Energien (oder Ramanverschiebungen). Als niedrige Energien sehen wir dabei solche an, die kleiner als etwa die Amplitude $\Delta_0$ der supraleitenden Energielücke sind. Wir betrachten zunächst streng tetragonale Systeme, welche eine Energielücke von der Form einer $d_{x^2-y^2}$-Welle haben. Man kann nun zeigen, daß im Falle des $A_{1g}$-Spektrums (und allen anderen Spektren außer dem $B_{1g}$-Spektrum) die Ramanintensität für $T = 0$ linear in der Ramanverschiebung ist. Das $B_{1g}$-Spektrum hat eine andere Eigenschaft. Die Energielücke besitzt $B_{1g}$-Symmetrie. Sie hat Knoten entlang der Diagonalen Γ-M der Brillouinzone. Dies ist ebenso der Fall bei der $B_{1g}$-Komponente des Ramanvertex. Dadurch entstehen zwei weitere Potenzen der Ramanverschiebung, so daß die Ramanintensität dann proportional zur dritten Potenz der Energie ist. Dies kann man experimentell in $Bi_2Sr_2CaCu_2O_8$ (Bi-2212) beobachten, nicht jedoch in Y-123. Für dieses Verhalten konnten wir eine Erklärung, die auf der Orthorhombizität der Hochtemperatursupraleiter basiert, geben. Beide Materialien, Bi-2212 und Y-123 besitzen eine leicht orthorhombisch verzerrte tetragonale Kristallstruktur. Solch eine orthorhombische Verzerrung kann nun auf zwei Arten geschehen. Die erste ist in Bi-2212 realisiert und erhält die Spiegelebenen welche die Lage der Knoten sowohl in der Lückenfunktion als auch in der $B_{1g}$-Komponente des

Ramanvertex definiert. Dadurch hat man in Bi-2122, ebenso wie in perfekt tetragonalen Systemen, ein kubisches Verhalten des $B_{1g}$-Spektrums bei niedrigen Energien. Die zweite Art wird durch Y-123 repräsentiert. Hier zerstört die orthorhombische Verzerrung besagte Spiegelebenen, und die Knoten der Lückenfunktion und diejenigen der $B_{1g}$-Komponente des Ramanvertex fallen nicht mehr zusammen. Dadurch erhält das Niederenergiespektrum einen starken linearen Anteil zusätzlich zum kubischen Anteil. In einer separaten Arbeit haben wir ein Verfahren angegeben, wie man die relative Verschiebung der Knoten in der Lückenfunktion und in der $B_{1g}$-Komponente des Ramanvertex bestimmen kann. Setzt man voraus, daß in einem orthorhombisch gestörten System die Lückenfunktion die Form $d + \alpha s$ einer Überlagerung einer $d$-Welle mit einer $s$-Welle annimmt, kommt die Bestimmung der relativen Verschiebung der Knoten einer Ermittlung des Parameters $\alpha$ gleich. Zur Durchführung des Verfahrens benötigt man das experimentell ermittelte Verhältnis der Stärke des linearen Anteils zum kubischen Anteil im Niederenergiespektrum. Weiterhin muß die elektronische Bandstruktur (etwa aus einer LMTO-Rechnung) bekannt sein. Wir merken in diesem Zusammenhang an, daß die Physik des Niederenergiespektrums sehr delikat ist. Dies liegt auf der Seite des Experiments daran, daß man energetisch schon sehr nahe am elastisch gestreuten Laserlicht ist und somit eine Trennung des um typischerweise sechs bis acht Größenordnungen intensiveren Laserlichts vom inelastisch gestreuten Licht schwierig ist. Auf der theoretischen Seite wird die klare Aussage der Linearität beziehungsweise Kubizität des Niederenergiespektrums durch die fehlende Betrachtung des Effektes von Verunreinigungen relativiert. Diese können – ebenso wie die orthorhombische Verzerrung – einen linearen Anteil zum kubischen Anteil des $B_{1g}$-Spektrums liefern.

## Vertexrenormierung

Ein weiterer Versuch, die Lage der Paarbrechungspeaks in den elektronischen Ramanspektren zu erklären, wurde von Manske *et al.* unternommen. In ihrer Arbeit zeigten sie, daß eine in der Standardtheorie der elektronischen Ramanstreuung (scheinbar) vernachlässigte Korrektur des Ramanvertex (durch eine Anziehung zwischen den Quasiteilchen) relevant für die Vorhersage der Lage des Paarbrechungspeaks im $B_{1g}$-Spektrum ist. Die Autoren präsentierten außer einer "‘erweiterten“ Theorie auch noch eine Modellrechnung, welche ein experimentell ermitteltes Ramanspektrum sehr gut fitten konnte. In der Modellrechnung wurde jedoch die $A_{1g}$-Komponente des Ramanvertex mit der "‘$A_{1g} + B_{2g}$“-Komponente verwechselt. Dies führt zu einem $A_{1g}$-Spektrum, das um mehr als eine Größenordnung von dem durch ihre "‘erweiterte“ Theorie vorausgesagten abweicht. Dadurch ist die Modellrechnung natürlich wertlos. Die Vertexrenormierung in der Theorie wurde jedoch auch schon von Devereaux *et al.* viel früher behandelt. In dieser Arbeit wurde gezeigt, daß besagte Vertexrenormierung zu einigen zusätzlichen Exciton-ähnlichen Polen etwas unterhalb von $2\Delta_0$ in der Tsuneto-Funktion führen. Diese Pole haben jedoch sehr geringes Spektralgewicht und sind dadurch für die Belange der Ramanstreuung irrelevant. Diese Punkte haben wir in einem Kommentar in der Physical Review B aufgezeigt.

# Ramanstreuung an Phononen

Der zweite Schwerpunkt der vorliegenden Arbeit betrifft die Ramanstreuung an Phononen. Phononen koppeln indirekt über eine Elektron-Loch-Anregung an das Laserlicht. Einfallendes Licht erzeugt ein Elektron-Loch-Paar. Dann streut das Elektron (oder das Loch) und erzeugt dabei ein Phonon. Das gestreute Elektron rekombiniert dann mit dem Loch und das gestreute Photon wird erzeugt. Es ist klar, daß an diesem Prozeß nur $\Gamma$-Punkt-Phononen beteiligt sein können. Insofern können die beteiligten Phononen also als diskrete Anregungen aufgefaßt werden. Die Elektron-Phonon-Kopplung zieht die Möglichkeit der Wechselwirkung von elektronischen Anregungen mit dem Phonon nach sich. Dies ist unabdingbar dafür, daß Ramanstreuung an Phononen überhaupt möglich ist. Es bewirkt aber auch die Interferenz der diskreten phononischen Anregung mit dem kontinuierlichen Elektron-Loch-Anregungsspektrum. Solch eine Interferenz wurde schon von Fano und von Anderson (in jeweils unterschiedlichem Kontext) untersucht; wir werden die durch Übertragung derer Methoden auf die Ramanstreuung an Phononen gewonnene Formel für die Ramanintensität *Fano-Formel* nennen. Eine wichtige Folgerung der Elektron-Phonon-Interferenz ist die Renormierung der Frequenz sowie der Lebensdauer der Phononen durch die Kopplung an das Elektron-Loch-Kontinuum. Beim Übergang vom normalleitenden zum supraleitenden Zustand eines Hochtemperatursupraleiters ändert sich das Elektron-Loch-Anregungsspektrum im Energiebereich unterhalb von etwa $3\Delta_0$ drastisch. Diese Änderung zieht dann eine solche der Renormierung der Phononen nach sich. In den Ramanspektren wirkt sich das dadurch aus, daß sich die Phononpeaks zum einen verschieben, und daß sie zum anderen ihre Breite ändern.

Das experimentell untersuchte Material war $HgBa_2Ca_3Cu_4O_{10+\delta}$ (Hg-1234). Wir entdeckten an zwei Phononen sehr starke Änderungen der Renormierung (stärker als alle zuvor an Hochtemperatursupraleitern gemessenen). Dieser überraschende Befund rief natürlich nach einer theoretischen Modellierung. Ein theoretisches Modell muß auf den berechneten Suszeptibilitäten der Elektron-Loch-Anregungen zum einem für den normalleitenden und zum anderen für den supraleitenden Zustand basieren. Dies wird dadurch verkompliziert, daß man sehr wenig über den normalleitenden Zustand weiß. Um dieses Problem zu umgehen, haben wir angenommen, daß der Einfluß der Elektron-Loch-Anregungen im Normalzustand des Supraleiters auf die betrachteten Phononen klein ist. Die auf dieser Annahme aufbauende Analyse der experimentell ermittelten Ramanspektren führt dann zu einer Abschätzung der Stärke der Elektron-Phonon-Kopplung. Diese Kopplung kann durch die Spektralfunktion $\alpha^2F(\omega)$ aus Eliashbergs Theorie charakterisiert werden. Aus diesem Grunde haben wir den Wert von McMillans daraus abgeleitetem Elektron-Phonon-Wechselwirkungsparameter $\lambda$, welcher nicht nur die Stärke der Elektron-Phonon-Wechselwirkung sondern im Rahmen von Eliashbergs Theorie auch die kritische Temperatur $T_c$ bestimmt, ermittelt. Zusammen mit Parametern, die aus den experimentell ermittelten Spektren entnommen wurden, führte unsere Theorie auf eine Abschätzung von $\lambda \approx 0.08$ für den jeweiligen Beitrag der beiden betrachteten Phononen. Wenn alle Phononen die gleiche Kopplungsstärke aufwiesen (was nicht der Fall ist), würde das bedeuten, daß der gesamte $\lambda$-Parameter den Wert 2 erreicht.

# Publications originating from this work

1. T. Strohm and M. Cardona
   *Electronic Raman scattering in* $YBa_2Cu_3O_7$ *and other superconducting cuprates*,
   Phys. Rev. B **55**, 12725 (1997).

2. M. Cardona, T. Strohm, and J. Kircher,
   *Raman scattering in high-*$T_c$ *superconductors: Electronic excitations*,
   in: *Spectroscopic Studies of Superconductors*,
   ed. I. Bozovic, Proc. SPIE **2696**, 182 (1996).

3. M. Cardona, T. Strohm, and X. Zhou,
   *Raman scattering by Electronic Excitations in High-*$T_c$ *Superconductors*,
   Physica C **282–287**, 2001 (1997).

4. T. Strohm and M. Cardona,
   *Determination of the d-wave/s-wave gap ratio in* $YBa_2Cu_3O_7$ *from electronic Raman scattering and the LMTO band structure*,
   Solid State Comm. **104**, 223 (1997).

5. V. G. Hadjiev, X. Zhou, T. Strohm and M. Cardona,
   *Strong superconductivity-induced phonon self-energy effects in* $HgBa_2Ca_3Cu_4O_{10+\delta}$,
   Phys. Rev. B **58**, 1043 (1998).

6. T. Strohm, D. Munzar, and M. Cardona,
   *Comment on "Screening of the* $B_{1g}$ *Raman response in d-wave superconductors"*,
   Phys. Rev. B **58**, 8839 (1998).

7. T. Strohm, V. Belitsky, V. Hadjiev, and M. Cardona,
   *Comment on "Raman Scattering Study on Fully Oxigenated* $YBa_2Cu_3O_7$ *Single Crystals: x-y Anisotropy in the Superconductivity-Induced Effects"*,
   Phys. Rev. Lett. **81**, 2180 (1998).

8. T. Strohm, M. Cardona, and A. A. Martin,
   *Electronic Raman scattering in high-*$T_c$ *superconductors*,
   to be published in: American Journal of Physics (1999).

9. V. G. Hadjiev, T. Strohm, M. Cardona, Z. L. Du, Y. Y. Xue, and C. W. Chu,
   *Raman Scattering from the Superconducting Phase ???*,
   ACS Symposium Series: Applications of Spectroscopy to Superconducting Materials (Washington, DC: ACS), in press (1999).

# Contents

# Chapter 1

# Introduction

## 1.1 History

In the history of physics, the advent of new technological achievements frequently has triggered the discovery of new physical phenomena. When Kammerlingh Onnes discovered in 1911 at the University of Leiden the *superconducting state* in solid mercury [1.1], this became possible because three years earlier he had succeeded in liquifying helium. Liquid helium was the key for accessing temperatures as low as a few Kelvin, necessary to reach the phase transition to the superconducting state at the *critical temperature* $T_c$.

For the theorists, the quest for a theory of the new state arose. The superconducting state is characterized mainly by two basic elementary properties, namely the *Meissner-Ochsenfeld effect* [1.2] (the *exclusion of magnetic flux* from the interior of a bulk superconductor), and the complete *vanishing of the dc electrical resistance.* A first step forward was undertaken when in 1935 F. and H. London explained the two basic electrodynamic properties of the superconducting state with the two London equations [1.3] in the framework of classical macroscopic electrodynamics.

Two other important properties of the superconducting state furthermore led closer to a theoretical explanation. Daunt and Mendelssohn [1.4] discovered the absence of thermoelectric power in the superconducting state, and Corak *et al.* [1.5] showed that for low temperatures well below $T_c$, the electronic specific heat obeys an exponential dependence on the temperature. These two effects suggested the presence of an *energy gap* $\Delta$ between the ground state of the system and its quasiparticle excitations. Another landmark was the suggestion by Fröhlich [1.6] in 1950 that the *electron-lattice interaction* is of crucial importance for the explanation of superconductivity. This proposal was confirmed soon thereafter by the discovery of the *isotope effect* [1.7], that is, the proportionality of the critical temperature $T_c$ to $M^{-1/2}$, the inverse square root of the mass of the element in elemental superconductors.

The final breakthrough, however, was the *pairing theory of superconductivity*, formulated by Bardeen, Cooper, and Schrieffer in 1956 (BCS-theory, see App. E) [1.8]. They showed that the Fermi sea ground state of an electron gas is unstable with respect to a weak attractive interaction between the electrons. Such an attraction causes the formation of *Cooper pairs* [1.9], which are pairs of electrons with opposite quasimomentum and spin. The spatial extension of these pairs is described by Pippard's *coherence length* $\xi_0$. The theory indeed showed the presence of an energy gap $2\Delta = 3.528 T_c$ in the excitation spectrum for the superconducting state, and explained most of the physical properties of the superconducting state.

The BCS-theory is a *weak-coupling theory*: the attractive electron-electron interaction must be small, otherwise the BCS-theory is not applicable. While the superconducting state of Al, In, and Sn can be described rather well within the BCS-theory, Pb and Hg deviate considerably, with $2\Delta = 4.3T_c$ and $2\Delta = 4.6T_c$, respectively, from the predicted BCS behavior. This deviation is mainly due to the crude description of the phonon-mediated attractive electron-electron interaction in the BCS-theory. The attractive interaction is realized by the exchange of virtual phonons and is based on Fröhlich's electron-lattice interaction. This is taken into account in the *Eliashberg-theory* [1.10] where the interaction is described by means of the function $\alpha^2 F(\omega)$, that is, the phonon density of states weighted by the electron-phonon coupling strength. Its predictions concerning the ratio $2\Delta/T_c$ in Pb and Hg agree well with the experiment.

The peaceful time of agreement between theory and experiment was disturbed again by the discovery of the *heavy-fermion superconductors* [1.11] which cannot be described by the Eliashberg theory. Examples for these systems are $CeCu_2Si_2$ and $UPt_3$, heavy-fermion superconductors always contain ions with $f$-electrons. The specific heat of these compounds is by orders of magnitude larger than in typical metals. This points to the existence of carriers with a mass much larger than the free electron mass, the heavy fermions. The low-temperature specific heat in these compounds appears to show a *power-law dependence*. Such a property could arise from a gap function which *vanishes at some points* (or lines) on the Fermi surface. Heavy-fermion superconductors, however, possess very low critical temperatures. This renders them experimentally difficult and may be the reason for their falling into oblivion.

This was the situation when in 1986 at the IBM research laboratory in Zürich, Bednorz and Müller succeeded in the epoch-making discovery of *high-temperature superconductivity* [1.12] in ceramic $La_{2-x}Ba_xCuO_4$ with a critical temperature of about 35 K. Soon after this remarkable event, high-temperature superconductivity was also found in $YBa_2Cu_3O_7$ [1.13] with $T_c \approx 92\,\mathrm{K}$, thus breaking the liquid-$N_2$ barrier, and in many similar layered materials based on copper-oxide planes.

The fact that the critical temperature of many of the high-temperature superconductors is higher than the liquification temperature of nitrogen opens the way for a technical application of superconductivity, because liquid nitrogen is cheap and easy to handle. Clear disadvantages for a technical application, however, are the low density of charge carriers (compared to metals), the marked anisotropy of the electronic properties (due to the layered structure), and the short coherence length $\xi_0$ which implies a low critical field $H_{c1}$.

For the high-temperature superconductors, there is no doubt that the superconductivity is based on *Cooper pairs* with *zero total quasimomentum* (the measured flux quantum is $hc/2e$) which are in the *spin singlet* state (may be deduced from Knight shift measurements), like in the BCS-theory.

Two other types of observations, however, cannot be explained by an isotropic theory like the BCS-theory: (1) the experiments which directly exploit the *spatial symmetry of the gap function*. A prominent example is the measurement of the trapped magnetic flux in a SQUID ring [1.14] which consists of two mutually rotated high-temperature superconductors. (2) experiments in which the *density of states* of quasiparticle excitations (or a quantity based on this) is probed. Photoelectron emission [1.15], infrared absorption [1.16], and Raman scattering [1.17] experiments show the existence of quasiparticle states for arbitrarily small excitations energies. This implies the vanishing of the gap function [1.18, 1.19] in certain regions on the Fermi surface. Results from specific heat measurements [1.20] also point in this direction. They show a linear dependence of the (electronic) specific heat on the temperature (for small temperatures). The penetration depth measurements [1.21] also support the conjecture that the gap function has *nodes*.

This picture of the phenomenon of high-temperature superconductivity, however, is far from being exhaustive. High-temperature superconductors possess a very difficult phase diagram [1.22], and provide further difficulties concerning, for instance, the normal state [1.23, 1.24], which cannot be described by a simple Fermi-liquid model.

## 1.2 Raman scattering in high-temperature superconductors

Raman scattering has played an important role in the investigation of the properties of high-temperature superconductors [1.25]. The dependence of the Raman efficiency on the directions of the polarization of the incident and scattered light yields several independent spectra which provide a considerable number of constraints on the assumed $k$-dependence of the gap function $\Delta_{\boldsymbol{k}}$. Raman scattering, however, is sensitive to the magnitude but not to the phase of the gap function.

The Raman spectra at temperatures below $T_c$ show, in most high-temperature superconductors, a clear gap-like structure which lies in the energy range of the optical phonons at the Γ-point. These phonons have been identified for most high-temperature superconductors [1.25], and the subtraction of the corresponding structures from the spectra has become a standard procedure to isolate electronic structures containing gap information. Electronic Raman scattering spectra are now available for many high-$T_c$ materials and, since they exhibit similar general features, most of these data are considered to be reliable. In this thesis (particularly in Chap. 2), we attempt to interpret these spectra from a theoretical point of view based on the full 3D one-electron band structure. We pay attention to both, line shapes and *absolute* scattering efficiencies.

## 1.3 A theoretical model for the Raman scattering by electronic excitations

The theory of electronic Raman scattering in superconductors was pioneered by Abrikosov and coworkers in two important papers [1.26, 1.27]. In the first, they developed a theory for the scattering efficiency of *isotropic* Fermi liquids under the assumption that the attractive interaction between quasiparticles can be neglected. In the second paper, they extended this approach to anisotropic systems, introduced the inverse effective mass vertex concept, and included Coulomb screening. The current form of the theory, developed mainly by Klein and Dierker [1.28], takes into account the attractive pairing interaction and emphasizes the role of gauge invariance as well as the polarization dependence for anisotropic gaps. In order to compare the theoretical predictions with the experiment, we evaluate the former numerically in a quantitative manner (including *absolute* scattering efficiencies) and compare them to the experimental findings.

Several calculations of the electronic Raman scattering efficiency of high-temperature superconductors have already been published. Some of them use highly simplified 2D band structures and a decomposition of the Raman vertex $\gamma_{\boldsymbol{k}}$ in Fermi surface (FS) harmonics [1.29] or Brillouin zone (BZ) harmonics, as well as FS integrations instead of the required BZ integrations [1.30, 1.31, 1.32]. The results of these calculations depend very strongly on the number of expansion coefficients used for $\gamma_{\boldsymbol{k}}$ and their relative values. Another approach [1.33] involves the use of band structures calculated in the framework of the local density approximation [1.34] (LDA) using the LMTO method [1.35, 1.36] (see App. B). Within the approximations of the LDA, this Raman vertex is exact, that is, the only errors made in such a calculation arise from limitations of the LDA method itself and from the discretization of the Brillouin zone or the Fermi surface. Some of these calculations, however, suffer from the fact that only the imaginary part of the Tsuneto function [1.37] has been used, and that only 2D integrations were performed [1.38].

## 1.4 Raman scattering by electronic excitations

The present approach to the Raman scattering by electronic excitations is based on the full 3D LDA-LMTO band structure. It uses a BZ integration (for comparison, a Fermi surface integration is also performed), screening effects are included, and both the real and imaginary part of the Tsuneto function are taken into account as required by the theory (see Sect. 2.3). Electronic Raman spectra are calculated for $YBa_2Cu_3O_7$ (Y-123) and $YBa_2Cu_4O_8$ (Y-124) and presented in Sect. 2.7. The orthorhombicity of the cuprates is also taken into account in the Raman vertex since we use as starting point the band structure of the *orthorhombic* materials.

The cuprates under consideration are not only of interest because of their superconducting, but also of their strange normal-conducting properties. Usual metals should show peaks in their Raman spectra at their plasma frequencies corresponding to Raman shifts of a few eV. The optimally doped cuprates, in contrast, show a very broad electronic background (from 0 to about 1 eV Raman shift), which is almost independent of temperature and frequency. The spectra of the underdoped high-temperature superconductors, such as Y-124, show some temperature dependence at low frequencies ($\hbar\omega \ll kT$). It is possible to explain these peculiarities, together with other properties, by assuming a certain form of the quasiparticle lifetime, as was done in the Marginal Fermi Liquid theory [1.23, 1.24]. We discuss this topic in Sect. 2.4.

For the superconducting state, various forms for the gap function have been proposed. That which has received most experimental support has $d_{x^2-y^2}$-symmetry, that is, $B_{1g}$ symmetry (see App. C) in tetragonal high-temperature superconductors. The power of Raman scattering to confirm such gap function has been questioned, because, among other difficulties, it only probes the *absolute* value of the gap function, that is, it cannot distinguish between a $d_{x^2-y^2}$-like gap function (e.g., $\cos 2\varphi$), and a $|\cos 2\varphi|$ gap function, which corresponds to anisotropic $s$- ($A_{1g}$-) symmetry. However, it was pointed out that addition of impurities can be used to effect the distinction [1.39] (see Subsect. 2.3.7).

## 1.5 Raman scattering by phonons

Raman scattering of light by optical phonons in solids essentially proceeds via electron-phonon interactions. Those phonons, which are strongly coupled to electrons occupying states near the Fermi surface (FS), can be very sensitive to changes in the vicinity of the FS. In superconductors, the opening of the superconducting gap results in a redistribution of electronic states and excitations in the immediate vicinity of the FS which in turn changes the phonon self-energy, that is, the contribution of the electron-phonon interaction to the phonon frequency and its linewidth. Superconductivity-induced phonon self-energy effects have been observed for a number of cuprates [1.40, 1.41, 1.42, 1.43, 1.44, 1.45] and theoretically studied for the case of $s$-wave [1.46] and $d$-wave [1.47, 1.48] superconductors. In particular, sizeable effects have been observed for the $B_{1g}$ out-of-phase plane oxygen phonon in $YBa_2Cu_3O_{7-\delta}$ (Y-123) [1.40, 1.42, 1.43] and for the $A_{1g}$ phonons in $HgBa_2Ca_2Cu_3O_{8+\delta}$ (Hg-1223) [1.45]. In addition, the appearance of a superconducting gap in the low-energy electronic excitations may also lead to resonance-like phenomena, for instance, increases in the Raman intensity of some phonons below the transition temperature $T_c$. Such increases have been seen in Y-123 [1.49], $YBa_2Cu_4O_8$ (Y-124) [1.50], and Hg-1223 [1.45]. Experimentally measured superconductivity-induced changes in phonon frequencies and linewidths, in conjunction with model calculations [1.46], have been used to estimate the magnitude of the superconducting gap in R-123 (R is a rare earth element) [1.42]. Information on the superconducting order parameter can also be inferred from the electronic peak that develops below $T_c$ due to quasiparticle creation through pair-breaking [1.32, 1.51], provided the peak is discernible. Similarities of model calculations of the phonon self-energy and the electronic Raman efficiency [1.52], with specific reference to $d$-wave paired superconductors, have been pointed out in [1.53]: at low frequencies, the imaginary part of the phonon self-energy of *tetragonal* superconductors varies with frequency as $\omega^3$ for the $B_{1g}$ and as $\omega$ for $A_{1g}$ spectra. Note, however, that in the *orthorhombically distorted* R-123 the tetragonal $B_{1g}$ and $A_{1g}$ symmetries are mixed [1.54].

In Sect. 3.5, we report a collosal superconductivity-induced phonon self-energy effect which we have discovered in microcrystalline $HgBa_2Ca_3Cu_4O_{10+\delta}$ (Hg-1234) superconductors. We have observed a remarkable frequency softening and a linewidth increase of vibrations along the $c$-axis involving the plane oxygen atoms with some admixture of calcium in a narrow temperature interval immediately below $T_c$, accompanied by a strikingly strong phonon intensity enhancement throughout the superconducting state. While rather elaborate theories exist for the self-energy effects of phonon frequencies and linewidths [1.46, 1.47], the corresponding effect on Raman intensities does not seem to have been theoretically treated. Moreover, the existing theories for the self-energy of phonons have so far not allowed the extraction of quantitative data concerning parameters relevant to the superconductivity from the available experimental results. We thus propose a simple quantum mechanical scheme which allows us to relate the enhancement of the Raman intensities observed in the superconducting state to the real part of the corresponding self-energy and to obtain semiquantitative information on the corresponding electron-phonon coupling constant.

# Chapter 2

# Electronic Raman scattering

## 2.1 Introduction

This chapter deals with electronic Raman scattering in superconducting cuprates and points out a way to explain the electronic Raman efficiency theoretically.

Section 2.2 introduces the theory of electronic Raman scattering and discusses the different aspects of the theory thoroughly and in a form which is applicable to metals in both the normal as well as the superconducting state. In the subsequent section, the theory is specialized to the superconducting state and the important Tsuneto-function is introduced. In addition to that, the effect of different nonidealities which are present in the experiment, as for instance impurities and a deviation of the crystal structure from the tetragonal symmetry, is discussed. Section 2.4 then briefly introduces a possible description of electronic Raman scattering in the normal state of the cuprate superconductors based on the Marginal Fermi Liquid (MFL) theory. Building on this preparatory discussion, we can then express the electronic Raman efficiency as a combination of some averages of certain $\boldsymbol{k}$-dependent functions over the Brillouin zone. The Sect. 2.5 introduces a method for a numerical evaluation of these averages and, therefore, shows how to determine the electronic Raman efficiency by numerical means. In Sect. 2.6 experimental results for the electronic Raman efficiency in the two compounds $\mathrm{YBa_2Cu_3O_7}$ (Y-123) and $\mathrm{YBa_2Cu_4O_8}$ (Y-124) are discussed. The purpose of Sect. 2.7 is to present the results of the numerical calculations and to compare them to the experimental findings.

The calculations in Sect. 2.7 are based on the “realistic” LDA-LMTO band structure, and use a $d_{x^2-y^2}$-like, band-independent gap function. In Sect. 2.8, we focus on some other interesting forms of the gap-function and use a model band-structure for the calculations. In nontetragonal superconductors, one may expect the presence of a $d_{x^2-y^2}$-like gap with a slight $s$-wave contribution. Section 2.9 introduces a method to determine the ratio of these two contributions to the gap-function. Finally, in Sect. 2.10 we discuss some extensions to the standard theory of electronic Raman scattering.

## 2.2 The theory of electronic Raman scattering

### 2.2.1 Photons and the electromagnetic field

*Raman scattering refers to the inelastic scattering of light.* In the typical experimental setup, a laser beam impinges on the sample (see Fig. 2.1). The coherence length of the laser beam in beam direction ($\sim 1\,\mathrm{m}$) is much larger than the size of the sample. As far as the sample is concerned, the vector potential of the laser beam therefore can be described by the plane wave

$$\boldsymbol{A}'_L(\boldsymbol{r},t) = A'_L \boldsymbol{e}'_L \exp i(\boldsymbol{k}'_L \boldsymbol{r} - \omega_L t)$$

with the amplitude $A'_L$, wavevector $\boldsymbol{k}'_L$, polarization $\boldsymbol{e}'_L$, and frequency $\omega_L \equiv ck'_L$.[1] The lateral size of the laser beam (typically $\sim 1.5\,\mathrm{mm}$), however, is often smaller than that of the sample. For the purpose of the theoretical treatment we therefore consider just a small sample, which is uniformly illuminated by the laser, and treat larger samples by using the illuminated area as the area $A_{\mathrm{Sa}}$ of the sample and the illuminated volume instead of the sample volume $V_{\mathrm{Sa}}$.

The plane wave then penetrates into the sample and creates inside an electromagnetic (elmag) field. This field can be calculated by means of Maxwell's equations and the (complex) dielectric constant $\epsilon$ of the sample, given by the *transversal* dielectric function $\epsilon(\boldsymbol{q},\omega)$ for $\omega = \omega_L$ and $\boldsymbol{q} \to 0$. The vector potential field inside of the sample is still a plane wave which, however, does not only experience refraction when crossing the surface, but also absorption inside the sample. The length scale in which it becomes damped is given by the penetration depth, which is equal to the inverse absorption coefficient. On scales much smaller than the penetration depth, the vector potential field inside of the sample can be described by an undamped plane wave. We denote its amplitude, wavevector, and polarization by $A_L$, $\boldsymbol{k}_L$, and $\boldsymbol{e}_L$, respectively. It is clear that for the case when the longitudinal size $L_{\mathrm{Sa}}$ of the sample is comparable to the penetration depth or even smaller, more than one single mode of the elmag field will be occupied with photons. The coherence length will be given by the penetration depth. In the upcoming theoretical treatment, we assume that the longitudinal size of the sample is much less than the penetration depth and neglect the damping effects. This, however, is problematic in typical high-$T_c$ superconductors, where the penetration depth is of the order of 100 nm or even less.

For normal incidence of the laser beam (which is the usual case in Raman scattering), and when neglecting multiple reflections at the sample surfaces, the amplitudes of the plane wave outside and inside the sample are related by Fresnel's equation, yielding $A_L = A'_L \cdot 2/(\tilde{n}+1)$, where the refractive index $\tilde{n}$ is related to the dielectric constant by the Maxwell relation $\tilde{n} = \sqrt{\epsilon}$, $\mathrm{Re}\,\tilde{n} > 0$.

If we describe the vector potential $\boldsymbol{A}_L$ inside the sample as a quantized field and use the sample volume $V_{\mathrm{Sa}}$ as quantization volume for the elmag field, then the laser light occupies the mode $(\boldsymbol{k}_L,\boldsymbol{e}_L)$ (which we call the *L-mode* and its quanta the *L-photons*) of the elmag field in the sample with a *macroscopic*[2] number $n_L$ of photons.

---

[1] We denote the length of vectors $\boldsymbol{v}$ by italic letters $v$, i.e. $v = |\boldsymbol{v}|$ throughout this chapter.

[2] This property makes it easy to relate the classical field amplitude $\boldsymbol{A}'_L$ to the quantum mechanical occupation number $n_L$ of the mode.

The interaction of the L-photons with the sample *opens up a decay channel for the L-photons*. We consider another mode, the *S-mode* ($\boldsymbol{k}_S$,$\boldsymbol{e}_S$) of the elmag field, carrying *S-photons*, and denote the decay rate of L-photons into the *empty* S-mode by $\Gamma_{L\to S}$. The vector potential field $\boldsymbol{A}_S$ related to the S-mode (which is also assumed to be a plane wave) then leaves the sample and creates the field $\boldsymbol{A}'_S$ with wavevector $\boldsymbol{k}'_S$ outside. The relation of $\boldsymbol{A}'_S$ and $\boldsymbol{A}_S$ is described by classical electrodynamics. Again for normal incidence, the Fresnel equations read $A'_S/A_S = 2\tilde{n}/(\tilde{n}+1)$, and the ratio of the intensities of the incoming light wave (with wavevector $\boldsymbol{k}'_L$) and the scattered light wave (with wavevector $\boldsymbol{k}'_S$) is related to the corresponding intensity ratio inside the sample by

$$(A'_S/A'_L)^2 = \left|\frac{4\tilde{n}}{(\tilde{n}+1)^2}\right|^2 (A_S/A_L)^2 \ . \tag{2.1}$$

### 2.2.2 The scattering efficiency

The intensity of the scattered wave is measured in the detector. For the description of the measured intensity, one defines the *differential Raman efficiency* $d^2\eta/(d\Omega\, d\hbar\omega)$ by making use of two *energy* currents (we use this term synonymous to "energy flux"). The first, denoted by $d^2I_{E,S}$, is the energy current of scattered photons with a wavevector lying in a cone $d\Omega$ around $\boldsymbol{k}'_S$ in $k$-space and having an energy lying in the interval $[\hbar\omega'_S \equiv \hbar c k'_S, \hbar\omega'_S + d\hbar\omega]$. Taking this quantity per unit angle and unit energy defines $d^2I_{E,S}/(d\Omega\, d\hbar\omega)$. The second is the energy current $I_{E,L}$ of photons which hit the sample. Then the differential Raman efficiency $d^2\eta/(d\Omega\, d\hbar\omega)$ is the quotient of these two energy currents. It has the dimension 1/Energy and is proportional to the thickness $L_{\mathrm{Sa}}$ of the sample (or the penetration depth of light in the sample if it is thicker than the inverse absorption coefficient $c/(\omega|\mathrm{Im}\,\tilde{n}|)$). This proportionality is removed by the definition of the quantity

$$\frac{d^2S}{d\Omega\, d\hbar\omega} = \frac{1}{L_{\mathrm{Sa}}}\frac{d^2\eta}{d\Omega\, d\hbar\omega} = \frac{1}{L_{\mathrm{Sa}}}\frac{1}{I_{E,L}}\frac{d^2I_{E,S}}{d\Omega\, d\hbar\omega} \tag{2.2}$$

which is called the *differential Raman efficiency* and has the dimensions 1/(Energy·Length). In the experiments, the energy is usually measured in wave numbers ($\mathrm{cm}^{-1}$), and therefore the differential Raman efficiency has the somehow strange dimensions $(\mathrm{cm}^{-1}\,\mathrm{cm}\,\mathrm{sr})^{-1}$.

When talking about the Raman efficiency, the Raman efficiency $S$, or the differential Raman efficiency, we shall *always* refer to the differential quantity defined in (2.2); if we refer to the differential Raman efficiency $d^2\eta/(d\Omega\, d\hbar\omega)$ it will be explicitly stated.

For the determination of the Raman efficiency we proceed as follows. The energy currents $I_{E,L}$ and $d^2I_{E,S}$ are related to the vector potentials $\boldsymbol{A}'_L$ and $\boldsymbol{A}'_S$, respectively. In the case of the incoming photons, the energy current is given by (we use *cgi units* throughout this chapter)

$$I_{E,L} = A_{\mathrm{Sa}}\frac{c}{8\pi}\frac{\omega_L^2}{c^2}{A'_L}^2 = \left|\frac{4\tilde{n}}{(\tilde{n}+1)^2}\right|^2 A_{\mathrm{Sa}}\frac{c}{8\pi}\frac{\omega_L^2}{c^2}A_L^2 \ ,$$

and is proportional to the surface area $A_{\mathrm{Sa}}$ of the sample (if we keep the vector potential $A'_L$ or—equivalently—the incoming energy current density fixed) and has the dimension Energy/Time. The determination of the scattered energy current $d^2I_{E,S}$ with wavevectors

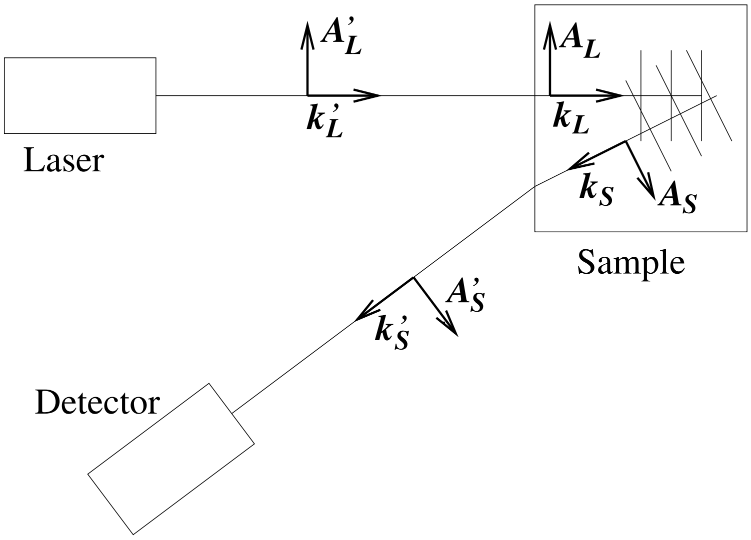

Figure 2.1: The definition of some quantities used in the discussion of Raman scattering.

in the cone[3][4] $d\Omega\, d\hbar\omega$ is a bit more difficult. If we consider just one mode, the S-mode, it is clear that the energy current is given by $I_{E,S} = \hbar\omega_S \Gamma_{L\to S}$ under the assumption that the time $1/\Gamma_{L\to S}$ is much larger than the one the scattered photons need to leave the sample. Otherwise, the assumption of an empty S-mode made in the definition of the decay rate $\Gamma_{L\to S}$ is not appropriate. Under the assumption that all other modes in the cone $d\Omega\, d\hbar\omega$ carry the same energy current as the S-mode, and that there are no interferences between the modes, the energy current $d^2 I_{E,S}$ is simply given by the number of modes in the cone times the energy current per mode. The number of photon states in the sample for a given polarization and per $k$-space volume $d^3k$ is $V_{\mathrm{Sa}}/(2\pi)^3$, and the energy current of the scattered photons is

$$\frac{d^2 I_{E,S}}{d\Omega\, d\hbar\omega} = \frac{V_{\mathrm{Sa}}}{(2\pi c)^3} \omega_S^3 \Gamma_{L\to S} \ .$$

This quantity has the dimension 1/Time (like the decay rate $\Gamma_{L\to S}$) and is proportional to the sample volume $V_{\mathrm{Sa}}$ or more exactly the illuminated volume (the decay rate is independent of the sample volume). This proportionality simply arises from the observation that the number of states in the cone $d\Omega\, d\hbar\omega$ is proportional to the sample volume.

At this point it already becomes clear that the quotient of energy currents leading to the differential Raman efficiency $d^2\eta/(d\Omega\, d\hbar\omega)$ is proportional to the sample thickness $L_{\mathrm{Sa}}$ (assuming that it is smaller than the penetration depth of light), just because the incoming energy current is proportional to the sample surface, and the energy current of the photons scattered into the cone $d\Omega\, d\hbar\omega$ is proportional to the sample volume. This proportionality is not present in the Raman efficiency $S$, which becomes

$$\frac{d^2 S}{d\Omega\, d\hbar\omega} = \frac{1}{L_{\mathrm{Sa}}} \frac{1}{I_{E,L}} \frac{d^2 I_{E,S}}{d\Omega\, d\hbar\omega} = \left| \frac{4\tilde{n}}{(1+\tilde{n})^2} \right|^2 \frac{1}{\pi^2} \frac{\omega_S^2}{\omega_L^2} \frac{\omega_S}{c^2 A_L^2} \Gamma_{L\to S} \ . \tag{2.3}$$

---

[3] Actually, this is just a slice of a cone!

[4] Note that there are two related cones, $d\Omega\, d\hbar\omega$ inside the sample, and $d\Omega'\, d\hbar\omega'$ outside. They turn out to contain the same number of modes of the elmag field.

The square of the vector potential $A_L$ has the dimension Energy/Length, and consequently the Raman efficiency (2.3) has the dimension 1/(Energy · Length).

### 2.2.3 Second quantization for photons

Having established the relation (2.3) between the Raman efficiency and the decay rate $\Gamma_{L\to S}$ for the L-photons in the sample, a major step in the calculation of the Raman efficiency is done. The following considerations do not depend anymore on issues related to the geometry of the sample or the change of the refractive index when passing the sample surface. One remark, however, still has to be given. It was stressed already, that inside the sample, we use the quantized description of the elmag field, whereas outside, the classical description is applied. Therefore, a relation between the amplitude $A_L$ of the plane-wave vector potential field of the laser beam and the occupation number $n_L$ of the L-mode inside the sample has to be given. This is simply given by identifying the expressions for the energy of the L-mode in the sample, expressed via the amplitude $A_L$ and the occupation number $n_L$, and yields the expression

$$n_L = V_{\mathrm{Sa}} \frac{1}{8\pi\hbar c^2} \omega_L A_L^2 \tag{2.4}$$

showing that $n_L$ is proportional to the sample volume, as expected.

The quantization of the elmag field inside the sample requires the introduction of the photon creation and annihilation operators. Consider again the plane-wave vector potential $\boldsymbol{A}(\boldsymbol{r},t)$ with wavevector $\boldsymbol{k}$ and a polarization represented by the unit vector $\boldsymbol{e}_{\boldsymbol{k}\lambda}$. This vector potential $\boldsymbol{A}(\boldsymbol{r},t)$, in the Heisenberg representation, is related to the mentioned operators by

$$\boldsymbol{A}(\boldsymbol{r},t) = \sqrt{\frac{2\pi\hbar c^2}{\Omega\omega}}\, \boldsymbol{e}_{\boldsymbol{k}\lambda} e^{i\boldsymbol{k}\boldsymbol{r}} \left( a_{\boldsymbol{k}\lambda} e^{-i\omega t} + a^+_{-\boldsymbol{k}\lambda} e^{i\omega t} \right) \ . \tag{2.5}$$

The operator $a_{\boldsymbol{k}\lambda}$ annihilates a photon of wavevector $\boldsymbol{k}$ and polarization $\boldsymbol{e}_{\boldsymbol{k}\lambda}$, and $a^+_{-\boldsymbol{k}\lambda}$ creates a photon with wavevector $-\boldsymbol{k}$ and polarization $\boldsymbol{e}_{\boldsymbol{k}\lambda}$. Both change the total momentum of the photon field by $-\boldsymbol{k}$ (see Eq. (1.5.15) in [2.1]).

Actually in (2.3) we have to use the velocity of light $c' = c/\tilde{n}$ in the medium, causing an additional factor $|1/\tilde{n}^2|$ to appear in terms which are proportional to the vector potential. In the calculation of the decay rate $\Gamma_{L\to S}$ in the next sections, however, we use the vacuum velocity of light, and account for the factor $|1/\tilde{n}^2|$ in (2.3), which becomes

$$\frac{d^2S}{d\Omega\, d\hbar\omega} = \left| \frac{4}{1+\tilde{n}^2} \right|^2 \frac{1}{\pi^2} \frac{\omega_S^2}{\omega_L^2} \frac{\omega_S}{c^2 A_L^2} \Gamma_{L\to S} \tag{2.6}$$

(cf. [2.2]).

### 2.2.4 The Hamiltonian

The sample will be described by a time-independent Hamiltonian $H$ of the form $H = H_{\mathrm{Sa}} + V + H_{\mathrm{elmag}}$, where $H_{\mathrm{Sa}}$ is the Hamiltonian of the sample without the elmag field,[5]

---

[5] without the external elmag field, to be more exact. The quantity $H_{\mathrm{Sa}}$ describes the system that is left over, when the laser is switched off, that is, includes the elmag interaction between charged particles in $H_{\mathrm{Sa}}$ etc.

which is given by $H_{\mathrm{elmag}}$. The interaction between the sample and the elmag field in the sample is represented by $V$. This separation allows the states of the sample to be divided into a part being related to the elmag degrees of freedom $|\psi_{\mathrm{elmag}}\rangle$ and the other degrees of freedom $|\psi_{\mathrm{Sa}}\rangle$.

The calculation of the decay rate $\Gamma_{L\to S}$ can be simplified considerably when moving to the Heisenberg representation with the elmag degrees of freedom (This is equal to taking $H_{\mathrm{elmag}}$ as the unperturbed Hamiltonian and moving to interaction representation). Then, $H_{\mathrm{elmag}}$ vanishes and the resulting Hamiltonian is given by

$$H(t) = H_{\mathrm{Sa}} + V(t) \ , \qquad V(t) = e^{iH_{\mathrm{elmag}}t/\hbar} V e^{-iH_{\mathrm{elmag}}t/\hbar} \ ,$$

where the interaction becomes time-dependent by virtue of the time-dependence of the vector potential $\boldsymbol{A} = \boldsymbol{A}(t)$. The states $|\psi_{\mathrm{elmag}}\rangle$ are independent of time now, whereas the states $|\psi_{\mathrm{Sa}}\rangle$ are still time-dependent. The time-dependence of the Hamiltonian allows for the use of *time-dependent perturbation theory* to calculate the decay rate $\Gamma_{L\to S}$.

### 2.2.5 Raman scattering in crystals

As a very important simplification, we assume the sample to be a crystal, that is, to possess a discrete translational symmetry. Then the elementary excitations in the sample can be classified by a quasimomentum $\boldsymbol{q}$. When the decay of an L-photon into an S-photon is accompanied by *one* such elementary excitation, the conservation law

$$\boldsymbol{k}_L - \boldsymbol{k}_S = \boldsymbol{q} + \boldsymbol{G}$$

(where $\boldsymbol{G}$ is a reciprocal lattice vector) holds. Similarly, homogeneity of the system with respect to time yields the energy conservation law

$$\omega_L - \omega_S = \omega \ ,$$

for the energy $\omega$ of the elementary excitation and the energies $\omega_L$ and $\omega_S$ of the photons taking part in the decay process.[6]

### 2.2.6 Different approaches

At least two approaches have been used to derive the decay rate $\Gamma_{L\to S}$ of electronic Raman scattering in superconductors with anisotropic Fermi surfaces. The first uses Green's functions [2.3, 2.4, 2.5, 2.6], and the second the kinetic equation [2.7, 2.8]. Both make use of the simplification of the Hamiltonian by $\boldsymbol{k}\cdot\boldsymbol{p}$ theory, which relates the Raman vertex $\gamma_{\boldsymbol{k}}$ to the inverse effective mass tensor [2.4, 2.9].

Instead of relating the Raman vertex to the inverse effective mass by using the effective mass approximation, it is in principle also possible to calculate the Raman vertex directly using numerical methods like, for instance, the LDA-LMTO, which is discussed in App. B.

---

[6] The symmetry of the crystal is a *discrete* translational symmetry, whereas homogeneity in time corresponds to a continuous translational symmetry. Therefore, the quasimomentum is conserved only up to a reciprocal lattice vector, while the energy is conserved strictly.

This procedure, however, is problematic because it involves the calculation of matrix elements of the momentum operator with respect to Bloch functions and is numerically very expensive. Another approach is to write the Raman vertex as a series of functions which are orthogonal in the Brillouin zone (or on the Fermi surface) and transform according to some irreducible representation of the crystal point symmetry group (see App. C). This method has been used for instance in [2.8] (see also Ref. [2.10] on Fermi-surface harmonics).

In the subsequent subsection, we first use time-independent perturbation theory to define a perturbation operator, the *effective Raman operator* $H_R$, which in first order time-dependent perturbation theory describes the transitions of the system. The *Golden Rule* is applied to determine the decay rate $\Gamma_{L\to S}$ which is related to the *Raman efficiency* by (2.6). The resulting equation can be connected to the imaginary part of the *Raman susceptibility* (defined in (2.29)). Having expressed the Raman efficiency by this quantity, the generalization to systems in the superconducting state, or including impurities, is relatively easy when using the formalism of diagrammatic perturbation theory (see App. D).

### 2.2.7 The transition rate for electronic Raman scattering

After having defined the differential Raman efficiency $d^2S/d\Omega d\hbar\omega$ in (2.2) and having related it to the decay rate $\Gamma_{L\to S}$ for L-photons in the sample in (2.6), we calculate the Raman efficiency for electronic Raman scattering by evaluating the decay rate $\Gamma_{L\to S}$.

The model used describes electrons in a crystal which will be treated in first quantization based on Bloch functions $|n\boldsymbol{k}\rangle$. Furthermore, the photons which constitute the photon field will be described in the form $|\{n_{\boldsymbol{k}\vec{\lambda}}\}\rangle$ using occupation number representation. The elementary electronic excitations appearing in the calculation are electron-hole excitations due to the fact that the number of electrons has to be conserved. Electron-electron interaction is neglected and will be treated perturbatively later when necessary. Hence, the Hamiltonian, after transformation to second quantization for electrons, will contain only terms bilinear in electron creation and annihilation operators of the form $\alpha_{ij}c_i^+c_j$, where $i$, $j$ denote Bloch states and $\alpha_{ij}$ are matrix elements with Bloch states. Furthermore we use the Hamiltonian $(1/2m_0)\sum_i \boldsymbol{p}_i^2$ for the kinetic energy of the electrons (the sum runs over all electrons in the system).[7] This kinetic energy is replaced by the operator $\boldsymbol{p}^2/2m_0$ in second quantization. This can be seen when following our prescription for the calculation which leads to the matrix elements $\alpha_{ij}$ above, and moving to second quantization eventually (see Eq. D.5).

The relevant states in the theory are composed of the state of the electronic system times the state of the photon system. Electronic excitations are always with respect to the Fermi sphere which is characterized by the Fermi energy $E_F$ and plays the role of the ground state. Therefore, matrix elements $\alpha_{ij} \equiv \langle i|\hat{\alpha}|j\rangle$ refer to electron-hole excitations with the electron in state $|i\rangle$ and energy $\epsilon_i - E_F < 0$, and the hole in state $|j\rangle$ and energy $\epsilon_j - E_F > 0$.

As stressed already, most of the states of the photon system are uninteresting for our purposes. Raman scattering is a process involving two specific photon modes, the incoming photons or L-photons ($\boldsymbol{k}_L$, $\boldsymbol{e}_L$) and the scattered photons or S-photons ($\boldsymbol{k}_S$, $\boldsymbol{e}_S$), and is

---

[7] Recall that a many-particle Hamiltonian $H$ in first quantization, which can be represented as a sum $H = \sum_i h_(\boldsymbol{r}_i, \boldsymbol{p}_i)$ of single-particle operators $h$, becomes $H = \sum_{\lambda\mu} \langle\lambda|h|\mu\rangle c_\lambda^+ c_\mu$ in second quantization. The sum $\sum_i$ runs over all electrons, while the sums $\sum_\lambda$, $\sum_\mu$ run over all single-particle states. See also App. D, Eq. (D.5).

described by means of the transition rate $\Gamma_{L\to S}$ from the incoming to the scattered photon. The initial state of the electron-photon system under consideration is therefore given by the electrons in the Fermi sphere times the photon field corresponding to the laser with $n_L$ photons in state $(\boldsymbol{k}_L, \boldsymbol{e}_L)$ and the photon field which is occupied by the scattering process with $n_S = 0$ photons in state $(\boldsymbol{k}_S, \boldsymbol{e}_S)$ (we are not including anti-Stokes scattering). The final state, after the Raman scattering process has happened, is given by *some* excited state of the electron system and the photon system in the state with $n_L - 1$ photons in state $(\boldsymbol{k}_L, \boldsymbol{e}_L)$ and $n_S = 1$ photon in state $(\boldsymbol{k}_S, \boldsymbol{e}_S)$. The initial and final states of the electron-photon system are therefore

$$\begin{aligned} |i\rangle &= |GS\rangle|n_L, n_S = 0\rangle \\ |f\rangle &= |f_{el}\rangle|n_L - 1, n_S = 1\rangle \ . \end{aligned} \tag{2.7}$$

According to (2.7), the matrix elements of bilinear combinations of photon creation and annihilation operators should all vanish except for the combinations $a_S^+ a_L$ and $a_L a_S^+$, where $a_L$ annihilates one photon in the state $(\boldsymbol{k}_L, \boldsymbol{e}_L)$, and $a_S^+$ creates another photon in the state $(\boldsymbol{k}_S, \boldsymbol{e}_S)$. The corresponding vector field thus can be written (in Heisenberg representation) in the form

$$\boldsymbol{A}(\boldsymbol{r}) = \boldsymbol{A}_L(\boldsymbol{r}) + \boldsymbol{A}_S(\boldsymbol{r}) \qquad \text{with} \qquad \begin{aligned} A_L(\boldsymbol{r}) &= A_L^- \boldsymbol{e}_L e^{+i\boldsymbol{k}_L \boldsymbol{r}} \\ A_S(\boldsymbol{r}) &= A_S^+ \boldsymbol{e}_S^* e^{-i\boldsymbol{k}_S \boldsymbol{r}} \end{aligned} \tag{2.8}$$

and the photon operators $A_L^-$ and $A_S^+$ are proportional to $a_L$ and $a_S^+$, respectively.[8] Note that these operators are not hermitian!

The Hamiltonian describing the electrons plus the electron-photon coupling then is given by substituting $\boldsymbol{p} \to \boldsymbol{p} - (e/c)\boldsymbol{A}(\boldsymbol{r})$ in the kinetic energy of the electrons:

$$H = \frac{1}{2m_0}\left(\boldsymbol{p} - \frac{e}{c}\boldsymbol{A}(\boldsymbol{r})\right)^2 \ . \tag{2.9}$$

When evaluating the square of the parenthesis we encounter an anticommutator $\{\boldsymbol{p}, \boldsymbol{A}(\boldsymbol{r})\}$ which is equal to $2\boldsymbol{A}(\boldsymbol{r})\boldsymbol{p} + (\hbar/i)\mathrm{div}\boldsymbol{A}(\boldsymbol{r})$. The second term of this expression vanishes in the Coulomb gauge. This implies $\boldsymbol{k}\boldsymbol{A}_{\boldsymbol{k}}(\boldsymbol{r}) = 0$ for the Fourier components of the vector potential and, therefore the requirement $\boldsymbol{e}_i \boldsymbol{k}_i = 0$ for $i = L, S$, that is, the polarization vectors are perpendicular to the momentum $\boldsymbol{k}$ of the photons. The Hamiltonian

$$H = H_0 + H_{\boldsymbol{Ap}} + H_{\boldsymbol{A}^2} \ , \qquad \begin{aligned} H_{\boldsymbol{Ap}} &= -\frac{e}{m_0 c}\boldsymbol{A}\boldsymbol{p} \\ H_{\boldsymbol{A}^2} &= \frac{e^2}{2m_0 c^2}\boldsymbol{A}^2 \end{aligned} \tag{2.10}$$

will be treated perturbatively in order to obtain the Raman transition rate. We identify the exponent of $e$, or equivalently of the vector field $\boldsymbol{A}(\boldsymbol{r})$, as the order of the perturbation. Absorption or emission processes involving only one photon, and therefore being of order $e^1$, are not of interest here since at least two photons are involved in the Raman process. We

---

[8] The annihilation operator $A_L^-$ (or $a_L$) always appears together with the space function $\exp(+i\boldsymbol{k}_L\boldsymbol{r})$ with a plus sign in the exponent, the operator *removes* the quasimomentum $\boldsymbol{k}_L$ from the photon system and the function $\exp(+i\boldsymbol{k}_L\boldsymbol{r})$ *adds* it to the electron system.

shall only consider processes of order $e^2$, being consistent with the initial and final states defined above.

Transition matrix elements of order $e^2$ are generated by the operator $H_{\boldsymbol{A}^2}$ taken in first order perturbation theory, and also by the operator $H_{\boldsymbol{Ap}}$ in second order perturbation theory. We first describe the treatment of $H_{\boldsymbol{A}^2}$. We consider $|f_{el}\rangle$ in (2.7) to be an electron-hole excitation with the hole of wavevector $\boldsymbol{k}$ in band $n_i$ and the electron with wavevector $\boldsymbol{k}'$ in band $n_f$. The transitions $|i\rangle \to |f\rangle$ defined in (2.7) when created by an operator $V$ are described by the matrix element $\langle n_f\boldsymbol{k}'|\langle n_L-1, n_S=1|V|n_L, n_S=0\rangle|n_i\boldsymbol{k}\rangle$. For these transitions, the translational invariance of the crystal lattice implies $\boldsymbol{k}_L-\boldsymbol{k}_S \equiv \boldsymbol{q} = \boldsymbol{k}'-\boldsymbol{k}$ (mod $\boldsymbol{G}$). Using this we denote the transition amplitude arising in first order perturbation theory from $H_{\boldsymbol{A}^2}$ by $M^{(1)}_{n_f,n_i}(\boldsymbol{q},\boldsymbol{k})$ and the one arising in second order from $H_{\boldsymbol{Ap}}$ by $M^{(2)}_{n_f,n_i}(\boldsymbol{q},\boldsymbol{k})$.

### 2.2.8 First order in $H_{\boldsymbol{A}^2}$

The transition amplitude $M^{(1)}_{n_f,n_i}(\boldsymbol{q},\boldsymbol{k})$ generated by $H_{\boldsymbol{A}^2}$ in first order perturbation theory is simply given by $\langle f|H_{\boldsymbol{A}^2}|i\rangle$, that is,

$$\begin{aligned} M^{(1)}_{n_f,n_i}(\boldsymbol{q},\boldsymbol{k}) &= \frac{e^2}{2m_0c^2}\langle n_f\boldsymbol{k}'|\langle n_L-1, n_S=1|\boldsymbol{A}^2|n_L, n_S=0\rangle|n_i\boldsymbol{k}\rangle \\ &= \frac{e^2}{2m_0c^2}\langle 2A_S^+A_L^-\rangle \boldsymbol{e}_S^*\boldsymbol{e}_L\langle n_f\boldsymbol{k}'|e^{i\boldsymbol{qr}}|n_i\boldsymbol{k}\rangle \ . \end{aligned}$$

The inner average is a photon field state average defined by the equation above; the matrix element with Bloch states an integration over the sample. The quantity $\boldsymbol{q} = \boldsymbol{k}_L - \boldsymbol{k}_S$ denotes the momentum transferred in the scattering process from the photon field to the electron system. Using $\psi_{n\boldsymbol{k}}(\boldsymbol{r}) = \exp(+i\boldsymbol{kr})u_{n\boldsymbol{k}}(\boldsymbol{r})$ for the Bloch functions, this reduces to $\delta_{\boldsymbol{k}'-(\boldsymbol{k}+\boldsymbol{q})}\cdot\int u^*_{n_f\boldsymbol{k}'}(\boldsymbol{r})u_{n_i\boldsymbol{k}}(\boldsymbol{r})$, where the integral[9] is $\sim \delta_{n_fn_i} + O(qa)^2$, the linear dimension of the crystal unit cell being denoted by $a$. Because $q \ll 1/a$ in the Raman process, we neglect the $(qa)^2$ order terms and write

$$M^{(1)}_{n_f,n_i}(\boldsymbol{q},\boldsymbol{k}) = r_0\langle A_S^+A_L^-\rangle \boldsymbol{e}_S^*\boldsymbol{e}_L\delta_{n_fn_i} \tag{2.11}$$

for the transition matrix element of the transition $|i\rangle \to |f\rangle$ with $|f_{el}\rangle$ carrying a hole $(n_i,\boldsymbol{k})$ and an electron $(n_f,\boldsymbol{k}+\boldsymbol{q})$ (see (2.7)). This transition matrix element is represented schematically in Fig. 2.2. For all other transitions, the transition matrix element vanishes because the quasimomentum[10] has to be conserved. The quantity $r_0 = e^2/(m_0c^2)$ in (2.11) is called the Thompson electron radius and the Kronecker symbol $\delta_{n_fn_i}$ expresses the fact that for $q \ll 1/a$ *only intraband* and *no interband* transitions are possible with this mechanism. This is a very important *selection rule* which arises from the fact that for fixed $\boldsymbol{k}$ the periodic parts of the Bloch functions of different bands are orthogonal.

It is clear that in a clean metal the transition under consideration only leads to elastic light scattering because the initial and final states must be the same. If impurities are present, or the crystal is in the superconducting state, Eq. (2.11) also leads to inelastic light scattering.

---

[9] Bloch functions $\psi_{n\boldsymbol{k}}(\boldsymbol{r})$ are orthogonal in the crystal: $\int_{\text{cry}}\psi^*_{n'\boldsymbol{k}'}(\boldsymbol{r})\psi_{n\boldsymbol{k}}(\boldsymbol{r})\,d^3r \sim \delta_{n'n}\delta_{\boldsymbol{k}'\boldsymbol{k}}$, whereas the lattice-periodic functions $u_{n\boldsymbol{k}}(\boldsymbol{r})$ are orthogonal *for fixed* $\boldsymbol{k}$ in the unit cell: $\int_{\text{u.cell}}u^*_{n'\boldsymbol{k}}(\boldsymbol{r})u_{n\boldsymbol{k}}(\boldsymbol{r})\,d^3r = \delta_{n'n}$.

[10] Note that Umklapp processes are neglected in the transition under consideration.

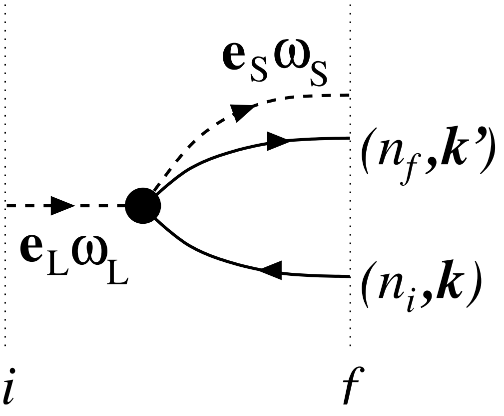

Figure 2.2: Diagram of the transition induced by the operator $H_{\boldsymbol{A}^2}$ and showing the vertex responsible for the transition. The vertical lines denote the initial and final state, respectively.

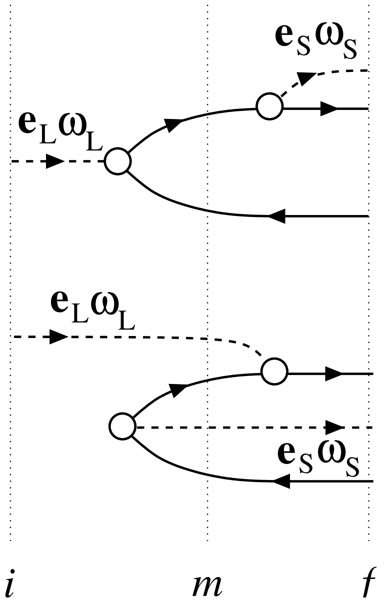

Figure 2.3: The two possibilities for annihilating a photon and creating another one along with an electronic pair excitation, involving an initial state $i$, an intermediate state $m$, and a final state $f$.

### 2.2.9 Second order in $H_{\boldsymbol{Ap}}$

The transitions generated by the operator $H_{\boldsymbol{Ap}}$ are emission and absorption when treated only up to first order perturbation theory. We are interested in two-photon processes and therefore apply second order perturbation theory to $H_{\boldsymbol{Ap}}$. The second order perturbation involves a *virtual* transition from a state $|i\rangle$ to an *intermediate* state[11] $|m\rangle$ and subsequently a transition to the final state $|f\rangle$, and sums over all possible intermediate states. Because of $\boldsymbol{A} = \boldsymbol{A}_L + \boldsymbol{A}_S$, two processes are possible: the first, annihilating a photon while going from $|i\rangle$ to $|m\rangle$ and creating a photon while going from $|m\rangle$ to $|f\rangle$ and vice versa for the second process (schematically shown in Fig. 2.3). The intermediate state of the photon field is $|n_L - 1, n_S = 0\rangle$ for the first case and $|n_L, n_S = 1\rangle$ for the second case. The matrix element for the transition $|i\rangle \to |m\rangle$ while absorbing a photon is

$$\begin{aligned} -\frac{e}{m_0 c}\langle m|\boldsymbol{A}_L\boldsymbol{p}|i\rangle &= -\frac{e}{m_0 c}\langle n_L - 1, n_S = 0|A_L^-|n_L, n_S = 0\rangle\times \\ &\quad \times \langle n_m\boldsymbol{k}'|\boldsymbol{e}_L e^{i\boldsymbol{k}_L\boldsymbol{r}}\boldsymbol{p}|n_i\boldsymbol{k}\rangle \\ &= -\frac{e}{m_0 c}(A_L^-)_{mi}\langle n_m\boldsymbol{k} + \boldsymbol{k}_L|\boldsymbol{e}_L\boldsymbol{p}|n_i\boldsymbol{k}\rangle\delta_{\boldsymbol{k}',\boldsymbol{k}+\boldsymbol{k}_L} \ . \end{aligned}$$

The sum over all intermediate states $|m\rangle$ is given now by a sum over all bands $n_m$, the other quantum numbers of $|m\rangle$ being fixed. The notation $(A_L^-)_{mi}$ refers to the matrix element of $A_L^-$ taken with the photon field parts of the states $|m\rangle$ and $|i\rangle$. Taking into account the energy difference of the initial and intermediate states to be $\epsilon_{n_i\boldsymbol{k}} - (\epsilon_{n_m,\boldsymbol{k}+\boldsymbol{k}_L} - \omega_L)$, and the fact that $(A_S^+)_{fm}(A_L^-)_{mi} = (A_L^-)_{fm}(A_S^+)_{mi} = \langle A_S^+A_L^-\rangle$ for the appropriate states, the transition matrix element is found to be

$$M^{(2)}_{n_f n_i}(\boldsymbol{q},\boldsymbol{k}) = r_0\langle A_S^+A_L^-\rangle\sum_{n_m}\Gamma^{(2)}_{n_f n_i;n_m}(\boldsymbol{q},\boldsymbol{k}) \tag{2.12}$$

with the expression from second order perturbation theory[12]

$$\begin{aligned} \Gamma^{(2)}_{n_f n_i;n_m}(\boldsymbol{q},\boldsymbol{k}) &= \frac{1}{m_0}\times \\ &\times\left[\frac{\langle n_f\boldsymbol{k}+\boldsymbol{q}|\boldsymbol{e}_S^*\boldsymbol{p}|n_m\boldsymbol{k}+\boldsymbol{k}_L\rangle\langle n_m\boldsymbol{k}+\boldsymbol{k}_L|\boldsymbol{e}_L\boldsymbol{p}|n_i\boldsymbol{k}\rangle}{\epsilon_{n_i\boldsymbol{k}} - \epsilon_{n_m\boldsymbol{k}+\boldsymbol{k}_L} + \hbar\omega_L + i0} + \right. \\ &\left. + \frac{\langle n_f\boldsymbol{k}+\boldsymbol{q}|\boldsymbol{e}_L\boldsymbol{p}|n_m\boldsymbol{k}-\boldsymbol{k}_S\rangle\langle n_m\boldsymbol{k}-\boldsymbol{k}_S|\boldsymbol{e}_S^*\boldsymbol{p}|n_i\boldsymbol{k}\rangle}{\epsilon_{n_i\boldsymbol{k}} - \epsilon_{n_m\boldsymbol{k}-\boldsymbol{k}_S} - \hbar\omega_S + i0}\right] \end{aligned} \tag{2.13}$$

and the two terms being related to the two processes in Fig. 2.3. At $T = 0$, the difference $\epsilon_{n_i\boldsymbol{k}} - \epsilon_{n_m\boldsymbol{k}+\boldsymbol{k}_L}$ is negative, so the first term may be resonant for certain electron-hole excitations whereas the second will never be. The wavevectors of light, $\boldsymbol{k}_L$ and $\boldsymbol{k}_S$, can usually be neglected in the matrix elements of Eq. (2.13) because $v_F \ll c$. For the same reason, $\epsilon_{n_m,\boldsymbol{k}+\boldsymbol{k}_L} \approx \epsilon_{n_m,\boldsymbol{k}}$. Therefore, we introduce the symbol $\Gamma^{(2)}_{n_f n_i;n_m}(\boldsymbol{k})$ to denote expression (2.13) with the light wavevectors set equal to zero.

---

[11] the transition to an *intermediate* state is called *virtual* if energy is not conserved. The violation of energy conservation appears only in perturbation theory. It is, however, possible if confined to a short time interval.

[12] Note that the application of the Golden Rule finally enforces energy conservation in the form of $\omega_L - \omega_S = \epsilon_{n_f\boldsymbol{k}} - \epsilon_{n_i\boldsymbol{k}}$.

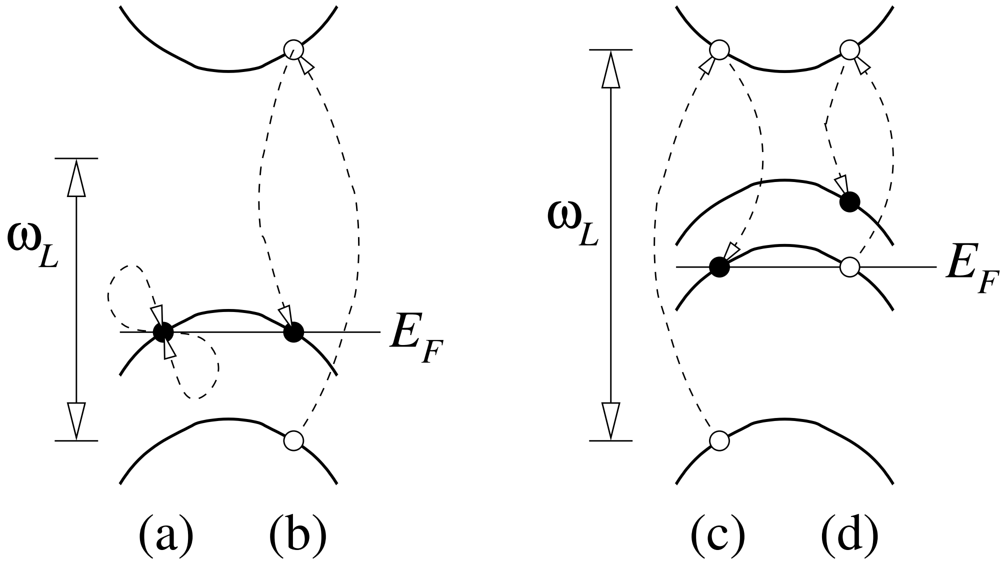

Figure 2.4: Four different cases for the second order transition. For the description refer to the text.

In Fig. 2.4, we show four different $(\boldsymbol{Ap})^2$ transitions which all contribute to Raman scattering. In case (a) the real and virtual transitions both are intraband transitions. This case is prohibited by the *selection rule* if the metal is clean (and not superconducting). The real and virtual transitions both are interband transitions in the other 3 cases. The first one (b) is above the resonance, the second one (c) is resonant, and the last one (d) is below the resonance.

### 2.2.10 Raman vertex

We find the total transition rate[13] $|i\rangle \to |f\rangle$, which for transitions of second order in the vector field can be expressed as

$$\begin{aligned} M_{n_f n_i}(\boldsymbol{q},\boldsymbol{k}) &= M^{(1)}_{n_f n_i}(\boldsymbol{q},\boldsymbol{k}) + M^{(2)}_{n_f n_i}(\boldsymbol{q},\boldsymbol{k}) \\ &= r_0 \langle A^+_S A^-_L \rangle \boldsymbol{e}^*_S \left[ \delta_{n_f n_i} + \sum_{n_m} \hat{\Gamma}^{(2)}_{n_f n_i; n_m}(\boldsymbol{q},\boldsymbol{k}) \right] \boldsymbol{e}_L \; . \end{aligned} \tag{2.14}$$

The symbol $\hat{\Gamma}^{(2)}_{n_f n_i; n_m}$ denotes the tensor that, when multiplied from the left by $\boldsymbol{e}^*_S$ and from the right by $\boldsymbol{e}_L$, yields the quantity $\Gamma^{(2)}_{n_f n_i; n_m}$ in (2.13). We define an *effective Raman operator* $H_R$ that reproduces the transition amplitude (2.14) in first order perturbation theory:

$$H_R = r_0 \langle A^+_S A^-_L \rangle \sum_{n_f, n_i, \boldsymbol{k}} \boldsymbol{e}^*_S \hat{\gamma}_{n_f n_i}(\boldsymbol{q},\boldsymbol{k}) \boldsymbol{e}_L |n_f; \boldsymbol{k}+\boldsymbol{q}\rangle\langle n_i; \boldsymbol{k}| \tag{2.15}$$

---

[13] Recall that $|f\rangle$ is given by (2.7) and $|f_{el}\rangle$ denotes an electron-hole excitation with quasimomentum $\boldsymbol{k}$.

where the second rank tensor $\hat{\gamma}_{n_f n_i}(\boldsymbol{q},\boldsymbol{k})$ is the (dimensionless) *nondiagonal Raman vertex tensor* which is given by

$$\hat{\gamma}_{n_f n_i}(\boldsymbol{q},\boldsymbol{k}) = \delta_{n_f n_i} + \sum_{n_m} \hat{\Gamma}^{(2)}_{n_f n_i; n_m}(\boldsymbol{q},\boldsymbol{k}) \ . \tag{2.16}$$

We introduce also the symbol $\gamma_{n_f n_i}$ to denote the *nondiagonal Raman vertex* for fixed light polarization vectors $\boldsymbol{e}_L$ and $\boldsymbol{e}^*_S$,

$$\gamma_{n_f n_i}(\boldsymbol{q},\boldsymbol{k}) = \boldsymbol{e}^*_S \hat{\gamma}_{n_f n_i}(\boldsymbol{q},\boldsymbol{k}) \boldsymbol{e}_L \ . \tag{2.17}$$

It can be easily seen that

$$\langle n_f; \boldsymbol{k}' | H_R | n_i; \boldsymbol{k} \rangle = M_{n_f n_i}(\boldsymbol{k}' - \boldsymbol{k}, \boldsymbol{k}) \ ,$$

in other words the transition rate $M_{n_f n_i}(\boldsymbol{q},\boldsymbol{k})$ can be obtained by just treating the effective Raman operator $H_R$ in first order perturbation theory, the second order effects via $H_{\boldsymbol{A}\boldsymbol{p}}$ are subsumed in (2.15).

We already mentioned that the product of $|\boldsymbol{q}|$ with the lattice constant $a$, that is, $a|\boldsymbol{q}|$ is of order $v_F/c$, and therefore the limit $\boldsymbol{q} \to 0+$ can be taken. We consequently introduce the notation

$$\gamma_{n_f n_i}(\boldsymbol{k}) = \lim_{\boldsymbol{q} \to 0+} \gamma_{n_f n_i}(\boldsymbol{q},\boldsymbol{k})$$

and replace $\boldsymbol{k}+\boldsymbol{q}$ by $\boldsymbol{k}$.

The perturbing operator $H_R$ must be a hermitian operator. This imposes the condition

$$\gamma_{n_f n_i}(\boldsymbol{k},\boldsymbol{q}) = \gamma^*_{n_i n_f}(\boldsymbol{k}+\boldsymbol{q}, -\boldsymbol{q}) \quad \text{or} \quad \gamma_{n_f n_i}(\boldsymbol{k}) = \gamma^*_{n_i n_f}(\boldsymbol{k}) \quad \text{for } \boldsymbol{q} \to 0 \tag{2.18}$$

on the Raman vertex and just states that the amplitudes of processes which are related by a time-reversal are related by complex conjugation.

The matrix $|n_f; \boldsymbol{k}+\boldsymbol{q}\rangle\langle n_i; \boldsymbol{k}|$ in (2.15) is analogous to the bilinear operator combination $c^+_{n_f,\boldsymbol{k}+\boldsymbol{q}} c_{n_i,\boldsymbol{k}}$ in the formalism of the second quantization. Definition (2.15) is therefore equivalent to

$$H_R = r_0 \langle A^+_S A^-_L \rangle \, \tilde{\rho}_{\boldsymbol{q}} \quad ; \qquad \tilde{\rho}_{\boldsymbol{q}} = \sum_{n_f, n_i, \boldsymbol{k}} \gamma_{n_f n_i}(\boldsymbol{k},\boldsymbol{q}) \, c^+_{n_f,\boldsymbol{k}+\boldsymbol{q}} c_{n_i,\boldsymbol{k}} \tag{2.19}$$

which is the effective Raman operator expressed in terms of fermionic creation and annihilation operators for Bloch electrons and the nondiagonal Raman vertex (2.16).

We next evaluate the factor $\langle A^+_S A^-_L \rangle$. Using the normalization inherent in (2.5), the quantities $A^+_S(t)$ and $A^-_L(t)$ are given explicitly by

$$A^-_L(t) = \sqrt{\frac{2\pi\hbar c^2}{V_{\text{Sa}}\omega_L}} e^{-i\omega_L t} a_{\boldsymbol{k}_L \lambda_L} \ , \quad A^+_S(t) = \sqrt{\frac{2\pi\hbar c^2}{V_{\text{Sa}}\omega_L}} e^{i\omega_S t} a^+_{\boldsymbol{k}_S \lambda_S} \ ,$$

and the matrix element $\langle A^+_S A^-_L \rangle$ becomes

$$\langle A^+_S A^-_L \rangle \equiv \langle n_L - 1, 1_S | A^+_S(t) A^-_L(t) | n_L 0_S \rangle = \frac{2\pi\hbar c^2}{V_{\text{Sa}}\sqrt{\omega_L \omega_S}} e^{-i\omega t} \sqrt{n_L} \tag{2.20}$$

where $\omega = \omega_L - \omega_S$. Note that $n_L$ is proportional to the sample volume, therefore $\langle A_S^+ A_L^- \rangle$ is proportional to $V_{\mathrm{Sa}}^{-1/2}$. The dimensions of $\langle A_S^+ A_L^- \rangle$ are Energy/Length, so that $H_R$ in (2.19) has the correct dimensions of an energy.

The effective Raman operator $H_R$ can be treated by methods which are essentially equivalent to Fermi's Golden Rule. As a result, the contribution of a certain transition $n_i \to n_m \to n_f$ at a certain point $\boldsymbol{k}$ in $k$-space, for a Raman shift $\epsilon_{n_f \boldsymbol{k}} - \epsilon_{n_i \boldsymbol{k}}$, has an amplitude given by the product of the transition matrix elements of the two virtual transitions divided by the corresponding resonance denominator.

We revisit our derivation of the Raman vertex now. For the calculation of the transition rate from $|i\rangle$ to $|f\rangle$, we made use of the Golden Rule. The Golden Rule states that the transition rate is given by

$$\Gamma_{i \to f} = \frac{2\pi}{\hbar} |\langle f|V|i\rangle|^2 \delta(E_f - E_i) \;, \tag{2.21}$$

where $H = H_0 + V$ is the Hamiltonian and $|i\rangle$ and $|f\rangle$ are eigenstates of $H_0$ with eigenvalues $E_i$ and $E_f$, respectively.

In our case, the perturbation is given by $V = H_{\boldsymbol{Ap}} + H_{\boldsymbol{A}^2}$. This gives rise to contributions to the transition rate which are proportional to (i) the term $|\langle f|H_{\boldsymbol{Ap}}|i\rangle|^2$, which corresponds to absorption/emission, and (ii) the term $|\langle f|H_{\boldsymbol{A}^2}|i\rangle|^2$, which is related to Raman scattering. Cross terms vanish identically.

It is clear that in higher order perturbation theory, the term $H_{\boldsymbol{Ap}}$ also will yield a contribution of fourth order in the vector potential $\boldsymbol{A}$ to the transition rate. In the approach given, we have tackled this problem by using Golden Rule. However, as a final state, we did not use the eigenstate $|f\rangle$ of $H_0$. Instead, we calculated the correction to $|f\rangle$ in first order (stationary) perturbation theory. This yields

$$|f\rangle^{(1)} = |f\rangle + \sum_{m \neq f} \frac{\langle m|V|f\rangle}{E_f - E_m} |m\rangle \;. \tag{2.22}$$

The state $|f\rangle^{(1)}$ was used in the Golden Rule (2.21). The resulting transition rate $\Gamma_{i \to f}$ then also contains contributions proportional to $(\boldsymbol{Ap})^4$ and $\boldsymbol{A}^2(\boldsymbol{Ap})^2$. Additionally appearing terms in order $\boldsymbol{A}^6$ and higher are neglected. This method yields the result (2.16) for the Raman vertex.

In a strict derivation of the transition rate, however, we should employ time-dependent perturbation theory in second order in the perturbation $V$. Performing this by using the time evolution matrix $U$ defined in App. D is rather straightforward. Two eigenstates $|i\rangle$ and $|f\rangle$ of $H_0$ are given at $t = 0$, when the perturbation $V$ is suddenly switched on. Then $|i\rangle$ evolves in time according to $H_0$, while $|f\rangle$ evolves according to the full Hamiltonian $H = H_0 + V$. The transition probability $P_{i \to f}(t)$ is given by $P_{i \to f}(t) = \langle i|f\rangle(t)$. The time evolution of $|f\rangle$ is expressed in second order in $V$ by using the evolution matrix $U$. Then, $\Gamma_{i \to f}$ can be calculated and the result (2.16) is recovered.

So far the derivation has been quite general. Before discussing the Raman vertex for a particular situation, we compare real intraband transitions to real interband transitions, that is, transitions with $n_f = n_i$ to transitions $n_f \neq n_i$ (if the bands $n_i$ and $n_f$ are degenerate, transitions connecting them count as interband transitions for the purpose of our discussion).

Because of energy conservation in a real transition, an intraband transition only contributes to the Raman spectrum at a vanishing Raman shift, the contribution is given by the Golden Rule and proportional to

$$|H_R|^2\delta(\omega)$$

where $\omega \equiv \omega_L - \omega_S$. The presence of lifetime broadening, induced, for instance, by impurity scattering may change this fact and allow for contributions to the Raman spectrum at $\omega \neq 0$. In the theory, the $\delta$-function in the equation above then is replaced by a Lorentzian whose width is determined by the inverse scattering time (for simple cases of impurity scattering).

A similar effect arises from superconductivity. In this case, the ground state of the system is very different from that of a Fermi liquid, and the $\delta$-function above must be replaced by the so-called Tsuneto-function, which in $\omega$-space is different from zero up to an energy of the order of the maximum of the superconducting gap.

Let us consider now a situation in which $\epsilon_{n_f\boldsymbol{k}} - \epsilon_{n_i\boldsymbol{k}}$ for $n_f \neq n_i$ is larger than a certain threshold $\delta_{\min}$ for all bands and all points in $k$-space. The threshold $\delta_{\min}$ also should be considerably larger than the inverse scattering length and/or the superconducting gap amplitude. Then the contributions from real interband transitions will appear in the Raman spectrum at Raman shifts larger than $\omega = \delta_{\min}$. If "broadening-like" effects, like impurity scattering, or superconducting pairing are present,[14] the Raman spectrum does not exhibit a sharp step at $\omega = \delta_{\min}$, but the spectrum may extend below this value for the Raman shift.

In many high-temperature superconductors such situation is obtains. The threshold $\delta_{\min}$ may be of the order of 50 meV, as can be inferred from the band structure (Fig. 2 of Ref. [2.11]); for Raman shifts lower than this value, the Raman spectrum essentially arises from real intraband transitions.

Therefore, we only consider real intraband transitions and introduce the *Raman vertex*

$$\gamma_n(\boldsymbol{k}) = \gamma_{nn}(\boldsymbol{k})$$

which is also called intraband or diagonal Raman vertex. This vertex has to be determined by Eq. (2.13), a rather formidable task. To evaluate this equation, matrix elements have to be known. Fortunately, an approximation known as *effective mass approximation* allows us to cast (2.13) into a form which can be related to the inverse effective mass tensor by means of a result of second order perturbation theory (see, e.g., App. E of Ref. [2.9]).

### 2.2.11 Effective mass approximation

In systems that exhibit translational invariance, the eigenstates of the single-particle Hamiltonian can be chosen to be eigenfunctions of the translation group as well. The resulting eigenstates then acquire the form $\psi_{n\boldsymbol{k}}(\boldsymbol{r}) = \exp(i\boldsymbol{k}\boldsymbol{r})u_{n\boldsymbol{k}}(\boldsymbol{r})$ as given by Bloch's theorem. Fixing the quasimomentum $\boldsymbol{k}$, the functions $u_{n\boldsymbol{k}}(\boldsymbol{r})$ are determined by a Hamiltonian $H_{\boldsymbol{k}}$ depending on $\boldsymbol{k}$ as a parameter. The eigenvalue problem then determines the eigenvalues $\epsilon_{n\boldsymbol{k}}$

---

[14] Actually these two cases are very different. Impurities produce an incoherent broadening, while superconducting pairing is described by a new (coherent) ground state which is different from that of a Fermi liquid.

for a fixed $\boldsymbol{k}$. Now the Hamiltonian $H_{\boldsymbol{k}}$ is quadratic in $\boldsymbol{k}$. Replacing $\boldsymbol{k}$ by $\boldsymbol{k}+\boldsymbol{q}$ yields two terms linear and quadratic in $\boldsymbol{q}$ in addition to $H_{\boldsymbol{k}}$. If we take $\boldsymbol{q}$ to be small (in comparison to the inverse lattice constant), we find using second order perturbation theory for the eigenvalues up to second order in $\boldsymbol{q}$ corrections that correspond to the first and second derivative, respectively, of the band structure with respect to the quasimomentum and therefore to the velocity and the inverse effective mass of the Bloch electrons, respectively. Proceeding along these lines leads to the equation

$$\begin{aligned}\frac{m_0}{\hbar^2}\frac{\partial^2\epsilon_{n\boldsymbol{k}}}{\partial k_i\partial k_j} =&\delta_{ij}+ \\ &+\frac{1}{m_0}\sum_{n'\neq n}\frac{\langle n\boldsymbol{k}|p_i|n'\boldsymbol{k}\rangle\langle n'\boldsymbol{k}|p_j|n\boldsymbol{k}\rangle+\langle n\boldsymbol{k}|p_j|n'\boldsymbol{k}\rangle\langle n'\boldsymbol{k}|p_i|n\boldsymbol{k}\rangle}{\epsilon_{n\boldsymbol{k}}-\epsilon_{n'\boldsymbol{k}}}\end{aligned} \tag{2.23}$$

which is called the $\boldsymbol{k}\cdot\boldsymbol{p}$ *effective mass theorem*. Between (2.16) in combination with (2.13), and the Eq. (2.23), there are only two essential differences. The first is the exclusion of the band $n'=n$ in the summation above, the other the absence of the laser frequencies $\omega_L$ and $\omega_S$ in the denominator of (2.23). The *effective mass approximation* reduces (2.16) and (2.13) to the form of (2.23) by just excluding the $n_m=n_i$ terms from the summation in (2.16) and neglecting the laser frequencies in the denominator of (2.13).

For the justification of this rule we first consider the error introduced by excluding the virtual intraband process from the sum in (2.16). Note again that for the case under consideration (with $n_i=n_f$) the frequencies $\omega_L$ and $\omega_S$ are equal. On the other hand, shifting states from $\boldsymbol{k}$ to $\boldsymbol{k}\pm\boldsymbol{k}_L$ or $\boldsymbol{k}\pm\boldsymbol{k}_S$ while keeping the band index fixed, just introduces correction of order $v/c$ to matrix elements. Therefore the two terms in (2.13) cancel for $n_i=n_m=n_f$ up to contributions of order $v/c$ and can be left out in the summation in (2.16) if there are nonvanishing contributions of $O(1)$.

Next we focus on the neglection of the laser energies in the denominators of (2.13) and denote the energy $\epsilon_{n_m\boldsymbol{k}}-\epsilon_{n_i\boldsymbol{k}}$ of the virtual electronic excitation by $\Delta\epsilon_m$. Furthermore all the matrix elements in (2.13) are taken as equal, the resulting right hand side of (2.13) is denoted by $r(\Delta\epsilon_m)$. Performing analogous steps with (2.23) and calling the resulting function $r_{ema}(\Delta\epsilon_m)$ we find the functions plotted in Fig. 2.5. Given a certain virtual transition $|i\rangle\to|m\rangle$ with a transition energy $\epsilon$, the factor $|r(\epsilon)|$ determines the weight of the contribution to the Raman efficiency. The figure shows that virtual intraband transitions do not contribute at all. Virtual transitions with $\epsilon\approx\omega_L$ can be in resonance with the incoming photon, and therefore contribute very strongly. For even larger values of $\epsilon$, the weight of the contribution decreases.

For the case of the effective mass formula the resonance behavior is characterized by the function $|r_{ema}(\epsilon)|$. This function weights very strongly the virtual transitions for $\Delta\epsilon_m\ll\omega_L$ and therefore is a very bad approximation for $|r(\epsilon)|$ in this regime. Around $\epsilon=\omega_L$, it does not resemble the resonance peak in the function $|r(\epsilon)|$ and is a bad approximation as well. However, for virtual transitions with $\epsilon\gg\omega_L$ it should be a very good approximation.

Assuming a sufficiently high minimum transition energy for virtual transitions, (2.16) becomes equivalent to the expression for the inverse effective mass from $\boldsymbol{k}\cdot\boldsymbol{p}$ theory and we can write

$$\gamma_n(\boldsymbol{k})=\frac{m}{\hbar^2}\sum_{i,j}\boldsymbol{e}^*_{S,i}\frac{\partial^2\epsilon_{n\boldsymbol{k}}}{\partial k_i\partial k_j}\boldsymbol{e}_{L,j}\ , \tag{2.24}$$

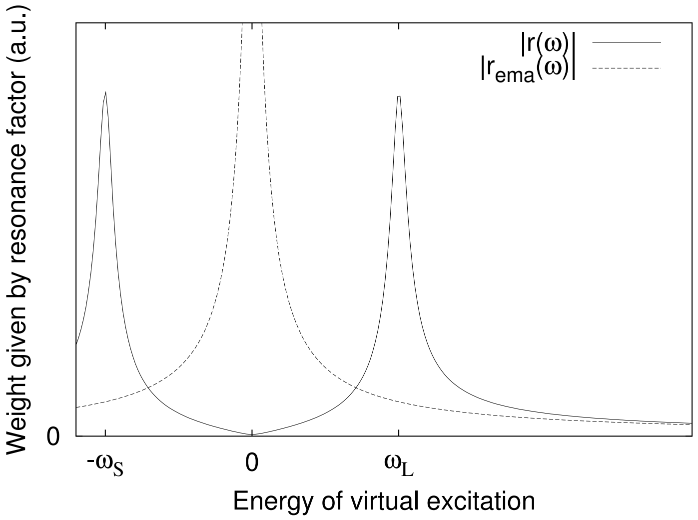

Figure 2.5: The weighting of the transition matrix elements in (2.23) by the numerator with and without the application of the effective mass approximation. The curve denoted $|r(\epsilon)|$ shows the exact case, and $|r_{ema}(\epsilon)|$ the case after applying the effective mass approximation.

that is, the Raman vertex is equal to the inverse effective mass contracted with the polarization vectors of the laser light and the scattered light.

We conclude this paragraph by stressing again that using the term $H_R$ from (2.19) in conjunction to the intraband Raman vertex $\gamma_{n\boldsymbol{k}} = \gamma_{nn}(\boldsymbol{k})$ from (2.16) as perturbation to the Hamiltonian for $\boldsymbol{A} = 0$ and treating this term in first order perturbation theory is equivalent to taking into consideration both terms, $H_A$ and $H_{\boldsymbol{A}^2}$ [2.4].

### 2.2.12 The tensorial nature of the Raman vertex

In the effective mass approximation (2.24), the tensorial nature of the Raman vertex can be easily seen. Let $\mathcal{G}$ denote the *point* group of a given Hamiltonian. Then the dispersion relation $\epsilon_{n\boldsymbol{k}}$ is invariant[15] with respect to the symmetry operations of this group, that is, for $G \in \mathcal{G}$, we have $\epsilon_{n\boldsymbol{k}} = \epsilon_{n,G\boldsymbol{k}}$. As a consequence, the inverse effective mass

$$\mu_{ij}^{-1}(\boldsymbol{k}) \equiv \frac{m}{\hbar^2} \frac{\partial^2 \epsilon_{n\boldsymbol{k}}}{\partial k_i \partial k_j}$$

transforms like a second rank tensor. This is also the case for the Raman vertex tensor $\hat{\gamma}_{\boldsymbol{k}}$ defined in (2.17).

In the case when the effective mass approximation is valid, the fact that the Raman vertex tensor $\hat{\gamma}_{\boldsymbol{k}}$ from (2.17) transforms like a second rank tensor can be inferred directly from the analogous property of the inverse effective mass tensor $\hat{\mu}^{-1}(\boldsymbol{k})$.

---

[15] The point group of a lattice is also the point group of the related reciprocal lattice. This is not true, however, for the space group. The reciprocal lattice of a body-centered cubic lattice, e.g., is a face-centered cubic lattice!

In the general case, the observation that $\boldsymbol{e}_S^* \hat{\gamma}_{\boldsymbol{k}} \boldsymbol{e}_L$ transforms like a scalar also yields the result that $\hat{\gamma}_{\boldsymbol{k}}$ corresponds to a second rank tensor.

For a crystal which possesses a certain point group symmetry, a tensor can be decomposed into components which each transforms according to some irreducible representation (IR) of the point group. Such decomposition is shown, as an example, in (C.25) for the case of the $C_{4v}$ point group. In the context of electronic Raman scattering, this decomposition is important when discussing the electronic screening of the electron-hole excitation created by Raman scattering. In Subsect. 2.3.6 we will show that the screening is proportional to the square of the Brillouin zone average $\langle \gamma_{\boldsymbol{k}} \lambda_{\boldsymbol{k}}(\omega) \rangle$, where $\lambda_{\boldsymbol{k}}(\omega)$ is a function with the complete symmetry of the point group, that is, transforms according to the $A_1$ IR of $C_{4v}$ (we continue using $C_{4v}$ as an example for the crystal point group). For all IR's $\mu$ different from $A_1$, the related component $\gamma_{\boldsymbol{k}}^{(\mu)}$ (called the $\mu$ component of $\gamma_{\boldsymbol{k}}$) of the Raman vertex tensor $\hat{\gamma}_{\boldsymbol{k}}$ implies the vanishing of $\langle \gamma_{\boldsymbol{k}}^{(\mu)} \lambda_{\boldsymbol{k}}(\omega) \rangle$ due to symmetry reasons. Therefore, we can conclude that electronic scattering is present only in the $A_1$ component of $\gamma_{\boldsymbol{k}}$ and, hence, only the $\mu$ component of the Raman tensor is screened.

Usually for a certain IR $\mu$, the $\mu$ component of the Raman vertex tensor can be "selected" by choosing a certain polarization configuration $(\boldsymbol{e}_s, \boldsymbol{e}_L)$, such that $\gamma_{\boldsymbol{k}}^{(\mu)} = \boldsymbol{e}_S^* \hat{\gamma}_{\boldsymbol{k}} \boldsymbol{e}_L$. For the case of $C_{4v}$ this is possible, and $(xy)$ selects the $B_2$ component of the Raman tensor (the $A_2$ component vanishes in the effective mass approximation). In conclusion the Raman efficiency in $(xy)$ is *not* influenced by electronic screening.

### 2.2.13 Scattering efficiency and Raman susceptibility

By lumping together all the transitions leading to Raman scattering and arising from the coupling of the photon field to the electrons, we defined the effective Raman operator in (2.19), which when applying the Golden Rule yields the decay rate $\Gamma_{L\to S}$. This decay rate, on the other hand, is related to the Raman efficiency by (2.6). Our final goal now is to express the decay rate $\Gamma_{L\to S}$ by a susceptibility which can be determined by diagrammatic perturbation theory. This is done via an intermediate step. The Golden Rule yields an expression which is proportional to a modified dynamical structure factor $\tilde{S}$ of the sample. In an isotropic situation (when the Raman vertex is independent of $\boldsymbol{k}$), this quantity is proportional to the dynamical structure factor $S(\boldsymbol{q}, \omega)$, which is a measure for *density-density fluctuations* in the sample. It is straightforward to relate $\tilde{S}(\boldsymbol{q}, \omega)$ to the imaginary part of a susceptibility, the Raman susceptibility $\chi_{Raman}$, by using the fluctuation-dissipation theorem.

To establish the relation of the decay rate $\Gamma(\boldsymbol{k}_L, \boldsymbol{e}_L; \boldsymbol{k}_S, \boldsymbol{e}_S) \equiv \Gamma_{L\to S}$ to the dynamical structure factor, we add the time evolution factor $e^{-i\omega t} = e^{-i(\omega_L - \omega_S)t}$ from the vector potential operators to the effective Raman operator (2.19) and use the *Golden Rule* to find the transition rate from a state $|i\rangle$ to a state $|f\rangle$ of the sample. Then, we sum over all final states $|f\rangle$ of the sample and do a thermal averaging over the initial states $|i\rangle$. The transition rate from a state with $n_L \equiv n_{\boldsymbol{k}_L \boldsymbol{e}_L}$ laser photons and no scattered photon to a state with $n_L - 1$ laser photons and $n_S \equiv n_{\boldsymbol{k}_S \boldsymbol{e}_S} = 1$ scattered photon at a temperature $T$ is given by the expression

$$\Gamma^T(\boldsymbol{k}_L, \boldsymbol{e}_L; \boldsymbol{k}_S, \boldsymbol{e}_S) = \frac{2\pi}{\hbar} r_0^2 \cdot \left| \langle A_S^+ A_L^- \rangle \right|^2 \cdot \tilde{S}^T(\boldsymbol{q}, \omega) \tag{2.25}$$

(the superscript $T$ denotes temperature dependence of the decay rate) whereas

$$\tilde{S}^T(\boldsymbol{q},\omega) = \sum_{i,f} \frac{e^{-\beta E_i}}{\mathcal{Z}_0} |\langle f|\tilde{\rho}_{\boldsymbol{q}}|i\rangle|^2 \delta(E_f - E_i + \hbar\omega) \tag{2.26}$$

is a *generalized dynamical structure factor* (of the sample!), which has the dimension 1/Energy and is proportional to the sample volume $V_{\rm Sa}$. The partition function is denoted by $\mathcal{Z}_0$, and $\beta$ is the inverse temperature in energy units. Notice at this point that the effective density operator $\tilde{\rho}_{\boldsymbol{q}}$ is defined by (2.19) using the Raman vertex $\gamma_{n_f n_i}(\boldsymbol{k},\boldsymbol{q})$ and the electron creation and annihilation operators. The Raman vertex $\gamma_{n_f n_i}(\boldsymbol{k},\boldsymbol{q})$ is meant for a *given polarization configuration* $(\boldsymbol{e}_L, \boldsymbol{e}_S)$ (see 2.17).

When using matrix notation, the Raman vertex would read

$$\gamma_{n_f n_i}(\boldsymbol{k},\boldsymbol{q}) = \sum_{i,j} \boldsymbol{e}^*_{S,i} \gamma_{n_f n_i;ij}(\boldsymbol{k},\boldsymbol{q}) \boldsymbol{e}_{L,j} \ , \tag{2.27}$$

and the Raman efficiency becomes

$$\frac{d^2S}{d\Omega d\hbar\omega}(\omega) = \sum_{i,j,k,l} \boldsymbol{e}^*_{S,i}\boldsymbol{e}^*_{S,j} \frac{d^2 S_{ijkl}}{d\Omega d\hbar\omega}(\omega) \boldsymbol{e}_{L,k}\boldsymbol{e}_{L,l}$$

where the 4th rank tensor $S_{ijkl}$ is independent of the polarization configuration (see [2.12], Eq. (2.55)).

We relate now the decay rate $\Gamma^T$ in (2.25) to the Raman efficiency defined in (2.6), use the expression (2.20) to relate the matrix element $\langle A^+_S A^-_L \rangle$ to the occupation number $n_L$, and (2.4) to relate $n_L$ to the (classical) vector potential field amplitude $A_L$. Then,

$$\frac{d^2S}{d\Omega\, d\hbar\omega}(\boldsymbol{q},\omega) = \left|\frac{4}{1+\tilde{n}}\right|^2 \frac{1}{V_{\rm Sa}} r_0^2 \left(\frac{\omega_S}{\omega_L}\right)^2 \tilde{S}(\boldsymbol{q},\omega) \ . \tag{2.28}$$

The factor $r_0^2/V_{\rm Sa}$ has the dimension 1/Length and is proportional to the sample volume $V_{\rm Sa}$. Together with the structure factor, the Raman efficiency consequently has the dimension 1/(Length · Energy) and does not depend on the sample volume.

Finally, one can define a retarded linear response function, the *retarded Raman susceptibility*

$$\chi^{\rm ret}_{\rm Raman}(\boldsymbol{q},t) = \frac{i}{\hbar}\Theta(t)\,{\rm Tr}\{\mathcal{Z}_0^{-1} e^{-\beta H_0} [\tilde{\rho}_{\boldsymbol{q}}(t), \tilde{\rho}_{-\boldsymbol{q}}(0)]\} \tag{2.29}$$

and its Fourier-transformed $\chi^{\rm ret}_{\rm Raman}(\boldsymbol{q},\omega)$. To relate the imaginary part of this quantity to the structure function $\tilde{S}^T(\boldsymbol{q},\omega)$, we use the fluctuation-dissipation theorem.[16] The result is

$$\tilde{S}^T(\boldsymbol{q},\omega) = -\frac{1}{\pi}(1+n_\omega)\,{\rm Im}\,\chi^{\rm ret}_{\rm Raman}(\boldsymbol{q},\omega) \tag{2.30}$$

with the Bose-Einstein factor $n_\omega = [\exp(\beta\omega) - 1]^{-1}$.

---

[16] See, e.g., Sect. 2.6 in the book of Rickayzen [2.13].

The derivation of (2.30) from (2.26) and (2.29) is standard. The trace is written as $\mathrm{Tr}\{O\} = \sum_i \langle i|O|i\rangle$, and in between the $\tilde{\rho}$ operators, a unit operator $\sum_f |f\rangle\langle f|$ is inserted. Taking then the imaginary part an comparing the result to (2.26), the fluctuation-dissipation theorem (2.30) is found.

We summarize the result for the Raman efficiency obtained so far. The relation to the imaginary part of the retarded Raman susceptibility, defined in (2.29), is given by

$$\frac{d^2S}{d\Omega\, d\hbar\omega}(\omega) = -\frac{1}{\pi}(1+n_\omega)\left|\frac{4}{1+\tilde{n}^2}\right|^2 \frac{r_0^2}{V_{\mathrm{Sa}}}\left(\frac{\omega_S}{\omega_L}\right)^2 \mathrm{Im}\,\chi_{\mathrm{Raman}}(\boldsymbol{q},\omega)\Bigg|_{|\boldsymbol{q}|\to 0+} . \tag{2.31}$$

When applying this formula, the following facts have to be kept in mind:

- The quantity $S$ (also known as $d^2S/d\Omega d\hbar\omega$) on the left hand side is the Raman efficiency per unit penetration depth as defined in (2.2).

- On the right hand side, there is a minus sign, because the imaginary part of a retarded susceptibility is always negative. We quote $\mathrm{Im}(\omega - \omega_0 + i0)^{-1} = -\pi\delta(\omega - \omega_0)$ as an example. The factor $1/\pi$ cancels the factor $\pi$ in the expression for *half* of the residue of the simple pole $(\omega - \omega_0 + i0)^{-1}$.

- The factor $1 + n_\omega$ takes into account stimulated emission of S-photons for temperatures $T > 0$. It becomes 1 for $k_BT \ll \omega$ and $k_BT/\omega$ for $k_BT \gg \omega$ and is important therefore only for finite temperatures and Raman shifts comparable to $k_BT$.

- The factor $|4/(1+\tilde{n}^2)|^2$ involves the refractive index $\tilde{n}$ and takes into account reflection losses etc. (see (2.6) and [2.2]).

- $V_{\mathrm{Sa}}$ represents the *illuminated* volume of the sample, that is, the illuminated area times the penetration depth.

- The factor $(\omega_S/\omega_L)^2$ would become $(\omega_S/\omega_L)$ when defining the scattering efficiency by the *number* of scattered photons normalized to the number of incoming photons. But we used energy current densities instead of particle current densities.

- The imaginary part $\mathrm{Im}\,\chi_{\mathrm{Raman}}$ of the Raman susceptibility is proportional to the sample volume $V_{\mathrm{Sa}}$ and cancels the factor $1/V_{\mathrm{Sa}}$ such that the Raman efficiency (per unit penetration depth) becomes independent of the sample size.

- The dependence of the Raman efficiency on the polarization configuration is put into the Raman susceptibility. The Raman vertex used in the definition (2.29) and (2.19) of the Raman susceptibility is given by (2.27).

The evaluation of the Raman susceptibility shall be given separately, (i) in Sect. 2.3 for the superconducting phase and for Raman shifts in the pair breaking region, and (ii) in Sec. 2.4 for large Raman shifts in the superconducting phase and for the normal phase.

### 2.2.14 The Raman susceptibility and Feynman diagrams

Equations (2.28) and (2.30) relate the Raman efficiency directly to the imaginary part of the Raman susceptibility. This is a very important result, because we will see that the Raman susceptibility is related to the polarization loops in the theory of Green's functions (see App. D). We can therefore employ Green's function techniques to calculate the Raman susceptibility, and will find this possibility *indispensable* when trying to *generalize* (2.26) to the case when the system is superconducting, includes impurities, or when electronic screening has to be taken into account.

Relating the Raman efficiency to the methods of Green functions, however, requires another intermediate step. This is the *time-ordered Raman susceptibility*, given by

$$\chi_{\text{Raman}}(\boldsymbol{q},t) = -\frac{i}{\hbar}\langle 0|T\{\tilde{\rho}_{\boldsymbol{q}}(t)\tilde{\rho}_{-\boldsymbol{q}}(0)\}|0\rangle \tag{2.32}$$

for the zero-temperature case. For finite temperatures, the generalization of the time-ordered Raman susceptibility requires the methods of the imaginary-time Green's functions (also called Matsubara Green's function. See [2.1], Chap. 3.2). It can be seen rather easily that the retarded and the time-ordered Raman susceptibility are related mutually by

$$\begin{aligned} \operatorname{Re}\chi_{\text{Raman}}(\boldsymbol{q},\omega) &= \operatorname{Re}\chi^{\text{ret}}_{\text{Raman}}(\boldsymbol{q},\omega) \\ \operatorname{Im}\chi_{\text{Raman}}(\boldsymbol{q},\omega) &= \operatorname{sign}(\omega)\operatorname{Im}\chi^{\text{ret}}_{\text{Raman}}(\boldsymbol{q},\omega)\ . \end{aligned} \tag{2.33}$$

But because in (2.30) we are interested usually only in nonnegative frequencies, it is possible to just consider the time-ordered Raman susceptibility.

We now express the time-ordered Raman susceptibility using Green's functions. Inserting the Raman vertex (2.16) into the definition of the time-ordered Raman susceptibility (2.32), and using the expression for the effective Raman density operator from (2.19), expectation values of the form (note (2.18))

$$\sum_{\boldsymbol{k}\boldsymbol{k}'}\gamma(\boldsymbol{k},\boldsymbol{q})\gamma(\boldsymbol{k}',-\boldsymbol{q})\langle 0|T\{c^{+}_{\boldsymbol{k}+\boldsymbol{q}}(t)c_{\boldsymbol{k}}(t)c^{+}_{\boldsymbol{k}'-\boldsymbol{q}}(0)c_{\boldsymbol{k}'}(0)\}|0\rangle \tag{2.34}$$

appear. Using Wick's theorem (see App. D), the time-ordered expectation value can be written as

$$\delta_{\boldsymbol{q},0}\Theta(\xi_{\boldsymbol{k}}-\xi_F)\Theta(\xi_{\boldsymbol{k}'}-\xi_F) - i^2 G(\boldsymbol{k}+\boldsymbol{q},t)G(\boldsymbol{k},-t)\delta_{\boldsymbol{k}+\boldsymbol{q},\boldsymbol{k}'}\ . \tag{2.35}$$

As already stressed and in view of the fact that $c \gg v_F$, we consider the case $\boldsymbol{q} \to 0$, but $\boldsymbol{q} \neq 0$, in Raman scattering. Using the expression (2.18) which relates the amplitude of time-reversal-related Raman processes, the time-ordered Raman susceptibility becomes

$$\chi_{\text{Raman}}(\boldsymbol{q},t) = \frac{i}{\hbar}\sum_{\boldsymbol{k}}|\gamma(\boldsymbol{k},\boldsymbol{q})|^2 G(\boldsymbol{k}+\boldsymbol{q},t)G(\boldsymbol{k},-t) \tag{2.36}$$

and is expressed in the diagram in Fig. 2.6 (for simplicity, we only take into account one electronic band. The extension to the case of more than one band is straightforward).

Figure 2.6 shows the diagram in the standard way. At the vertex $\gamma_{\boldsymbol{k}}$, an incoming photon of wave vector $\boldsymbol{k}_L$ and frequency $\omega_L$ is annihilated, an electron-hole pair with a wave vector of $\boldsymbol{q}$ is created, while a scattered photon of wave vector $\boldsymbol{k}_S$ and frequency $\omega_S$ is created. *The* *fact that the Raman vertex appears twice in the diagram, is directly related to the Golden Rule, in which it also appears quadratically.* The $\delta$-function in the Golden Rule is given by the imaginary part of the self-energy corresponding to the polarization-loop-like diagram in Fig. 2.6.

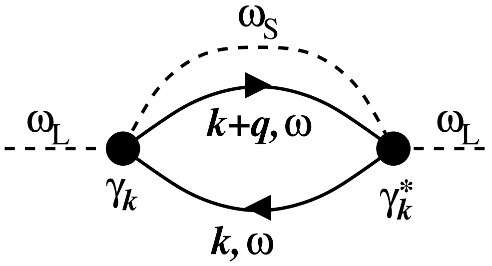

Figure 2.6: The polarization loop for the Raman susceptibility.

Remembering that the Raman vertex is a sum of two contributions, namely the vertices shown in Figs. 2.2 and 2.3, we can consider the Raman susceptibility to consist of the four contributions in Fig. 2.7.

The panels (a) and (d) in Fig. 2.7 show the contributions from scattering via the Hamiltonians $H_{\boldsymbol{Ap}}$ and $H_{\boldsymbol{A}^2}$, respectively. The other two panels (b) and (c) are interference contributions.

We call the vertex in Fig. 2.2 the *ρ-part of the Raman vertex*, because in the isotropic case, when $\gamma_{\boldsymbol{k}}$ is $\boldsymbol{k}$-independent, Fig. 2.7(a) describes the density-density response function (susceptibility). The vertex in Fig. 2.3 will be called the *jj-part of the Raman vertex*, because the vertices are related to matrix elements of the momentum operator and therefore to the current operator.

The vertical lines in the four diagrams of Fig. 2.7 denote the final state of the Raman scattering process for which energy conservation is enforced. Just calculating the diagram (d) according to Feynman's rules and ignoring the vertical line, would give a wrong result, because it contains also contributions, which are renormalizing the dielectric function, that is, they are related to light absorption and not Raman scattering (see Subsect. 3.4.1).

### 2.2.15 Some preliminary words about electronic screening

The electronic screening caused by the presence of the Coulomb interaction is treated using quantum many-body theory and the random phase approximation (RPA). The effect of screening an electron-hole excitation (whose electron possesses a wavevector $\boldsymbol{k}$ and is in band $n_f$, and whose hole possesses a wavevector $-\boldsymbol{k}$ and is in band $n_i$) on an electronic susceptibility is given in the framework of this approximation by the equation equivalent to the sum of the diagrams shown in Fig. 2.8(a) which involves the *effective* or *screened* Coulomb interaction depicted by the double wavy line. This effective Coulomb interaction is defined by the series in Fig. 2.8(b), a summation over the quantum numbers $(\alpha, \beta, \boldsymbol{q})$, $(\alpha, \beta, \boldsymbol{q})$, etc., is implied (Greek letters denote band indices). The screening is related to the *longitudinal* dielectric function, whereas the refractive index in (2.31) is related to the *transversal* dielectric function.

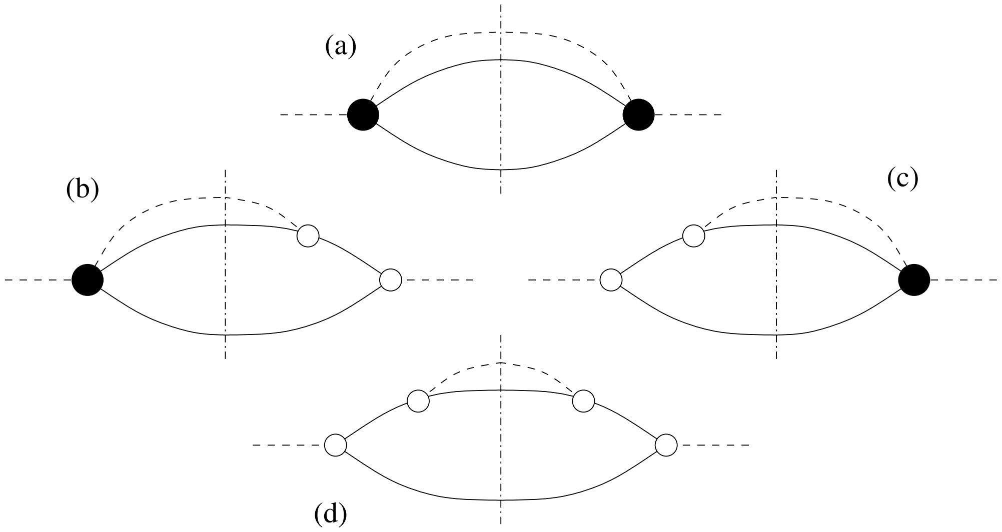

Figure 2.7: Diagrams for the four lowest order contributions to electronic Raman scattering.

The following discussion of electronic screening is based upon the assumption [2.5] that *the Coulomb matrix element between states in one and only one band is much larger than between states in different bands.*

We start the discussion with the $\rho$-part of the Raman vertex, the easier one. In the diagram of Fig. 2.2, there is only one electron-hole excitation to be screened. If we screen the electron-hole pair by the effective Coulomb interaction, we obtain the diagram in Fig. 2.9(b) *in addition* to the one in Fig. 2.2. The selection rules tell us that the electron-hole excitation created by the light is an intraband excitation, that is, $\alpha = \beta$. The effective Coulomb interaction is large if all the states involved in the matrix element are from the same band. Therefore, the diagram with $\alpha = \beta = \gamma = \delta$ is larger than the other ones which will be neglected. We conclude that *the electronic screening is intraband screening only* for the $\rho$-part of the Raman vertex.

The $jj$-part of the Raman vertex (Fig. 2.3) is more delicate, because it can be screened in two different places: after the creation of the initial electron-hole pair, that is, in the intermediate state with no photons, or after the emission of the scattered photon, denoted by A and B, respectively, in the diagram (a) of Fig. 2.9. Let us look closer to the case A. The incoming photon is annihilated and an electron-hole pair is created in the first vertex. The selection rules for the $\boldsymbol{Ap}$ vertex require this electron-hole pair to correspond to an interband excitation, and therefore the states $\alpha$ and $\beta$ must be in different bands. The Coulomb matrix element related to case A therefore involves states from different bands and is consequently very small. *We will therefore neglect electronic screening of the electron-hole pair present in the intermediate state.*

The discussion of case B is similar to the related issue for the $\rho$-part of the Raman vertex. The selection rules demand $\gamma \neq \delta$. The emission of the scattered light causes a transition of the electron (or hole) from band $\gamma$ to $\epsilon$. Therefore, both cases, $\delta = \epsilon$ and $\delta \neq \epsilon$ are possible. The one which will not be neglected has $\delta = \epsilon = \xi = \eta$. And consequently, from the transitions generated by the $\boldsymbol{Ap}$ vertex *only the intraband transitions will be screened.*

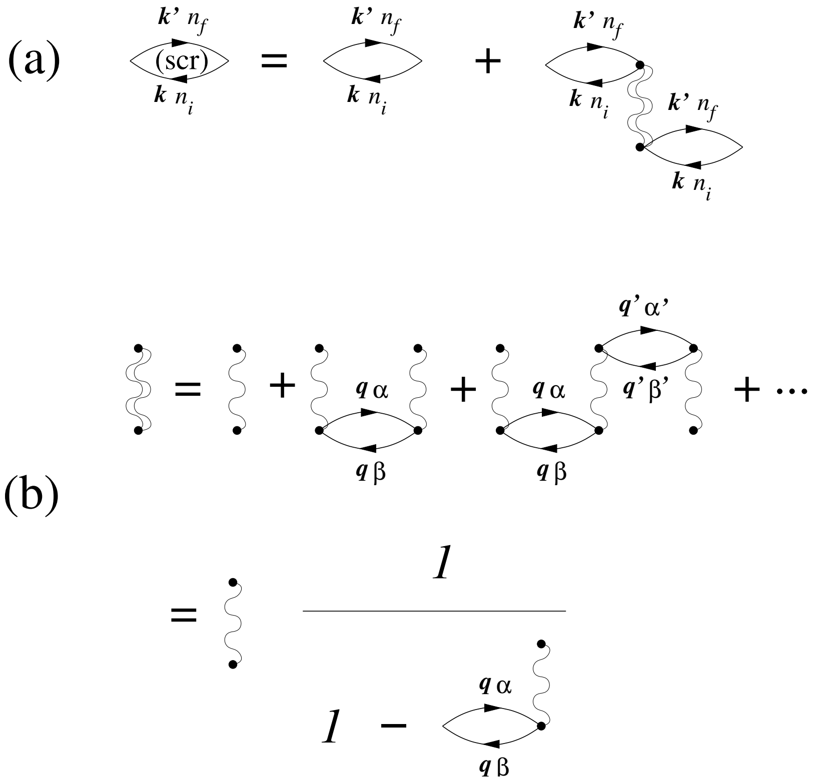

Figure 2.8: (a) Electronic screening of an electron-hole loop, and (b) the effective Coulomb interaction. A summation over the quantum numbers $(\alpha, \beta, \boldsymbol{q})$, $(\alpha, \beta, \boldsymbol{q})$, and so on, is implied (Greek letters denote band indices).

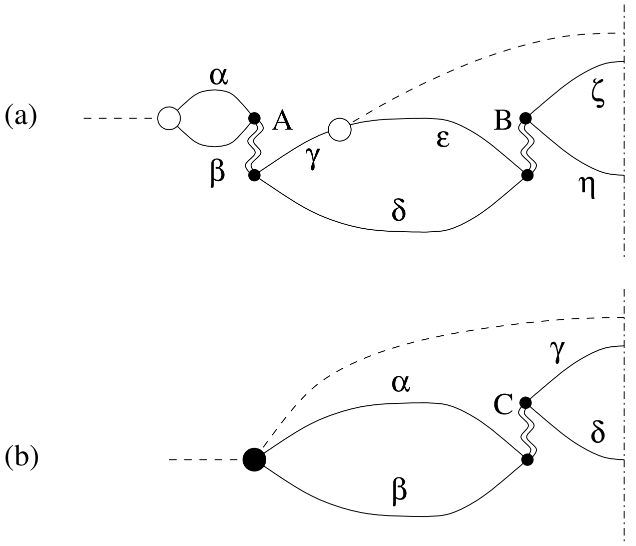

Figure 2.9: Screening the vertices. (a) the $jj$-part of the Raman vertex, and (b) the $\rho$-part of the Raman vertex. The Greek letters denote band indices.

### 2.2.16 Effective mass approximation and high-$T_c$ superconductors

According to the LMTO calculations, in the band structure of Y-123 and Y-124, there are bands above a band gap between approximately 2 eV and 2.5 eV above the Fermi energy. These bands can present a problem with respect to the discussion on resonance effects in Subsect. 2.2.11, because they are almost resonant for typical laser wavelengths like 514.5 nm. The same is true for the conduction bands, which extend until 2 eV above the Fermi surface. Note that due to the strong on-site repulsion at the Cu atoms, correlation effects are expected to strongly influence the electronic structure. It is possible that at energies of the order of 1 eV the Fermi surface the picture of the Hubbard bands[2.14, 2.15, 2.16] is a better description of the band structure and may explain the weak dependence of the Raman spectra on the laser frequency observed for laser frequencies in the visible range. The band structure shows many bands at about the laser frequency below the Fermi energy. These should yield resonant contributions to the Raman efficiency.

Because the Raman vertex $\gamma_{\boldsymbol{k}}$ is, in the given approximation, the second derivative of the energy with respect to $\boldsymbol{k}$, the $A_{2g}$ component for tetragonal crystals vanishes in this version of the theory (the irreducible representation $A_{2g}$ corresponds to the symmetry of an antisymmetric tensor). If one considers once more the effects of a nearby resonance, it can be easily seen that the Raman tensor does not have to be symmetric. This stresses again the questionability of the effective mass approach if the scattering is resonant.

## 2.3 The superconducting state

### 2.3.1 Introduction

The function which describes the excitations in the superconducting state is the *Tsuneto-function*. This function therefore plays a very important role in the theory of electronic Raman scattering and will be discussed in great detail here.

In a first part, we derive the Tsuneto-function using the formalism of Green's functions involving Matsubara-frequencies[17] and discuss its poles. Subsequently a short discussion of vertex corrections follows. Then the *Fermi-surface Tsuneto-function* is defined and calculated. This function is essentially the Tsuneto-function integrated perpendicular to the Fermi-surface. Instead of calculating $k$-space averages involving the Tsuneto-function, in

---

[17] The main difference between the Green's functions $G$ for $T = 0$ and $G^T$ for $T \neq 0$ is an additional Boltzmann factor $\exp(-\beta H)/\operatorname{Tr}\exp(-\beta H)$ in the average which defines $G^T$. As a consequence, there are *two* exponentials $\exp(-\beta H)$ and $\exp(\pm iHt/\hbar)$ in the expression for $G^T$ which both have to be expanded in perturbation series, making this task very complicated. In the *Matsubara-formalism* [2.17, 2.1, 2.13], the inverse temperature $\beta$ is regarded as imaginary part of a complex time variable $\tilde{t} = t \pm i\hbar\beta$, and the two exponentials are treated as one. This leads to the definition of the *imaginary-time* or *Matsubara Green's function* $\mathcal{G}(\tau)$ with $\tau = it$. For Matsubara Green's functions, the diagram rules from diagrammatic perturbation theory are applicable, therefore it can be expanded in a series of Feynman diagrams. The temperature-dependent Green's function $G^T$, however, does not have a diagrammatic expansion, but it can be determined from $\mathcal{G}$ by an analytic continuation. It follows from the definition of the Matsubara Green's function that $\mathcal{G}(\tau) = -\mathcal{G}(\tau + \beta)$ for fermions, and $\mathcal{G}(\tau) = +\mathcal{G}(\tau + \beta)$ for bosons (with $-\beta < \tau < 0$ in both cases). Therefore, the Matsubara Green's function is *periodic in* $\tau$ and the Fourier transform is given by the coefficients $\mathcal{G}_n \equiv \mathcal{G}(i\omega_n)$ (where $n$ is an integer number); the frequencies $\omega_n$ are called *Matsubara frequencies* and given by $\omega_n = 2\pi(n + 1)/\beta$ for fermions and by $\nu_n = 2\pi n/\beta$ for bosons.

some cases one can do $\varphi$-integrations[18] involving the Fermi-surface Tsuneto-function. Especially for numerical applications, this is much easier than the $k$-space integrations.

A next point is the discussion of some limiting cases and singularities which arise when the imaginary part of the Raman susceptibility is calculated. Then electronic screening is discussed. The effects of impurities, nontetragonality and the presence of multiple bands are also treated. Under some particular circumstances the electronic screening can *enhance* the imaginary part of the Raman susceptibility. This effect of *antiscreening* is also investigated.

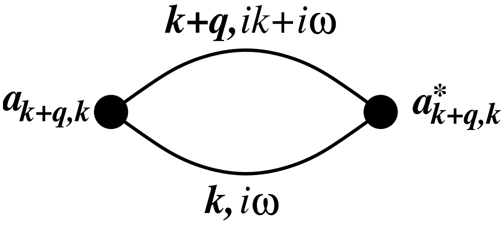

Figure 2.10: A polarization loop.

### 2.3.2 The Tsuneto-function

The Tsuneto-function is the basic function for the calculation of polarization loops in the superconducting state. To determine this function, we use the temperature-dependent Matsubara technique [2.17, 2.13, 2.1, 2.18] and employ Nambu's formalism [2.19, 2.18]. In this formalism, the Green's function of a quasiparticle pair is the $2 \times 2$-matrix

$$\hat{\mathcal{G}}(\boldsymbol{k}, ik_0) = \frac{ik_0 + \xi_{\boldsymbol{k}}\hat{\tau}_3 + \Delta_{\boldsymbol{k}}\hat{\tau}_1}{(ik_0)^2 - E_{\boldsymbol{k}}^2} \ , \tag{2.37}$$

where $ik_0$ is a fermionic Matsubara frequency, $E_{\boldsymbol{k}} = \sqrt{\xi_{\boldsymbol{k}}^2 + \Delta_{\boldsymbol{k}}^2}$ is the quasiparticle dispersion, $\epsilon_{\boldsymbol{k}}$ is the dispersion relation of the electrons, $\xi_{\boldsymbol{k}} = \epsilon_{\boldsymbol{k}} - \mu$ the dispersion relation measured with respect to the chemical potential, $\Delta_{\boldsymbol{k}}$ is the gap function, and $\hat{\tau}_i$ are the Pauli matrices. When calculating polarization loops (Fig. 2.10) for the superconducting state, the symmetry of the vertices $a_{\boldsymbol{k}+\boldsymbol{q},\boldsymbol{k}}$ with respect to the transformation $\boldsymbol{k} \rightarrow -\boldsymbol{k}$ plays an important role. For a current-current polarization loop, which is the quantity to be calculated when determining the infrared absorption, the vertex in the case $\boldsymbol{q} = 0$ is proportional to the momentum operator, and therefore changes sign when $\boldsymbol{k}$ does. The density vertex in the density-density polarization loop which, for example, occurs in the calculation of ultrasonic attenuation, or the Raman vertex, both do not change sign when $\boldsymbol{k}$ does. These two cases are distinguished in the Nambu-formalism in that for the first case, the vertex is proportional to $\hat{\tau}_0$, and in the second to $\hat{\tau}_3$ (see [2.18]). We are going to calculate a loop with vertices of the second type by evaluating the so-called *Tsuneto-function* [2.20], defined by the diagram in Fig. 2.10

$$\lambda_{\boldsymbol{k}}(i\omega) \equiv -\frac{1}{\beta} \sum_{ik_0} \mathrm{Tr}\left[\hat{\mathcal{G}}(\boldsymbol{k}+\boldsymbol{q}, ik_0 + i\omega)\hat{\tau}_3\hat{\mathcal{G}}(\boldsymbol{k}, ik_0)\hat{\tau}_3\right] \ . \tag{2.38}$$

---

[18] The variable $\varphi$ denotes the azimuthal angle in the two-dimensional $(k_x, k_y)$ space. It is defined by $\tan\varphi = k_y/k_x$, and $\varphi = 0$ corresponds to the $k_x$-axis.

| $i$ | $z_i$ | $n_F(z_i)\,\mathrm{Res}_{z=z_i}\,\mathcal{L}(\boldsymbol{k},z,\boldsymbol{q},i\omega)$ |
|---|---|---|
| 1 | $-i\omega+E'$ | $n_F(E')\cdot\frac{E'(E'-i\omega)+\epsilon'\epsilon-\Delta'\Delta}{(2E')[(E'-i\omega)^2-E^2]}$ |
| 2 | $-i\omega-E'$ | $[1-n_F(E')]\cdot\frac{E'(E'+i\omega)+\epsilon'\epsilon-\Delta'\Delta}{(-2E')[(E'+i\omega)^2-E^2]}$ |
| 3 | $E$ | $n_F(E)\cdot\frac{E(E+i\omega)+\epsilon'\epsilon-\Delta'\Delta}{[(E+i\omega)^2-E'^2](2E)}$ |
| 4 | $-E$ | $[1-n_F(E)]\cdot\frac{E(E-i\omega)+\epsilon'\epsilon-\Delta'\Delta}{[(E-i\omega)^2-E'^2](-2E)}$ |

Table 2.1: Poles of the density-density polarization loop. The unprimed quantities $E$, $\epsilon$, and $\Delta$ have an index $\boldsymbol{k}$, the respective primed quantities have an index $\boldsymbol{k}+\boldsymbol{q}$.

In this expression, the trace of products of the form $\hat{\tau}_i\hat{\tau}_3\hat{\tau}_j\hat{\tau}_3$ is taken. The trace of $\hat{\tau}_0$ is 2 whereas for all other Pauli matrices it vanishes. Of the products $\hat{\tau}_i\hat{\tau}_j$, only those with $i=j$ are proportional to $\hat{\tau}_0$, therefore in the product $\hat{\tau}_i\hat{\tau}_3\hat{\tau}_j\hat{\tau}_3$, the condition $i=j$ has to be fulfilled. The combinations contributing to the trace then are $(\hat{\tau}_0\hat{\tau}_3)^2=\hat{\tau}_0$ as well as $(\hat{\tau}_3\hat{\tau}_3)^2=\hat{\tau}_0$ and $(\hat{\tau}_1\hat{\tau}_3)^2=(-i\hat{\tau}_2)^2=-\hat{\tau}_0$. The trace in (2.38) thus becomes

$$\mathcal{L}(\boldsymbol{k},ik_0,\boldsymbol{q},i\omega)=2\cdot\frac{(ik_0+i\omega)ik_0+\xi_{\boldsymbol{k}+\boldsymbol{q}}\xi_{\boldsymbol{k}}-\Delta_{\boldsymbol{k}+\boldsymbol{q}}\Delta_{\boldsymbol{k}}}{[(ik_0+i\omega)^2-E^2_{\boldsymbol{k}+\boldsymbol{q}}][(ik_0)^2-E^2_{\boldsymbol{k}}]}\ . \tag{2.39}$$

Note that replacing the two $\hat{\tau}_3$ vertices in (2.38) by $\hat{\tau}_0$ yields the same result with the exception that the term $-\Delta_{\boldsymbol{k}+\boldsymbol{q}}\Delta_{\boldsymbol{k}}$ has a plus sign. In order to evaluate the Matsubara sum in (2.38), we have to determine the residues of the 4 poles $z_i$ of the expression (2.39) in the complex $ik_0$ plane, and multiply every residue with the value of the Fermi function $n_F(z_i)$ at the pole. The resulting four contributions to $\mathcal{L}(\boldsymbol{k},ik_0,\boldsymbol{q},i\omega)$ are given in Tab. 2.1.

For Raman scattering, the limit $\boldsymbol{q}\to 0+$ is adequate. It implies that the residues at poles 1 and 4 become equal except for a minus sign. The same happens for the other two poles. Adding the four terms together yields

$$\begin{aligned}\lambda_{\boldsymbol{k}}(i\omega)&=[1-2n_F(E_{\boldsymbol{k}})]\times\\&\quad\left[\frac{E_{\boldsymbol{k}}(E_{\boldsymbol{k}}-i\omega)+\xi^2_{\boldsymbol{k}}-\Delta^2_{\boldsymbol{k}}}{2E_{\boldsymbol{k}}[(E_{\boldsymbol{k}}-i\omega)^2-E^2_{\boldsymbol{k}}]}+\frac{E_{\boldsymbol{k}}(E_{\boldsymbol{k}}+i\omega)+\xi^2_{\boldsymbol{k}}-\Delta^2_{\boldsymbol{k}}}{2E_{\boldsymbol{k}}[(E_{\boldsymbol{k}}+i\omega)^2-E^2_{\boldsymbol{k}}]}\right]\\&=-\tanh\left(\frac{E_{\boldsymbol{k}}}{2k_BT}\right)\frac{\Delta^2_{\boldsymbol{k}}}{i\omega E_{\boldsymbol{k}}}\left[\frac{1}{i\omega-2E_{\boldsymbol{k}}}+\frac{1}{i\omega+2E_{\boldsymbol{k}}}\right]\ .\end{aligned} \tag{2.40}$$

The factor $1/i\omega$ vanishes when doing a decomposition in partial fractions, the final result is

$$\lambda_{\boldsymbol{k}}(i\omega)=-2\tanh\left(\frac{E_{\boldsymbol{k}}}{2k_BT}\right)\frac{\Delta^2_{\boldsymbol{k}}}{E^2_{\boldsymbol{k}}}\left[\frac{1}{i\omega-2E_{\boldsymbol{k}}}-\frac{1}{i\omega+2E_{\boldsymbol{k}}}\right]\ . \tag{2.41}$$

This function is the *Tsuneto-function* for bosonic Matsubara frequencies $i\omega$. The retarded analytical continuation is performed by substituting $i\omega$ by $\omega+i\delta$. This yields for $T=0$ the *retarded Tsuneto-function*

$$\lambda_{\boldsymbol{k}}(\omega)=\frac{|\Delta_{\boldsymbol{k}}|^2}{E^2_{\boldsymbol{k}}}\left[\frac{1}{\omega-2E_{\boldsymbol{k}}+i\delta}-\frac{1}{\omega+2E_{\boldsymbol{k}}+i\delta}\right]\ . \tag{2.42}$$

This function $\lambda_{\boldsymbol{k}}(\omega)$ has two poles, at $\omega = \pm 2E_{\boldsymbol{k}} - i\delta$, corresponding to the excitation energy of a pair $(\boldsymbol{k}, -\boldsymbol{k})$ of quasiparticles. It is a retarded function being analytic in the upper half plane (UHP) of the complex frequency plane. Note that $\lambda_{\boldsymbol{k}}$ obeys the symmetry relation

$$\lambda^*_{\boldsymbol{k}}(\omega) = \lambda_{\boldsymbol{k}}(-\omega) \qquad \text{or} \qquad \begin{array}{l} \operatorname{Re}\lambda_{\boldsymbol{k}}(-\omega) = \operatorname{Re}\lambda_{\boldsymbol{k}}(\omega) \\ \operatorname{Im}\lambda_{\boldsymbol{k}}(-\omega) = -\operatorname{Im}\lambda_{\boldsymbol{k}}(\omega)\ . \end{array} \tag{2.43}$$

This relation is mandatory for a susceptibility (such as $\lambda_{\boldsymbol{k}}(\omega)$). Due to the fact that $\lambda_{\boldsymbol{k}}(\omega)$ is analytic in the UHP of the complex $\omega$-plane, the Kramers-Kronig relations (KKR) are applicable. They are given by

$$\begin{aligned} \operatorname{Re}\lambda_{\boldsymbol{k}}(\omega) &= \frac{1}{\pi}\int_{-\infty}^{\infty}\frac{d\omega'}{\omega'-\omega}\operatorname{Im}\lambda_{\boldsymbol{k}}(\omega') \\ \operatorname{Im}\lambda_{\boldsymbol{k}}(\omega) &= -\frac{1}{\pi}\int_{-\infty}^{\infty}\frac{d\omega'}{\omega'-\omega}\operatorname{Re}\lambda_{\boldsymbol{k}}(\omega')\ . \end{aligned} \tag{2.44}$$

The symmetry (2.43) may be included explicitly in the KKR; then the integrals extend over positive frequencies only.

### 2.3.3 The Fermi-surface Tsuneto-function

In the numerics section of this chapter (Sect. 2.5), we have to perform Brillouin zone averages of $\boldsymbol{k}$-dependent functions (e.g. the Raman vertex) $f_{\boldsymbol{k}}$ weighted by the Tsuneto-function

$$\langle f_{\boldsymbol{k}}\lambda_{\boldsymbol{k}}(\omega)\rangle_{BZ} \equiv V\int_{BZ}\frac{d^2k}{(2\pi)^2}f_{\boldsymbol{k}}\lambda_{\boldsymbol{k}}(\omega)\ .$$

These averages can be approximated by Fermi surface averages if $f_{\boldsymbol{k}}$ is a function of the angle $\varphi$ only. To show the explicit relation among the BZ and the FS integrations, we use a circular two-dimensional Fermi surface $|\boldsymbol{k}| = k_F$ and introduce radial coordinates:

$$\langle a_{\boldsymbol{k}}\lambda_{\boldsymbol{k}}(\omega)\rangle_{BZ} = \int\frac{d\varphi}{2\pi}a_\varphi\cdot V\int\frac{k\,dk}{2\pi}\lambda_{\boldsymbol{k}}(\omega) \equiv \langle a_\varphi\lambda^{FS}_\varphi(\omega)\rangle_{FS}\ ,$$

where $a_\varphi = a_{\boldsymbol{k}(\varphi)}$ is a function only depending on $\varphi$, and $\lambda^{FS}_\varphi(\omega)$ is the *Fermi-surface Tsuneto-function* (FS-Tsuneto-function) defined by

$$\lambda^{FS}_\varphi(\omega) \equiv V\int\frac{k\,dk}{2\pi}\lambda_{\boldsymbol{k}}(\omega)\ . \tag{2.45}$$

To evaluate (2.45), we write the dispersion law as $\epsilon_{\boldsymbol{k}} = \epsilon_k = v_F\cdot(k-k_F)$, the quasiparticle dispersion as $E^2_{\boldsymbol{k}} = \epsilon^2_k + |\Delta_\varphi|^2$ (perpendicular to the FS, only $\epsilon_k$ changes, and parallel to it, only $\Delta_\varphi$ changes), and restrict the BZ-integration to a ring $k_F - \delta k < k < k_F + \delta k$ around the Fermi surface. Introducing also $\tilde{k} = k + k_F$ yields

$$\lambda^{FS}_\varphi(\omega) \approx \frac{V}{2\pi}\int_{-\delta k}^{\delta k}(\tilde{k}+k_F)\lambda_{k=\tilde{k}-k_F,\varphi}(\omega)\,d\tilde{k}\ .$$

Let us now write $\lambda_{E,\varphi} \equiv \lambda_{\tilde{k}=\tilde{k}(E),\varphi}$ which is an even function in $\tilde{k}$. Therefore the term $\tilde{k}\lambda_{\tilde{k}}$ is odd in $\tilde{k}$ and drops out of the integral. Writing $\Delta$ for $|\Delta_{\boldsymbol{k}}|$ and using $d\tilde{k}/dE = EdE/(v_F\sqrt{E^2-\Delta^2})$ and $E_c = E(\delta k + k_F)$, we obtain

$$\lambda_\varphi^{FS}(\omega) \approx 2\frac{V}{2\pi}\frac{k_F}{v_F}\int_0^{E_c} \frac{E\,dE}{v_F\sqrt{E^2-\Delta^2}}\lambda_{E,\varphi}(\omega)\ . \tag{2.46}$$

Because of $\operatorname{Im}\lambda_{\boldsymbol{k}}(\omega) = (|\Delta_{\boldsymbol{k}}|^2/E_{\boldsymbol{k}}^2)[-\pi\delta(\omega-2E_{\boldsymbol{k}}) + \pi\delta(\omega+2E_{\boldsymbol{k}})]$, the imaginary part $\operatorname{Im}\lambda_\varphi^{FS}(\omega)$ is easily evaluated:

$$\begin{aligned}\operatorname{Im}\lambda_\varphi^{FS}(\omega) &\approx 2\frac{V}{2\pi}\frac{k_F}{v_F}\int_0^{E_c}\frac{E\,dE}{\sqrt{E^2-\Delta^2}}\left(+\pi\frac{\Delta^2}{E^2}\right)\delta(2E+\omega)\\ &\approx -\pi\frac{V}{2\pi}\frac{k_F}{v_F}\frac{4\Delta^2}{\omega\sqrt{\omega^2-4\Delta^2}} \qquad \text{for } |\omega| \geq 2\Delta\ .\end{aligned} \tag{2.47}$$

For the case $|\omega| < 2\Delta$, (2.47) vanishes. Note that (2.47) is an odd function of $\omega$ as required by (2.43). The prefactor $Vk_F/(2\pi v_F)$ is the density of states $\mathcal{N}_F(\varphi)$ at the Fermi surface per spin and per unit angle $\varphi$ in the two-dimensional $k$-space. Note that the term $\epsilon_{\boldsymbol{k}}$ has disappeared from the denominator in (2.47). The imaginary part of $\lambda_\varphi^{FS}(\omega)$ is now a function of $\omega/2\Delta$ only.

The integral appearing in the calculation of $\operatorname{Re}\lambda_\varphi^{FS}(\omega)$ is more complicated. It is sufficient, to consider only positive frequencies $\omega > 0$, because according to (2.43), $\operatorname{Re}\lambda_\varphi^{FS}(\omega)$ is an even function of frequency.

In order to be consistent with the approximations leading to (2.47) we perform a Kramers-Kronig transformation (KKT) given by (2.44) to obtain $\operatorname{Re}\lambda_\varphi^{FS}(\omega)$ from the former quantity. Using (2.47) and $\tilde{\omega} = \omega'/(2\Delta)$, we find

$$\operatorname{Re}\lambda_\varphi^{FS}(\omega) = -\mathcal{N}_F(\varphi)\frac{2\Delta}{\omega}\left(\int_{-\infty}^{-1} + \int_1^\infty\right)\frac{d\tilde{\omega}}{\tilde{\omega}\sqrt{\tilde{\omega}^2-1}(\tilde{\omega}-\omega/(2\Delta))}\ . \tag{2.48}$$

Taking into consideration that $\tilde{\omega}^{-1}(\tilde{\omega}-\omega/2\Delta)^{-1} = (2\Delta/\omega)[(\tilde{\omega}-\omega/2\Delta)^{-1} - \tilde{\omega}^{-1}]$ and the cancellation of the odd term in (2.48) gives

$$\operatorname{Re}\lambda_\varphi^{FS}(\omega) = -\mathcal{N}_F(\varphi)\frac{2\Delta}{\omega}\left(\int_{-\infty}^{-1} + \int_1^\infty\right)\frac{d\tilde{\omega}}{\sqrt{\tilde{\omega}^2-1}(\tilde{\omega}-\omega/(2\Delta))}\ .$$

The integrals above can be written in the analytic form

$$\begin{cases}\frac{4\Delta}{\sqrt{4\Delta^2-\omega^2}}\arctan\frac{\omega}{\sqrt{4\Delta^2-\omega^2}} & \text{for } \omega < 2\Delta\\ \frac{2\Delta}{\sqrt{\omega^2-4\Delta^2}}\ln\left|\frac{\omega-\sqrt{\omega^2-4\Delta^2}}{\omega+\sqrt{\omega^2-4\Delta^2}}\right| & \text{for } \omega > 2\Delta\ .\end{cases}$$

As a final result, the function $\lambda_\varphi^{FS}(\omega)$ can be written as

$$\operatorname{Im}\lambda_\varphi^{FS}(\omega) = -\pi\mathcal{N}_F(\varphi)\frac{2|\Delta_\varphi|}{\omega}\begin{cases}0 & \text{for } \omega < 2|\Delta_\varphi|\\ \frac{2|\Delta_\varphi|}{\sqrt{\omega^2-4\Delta^2}} & \text{for } \omega > 2|\Delta_\varphi|\end{cases} \tag{2.49}$$

$$\begin{aligned}\operatorname{Re}\lambda_\varphi^{FS}(\omega) &= -\pi\mathcal{N}_F(\varphi)\frac{2|\Delta_\varphi|}{\omega}\times\\ &\times\begin{cases}2\frac{1}{\pi}\frac{2|\Delta_\varphi|}{\sqrt{4\Delta^2-\omega^2}}\arctan\frac{\omega}{\sqrt{4\Delta^2-\omega^2}} & \text{for } \omega < 2|\Delta_\varphi|\\ \frac{1}{\pi}\frac{2|\Delta_\varphi|}{\sqrt{\omega^2-4\Delta^2}}\ln\left|\frac{\omega-\sqrt{\omega^2-4\Delta^2}}{\omega+\sqrt{\omega^2-4\Delta^2}}\right| & \text{for } \omega > 2|\Delta_\varphi|\end{cases}\end{aligned} \tag{2.50}$$

with the density of states $\mathcal{N}_F(\varphi) = (2\pi)^{-1} V k_F / v_F$. The logarithm in (2.50) has to be taken positive for positive frequencies and negative for negative frequencies (i.e. it has to be multiplied by $\operatorname{sign}\omega$). The imaginary part is an odd function and the real part an even function of frequency, as demanded by (2.43).

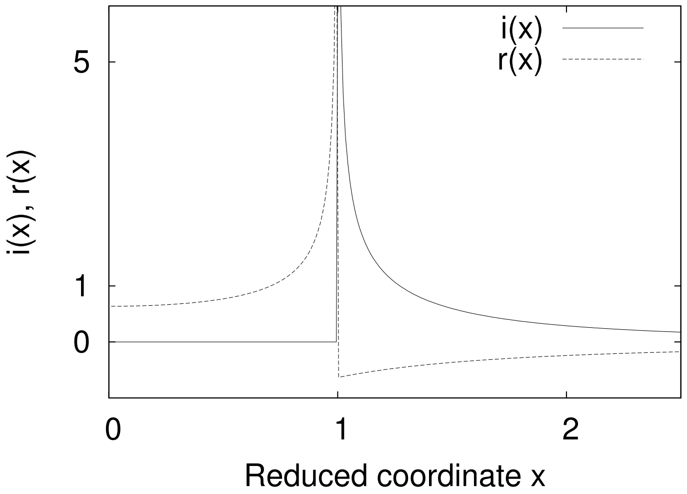

Figure 2.11: The functions $L_i(x)$ and $L_r(x)$ are up to a constant equal to the imaginary and real part of the FS-Tsuneto-Function, respectively. The $x$-coordinate corresponds to the reduced frequency $\tilde{\omega} = \omega/(2|\Delta_\varphi|)$.

In Fig. 2.11, the functions $L_i(\tilde{\omega})$ and $L_r(\tilde{\omega})$, defined by

$$\operatorname{Im}\lambda_\varphi^{FS}(\omega) = -\pi\mathcal{N}_F(\varphi)\cdot L_i\left(\frac{\omega}{2|\Delta_\varphi|}\right) \quad , \quad \operatorname{Re}\lambda_\varphi^{FS}(\omega) = -\pi\mathcal{N}_F(\varphi)\cdot L_r\left(\frac{\omega}{2|\Delta_\varphi|}\right)$$

are plotted versus the reduced frequency $\tilde{\omega} = \omega/(2|\Delta_\varphi|)$. We discuss first the imaginary part $\operatorname{Im}\lambda_\varphi^{FS}(\omega)$. This is the negative of the density for quasiparticle excitations at the point specified by the angle $\varphi$ on the Fermi surface. At this point, the gap has a value of $\Delta_\varphi$, and therefore the function vanishes for frequencies $\omega$ less than twice this value. At $\tilde{\omega} = 1$, the function has a inverse square root singularity, $L_i(\tilde{\omega}) \sim 1/\sqrt{2(\tilde{\omega}-1)}$ which is due to the fact that the group velocity of the quasiparticles vanishes at $\tilde{\omega} = 1$. For large frequencies $\tilde{\omega} \gg 1$, the function $L_i(\tilde{\omega})$ behaves like $\tilde{\omega}^{-2}$.

The real part $\operatorname{Re}\lambda_\varphi^{FS}(\omega)$ is just the Kramers-Kronig transform of the corresponding imaginary part. At $\tilde{\omega} = 0$ it takes on the value $2/\pi$. For $\tilde{\omega} \to 1$ but $\tilde{\omega} > 1$, it behaves like $L_r(\tilde{\omega}) \sim 1/\sqrt{2(1-\tilde{\omega})}$, and for $\tilde{\omega} \to 1$ but $\tilde{\omega} > 1$, it becomes $-2/\pi$. Note that there is no pole here! In the case $\tilde{\omega} \gg 1$, the asymptotic expression $L_r(\tilde{\omega}) \sim -(1/\pi)\tilde{\omega}^{-2}\ln(4\tilde{\omega}^2)$ is valid.

## 2.3.4 Low-frequency asymptotic laws

In the next paragraph, it is shown that the frequency-dependent Raman efficiency, which is proportional to the Raman susceptibility, is given by Brillouin-zone averages involving products of some integer powers of the Raman vertex $\gamma_{\boldsymbol{k}}$ with the Tsuneto-function $\lambda_{\boldsymbol{k}}(\omega)$. Taking this for granted, the Raman efficiency can be shown to obey a very simple power-law frequency-dependence for frequencies low compared to the gap amplitude. The power-law dependence can be proved by applying straightforward scaling arguments which are extensively discussed in Sect. 2.9.

### 2.3.5 Zero-slope points of the gap-function

In this short paragraph, we show that points where the first derivative of the gap-function $\Delta_\varphi$ with respect to $\varphi$ vanishes, produce singularities in the imaginary part of the Raman susceptibility at a Raman shift which corresponds to the value of the gap-function at the zero-slope point.

As a model for the zero-slope point we take the gap-function $\Delta_\varphi = \Delta_0 - (\Delta_1/2)\,\varphi^2$ ($\Delta_0$ and $\Delta_1$ both are larger than zero, the case $\Delta_1 < 0 < \Delta_0$ is trivial) which has a zero-slope point at $\varphi = 0$ with a value for the gap of $\Delta_0$.

The imaginary part of the unscreened Raman susceptibility is given by the Fermi surface average $\langle \gamma_\varphi^2 \lambda_\varphi^{FS}(\omega)\rangle_{FS}$. We are going to investigate now the region around $\omega = 2\Delta_0$ and therefore introduce a variable $\delta$ by writing $\omega = 2\Delta_0 + \delta$. It is clear that for the case under discussion the $\varphi$-integration just has to be done in an interval from 0 to some small angle $\epsilon$ which has to be larger than $\sqrt{\delta_{max}/\Delta_1}$, if $\delta_{\max}$ is the maximum absolute value for $\delta$ to be considered.

The Raman vertex $\gamma_\varphi$ is assumed not to vanish at $\varphi = 0$, an can therefore be approximated by a constant $\gamma_0$ in the interval under consideration. As a consequence, we have to discuss only the integral

$$I(\delta) = \int_0^\epsilon d\varphi\ \mathrm{Im}\,\lambda_\varphi^{FS}(2\Delta_0 + \delta)\ .$$

Using (2.49) one notes immediately, that the factor $4|\Delta_\varphi|^2/\omega$ is almost constant in the integration interval an can be taken out of the integral.

We consider first the case $\delta > 0$ for which the imaginary part of the Tsuneto-function never vanishes. The combination $\omega^2 - |2\Delta_\varphi|^2$ equals to $\delta^2 + 4\Delta_0\delta + 4\Delta_0\Delta_1\varphi^2 + \Delta_1^2\varphi^4$. We neglect the term proportional to $\varphi^4$, because for sufficiently small $\epsilon$, this term is much smaller than the one quadratic in $\varphi$. The integral then becomes

$$I(\delta) = 2\Delta_0 \int_0^\epsilon d\varphi\, \frac{1}{\sqrt{\delta^2 + 4\Delta_0\delta + 4\Delta_0\Delta_1\varphi^2}} \sim C - \frac{1}{2}\ln(\delta^2 + 4\Delta_0\delta)$$

where $C$ is some constant. The term $\delta^2$ can be neglected for small values of $\delta$. Therefore, the imaginary part of the Raman susceptibility behaves like $-\ln(4\Delta_0\delta)/2$ for $\delta > 0$.

Next the case $\delta < 0$. Take $\delta$ fixed, then $\omega = 2\Delta_0 + \delta < 2\Delta_\varphi$ in the interval from 0 to some $\varphi_0(\delta)$. The integration then involves the $\varphi$-interval from $\varphi_0(\delta)$ to $\epsilon$ only, and is dependent on $\delta$. Taking this into consideration and performing steps similar to the ones from the former case, we obtain the asymptotic behavior $-\ln(-4\Delta_0\delta)/2$ for the imaginary part of the Raman susceptibility at the singularity. This is the same result as in the former case, but it arises by a delicate cancellation here.

If the Raman vertex becomes zero at $\varphi = 0$, the replacement of $\gamma_\varphi$ by a constant $\gamma_0$ in the Fermi-surface average is not possible. Instead, it should be replaced by a constant times a positive integer power of the angle $\varphi$. Repeating the calculation above, one can easily show that the asymptotic behavior at the singularity does not change.

In the next paragraphs, we show that electronic screening is very important for electronic Raman scattering and can remove the logarithmic singularities mentioned above. We anticipate the result for the imaginary part of the screened Raman susceptibility, which is given by the expression

$$\langle \gamma_\varphi^2 \lambda_\varphi^{FS}(\omega) \rangle_{FS} - \frac{\langle \gamma_\varphi \lambda_\varphi^{FS}(\omega) \rangle_{FS}^2}{\langle \lambda_\varphi^{FS}(\omega) \rangle_{FS}} \,, \tag{2.51}$$

(cf. Eq. (2.52) discussed in the next subsection) whose first term is the unscreened contribution, whereas the second one represents the electronic screening. An important property of (2.51) is its invariance under the replacement $\gamma_\varphi \to \gamma_\varphi + \text{const}$. *Contributions to the Raman susceptibility which are due to a constant part of the Raman vertex always vanish when the Raman susceptibility is screened!*

Consider again an integration along a short interval from 0 to $\epsilon$, and approximating the Raman vertex by a constant $\gamma_0 \neq 0$, we can again take it out of the averages in the screening contribution: The whole expression (2.51) vanishes. Therefore we conclude that the logarithmic singularities present in the imaginary part of the unscreened Raman susceptibility are cancelled by similar logarithmic singularities in the screening contribution. The imaginary part of the screened Raman susceptibility then is continuous at Raman shifts where the corresponding unscreened quantity has a singularity.

There is one exception to the observation above. In some cases, the screening term of (2.51) vanishes identically by symmetry. Then the logarithmic singularity is not removed. This, however, can be achieved when taking into account vertex renormalizations (see [2.21]).

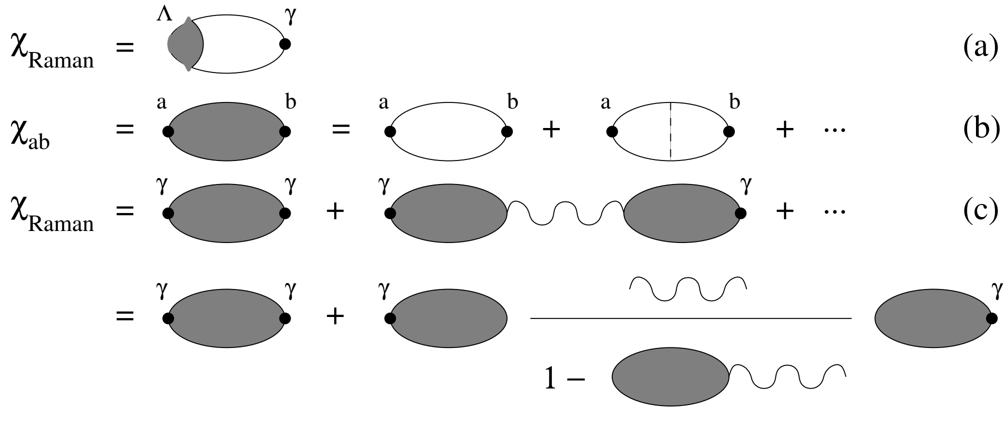

Figure 2.12: Incorporation of screening effects into the theory of Raman scattering by electronic excitations in HTSC. The grey shaded bubbles are sums of ladders contracted with vertices $a$ and $b$. Wavy lines correspond to the long-range Coulomb interaction, dashed lines to the attractive pairing interaction. The equation on the last line corresponds to Eq. (2.52).

### 2.3.6 Electronic screening

As pointed out in Ref. [2.5], the Raman susceptibility due to pair-breaking processes and including electronic screening is given by a polarization-like bubble consisting of a renormalized Raman vertex $\Lambda_{\boldsymbol{k}}$, a Raman vertex $\gamma_{\boldsymbol{k}}$, and in between two Green's function lines for bogolons (which are also called Bogoliubov quasiparticles) (Fig. 2.12(a)). The vertex renormalization includes corrections for Cooper-pair-producing attractive interaction as well as the repulsive Coulomb interaction, the Dyson equation for the vertex $\Lambda_{\boldsymbol{k}}$ in the limit $\boldsymbol{q} \to 0$ is given by Fig. 13 in Ref. [2.5].

To show more clearly the effect of screening, we write the equation for the Raman susceptibility as given in Fig. 2.12(b) and 2.12(c). Figure 2.12(b) (with $a = \gamma_{\boldsymbol{k}}$ and $b = \gamma_{\boldsymbol{k}}$) shows the unscreened susceptibility $\chi_{\gamma\gamma}$ given by a bare polarization bubble with two Raman vertices $\gamma_{\boldsymbol{k}}$ and the contraction of a BCS-like ladder sum with two Raman vertices. Therefore, $\chi_{\gamma\gamma}$ includes the attractive Cooper-pair-producing BCS interaction. We will see in the discussion in Sect. 2.10 (see also [2.18]) that the inclusion of the repulsive Coulomb interaction in the dash-dotted line in (b) is necessary in order to be consistent with the Ward identities (which correspond to local conservation laws) [2.22, 2.1, 2.18].

We include Coulomb screening by virtue of a RPA-like sum given in Fig. 2.12c. The effect of screening on the electronic Raman scattering can now easily be seen [2.4]. If we denote by $\chi_{ab}$ a bubble, renormalized by pairing interaction, with vertices $a$ and $b$ at the ends as in Fig. 2.12b, the RPA-chain can be easily summed (see Fig. 2.12c) yielding

$$\begin{aligned} \chi_{\text{Raman}}(\boldsymbol{q} \to 0, \omega) &= \chi_{\gamma\gamma}(\omega) - \left.\frac{\chi_{\gamma 1}^2(\omega)}{\chi_{11}(\omega) - V_{\boldsymbol{q}}^{-1}}\right|_{\boldsymbol{q}\to 0} \\ \chi_{\text{Raman}}(\boldsymbol{q} \to 0, \omega) &= \chi_{\gamma\gamma}(\omega) - \frac{\chi_{\gamma 1}^2(\omega)}{\chi_{11}(\omega)} \end{aligned} \tag{2.52}$$

in the long wavelength limit. In Eq. (2.52) we have used the fact that $V_{\boldsymbol{q}}/(1-\chi_{11}V_{\boldsymbol{q}})$ equals $-\chi_{11}^{-1}$ in the limit $\boldsymbol{q} \to \infty$.

Without taking into account Coulomb interaction, the Green's functions have a well-known massless pole (Goldstone mode) which is a consequence of the breaking of gauge symmetry in the superconducting phase (see, e.g. [2.23, 2.5]). Coulomb interaction makes this pole acquire a finite mass (which can be shown to correspond to the plasma frequency), so if we correctly include Coulomb screening (not done in Ref. [2.24]) we no longer have a Goldstone mode, but a massive Anderson-Bogoliubov mode [2.23, 2.5, 2.25]. This mode has the energy $\hbar\omega_p$ ($\omega_p$ is the plasma frequency) at the $\Gamma$-point and is therefore negligible for the low energy behavior of the Raman spectra.

The susceptibilities $\chi_{ab}$ in Fig. 2.12(b) are like a ladder sum contracted with vertices $a_{\boldsymbol{k}}$ and $b_{\boldsymbol{k}}$ and can be written as a sum

$$\chi_{ab}(\boldsymbol{q}{=}0, \omega) = \sum_{\boldsymbol{k}} a_{\boldsymbol{k}} b_{\boldsymbol{k}} \lambda_{\boldsymbol{k}}(\omega) \tag{2.53}$$

which involves the Tsuneto function [2.20] $\lambda_{\boldsymbol{k}}(\omega)$. For small values of $\boldsymbol{q}$ (compared to the inverse coherence length $\xi$ and the Fermi wave vector $k_F$), the attractive interaction does not have to be taken into account in the summation of the ladder, and the Tsuneto function is given simply by a unmodified bubble (the first term in the series in Fig. 2.12(b) only) and can be easily evaluated to be

$$\begin{aligned}\lambda_{\boldsymbol{k}}(\omega) =& \frac{\Delta_{\boldsymbol{k}}^2}{E_{\boldsymbol{k}}^2} \tanh\left(\frac{E_{\boldsymbol{k}}}{2T}\right) \times \\ & \times \left(\frac{1}{2E_{\boldsymbol{k}} + \omega + i0} + \frac{1}{2E_{\boldsymbol{k}} - \omega - i0}\right) ,\end{aligned} \tag{2.54}$$

as it was done in Subsect. 2.3.2.

Equation (2.54) involves the gap function $\Delta_{\boldsymbol{k}}$ (which depends on temperature) and the quasiparticle dispersion relation $E_{\boldsymbol{k}}^2 = \xi_{\boldsymbol{k}}^2 + \Delta_{\boldsymbol{k}}^2$ with $\xi_{\boldsymbol{k}}^2 = (\epsilon_{\boldsymbol{k}} - \epsilon_F)^2$. The constants $\hbar$ and $k_B$ have been set equal to 1. As already mentioned, vertex corrections due to the pairing interaction are neglected. This approximation is valid for $q \ll \xi^{-1}, k_F$ (Ref. [2.25]) and $\omega \ll \omega_p$, because the Anderson-Bogoliubov pole at the plasma frequency need no longer be included.

An important fact in the expressions above is that they contain only the absolute square of the gap function, that is, Raman scattering is *not phase sensitive*, and consequently cannot distinguish between a strongly anisotropic $s$-wave gap $|d_{x^2-y^2}|$ and a $d_{x^2-y^2}$-wave gap (see App. E concerning the different possible symmetries of the gap function).

In the preceding calculation of the unscreened correlation functions $\chi_{ab}$, we have neglected impurity scattering as well as scattering between quasiparticles (collisionless regime). In isotropic $s$-wave superconductors at $T = 0$ and for Raman shifts $\omega \ll 2\Delta$, it is reasonable to neglect impurity scattering, because in this regime pair breaking by impurity scattering is not possible [2.26]. Also, the scattering between quasiparticles can be neglected because their density is very small at low temperatures $T \ll T_c$. For $d$-wave superconductors, however, this is no longer correct. The effect of impurities will be discussed in the next subsection, whereas a discussion about scattering between quasiparticles can be found in Sec. 2.4.

The second term of (2.52), representing screening, vanishes if the average of $\gamma_{\boldsymbol{k}}\lambda_{\boldsymbol{k}}$ does. The Tsuneto function is fully symmetric, that is, has $A_{1g}$ ($D_{4h}$ group) or $A_g$ ($D_{2h}$) symmetry regardless of gap symmetry (for the notation of the irreducible representations of point groups, refer to [2.12], pg. 46f). As a consequence, the screening term vanishes unless the Raman vertex has the same symmetry as the crystal. In the tetragonal case, $A_{1g}$-like vertices are screened, but $B_{1g}$- and $B_{2g}$-like are not [2.27]. This is different for orthorhombic HTSC of the YBCO-type. In this case the Tsuneto function has $A_1$ symmetry, and the same is true for the $d_{x^2-y^2}$-like component of the inverse effective mass ($B_{1g}$ representation of $D_{4h}$ group, $A_g$ of $D_{2h}$). Consequently, in these orthorhombic crystals the $B_{1g}$ component is also screened. This discussion is also applicable to BISCO, but with interchanged roles of $B_{1g}$ and $B_{2g}$ modes because of the different orientation of the crystallographic unit cell with respect to the Cu-O bonds.

In tetragonal systems, the $B_{1g}$ component of the Raman vertex has nodes at the same position as the gap function. This has severe consequences for the low-energy part of the spectra [2.25]. In two dimensions, the existence of the nodes of the gap function in the case of a $d_{x^2-y^2}$ gap results in a linear density of states at low energies [2.28]. If the vertex has a finite value in this region, the imaginary part of the Raman susceptibility is also linear in the frequency. If the vertex has a node, however, its magnitude squared becomes quadratic with respect to the gap on the Fermi surface. This causes two additional powers of the frequency to appear, the $B_{1g}$ component of the scattering efficiency becomes cubic for the YBCO type at low frequencies [2.8]. Two effects can alter this behavior: an orthorhombic distortion and impurities.

In our calculations, we focus on a $d_{x^2-y^2}$-like gap function which is only a function of the direction in $k$-space, but not of the magnitude of $\boldsymbol{k}$, since the values of the *gap functions* sufficiently far from the Fermi surface do not affect the results. We are using the same gap function for all bands involved. The asymptotic behavior just mentioned is not changed by using a gap function $\Delta_{\boldsymbol{k}} = \Delta_0(k_x^2 - k_y^2)/k$ instead of $\Delta_\varphi = \Delta_0 \cos(2\varphi)$.

### 2.3.7 Effect of impurities

In contrast to scattering by nonmagnetic impurities in conventional (isotropic) superconductors, impurity scattering plays an important role for superconductors with anisotropic gaps and its effect on the Raman spectrum is most pronounced for superconductors which exhibit regions in $k$-space where the gap almost or completely vanishes.

The formalism for the theoretical discussion of the impurity effects was set up in [2.29, 2.30] for heavy-fermion systems. It was applied to $d$-wave gaps in high-temperature superconductors in [2.31], where the current-current susceptibility (i.e., the effect on infrared absorption) was calculated. In Ref. [2.32], the effect of impurities on the density of states of $d$-wave and $|d|$-wave superconductors was compared, and it was shown that *impurities may provide a means for distinguishing between these gap functions*. Finally, in [2.33], this discussion was extended to the case of the unscreened Raman efficiency.

It was shown in Refs. [2.32, 2.33] that in the case of $d$-wave pairing, impurity scattering can be described by extending the nodal points on the 2D Fermi surface to small finite regions with vanishing gap. This causes a nonvanishing density of states at the Fermi energy. For anisotropic $s$-wave pairing the gap anisotropy becomes smeared out leading to an increase of the minimum gap value $\Delta_{\text{min}}$. In the case of a $|d_{x^2-y^2}|$ gap, this minimum gap increases monotonically with the impurity concentration $n_i$ for small values of $n_i$.

The renormalization of the gap function by the presence of impurities causes an additional contribution to the Raman spectra, which is linear in the Raman shift $\omega$ for small Raman shifts $\omega$ [2.33]. This has consequences for the $B_{1g}$ spectrum of a *tetragonal* crystal, which, in the clean limit, should have a cubic $\omega$-dependence, because a linear frequency dependence is added. As will be discussed in the next subsection, the orthorhombicity of the YBCO compounds also causes a linear addition to the cubic behavior of the spectrum in the $B_{1g}$ channel.

In the case of a $|d_{x^2-y^2}|$-like, $A_g$ symmetry gap function the impurity-induced minimal gap $\Delta_{\text{min}}$ reflects itself in an excitation-free below a Raman shift of $2\Delta_{\text{min}}$.

### 2.3.8 Effect of orthorhombic distortion

As already mentioned, orthorhombic distortions of the tetragonal symmetry have a different effect on Y-123 and on $Bi_2Sr_2CaCu_2O_8$ (Bi-2212). Consider the $B_{1g}\,(D_{4h})$ component of the inverse effective mass tensor in a *tetragonal* high-$T_c$ superconductor with a $d_{x^2-y^2}$-like gap. The $B_{1g}\,(D_{4h})$ inverse effective mass has its nodes in directions bisectioning the copper-oxygen bonds along $x$ and $y$. The same is true for the gap function. As mentioned above, this results in the $\omega^3$-dependence of the Raman efficiency for $B_{1g}\,(D_{4h})$ scattering, in contrast to the $\omega$-dependence predicted for $A_{1g}$ and $B_{2g}$ scattering. Let us now consider the orthorhombic distortion present in Y-123. The zeros of the $B_{1g}\,(D_{4h})$ inverse effective mass shift because there are no longer mirror planes through the (110) axes. For this reason, the low-energy part of the spectrum acquires a linear component in addition to the $\omega^3$ component of the $D_{4h}$ case.

In Bi-2212 the situation is different because the orthorhombic crystallographic cell is rotated by 45° with respect to the $a$- and $b$-axes, thus preserving the $[a \pm b, c]$ mirror planes. Consequently, the $B_{1g}$ zeros stay at the same position, the low-energy efficiency acquires no linear component.

For a more elaborate discussion of the orthorhombic distortion and its effect on Raman scattering, see Sect. 2.9 and [2.28].

### 2.3.9 Effect of multilayers

In systems with one Cu-O$_2$ plane per primitive cell there is only one Fermi surface and the fluctuations of the inverse effective mass are essentially intraband fluctuations, which are very sensitive to the scattering polarizations. The scattering related to the average inverse effective mass is fully screened. The simplest $A_{1g}\,(D_{4h})$ scattering is related to a Raman vertex component of the form $\cos 4\varphi$ while $B_{1g}\,(D_{4h})$ scattering is obtained for a $\cos 2\varphi$ vertex. In multilayer systems, interband fluctuations between the various sheets FS are also important. The lowest component of such fluctuations corresponds to different *average* inverse effective masses in each FS sheet. Such fluctuations do not depend on the scattering polarizations and lead to unscreened scattering of $A_g$ symmetry.

### 2.3.10 Effect of a sign change of $\gamma_{\boldsymbol{k}}$ on the Fermi surface

The behavior of the Raman vertex near the Fermi surface, especially its sign, is crucial for the scattering efficiency and, in particular, for the effect of screening. *Antiscreening*, that is, an *enhancement* of the scattering efficiency by screening, can occur if the Raman vertex changes sign on the Fermi surface. This can be seen by considering the screening part

$$\operatorname{Im}\chi_{\mathrm{Scr}} = -\operatorname{Im}\frac{\chi_{\gamma 1}^2}{\chi_{11}} \tag{2.55}$$

of the Raman susceptibility. A positive value of $\operatorname{Im}\chi_{\mathrm{Scr}}$ enhances the efficiency, that is, corresponds to antiscreening.

To show how antiscreening arises, we first write the screening term $\operatorname{Im}\chi_{\mathrm{scr}}$ in terms of the real and imaginary parts $\lambda' \equiv \operatorname{Re}\lambda$ and $\lambda'' \equiv \operatorname{Im}\lambda$ of the Tsuneto function and its contribution to the Raman vertex $\gamma_{\boldsymbol{k}}$ as

$$\operatorname{Im}\chi_{\mathrm{Scr}} = \frac{\langle\gamma\lambda'\rangle^2\langle\lambda''\rangle - \langle\gamma\lambda''\rangle^2\langle\lambda''\rangle - 2\langle\gamma\lambda'\rangle\langle\gamma\lambda''\rangle\langle\lambda'\rangle}{\langle\lambda'\rangle^2 + \langle\lambda''\rangle^2}\;. \tag{2.56}$$

The imaginary part of the Tsuneto function $\lambda''$ is a positive function. Consequently, the quantity $\langle\lambda''\rangle$ is a positive function of the Raman shift $\omega$. If $\gamma_{\boldsymbol{k}}$ changes sign in a region around the Fermi surface, it is possible that $\langle\gamma\lambda''\rangle$ changes sign as a function of $\omega$, that is, has a zero. At the position of this zero, the second and the third term in the numerator of (2.56) vanish. The first term, $\langle\gamma\lambda'\rangle^2\langle\lambda''\rangle$, is positive and can become dominant in Eq. (2.56). In this case antiscreening results. In the next paragraph it will be shown that antiscreening is particularly sensitive to the sign of the Raman vertex on parts of the Fermi surface around the directions of the nodes of the gap function $\Delta_{\boldsymbol{k}}$.

### 2.3.11 Antiscreening and the sign of the Raman vertex

In Subsect. 2.3.10, we pointed out that the effect of antiscreening results from sign changes of the Raman vertex $\gamma_{\boldsymbol{k}}$, that is, the inverse effective mass, on the Fermi surface. In this paragraph we present a different proof using a power expansion of $\gamma_{\boldsymbol{k}}$.

For very low frequencies $\omega \ll \Delta_0$, only the regions around the node directions of the gap function (we assume a $d_{x^2-y^2}$-like gap) contribute to the susceptibility. We focus on a specific node of the gap function and define the point $\boldsymbol{k}_0$ as the point of intersection of the node line of the gap function and a specific sheet of the Fermi surface. Then we introduce an orthonormal coordinate system $\{k, k_\perp\}$ in the $a$-$b$-plane in $k$-space with the origin at $\boldsymbol{k}_0$, rotated in such a way that the $k_\perp$-axis is perpendicular to the node line and assume that this is tangent to the Fermi surface. We write the Raman vertex as a series $\gamma(\boldsymbol{k}) = \sum_i \gamma_i (k_\perp/k_c)^i$ (where $k_c$ is a cutoff), using the assumption that $\partial\gamma/\partial k = 0$. This approximation is justified since contributions to the Raman susceptibility mostly arise from a narrow region around the Fermi surface). We write Eq. (2.56) as

$$\operatorname{Im}\chi_{\mathrm{Scr}} = \sum_i \operatorname{Im}\chi_{\mathrm{Scr}}^{(i)} \; , \tag{2.57}$$

whereas $\operatorname{Im}\chi_{\mathrm{Scr}}^{(i)}$ contains the $i$th powers in $k_\perp$ from the expansion of $\gamma_{\boldsymbol{k}}$. The first three terms in this sum are

$$\begin{aligned}
\operatorname{Im}\chi_{\mathrm{Scr}}^{(0)} &= -\gamma_0^2\langle\lambda''\rangle \\
\operatorname{Im}\chi_{\mathrm{Scr}}^{(1)} &= -2\gamma_0\gamma_1\langle k_\perp\lambda''\rangle \\
\operatorname{Im}\chi_{\mathrm{Scr}}^{(2)} &= -2\gamma_0\gamma_2\langle k_\perp^2\lambda''\rangle \\
&- \gamma_1^2 \frac{\langle\lambda''\rangle(\langle k_\perp\lambda''\rangle^2 - \langle k_\perp\lambda'\rangle^2) + 2\langle\lambda'\rangle\langle k_\perp\lambda'\rangle\langle k_\perp\lambda''\rangle}{\langle\lambda'\rangle^2 + \langle\lambda''\rangle^2} \; .
\end{aligned}$$

Now we investigate the behavior of $\langle k_\perp^i\lambda''\rangle$ in the low frequency limit. We set $v_F = 1$ and $\Delta_0 = 1$ (this represents a simple change in units). Then, $E_{\boldsymbol{k}} = k$ ($E_{\boldsymbol{k}}$ is constant as function of $k_\perp$ by definition), $\Delta_{\boldsymbol{k}} = k_\perp$, and therefore $\Delta_{\boldsymbol{k}}^2/E_{\boldsymbol{k}}^2 = k_\perp^2/k^2$ and $\lambda'' \sim (k_\perp/k)^2 \cdot \delta(2k-\omega)$ from Eq. (2.54). We perform a 2D BZ integration which has to be cut off at a value proportional to $\omega$ in the $k_\perp$ integration,

$$\langle k_\perp^i\lambda''\rangle \sim \int dk_\perp\, dk\, k_\perp^i \cdot \frac{k_\perp^2}{k^2}\delta(2k-\omega) \; . \tag{2.58}$$

Introducing polar coordinates $k_0$ and $\varphi_k$ by $k_0^2 = k_\perp^2 + k^2$ and $\tan\varphi_k = k/k_\perp$, this yields the low frequency behavior

$$\langle k_\perp^i\lambda''\rangle \sim \int d\varphi_k\, \cos^{2+i}\varphi_k \int dk_0\, k_0^{1+i}\,\delta(2k_0-\omega) \sim \omega^{1+i} \; , \tag{2.59}$$

the prefactor vanishes if $i$ is odd. The same is true for the real part $\langle k_\perp^i \lambda' \rangle$. Note that the proportionality constant in (2.59) is positive. This implies that $\operatorname{Im}\chi_{\mathrm{Scr}}^{(i)} \sim \omega^{i+1}$ and

$$\operatorname{Im}\chi_{\mathrm{Scr}} = -\left(\alpha_0\gamma_0^2\omega + (\alpha_1\gamma_0\gamma_2 + \alpha_2\gamma_1^2)\omega^3 + O(\omega^4)\right) \tag{2.60}$$

with positive constants $\alpha_0$ and $\alpha_1$. The sign of $\alpha_2$ depends on the specific case.

For a tetragonal Fermi surface, we only have to focus on the $A_{1g}$ mode because the screening contributions to the other components vanish by symmetry. The $A_{1g}$ symmetry implies $\gamma_1 = 0$ because of the $\sigma_d$ symmetry operation (reflection at $\Gamma S$) which transforms $\gamma_1 k_\perp \to -\gamma_1 k_\perp$. Then, the screening term for low frequencies can be written as

$$\operatorname{Im}\chi_{\mathrm{Scr}} = -\left(\alpha_0\gamma_0^2\omega + \alpha_2\gamma_0\gamma_2\omega^3 + \cdots\right) \ . \tag{2.61}$$

If there are nodes in the Raman vertex near the node of the gap function, then $\gamma_0\gamma_2 < 0$, that is, the screening term is negative for very small $\omega$, but eventually crosses zero because of the $\omega^3$ contribution. For large $\omega \gtrsim 2\Delta_0$, the approximation $\langle\gamma\lambda\rangle \approx \langle\gamma\rangle\langle\lambda\rangle$ yields $\chi_{\mathrm{Scr}} = -\langle\gamma\rangle^2\chi_{11}$, which is the screening term for an isotropic Fermi surface with a scalar Raman vertex $\langle\gamma\rangle$, and therefore negative. If the Raman vertex does not show nodes near the node of the gap function, $\gamma_0\gamma_2$ is larger than zero, and the screening term is not likely to change sign.

In the orthorhombic case of a weakly distorted tetragonality, the $B_{1g}$ $(D_{4h})$ zero in the Raman vertex may shift with respect to the gap node. This can be described by a small $\gamma_0 \neq 0$ and $\gamma_1 \neq 0$; we neglect $\gamma_2$. The low frequency screening term then has the form

$$\operatorname{Im}\chi_{\mathrm{Scr}} = -\left(\alpha_0\gamma_0^2\omega + \alpha_2\gamma_1^2\omega^3 \cdots\right) \ . \tag{2.62}$$

Whether antiscreening exists or not depends on the sign of $\alpha_2$.

It can be seen that for small values of $\gamma_0$, the antiscreening can start already at very small Raman shifts as is the case in the calculations, Fig. 2.19, $B_{1g}$ panel.

## 2.4 The normal state

In the normal phase, the exact mechanism responsible for the observed finite Raman intensity which is almost constant over a broad frequency and temperature range, is not known. Here, we assume a finite lifetime of the quasiparticles since the low-frequency scattering vanishes in the clean limit. Candidates for this scattering are the quasiparticle-quasiparticle scattering in Marginal Fermi Liquid theory (MFL) [2.34], impurity scattering [2.30] or scattering due to spin fluctuations [2.35]. A self energy with nonvanishing imaginary part yields a susceptibility of the form

$$\chi_{ab}(\boldsymbol{q}{=}0,\omega) = \sum_{\boldsymbol{k}} a_{\boldsymbol{k}} b_{\boldsymbol{k}} \nu_{\boldsymbol{k}}(\omega) \tag{2.63}$$

with the relaxation kernel (the function $f'$ is the derivative of the Fermi function with respect to the energy)

$$\nu_{\boldsymbol{k}}(\omega) = -f'(\xi_{\boldsymbol{k}})\frac{i\Gamma_{\boldsymbol{k}}}{\omega + i\Gamma_{\boldsymbol{k}}} \tag{2.64}$$

and its imaginary part [2.36, 2.37]

$$\operatorname{Im}\nu_{\boldsymbol{k}}(\omega) = -f'(\xi_{\boldsymbol{k}})\frac{\omega\Gamma_{\boldsymbol{k}}}{\omega^2 + \Gamma_{\boldsymbol{k}}^2} \ . \tag{2.65}$$

This can easily be seen by evaluating a bubble with two Green's function lines for quasiparticles with an imaginary part $\Gamma_{\boldsymbol{k}}$ of the self energy.

Note that in the superconducting phase for Raman shifts larger than $\sim\Delta$, the relaxation effects described by (2.65) are also of importance.

To describe the constant background in the Raman spectra in the normal phase, one can adopt the frequency-dependent quasiparticle scattering rate of MFL theory [2.34, 2.38]

$$\Gamma_{\boldsymbol{k}}(\omega) \sim \max(\alpha T, \beta\omega) \ . \tag{2.66}$$

In order to evaluate the real part of $\nu_{\boldsymbol{k}}$ using causality arguments, and to prevent divergences, we introduce a high-frequency cutoff $\omega_C$. Note that the nearly antiferromagnetic Fermi liquid (NAFL) [2.39, 2.40] and also the nested Fermi liquid (NFL) [2.41] yield a very similar quasiparticle scattering rate. The former can also provide a mechanism, which accounts for $d_{x^2-y^2}$-pairing. Similar results are obtained for Luttinger liquids [2.42].

Equation (2.66) yields a scattering continuum which is constant for frequencies smaller than $\min(\alpha T/\beta, T)$ and for frequencies larger than the temperature $T$, but with different intensities. In the first case, $\Gamma_{\boldsymbol{k}}$ is proportional to the temperature, that is, $\operatorname{Im}\chi \sim \omega/T$. Multiplying by the Bose factor $1 + n_\omega \sim T/\omega$ a frequency- and temperature-independent Raman efficiency is found. In the second case, $\Gamma_{\boldsymbol{k}} \sim \omega$, and, consequently, $\operatorname{Im}\chi = \text{const}$. The Bose factor is also constant and one is left with a constant Raman efficiency. Note that in the first case, $\operatorname{Im}\chi$ cancels the $\omega$- and $T$-dependence of the Bose factor. It has been shown [2.43, 2.44, 2.38], that $\mathrm{YBa_2Cu_4O_8}$ does not exhibit this behavior. This has been attributed to the breakdown of MFL theory for not optimally doped cuprates [2.38]. Actually, in this case the spectra are nearly temperature independent *after* dividing them by the Bose factor. We shall address this question once more at the end of this section.

We start the discussion of quasiparticle-quasiparticle (qp-qp) scattering, and its influence on electronic Raman scattering, with the case of a $d_{x^2-y^2}$ gap. Suppose the nodes of this gap have a width $\delta_0$ in $k$-space on the Fermi surface due to impurity scattering. We use the model of Eq. (2.65) with a quasiparticle scattering rate $\Gamma_{\boldsymbol{k}}$ independent of $\boldsymbol{k}$ and discuss first the case $T = 0$. Then it can be seen that the contribution of qp-qp scattering to the imaginary part of the Raman susceptibility (2.29) for low frequencies $\omega \ll \Delta_{\max}$ is proportional to the Drude-like factor $\omega\Gamma/(\omega^2+\Gamma^2)$ (which is, for small $\omega$ and low temperatures $T < \omega$, linear in $\omega$ if $\Gamma = \text{const}$ (semiconductors) or $\Gamma \sim \max(\omega^2, T^2)$ (FL), but constant as a function of $\omega$ if $\Gamma \sim \max(\omega, T)$ (MFL) (see also [2.45]). In the tetragonal case, it is also proportional to the density of states at the Fermi surface and in the case of $A_{1g}$ and $B_{2g}$ polarizations to the width $\delta_0$, and in the case of $B_{1g}$ to the third power $\delta_0^3$ of the width $\delta_0$. The discussion for BISCO is analogous with the exception that $B_{1g}$ and $B_{2g}$ exchange their role.

Finite, but small temperatures $T \ll \Delta_{\max}$ have the effect of enlarging the widths $\delta_0$ linearly in temperature, that is, the temperature dependence of the contribution from qp-qp scattering is proportional to $\text{const} + T$. Note that for $T \gtrsim 0$, the Bose factor changes the linear-in-$\omega$ dependence to a constant.

For the anisotropic $s$-wave gap of the form $|d_{x^2-y^2}|$ which acquires a finite minimum gap $\Delta_{\text{min}}$ due to the presence of impurities [2.33], the situation is different. The frequency dependence is also given by the factor $\omega\Gamma/(\omega^2+\Gamma^2)$ in addition to the Bose factor. But the temperature dependence is different. For temperatures $T \ll \Delta_{\text{min}}$ smaller than the minimal gap, the density of quasiparticles is proportional to $\exp(-\Delta_{\text{min}}/kT)$, that is, the contribution of qp-qp scattering to the Raman efficiency is exponentially small. At $kT \approx \Delta_{\text{min}}$, this exponential dependence on $T$ crosses over to a power law.

The background electronic Raman spectrum in the normal phase has been observed to be independent of temperature for nearly optimally doped high-$T_c$ compounds only. In the overdoped and underdoped case, the materials seem to show Fermi liquid-like behavior concerning the quasiparticle scattering rate $\Gamma_{\boldsymbol{k}}$ (for small $\omega$) [2.38, 2.44]. The temperature dependence of the scattering rate $\Gamma_{\boldsymbol{k}}$, as defined in (2.65), has been measured [2.46] for optimally doped and overdoped Bi-2212, and, especially in the case of the $B_{2g}\,(D_{4h})$ mode, the optimally doped sample shows $\Gamma = \alpha T$, whereas for the overdoped sample $\Gamma = \alpha' T^2 + \Gamma_0$. Therefore, the overdoped sample shows a normal Fermi liquid behavior, that is, $\Gamma \sim \max(\omega^2, T^2)$. The $B_{1g}\,(D_{4h})$ mode result for the optimally doped sample yields the puzzling quasiparticle scattering rate $\Gamma = \text{const}$.

## 2.5 The numerical calculation: `massf`

### 2.5.1 Prerequisites and definitions

The `massf` program which we are going to discuss in this chapter performs the $k$-space integrations required for the calculation of the Raman efficiency for electronic Raman scattering in superconductors by making use of the Eqs. (2.28), (2.30) in relation with (2.52). We start this section by defining the choice for the primitive cell, its decomposition into integration cells ("discretization") and the treatment of symmetries.

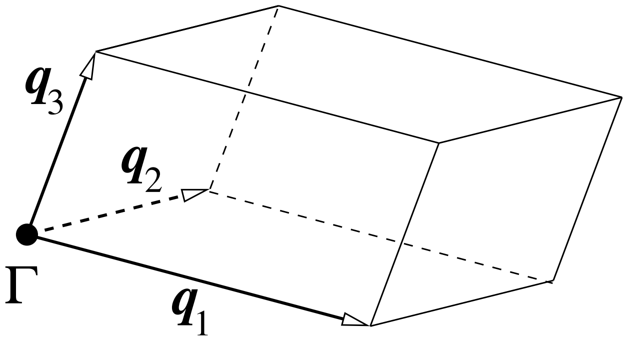

Figure 2.13: Vectors used in the definition of the primitive cell.

The choice of the primitive cell to be used in `massf` is dictated by the output of the LMTO-calculations [2.11] which is used as an input to the `massf` program. The *primitive cell* is spanned by the three reciprocal lattice vectors $\boldsymbol{q}_i$ $(i = 0, 1, 2)$. Therefore, the $\Gamma$-point is *at the corner* of the primitive cell and the primitive cell does *not* correspond to the standard (Wigner-Seitz) first Brillouin zone. In order to perform the integrations in $k$-space, one can use the given primitive cell or the standard first Brillouin zone as the integration volume either: we shall use the former.

*Primitive cell:* The primitive cell is given by the set of all $k$-space points $\boldsymbol{k} = \sum_i \alpha_i \boldsymbol{q}_i$ with $0 \leq \alpha_i < 1$.

All the physical quantities which are defined in $k$-space are given on points of a *discretization lattice.* [19] This lattice defines $N_c = N_1 \cdot N_2 \cdot N_3$ points within the primitive cell. They are given by the vectors $\boldsymbol{k} = \sum_i n_i \boldsymbol{t}_i$ where $n_i = 0, \ldots, N_i - 1$ is an integer and $\boldsymbol{t}_i = \boldsymbol{q}_i / N_i$ are the translation vectors of the discretization lattice.

*Lattice cell:* The lattice cell referred to as $\boldsymbol{k}_c = \sum_i n_i \boldsymbol{t}_i$ is given by the set of all $\boldsymbol{k} = \boldsymbol{k}_c + \sum_i \alpha_i \boldsymbol{t}_i$ with $0 \leq \alpha_i < 1$. The notion "lattice" refers to the discretization of $k$-space in this context.

Derivatives of functions $f(\boldsymbol{k})$ with respect to the components of $\boldsymbol{k}$ are done by calculating differences on the lattice. The basis of the lattice is not necessarily an orthonormal one, therefore co- and contravariant vector components differ. To circumvent the use of two different sets of vector components, we introduce an orthonormal basis $\{\boldsymbol{e}_i\}$ and give vector components *always* with respect to this basis.

### 2.5.2 Symmetries

If the direct lattice of the crystal has a certain point group symmetry, this property also holds for the reciprocal lattice. Physical quantities $Q(\boldsymbol{k})$ which have the property $Q(\boldsymbol{k}) = Q(S\boldsymbol{k})$ for all the symmetry operations $S$ of the given symmetry group of the reciprocal lattice can be fully represented by giving their values only on a subset of the $N_c$ lattice points. We call those points the irreducible $\boldsymbol{k}$-points and denote them by $\boldsymbol{k}_i$ where $i = 0, \ldots, N_{irr}$. (In the notation of group theory [2.47], a vector $\boldsymbol{k}_i$ is called a representative of star$\{\boldsymbol{k}_i\}$ which is the set of vectors $\{S\boldsymbol{k}_i\}$.)

This classification of $k$-space points defines a mapping which maps the triple $(n_1, n_2, n_3)$ identifying a lattice point to the index $i$ of the associated irreducible $\boldsymbol{k}$-point $\boldsymbol{k}_i$, $i = i(n_1, n_2, n_3)$.

The gap function $\Delta_{\boldsymbol{k}}$ does, in general, *not* have the property $\Delta_{\boldsymbol{k}} = \Delta_{S\boldsymbol{k}}$, that is, it does not always have the full point group symmetry (for the symmetry properties of the gap function, refer to App. E). Therefore it cannot be represented using the concept of irreducible $\boldsymbol{k}$-points. We must instead either use all $\boldsymbol{k}$-points or use only the irreducible $\boldsymbol{k}$-points and giving the irreducible representation according to which the gap function transforms. The latter choice has the advantage that symmetry properties hold exactly (without numerical errors) but the disadvantage that it does not allow for gap functions of accidentally mixed symmetry. A further complication in this context is the choice of the primitive cell. Usually, the gap-function is defined as a function of the angle $\varphi$ in the $k_x$-$k_y$-plane of $k$-space. When iterating through the $\boldsymbol{k}$-points of the primitive cell, we calculate the angle $\varphi$ for each of the $\boldsymbol{k}$-points and use $\varphi$ to determine the value of the gap function. The $k$-space angles for our choice of the primitive cell, however, all lie in an interval of length $\pi/2$. For the

---

[19] Also called *the lattice* or *integration lattice.*

calculation of the gap function, we need angles $\varphi$ from 0 to $\pi$. We accomplish this by first mapping the $k$-space points in the primitive cell to the corresponding $k$-space points of the first Brillouin zone (by adding multiples of the translation vectors $\boldsymbol{q}_i$) and then calculating the corresponding angle $\varphi$.

Among other things the `massf` program calculates 4th rank tensors as function of frequency. These tensors consist out of $3^4 = 81$ elements and occupy a large amount of computer memory. We can lower the requirements by considering the symmetry of the tensors. In the case under consideration, the 4th rank tensors are given by a product of two 2nd rank tensors, $t_{ijkl} = g_{ij}g_{kl}$, where the 2nd rank tensor $g_{ij}$ corresponds to the Raman vertex or, when applying the effective mass approximation, the inverse effective mass tensor. The 4th rank tensor formed in such a way is symmetric when interchanging the first index pair with the second one. We denote this symmetry operation by the *permutation* (1 3)(2 4) (see Chap. 15 in [2.47] on the Permutation Group). In the framework of the effective mass approximation, the tensor $g_{ij}$ is given by a second derivative and, as a consequence, symmetric under the permutations (1 2) and (3 4). Note that this is independent of the point group of the crystal! When investigating the group generated by former three permutations, it turns out that the tensor $t_{ijkl}$ only possesses 21 independent elements. Note that this group is only a subgroup of the symmetry group of a 4th rank tensor. Considering the whole symmetry group of the tensor would reduce the number of elements to 9 in the orthorhombic case (see App. C).

### 2.5.3 The `massf` program

The Raman efficiency $I(\omega)$ as a function of the Raman shift $\omega$ is calculated by the program `massf`, which was written in two versions, `massf-fs`, and `massf-k`, the first uses Fermi surface integrations and the second full $k$-space integrations. The program uses as an input the band structure $\epsilon_{n\boldsymbol{k}}$ as calculated by the LMTO program [2.48] as well as the appropriate gap function $\Delta_{\boldsymbol{k}}$ (or $\Delta_\varphi$) and calculates the density of states (DOS) $\mathcal{N}_F$ at the Fermi surface and as well averages

$$\langle \mu_{ij}^{-1} \rangle \ , \quad \langle \mu_{ij}^{-1} \mu_{kl}^{-1} \rangle$$

as well as

$$\langle \lambda(\omega) \rangle \ , \quad \langle \mu_{ij}^{-1} \lambda(\omega) \rangle \ , \quad \langle \mu_{ij}^{-1} \mu_{kl}^{-1} \lambda(\omega) \rangle$$

for given cartesian indices $i$, $j$, $k$, and $l$ and given values of the frequency $\omega$. This chapter serves the purpose of describing the details of the `massf` program.

### 2.5.4 Initialization and the LMTO output file

First of all we describe the initialization of the most important data structures used in `massf` which will store the data contained in the input file to `massf`, and produced as an output file by the LMTO program. We use the notation of the programming language C [2.49], which for the case of arrays has the form

$$\textit{type}\ \texttt{a}[d_1] \cdots [d_n]$$

for an array $a_{i_1 \cdots i_n}$ with $i_j = 0, \ldots, d_j - 1$, $j = 1, \ldots, n$. The *type* denotes the type of the array which is `int` for $a_{i_1 \cdots i_n} \in \mathbb{N}$ and `double` for $a_{i_1 \cdots i_n} \in \mathbb{R}$.

The initialized data structures are:

`int n[3]`
: Contains the numbers $N_1$, $N_2$, and $N_3$ of points in each of the directions in $k$-space.

`int nkp`
: The number $N_{irr}$ of irreducible $\boldsymbol{k}$-points.

`int nband`
: The number $N_b$ of energy bands.

`int iqp[`$N_1$`][`$N_2$`][`$N_3$`]`
: This 3-dimensional array maps the $N_c$ points of the first Brillouin zone onto an integer number, the number of the irreducible $\boldsymbol{k}$-point associated to. It is the implementation of the $\mathbb{N}^3 \to \mathbb{N}$ mapping defined in the last section.

`double qb[3][3]`
: A $3 \times 3$ matrix containing the primitive lattice vectors $\boldsymbol{q}_i$ of the reciprocal lattice. These vectors are converted from the unit $2\pi/3.87$ Å in the input file to the unit $1/a_B$. The first index of `qb` corresponds to the vector components, the second one to the index of the primitive lattice vectors. Therefore, `qb[`$i$`][`$j$`]` $= \boldsymbol{e}_i \boldsymbol{q}_j$.

`double eb[`$N_b$`][`$N_{irr}$`]`
: These are the energy bands $\epsilon_n(\boldsymbol{k})$. The first index is the band index and the second the number of the irreducible $\boldsymbol{k}$-point. The energy bands in the input file are given in Rydberg (Ry) units and are converted to Hartree (1 Ha = 2 Ry) units. After the conversion, the Fermi energy is zero.

In the superconducting state, the gap function also has to be specified. This function is used to calculate the Tsuneto-function $\lambda_{\boldsymbol{k}}(\omega)$ on the same $k$-space lattice on which the energy bands are defined. For convenience, we give the explicit form of the Tsuneto-function, which is

$$\mathrm{Re}\,\bar{\lambda}_{\boldsymbol{k}}(\bar{\omega}) = \begin{cases} \dfrac{2}{\pi}\dfrac{1}{\sqrt{1-\bar{\omega}^2}}\,\mathrm{atan}\left(\dfrac{\bar{\omega}}{\sqrt{1-\bar{\omega}^2}}\right) & ;\ \bar{\omega} < 1 \\ \dfrac{1}{\pi}\dfrac{1}{\sqrt{\bar{\omega}^2-1}}\log\left|\dfrac{\bar{\omega}-\sqrt{\bar{\omega}^2-1}}{\bar{\omega}+\sqrt{\bar{\omega}^2-1}}\right| & ;\ \bar{\omega} > 1 \end{cases} \tag{2.67}$$

for the real part, and

$$\mathrm{Im}\,\bar{\lambda}_{\boldsymbol{k}}(\bar{\omega}) = \begin{cases} 0 & ;\ \bar{\omega} < 1 \\ \dfrac{1}{\sqrt{\bar{\omega}^2-1}} & ;\ \bar{\omega} > 1 \end{cases} \tag{2.68}$$

for the imaginary part, where $\lambda_{\boldsymbol{k}}(\omega) = 2|\Delta_{\boldsymbol{k}}|\,\bar{\lambda}_{\boldsymbol{k}}(\bar{\omega})$ and $\bar{\omega} = \omega/(2|\Delta_{\boldsymbol{k}}|)$ in both cases.

These functions have been calculated on the discretization lattice for several frequencies $\omega_i = i \cdot \omega_{max}/(N_{om}-1)$ with $i = 0, \ldots, N_{om}-1$ and stored in the two 4-dimensional arrays

`double re_tsu[`$N_1$`][`$N_2$`][`$N_3$`][`$N_{om}$`]`
`double im_tsu[`$N_1$`][`$N_2$`][`$N_3$`][`$N_{om}$`]` .

Here, $N_{om}$ is the number of points in $\omega$-space. For reasons related to numerical errors, a cutoff has been used. This cutoff is related to the singularity of the Tsuneto-function at $\omega = 2|\Delta_{\boldsymbol{k}}|$ and is implemented by setting the values of the Tsuneto-function for arguments $\omega$ with $|\bar{\omega} - 1| < \epsilon_{\bar{\omega}}$ to the respective values at the limits of this frequency interval.

### 2.5.5 Velocity

After the initialization, `massf` calculates the first derivative of $\epsilon_{n\boldsymbol{k}}$ with respect the $\boldsymbol{k}$ which we will call the *velocity*, defined by

$$\epsilon_n(\boldsymbol{k}+\vec{\delta}) = \epsilon_n(\boldsymbol{k}) + \boldsymbol{v}_n(\boldsymbol{k})\cdot\vec{\delta} + O(\delta^2)\ . \tag{2.69}$$

If the primitive vectors $\{\boldsymbol{q}_i\}$ do not form an orthonormal basis, one has to be careful when calculating the vector magnitudes. Therefore we introduce the velocity vector components with respect to a cartesian basis $\{\boldsymbol{e}_i\}$ and define $\boldsymbol{v}_n = \sum_i v_{ni}\boldsymbol{e}_i$. The differentiation on the lattice then yields

$$\Delta\epsilon_{ni}(\boldsymbol{k}) \equiv \epsilon_n(\boldsymbol{k}+\boldsymbol{t}_i) - \epsilon_n(\boldsymbol{k}-\boldsymbol{t}_i) = 2\boldsymbol{v}_n(\boldsymbol{k})\boldsymbol{t}_i \tag{2.70}$$

or, if we introduce the matrix $Q_{ij} = \boldsymbol{t}_i\boldsymbol{e}_j$,

$$\Delta\epsilon_{ni}(\boldsymbol{k}) = 2\boldsymbol{t}_i\boldsymbol{v}_n(\boldsymbol{k}) = 2\sum_j(\boldsymbol{t}_i\boldsymbol{e}_j)\cdot(\boldsymbol{e}_j\boldsymbol{v}_n(\boldsymbol{k})) = 2\sum_j Q_{ij}v_{nj}(\boldsymbol{k}) \tag{2.71}$$

which gives $\{v_{nj}(\boldsymbol{k})\}$ when inverted. This has to be calculated for all $\boldsymbol{k}$-points on the discretization lattice. Boundary conditions are determined by the translational symmetry of the primitive cell.

The calculation of the velocity serves two purposes. First it is an intermediate step for the calculation of the inverse effective mass, second, the inverse of its *absolute magnitude* determines the local contribution of an element of the Fermi surface to the density of states at the Fermi surface.

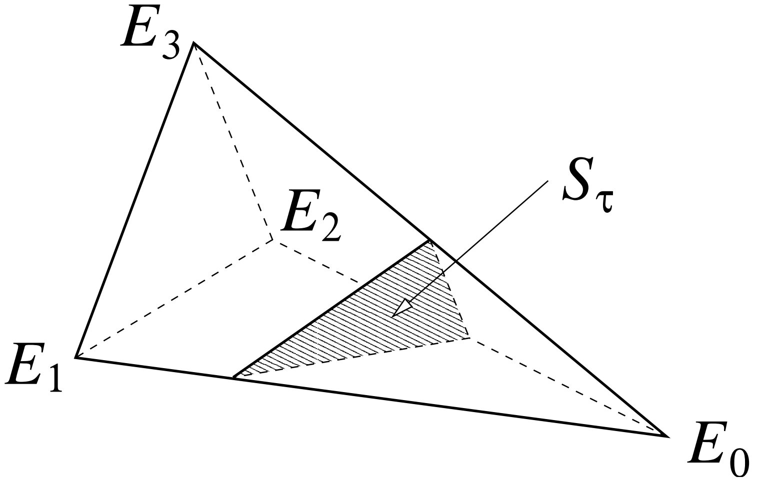

Figure 2.14: The Fermi surface crossing a tetrahedron $\tau$ with a plane intersecting it ($E_0 < 0 < E_1, E_2, E_3$). The intersection has the surface area $S_\tau$.

### 2.5.6 Tetrahedron integration

The Fermi surface integration is done using the *tetrahedron method*. This method decomposes each of the $N_c$ lattice cells spanned by the vectors $\boldsymbol{t}_i$ in the primitive cell into six tetrahedra and uses the $6N_c$ tetrahedra as integration cells. When performing the Fermi surface integration, only tetrahedra which are crosses by the Fermi surface, have to be taken into account. To check whether the Fermi surface of a particular electronic band passes through a particular tetrahedron, it just has to be determined whether the energies $\epsilon_n(\boldsymbol{k}) - \epsilon_F$ given by the electronic band and taken at the four tetrahedron corners have the same sign. The Fermi surface, which is approximated by a plane inside a tetrahedron, always cuts an area enclosed by a polygon with three or four corners out of the tetrahedron (except for uninteresting pathological cases of lower dimension), whose surface area can be easily determined. This property is one of the main advantages of the tetrahedron decomposition. If we would use the plain lattice cell as integration cell, the Fermi surface could cut a polygon with 3, 4, 5, or even 6 corners out of the integration cell. Determining the surface area of such a polygon would unnecessarily complicate the program.

Suppose a $\boldsymbol{k}$-dependent physical quantity $p(\boldsymbol{k})$ has to be integrated over the Fermi surface. If $p_j = p(\boldsymbol{k}_j)$ for some point $\boldsymbol{k}_j$ on the Fermi surface in the tetrahedron $j$, and $S_j$ equals the area of the Fermi surface in the tetrahedron $j$, then the Fermi surface integral is approximated by

$$P = \sum_j p_j S_j \ ,$$

this is the method used by `massf` for performing Fermi surface integrals.

For the integration we finally need the surface area $S_\tau$ of that part of the Fermi surface intersecting a tetrahedron $\tau$ under consideration. We linearize the bands $\epsilon_n(\boldsymbol{k})$ inside the tetrahedron $\tau$ by using the values of the dispersion relation at the four corners of the tetrahedron. Then, the Fermi surface defined by $\epsilon_n(\boldsymbol{k}) = \epsilon_F$ becomes a plane. As already mentioned, a plane crossing a tetrahedron always cuts a flat polygon with either three or four corners out of the tetrahedron, therefore its surface area $S_\tau$ is determined easily. The required FS averages eventually are given by

$$\begin{aligned} S &= \sum_\tau S_\tau \ ; & \langle \lambda(\omega) \rangle &= S^{-1} \sum_\tau \lambda_\tau(\omega) S_\tau \ ; \\ \langle \mu_{ij}^{-1} \rangle &= S^{-1} \sum_\tau \mu_{ij}^{-1}(\tau) S_\tau \ ; & \langle \mu_{ij}^{-1} \mu_{kl}^{-1} \rangle &= S^{-1} \sum_\tau \mu_{ij}^{-1}(\tau) \mu_{kl}^{-1}(\tau) S_\tau \ , \end{aligned} \tag{2.72}$$

where $\mu_{ij}^{-1}(\tau)$ and $\lambda_\tau(\omega)$ are the values of the inverse effective mass tensor and the Tsuneto-function, respectively, for tetrahedron $\tau$. The density of states at the Fermi level is given by

$$\mathcal{N}_F \sim \int \frac{dS_F}{\hbar |\boldsymbol{v}(\boldsymbol{k})|} \quad \text{or} \quad \mathcal{N}_F \sim \frac{1}{\hbar} \sum_\tau \frac{S_\tau}{|\boldsymbol{v}(\tau)|}$$

where $\boldsymbol{v}(\tau)$ denotes the velocity at some point inside of tetrahedron $\tau$.

### 2.5.7 Inverse effective mass

The calculation of the second derivatives of the bands is done in combination with the integration and therefore in a manner different from that of the velocities.

The lattice cells each are decomposed into 6 tetrahedra (see Fig. 2.15), numbered $i =$

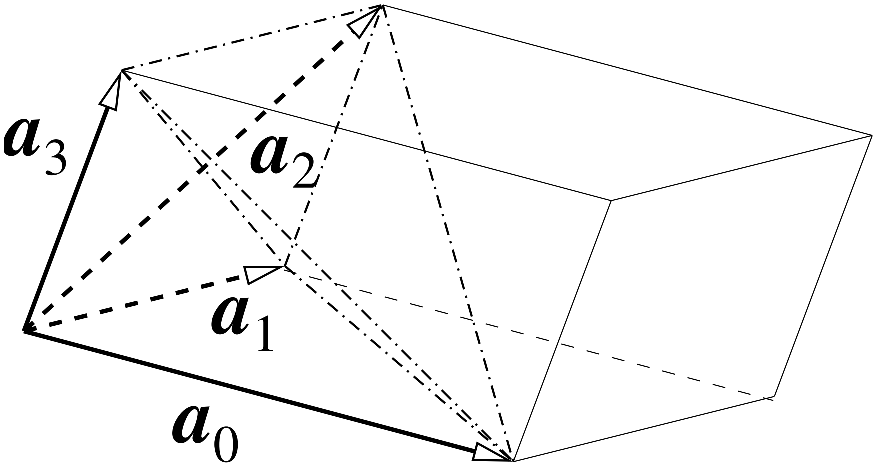

Figure 2.15: The definition of a tetrahedron inside the integration cell denoted by $\boldsymbol{k}_c$ using four vectors $\boldsymbol{a}_i$.

$0,\ldots,5$.[20] The corners of these tetrahedra are specified by four vectors $\boldsymbol{a}_{ij}$, $j = 0,\ldots,3$:

$$\boldsymbol{a}_{ij} = \sum_k d_{ijk} \boldsymbol{t}_k \ . \tag{2.73}$$

The quantities $d_{ijk}$ are the only vector components in this section which are *not* given in a cartesian basis but in the basis of the vectors $\{\boldsymbol{t}_i\}$. The $4 \times 6 \times 3 = 72$ values of $d_{ijk}$ are stored in the array `int ind[4][6][3]`.

The calculation of the inverse effective mass tensor $\hat{\mu}^{-1}$ is based on the formula

$$\boldsymbol{v}(\boldsymbol{k} + \vec{\delta}) = \boldsymbol{v}(\boldsymbol{k}) + \hat{\mu}^{-1}(\boldsymbol{k})\vec{\delta} + O(\vec{\delta}^2) \ . \tag{2.74}$$

We put the three vectors $\boldsymbol{t}_j = \boldsymbol{a}_{j+1} - \boldsymbol{a}_0$, $j = 0\ldots2$ constituting the tetrahedron for $\delta$. The equation defining the inverse effective mass tensor then reads

$$\delta\boldsymbol{v}(\boldsymbol{t}_j) \equiv \boldsymbol{v}(\boldsymbol{a}_0 + \boldsymbol{t}_j) - \boldsymbol{v}(\boldsymbol{a}_0) = \hat{\mu}^{-1}(\boldsymbol{a}_0 + \epsilon\boldsymbol{t}_j)\boldsymbol{t}_j \tag{2.75}$$

on the discretization lattice ($0 < \epsilon < 1$). We next convert (2.75) to the cartesian basis by inserting the unit matrix $\sum_k \boldsymbol{e}_k\boldsymbol{e}_k$ (outer product) and multiplying the equation on the right with $\boldsymbol{e}_i$ which yields

$$\boldsymbol{e}_i\delta\boldsymbol{v}(\boldsymbol{t}_j) = \sum_k \boldsymbol{e}_i\hat{\mu}^{-1}\boldsymbol{e}_k Q_{jk} \ . \tag{2.76}$$

If we introduce the matrix

$$\hat{V} = (V_{ij}) \quad , \quad V_{ij} = \boldsymbol{e}_i\delta\boldsymbol{v}(\boldsymbol{t}_j)$$

and invert (2.76), we obtain the equation

$$\boldsymbol{e}_i\hat{\mu}^{-1}\boldsymbol{e}_k = (\hat{V}\hat{Q}^{T\,-1})_{ik} \tag{2.77}$$

---

[20] Arrays in the programming language C are always indexed from 0 on, we also use this convention here.

for the cartesian components of the inverse effective mass tensor.

Note that each of the three equations (2.75) uses the inverse effective mass $\hat{\mu}^{-1}$ at a slightly different point in the tetrahedron. Therefore, the matrix $\hat{\mu}^{-1}$ calculated using (2.77) is not necessarily symmetric. We neglect the antisymmetric part of $\hat{\mu}^{-1}$, this symmetrization amounts to some kind of averaging of $\hat{\mu}^{-1}$ inside the tetrahedron.

The data structures used for the tetrahedron integration and the calculation of the inverse effective mass are

`double qmat[3][3]`
: This matrix contains just the elements of the transposed of $(Q_{ij})$, that is, `qmat[`$i$`][`$j$`]` $= Q_{ji}$.

`double invqmat[3][3]`
: The components of $(Q_{ij})^{T\,-1}$ are stored here. The identity $\sum_j$ `qmat[`$i$`][`$j$`]` $\cdot$ `invqmat[`$j$`][`$k$`]` $= \delta_{ik}$ holds.

`double vmat[3][3]`
: These are the components of the matrix $\hat{V}$. It is `vmat[`$i$`][`$j$`]` $= V_{ij}$.

`double invmass[3][3]`
: This matrix corresponds to the inverse effective mass $\hat{\mu}^{-1}$. To be more specific, its cartesian components are given by `invmass[`$i$`][`$j$`]` $= \boldsymbol{e}_i\hat{\mu}^{-1}\boldsymbol{e}_j$.

`int ind[6][4][3]`
: These are the integer numbers $d_{ijk}$ specifying the 3 cartesian components of the 4 corners of each of the 6 tetrahedra inside a lattice cell. *These are NOT cartesian components, but just the numbers $d_{ijk}$ defined in (2.73).*

## 2.6 Experimental results

The experimental determination of *absolute* Raman scattering intensities is plagued by a number of difficulties (a reason why usually "relative units" are found in the literature). The first is related to the presence of elastically scattered light in the spectra, in particular when nonideal sample surfaces are involved. Depending on the quality of the spectrometer this leads to contributions extending typically, for the parameters of the present work, up to 50 cm$^{-1}$ from the center of the laser line. These contributions can be filtered out using a premonochromator or notch filters but, in any case, Raman scattering measurements below 50 cm$^{-1}$ remain difficult. The measurements discussed here have been performed by comparison with the known efficiency of a silicon crystal after correcting for differences in the scattering volumes. The procedure leads to errors of about 50%.

We use for comparison with the calculation the experimental data of Krantz *et al.* [2.50] in the case of Y-123, and Donovan *et al.* [2.43] in the case of Y-124. Our Figs. 2.16 and 2.17 are taken from these publications. In the case of Fig. 2.16 we have corrected a scale error in the abscissa found in Ref. [2.50]. In the case of Fig. 2.17 we have calculated the $A_{1g}$ component from the experimental results for the $(x'x')$ and $(xy)$ polarizations.

The classification of the measured spectra according to irreducible representations of the symmetry group of the crystal is performed with the use of the Raman tensor $\hat{R}$ which is related to the Raman efficiency through the expression $I \sim \left|\boldsymbol{e}_L\hat{R}\boldsymbol{e}_S\right|^2$, bilinear in the Raman

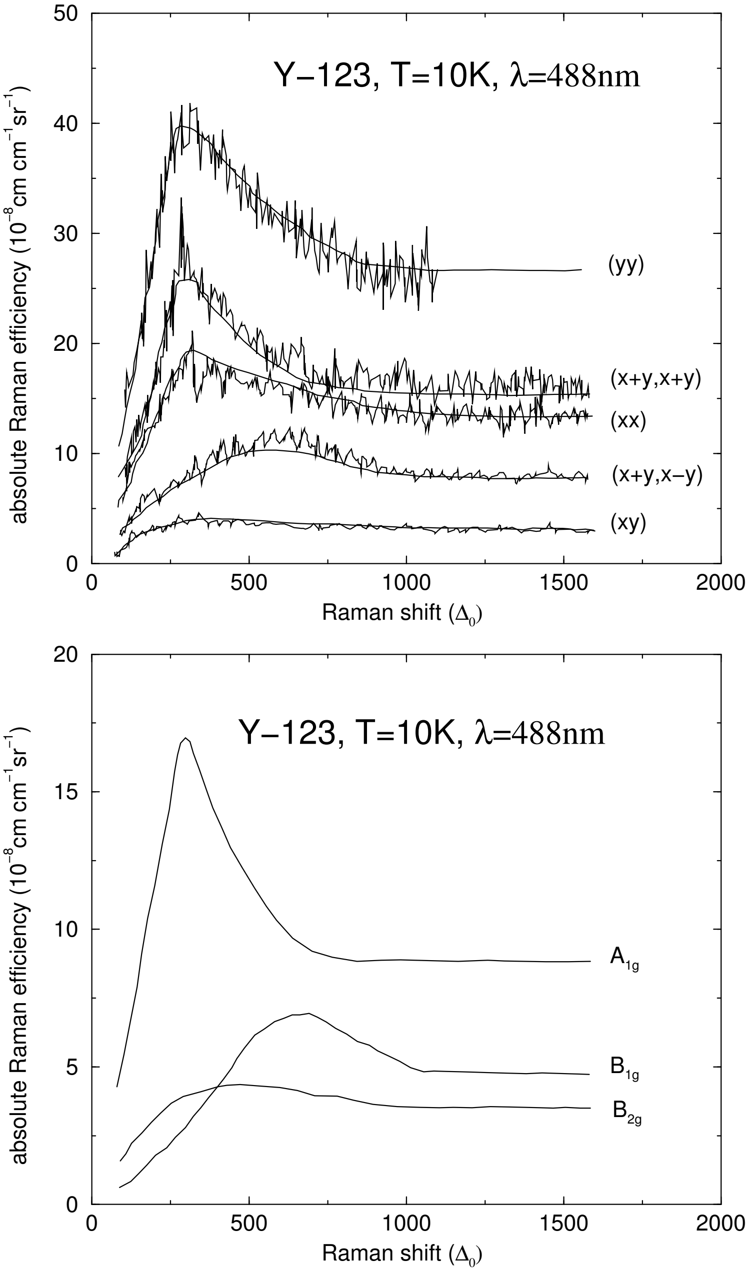

Figure 2.16: Experimental Raman scattering efficiencies for Y-123 from Ref. [2.50]. The vertical scales are absolute Raman efficiencies, measured at $T = 10\,\mathrm{K}$ and an exciting laser wavelength of $\lambda = 488\,\mathrm{nm}$ (Note that a scale error found in Ref. [2.50] has been corrected). The $A_{1g}$ component extracted according to $I_{A_{1g}} = (I_{xx} + I_{yy})/2 - I_{x'y'}$ is plotted in the lower panel together with the quasitetragonal $B_{1g}$ and $B_{2g}$ components.

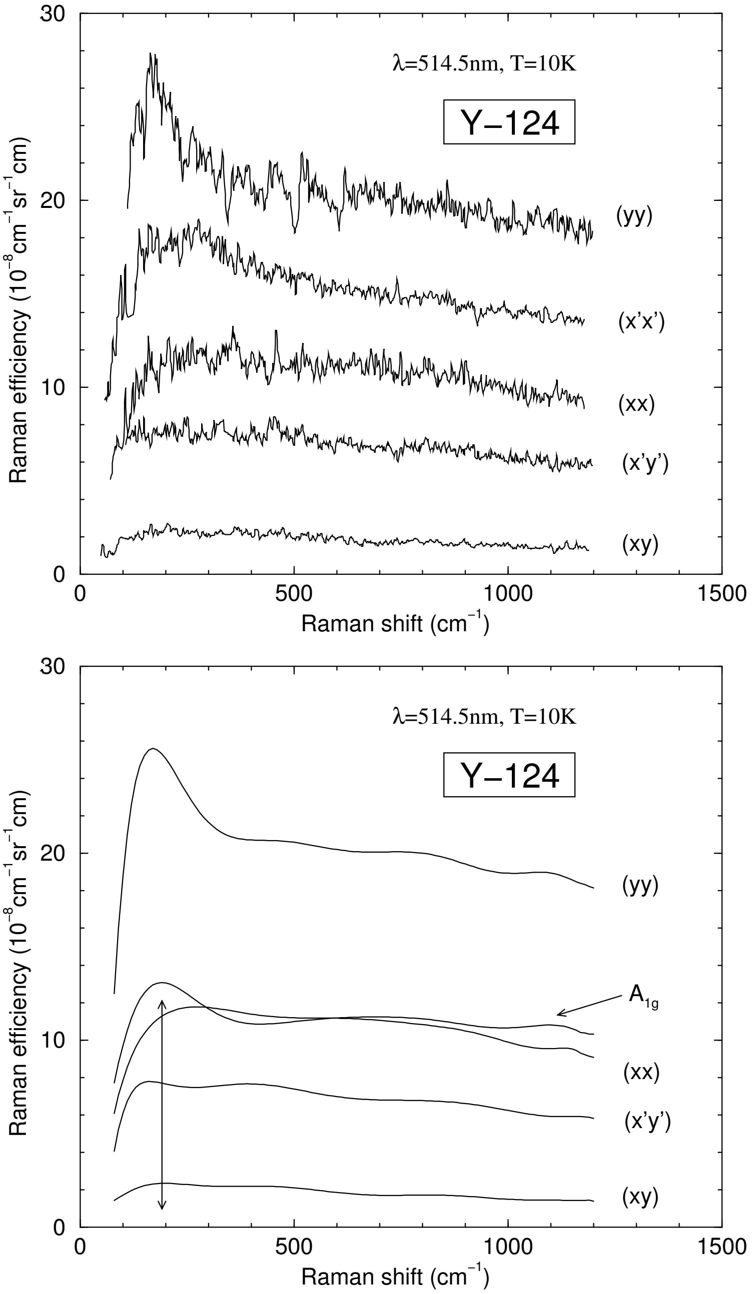

Figure 2.17: Upper panel: experimental absolute Raman efficiencies given for the five specified polarization configurations for Y-124 from Ref. [2.43]. These data are taken at $T = 10\,\mathrm{K}$ with an exciting laser wavelength of $\lambda = 514.5\,\mathrm{nm}$. Lower panel: smoothed curves and the $A_{1g}$ spectrum additionally extracted from the former. In both panels, consecutive offsets of $0, 1, \ldots, 4 \times 2.5\,\mathrm{cm}^{-1}\mathrm{sr}^{-1}\mathrm{cm}$ were used.

tensor. In the calculations, the Raman tensor does not appear explicitly, the inverse effective mass $\partial^2 E/(\partial k_i \partial k_j)$ playing its role. It is important to note that the Raman efficiency, as given by the theory (Eqs. (2.28), (2.30), and (2.52)), is bilinear in the inverse effective mass of the Raman vertex (including the screening part!), that is, contains the same interferences as the approach involving the Raman tensor. Note that the Tsuneto function $\lambda$ is fully symmetric. In the normal phase, the scattering kernel $\nu$ has been assumed to be the same for all scattering channels.

In most of the measurements of the Raman efficiency in orthorhombic high-$T_c$ superconductors, an $A_{1g}$ component is given. Strictly, this irreducible representation notation is not appropriate to $D_{2h}$ but only to $D_{4h}$. In orthorhombic crystals, the Raman tensor has two $A_g$ components ($R_{xx}$ and $R_{yy}$) which correspond to the $A_{1g}$ ($R_{xx} + R_{yy}$) and $B_{1g}$ ($R_{xx} - R_{yy}$) components of the tetragonal $D_{4h}$ case, and which are not distinguishable in $D_{2h}$ because they transform in the same way. Nevertheless, quantities can be constructed in the orthorhombic case which correspond to the tetragonal $A_{1g}$ component.

One of these is $I^{(1)} = (I_{xx} + I_{yy})/2 - I_{x'y'}$ from the experimental spectra. Both, $I_{xx}$ and $I_{yy}$ contain $A_{1g}$ and $B_{1g}$ ($D_{4h}$), and also an interference term (present only in the case of orthorhombic $D_{2h}$ symmetry) which cancels when $I_{xx}$ and $I_{yy}$ are added. The $I_{x'y'}$ efficiency contains $B_{1g}$ and $A_{2g}$ ($D_{4h}$). If we assume that the antisymmetric component ($A_{2g}$ in $D_{4h}$) of the Raman tensor $\hat{R}$ vanishes (i.e. $I_{xy} = I_{yx}$), $I_{x'y'}$ corresponds to tetragonal $B_{1g}$ and cancels the $B_{1g}$ contribution in $I_{xx}$ and $I_{yy}$. Provided that the $A_{2g}$ component of the Raman tensor vanishes, $I^{(1)}$ corresponds to the $I_{A_{1g}}$ of the tetragonal case. Note that the antisymmetric component $(R_{xy} - R_{yx})/2$ of the Raman tensor vanishes in the inverse effective mass vertex theory given in Sec. 2.2 because of $\gamma_{xy} = \gamma_{yx}$ regardless of the symmetry of the crystal, and also in the experiment in the case of tetragonal crystals but not necessarily for orthorhombic crystals. The equality of $I_{xy}$ and $I_{yx}$ in the calculation is an artifact of the theory and results from making use of the effective mass approximation.

A second possible construction for $A_{1g}$ is $I^{(2)} = I_{x'x'} - I_{xy}$. The $I_{x'x'}$ efficiency contains $A_{1g}$ and $B_{2g}$ contributions. The interference term of these two contributions vanishes in the tetragonal as well as the orthorhombic case. Both, $B_{2g}$ ($D_{4h}$) and $A_{2g}$ are contained in $I_{xy}$. But if the (antisymmetric) $A_{2g}$ component of the Raman tensor vanishes, $I^{(2)}$ also corresponds to the $I_{A_{1g}}$ of the tetragonal case. In one of the experimental works [2.50] a different method to extract the $A_{1g}$ component was used. Both of the expressions for $I^{(1)}$ and $I^{(2)}$ contain contributions of the $A_{2g}$ ($D_{4h}$) Raman tensor component. This component may be present in the experiment, but not in the inverse effective mass based theory, a fact, that has to be kept in mind when comparing the numerical results to the measurements. Note that the Raman efficiencies in $(xy)$ and $(x'y')$ polarization configurations also contain contributions from the antisymmetric part of the Raman tensor. In view of these uncertainties in $A_{1g}$ we mainly focus in the next section on the directly observable components of the Raman tensor.

We conclude this section by taking up again the question of the validity of the effective mass approximation. In the experiment, this can be checked in two ways. First, via the dependence of the spectra on the laser frequency which should make it possible to distinguish the contributions to the Raman efficiency resulting from resonant and nonresonant transitions, respectively. The second way involves the measurement of the $A_{2g}$ component of the inverse effective mass. If the effective mass approximation is valid, the Raman vertex should be symmetric ($\gamma_{xy} = \gamma_{yx}$), that is, the $A_{2g}$ ($D_{4h}$) component should vanishes. A nonvanishing $A_{2g}$ component of the measured scattering would cast doubts on the appropriateness of the effective mass approximation.

## 2.7 Numerical results and comparison to experimental results

In this section we present the results of the calculation of the Raman efficiency for the Y-123 and Y-124 compounds. In both cases, the dispersion relation $\epsilon_n(\boldsymbol{k})$ was obtained from a full LDA-LMTO calculation (in the atomic spheres approximation ASA). The gap function $\Delta_n(\boldsymbol{k})$ which was used in the calculation is a simple band-independent $d_{x^2-y^2}$-wave of the form $\Delta_n(\boldsymbol{k}) = \Delta_0 \cos(2\varphi)$.

To carry out the numerical BZ and FS integrations, we employed the tetrahedron approach as discussed in Sect. 2.5, see also Refs. [2.51, 2.52]. The convergence of the integrations was checked by using different discretization lattices. In Figs. 2.18 and 2.19, the results of full BZ integrations for Y-123 and Y-124, respectively, are plotted. The corresponding spectra obtained through FS integrations can be seen in Ref. [2.42], they are almost identical to the latter ones. The Bose factor in the expression (2.30) has been omitted, hence the results apply to zero temperature. In both figures, the Raman shift is given in units of the gap amplitude $\Delta_0$. Since the calculated scattering efficiencies for BZ integrations, contrary to FS integrations, are not only a function of the reduced frequency but depend also weakly on the value of $\Delta_0$ (In the FS integration, but not in the BZ-integration, the step leading from (2.46) to (2.47) can be performed; this makes the FS-Tsuneto-function a function of $\omega/(2\Delta_0)$ only), we took for the calculations $\Delta_0 = 220\,\mathrm{cm}^{-1}$. This value of $\Delta_0$ falls in the range of $\Delta_0$'s determined by Raman scattering and other methods. The $\delta$-function peaks in the Tsuneto-function have been broadened phenomenologically by introducing a finite imaginary part $\Gamma = 0.3\Delta_0$ of the frequency variable $\omega$.

Figures 2.18 and 2.19 display spectra for each of the polarization configurations $(yy)$, $(x'x')$, $(xx)$, $(x'y')$, and $(xy)$, as well as the symmetry component $A_{1g}$ ($D_{4h}$) (defined by $I_{A_{1g}} = I_{x'x'} - I_{xy}$), the unscreened intensities, the screening part (2.55), and the total intensities, equal to the difference between unscreened and screening parts. Note that the $(x'y')$ configuration corresponds to the $B_{1g}$ ($D_{4h}$) component because of the vanishing of the $A_{2g}$ component in the theory.

We discuss first the results for Y-123. The $A_{1g}$ component (in the rest of this section we use tetragonal notation unless explicitly stated) is subject to rather strong screening, however its unscreened part is comparable to that of the $B_{1g}$ component. The relation between the unscreened and the screened (total) spectral weight of the $A_{1g}$ component is about three. Nevertheless, the shapes of the unscreened and the screened parts are the same and, consequently, *there is almost no shift in the peak position due to screening* (contrary to the results of Ref. [2.8]). The peak is located almost exactly at $2\Delta_0$. Note that there is no antiscreening in the $A_{1g}$ component. The low-energy part of all $A_{1g}$ spectra (screened and unscreened) is linear, as predicted by the theory.

As already mentioned, the $(x'y')$ component (equal to the $B_{1g}$ component in the nonresonant case) is almost four times stronger than its screened $A_{1g}$ counterpart. The screening

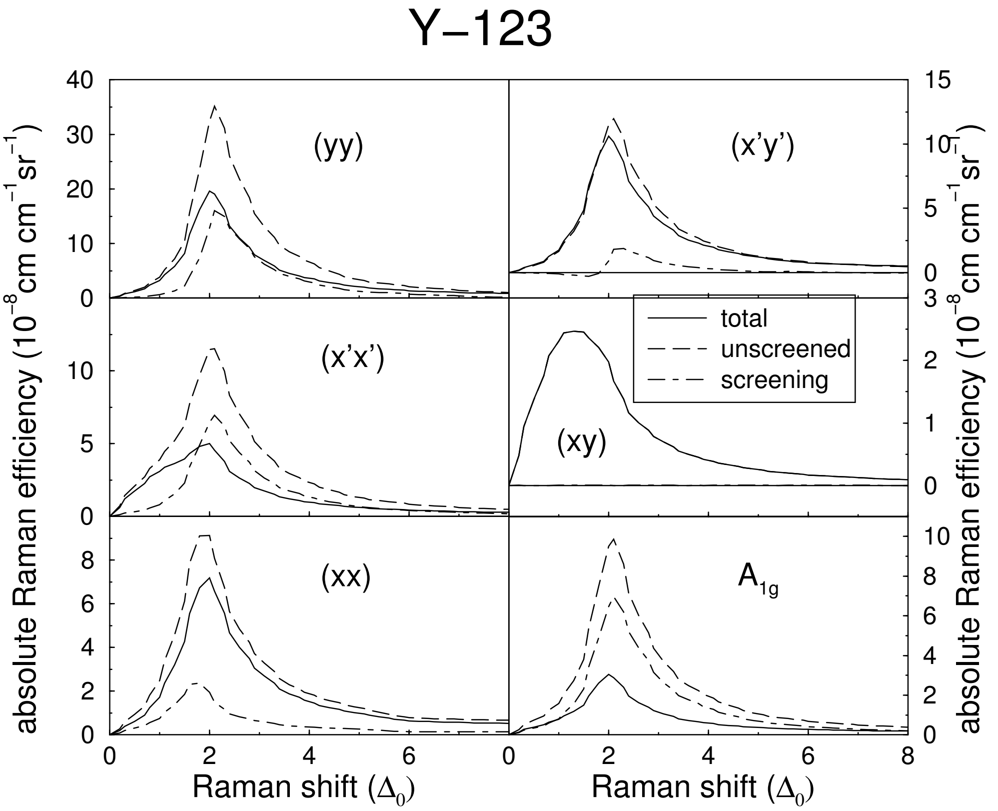

Figure 2.18: Results of the BZ integration leading to the electronic Raman scattering efficiencies for Y-123. Given in the five panels are absolute efficiencies for electronic Raman scattering. The upper three curves are labelled using the irreducible representation ($D_{4h}$) of the Raman tensor, the lower two panels with the polarization geometry. Each of the five panels contains the total absolute Raman efficiency according to Eq. (2.28) and (2.30) and its two constituents, the unscreened and the screening part according to Eq. (2.52).

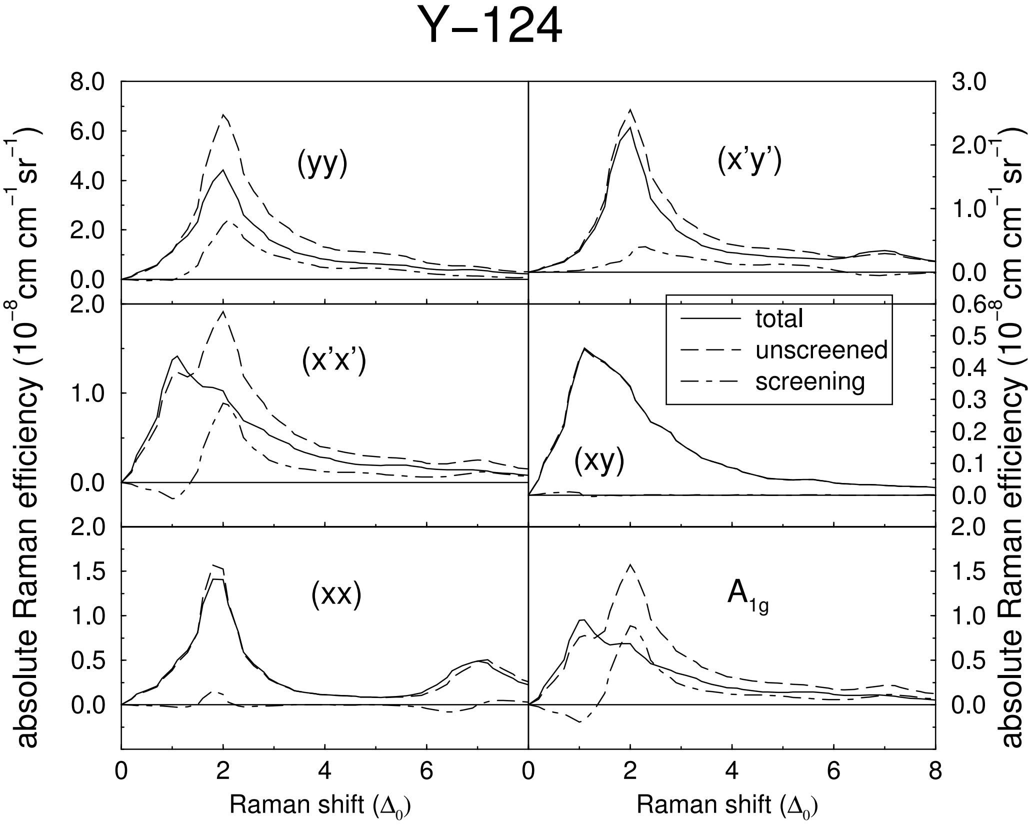

Figure 2.19: Results of the Brillouin zone integration for Y-124. For details see the caption of Fig. 2.18.

is very small, its nonvanishing being an effect of the distorted tetragonality of the crystal. There is, in this case, a very small amount of antiscreening in the region below $2\Delta_0$. As in the case of the $A_{1g}$ component, the $(x'y')$ component peaks at almost exactly the $2\Delta_0$ frequency shift. The low-frequency part has an $\alpha\omega + \beta\omega^3$ frequency dependence (see Sect. 2.9 and [2.28]), the linear part arising from the distorted tetragonality, that is, the fact that the $B_{1g}$ inverse effective mass does not vanish at exactly the same position on the Fermi surface as the gap function does.

The efficiency of the peak in the $(xy)$ configuration (equal to the $B_{2g}$ component in the nonresonant case) is also four or five times smaller than that of the $A_{1g}$ peak. The $(xy)$ peak is located at about $1.3\Delta_0$, as expected from the fact that in the neighborhood of the region where the gap is large (along the $k_x$ and $k_y$ axes), the $B_{2g}$ component of the inverse effective mass vanishes. Consequently, the peak is not as sharp as in the former cases and screening vanishes since these spectra correspond to a nonsymmetric $(B_{1g})$ representation of the orthorhombic group $(D_{2h})$. Note that this is only valid for the Y-123 crystal, but not for Bi-2212 (refer to Sect. 2.9 and [2.28]).

In the $A_{1g}$ and $(x'y')$ spectra there should be a small peak at about $\omega = 2\sqrt{\epsilon_{\mathrm{vH}}^2 + \Delta_{\max}^2} \approx 3.9\Delta_0$ due to the van Hove singularity[21] on the $k_x$-axis near the $X$-point. The corresponding structure, however, is very weak, and barely visible in Fig. 2.18. This is not unexpected for a 3D calculation. These peaks appear strongly when 2D calculations are performed through BZ integrations [2.24].

In general, the efficiencies in Y-124 (Fig. 2.19) are about a factor of three less than those for its Y-123 counterpart. Moreover, the screening of the $A_{1g}$ component of Y-123 is much stronger than that of Y-124. This may be, at least in part, due to the additional chain band: The $(yy)$ component of Y-124 is less screened than the $(yy)$ component of Y-123. At low frequencies, we correspondingly have antiscreening even in $A_{1g}$, a fact which reveals itself as a change of sign of the inverse effective mass on the Fermi surface (see Sec. 2.3). Due to this antiscreening, the peak in the $A_{1g}$ spectrum is shifted from $2\Delta_0$ towards approximately $1.6\Delta_0$. In contrast to the situation in Y-123, the Y-124 spectra show clearly the influence of the van Hove singularity on the spectra, as a small hump (vH) located near $2\sqrt{\epsilon_{\mathrm{vH}}^2 + \Delta_{\max}^2} \approx 7\Delta_0$. In the $A_{1g}$ spectrum this hump is almost screened out whereas in the $(x'y')$ spectrum it appears slightly increased by the influence of antiscreening.

To compare these predictions with the experiment let us first focus on the peak positions. The experimental results for Y-123 (Fig. 2.16, lower part) clearly show that the position of the $(yy)$, $(x'x')$ and $(xx)$ peaks is at about $300\,\mathrm{cm}^{-1}$, whereas the $(x'y')$ peak is located at $600\,\mathrm{cm}^{-1}$, that is, at twice the frequency of the former. This fact is in sharp contrast with the calculated spectra and has been at the center of the controversy concerning the topic at hand [2.53, 2.54]. It has been suggested by Devereaux *et al.* [2.8, 2.54] that the $B_{1g}$ component peaks at $2\Delta_0$, and the $A_{1g}$ component becomes shifted down to almost $\Delta_0$ by the screening. This interpretation contradicts our numerical results which clearly suggest that the influence of screening on the position of the $A_{1g}$ mode is usually smaller. The frequency renormalizations of phonons around $T_c$ also seem to contradict the interpretation

---

[21] The band-structure calculations [2.11] predict a van Hove singularity in the band structure of optimally-doped Y-123. This saddle-point is located on the $k_x$-axis near the $X$-point. Together with the fact that the $d_{x^2-y^2}$-like gap function has zero slope on the $k_x$-axis, this causes a peak in the Raman efficiency (see Subsect. 2.3.5).

in Refs. [2.8] and [2.54]. It has been shown [2.55] that lowering the temperature of the sample in the superconducting phase causes the $A_{1g}$ $435\,\mathrm{cm}^{-1}$ phonon (plane-oxygen, in-phase) to shift up in frequency and the $B_{1g}$ ($D_{4h}$ notation) $340\,\mathrm{cm}^{-1}$ phonon (plane-oxygen, out-of-phase) to shift down. This, in turn, implies a value of the gap parameter $2\Delta_0$ between $300\,\mathrm{cm}^{-1}$ and $360\,\mathrm{cm}^{-1}$ and is consistent with our interpretation of the electronic Raman spectra with the $A_{1g}$ peak at $2\Delta_0$.

Note that the $(yy)$, $(x'x')$ and $(xx)$ spectra do *not* contain contributions of the $A_{2g}$ ($D_{4h}$) antisymmetric component of the Raman tensor while the $(x'y')$ component does. Hence, the experimental results may suggest that the shift of the position of the $(x'y')$ spectrum with respect to the peak position of the other spectra maybe due to resonance effects. The $(xy)$ spectrum is also influenced by the $A_{2g}$ component. It is difficult to determine its peak position from Fig. 2.18, but it seems to be located at the same position as that of the $(yy)$, $(x'x')$ and $(xx)$ configurations. The calculation predicts it to be located at about $1.3\Delta_0$, the shift to $2\Delta_0$ can also be attributed to the existence of an $A_{2g}$ component, like in the case of the $(x'y')$ configuration.

To compare the relative intensities of the spectra with different polarizations, we refer to Table 2.2, which lists them together with the corresponding absolute intensities, both at the peak position. The detailed results of our FS integration have already been reported earlier [2.42]. We begin with Y-123 (upper panel in Table 2.2) and compare the BZ integration results to the experimental ones. With the possible exception of the $A_{1g}$ component (and the $(x'x')$ component, which is very similar to the $A_{1g}$ counterpart), the agreement is rather good. The deviation of the $A_{1g}$ component may be attributed to screening, which is very sensitive to sign changes and other details of the Raman vertex near the Fermi surface (such as details of the band structure and especially the exact position of the Fermi energy).

The second compound, Y-124 (lower panel in Table 2.2), also shows reasonable agreement between the results of the BZ integration and the experiment. However, we also have problems with the $A_{1g}$ component, as we did for Y-123.

The measured absolute intensities agree particularly well with the calculations in the case of Y-123. With the exception of $A_{1g}$, the discrepancy between theory and experiment is only a factor of two, which can easily be related to the difficulties in measuring absolute scattering cross sections. In the case of Y-124, the discrepancy is a bit larger, but a factor of four can still be considered good. We should also keep in mind that resonances of $\omega_L$ or $\omega_S$ with virtual interband transitions are expected to enhance the simple inverse effective mass Raman vertex, a fact which could also explain why the measured scattering efficiencies are usually larger than the calculated ones.

We close the discussion of the numerical results with a remark about the Fermi surface integration. For Y-124, the results of the former correspond rather closely to the results from the BZ integration. The situation is different for Y-123. Here, the $(xx)$ peak height is almost a factor of four larger in the FS integration than in the BZ integration. This is likely to result from the close proximity of the van Hove singularity to the FS in the case of Y-123 (25 meV), as compared to Y-124 (110 meV) [2.11].

To verify the predictions related to the effect of orthorhombic distortions, as discussed in Sec. 2.3, we performed a fit of the function $\alpha\omega + \beta\omega^3$ to the low-frequency part of the $B_{1g}$ data for Y-123 reported in Ref. [2.50] and Ref. [2.56] as well as for Bi-2212 (taken from Ref. [2.57]) and to the results of our numerical calculations for Y-123. The ratios of the

| **Y-123** | FS integration [2.42] | | BZ integration | | Experiment [2.50] | |
|---|---|---|---|---|---|---|
| Polarization | absolute | relative | absolute | relative | absolute | relative |
| $yy$ | 20.0 | 1.00 | 19.6 | 1.00 | 40 | 1.00 |
| $xx$ | 28.0 | 1.40 | 7.2 | 0.37 | 19 | 0.48 |
| $xy$ | 3.0 | 0.15 | 2.5 | 0.13 | 4 | 0.10 |
| $x'x'$ | | | 5.0 | 0.26 | 26 | 0.65 |
| $x'y'$ | 4.8 | 0.24 | 10.6 | 0.54 | 12 | 0.30 |
| $A_{1g}$ | 19.2 | 0.96 | 3.0 | 0.15 | 18 | 0.45 |

| **Y-124** | FS integration [2.42] | | BZ integration | | Experiment [2.43] | |
|---|---|---|---|---|---|---|
| Polarization | absolute | relative | absolute | relative | absolute | relative |
| $yy$ | 6.3 | 1.00 | 4.4 | 1.00 | 18.0 | 1.00 |
| $xx$ | 1.5 | 0.24 | 1.4 | 0.32 | 7.2 | 0.40 |
| $xy$ | 1.1 | 0.17 | 0.5 | 0.11 | 2.6 | 0.14 |
| $x'x'$ | | | 1.4 | 0.32 | 12.0 | 0.66 |
| $x'y'$ | 2.8 | 0.44 | 2.3 | 0.52 | 5.6 | 0.31 |
| $A_{1g}$ | 1.1 | 0.17 | 1.0 | 0.23 | 6.9 | 0.38 |

Table 2.2: Comparison of the experimental peak scattering efficiencies given in units of $10^{-8}\,\mathrm{cm\,cm^{-1}\,sr^{-1}}$ to the theoretical predictions (from Fermi surface integrations, Ref. [2.42], as well as Brillouin zone integrations, present work) for Y-123 and Y-124.

cubic vs. the linear part (at $\omega = 300\,\mathrm{cm}^{-1}$) of the fit to the low-frequency efficiency are given in Table 2.3.

Both measurements for Y-123 agree in their large linear part, which should arise from the lack of exact tetragonality, and also from the presence of impurities. The results of the BZ integration show a smaller linear part, because they do not take into account the influence of impurities. Finally, the result for Bi-2212 is completely different from the former results for Y-123. The linear part almost vanishes, in agreement with the preceding discussion.

In spite of the striking ability to predict not only general features of the observed spectra but also their peak intensities in absolute units, our calculations are not able to predict the relative positions of the $A_{1g}$ and $B_{1g}$ peaks. According to Figs. 2.18 and 2.19 the $A_{1g}$ spectrum should peak only slightly below $2\Delta_0$ while $B_{1g}$ should peak at $2\Delta_0$. The

| HTSC | cubic:linear in $B_{1g}$ | Reference |
|---|---|---|
| Y-123 | 1 | Krantz *et al.* [2.50] |
| Y-123 | 1 | Hackl *et al.* [2.56] |
| Y-123 | 0.35 | BZ integration |
| Bi-2212 | 0.07 | Staufer *et al.* [2.57] |

Table 2.3: The ratio between the linear and cubic parts of the low energy Raman efficiency in $B_{1g}\,(D_{4h})$ configuration of several high-$T_c$ compounds at a Raman shift of $\omega = 300\,\mathrm{cm}^{-1}$.

experimental data of Figs. 2.16 and 2.17, however, indicate that the $B_{1g}$ spectra peak nearly at twice the frequency of $A_{1g}$. Since the observed $A_{1g}$ peak is considerably sharper than that of the $B_{1g}$ spectrum, we may want to assign the $A_{1g}$ peak to $2\Delta_0$. Our calculations show that it is impossible to reproduce both peak frequencies with a simple gap of the form $\Delta_0 \cos 2\varphi$ where $\varphi$ is the direction of the $\boldsymbol{k}$-vector. A reasonable fit was obtained in Ref. [2.50] with a two-dimensional FS which did not take into account the chain component and assigned $d$- and $s$-like gaps to the two bonding and antibonding sheets of the FS of the two planes in an *ad hoc* way. Within the present 3-dimensional band structure the FS cannot be broken up into bonding and antibonding plane and chain components since such sheets are interconnected at general points of $k$-space. It is nevertheless clear that there is no reason why the gap function should be the same in the various sheets for a given $\boldsymbol{k}$-direction. Thus the remaining discrepancy in the peak positions between theory and experiment could be due to a more complicated $\Delta_{n\boldsymbol{k}}$ than a simple $\Delta_0 \cos 2\varphi$ used here. Another possible source of this discrepancy is scattering through additional excitations of a type not considered here (e.g. magnetic excitations) contributing to and broadening the $B_{1g}$ peak.

A BCS-like theory, which involves an attractive pairing potential as well as the repulsive Coulomb potential and postulates an anisotropic $d_{x^2-y^2}$-like gap function in connection with the effective mass approximation yields absolute Raman scattering efficiencies which are in significant agreement with the experimental spectra. There is one exception, the relative peak positions of the $A_{1g}$ and the $B_{1g}$ components. The theory predicts them to be both located near $\omega = 2\Delta_0$, but the experiment shows the peak in $B_{1g}$ at almost twice the frequency of the peak in $A_{1g}$. The weak $B_{2g}$ spectrum agrees in intensity and peak position with calculations for a $d_{x^2-y^2}$-like gap. The results of other experiments, involving the temperature dependence of phonon frequencies [2.55], suggest that the $A_{1g}$ peak position corresponds to the gap amplitude $2\Delta_0$. The shifting of the $B_{1g}$ peak towards higher frequencies may have an origin different from the mass-fluctuation-modified charge-density excitations described in the theoretical part of this paper but could also be due to a multi-sheeted gap function, more complicated than the simple $d_{x^2-y^2}$-like $\Delta_0 \cos 2\varphi$ gap assumed in our calculations. The initial variation of the $A_{1g}$ and $B_{1g}$ scattering efficiencies vs. $\omega$ are linear as expected for that gap. The $B_{1g}$ symmetry becomes $A_g$ in the presence of the orthorhombic distortion related to the chains. Consequently, the scattering efficiency at low frequency is not proportional to $\omega^3$ but should have a small linear component which is found both in the calculated and the measured spectra. In the corresponding spectrum of Bi-2212, with and orthorhombic distortion along $(x + y)$, the $B_{1g}$ $(D_{4h})$ excitations also have a nonsymmetric $B_{1g}$ $(D_{2h})$ orthorhombic character. Consequently, for small $\omega$ no component linear in $\omega$ is found in the measured spectra.

We have performed our calculations using either BZ or FS integration. In the case of Y-124 the spectra so obtained are very similar. For Y-123 quantitative differences appear; they are probably related to the presence of a van Hove singularity rather close to the FS. These singularities appear as weak structures in the calculated spectra, as expected for a 3D band structure.

## 2.8 Other forms for the gap function

In this section, we present the results for the electronic Raman efficiency for forms of the gap function different from the $d_{x^2-y^2}$-ansatz we used in the former sections. Another difference to the treatment in the last sections is the band structure employed. Here, we use a simple model band structure whereas in the former section, the full LDA-LMTO band structure was used.

One simple band structure which can be inserted into the theory is an analytical expression with a small number of parameters as a model for a single-band band structure. In this case, though, Raman scattering can occur only via the $\boldsymbol{A}^2$ vertex because virtual interband transitions (i.e. transitions of the type $|i\rangle \rightarrow |m\rangle \rightarrow |f\rangle$ with $|i\rangle \neq |m\rangle$ and $|m\rangle \neq |f\rangle$) do not exist in the one-band model, and therefore transition matrix elements of the operator $\boldsymbol{p} \cdot \boldsymbol{A}$ vanish due to its negative parity. If virtual interband transitions are not important in the situation under consideration, the use of a single-band band structure may be an acceptable choice. But we can do better anyhow: the band structure $\epsilon_{\boldsymbol{k}}$ is not needed directly for the calculation of the Raman efficiency using the expression

$$I(\omega) \sim \langle \gamma_{\boldsymbol{k}}^2 \lambda_{\boldsymbol{k}}(\omega) \rangle - \frac{\langle \gamma_{\boldsymbol{k}} \lambda_{\boldsymbol{k}}(\omega) \rangle^2}{\langle \lambda_{\boldsymbol{k}}(\omega) \rangle} \tag{2.78}$$

but just in the form of the $\boldsymbol{k}$-dependent Raman vertex. The Raman vertex, however, already combines transitions via the $\boldsymbol{A}^2$ and $\boldsymbol{p} \cdot \boldsymbol{A}$ vertices and the modeling of the Raman vertex by an parametrized analytical expression therefore seems to be a more clever choice than simply modeling the electronic band structure. This conclusion, however, depends heavily on the details of the problem to be analyzed.

### 2.8.1 A gap function of type $s + d$

The first class of gap dependencies on $\varphi$ that was investigated has the form of an extended $s$-like function having the full $A_{1g}$ symmetry of the tetragonal $D_{4h}$ point group,

$$\Delta(\varphi) = \Delta_0 + \Delta_1 \cos(4\varphi) \ .$$

We especially focused on the values of $\Delta_0 = 0.7$ and $\Delta_1 = 1$. This form for a gap function was suggested in recent work of B. Brandow [2.58].

In the ΓX (01) and ΓY (10) directions, this gap function has a maximum value of $\Delta_0 + \Delta_1$ with the same phase (positive) in both directions. In the ΓM (11) direction, it has a value of $\Delta_0 - \Delta_1$, which is negative. In between, there are two nodes (per quadrant in k-space).

Consequently, the derivative of the gap with respect to $\varphi$ vanishes in two nonequivalent directions, ΓX and ΓM, where it takes on different values. If the Raman vertex does not vanish in either of these directions, the unscreened Raman efficiency has two logarithmic singularities, at Raman shifts $\Delta_0 + \Delta_1$ and $\Delta_0 - \Delta_1$. The logarithmic singularities can be understood as arising from critical points in the two dimensional space represented by $\varphi$ and $dk/dE$. These peaks can be identified in all spectra for $A_{1g}$ Raman vertices, especially in the spectrum calculated for the (unscreened) isotropic Raman vertex $\gamma_\varphi = 1$ in Fig. 2.20 which also shows the exact cancellation of the unscreened term by the screening term.

For a slightly nonisotropic $A_{1g}$ vertex (Fig. 2.21) of the form $\gamma_\varphi = 1 + (1/2)\cos(4\varphi)$ the screened spectrum does no longer vanish identically. An interesting property of this case is that the peak at higher frequency is screened more strongly than that at lower frequency: The screened spectrum consists of a single peak at the position $\Delta_0 - \Delta_1$.

Raman vertices of $A_{1g}$ symmetry which change sign on the Fermi surface produce antiscreening which is strongest in the frequency range of the gap function at the node position of the Raman vertex. In Fig. 2.22 the results for an $A_{1g}$ vertex of the form $\gamma_\varphi = 1+(3/2)\cos(4\varphi)$ are displayed. This Raman vertex changes sign near the ΓM direction, where the gap function takes approximately the value $\Delta_0 - \Delta_1$. At this frequency, Fig. 2.22 shows strong antiscreening that enhances drastically the unscreened spectrum.

Figure 2.23 shows the effect of the $A_{1g}$ vertex $\gamma_\varphi = 1 - (3/2)\cos(4\varphi)$ which is large in ΓM direction and small in ΓX direction. The nodes are close to the ΓX direction where the gap function is almost $\Delta_0 + \Delta_1$. Exactly in this frequency range, antiscreening occurs.

In the case of a vertex with $B_{1g}$ symmetry (Fig. 2.24), the singularity at $\Delta_0 - \Delta_1$ appears as an almost invisible kink, because the ΓM direction is not sampled due to the vanishing Raman vertex. Furthermore, the low-energy spectrum is linear in the Raman shift! This is due to the fact that the gap does not vanish in the ΓM direction, where the $B_{1g}$ vertex vanishes. In the case of a $d$-wave gap function in tetragonal high-$T_c$'s, the node of the gap function and the node of the $B_{1g}$ vertex coincide. This produces a low-frequency behavior of the imaginary part of the Raman susceptibility which is cubic. This behavior has been verified in some important cases (e.g. Bi-2212).

To summarize, the screened Raman efficiency for different choices of an $A_{1g}$ vertex shows a peak at the frequency $\Delta_0 - \Delta_1$ and a small, strongly screened feature at the frequency $\Delta_0 + \Delta_1$. In the case of a $B_{1g}$ vertex, the situation is reversed. At the frequency $\Delta_0 - \Delta_1$ there is only a very tiny kink. The strong peak is located at the frequency $\Delta_0 + \Delta_1$.

## 2.9 The $s$-wave/$d$-wave gap ratio in nontetragonal HTSC

There are two distinct ways to distort the tetragonal ($D_{4h}$ point group) symmetry of the Cu-O plane of high-temperature superconductors (HTC). One way is realized in Y-123. The presence of the Cu-O chains increases the distance of two Cu ions in the plane in $y$-direction, but leaves their distance in $x$-direction almost unchanged (see Fig.2.25, left panel). The initially tetragonal primitive unit cell becomes orthorhombic in this way, the tetragonal $B_{1g}$ irreducible representation (IR) corresponds the the orthorhombic $A_g$ IR. Consider a $d_{x^2-y^2}$-like gap function in tetragonal Y-123. The presence of the $\sigma_{x'}$ and $\sigma_{y'}$ mirror planes guarantees that the nodes of the gap function coincide with the nodes the the $B_{1g}$ component (corresponding to the $(x'y')$ polarization) of the Raman vertex. In orthorhombically distorted Y-123 there are no $\sigma_{x'}$ and $\sigma_{y'}$ mirror planes, and the coincidence of the gap function nodes and the $(x'y')$ component of the Raman vertex is not enforced by the point group symmetry of the crystal.

In Bi-2212 the situation is different. The tetragonal symmetry becomes broken, because the Cu-O square in the primitive unit cell actually has sides of equal length, but the angles deviate slightly from $\pi/2$. Therefore, the approximate square actually is a rhombohedron,

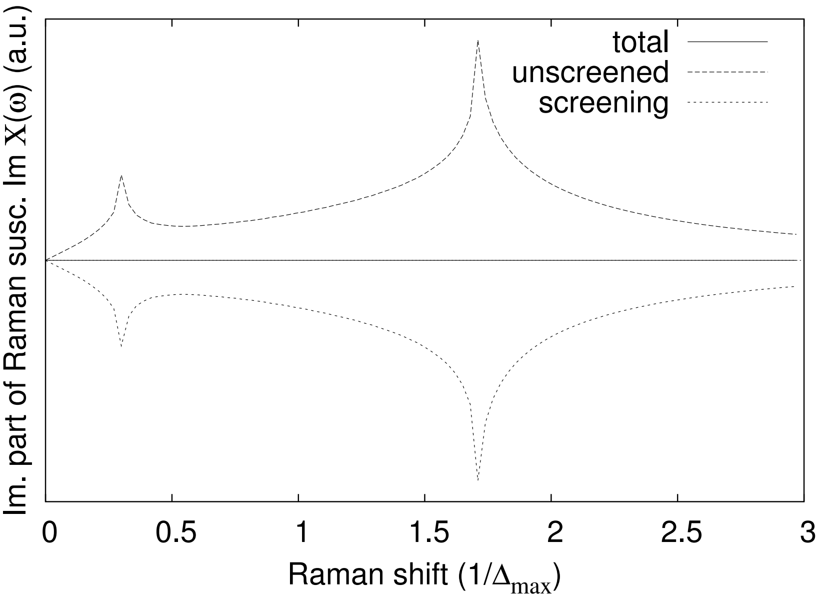

Figure 2.20: Imaginary part of the Raman susceptibility for $A_{1g}$ polarization and an isotropic Raman vertex $\gamma_\varphi = 1$.

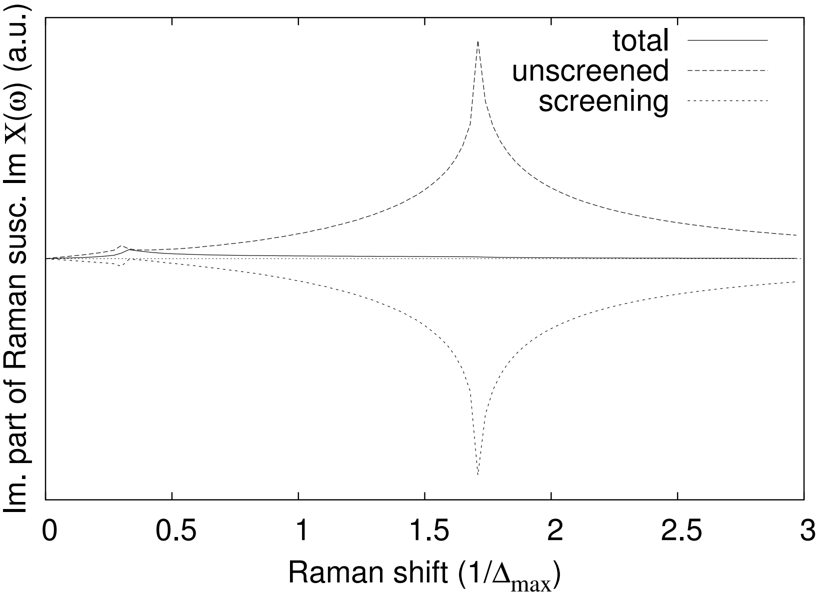

Figure 2.21: As in Fig. 2.20 but with a slightly anisotropic Raman vertex $\gamma_\varphi = 1 + (1/2)\cos(4\varphi)$.

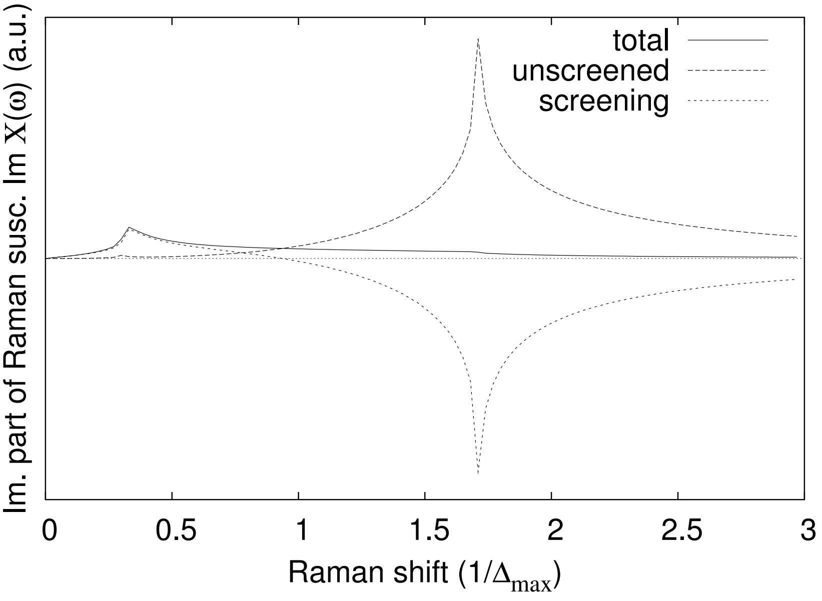

Figure 2.22: As in Fig. 2.20 but with a very anisotropic Raman vertex $\gamma_\varphi = 1 + (3/2)\cos(4\varphi)$ which changes sign on the Fermi surface close to the ΓM direction.

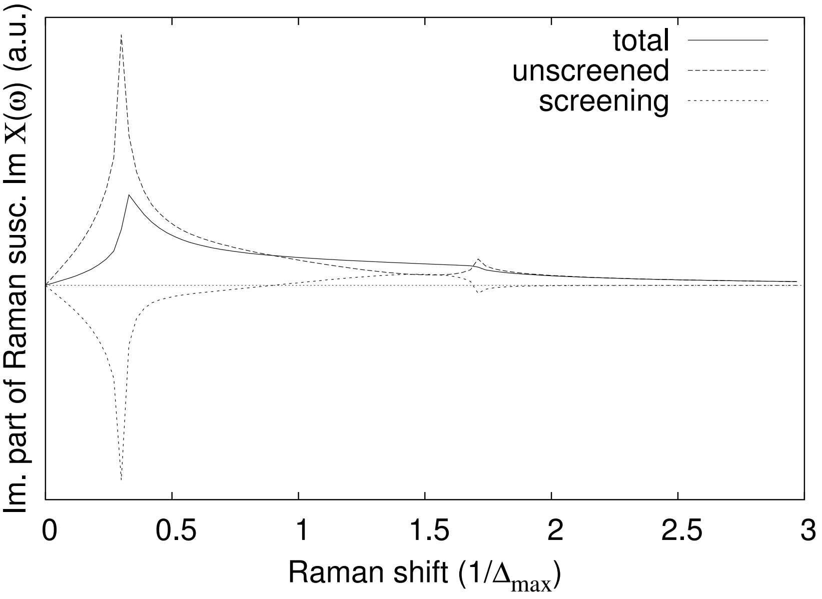

Figure 2.23: As in Fig. 2.20 but with a very anisotropic Raman vertex $\gamma_\varphi = 1 - (3/2)\cos(4\varphi)$ which changes sign on the Fermi surface close to the ΓX direction. Note the antiscreening in the 0.9 to 1.7 Raman shift region.

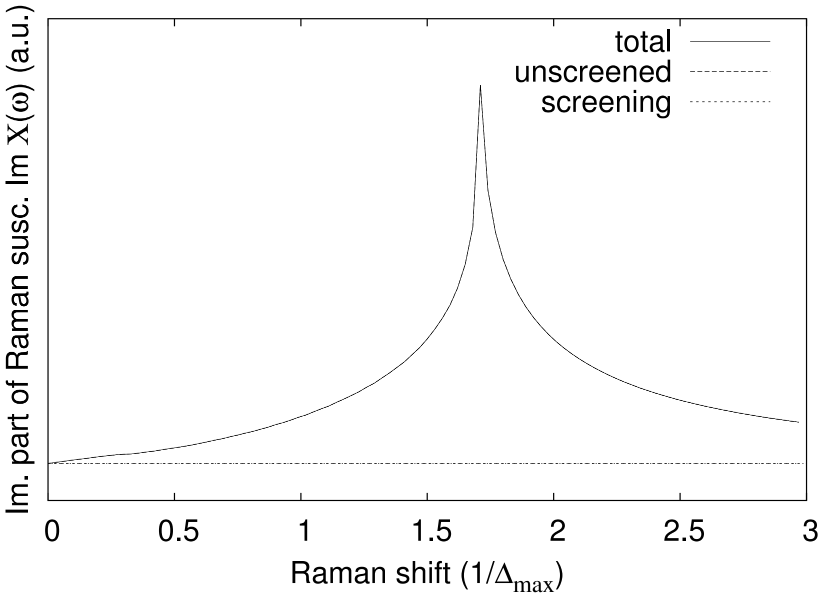

Figure 2.24: Imaginary part of the Raman susceptibility for $B_{1g}$ polarization and a $d$-wave Raman vertex $\gamma_\varphi = \cos(2\varphi)$.

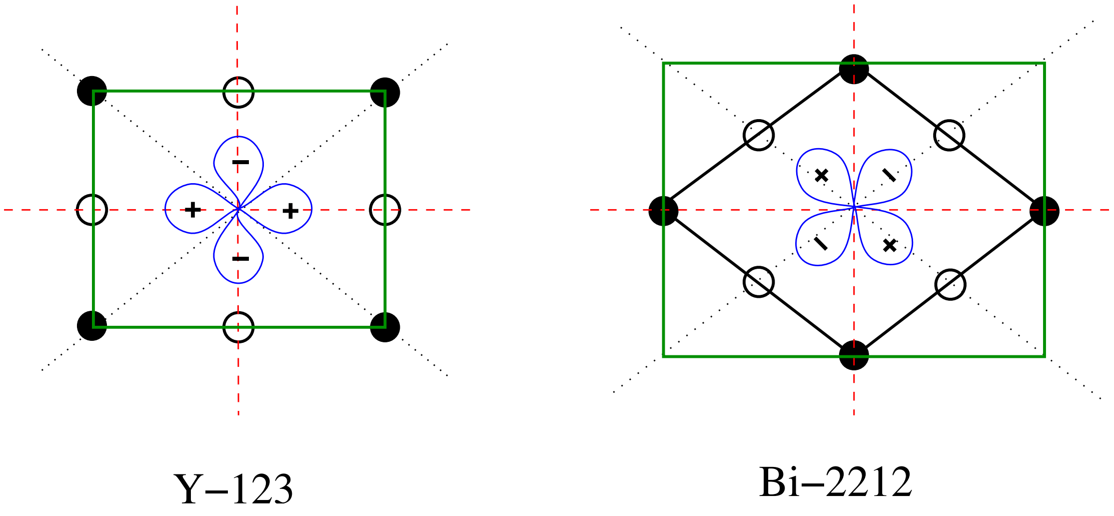

Figure 2.25: The two possibilities of deforming a tetragonal crystal into an orthorhombic one in the case of high-$T_c$ cuprates.

which has orthorhombic symmetry. To make this obvious, we choose a symmetry-adapted unit cell with twice the size of the primitive unit cell (see Fig.2.25, right panel). Considering again a $d_{x^2-y^2}$-like gap function, it is obvious that the gap nodes and the nodes of the $(x'y')$ polarization related Raman vertex component coincide as required by the presence of the $\sigma_{x'}$ and $\sigma_{y'}$ mirror planes even in the orthorhombic case.

This section deals with Y-123-like orthorhombic HTSC. Due to the fact that the $d_{x^2-y^2}$-like wave function transforms according to the $A_g$ $(D_{2h})$ IR, like the $s$-wave gap function does, both functions may mix. Therefore, and because the deviation from the tetragonal case is small, the gap function in Y-123 should mainly be $d_{x^2-y^2}$-like, with a small $s$-wave component [2.59, 2.60, 2.61, 2.62, 2.63]. In this section, we present a method to determine the position of the nodes of the gap function in nontetragonal high-$T_c$ superconductors. We write this gap function in the form

$$\Delta_\phi = \Delta_0 \cdot [\cos(2\phi) + r] \ , \tag{2.79}$$

($\Delta_0$ as well as $r$ are assumed to be real) where $\phi$ is the polar angle in the $k_x$-$k_y$-plane ($\phi = 0$ corresponds to the $\Gamma$X direction), and demonstrate how to determine the parameter $r$ using electronic Raman scattering together with LDA-LMTO band structure calculations [2.64].

It is well known [2.65, 2.27] that *tetragonal* high-$T_c$ superconductors show a low-energy Raman spectrum in $B_{1g}$ polarization configuration which is cubic in the Raman shift, that is, $I(\omega) \sim \omega^3$. There are two principal conditions which can alter this low-frequency law, the presence of impurities [2.32, 2.66], and an orthorhombic distortion [2.63, 2.27] like the one present in the high-$T_c$ superconductors (HTSC) in which the tetragonal $D_{4h}$ point group symmetry is broken by the presence of the Cu-O chains. Either of the two circumstances leads to an additional contribution to the low-frequency regime linear in the Raman shift. This makes the low-energy spectrum acquire the form

$$I(\omega) \sim \alpha \frac{\omega}{\omega_0} + \left(\frac{\omega}{\omega_0}\right)^3 \tag{2.80}$$

with two parameters $\omega_0$ and $\alpha$ which can be determined from fits to the low-energy regime of the experimental results from electronic Raman scattering [2.27]. In view of the fact that the results do not change very much from sample to sample, at least in optimally doped samples [2.67], we neglect impurity scattering.

According to the theory of electronic Raman scattering in anisotropic superconductors [2.65, 2.27, 2.68] the scattering efficiency in $B_{1g}$ polarization at $T = 0$ is given by the Fermi surface (FS) average

$$I(\omega) \sim \langle \gamma^2_{B_{1g}}(\phi) \lambda_{\mathrm{FS}}(\phi, \omega) \rangle \ , \tag{2.81}$$

in which the influence of impurities has been neglected. Here $\gamma_{B_{1g}}(\phi)$ denotes the $B_{1g}$ component of the inverse effective mass and $\lambda_{\mathrm{FS}}(\phi, \omega)$ is the imaginary part of the Tsuneto-function which for $\omega > 2|\Delta_\phi|$ is given by

$$\lambda_{\mathrm{FS}}(\phi, \omega) \sim \frac{|\Delta_\phi|^2}{\omega \sqrt{\omega^2 - 4|\Delta_\phi|^2}} \ . \tag{2.82}$$

and vanishes for $\omega < 2|\Delta_\phi|$. Note that in general $I(\omega)$ is given by a Brillouin zone (BZ) average. However, under the reasonable assumption that $\gamma_{\boldsymbol{k}}$ and $\Delta_{\boldsymbol{k}}$ do not change much close and perpendicular to the FS, the average over the BZ can be reduced to the FS average of Eq. (2.81).

At this point we introduce another angular variable $\varphi$ defined as $\varphi = \phi - \phi_0$ where $\phi_0$ is the position of the node of the gap function in the ΓX-ΓY quadrant and corresponds to the ΓM direction in tetragonal systems. From inspection of the Tsuneto-function, it is clear that the Raman response at a certain Raman shift $\omega$ arises from those regions on the Fermi surface where twice the gap is smaller than $\omega$. Therefore, in the calculation of the low-energy Raman efficiency ($\omega \ll 2\Delta_0$), we only have to take into consideration those regions of the FS which are close to the gap nodes. We shall focus our attention on one of these gap nodes and, later on, treat the other three gap nodes by using symmetry arguments. The vanishing of the gap function at $\varphi = 0$ allows us to approximate it by $\Delta(\varphi) = \Delta_1\varphi$. We treat the inverse effective mass $\gamma$ also in a linear approximation, $\gamma_{B_{1g}}(\varphi) = \gamma_0 + \gamma_1\varphi$, $\gamma_0$ being the value of $\gamma(\varphi) \equiv \gamma_{B_{1g}}(\varphi)$ at the position $\varphi = 0$ of the gap node, and $\gamma_1$ its slope. This approximation allows us to analytically evaluate the FS-average in Eq. (2.81) in the low-frequency regime. The result is given by the expression

$$I(\omega) \sim \alpha_1\omega + \alpha_2\omega^2 + \alpha_3\omega^3 \tag{2.83}$$

with the coefficients

$$\alpha_1 = \frac{\pi}{2}\frac{\gamma_0^2}{8\Delta_1}\ , \quad \alpha_2 = C\frac{\gamma_0\gamma_1}{8\Delta_1^2}\ , \quad \alpha_3 = \frac{3\pi}{8}\frac{\gamma_1^2}{32\Delta_1^3}\ . \tag{2.84}$$

The proportionality constant $C$ in the equation for $\alpha_2$ actually vanishes in our linear approximation for $\Delta(\varphi)$ and $\gamma(\varphi)$. In an exact calculation, this constant would also be zero if we include all nodes of the gap function in the $0 < \varphi < 2\pi$ domain: the $D_{2h}$ symmetry operations $\sigma_x$ and $\sigma_y$ can be used to map the other three nodes on the first one. Upon application of the $\sigma_x$ or $\sigma_y$ symmetry operations, the constant $\gamma_1$ changes sign. As a result, the total quadratic contribution in Eq. (2.83) vanishes and the final result is given by Eq. (2.83) with $\alpha_2 = 0$ and $\alpha_1$, $\alpha_3$ given by Eq. (2.84).

To determine the ratio $\gamma_0/\gamma_1$ at the gap node, we compare these results with the experimental values of $\alpha$ and $\omega_0$ determined with Eq. (2.80) and obtain the relation

$$\alpha = \frac{\alpha_1\omega_0}{\alpha_3\omega_0^3} = \frac{4}{3}\left(\frac{2\Delta_1}{\omega_0}\right)^2 \cdot \left(\frac{\gamma_0}{\gamma_1}\right)^2\ , \tag{2.85}$$

which expresses the fact that the position of a node of the gap function and the ratio of the value and the first derivative of $\gamma(\phi)$ at that position are related. Furthermore, the latter ratio is related to that of the linear and cubic parts in the low-energy electronic Raman spectrum in $B_{1g}$ polarization. Note that Eq. (2.85) also works for tetragonal superconductors: For Bi-2212, there is no linear contribution [2.63] in the low-energy part of the electronic Raman spectrum, therefore $\alpha = 0$, and Eq. (2.85) yields $\gamma_0 = 0$. This means that the nodes of the gap function and the node of the $B_{1g}$ component of the inverse effective mass $\gamma$ are at the same position.

The presence of impurities also may give rise to a linear part in the low-energy electronic Raman spectrum [2.32, 2.66]. This leads to an overestimate of the parameter $\alpha$ in Eq. (2.80) and, according to Eq. (2.85), to an underestimate of $\gamma_0/\gamma_1$ at the gap node. While this fact should be kept in mind when we extract the parameter $r$, we have given arguments that suggest that impurity effects can be neglected.

The availability of the LDA-LMTO band structure allows us to calculate the inverse effective mass $\gamma(\phi)$ and, therefore, $\gamma(\phi)/\gamma'(\phi)$ as a function of $\phi$. This enables us to localize the point $\varphi_0$ on the Fermi surface, where $\gamma(\phi)/\gamma'(\phi)$ assumes the value $\gamma_0/\gamma_1$. This is the position of the gap node and, thus, yields the value of $r$ in Eq. (2.79).

In the next few paragraphs, we shall give an example of the use of the method outlined above to evaluate $r$. It turns out that sometimes we find more than one solution for the position of the gap node in the ΓX-ΓY quadrant. Within the framework of this method, no further information on which of the two values is the correct one is available.

In the case of $YBa_2Cu_3O_7$ a further complication arises: the existence of two Cu-O plane bands (we call them $a$ and $b$, antibonding and bonding with respect to inversion) which are both superconducting. Each of these bands defines a sheet of the FS. Therefore, we have two different inverse effective masses $\gamma_a(\phi)$ and $\gamma_b(\phi)$ as well as two different gap functions $\Delta_\phi^{(a)}$ and $\Delta_\phi^{(b)}$ and, as a consequence, two different Tsuneto-functions $\lambda_a(\phi,\omega)$ and $\lambda_b(\phi,\omega)$. The fact that the Fermi sheets of the two plane bands are rather close in $k$-space implies $\Delta_\phi^{(a)} \approx \Delta_\phi^{(b)}$, as well as $\lambda_a(\omega) \approx \lambda_b(\omega)$, and therefore

$$\langle \gamma_a^2 \lambda_a \rangle + \langle \gamma_b^2 \lambda_b \rangle \approx \langle (\gamma_a^2 + \gamma_b^2)\lambda \rangle \tag{2.86}$$

holds. Hence, the one-band expression in Eq. (2.83) is still valid if we replace $\gamma_0^2$ by $\gamma_{a,0}^2 + \gamma_{b,0}^2$ and $\gamma_0\gamma_1$ by $\gamma_{a,0}\gamma_{a,1} + \gamma_{b,0}\gamma_{b,1}$. Note that we neglect a possible influence of a nonvanishing gap function in the strongly orthorhombic Cu-O chains on the Raman efficiency and a term which is due to the mixing of the bands [2.69].

From the experimental electronic Raman spectrum in $B_{1g}$ polarization for $YBa_2Cu_3O_7$ [2.70] in Fig. 2.26 we determined a coefficient $\alpha = 1$ at $\omega_0 = 300\,\mathrm{cm}^{-1}$. Furthermore, the LDA-LMTO band structure yields the functions $\gamma_{a,B_{1g}}(\phi)$ and $\gamma_{b,B_{1g}}(\phi)$ which are plotted in Fig. 2.27 together with the function

$$\Lambda(\phi) = \left| \frac{\gamma_{a,0}^2 + \gamma_{b,0}^2}{\gamma_{a,0}\gamma_{a,1} + \gamma_{b,0}\gamma_{b,1}} \right| . \tag{2.87}$$

Note that the $k_x$-$k_y$-plane angle $\phi$ denotes $\phi = \arctan(k_y/k_x)$ and $\phi = 0$ is given by the ΓX direction. For the slope $\Delta_1$ of the gap function $\Delta_\varphi$ at its node, we take the value $\Delta_1 = 450\,\mathrm{cm}^{-1}\mathrm{rad}^{-1}$, which is supported by several experiments [2.65]. According to Eq. (2.85), these values for $\alpha$, $\omega_0$ and $\Delta_1$ require the functions $\Lambda(\phi)$ to take on the value 0.3 at the position $\phi_0$ of the gap node, which leads to (see Fig. 2.27)

$$\phi_0 = 0.57\,\mathrm{rad} = 33^\circ \quad \text{and} \quad r = -0.42 \tag{2.88}$$

or

$$\phi_0 = 0.68\,\mathrm{rad} = 39^\circ \quad \text{and} \quad r = -0.21 \tag{2.89}$$

as a second possibility.

Note that the function $\Lambda(\phi)$ in Fig. 2.27 has a local minimum in the region between 0.3 and 1 rad with a value of 0.06. If the gap node were at the position of this minimum, the linear part in the low-energy spectrum would vanish. The value of 0.06 corresponds to a value of $\alpha = 0.04$ at $\omega_0 = 300\,\mathrm{cm}^{-1}$. This value can be higher in an experiment due to the presence of impurities. The band structure calculation yields $\alpha = 0.04$ as a lower bound for the linear part in the electronic Raman spectrum.

A second remark concerns the reliability of the LDA-LMTO band structure. It is believed that this band structure is reasonable in the vicinity of the Fermi surface. A more serious problem may be resonance effects changing the nonresonant inverse effective mass vertex used here. They could, of course, be included in the calculation with additional computational work. However, consideration of these has not been necessary for the semiquantitative interpretation of absolute scattering intensities [2.27, 2.71].

We summarize: in this section, we have presented a method to determine the position of the nodes of the gap function for nontetragonal high-$T_c$ superconductors using inverse effective masses obtained from LMTO band structure calculations and the Raman efficiency at low energies. The method has been applied to the case of $YBa_2Cu_3O_7$ for which a result is given.

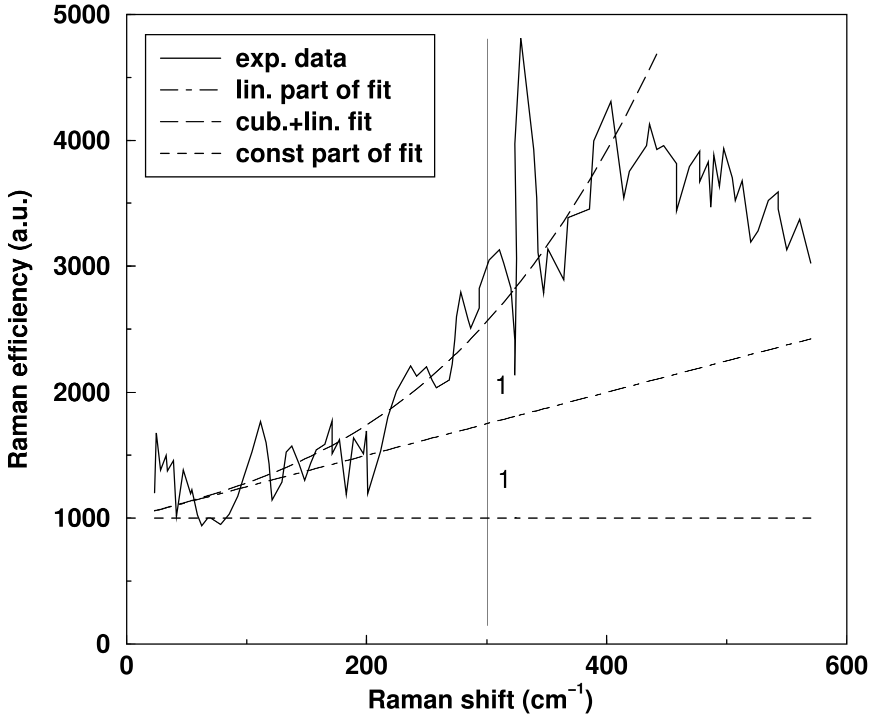

Figure 2.26: Linear and cubic part of the low-energy region of the $B_{1g}$ scattering efficiency for Y-123 from the experiment [2.70].

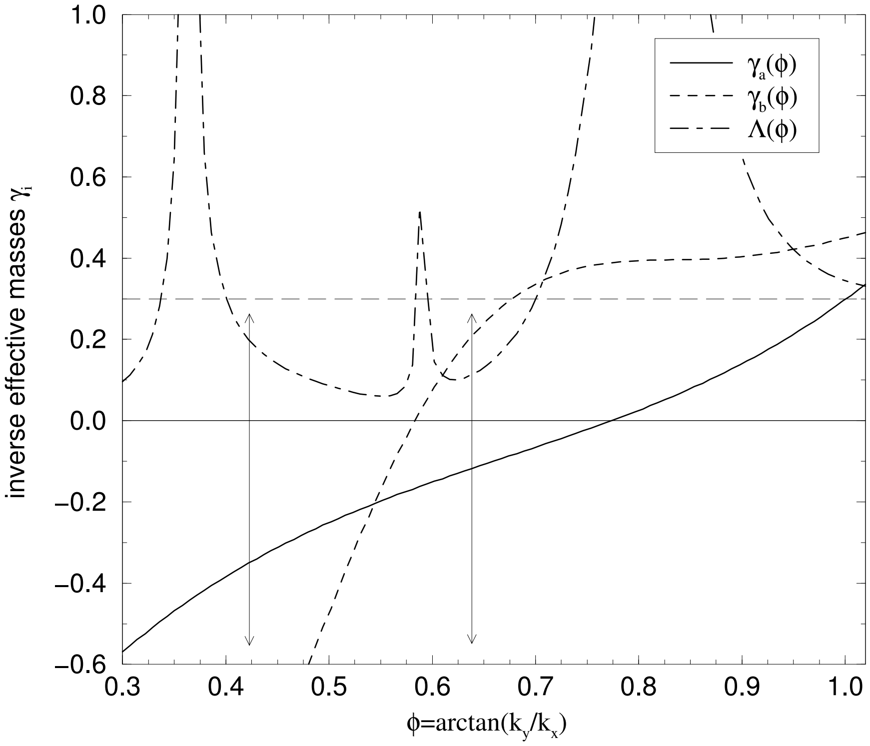

Figure 2.27: Inverse effective masses for the Cu-O plane bands on the Fermi surface around the ΓM direction for Y-123 from a LDA-LMTO calculation [2.27].

## 2.10 Extensions and other aspects of the theory

### 2.10.1 A comment on vertex renormalizations

Manske *et al.* presented in Ref. [2.21] a calculation of electronic Raman scattering in clean $d$-wave superconductors in which the $B_{1g}$ electronic Raman response is affected by electronic screening. They claimed that this screening suffices to explain drastic differences between experiments and previous calculations. We show that these differences remain after errors in Ref. [2.21] are corrected.

In Ref. [2.21], Manske *et al.* propose a modified theory for the explanation of the electronic Raman scattering in clean $d$-wave high-$T_c$ superconductors for incoming and scattered light wave vectors perpendicular to the CuO planes. Their Fermi-liquid-like theory is based on a simple $t$-$t'$ model band structure. It involves a renormalization of the Raman vertex $\gamma_{\boldsymbol{k}}$ by a pairing interaction $V(\boldsymbol{k},\boldsymbol{k}')$ and a short-range interaction $U_q$ (in Ref. [2.21], $U_q$ is taken as independent of $q$, otherwise their Eq. (6) is wrong) in a ladder approximation, and additionally by the short-range interaction $U_q$ in RPA. An expression for the Raman response function is obtained and it is claimed that for certain values of the parameters of the model band structure, it reproduces the measured Raman spectra in $YBa_2Cu_3O_7$ (Y-123).

Here, we want to point out some mistakes in Ref. [2.21], which invalidate the conclusions and also make some comments concerning the proposed theory.

(1) The expression for the $A_{1g}$ component of the Raman vertex $\gamma_{A_{1g}}$ given in Eq. (5) of Ref. [2.21] is clearly not fully symmetric with respect to the $D_{4h}$ point group and therefore incorrect (actually, it has "$A_{1g}+B_{2g}$" symmetry). The correct expression is

$$\gamma_k^{A_{1g}} \propto t[\cos(k_x)+\cos(k_y)-4B\cos(k_x)\cos(k_y)] \ . \tag{2.90}$$

instead of

$$\gamma_k^{A_{1g}} \propto t[\cos(k_x)\cos(k_y)-4B\cos(k_x)\cos(k_y)] \ . \tag{2.91}$$

The wrong expression for this vertex was used together with Eq. (11) of Ref. [2.21] to calculate the Raman response function $\chi_{A_{1g}}(\omega)$. Consequently, the computed $A_{1g}$ spectrum shown as solid line in their Fig. 3 must also be incorrect. Using the same parameters for the band structure as in Ref. [2.21], we repeated the calculation of $\operatorname{Im}\chi_{A_{1g}}$ with the correct vertex (2.90) and obtained the result given in our Fig. 2.28, which is by almost *two orders of magnitude* smaller than that given in Ref. [2.21]. Even the unscreened part (i.e., $2\operatorname{Im}\langle\gamma^2_{A_{1g}}\Delta^2_{\boldsymbol{k}}\rangle$ in the notation used by Manske *et al.*) is one order of magnitude smaller than the fully screened one of Ref. [2.21]. Note that also the peak position of the $A_{1g}$ spectrum now corresponds almost to the peak position of the $B_{1g}$ Raman spectrum. Therefore, the difference in the peak position of the $A_{1g}$ and $B_{1g}$ Raman spectra is not explained by the Ansatz of Manske *et al.* nor is the ratio of the peak strenghts.

We also plotted in Fig. 2.28 the $B_{2g}$ component of the Raman spectrum which is almost identical to the wrong $A_{1g}$ Raman spectrum. This is due to the fact that the wrong Raman vertex is equal to $\gamma^{A_{1g}}+\gamma^{B_{2g}}$ and that the magnitude of the $A_{1g}$ Raman spectrum is much smaller than that of the $B_{2g}$ Raman spectrum. The result that the peak in the $B_{2g}$ spectrum occurs at a lower Raman shift than that in the $B_{1g}$ spectrum is simply due to the fact that the $B_{2g}$ Raman vertex vanishes in $k$-space directions where the gap function $\Delta_{\boldsymbol{k}}$ has its maxima. The small magnitudes of both screened and unscreened $A_{1g}$ spectra in Fig. 2.28 result from the fortuitously small values of the Raman vertex of Eq. (1) on the Fermi surface as illustrated in Fig. 2.29. Note that the $B_{1g}$ Raman spectrum in Fig. 2.28 does not exhibit a strictly cubic low-energy behavior. This is due to the fact that we are using a broadened (but still causal) Tsuneto-function in the numerical integration of the Brillouin zone averages and has little influence on the Raman spectra at energies comparable to the gap amplitude or larger.

(2) The band structure parameters used for the calculation of the Raman response in Ref. [2.21] are also questionable. They correspond to a filling of 1.2 electrons per plane band and unit cell. Band structure calculations and ARPES measurements [2.72] suggest the filling to be in the range from 0.6 to 0.8 electrons per plane band and unit cell.

(3) It is important also to include in the theory the renormalization of the Raman vertex by the pairing interaction $V(\boldsymbol{k}, \boldsymbol{k}')$ in the RPA-like term (last term in Eq. (6) and last diagram in Fig. 1 of Ref. [2.21]). The fact that the interaction $U_q$ is of short-range implies that the contribution of the pairing interaction to the RPA-like term is of the same order of magnitude as the contribution of the short-range interaction $U_q$. If a long-range interaction of the Coulomb-type were involved, taking into account the pairing interaction $V(\boldsymbol{k}, \boldsymbol{k}')$ would not be necessary because the Coulomb interaction is much more important than the pairing interaction in the $\boldsymbol{q} \to 0$ limit.

(4) The expression for the $B_{1g}$ component of the Raman response given in Eq. (12) of Ref. [2.21] already was given in Ref. [2.25], Eq. (C23), with the only exception that in Ref. [2.21] the interaction $V$ in the $B_{1g}$ channel is expressed by Tsuneto-function weighted Brillouin zone averages of combinations of the quasiparticle energies $\epsilon_{\boldsymbol{k}}$ and the gap function $\Delta_{\boldsymbol{k}}$.

In conclusion, the theory given by Manske *et al.*, if correctly formulated, does not explain the anomalies observed in the electronic Raman spectra of $d$-wave superconductors.

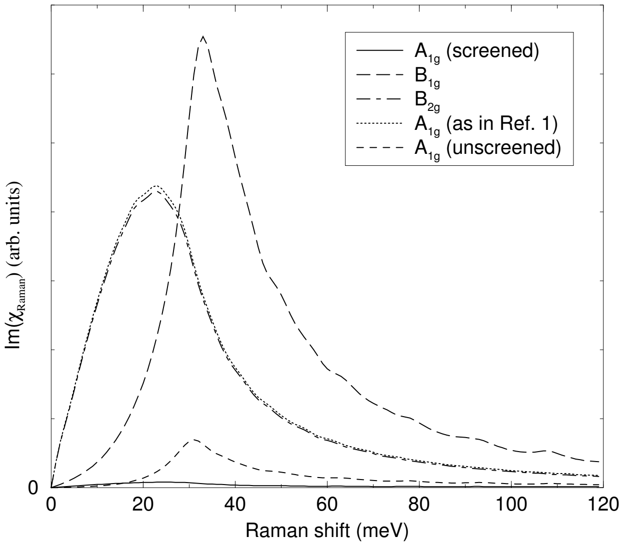

Figure 2.28: Imaginary part of the Raman response for different polarization configurations. The thin solid, long-dashed, and dot-dashed lines are our results for the $A_{1g}$, $B_{1g}$, and $B_{2g}$ irreducible representations, respectively. The thick solid line corresponds to the Raman spectrum calculated with the wrong Raman vertex $\gamma_{A_{1g}}$ in Ref. [2.21] while the short-dashed line is the result for the unscreened $A_{1g}$ Raman spectrum and the dotted line corresponds to the screening part contained in the result for $B_{1g}$.

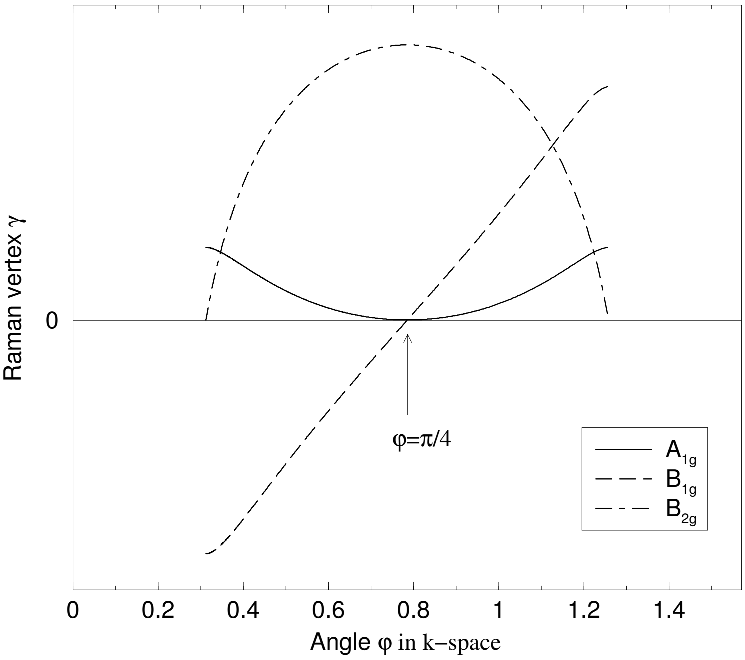

Figure 2.29: Irreducible components of the Raman vertex on the Fermi surface as a function of the angle in the first quadrant of the Brillouin zone.

# Chapter 3

# Phonon Raman scattering

## 3.1 Introduction

The presence of electron-phonon coupling in systems which possess electron-hole excitations and phononic excitations introduces two new physical processes: (i) the electronic Raman efficiency is changed as a consequence of the new decay channel for electron-hole pairs to recombine via the creation of a phonon, and (ii) the indirect coupling of light to the phonons via an intermediate electron-hole excitation gives rise to *phonon Raman scattering*. The chapter at hand serves the purpose of reviewing and investigating these effects.

An implication of the very large magnitude of the speed of light in comparison to the Fermi velocity is that an electron-hole pair, which was created by inelastic scattering of light, has zero total quasimomentum. One of the constituents of the electron-hole pair may scatter and thereby create a phonon. This process has a nonvanishing amplitude only if the electron-hole pair resulting from the scattering process may recombine later via the creation of light. This implies the vanishing of the quasimomentum of the phonons which participate in the electron-phonon coupling. *The phonons which have to be considered when discussing Raman scattering in the presence of electron-phonon coupling have a vanishing quasimomentum, that is, are* $\Gamma$*-point phonons.*

The system to be considered for the discussion of Raman scattering consists of a continuous spectrum of electron-hole excitations and one (or a small number of) discrete phonon excitation (the $\Gamma$-point phonon). The physical effects of the coupling of a discrete excitation to a continuous excitation spectrum has been studied first by Fano [3.1] in the context of energy loss spectroscopy where the discrete levels of an atom are involved in the discrete excitation, and by Anderson [3.2] (see also [3.3], Chap. 4.2) who discussed the coupling of a single impurity state to a continuous spectrum of electron-hole excitations. Although the physics of phonon Raman scattering is obviously different from the absorption by atomic levels, the effect of the coupling of a continuous spectrum of electron-hole excitations to a discrete phonon excitation is called the *Fano effect* in the framework of the theory of Raman scattering. We will go further and call the theory of electronic Raman scattering, after extending it to include the Fano effect, the *Fano theory*.

The general theory of Raman scattering is described in a very comprehensive manner by Enderlein and coworkers [3.4], an application to insulators is described by Mills and Burstein [3.5]. The formulation of the theory of Raman scattering using the temperature-dependent diagram technique has been given by Kawabata [3.6]. In the context of isotropic superconductivity, the Raman efficiency is calculated by Klein and Dierker [3.7].

A recent treatment of the Fano effect in the light of Feynman diagrams was presented by Belitsky and coworkers [3.8]. Itai [3.9] discusses the Fano effect in presence of impurity scattering.

In Sect. 3.2 the definition and interpretation of the Raman vertex is reviewed. Then the electron-phonon vertex and the photon-phonon vertex are introduced and discussed. The Green's function for the electronic excitations and the phonons are defined and the basic polarization loop is reviewed. The Fano theory with certain simplifying assumptions is given in Sect. 3.3, and its different contributions are explained. In Sect. 3.4 we generalize this theory and introduce the concept of a renormalized phonon intensity which is used in the interpretation of the experiment presented in Sect. 3.5. Also, the concepts of anharmonic decay and the Eliashberg-functions, which are playing an important role in the theory of superconductivity, are introduced. Finally, in Sect. 3.5, which is the central section in this chapter, we describe a Raman scattering experiment and try to understand it by means of the theory presented in the other sections of this chapter.

The material presented in Sect. 3.5, and concerning the Raman scattering experiment, is based on a publication by Hadjiev and coworkers [3.10].

## 3.2 The photon-phonon vertex and other prerequisities

In App. A we have shown how a coupling of electronic excitations to phonons arises. A consequence of this coupling is that phonons are "seen" in electronic Raman scattering. The discrete phonon excitation which is involved in Raman scattering is interfering with the electron-hole continuum. For the sake of giving later an elementary theory of the *Fano effect*, we will recall the properties of the vertices which are important in this theory.

**Raman vertex.** The *Raman vertex* $\gamma_{\boldsymbol{k}}$ (shown in Fig. 3.1) describes the transition amplitude for the inelastic scattering of light by creating a pair-excitation[1] in the electron system of the specimen under consideration. This process is described by the diagram in Fig. 3.1. The Raman vertex (2.17) corresponds to a second rank tensor since it must be contracted with the electric field vector of the incident and the scattered light. It also depends on the vector $\boldsymbol{k}$ characterizing the electronic pair-excitation. Due to the fact that the velocity of light is much larger than typical Fermi velocities, the total quasimomentum $\boldsymbol{q}$ transferred to the solid in the scattering process is approximately zero (it is two or three orders of magnitude less than the $\boldsymbol{k}$-vector at the BZ boundary). As was already shown in Chap. 2, the Raman vertex (2.16) is the result of summing two different diagrams (Figs. 2.2 and 2.3), both second order in light, describing inelastic scattering of light on an electron system. The Raman vertex shows a dependence on the light frequency $\omega_L$ which may be in resonance with electronic pair-excitations for some values of $\omega_L$.

**Electron-phonon vertex.** The coupling of electrons to phonons is quantified by the *electron-phonon vertex* $g_{\boldsymbol{k}}$ describing the process of the destruction of a phonon by creating an electronic pair-excitation or vice versa and is illustrated in Fig. 3.2. If the

---

[1] Only electronic *pair* excitations are of interest here, because the particle number has to be conserved.

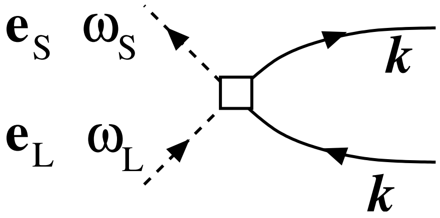

Figure 3.1: The Raman vertex $\gamma_{\boldsymbol{k}}$ for scattering by electronic excitations. Incoming and scattered light have the frequencies $\omega_L$ and $\omega_S$ as well as the polarizations $\boldsymbol{e}_L$ and $\boldsymbol{e}_S$, respectively.

total quasimomentum $\boldsymbol{q}$ of the electronic pair-excitation is zero, this is also the case for the phonon, and therefore we will restrict to Γ-point phonons.[2]

The electron-phonon vertex is a $\boldsymbol{k}$-dependent scalar. [3] In general, it also has a phonon branch index, but here and in most of the following material we will consider only nondegenerate optical phonons.

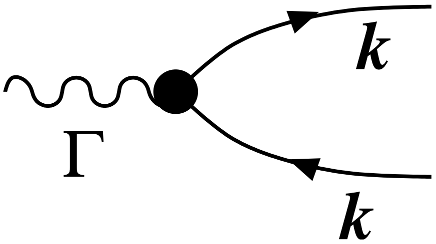

Figure 3.2: The electron-phonon vertex $g_{\boldsymbol{k}}$.

**Photon-phonon vertex.** Phonon Raman scattering can be repesented by the photon-phonon vertex $T_p$ which describes the transition amplitude for inelastic light scattering by creating a phonon. One possible mechanism for this process is the coupling of the electric fields of the light waves to the ionic charges in an ionic crystal. When developing a theory for this process, one would start with the Hamiltonian of the ion system coupled to the electromagnetic field. The kinetic part of this operator is given by $(1/2M_{\rm ion})\sum_i(\boldsymbol{P}_i+(q_{\rm ion}/c)\boldsymbol{A}(\boldsymbol{R}_i))^2$, where the sum runs over all ions in the lattice, $\boldsymbol{R}_i$ and $\boldsymbol{P}_i$ are the position and momentum operators, respectively, of ion $i$, and for simplicity all the ions are assumed to have the same mass $M_{\rm ion}$ and charge $q_{\rm ion}$. The vertex which describes the direct photon-phonon coupling originates from the term $H_{\boldsymbol{Ap},\rm ion} = (q_{\rm ion}/cM_{\rm ion})\sum_i \boldsymbol{P}_i\boldsymbol{A}(\boldsymbol{R}_i)$ which has to be taken in second order perturbation theory and then leads to processes in which the inelastic scattering of light creates a *pair* of phonons (shown in Fig. 3.3(a)). We will not consider this process further, because it is quadratic in

---

[2] Actually some care is needed here. If we talk of Γ-point phonons it is always meant $\boldsymbol{q}\to 0$, but $\boldsymbol{q}\neq 0$. For $\boldsymbol{q}=0$, the acoustical phonon degenerates into static strain which does not contribute to the dynamics of the electron-phonon system.

[3] If there is no degeneracy. Otherwise it will be a quantity which transforms according to a certain irreducible representation of the crystal point group.

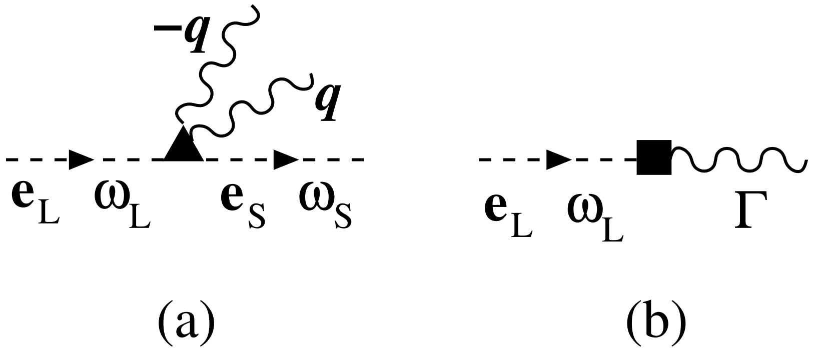

Figure 3.3: (a) Direct inelastic light scattering by phonons, and (b) light absorption by phonons.

the phonon, and expected to be small because the large ionic mass appears in the denominator.

A process which leads to inelastic scattering of light and the creation of *one* phonon is shown in Fig. 3.4. It involves the creation and destruction of an electronic pair-excitation. This is the basic diagram for phonon Raman scattering.

In optical absorption, the creation of a phonon in conjunction with the absorption of a photon is described by $H_{\boldsymbol{Ap},\mathrm{ion}}$ in first order perturbation theory. Usually (if not forbidden by selection rules) the diagram in Fig. 3.3(b) is the dominant process leading to light absorption via a phonon.

From the diagram in Fig. 3.4 it is clear that phonon Raman scattering is sensitive only to even-parity phonons (we consider a crystal with an inversion center), because the incoming and scattered photon have the same parity. *Raman scattering is sensitive to even Γ-point phonons only.* In optical absorption this is different. From Fig. 3.3(b) we infer that the involved Γ-point phonons have to have odd parity, because the photons do so. Considering the coupling which is proportional to the dipol momentum of the optical Γ-point phonon, and noticing that even-parity phonons have a vanishing dipol momentum yields to the same result.

Electronic Raman scattering and phonon Raman scattering are of quite different nature. In electronic Raman scattering, the Raman shift (i.e. the difference between the energy of the incoming laser light $\omega_L$ and the energy of the scattered light $\omega_S$) corresponds directly to the energy of the electron-hole excitation created in the scattering process. In an intrinsic semiconductor with a gap energy $E_g$ and at $T = 0$, the electronic Raman spectrum will vanish from 0 to $E_g$ Raman shift (except for excitons). For phonons, this is different. The first step in phonon Raman scattering (Fig. 3.4) is the creation of a *virtual* electron-hole pair with an energy of $\epsilon_{e-h}$ and a transition amplitude which is proportional to $(\epsilon_{e-h} - \omega_L)^{-1}$. Then the scattering of the hole (electron) while creating a phonon with energy $\omega_\Gamma$, which changes the energy of the electron-hole excitation to $\epsilon'_{e-h}$, and possesses a transition amplitude proportional to $\epsilon'_{e-h} + \omega_\Gamma - \omega_L$. Eventually, the virtual electron-hole pair is destroyed, the transition amplitude for this is proportional to $\epsilon'_{e-h} - \omega_S$. The process is important close to the resonance, that is, the electron-hole excitations which are mainly involved in phonon Raman scattering have an energy of approximately the photon energy $\omega_L$. They are not directly related to the electron-hole excitations which are responsible for electronic Raman scattering at energies close to the energy of the phonon.

Note that for a scaling $\boldsymbol{A}_L \rightarrow \alpha \boldsymbol{A}_L$ of the laser light amplitude, the photon-phonon vertex scales as $T_p \rightarrow \alpha^2 T_p$ just as the Raman vertex does. This is due to the occurrence of the two $\boldsymbol{A} \cdot \boldsymbol{p}$ vertices in the diagram in Fig. 3.4.

Like the Raman tensor, the photon-phonon vertex corresponds to a second rank tensor (we again only consider the case of no phonon degeneracy). But as a contrast, it is *not dependent* on $\boldsymbol{k}$. When evaluating the diagram in Fig. 3.4, the $\boldsymbol{k}$-dependence is integrated out. The diagram in Fig. 3.5 is not a contribution to the photon-phonon vertex but will turn out to be just a part of the renormalization of the electronic Raman vertex.

To prevent from falling into the trap of identifying the coupling constants $V$ in the processes given by the diagrams in Figs. 3.4 and 3.5, respectively, we note that usually these electron-phonon matrix elements $V$ involve completely different electronic states. In Fig. 3.4 it involves either only occupied or occupied states and in Fig. 3.4 an electron-hole excitation.

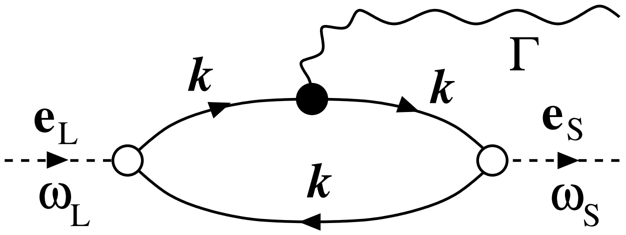

Figure 3.4: The photon-phonon vertex $T_p$ involving an electronic pair-excitation is given by this diagram.

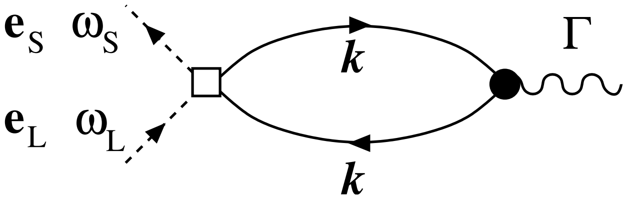

Figure 3.5: This is *not* a contribution to the photon-phonon vertex $T_p$ but to the renormalization of the Raman vertex $\gamma_{\boldsymbol{k}}$.

**The bare Green's functions.** The elementary excitations in the Fano process are the electronic pair-excitation continuum and the discrete phonon excitation (the Γ-point phonon). Electronic pair-excitations appear in the Fano theory as *polarization loops*, the most general one (Fig. 3.6) describes the creation of an electron-hole pair via a vertex $a_{\boldsymbol{kq}}$, the electron having an energy $\nu + \omega$ ($\hbar = 1$ here) and quasimomentum $\boldsymbol{k} + \boldsymbol{q}$ and the hole having energy $-\nu$ and quasimomentum $\boldsymbol{k}$.[4] The electron-hole pair then is destroyed via a

---

[4] In the formalism applied here (see Sect. 2.8 in [3.3]), electron and holes have the same dispersion relation $\epsilon_{\boldsymbol{k}}$. The Green's functions, however, distinguishes between electrons and holes: it has a pole in the lower half of the complex frequency plane for $\epsilon_{\boldsymbol{k}} > \epsilon_F$ (electrons), and in the upper half for $\epsilon_{\boldsymbol{k}} < \epsilon_F$

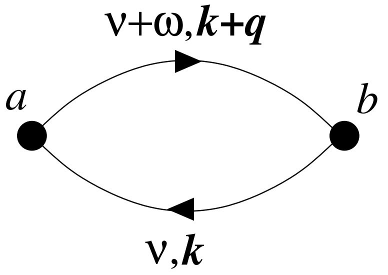

Figure 3.6: The basic polarization loop.

vertex $b_{\boldsymbol{kq}}$. The Green's function[5] of the electron is given by

$$G(\boldsymbol{k},\omega)=\frac{1}{\omega-\epsilon_{\boldsymbol{k}}+i\delta_{\boldsymbol{k}}}\ ,\qquad \delta_{\boldsymbol{k}}=\delta\cdot\mathrm{sign}(\epsilon_{\boldsymbol{k}}-\epsilon_F) \tag{3.1}$$

and the Feynman diagram (called polarization loop) in Fig. 3.6 translates to the expression

$$\chi^{(0)}_{to,ab}(\boldsymbol{q},\omega)=2i\int d\nu\sum_k a_{\boldsymbol{kq}}b^*_{\boldsymbol{kq}}G(\boldsymbol{k}+\boldsymbol{q},\nu+\omega)G(\boldsymbol{k},\nu)\ . \tag{3.2}$$

The function $\chi^{(0)}_{to,ab}(\boldsymbol{q},\omega)$ is called a *susceptibility*.[6] In the Fano theory, electron-hole pairs are always created by light via the Raman vertex or by a phonon via the electron-phonon vertex. In the first case, the quasimomentum $\boldsymbol{q}$ of the pair vanishes. In the second case $\boldsymbol{q}$ also vanishes, because the phonon itself was either created by an electron-hole excitation or by inelastic light scattering. Therefore we are interested only in pair-excitations or phonons at the Γ-point, that is, with $\boldsymbol{q}\approx 0$. The polarization loop then reads

$$\chi^{(0)}_{to,ab}(\omega)=\int d\nu\sum_k a_{\boldsymbol{k}}b^*_{\boldsymbol{k}}G(\boldsymbol{k},\nu+\omega)G(\boldsymbol{k},\nu)\ .$$

If the Fano theory we will introduce a further simplification by assuming that the vertices are independent of $\boldsymbol{k}$. Consequently the susceptibility acquires the form

$$\chi^{(0)}_{to,ab}(\omega)=ab^*\sum_k G(\boldsymbol{k},\nu+\omega)G(\boldsymbol{k},\nu)\equiv ab^*\chi_{to,0}(\omega)\ , \tag{3.3}$$

---

(holes). A consequence is the vanishing of the frequency integral in the expression for the polarization loop if $\boldsymbol{k}$ and $\boldsymbol{k}+\boldsymbol{q}$ are both either below or above the Fermi energy. Nonvanishing contributions to the polarization loop only arise if one of the two particles is above and the other below the Fermi surface. In this case, the difference $\epsilon_{\boldsymbol{k}+\boldsymbol{q}}-\epsilon_{\boldsymbol{k}}$ appears as excitation energy when performing the frequency integration. As a conclusion, we label both electron lines in the polarization loop with frequency and quasimomentum of electrons, not holes, and take into account the particle number conservation by two arrows pointing in opposite direction.

[5] These are *time-ordered* Green's functions for which the diagrammatic perturbation expansion is valid. We only employ them in the calculation of the polarization loop. For all other purposes we make use of the retarded Green's functions, because they also obey a Dyson equation and are directly related to observable quantities. The retarded Green's functions fulfill the Kramers-Kronig relations. For a time-ordered Green's function $G(\omega)$ and a retarded Green's function $G_{ret}(\omega)$, the relations $\mathrm{Im}\,G(\omega)=\mathrm{sign}(\omega)\,\mathrm{Im}\,G_{ret}(\omega)$ and $\mathrm{Re}\,G(\omega)=\mathrm{Re}\,G_{ret}(\omega)$ are valid.

[6] More specific, it is a time-ordered susceptibility (hence the subscript *to*), because the Green's function used to define it is time-ordered as well. The second subscript *ab* refers to the vertices, and the superscript (0) indicates that it is a *bare*, i.e., not renormalized, susceptibility.

and can be expressed by the function $\chi_{to,0}(\omega)$ which is defined by (3.3) and can be interpreted as the Green's function of an electron-hole pair (or electronic susceptibility) because it's imaginary part is proportional to the density of electron-hole excitations. The *retarded* susceptibilities $\chi^{(0)}_{ab}(\omega)$ and $\chi_0(\omega)$ corresponding to the time-ordered susceptibilities $\chi^{(0)}_{to,ab}(\omega)$ and $\chi_{to,0}(\omega)$, respectively, shall be used extensively in the Fano theory. We introduce their real and imaginary parts of $\chi_0(\omega)$ in the form

$$\rho(\omega) = -\frac{1}{\pi}\,\mathrm{Im}\,\chi_0(\omega) \qquad \text{and} \qquad R(\omega) = \mathrm{Re}\,\chi_0(\omega)\ .$$

The imaginary part $\rho(\omega)$ of $-(1/\pi)\chi_0(\omega)$ is a *spectral density function* for the electron-hole excitations and the real part $R(\omega)$ is connected with $\rho(\omega)$ via a Kramers-Kronig relation, because $\chi_0(\omega)$ is analytic in the upper half plane of the complex frequency $\omega$.

The *screening* of the polarization loop by electrons can easily be incorporated in the present formalism by using the same method as in Chap. 8 and replacing the susceptibilities $\chi$ by the corresponding screened susceptibilities $\chi/\epsilon$.

The *phonon excitation* is taken to be an optical phonon close to the $\Gamma$-point with a (bare) frequency of $\omega_{p,0}$. Its Green's function[7] is given by

$$D_0(\omega) = \frac{1}{\omega - \omega_{p,0} + i\delta} - \frac{1}{\omega + \omega_{p,0} + i\delta} = \frac{2\omega_{p,0}}{\omega^2 - \omega_{p,0}^2 + i\delta\,\mathrm{sign}(\omega)}\ .$$

We have included phonons with negative frequency ("traveling in negative time direction") in the Green's function $D_0(\omega)$. They are necessary if we are interested in frequencies much less than the bare phonon frequency $\omega_{p,0}$ and also because the relation $D_0(-\omega) = D_0^*(\omega)$ has to be fulfilled. If these things are not of importance, the approximation

$$D_0(\omega) = \frac{1}{\omega - \omega_{p,0} + i\delta} \tag{3.4}$$

may be used.[8]

The Fano theory renormalizes the Raman susceptibility $\chi_{Raman}(\omega)$ by multiplying it with a functional of the phonon Green's function $D_0(\omega)$, the vertices $T_e$, $T_p$, and $V$, and the polarization loop $\chi_0(\omega)$, see (3.10). This renormalization should not alter the property of $\chi_{Raman}(\omega)$ with respect to the transformation $\omega \to -\omega$ and this is guaranteed if $D_0(-\omega) = D_0^*(\omega)$.

## 3.3 Elementary Fano theory

After the preparations and definitions introduced in the last section, we are well armed to tackle the problem of giving a first elementary version of the Fano theory. The notion

---

[7] This is the retarded phonon Green's function for $T = 0$. We are not going to use the time-ordered Green's function because all the renormalizations are done with the Dyson equation and this equation is valid for the time-ordered and the retarded Green's function as well. In Sect. 3.4.6 we renormalize the electron and this would require the time-ordered phonon Green's function, but there we employ the imaginary-time Green's function.

[8] The reader may have the impression that we are somehow picky about the behavior of the Green's functions upon the transformation $\omega \to -\omega$. But the importance of this property should not be underestimated, especially not when calculating the real part of a Green's function from its imaginary part (or vice versa) by means of a Kramers-Kronig transformation.

*elementary Fano theory* is coined by the request for maximum simplicity while still showing the physical principles of the Fano effect.

### 3.3.1 The different contributions

**Renormalizing the electronic Raman efficiency.** Now we are prepared to give an elementary Fano theory. As already announced, our elementary Fano theory will *neglect* the $\boldsymbol{k}$-dependence of the vertices, we write in the following the $\boldsymbol{k}$-independent vertices as

$$\gamma_{\boldsymbol{k}} \to T_e \ , \qquad g_{\boldsymbol{k}} \to V$$

and also treat all vertices $T_e$, $V$, and $T_p$ as *real* quantities. In the next section, this restriction will be removed.

First of all, we recall the theory of electronic Raman scattering [3.7, 3.6]. In this theory, the Raman efficiency $I(\omega)$ is proportional to the imaginary part of the Raman susceptibility $\chi_{Raman}(\omega)$,[9] which, in the easiest case of vanishing screening and a $\boldsymbol{k}$-independent Raman vertex $T_e$, is given by the electron-hole susceptibility $\chi_0(\omega)$ with total quasimomentum $\boldsymbol{q} = 0$ (Fig. 3.7(a)) multiplied by the square of the vertex,

$$\chi_{Raman}(\omega) = T_e^2 \chi_0(\omega) \ .$$

Taking into consideration the electron-phonon coupling processes described in the last paragraphs an electron-hole excitation can be destroyed by creating a phonon. Processes of this kind give rise to an infinite amount of contributions to the electronic Raman scattering shown in Fig. 3.7(b), and consequently renormalize the Raman susceptibility. We call the electronic Raman susceptibility renormalized by electron-phonon interactions the *Fano susceptibility* $\chi_{Fano}$, illustrated by

$$\chi_{Raman} \xrightarrow{\text{el-p coupling}} \chi_{Fano} \ .$$

All these different contributions constitute a geometric series and, therefore, can be summed up (Fig. 3.8). We define the *renormalized phonon Green's function* $D(\omega)$

$$D = D_0 + D_0 V \chi_0 V D_0 + D_0 V \chi_0 V D_0 V \chi_0 V D_0 + \cdots$$

dropping the frequency-dependence of the Green's functions in this and the subsequent equations whenever convenient.[10] The summation yields the *phonon Dyson equation*

$$D^{-1}(\omega) = D_0^{-1}(\omega) - V^2 \chi_0(\omega) \ . \tag{3.5}$$

As a consequence, the renormalized electronic Raman scattering is described by the sum of the Green's functions $\chi_{el}^{(0)}(\omega)$ and $\chi_{el}^{(1)}(\omega)$ shown in Fig. 3.9. The sum of the diagrams (a)

---

[9] Actually, the Raman efficiency $I(\omega)$ is a 4th rank tensor, because it is proportional to the square of the Raman vertex $\gamma_{\boldsymbol{k}}$, which is a 2nd rank tensor and has to be multiplied with the polarization vectors $\boldsymbol{e}_L$ and $\boldsymbol{e}_S$ of the incoming and the scattered light, respectively. In the discussion at hand, we fixed the polarization vectors, and therefore the Raman efficiency appears as a scalar.

[10] This equation tells us that the combination $V^2 \chi_0 D_0$ is dimensionless. Green's functions always have the unit 1/eV, consequently the vertices have the unit eV.

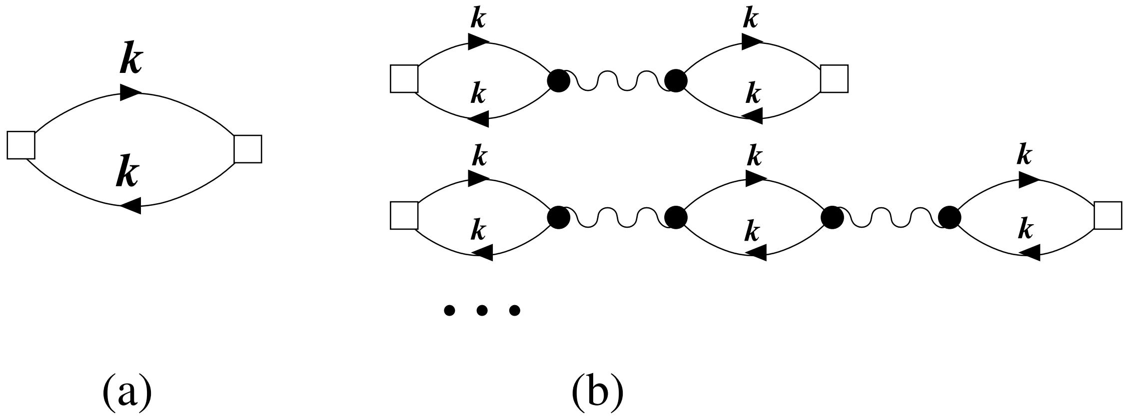

Figure 3.7: (a) The diagram describing bare electronic Raman scattering, and (b) the first two diagrams out of an infinite series which results in the renormalization of the electronic Raman scattering by electron-phonon interaction. The photon lines which correspond to the incoming and scattered light, respectively, have been omitted (cf. Fig. 2.6).

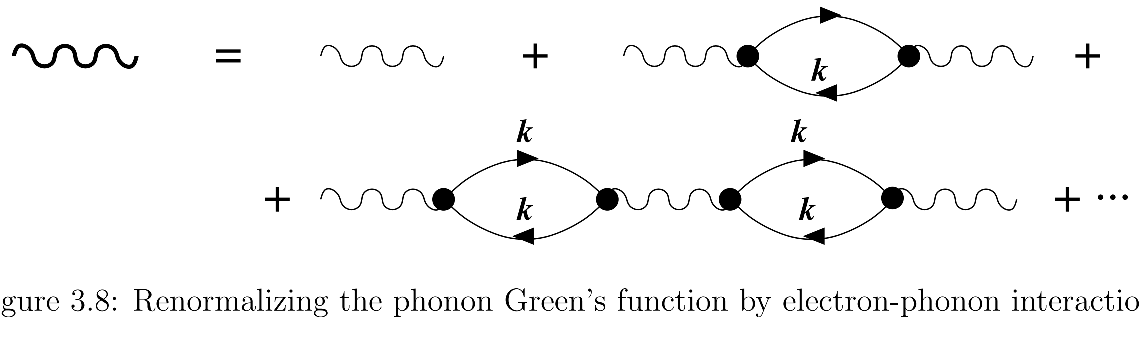

Figure 3.8: Renormalizing the phonon Green's function by electron-phonon interaction.

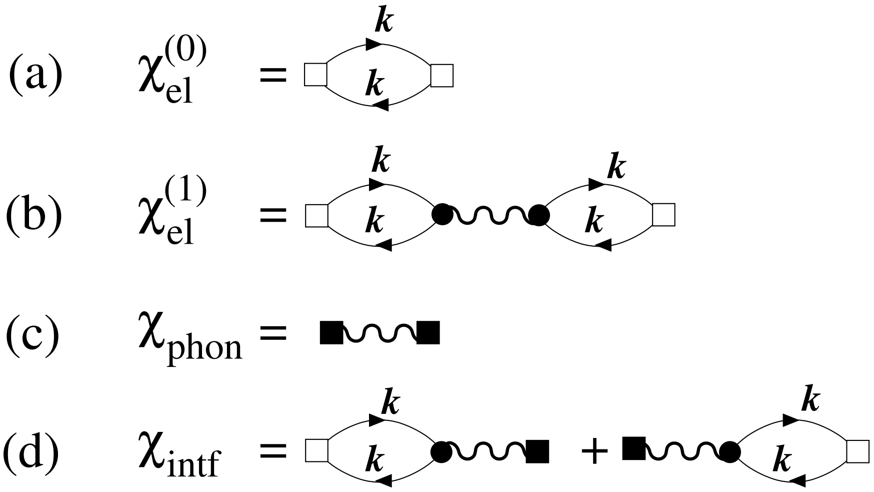

Figure 3.9: The different contributions to the Fano susceptibility. Panel (a) represents the bare electronic Raman susceptibility which is equal to the Fano susceptibility in the limit of vanishing electron-phonon coupling. Panel (b) depicts the renormalization of the electronic Raman susceptibility by electron-phonon interaction. Show in panel (c) is the contribution from phonon Raman scattering to the Fano susceptibility. The black-box vertices are an abbreviation for the photon-phonon vertex as shown in Fig. 3.4 with omitted photon lines. Finally, panel (d) depicts the contributions which result from the interference of electronic and phonon Raman scattering.

and (b) in Fig. 3.9 is equivalent to the sum of all diagrams in Fig. 3.7, therefore the sum of the Green's functions is given by

$$\begin{aligned}\chi_{el}(\omega) &\equiv \chi_{el}^{(0)}(\omega) + \chi_{el}^{(1)}(\omega) \\ &= T_e^2\left(\chi_0 + \chi_0 V D V \chi_0\right) = \frac{T_e^2}{|D|^{-2}}\left(\chi_0 |D|^{-2} + V^2 \chi_0^2 D^{*\,-1}\right) \ .\end{aligned}$$

If we now use the Dyson equation (3.5) of the renormalized phonon, we get the expression

$$\chi_{el} = \frac{T_e^2}{|D|^{-2}}\left\{\chi_0 \left|D_0^{-1} - V^2\chi_0\right|^2 + V^2\chi_0^2\left(D_0^{-1} - V^2\chi_0^*\right)\right\} \ .$$

The two terms proportional to $V^4$ in this expression drop out. Considering the fact that $D_0^{-1} = \omega - \omega_{p,0}$ is real,[11] and taking the imaginary part of the expression, the two terms proportional to $V^2$ also cancel, and we are left with

$$\mathrm{Im}\,\chi_{el} = T_e^2\,\mathrm{Im}\,\chi_0 \cdot \frac{D_0^{-2}}{|D|^{-2}} = \mathrm{Im}\,\chi_{Raman} \cdot \frac{D_0^{-2}}{|D|^{-2}} \ .$$

The renormalization of the Raman susceptibility by the electron-phonon interaction therefore is given by multiplying it with the absolute square of the ratio of renormalized phonon

---

[11] We just adhere to the definition of the bare phonon Green's function. The limit $\delta \to 0$ in (3.4) implies that $D_0^{-1}$ is real. This is *not true*, however, for $D_0$.

Green's function to bare phonon Green's function. Expressing this ratio with bare quantities by using the phonon Dyson equation and the approximation (3.4) yields

$$\operatorname{Im}\chi_{el}(\omega) = -\pi T_e^2\rho(\omega)\cdot\frac{(\omega-\omega_{p,0})^2}{[\omega-\omega_{p,0}-V^2R(\omega)]^2+[\pi V^2\rho(\omega)]^2}\ . \tag{3.6}$$

For large frequencies (higher than these of typical electron-hole excitations), the Green's function $\chi_0$ vanishes as $\omega^{-1}$. Therefore, the ratio $D_0^{-2}/|D|^{-2}$ becomes one in this limit and the renormalization of the electronic Raman efficiency vanishes. The quotient in (3.6) should be even with respect to $\omega \to -\omega$ and it is if the exact result for $D_0$ instead of the approximation (3.4) is used. Therefore, (3.6) transforms like $\operatorname{Im}\chi_0(\omega)$ for $\omega \to -\omega$.

To gain further insight in the renormalization expressed by (3.6), we assume that $R(\omega) \approx R_0$ and $\rho(\omega) \approx \rho_0$ are constant in the region of interest. We introduce the *renormalized phonon frequency* $\omega_p$ and the *linewidth* $\Gamma_p$ (HWHM) by

$$\omega_p \equiv \omega_{p,0} + V^2R_0 \qquad \text{and} \qquad \Gamma_p \equiv \pi V^2\rho_0 \tag{3.7}$$

and write

$$\frac{D_0^{-2}}{|D|^{-2}} = \frac{(\omega-\omega_{p,0})^2}{(\omega-\omega_p)^2+\Gamma_p^2}$$

which shows a peak at *about* the renormalized phonon frequency $\omega_p$ and a zero, called *antiresonance*, at the bare phonon frequency $\omega_{p,0}$ (see Fig. 3.10). It is clear, that the peak of $\operatorname{Im}\chi_{el}$ is only approximately located at $\omega_p$ because of the frequency dependence of the numerator of (3.6).

**Direct phonon Raman scattering.** The fact that in addition to the process given in Fig. 3.1 and described by the Raman vertex, inelastic scattering of light also occurs via the diagram in Fig. 3.4 gives rise to further contributions to Raman scattering. The first of these is the *direct phonon Raman scattering* described by the Green's function depicted in Fig. 3.9(c) and denoted by $\chi_{phon}(\omega)$. It is given by[12]

$$\operatorname{Im}\chi_{phon} = T_p^2\operatorname{Im}D = T_p^2\frac{1}{|D|^{-2}}\operatorname{Im}\left(D^{*\,-1}\right)$$

which by again taking into consideration the phonon Dyson equation (3.5) takes the form

$$\operatorname{Im}\chi_{phon} = T_e^2\operatorname{Im}\chi_0(\omega)\cdot\frac{\left(\frac{T_pV}{T_e}\right)^2}{|D|^{-2}} \tag{3.8}$$

and consists of the electronic Raman efficiency multiplied by a Lorentzian centered at the renormalized phonon frequency $\omega_p = \omega_{p,0} + V^2R_0$ and having a width $\pi V^2\rho_0$. The contribution (3.8) appears to be independent of $T_e$, but the Raman vertex is hidden in the photon-phonon vertex $T_p$ defined in Fig. 3.4.

**Interference terms.** In addition to the contributions already treated, there are interference terms between electronic and phonon Raman scattering. The two interference terms, whose diagrams are depicted in Fig. 3.9(d), are denoted by $\chi_{intf}$ and can be written as

$$\operatorname{Im}\chi_{Intf} = 2T_eVT_p\operatorname{Im}(\chi_0D) = \frac{2T_eVT_p}{|D|^{-2}}\operatorname{Im}\left(\chi_0D^{*-1}\right)\ ,$$

---

[12] The *spectral function* of the phonon is given by $-\pi^{-1}\operatorname{Im}D_{ret}(\omega)$.

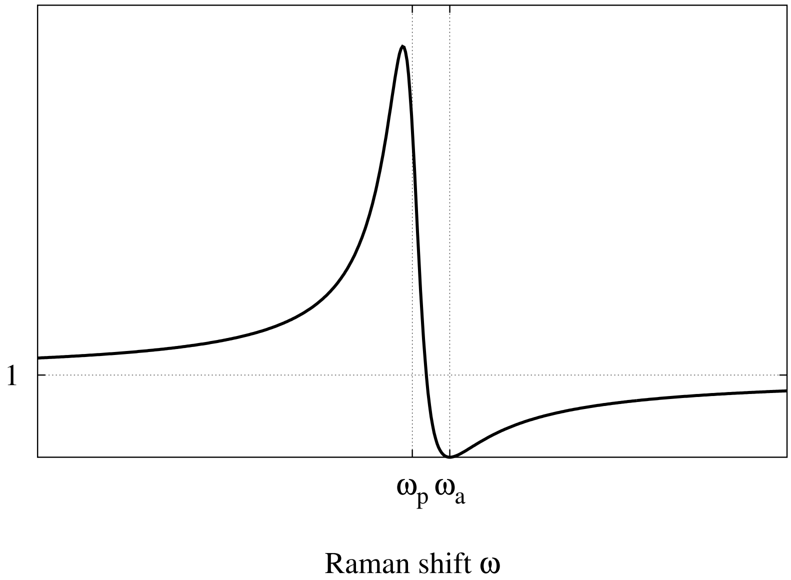

Figure 3.10: The function $D_0^{-2}/|D|^{-2}$ which when multiplied by the imaginary part of the electronic Raman susceptibility in *absence* of electron-phonon interaction yields the imaginary part of the electronic Raman susceptibility in *presence* of electron-phonon interaction. Note that the maximum and the renormalized phonon frequency $\omega_p$ do *not* correspond.

Using the phonon Dyson equation (3.5), they can be transformed into

$$\operatorname{Im}\chi_{Intf} = T_e^2 \operatorname{Im}\chi_0(\omega) \cdot \frac{2\frac{T_p V}{T_e} D_0^{-1}}{|D|^{-2}} \,. \tag{3.9}$$

Similarly to the term $\chi_{el}$, this interference term shows a peak at the renormalized phonon frequency $\omega_p$ and an antiresonance at the bare phonon frequency $\omega_{p,0}$.

### 3.3.2 The Fano result

Summing up all the contributions (3.6), (3.8), and (3.9) to the Fano susceptibility $\chi_{Fano} \equiv \chi_{el} + \chi_{phon} + \chi_{intf}$, we arrive to the result of renormalizing the electronic Raman susceptibility by introducing electron-phonon coupling,

$$\operatorname{Im}\chi_{Fano} = T_e^2 \operatorname{Im}\chi_0 \cdot \frac{\left(D_0^{-1} + \frac{T_p V}{T_e}\right)^2}{\left[D_0^{-1} - V^2 \operatorname{Re}\chi_0\right]^2 + \left[V^2 \operatorname{Im}\chi_0\right]^2} \,. \tag{3.10}$$

This expression is called the *Fano-Breit-Wigner equation.* It contains all contributions to Raman scattering in a system of coupled electrons and a phonon.

For vanishing electron-phonon coupling $V = 0$ the quotient in (3.10) becomes 1 and we recover the known formula for electronic Raman scattering. For vanishing photon-phonon coupling $T_p = 0$, the result (3.6) is recovered, therefore phonons are seen in the Raman spectra even if they do not couple via $T_p$ to light. The absence of electronic pair excitations makes $\operatorname{Im}\chi_{Fano}$ to vanish completely. This is not trivial to see in the formalism, because $\operatorname{Im}\chi_{Fano}$ contains the phonon-part $\operatorname{Im}\chi_{phon} = |T_p|^2 \operatorname{Im} D$, and for $\rho(\omega) \equiv 0$ the spectral density $\operatorname{Im} D$ will be a $\delta$-function, in the experiment somehow broadened. But nevertheless $\operatorname{Im}\chi_{phon}$ vanishes for $\rho(\omega) \equiv 0$ because the vertex $T_p$ defined by the diagram in Fig. 3.4 does.

**The usual parametrization.** In the literature [3.11], the Fano formula (3.10) is usually presented in terms of the parameters $q$ and $\epsilon$ and reads

$$I(\omega) = I_{el}(\omega)\frac{|q+\epsilon|^2}{1+\epsilon^2} \ . \tag{3.11}$$

Comparing to (3.10), the parameters[13] $\epsilon$ and $q$ can be related to the microscopic parameters as

$$\begin{aligned} q(\omega) &= \frac{\frac{T_pV}{T_e} + V^2R(\omega)}{\pi V^2\rho(\omega)} = \frac{\omega_p - \omega_a}{\Gamma_p} \\ \epsilon(\omega) &= \frac{\omega - \omega_{p,0} - V^2R(\omega)}{\pi V^2\rho(\omega)} = \frac{\omega - \omega_p}{\Gamma_p} \end{aligned} \tag{3.12}$$

For the case of frequency-independent functions $R(\omega)$ and $\rho(\omega)$ (this is actually the case when the parametrization (3.11) makes sense), the variable $\epsilon$ represents the frequency in reduced units, having the property that $\epsilon = 0$ for $\omega = \omega_{p,0}$. The parameter $q$, called the *Fano asymmetry parameter*, gives the approximate distance between the antiresonance and the position of the maximum, in units of the phonon linewidth $\Gamma_p$. For small values of $q$, the antiresonance is very close to the position of the peak (in comparison to the phonon linewidth $\Gamma_p$). For large values of $q$, the numerator of (3.11) is almost constant around $\omega_p$, and the phonon peak is almost Lorentzian.

In the discussion of the limit $V \to 0$ we will take $R(\omega) = R_0$ and $\rho(\omega) = \rho_0$. Then $q = O(1/V)$, and $\epsilon = O(1/V^2)$, therefore in this limit $q/\epsilon \to 0$, and $|q+\epsilon|^2/(1+\epsilon^2) \to 1$. For vanishing electron-phonon coupling, the quotient in (3.10) becomes one.

**Location of the peak.** An important topic in this context is the *location of the phonon peak*. For a bare Green's function $\chi_0$ which does not vary too much in a region of width $\Gamma_p$ around the renormalized phonon frequency[14] $\omega_p$, the location of the phonon peak can be defined by the requirement that the first derivative of $\operatorname{Im}\chi_{Fano}$ vanishes. If we use the approximation (3.4) and the notation $\omega_a = \omega_{p,0} - T_pV/T_e$ for the location of the antiresonance and $I_{el} = T_e^2 \operatorname{Im}\chi_0$ for the bare electronic Raman efficiency, the imaginary part of the Fano susceptibility $\chi_{Fano}$ is given by

$$I_{el}\frac{(\omega-\omega_a)^2}{(\omega-\omega_p)^2+\Gamma_p^2} \tag{3.13}$$

whose first derivative has to vanish. This is fulfilled for the two frequencies

$$\omega = \tilde{\omega}_p \equiv \omega_p - \frac{\Gamma_p^2}{\omega_a - \omega_p} \qquad \text{and} \qquad \omega = \omega_a \ ,$$

---

[13] Usually, in (3.12) the functions $R(\omega)$ and $\rho(\omega)$ are taken to be constant (at least closed to $\omega_p$). Then, $q$ becomes a constant, and $\epsilon$ a (dimensionless) variable.

[14] This is a *nonlinear* condition because $\omega_p$ is determined by an equation which contains the Green's function $\chi_0$!

the first of these expressions given is the location of the phonon peak. If the conditions

$$\left|\frac{\Gamma_p^2}{\omega_a - \omega_p}\right| \ll \Gamma_p \qquad \text{or} \qquad \rho_0 \ll \left|\frac{T_p}{T_e V} + R_0\right| \qquad \text{or} \qquad q \gg 1$$

are fulfilled, the position of the peak $\tilde{\omega}_p$ can be identified with the renormalized phonon frequency $\omega_p$.

For a nonconstant Green's function $\chi_0$, the situation is much more complicated. In this case we just discuss the location of the minima of the expression $[D_0^{-1} - V^2 \operatorname{Re}\chi_0]^2$ in the denominator of the Fano formula (3.10). The minima are determined by

$$D_0^{-1}(\omega_m) = V^2 R(\omega_m) \ .$$

Using again the approximation (3.4) for $D_0$, this is equivalent to

$$\omega_m - \omega_{p,0} = V^2 R(\omega_m) \tag{3.14}$$

which may have more than one solution for $\omega_m$. We consider an electron-hole spectral density $\rho(\omega)$ which is Lorentzian around $\omega_e \approx \omega_{p,0}$ as shown in Fig. 3.11. The real part $R(\omega)$ crosses the line $V^{-2}(\omega - \omega_{p,0})$ at three points, the minima $\omega_m$. The Fano function shows indeed two peaks at the leftmost and rightmost of the minima. At the minimum in the middle, there is no peak because the term $[\pi V^2 \rho(\omega)]^2$ in the denominator of the Fano formula very large, therefore the third peak can be considered to be extremely broad (overdamped). This examination clearly shows that the position of the peak(s) in the Raman spectra produced by the existence of a phonon are not necessarily closely related to the renormalized phonon frequency $\omega_p$. Note that the example under consideration is somehow contrived because the coupling matrix element $V$ used is very large and the number of electrons coupling to the phonon is very small. This is why the electronic peak at $\omega_e$ in Fig. 3.11 is washed out as a result of the coupling to the phonons.

Relaxing the approximation (3.4) shows that the linear function $\omega - \omega_{p,0}$ in (3.14) should be replaced by the parabola $(\omega^2 - \omega_{p,0}^2)/2\omega_{p,0}$ which is centered around $\omega = 0$ and has a slope of 1 at the $\omega = \omega_{p,0}$ node, and therefore this case is similar to the previous one.

**Discussion of the different contributions.** Now we are prepared to discuss the different contributions to the Fano efficiency which are plotted in Fig.3.12. In this figure, the bare electronic Raman susceptibility was set equal to 1. The renormalized electronic contribution $\chi_{el}$ approaches 1 for $|\omega - \omega_p| \gg \Gamma_p$ and vanishes quadratically with the frequency $\omega$ at $\omega = \omega_{p,0}$, the bare phonon frequency. Furthermore, the contribution coming from the renormalized phonon is just a Lorentzian with a width of $\Gamma_p$ and centered around $\omega = \omega_p$. The interference contribution $\chi_{intf}$ vanishes linearly with frequency at $\omega = \omega_{p,0}$ where the electronic contribution also vanishes. Finally, the sum $\chi_{Fano}$ of all these contributions vanishes at the antiresonance $\omega_a$. At this frequency the electronic and phonon contributions are exactly the same and are cancelled by the interference term meaning that the electronic and phonon contributions are out of phase at the antiresonance.

**Complex vertices.** Let us turn to the discussion of how complex[15] vertices would change our result (3.10) for the Fano formula obtained so far. The important point here

---

[15] A real number is also a complex number. But here we refer to nonreal complex numbers.

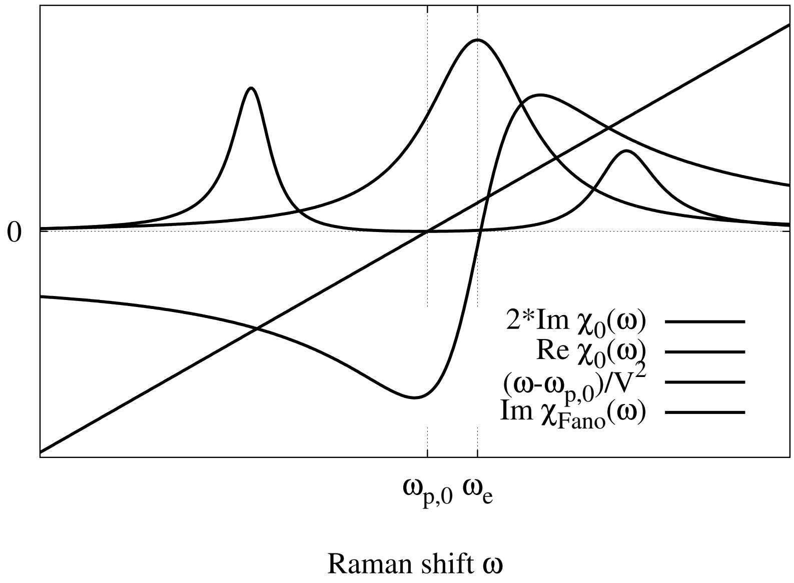

Figure 3.11: Determining the position of the peaks predicted by the Fano formula.

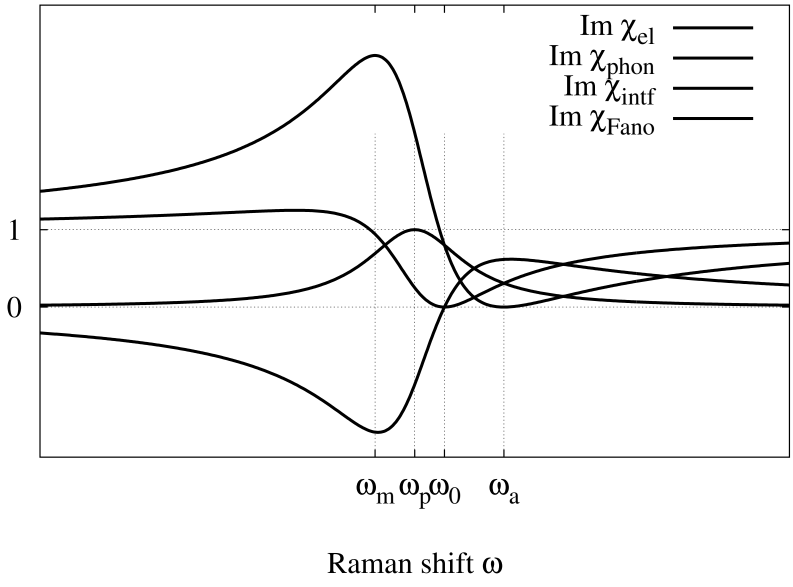

Figure 3.12: The different contributions to $\chi_{Fano}(\omega)$ as a function of frequency $\omega$.

shall be illustrated for the case of the electron-phonon vertex $V$ describing the process of *creating* an electron-hole pair while *destroying* a phonon. The magnitude of the transition amplitude for this process is the same as for the *conjugated* (or time-reversed) process, that is the creation of a phonon by recombination of an electron-hole pair while the phase of $V$ is complex conjugated for the conjugated process. The transition amplitude of the first is given by $V$, that of the second by $V^*$ (see Fig. 3.13(a)) as explained in Chap. 9. Let us now revise the derivation of the Fano formula in that light.

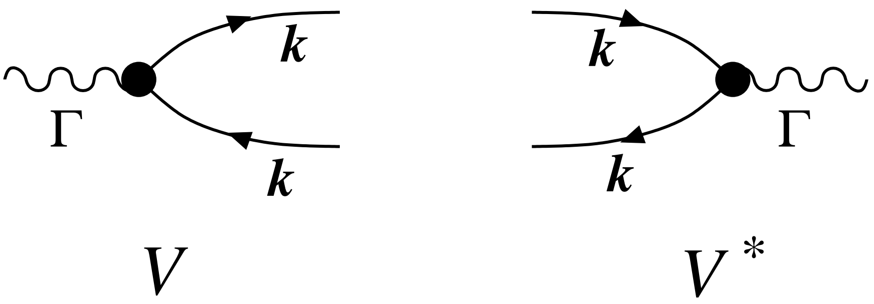

Figure 3.13: The creation of an electron-hole pair by destroying a phonon and the time-reversed process.

In the contributions Fig. 3.9(a) and (b), the Raman vertex occurs in complex conjugated pairs. This is also the case for the vertex $T_p$ in the diagram Fig. 3.9(c). The two electron-phonon vertices in Fig. 3.9(b) are conjugated as well, therefore leaving a factor $|V|^2$. This is also the case for the renormalized phonon (see Fig. 3.8). As a consequence the vertices in the contributions $\chi_{el}$ and $\chi_{phon}$ only occur in the combinations $|T_e|^2$, $|T_p|^2$, and $|V|^2$. In the interference contribution Fig. 3.9(d), the vertices in the first diagrams are $T_e V^* T_p^*$ and in the second part the complex conjugated vertices $(T_e V^* T_p^*)^*$. The combination of these two terms occurring in $\chi_{intf}$ is therefore $2|T_e|^2 \operatorname{Re}(T_p V/T_e)$. Adding again the three contributions as in (3.10) shows that the square in the numerator in the Fano formula has to be replaced by an absolute square $|\cdots|^2$. As a conclusion, the vertex squares in the Fano formula (3.10) as well as the numerator $(\cdots)^2$ both should be interpreted as absolute squares, but the combination $T_p V/T_e$ is to be interpreted as complex now. This has the consequence that the frequency $\omega_a$ of the antiresonance is no longer real: *the Fano efficiency at the antiresonance does no longer vanish.*

**Complex vertices and a noninteracting background.** For the purpose of fitting the Fano formula to experimental spectra, the consideration of the possibility of complex vertices augments the number of fitting parameters by 2 phases, making the fitting process much more difficult. We show subsequently that under the assumption of a constant electron-hole susceptibility $\chi_0$ the introduction of complex vertices in the theory just amounts to an additional constant noninteracting background in the spectra accompanied by a renormalization of the parameters in the Fano formula [3.12].

For a constant $\chi_0(\omega)$ we write the Fano formula in the form (3.13) where $\omega_a = \omega_a' + i\omega_a''$ becomes complex. Then we introduce a Fano formula with renormalized parameters $\tilde{I}_0$, $\tilde{\omega}_a$, $\tilde{\omega}_p$, and $\tilde{\Gamma}_p$ plus a constant background $\tilde{I}_b$, the renormalized position of the antiresonance $\tilde{\omega}_a$

now being a real quantity, and equate both forms:

$$\tilde{I}_0 \frac{(\omega-\tilde{\omega}_a)^2}{(\omega-\tilde{\omega}_p)^2+\tilde{\Gamma}_p^2} + \tilde{I}_b = I_0 \frac{|\omega-\omega_a'-i\omega_a''|^2}{(\omega-\omega_p)^2+\Gamma_p^2} \ ,$$

with two sets of five parameters on each side of the equation. Multiplying the equation by the two denominators leads to an equation of two polynomials of fourth order in $\omega$ allowing for the determination of 5 relations and, consequently of one set of parameters as a function of the other set, in the form

$$(\tilde{I}_0, \tilde{\omega}_p, \tilde{\Gamma}_p, \tilde{\omega}_a, \tilde{I}_b) = f(I_0, \omega_p, \Gamma_p, \omega_a', \omega_a'') \ .$$

This proves the assertion and gives a method to substitute a constant background by a complex combination $T_pV/T_e$ of vertices. We stress again that the requirement that the real and imaginary part of the function $V^2\chi_0(\omega)$ have to be constants for the statement above to hold. Strictly this is not possible because $\chi_0(\omega)$ is an analytic function in the upper half plane of the complex frequency plane.

**Determining Fano parameters from the experiment; Fitting issues.** We start with the Fano formula

$$I(\omega) = \alpha \cdot \frac{(\omega-\omega_a)^2}{(\omega-\omega_p)^2+\Gamma_p^2} \tag{3.15}$$

whose parameters $\alpha$, $\omega_a$, $\omega_p$, and $\Gamma_p$ are determined by fitting (3.15) to the experimental spectra. Usually Raman intensities are determined in arbitrary units in the experiment, therefore $\alpha$ is a scaling constant without physical meaning.

If the density $\rho(\omega)$ of electron-hole excitations is known in the system under consideration, the absolute value of the electron-phonon vertex can already be determined by using $\Gamma_p = |V|^2\rho(\omega=\omega_p)$. A Kramers-Kronig transformation gives us $R(\omega)$ and, correspondingly, the bare phonon frequency $\omega_p^0 = \omega_p - |V|^2R(\omega_p)$. The absolute value of the vertex product $T_pV/T_e$ is then calculated from $\omega_a = \omega_p^0 + T_pV/T_e$, and the quotient of the vertices $|T_e|$ and $|T_p|$ is given by dividing that by $|V|$. Note that $|T_e|$ and $|T_p|$ individually cannot be determined if the experiment only gives the Raman intensity up to an unknown constant.

## 3.4 More sophisticated concepts

In Subsect. 3.4.1 we motivate the definition of the *integrated phonon-intensity*. A phonon broadening mechanism which is often as important as the one made possible by electron-phonon coupling, the *anharmonic decay*, is discussed in the Subsects. 3.4.2 and 3.4.3.

An *effective phonon-phonon interaction* plays a role in the explanation of our experiment and is introduced in Subsect. 3.4.4. In Subsect. 3.4.5 we discuss how the formalism presented here can be applied to the case of *optical absorption*, and finally, in Subsect. 3.4.6, the *renormalization of the electron* by the presence of the electron-phonon interaction leads to the definition of the *Eliashberg-function*.

### 3.4.1 Final states and the renormalized phonon intensity

To quantify the effect of electron-phonon coupling on the phonon, we define a *renormalized phonon intensity*. Within the formalism used so far, which comprises the diagrams in

Fig. 3.9, it is not a priori clear how to do this. The integrated intensity of the bare phonon could be defined by its *spectral weight*, that is

$$I_p^0 = -\frac{1}{\pi} T_p^2 \int_0^\infty d\omega \, \operatorname{Im} D_0(\omega) = T_p^2 \ , \tag{3.16}$$

but then the question arises of how to generalize this expression to the case of nonvanishing electron-phonon interaction. Let us focus again on Fig. 3.9. Taking into consideration diagram (c) and substituting $D$ for $D_0$ in (3.16) does not yield the desired result, because the renormalization of the phonon in (3.16) does *not* change its integrated spectral weight.

Another possibility would be to take the Fano result $\chi_{Fano}$ and just subtract the bare electron-hole susceptibility $\chi_0$. Even this method—as straightforward as it seems—does not yield the desired result.

An appropriate classification of the contributions to $\chi_{Fano}$ into an electronic and a phonon contribution requires the introduction of the *final-state formalism*. To introduce this formalism, we first note the identity

$$\begin{aligned}\operatorname{Im}(AB\cdots YZ) = &\operatorname{Im}(A)(B\cdots YZ)^* + A\operatorname{Im}(B)(\cdots YZ)^* + \\ &+ \cdots + \\ &+ AB\cdots \operatorname{Im}(Y)Z^* + AB\cdots Y\operatorname{Im}(Z)\end{aligned}$$

for the imaginary part of products of complex numbers. As we are always interested in the imaginary part of susceptibilities, and the individual diagrams contributing to the susceptibilities are products of complex-valued Green's functions, we shall apply latter identity. The second order contribution to the phonon renormalization then is written as (assuming real vertices)

$$\operatorname{Im}(D_0V\chi_0VD_0) = V^2[\operatorname{Im}(D_0){\chi_0}^*D_0^* + D_0\operatorname{Im}(\chi_0)D_0^* + D_0\chi_0\operatorname{Im}(D_0)]$$

and plotted in Fig. 3.14(a). We agree to denote the imaginary part of a Green's function by a vertical line through the diagram. Then the rule for calculating the imaginary part of some diagram is as follows. Take the sum of all possibilities drawing vertical lines through the individual components of a diagram. A diagram with a vertical line is translated into an equation by putting the complex conjugated Green's function to the left of the vertical line, the imaginary part of the Green's function for the part of the diagram cut by the vertical line, and the plain Green's function for the diagram parts to the left of the vertical line.

Now we have a method at hand to classify the contributions to the imaginary part of the Fano susceptibility into contributions with electron-hole final states and contributions with a renormalized phonon as final state. Latter contributions are given by Fig. 3.14(b) whose imaginary part is

$$\begin{aligned}\operatorname{Im}\chi_{rp}(\omega) &= T_p\operatorname{Im}(D)T_p^* + [T_p\operatorname{Im}(D)V{\chi_0}^*T_e^* + \text{c.c.}] \\ &\quad + T_e\chi_0V^*\operatorname{Im}(D)V{\chi_0}^*T_e^* \\ &= |T_p + T_eV^*\chi_0(\omega)|^2\operatorname{Im}D(\omega) \ .\end{aligned} \tag{3.17}$$

The total intensity of the renormalized phonon is given by the integral over $\operatorname{Im}\chi_{rp}(\omega)$. The main contribution to this integral comes from the region around $\omega_p$, the renormalized

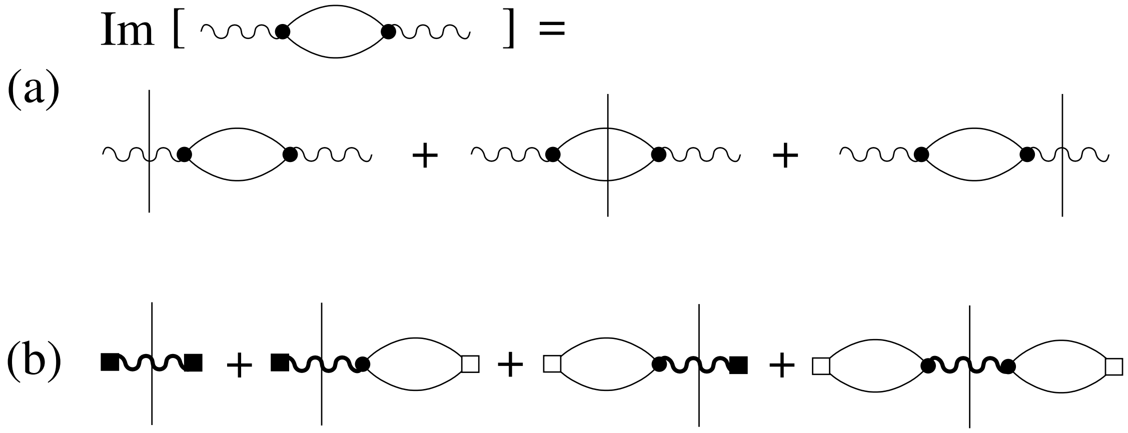

Figure 3.14: (a) a final-state diagram, and (b) the contributions with a renormalized phonon as final state.

phonon frequency. Therefore we approximate the prefactor of $\operatorname{Im} D$ in (3.17) by its value at the renormalized phonon position $\omega_p$. The frequency integration over $\operatorname{Im} D(\omega)$ yields $-\pi$, therefore we have

$$I_p = -\frac{1}{\pi} \int d\omega \operatorname{Im} \chi_{rp}(\omega) \approx |T_p + T_e V^* \chi_0(\omega_p)|^2 \tag{3.18}$$

which reduces to (3.16) for $V = 0$. The change of the phonon intensity by coupling it to electron-hole excitations is given by

$$I_p / I_p^0 \approx \left| 1 + \frac{T_e V^*}{T_p} \chi_0(\omega_p) \right|^2 .$$

Using the parameter $q = q(\omega_p)$ and $I_{el} = I_{el}(\omega_p)$ as defined in (3.12), as well as the notation introduced in (3.7), the phonon intensity can be written in the form

$$I_p \approx \pi I_{el} \left[ q + 1 \right]^2 \Gamma_p \tag{3.19}$$

in which all parameters can be determined from the experiment.

### 3.4.2 Another phonon broadening mechanism: Anharmonic decay

In the next section we will discuss the temperature-dependence of the linewidth of phonons. We have seen in Sect. 3.3 that one effect causing the phonon to acquire a finite linewidth is the possibility of decaying into electron-hole excitations due to the presence of the electron-phonon interaction. In real systems, there is another important decay mechanism for phonons: the decay into two phonons [3.13, 3.14] that we discuss next.

We denote (see Fig. 3.15) the cartesian component $i$ of the displacement of the ion located in the crystal at the position $\boldsymbol{R}_{l\alpha} = \sum l_i \boldsymbol{t}_i + \boldsymbol{d}_\alpha$ ($\boldsymbol{t}_i$ are the translation vectors of the crystal and $\boldsymbol{d}_\alpha$ is the position of the ion $\alpha$ in a cell with respect to the cell origin) by $u_i(\boldsymbol{l}\alpha)$. Terms of the ion-ion interaction potential in third and higher order in $u_i(\boldsymbol{l}\alpha)$ have been neglected

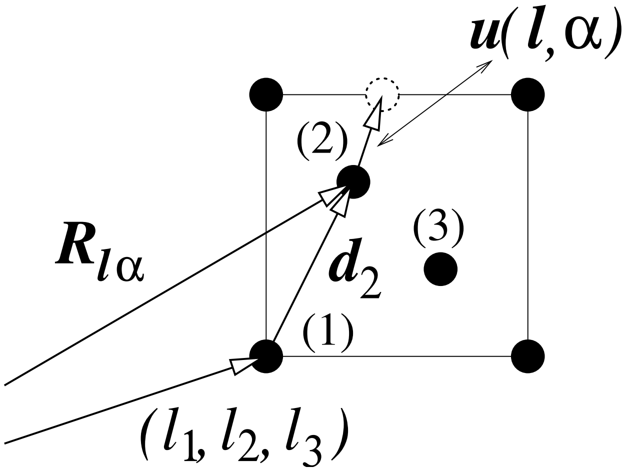

Figure 3.15: The notation used in the discussion of the anharmonic decay. The ion denoted by (2) is displaced from its equilibrium position to a new position (dotted circle). The vector $\boldsymbol{l}$ refers to the unit cell of the ion whereas the index $\alpha$ counts the individual ions in the unit cell.

in the harmonic approximation. Taking into consideration these third order terms adds a contribution of the form

$$\sum_{\boldsymbol{l}\alpha i}\sum_{\boldsymbol{m}\beta j}\sum_{\boldsymbol{n}\gamma k}\Phi_{ijk}\begin{pmatrix}\boldsymbol{l} & \boldsymbol{m} & \boldsymbol{n}\\ \alpha & \beta & \gamma\end{pmatrix}\cdot u_i(\boldsymbol{l}\alpha)u_j(\boldsymbol{m}\beta)u_k(\boldsymbol{n}\gamma)$$

to the harmonic Hamiltonian, where $\Phi_{ijk}$ is the potential describing the effective ion-ion interactions in the crystal. Transforming this contribution to normal coordinates and introducing the same phonon creation and destruction operators $a_{\boldsymbol{k}\lambda}$ and $a^{+}_{\boldsymbol{k}\lambda}$ as used in the harmonic approximation transforms this term into

$$\sum_{\boldsymbol{k}\lambda}\sum_{\boldsymbol{k}'\lambda'}\sum_{\boldsymbol{k}''\lambda''}V_3\begin{pmatrix}\lambda & \lambda' & \lambda''\\ \boldsymbol{k} & \boldsymbol{k}' & \boldsymbol{k}''\end{pmatrix}(a_{\boldsymbol{k}\lambda}+a^{+}_{-\boldsymbol{k}\lambda})(a_{\boldsymbol{k}'\lambda'}+a^{+}_{-\boldsymbol{k}'\lambda'})(a_{\boldsymbol{k}''\lambda''}+a^{+}_{-\boldsymbol{k}''\lambda''}) \qquad (3.20)$$

where the matrix $V_3$ is related to $\Phi$ and does not vanish only if $\boldsymbol{k}+\boldsymbol{k}'+\boldsymbol{k}''=0$, modulo a reciprocal lattice vector.

The decay of a phonon into two phonons is caused by terms in (3.10) of the form $a^{+}a^{+}a$, consisting of two creation and one destruction operators in the Hamiltonian. Because of the fact that this decay only exists if terms beyond the harmonic ones are taken into account in the Hamiltonian, it is called *anharmonic decay*.

**Diagramatics.** In the perturbational calculation of the contributions of the anharmonic decay to the phonon self-energy, the third-order contribution (3.20) has to be taken in second order of the matrix element $V_3$ (which is sixth order in the ion displacement), see Fig. 3.16(a). Therefore, the contribution of fourth order (in the ion displacement) to the linewidth could be as important as the third order term in Fig. 3.16(a). However, the fourth order term of Fig. 3.16(b) contributes only to the phonon lineshift, but not to the phonon linewidth. We focus consequently on the contribution in Fig. 3.16(a).

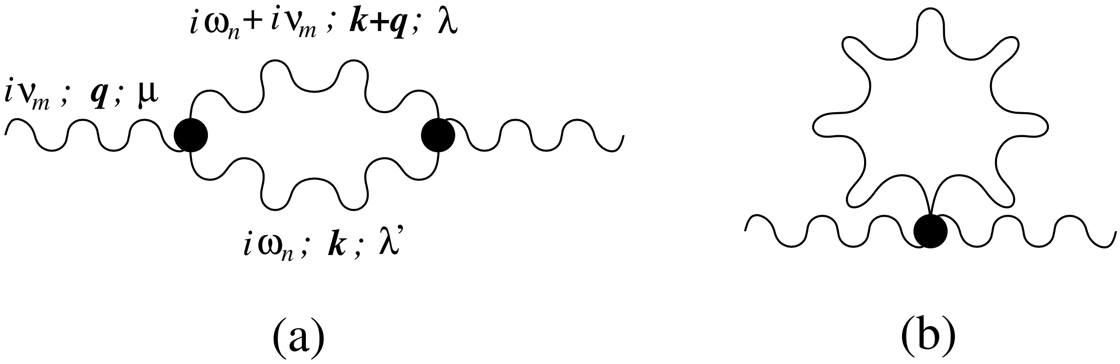

(a) (b)

Figure 3.16: Two contributions to the phonon self-energy arising from anharmonic ion-ion interaction terms in the Hamiltonian.

We use the temperature-dependent Matsubara-technique to evaluate the temperature-dependence of the linewidth that follows from the diagram in Fig. 3.16. Using this technique, the phonon self-energy is given by

$$\begin{aligned}\Pi_\mu(\boldsymbol{q}, i\nu_m) &= \frac{1}{\Omega}\sum_{\boldsymbol{k}}\sum_{\lambda,\lambda'} V_3^2 \left(\begin{array}{c|c|c} \mu & \lambda & \lambda' \\ \boldsymbol{q} & \boldsymbol{k}+\boldsymbol{q} & -\boldsymbol{k} \end{array}\right) \times \\ &\qquad \times \left(-\frac{1}{\beta}\right) \sum_{i\omega_n} D_\lambda^{(0)}(\boldsymbol{k}+\boldsymbol{q}, i\omega_n + i\nu_m) D_{\lambda'}^{(0)}(-\boldsymbol{k}, -i\omega_n) \\ &= \frac{1}{\Omega}\sum_{\boldsymbol{k}}\sum_{\lambda,\lambda'} V_3^2 \left(\begin{array}{c|c|c} \mu & \lambda & \lambda' \\ \boldsymbol{q} & \boldsymbol{k}+\boldsymbol{q} & -\boldsymbol{k} \end{array}\right) \times \pi_\mu^{\lambda\lambda'}(\boldsymbol{q}, i\nu_m; \boldsymbol{k})\ .\end{aligned} \tag{3.21}$$

We introduce the expression

$$D_\lambda^{(0)}(\boldsymbol{q}, i\omega_n) = \frac{1}{i\omega_n - \omega_{\boldsymbol{q}}^\lambda} - \frac{1}{i\omega_n + \omega_{\boldsymbol{q}}^\lambda} = \sum_{\epsilon=\pm 1} \frac{\epsilon}{i\omega_n - \epsilon\omega_{\boldsymbol{q}}^\lambda} \tag{3.22}$$

for the temperature-dependent phonon Green's function. The function $\pi_\mu^{\lambda\lambda'}$ defined in (3.21) becomes

$$\pi_\mu^{\lambda\lambda'}(\boldsymbol{q}, i\nu_m; \boldsymbol{k}) = \sum_{\epsilon\epsilon'} \left(-\frac{1}{\beta}\right) \sum_{i\omega_n} \left[\frac{\epsilon}{i\omega_n + i\nu_m - \epsilon\omega_{\boldsymbol{k}+\boldsymbol{q}}^\lambda} \cdot \frac{\epsilon'}{-i\omega_n - \epsilon'\omega_{-\boldsymbol{k}}^{\lambda'}}\right]\ . \tag{3.23}$$

We perform the $i\omega_n$-summation by converting the sum of (3.23) into an integral and the integral via the Poisson sum formula into a sum over residua. Noting that $n_B(-i\nu_m + \epsilon\omega_{\boldsymbol{k}+\boldsymbol{q}}^\lambda) = n_B(\epsilon\omega_{\boldsymbol{k}+\boldsymbol{q}}^\lambda)$ because $i\nu_m$ is a bosonic Matsubara-frequency, and that $n_B(\omega) + n_B(-\omega) + 1 = 0$, we obtain

$$\begin{aligned}\pi_\mu^{\lambda\lambda'}(\boldsymbol{q}, i\nu_m; \boldsymbol{k}) &= \left[n_B(\omega_{-\boldsymbol{k}}^{\lambda'}) - n_B(\omega_{\boldsymbol{k}+\boldsymbol{q}}^\lambda)\right] \left[\frac{1}{i\nu_m - (\omega_{-\boldsymbol{k}}^{\lambda'} - \omega_{\boldsymbol{k}+\boldsymbol{q}}^\lambda)} + \text{c.c}\right] + \\ &\quad + \left[1 + n_B(\omega_{-\boldsymbol{k}}^{\lambda'}) + n_B(\omega_{\boldsymbol{k}+\boldsymbol{q}}^\lambda)\right] \left[\frac{1}{i\nu_m - (\omega_{-\boldsymbol{k}}^{\lambda'} + \omega_{\boldsymbol{k}+\boldsymbol{q}}^\lambda)} + \text{c.c}\right]\end{aligned} \tag{3.24}$$

Replacing this into (3.21) we find the desired result for the phonon self-energy contribution of the diagram in Fig. 3.16(a).

The four terms in (3.24) arise from the fact that *both* phonon Green's functions in the diagram (Fig. 3.16(a)) have *two* poles each at $\pm\omega_{\boldsymbol{k}}^{\lambda}$ (for a phonon with quasimomentum $\boldsymbol{k}$ and of branch $\lambda$). This is necessary for the symmetry $D(-\omega) = D^*(\omega)$ of the phonon Green's functions to hold.

As appropriate to Raman scattering we consider an *optical* Γ-point phonon $\omega_\Gamma^\mu$, that is, $\boldsymbol{q} = 0$, decaying into two phonons $\omega_{\boldsymbol{k}}^{\lambda}$ and $\omega_{-\boldsymbol{k}}^{\lambda'}$. The first two terms in (3.24) contribute to the linewidth of the Γ-point phonon $\omega_\Gamma^\mu$ if $\omega_\Gamma^\mu = \left|\omega_{\boldsymbol{k}}^{\lambda} - \omega_{-\boldsymbol{k}}^{\lambda'}\right|$. The thermal prefactor $n_B(\omega_{\boldsymbol{k}}^{\lambda}) - n_B(\omega_{-\boldsymbol{k}}^{\lambda'})$ is usually very small and allows us to neglect the corresponding terms if $T \ll T_{Debye}$.

The second summand in (3.24) describes the main contribution to the phonon linewidth by anharmonic decay. This summand becomes important if the relation

$$\omega_\Gamma^\mu = \omega_{\boldsymbol{k}}^{\lambda} + \omega_{-\boldsymbol{k}}^{\lambda'} \tag{3.25}$$

is fulfilled. If the two phonons resulting from the decay are from the same branch, the equation (3.25) can be written as

$$\omega_\Gamma^\mu = 2\omega_{\boldsymbol{k}}^{\lambda} \ ,$$

where we have made use of the relation $\omega_{-\boldsymbol{k}}^{\lambda} = \omega_{\boldsymbol{k}}^{\lambda}$.

Within this scenario, the contribution to the linewidth arising from (3.24) is proportional to $1 + 2n_B(\omega_{\boldsymbol{k}}^{\lambda}) = 1 + 2n_B(\omega_\Gamma^\mu/2)$. We thus write the temperature dependent linewidth as

$$\Gamma_{anh}(T) = [1 + n_B(\omega_p/2)] \cdot \Gamma_{anh}(0) \ . \tag{3.26}$$

We are going to use this formula in the upcoming discussion of experimentally measured spectra in Hg-1234.

### 3.4.3 Fano effect and other self-energy contributions

Let us again pick up the topic of Subsect. 3.4.1. What influence do additional phonon decay mechanisms have on Eq. (3.19)? We consider a specific example: the anharmonic decay of the phonon. The renormalized phonon Green's function is given by the Dyson equation

$$D^{-1} = D_0^{-1} - V^2\chi_0 - U^2\chi_{2p}$$

where $U$ is the vertex for the anharmonic decay of one phonon into two phonons and $\chi_{2p}$ is the polarization loop with 2 phonons. The imaginary part of $\chi_{2p}$ is basically the 2-phonon density of states.

This yields a phonon spectral function

$$\begin{aligned} &-\frac{1}{\pi}\operatorname{Im} D(\omega) = \\ &-\frac{1}{\pi}\frac{V^2\operatorname{Im}\chi_0(\omega) + U^2\operatorname{Im}\chi_{2p}(\omega)}{(\omega - \omega_p^0 - V^2\operatorname{Re}\chi_0 - U^2\operatorname{Re}\chi_{2p})^2 + (V^2\operatorname{Im}\chi_0 + U^2\operatorname{Im}\chi_{2p})^2} \ . \end{aligned} \tag{3.27}$$

Defining the renormalized phonon frequency $\omega_p$ by the (nonlinear) condition

$$\omega_p^0 - V^2\operatorname{Re}\chi_0(\omega_p) - U^2\operatorname{Re}\chi_{2p}(\omega_p) = \omega_p$$

and introducing the symbols

$$\begin{aligned}\Gamma_{ep} &= -V^2\,\mathrm{Im}\,\chi_0(\omega_p)\\ \Gamma_{anh} &= -U^2\,\mathrm{Im}\,\chi_{2p}(\omega_p)\\ \Gamma &= \Gamma_{ep}+\Gamma_{anh}\\ \Delta &= \omega_p-\omega_p^0\end{aligned} \tag{3.28}$$

allows us to write

$$-\frac{1}{\pi}\,\mathrm{Im}\,D(\omega)=\frac{\Gamma/\pi}{(\omega-\omega_p^0-\Delta)^2+\Gamma^2}\ .$$

Substituting this in (3.17) and taking into consideration that $\int \mathrm{Im}\,D=-\pi$ we see that (3.18) remains valid with the quantities $\Gamma_p$ and $q$ in (3.19) interpreted as arising from electron-phonon coupling only.

### 3.4.4 Phonon-phonon interferences mediated by electronic excitations

High-temperature superconductors have complex structures with about ten or more atoms per primitive cell. Therefore they possess a considerable number of optical phonons. The system Y-123 has 13 atoms per unit cell and, correspondingly, $3\cdot 13-3=36$ optical phonons, 15 of them are even with respect to the inversion center (e.g. at the site of the Y atom), 4 out of these 15 Raman active phonons are of $A_{1g}$ $(D_{4h})$ symmetry and are visible in the $A_{1g}$ electronic Raman spectra. In the Hg-1234 $A_{1g}$ spectra there are 2 very intense phonons seen in the region from $200\,\mathrm{cm}^{-1}$ to $400\,\mathrm{cm}^{-1}$. They are close to each other in energy. One is tempted to use the simple Fano theory given in the last section to describe both phonons and use a parametrized form of the Raman efficiency for describing the spectra. Call $I_{p,1}(\omega)$ and $I_{p,2}(\omega)$ the Fano intensities for Raman scattering involving one phonon with a frequencies $\omega_1$ and $\omega_2$, respectively. These intensities each contain a phonon plus the electronic background. For describing the two phonons, one could add both intensities and subtract from this one electronic background $I_{el}(\omega)$, writing

$$I_{2-p}(\omega)\approx I_{p,1}(\omega)+I_{p,2}(\omega)-I_{el}(\omega)\ . \tag{3.29}$$

This attempt fails in the interesting case of 2 phonons which are coupled strongly to the electronic background and which are close to each other in terms of frequency. For such situation, the function $I_{2-p}(\omega)$ is plotted in Fig. 3.17 and shows a *negative intensity* in some frequency regions. It is clear that a *two-phonon fitting formula* produced using the prescription above and employing it for fitting parameters from the experimental data is doomed to fail.

Where do the negative intensities come from? The recipe for determining $I_{2-p}(\omega)$ above does not work, because it omits important interference contributions coming into the game when considering two different phonons. A typical representative of the class of contributions to the scattering cross section omitted is given by the diagram in Fig. 3.18. It describes the destruction of a phonon 1 accompanied by a polarization of the electronic system, in other words the creation of an electron-hole excitation, and the subsequent recombination of the electron-hole excitation connected with the creation of a phonon 2. This process is virtual

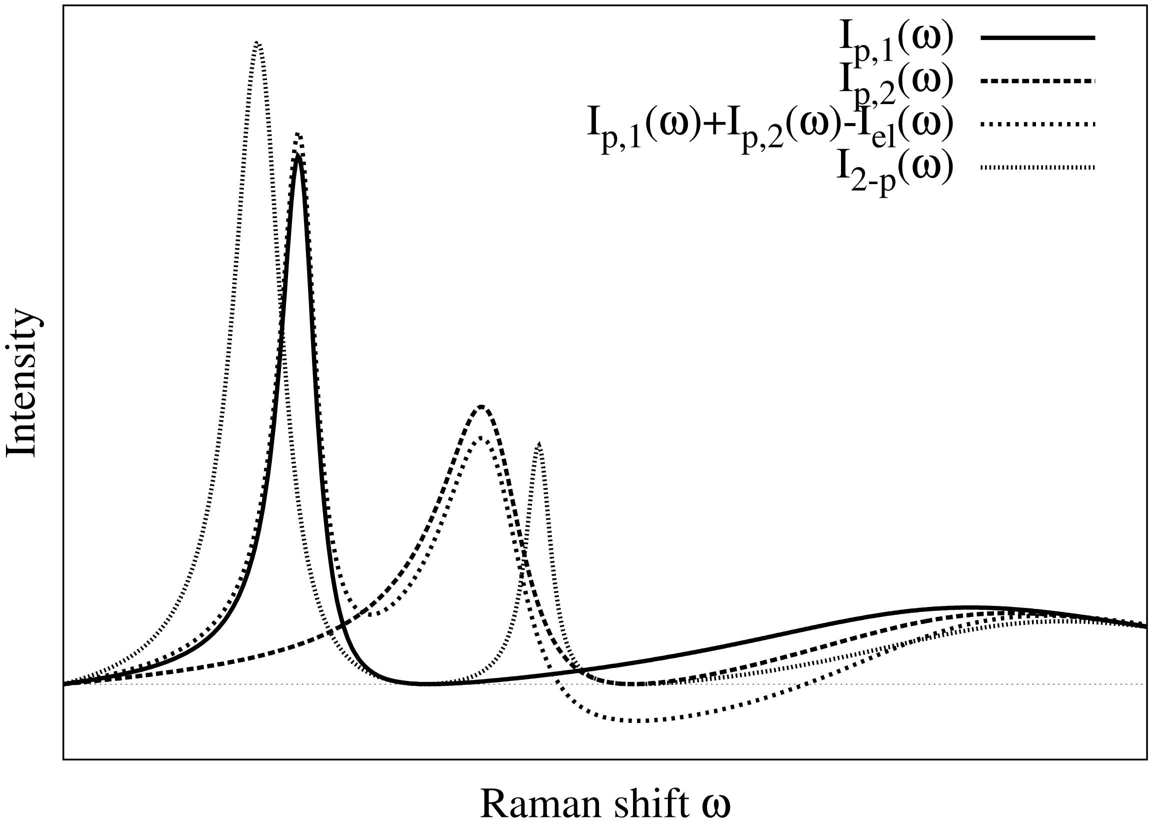

Figure 3.17: The intensity $I_{p,1}$ ($I_{p,2}$) results from coupling a phonon with frequency $\omega_1$ ($\omega_2$) to a continuum of electron-hole excitations. The curve denoted by $I_{p,1}(\omega) + I_{p,2}(\omega) - I_{el}(\omega)$ shows the approximation (3.29) to the 2-phonon Raman efficiency. The correct expression for the 2-phonon Raman efficiency is denoted by $I_{2-p}(\omega)$ and given by (3.32).

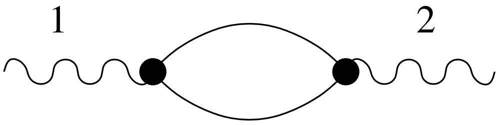

Figure 3.18: A typical diagram describing phonon-phonon coupling via the electronic continuum.

as long as the phonons are not degenerate, but still gives an important contribution to the scattering intensity $I_{2-p}(\omega)$.

In the following paragraph we give a generalization of the Fano theory to the case in which 2 phonons are present diagram in Fig. 3.18 is important. Like in the elementary Fano theory, we assume that the vertices are real scalar quantities, independent of $\boldsymbol{k}$. The frequencies and electron-phonon matrix elements of the two phonons will be denoted by $\omega_1$ and $\omega_2$, $V_1$ and $V_2$.

The derivation of the Fano formula in Sect. 3.3 was based on the renormalization of the discrete phonon by interaction with the continuum of electronic excitations. Because of practical considerations this time we are going to renormalize the electron-hole Green's function $\chi_0$. This is done by summing all the diagrams in Fig. 3.7 without the vertices $T_e$ at either end of each diagram. With respect to phonon lines we have to take all combinations possible with the two phonons present in the system under consideration. The second order phonon diagram (Fig. 3.7(b), bottom) therefore becomes a total of four diagrams. It is clear that the renormalized pair Green's function $\chi$ is given by the Dyson equation

$$\chi^{-1}(\omega) = {\chi_0}^{-1}(\omega) - V_1^2 D_1^{(0)}(\omega) - V_2^2 D_2^{(0)}(\omega) \tag{3.30}$$

with both phonons described by their respective bare Green's function $D_i^{(0)}(\omega)$ playing the same role in the renormalization of the bare Green's function $\chi_0$. Taking the imaginary part of the Dyson equation (3.30) yields the expression

$$\operatorname{Im}\chi = \frac{\operatorname{Im}\chi_0}{\left|1 - (V_1^2 D_1^{(0)} + V_2^2 D_2^{(0)})\chi_0\right|^2} \; .$$

where it was used that the imaginary part of $D_i^{(0)}$ vanishes (see the discussion in Subsect. 3.3.1). This is true for $\omega \neq \omega_{0,i}$ and bare phonons. For phonons already broadened by processes other than the decay into an electron-hole pair, the situation is more complicated and $\operatorname{Im} D_i^{(0)}$ may not be negligible.

Finally we multiply the expression for $\operatorname{Im}\chi$ as given above by $(D_1^{(0)} D_2^{(0)})^{-1}$ or $(\omega - \omega_{0,1})(\omega - \omega_{0,2})$ to end up with the expression

$$\operatorname{Im}\chi = \operatorname{Im}\chi_0 \frac{(\omega - \omega_{0,1})(\omega - \omega_{0,2})}{\left\{ \begin{array}{c} \left[ \begin{array}{c} (\omega - \omega_{0,1})(\omega - \omega_{0,2}) \\ -(V_1^2(\omega - \omega_{0,2}) + V_2^2(\omega - \omega_{0,1}))\operatorname{Re}\chi_0 \end{array} \right]^2 \\ +[(V_1^2(\omega - \omega_{0,2}) + V_2^2(\omega - \omega_{0,1}))\operatorname{Im}\chi_0]^2 \end{array} \right\}} \tag{3.31}$$

for the renormalized electron-hole susceptibility $\chi$ which is shown in the first column of the first row of Fig. 3.19.

So far we have calculated the renormalized pair Green's function $\chi(\omega)$. Adding the contributions of phonon Raman scattering and the interference terms which are analogous to the ones discussed in Subsect. 3.3.1) is straightforward now. Keeping in mind the presence of two phonons in the system, the additional contributions are given in Fig. 3.19 with one exception: the two diagrams describing the phonon Raman scattering by the *bare* phonons 1 and 2. These two diagrams vanish in the Fano formula because they do not have an imaginary

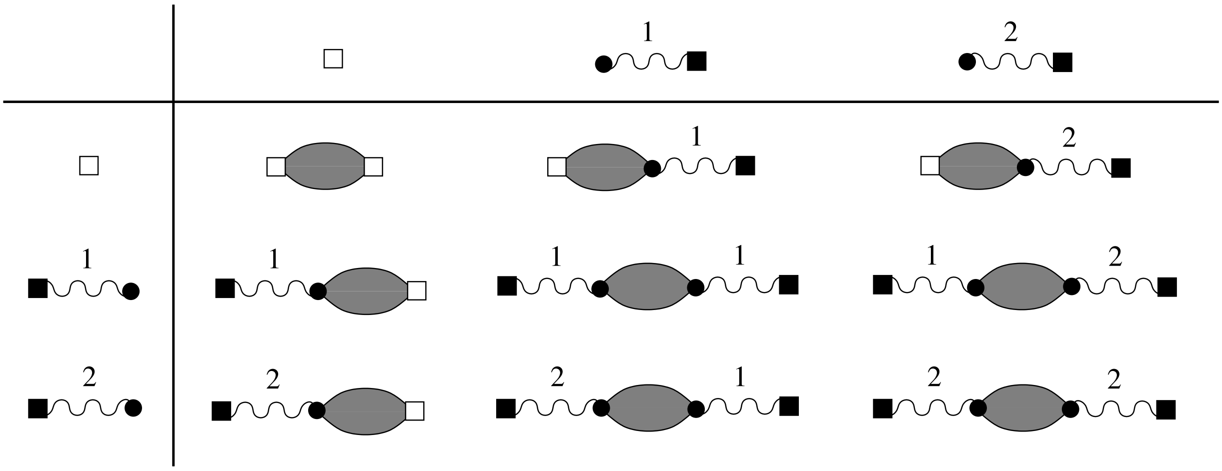

Figure 3.19: The diagrams contributing with their imaginary part to the 2-phonon Fano formula. The wavy lines with number $i$ refer to the phonon $i$. The polarization loops correspond to the *renormalized* electronic susceptibility (renormalized by electron-phonon interaction). An open box corresponds to the Raman vertex $T_e$. A filled box (filled circle) attached to a phonon line $i$ represents the photon-phonon vertex $T_{p,i}$ (electron-phonon vertex $V_i$.

part.[16] The sum of the susceptibilities of the 9 diagrams in Fig. 3.19 thus becomes

$$\begin{aligned}\operatorname{Im}\chi_{Fano}(\omega) &= \left|T_e + T_{p,1}D_1^{(0)}V_1 + T_{p,2}D_2^{(0)}V_2\right|^2 \operatorname{Im}\chi(\omega) \\ &= |T_e|^2 \frac{\left|(\omega-\omega_{0,1})(\omega-\omega_{0,2}) + \frac{T_{p1}V_1}{T_e}(\omega-\omega_{0,2}) + \frac{T_{p2}V_2}{T_e}(\omega-\omega_{0,1})\right|^2}{\{\cdots\}}\end{aligned} \tag{3.32}$$

where the expression in braces is the same as in (3.31). Equation (3.32) is the result for the 2-phonon Fano theory. In Fig. 3.17 we also plotted the 2-phonon Fano formula. The difference between the "first guess" curve denoted by $I_{p,1}(\omega) + I_{p,2}(\omega) - I_{el}(\omega)$ and the curve given by (3.32) and denoted $I_{2-p}(\omega)$ in Fig. 3.17 is due to the 2 interference terms in row 2, column 3 and row 3, column 2 of Fig. 3.19. The 2-phonon Fano formula shows two exact antiresonances and the phonons are repelled from each other when comparing them to the corresponding phonons in the 1-phonon Fano curves $I_{p,1}(\omega)$ and $I_{p,2}(\omega)$. This effect corresponds to level-repulsion in second order perturbation theory.

### 3.4.5 The case of infrared absorption

The Fano effect is also important and has an influence on optical absorption by infrared-active phonons. The calculation of the real part of the optical conductivity $\sigma(\omega)$ (proportional to $\omega \operatorname{Im}\epsilon(\omega)$) in presence of electron-phonon coupling parallels that of the imaginary part of the Raman susceptibility with the only difference that the vertices $T_e$, $T_p$, and $V$ have

---

[16] Note, however, that they have to be taken into account when discussing sum rules (pay attention to [3.15]) of the kind $\int d\omega \operatorname{Im}\chi_{Fano}(\omega)$.

to be reinterpreted in physical terms. This subsection serves the purpose of a comparison of the vertices for the cases of Raman scattering and optical absorption.

**The photon-electron vertex $T_e$.** We start with the vertex $T_e$ coupling the incident light to the electronic continuum. In Raman scattering, this vertex is of second order in the light field, and consists of two contributions: the elementary vertex[17] $\boldsymbol{A}^2\rho$ which contributes a density-density-like polarization loop allowing for intraband transitions only, and a vertex proportional to $(\boldsymbol{A}\cdot\boldsymbol{j})^2$, allowing additionally for interband transitions, and contributing also a density-density-like polarization loop to the Raman susceptibility (density-density-like as far as the parity of the vertex is concerned). The total polarization loop arising from these two contributions is density-density-like and therefore related to the *longitudinal* dielectric function.

In the case of optical absorption, the role of the vertex $T_e$ is played by the combination $\boldsymbol{A}\cdot\boldsymbol{j}$. This yields a current-current-like polarization loop and produces only electron-hole excitations with negative parity; it does not allow for intraband excitations. Therefore, the effect of Coulomb screening on the relevant polarization loop is marginal. The negative parity of the electron-hole pairs excited by light is an important selection rule in optical absorption. The current-current-like polarization loop is related to the *transverse* dielectric function.

**The photon-phonon vertex $T_p$.** In Raman scattering, the photon-phonon vertex $T_p$ is represented by the diagram of Fig. 3.4. Due to the fact that the $\boldsymbol{A}\cdot\boldsymbol{j}$ vertices in Fig. 3.4 have negative parity, this is also true for the electron-hole pairs before and after the creation of the phonon. Therefore, the phonon involved must be *even*.[18] This is an important selection rule!

In crystals possessing optical modes with a nonvanishing dipole moment (these modes must necessarily have *odd* parity!) the light directly couples to the transverse component of the odd phonons. The corresponding vertex is proportional to $\boldsymbol{A}\cdot\boldsymbol{d}$, where $\boldsymbol{d}$ is the dipole moment of the phonon. Note that a diagram analogous to the one in Fig. 3.4 does not exist in optical absorption.

**The electron-phonon vertex $V$.** The electron-phonon vertex $V$ plays a similar role in Raman scattering and in optical absorption.

### 3.4.6 Renormalizing the electron

Electron-phonon interaction renormalizes not only the phonon but also the electronic excitations. To see this, we calculate the self-energy of the electron due to the presence of the electron-phonon interaction in the Hartree-Fock approximation. The Hartree-term, that is, the tadpole depicted in Fig. 3.20(a) only does not vanish for a $\boldsymbol{q}=0$ phonon. This is not meant to be a $\boldsymbol{q}\neq 0$ phonon in the $\boldsymbol{q}\to 0$ limit, as is usually the case in Raman scattering, but an exact $\boldsymbol{q}=0$ phonon representing a static strain in the crystal and therefore not having to be considered in our case. The exchange-type Fock-term in Fig. 3.20(b) is the

---

[17] By the notation $\boldsymbol{A}^2\rho$ we refer to the vertex discussed in Subsect 2.2.8, $(\boldsymbol{A}\cdot\boldsymbol{j})^2$ denotes the vertex of Subsect 2.2.9. We use the density $\rho$ and current density $\boldsymbol{j}$ (instead of the quasimomentum $\boldsymbol{p}$) to clarify the relation of the electronic Raman susceptibility to the density-density and current-current response functions.

[18] It is clear that the crystal must possess inversion symmetry. Otherwise there are no irreducible representations of the crystal's symmetry group which correspond to positive and negative parity, respectively.

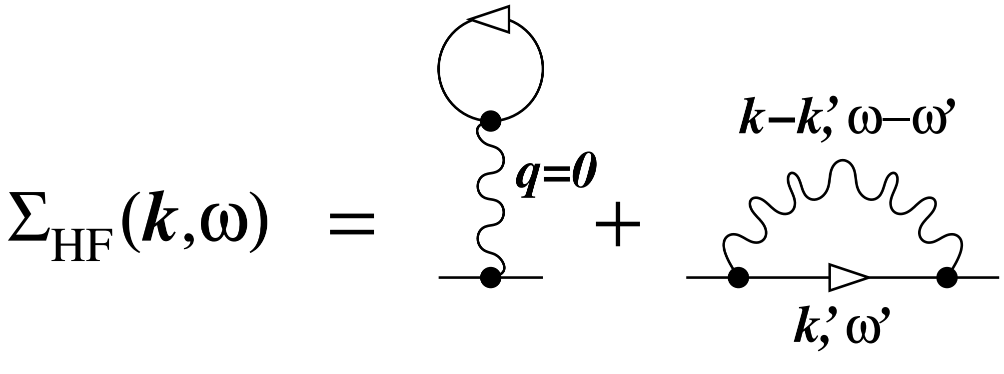

Figure 3.20: The contributions to the electron self-energy in Hartree-Fock approximation.

term we are interested in. Using the temperature-dependent Matsubara-formalism and the bare electron and phonon Green's functions $\mathcal{G}_0$ and $\mathcal{D}_0$, the self-energy of the electron is given by

$$\Sigma(\boldsymbol{k}, i\omega_n) = \sum_{\boldsymbol{k}'} |g_{\boldsymbol{k}\boldsymbol{k}'}|^2 (-k_B T) \sum_{i\omega_{n'}} \mathcal{G}_0(\boldsymbol{k}', i\omega_{n'}) \mathcal{D}_0(\boldsymbol{k}-\boldsymbol{k}', i\omega_n - i\omega_{n'}) \; .$$

Performing the summation over $i\omega_n$ (both frequencies $i\omega_n$ and $i\omega_{n'}$ are Fermi-frequencies!) by changing the sum into an integral and using the residue theorem we find

$$\begin{aligned}\Sigma(\boldsymbol{k}, i\omega_n) = & \sum_{\boldsymbol{k}'} |g_{\boldsymbol{k}\boldsymbol{k}'}|^2 \times \\ & \times \left\{ \frac{n_B(\omega_{\boldsymbol{k}-\boldsymbol{k}'}) + n_F(\xi_{\boldsymbol{k}'})}{i\omega_n - \xi_{\boldsymbol{k}'} + \omega_{\boldsymbol{k}-\boldsymbol{k}'}} + \frac{1 + n_B(\omega_{\boldsymbol{k}-\boldsymbol{k}'}) - n_F(\xi_{\boldsymbol{k}'})}{i\omega_n - \xi_{\boldsymbol{k}'} - \omega_{\boldsymbol{k}-\boldsymbol{k}'}} \right\}\end{aligned}$$

which we are going to evaluate for the case $T = 0$.[19] Then, the Bose functions $n_B$ vanish, and the Fermi functions $n_F$ become step functions. Performing also the analytic continuations, the retarded self-energy is given by

$$\begin{aligned}\Sigma_{ret}(\boldsymbol{k}, \omega) &= \sum_{\boldsymbol{k}'} |g_{\boldsymbol{k}\boldsymbol{k}'}|^2 \left\{ \frac{\Theta(-\xi_{\boldsymbol{k}})}{\omega - \xi_{\boldsymbol{k}'} + \omega_{\boldsymbol{k}-\boldsymbol{k}'} + i\delta} + \frac{\Theta(\xi_{\boldsymbol{k}})}{\omega - \xi_{\boldsymbol{k}'} - \omega_{\boldsymbol{k}-\boldsymbol{k}'} + i\delta} \right\} \\ &= \int_0^\infty d\epsilon' \, d\omega' \sum_{\boldsymbol{k}'} |g_{\boldsymbol{k}\boldsymbol{k}'}|^2 \delta(\omega' - \omega_{\boldsymbol{k}-\boldsymbol{k}'}) \delta(\epsilon' - \xi_{\boldsymbol{k}'}) \times \\ &\quad \times \left\{ \frac{1}{\omega + (\epsilon' + \omega') + i\delta} + \frac{1}{\omega - (\epsilon' + \omega') + i\delta} \right\} \; .\end{aligned} \tag{3.33}$$

To describe the superconductor in a dirty limit, we define the *averaged electron self-energy* $\Sigma_{ret}(\omega)$ by averaging the electron self-energy (3.33) over the Fermi surface yielding

$$\Sigma_{ret}(\omega) \equiv \langle \Sigma_{ret}(\boldsymbol{k}, \omega) \rangle_{FS} = \frac{\sum_{\boldsymbol{k}} \Sigma_{ret}(\boldsymbol{k}, \omega) \delta(\epsilon_{\boldsymbol{k}})}{\sum_{\boldsymbol{k}} \delta(\epsilon_{\boldsymbol{k}})} \tag{3.34}$$

---

[19] This is easier that using the $T = 0$ Green's functions formalism.

where the sum in the denominator is the density of states at the Fermi energy, $N_F = 2\sum_{\boldsymbol{k}}\delta(\epsilon_{\boldsymbol{k}})$. Using this we write the average electron self-energy (3.34) in the form

$$\Sigma_{ret}(\omega) = \int_0^\infty d\epsilon'\, d\omega'\, \alpha^2 F(\omega') \left\{ \frac{1}{\omega + \epsilon' + \omega' + i\delta} + \frac{1}{\omega - (\epsilon' + \omega') + i\delta} \right\}$$

and introduce a function which is very important in the theory of superconductivity, the *Eliashberg-function*[20]

$$\alpha^2 F(\omega) = \frac{2}{N_F} \sum_{\boldsymbol{k}\boldsymbol{k}'} |g_{\boldsymbol{k}\boldsymbol{k}'}|^2 \delta(\omega - \omega_{\boldsymbol{k}-\boldsymbol{k}'}) \delta(\epsilon_{\boldsymbol{k}'}) \delta(\epsilon_{\boldsymbol{k}}) \ .$$

In the definition of the Eliashberg-function we have approximated the function $\delta(\epsilon' - \epsilon_{\boldsymbol{k}'})$ by $\delta(\epsilon')$ making the Eliashberg-function independent of $\epsilon'$. The justification of this is somewhat complicated. We refer to page 17 of [3.16]. The $\epsilon'$-integration is now trivial and, closed to the Fermi surface, the electron self-energy can be written in the form

$$\Sigma_{ret}(\omega) = -2\omega \int \frac{d\omega'}{\omega'} \alpha^2 F(\omega') + O(\omega^2) \equiv -\lambda\omega + O(\omega^2) \ . \tag{3.35}$$

Equation (3.35) defines the *McMillan* parameter $\lambda$ that characterizes the average strength of the electron-phonon interaction. We shall illustrate this by presenting an example, the evaluation of the effective mass of "dressed" electrons, whose Green's function is given by

$$G^{-1}(\boldsymbol{k}, \omega) = G_0^{-1}(\boldsymbol{k}, \omega) - \Sigma(\boldsymbol{k}, \omega) \ .$$

Using the $\boldsymbol{k}$-independent self-energy calculated above and noting that the excitation spectrum of the dressed electrons is given by the poles of the Green's function $G$, we obtain

$$\epsilon^*_{\boldsymbol{k}} = \frac{\epsilon_{\boldsymbol{k}}}{1+\lambda} = \frac{m}{m^*}\epsilon_{\boldsymbol{k}} \ , \qquad \text{i.e.} \qquad m^* = (1+\lambda)m$$

expressing the fact that the electron-phonon coupling causes an electron mass enhanced by a factor of $1 + \lambda$.

## 3.5 The Fano-effect and superconductivity

This section is concerned with the work in [3.10]. In this publication experimental data is illustrating the renormalization of two particular phonons by the superconducting transition in the high-temperature superconductor $HgBa_2Ca_3Cu_4O_{10+\delta}$. Theoretical considerations in addition to the discussion and interpretation of the experimental data complete the presentation.

---

[20] One comment on the unconventional symbol $\alpha^2 F$ denoting the Eliashberg-function. It does *not* imply a product $\alpha \cdot \alpha \cdot F$, but just serves as a mnemonic for the physical meaning of the Eliashberg-function: it is "like" a squared matrix element ($g^2_{\boldsymbol{k}\boldsymbol{k}'}$) times a one-phonon density of states.

### 3.5.1 Introduction

After having introduced the basic notions of Fano theory, we are going to discuss the change of phonon renormalization when entering the superconducting state at $T = T_c$ of a high-temperature superconductor. We shall present an experimental data and explain them by means of an appropriate theoretical formalism.

The reason for a drastic change in the renormalization of phonons by electron-phonon interaction when going from the normal to the superconducting state lies in the restructuration of the electronic system by the appearance of a superconducting gap at $T = T_c$. In high-temperature superconductors the energy scale of optical phonons and that of the superconducting gap happen to be the same. Therefore, the change of the electronic polarization induced by the opening of the superconducting gap has a large influence on the phonon self-energy and implies a change of the phonon parameters.

These *superconductivity-induced phonon self-energy effects* already have been observed for a number of superconducting cuprates. The measurements usually have been motivated by the interest in the size of the superconducting gap, which can be inferred from the knowledge of the temperature-dependence of the phonon self-energy for particular phonons, and the magnitude of the electron-phonon interaction. The first phonon *softening* measured was that of the $B_{1g}$-like O(2)/O(3) out-of-phase phonon at $340\,\mathrm{cm}^{-1}$ in Y-123, observed by Macfarlane and coworkers [3.17] in ceramic Y-123 and by Thomsen and coworkers [3.18] in Y-123 single crystals. The corresponding $A_{1g}$-like phonon [O(2)/O(3) in-phase displacements along the $c$-axis, at $440\,\mathrm{cm}^{-1}$] was later shown by Horn and coworkers [3.19] to *harden*. Cooper and colleagues [3.20] and by Friedl and coworkers [3.21] also demonstrated that the $B_{1g}$ phonon in Y-123 broadens below $T_c$.

Phonon Raman scattering measurements have already been done in the whole series of $\mathrm{HgBa_2Ca_{n-1}Cu_nO_{2n+2+\delta}}$ high-temperature superconductors where $n = 1, \ldots, 5$ and are reported, for example, by Zhou and colleagues in [3.22]. The Hg-1223 compound, in particular, has been addressed in [3.23].

There are also some theoretical investigations of this effect available. Zeyher and Zwicknagl [3.24] have treated the problem in the framework of Eliashberg-theory for an $s$-wave superconductor and an optical phonon. Later on, Nicol and Carbotte [3.25, 3.26] have extended this model to the case of an anisotropic $d$-wave superconductor. Devereaux [3.27] calculated the phonon self-energy in a 2-dimensional one-band Landau liquid model with circular Fermi surface using the BCS pairing scenario with a $d$-wave gap and compared the results to measurements which have been performed at $\mathrm{Bi_2Sr_2CaCu_2O_8}$ (Bi-2212) and $\mathrm{YBa_2Cu_3O_7}$ (Y-123). In a further paper, Devereaux and coworkers [3.28] contrasted the self-energy effect for $B_{1g}$ phonons to that of $A_{1g}$ phonons using a model of the electronic system coupling via charge density fluctuations to phonons.

The experiment we are going to discuss as an illustration of electron-phonon interaction in the superconducting state was performed by Hadjiev and coworkers [3.10] using as a sample a $\mathrm{HgBa_2Ca_3Cu_4O_{10+\delta}}$ (Hg-1234) high-temperature superconductor, and it was found to show a drastic phonon frequency softening (i.e. lowering of the frequency) as well as a linewidth increase for particular vibration modes with ion displacements directed along the crystal $c$-axis when entering the superconducting state from $T > T_c$ to $T < T_c$. Additionally, the Raman peaks of the phonons also show a strong intensity enhancement by a factor of about 10 when entering the superconducting state. These phonons are observed in $(x'x')$

polarization which corresponds to $A_{1g} + B_{2g}$ in tetragonal notation.

**The experimental setup.** The Hg-1234 sample used in the experiment is a microcrystalline pellet prepared by a high-pressure technique [3.29]. The transition temperature was determined to be $T_c = 123\,\mathrm{K}$ by the method of zero of resistance. By X-ray diffraction analysis it was confirmed that Hg-1234 was the main phase in the pellet, but the presence of other phases like Hg-1223 cannot be ruled out completely. The Raman measurements have been performed by focusing the laser light to single crystalline grains in the pellet with microscope optics. The focusing diameter was about 2–3 $\mu$m. By putting the pellet inside of a continuous-flow liquid helium cryostat, it became possible to vary the temperature of the pellets continuously in the range from 4 K to room temperature. Local overheating of the sample by the laser light was kept low by using light of only moderate power, and was estimated to amount to no more that 5–10 K.

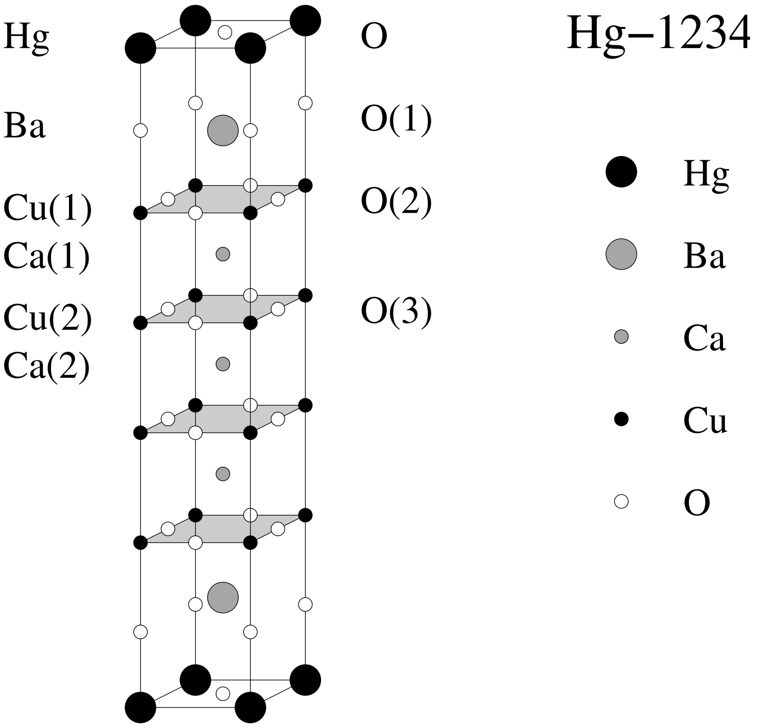

Figure 3.21: The unit cell of the high-$T_c$ superconductor $HgBa_2Ca_3Cu_4O_{10+\delta}$ (Hg-1234).

**Predicted phonons.** The cuprate superconductor under consideration crystallizes in the P4/mmm space group, having the tetragonal $D_{4h}$ point group [3.30] (see Fig. 3.21). A group-theoretical analysis of the Γ-point phonons of Hg-1234 was presented in Chap. 4 and showed the presence of $7\,A_{1g}$, $2\,B_{1g}$, and $9\,E_g$ Raman-allowed modes. In particular, there are no $B_{2g}$ phonon modes. From this fact we deduce that the phonons seen in $(x'x')$ polarization are $A_{1g}$ phonons. The 7 modes transforming according to the $A_{1g}$ representation of the tetragonal $D_{4h}$ group are composed out of the displacement patterns which are even with respect to the crystal inversion center located at the Hg site and involve the Ba, Ca, Cu(1), Cu(2), O(1), O(2), and O(3) ions. By comparison to the system Tl-1234, which has the same group-theoretical symmetry properties, we conclude that the heavy Ba and

| phonon | frequency |
|---|---|
| O(2)-O(3) in-phase | $246\,\mathrm{cm}^{-1}$ |
| O(2)-O(3) out-of-phase | $369\,\mathrm{cm}^{-1}$ |
| O(2)-O(3) in-phase, Ca out-of-phase | $450\,\mathrm{cm}^{-1}$ |

Table 3.1: Phonon frequencies predicted for Tl-1234. Taken from [3.31]. For the crystal structure see Fig. 3.21.

Cu ions should have the lowest frequencies, followed by the Ca, O(2), and O(3) ions, and finally by the apex oxygen O(1) vibration having the highest frequency. Table 3.1 shows the frequencies predicted by calculations based on a particular kind of shell model by Kulkarni and coworkers [3.31]. This information will help us to assign the phonon peaks observed in the experiment to the predicted phonon modes [3.22].

### 3.5.2 Experimental results

**Presentation of the spectra.** Figure 3.22 shows polarized Raman spectra of Hg-1234 measured at 4.5 K and at room temperature. The spectra were recorded in three different polarization configurations. In Fig. 3.22(a) the polarization is $(x'x')$, this corresponds to a mixed symmetry of $A_{1g} + B_{2g}$ in tetragonal notation. We already mentioned the fact that in the ideal Hg-1234 crystal structure there are no $B_{2g}$ phonons. Hence, all the phonons seen in the $(x'x')$ spectrum have $A_{1g}$ symmetry. The spectrum in Fig. 3.22(b) was measured in $(x'y')$ configuration and is therefore related to the Raman vertices transforming like $B_{1g}$. Finally, Fig. 3.22(c) was measured in $(zz)$ polarization and therefore also has $A_{1g}$ symmetry properties.

We start describing the $(zz)$ spectra shown in Fig. 3.22(c). At room temperature two clear Raman peaks at 574, and $487\,\mathrm{cm}^{-1}$ and a shoulder at $532\,\mathrm{cm}^{-1}$ can be identified. At helium temperature, they can be better resolved, especially the shoulder at $532\,\mathrm{cm}^{-1}$ becomes a peak. The strong peaks at 574, 532, and $487\,\mathrm{cm}^{-1}$ have been assigned to vibrations of the apex oxygen along the $c$-axis and to mixed modes of apex and excess oxygen at different positions in the Hg plane [3.22].

Let us return to the $(x'x')$ spectra in Fig. 3.22(a). For this polarization configuration, and at room temperature, three weak phonon-like structures are observable at 240, 390, and $410\,\mathrm{cm}^{-1}$ which, as already mentioned, must have $A_{1g}$ symmetry. The phonons at 240 and $390\,\mathrm{cm}^{-1}$ exhibit strong coupling with the scattering continuum manifested by a clear asymmetric lineshape, with antiresonances to the right of the phonons. The peak at $410\,\mathrm{cm}^{-1}$ has a symmetric lineshape and very low intensity. At low temperature, in the superconducting state, the two lower frequency phonons show an obvious change of their position, linewidth and, especially, the scattering intensity. Except for a change in intensity, there is no visible change of the $410\,\mathrm{cm}^{-1}$ phonon self-energy when going from the normal conducting to the superconducting state.

In addition to the three phonon-like features described, there are two relatively sharp Raman features at 485 and $575\,\mathrm{cm}^{-1}$ on the top of the $A_{1g} + B_{2g}$ superconductivity-induced electronic peak. Comparing these to the spectra given in Fig. 3.22(c), one finds that the position of the peaks *correlates* with that of the mainly $zz$-polarized vibrations of the excess and apex oxygen atoms. It is important to note that this is not because of polarization leakage, but must be an intrinsic effect. The lineshape of the $575\,\mathrm{cm}^{-1}$ phonon in $zz$-polarization is almost independent of temperature while the $575\,\mathrm{cm}^{-1}$ peak in the $x'x'$ spectra only exists in the superconducting phase.

The two phonons of $B_{1g}$ symmetry which are predicted by group theory are hardly seen in the room temperature spectrum of Fig. 3.22(b). Except for some Raman features that coincide in position with the peaks in the $x'x'$-spectra, likely due to polarization leakage, a relatively broad peak appears at $690\,\mathrm{cm}^{-1}$ that can be attributed to superconductivity-induced $B_{1g}$ excitations of electronic origin. From now on we focus on the $(x'x')$ spectra.

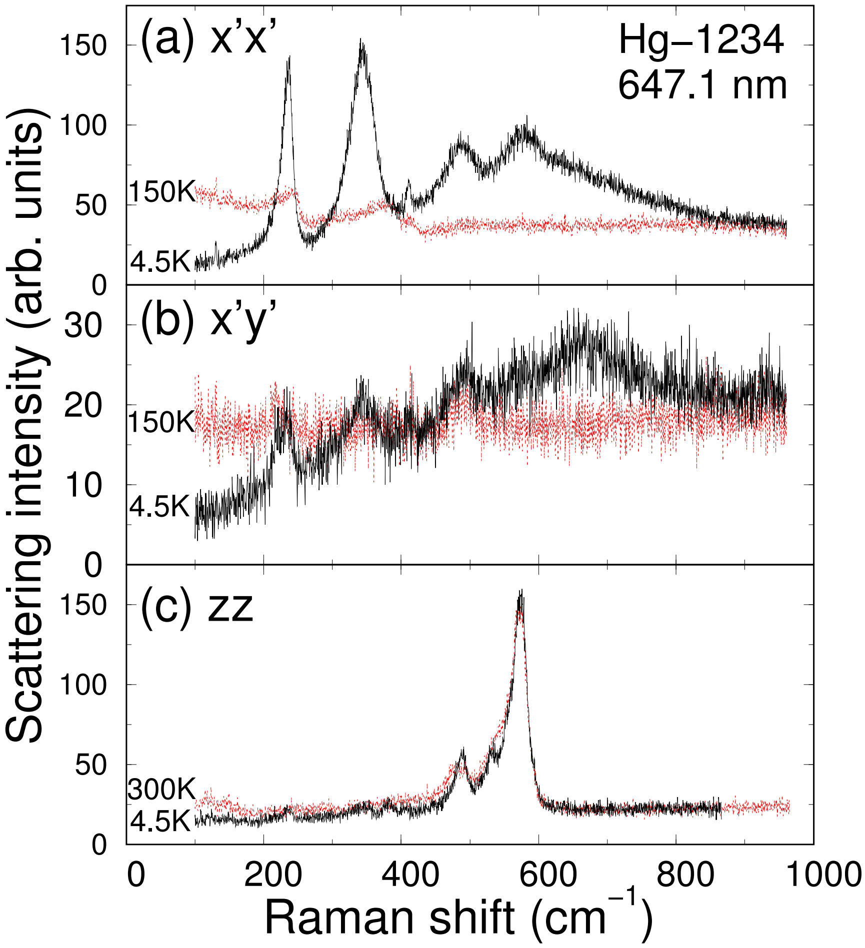

Figure 3.22: Polarized Raman spectra of Hg-1234 single crystalline grains measured at room temperature and at 4.5 K with 647.1 nm laser excitation. The spectra (a) and (b) were taken from the same grain, whereas those in (c) were measured from another grain oriented with the $ac$-plane normal to the direction of incidence of the light.

**Phonon assignment.** We discuss next the assignment of the $A_{1g}$ phonons at 240, 390 and $410\,\mathrm{cm}^{-1}$. The symmetry and frequency of these phonons suggest that they involve vibrations along the $c$-axis of plane oxygen atoms and of the Ca: the vibrations of Ba and Cu in the planes usually have frequencies below 200 cm$^{-1}$ in the structurally similar superconducting cuprates; the $A_{1g}$ apex oxygen vibration is seen at 574 cm$^{-1}$ in Fig. 3.22(c). Since Ca has the lightest mass among the cations in Hg-1234, its frequency is expected to be close to that of the low frequency (bond bending) oxygen vibrations and the Ca vibrations may therefore mix with the latter. This gives a total of three Raman active $A_{1g}$ modes in the 200–450 cm$^{-1}$ region involving pairs of planes. Lattice dynamical calculations for the isomorphic Tl-1234 compound [3.31] indeed show that the vibrations of Ca and plane oxygen atoms are mixed. In the paper of Kulkarni and coworkers [3.31], it was calculated for Tl-1234 that the mixed vibrations along the $c$-axis of oxygen in the CuO$_2$ planes and Ca moving in-phase and out-of-phase with the oxygen atoms take palce at 246 and 450 cm$^{-1}$, respectively. One phonon corresponds nearly exclusively to the vibration against each other of the two CuO$_2$ layers which are separated by Ca atoms. This phonon has a small admixture of calcium and should be found at 369 cm$^{-1}$. Unfortunately, there are no experimental data available so far for Tl-1234 that may check the model of the lattice dynamical predictions, which, in any case, are known to be rather unreliable, especially concerning eigenvectors [3.32]. *Ab initio* calculations, based on the electronic total energy [3.33, 3.34], would be highly desirable in order to achieve a reliable assignment of the frequencies and eigenvectors of the three $A_{1g}$ modes under discussion. Nevertheless even these calculations are known to lead to considerable errors in the phonon eigenvectors, especially when phonon frequencies corresponding to the same symmetry are close to each other. A way to solve this problem is to determine the eigenvectors experimentally by isotopic substitution [3.32], an investigation which has not yet been performed for the Hg-based superconductors. As a possible way out of this impass we examine the possibility of adopting the eigenvalues and eigenvectors calculated for Tl-1234 for the interpretation of our data concerning the 240, 390 and 410 cm$^{-1}$ phonons of Hg-1234. The similarity of the electron-phonon coupling strength of the modes at 240 and 390 cm$^{-1}$, as displayed by their lineshape and dependence of Raman intensity on temperature, suggests that these two phonons should have similar vibrational patterns. In addition, the phonons at 265 and 400 cm$^{-1}$ in Hg-1223 have similar temperature dependence as those at 240 and 390 cm$^{-1}$ in Hg-1234 [3.23]. In the Hg-1223 compound there are only two Raman active mixed plane-oxygen and Ca modes [3.31]. Therefore, we assign the $A_{1g}$ modes at 240 and 390 cm$^{-1}$ in Hg-1234 to the mixed Ca and oxygen modes and that at 410 cm$^{-1}$ to nearly pure plane oxygen vibrations along the $c$-axis. The weak electron-phonon coupling observed for the 410 cm$^{-1}$ phonon would then have to result from some cancellation within each pair of CuO$_2$ planes sandwiching the Ca plane, possibly related to the fact that those CuO$_2$ planes move in opposite direction.

**Fitting the Fano parameters.** To show more clearly the dependence of the phonon self-energy on temperature, the $(x'x')$ polarized Raman spectrum of Hg-1234 has been measured for several temperatures between 4.5 K and 295 K, see Fig. 3.23. The 240 and 390 cm$^{-1}$ phonon peaks display clear asymmetric lineshapes with a characteristic antiresonance at the higher frequency side in the whole range from room temperature (but much stronger asymmetric above $T_c$, see $q$ in Fig. 3.24) to 4.5 K, a fact which suggests an interaction between the discrete phonon states and the electronic continuum, as found for other cuprates [3.20, 3.21, 3.23]. We have fitted the measured phonon peaks with a standard Fano

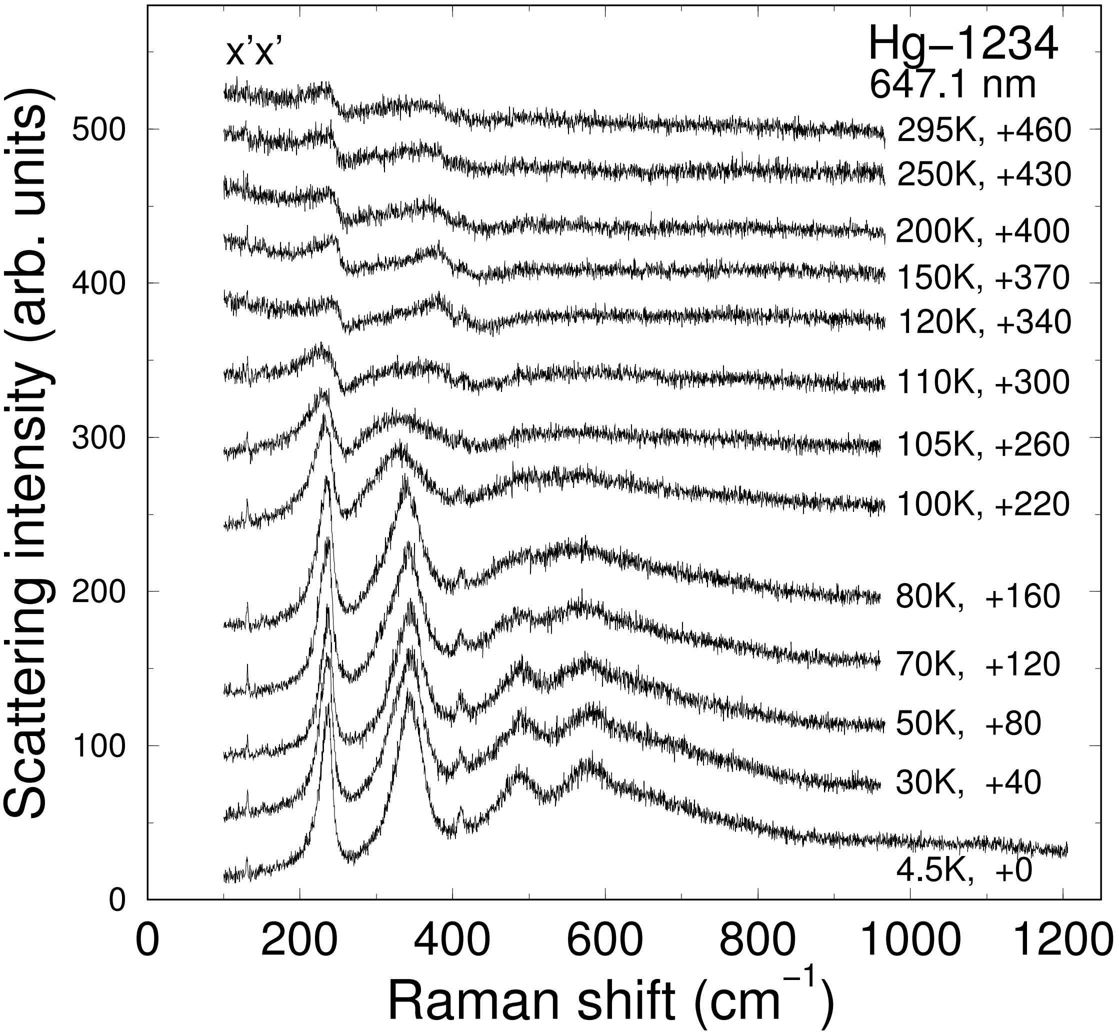

Figure 3.23: Raman spectra of Hg-1234 measured at various temperatures between room temperature and 4.5 K in $x'x'$ polarization. The numbers in the right column give the offset of the spectra with respect to that at the bottom.

function (3.11) [the parameters $q$ and $\epsilon$ are related to $\omega_p$, $\omega_a$, and $\Gamma_p$ by (3.12)]

$$I(\omega) = I_c \frac{|q+\epsilon|^2}{1+\epsilon^2} + I_b(\omega) \ , \tag{3.36}$$

in which $\epsilon = (\omega - \omega_p)/\Gamma_p$ with the renormalized phonon frequency $\omega_p = \omega_p^0 + \delta\omega_p$, $\omega_p^0$ is the "bare" phonon frequency, $q$ the asymmetry parameter, $\Gamma_p$ the linewidth (the half width at half maximum, HWHM), $I_c$ a quantity proportional to the square of the Raman vertex of that part of the electronic continuum that interferes with the phonon (assuming to be constant in the phonon region). Additionally, we have added the contribution $I_b$ representing a possible noninterfering background. Raman spectra and the fitted Fano profiles of the 240 and $390\,\mathrm{cm}^{-1}$ phonons are shown in Figs. 3.24(a) and 3.24(a), respectively. The fitted values of the Fano parameters (except for the trivial background $I_b$) and the *renormalized phonon intensity* [3.35] [see Subsect. 3.4.1 and in particular (3.19)]

$$I_p \equiv \pi[I(\omega_p) - I_b(\omega_p)]\Gamma_p = \pi I_c q^2 \Gamma_p \tag{3.37}$$

of the 240 and $390\,\mathrm{cm}^{-1}$ peaks are plotted versus temperature in Figs. 3.24(b) and 3.25(b) (We assume that $q$ is real. An imaginary part of $q$ can be represented by a noninteracting electronic background, that is by $I_b$, as shown in Subsect. 3.3.2 and also in [3.12]). Note that $I_c$ and $I_b$ are intensities per unit frequency while $I_p$ is the *integrated* intensity of the discrete phonon excitation.

Apart from some differences in details, the temperature dependencies of frequency, linewidth and intensity of the 240 and $390\,\mathrm{cm}^{-1}$ peaks display a remarkable abrupt change in a narrow temperature interval (10–15 K) right below $T_c$. Using the phonon frequencies $\omega_p^N$ and $\omega_p^S$ in the normal state and in the superconducting state, the relative softening $(\omega_p^N - \omega_p^S)/\omega_p^N$ of the 240 and $390\,\mathrm{cm}^{-1}$ phonons is 6 % and 18 %, respectively. The phonon linewidth goes through a maximum below $T_c$ with an overall change in linewidths $(\delta\Gamma_p)_{max}/\omega_p^N$ equal to 10 % for the phonon at $240\,\mathrm{cm}^{-1}$ and 40 % for that at $390\,\mathrm{cm}^{-1}$.

**Linewidths and anharmonic broadening.** In the normal state, the linewidths of the 240 and $390\,\mathrm{cm}^{-1}$ phonons increase with increasing temperature. Assuming that the electronic susceptibility in the normal state is temperature independent, this indicates the presence of another phonon decay channel beside decay into an electron-hole pair. We are going to describe this additional channel as an anharmonic decay into two phonons. This process has been treated theoretically in Subsect. 3.4.2 and implies a temperature-dependence of that contribution to the phonon linewidth of the form (3.26).

An additional nearly temperature independent contribution $\Gamma_b$ to the linewidth may result from elastic scattering by defects and, in the normal state, to the coupling of the phonon to the structureless continuum of electronic excitations. We have fitted the temperature dependence of the phonon linewidths $\Gamma_p(T)$ at $240\,\mathrm{cm}^{-1}$ (Fig. 3.24(b)) and $390\,\mathrm{cm}^{-1}$ (Fig. 3.25(b)) in the normal state with the function (see Eq. (3.26))

$$\Gamma_p^N(T) = \Gamma_{anh}^0 \left[ 1 + 2 \left( \exp \frac{\hbar\omega_p}{2k_BT} - 1 \right)^{-1} \right] + \Gamma_b \ . \tag{3.38}$$

Note that $\Gamma_p^N(T{=}0) = \Gamma_{anh}^0 + \Gamma_b$ is the sum of the temperature-dependent part of $\Gamma_p^N(T)$ at $T = 0$ and the temperature-independent part $\Gamma_b$. Consequently, the *change* in linewidth

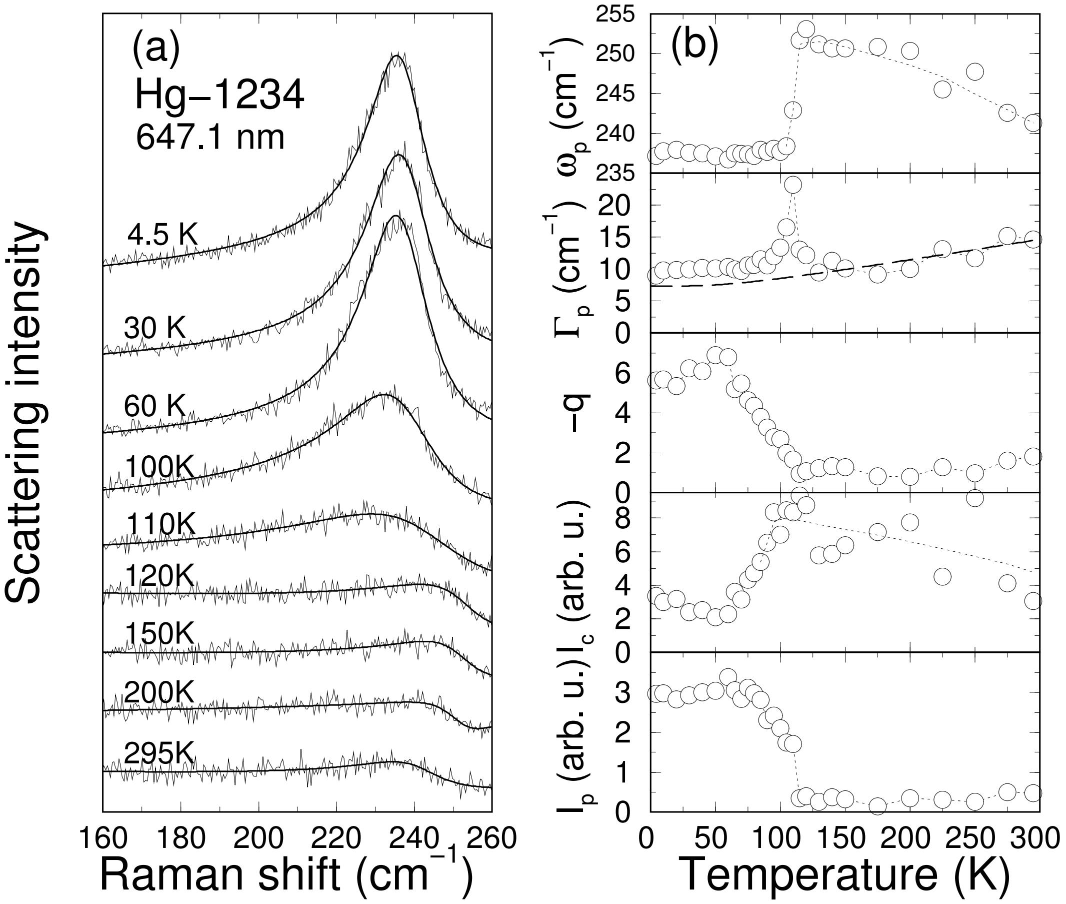

Figure 3.24: Raman spectra of the $A_{1g}$ mode at $240\,\mathrm{cm}^{-1}$ measured in $x'x'$ polarization with the 647.1 nm laser line at different temperatures and the corresponding fitted Fano profiles (a). The fitted frequency, linewidth $\Gamma_p$ (HWHM), asymmetry parameter $q$ and the phonon intensity are plotted in (b) as open circles. Smooth dotted lines are given as a guide to the eye. The dashed line in the linewidth panel represents a fit to the widths found above $T_c$ with the function in (3.38), taking $\omega_p = 240\,\mathrm{cm}^{-1}$. This fit yields $\Gamma^0_{anh} = 3\,\mathrm{cm}^{-1}$ and $\Gamma_b = 4.4\,\mathrm{cm}^{-1}$.

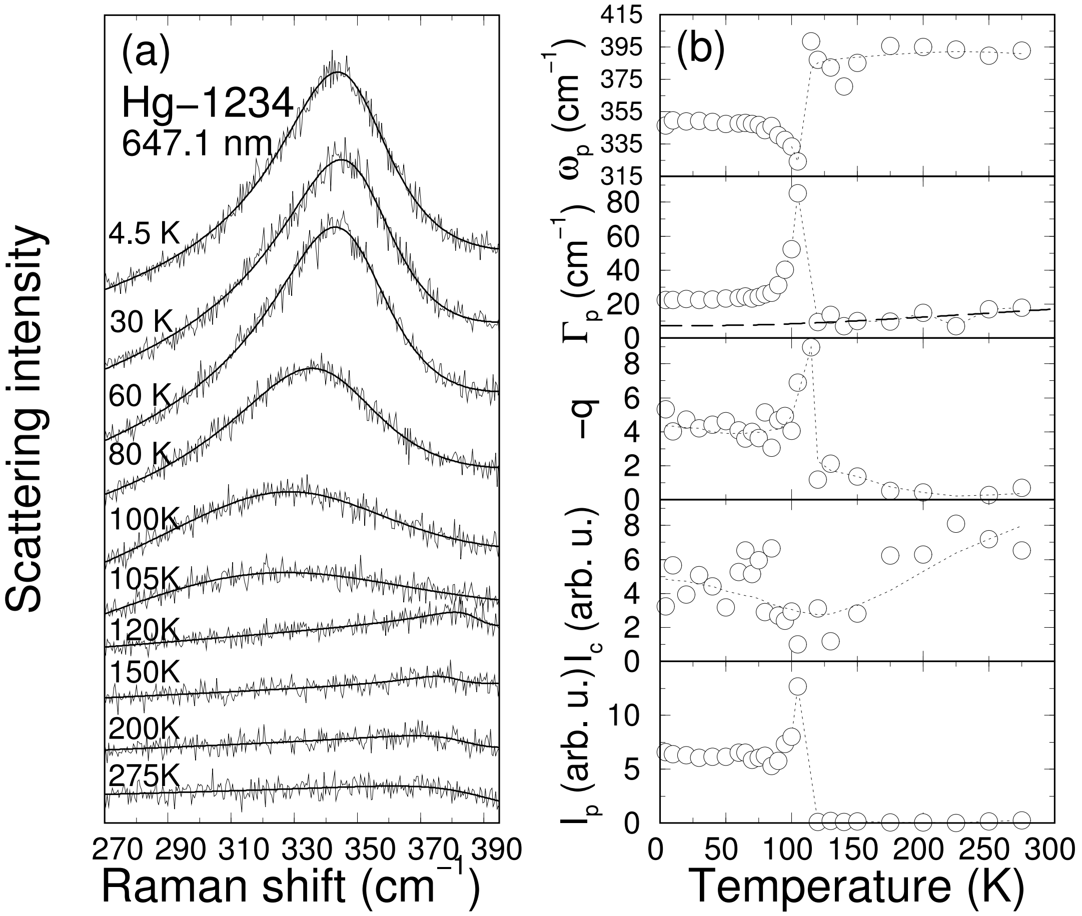

Figure 3.25: Raman spectra covering the 390 cm$^{-1}$ $A_{1g}$ mode measured in $x'x'$ polarization with the 647.1 nm laser line at different temperatures and the corresponding fits with Fano profiles (a). The fitted frequencies, linewidths $\Gamma_0$ (HWHM), lineshape parameters $q$ and the phonon intensity are represented in (b) by open circles. Smooth dotted lines through the points are given as a guide to the eye. The dashed line in the linewidth panel represents a fit to the widths found above $T_c$ with the function in (3.38), taking $\omega_p = 390\,\text{cm}^{-1}$. This fit yields $\Gamma^0_{anh} = 7.3\,\text{cm}^{-1}$.

due to the superconducting transition is given by the linewidth at $T = 0$ minus $\Gamma_p^N(T{=}0)$, that is $\delta\Gamma_p = \Gamma_p(0) - (\Gamma_{anh}^0 + \Gamma_b)$. The dashed line in Fig. 3.24(b) represents the fit with Eq. (3.38) (linewidths are given as HWHM) with $\Gamma_{anh}^0 = 3\,\mathrm{cm}^{-1}$ and $\Gamma_b = 4.4\,\mathrm{cm}^{-1}$ taking $\omega_p = 240\,\mathrm{cm}^{-1}$ (these quantities have rather large error bars). The fit allows us to distinguish between the temperature-dependent contribution $\Gamma_{anh}$, and the constant contribution $\Gamma_b$ to the linewidth, of which the latter is likely to be due to the interaction of the $240\,\mathrm{cm}^{-1}$ phonon with electronic excitations in the normal state and/or impurity scattering. The fit of the temperature dependence of the $390\,\mathrm{cm}^{-1}$ phonon linewidth with Eq. (3.38) yields $\Gamma_b \approx 0$. The results of such a fit are represented by the dashed line in Fig. 3.25(b). The fitting parameters for this case are $\Gamma_{anh}^0 = 7.3\,\mathrm{cm}^{-1}$ for $\omega_p = 390\,\mathrm{cm}^{-1}$. The strongest change in the phonon linewidth takes place just below $T_c$, as would be expected for a crossover of the opening superconducting gap and the phonon energy. When further lowering the temperature the linewidth remains nearly constant.

### 3.5.3 Discussion and model

**Introduction and assumptions.** The expression (3.36) for the Raman efficiency of a system with a phonon coupled to a continuum of electronic excitations can be written in terms of microscopic parameters [3.11, 3.8] (neglecting for simplicity other phonon renormalization mechanisms as, for instance, anharmonic decay)

$$I(\omega) \sim \pi T_e^2 \rho(\omega) \frac{\left(\omega - \omega_p^0 + \frac{T_p V}{T_e}\right)^2}{\left(\omega - \omega_p^0 - V^2 R(\omega)\right)^2 + \left(\pi V^2 \rho(\omega)\right)^2} \tag{3.39}$$

where $T_e$, $T_p$, and $V$ are the vertices describing the coupling of the electron-hole excitations to the photons (Raman vertex), the coupling of the phonons to the photons, and the electron-phonon coupling, respectively. The bare phonon frequency is $\omega_p^0$. The spectral function of the electrons $\rho(\omega)$ and the function $R(\omega)$ are related to the imaginary and the real part of the *retarded* electronic polarizability $\Pi(\omega)$ at $\boldsymbol{q} = 0$ by

$$\rho(\omega) = -\frac{1}{\pi}\,\mathrm{Im}\,\Pi(\omega) \qquad \text{and} \qquad R(\omega) = \mathrm{Re}\,\Pi(\omega)\ , \tag{3.40}$$

respectively. A Kramers-Kronig relation allows us to calculate $R(\omega)$ from $\rho(\omega)$. Note that $\rho(\omega)$ is an odd function of $\omega$, this is a general property of retarded correlation functions (see the discussion at the end of Sect 3.2) and has to be kept in mind when performing the Kramers-Kronig transformation.

In Eq. (3.39), it is implicitly assumed that the vertices $T_e$, $T_p$, and $V$ are all independent of energy and quasimomentum (these assumptions are justified by the small range of energies covered by the Raman spectra) and are taken to be real. We will also assume that the vertices $T_e$ and $T_p$ do not change much[21] when crossing the superconducting phase transition

---

[21] The change of the electronic Raman susceptibility across $T_c$ mainly is due to the change of the Green's function of the electron. The vertex $T_e$ is given by (2.16) and (2.13) and, therefore, is dependent on the electronic Green's function (see also Fig. 2.3). The intermediate state (denoted by $m$ in Fig. 2.3)), however, is an interband electron-hole excitation. The susceptibility for electron-hole interband excitations does not change essentially across $T_c$ and, hence, the Raman vertex $T_e$ is constant across $T_c$ in good approximation.

at $T = T_c$. These vertices include electronic transitions to intermediate states (with $\boldsymbol{k}$-conservation) which may have energies close to those of laser photons $\omega_L$. The band structure changes at $T_c$ only in a region of width approximately twice the maximum gap $2\Delta_0$ around the Fermi energy. Therefore, and because of the fact that $2\Delta_0$ is considerably less than the typical lifetime broadening of interband transitions, the resonance conditions should not change much upon crossing $T_c$. Hence, the Raman vertex $T_e$ can be assumed to be the same in the normal as in the superconducting state. This assumption has received ample confirmation in the cases of Y-123 [3.36] and Y-124 [3.37, 3.38]. The vertex $T_p$ involves first absorbing a photon, then emitting a phonon and after that emitting the scattered photon. Also in this case, and for the same reasons, it is unlikely that $T_p$ would change when crossing $T_c$.

We conclude from Eq. (3.39) that the broadening of the phonon due to the coupling to the continuum of excitations is given by [3.21]

$$\Gamma = \pi V^2 \rho(\omega_p) \tag{3.41}$$

Note that anharmonic broadening $\Gamma_{anh}$ can be included by replacing the term $\pi V^2 \rho(\omega)$ in Eq. (3.39) by $\pi V^2 \rho(\omega) + \Gamma_{anh}$ provided the real part of the self energy $\delta\omega_p^{anh}$ given by anharmonic broadening does not vary much around $\omega_p^0$. In this case $\delta\omega_p^{anh}$ can be absorbed as a frequency shift into $\omega_p^0$ (i.e. we replace $\omega_p^0 + \delta\omega_p^{anh}(\omega_p^0)$ by $\omega_p^0$ in Eq. (3.39)).

**Ratio of vertices; electronic continuum.** If we attempt to determine $V$ by fitting experimental data with (3.41), we are faced with a problem. When trying to calculate $V$ from the linewidth, we need to know the electron spectral function $\rho(\omega)$. In the case of vanishing electron-phonon coupling $V$, Eq. (3.39) gives $I(\omega) \sim \pi T_e^2 \rho(\omega)$. Although $T_e$ is unknown it can be taken as a scaling factor when we represent the data in arbitrary units. On the other hand, from the theory of electronic Raman scattering in the superconducting state, we know that for tetragonal superconductors with a gap function of $k_x^2 - k_y^2$ symmetry ($B_{1g}$ in the $D_{4h}$ point group) the function $\rho(\omega)$ is linear in $\omega$ in the low-frequency regime ($\omega \lesssim \Delta_0$) (see [3.37, 3.39]). Under this assumption and using Eq. (3.41), we can calculate the ratio of the electron-phonon coupling constants for the two particular phonons at $390\,\mathrm{cm}^{-1}$ and at $240\,\mathrm{cm}^{-1}$ *in the superconducting state* to be

$$\frac{V_{390}^2}{V_{240}^2} = \frac{\Gamma_{390}}{\Gamma_{240}} \cdot \frac{240\,\mathrm{cm}^{-1}}{390\,\mathrm{cm}^{-1}} \tag{3.42}$$

which yields $V_{390}/V_{240} \approx 1.5$.

**Temperature-dependence of the vertex $V$.** The second possibility to obtain information about $V$ from experimental spectra makes use of the frequency shift $\delta\omega_p = -V^2 R(\omega_p)$. For this purpose we must know the unrenormalized energy which is, in principle, not an observable.

This problem can be overcome through the kindness of nature: in the material at hand the experimental data for the *normal state* suggest that $V$, and thus the phonon self-energy, is rather small. Nearly negligible electronic self-energy contributions to $\Gamma_p$ in the normal state can be inferred from Figs. 3.24(b) and 3.25(b). The increase in $\Gamma$ observed below $T_c$, in spite of the decrease in the electronic continuum at frequencies below $\approx 400\,\mathrm{cm}^{-1}$, also confirms the fact that $V$ in the superconducting state is much larger than in the normal state. We shall make use of this fact to obtain the real and imaginary parts of the self energy in the superconducting state by referring the corresponding frequencies and widths to those in the normal state (which are assumed to vanish).

We note, however, that values of the Fano parameter $q$ of the order of one are found for the two phonons in the normal state. Correspondingly, sigmoid-type spectra can be seen for these phonons in Fig. 3.23 in spite of their meager strength. The expression for $q$ is (see Eqs. (3.36) and (3.39))

$$q = \frac{VT_p/T_e + V^2 R(\omega)}{\pi V^2 \rho(\omega)} \ . \tag{3.43}$$

The weak phonon spectra observed in the normal state allow us to set $T_p \approx 0$. The values of $q \approx 1$ found experimentally thus imply that $R \approx \rho$.

The reason why $V$ in the normal state differs from that in the superconducting state can be attributed to the fact that $V$ has to be interpreted as a kind of averaged $\boldsymbol{k}$-dependent matrix element $g_{\boldsymbol{k}}$. For anisotropic vertices $\gamma_{\boldsymbol{k}}$ and $g_{\boldsymbol{k}}$, the polarization loops[22] $\langle \gamma_{\boldsymbol{k}}^2 \chi_{\boldsymbol{k}}(\omega) \rangle$ and $\langle g_{\boldsymbol{k}}^2 \chi_{\boldsymbol{k}}(\omega) \rangle$ usually do not have a property which they share in the isotropic case: they are not anymore functions mutually proportional in $\omega$. Therefore, if we try to define *effective* isotropic vertices by

$$\langle \gamma_{\boldsymbol{k}}^2 \chi_{\boldsymbol{k}}(\omega) \rangle = T_e^2 \rho(\omega)$$
$$\langle g_{\boldsymbol{k}}^2 \chi_{\boldsymbol{k}}(\omega) \rangle = V^2 \rho'(\omega)$$

we have to keep in mind that there appear two different spectral functions $\rho(\omega)$ and $\rho'(\omega)$. In the isotropic case, the spectral density $\rho(\omega)$ is deduced from the overall electronic Raman spectrum which is proportional to $\langle \gamma_{\boldsymbol{k}}^2 \chi_{\boldsymbol{k}}(\omega) \rangle$ and the fact that $\rho(\omega)$ is equal to $\rho'(\omega)$ yields the function $\langle g_{\boldsymbol{k}}^2 \chi_{\boldsymbol{k}}(\omega) \rangle$ up to a multiplicative constant. This is no longer true for anisotropic vertices. This deficiency, however, can be repaired by the following reasoning.

We express the electron-phonon vertex by a multiple of the Raman vertex $\gamma_{\boldsymbol{k}}$, plus a variation $\delta g_{\boldsymbol{k}}$ writing

$$g_{\boldsymbol{k}} = \alpha \gamma_{\boldsymbol{k}} + \delta g_{\boldsymbol{k}} \ ,$$

where a condition has yet to be given so as to specify the normalization of $\delta g_{\boldsymbol{k}}$. Then the phonon self-energy is given by

$$\begin{aligned} \langle g_{\boldsymbol{k}}^2 \chi_{\boldsymbol{k}}(\omega) \rangle = {} & \alpha^2 \langle \gamma_{\boldsymbol{k}}^2 \chi_{\boldsymbol{k}}(\omega) \rangle + \\ & + 2\alpha \langle (\delta g_{\boldsymbol{k}}) \gamma_{\boldsymbol{k}} \chi_{\boldsymbol{k}}(\omega) \rangle \\ & + \langle (\delta g_{\boldsymbol{k}})^2 \chi_{\boldsymbol{k}}(\omega) \rangle \end{aligned}$$

where the mentioned condition will be fixed now by requiring the term proportional to $\delta g_{\boldsymbol{k}}$ to vanish. It is clear that this proceeding implies a temperature-dependent coefficient $\alpha$, because the susceptibility $\chi_{\boldsymbol{k}}(\omega)$ itself is temperature-dependent. The function $\rho(\omega)$ now will be *defined* by

$$\langle \gamma_{\boldsymbol{k}}^2 \chi_{\boldsymbol{k}}(\omega) \rangle \equiv T_e^2 \rho(\omega)$$

specifying also the effective Raman vertex $T_e$. The phonon self-energy assumes the form

$$\langle g_{\boldsymbol{k}}^2 \chi_{\boldsymbol{k}}(\omega) \rangle = \alpha^2 T_e^2 \rho(\omega) + \langle (\delta g_{\boldsymbol{k}})^2 \chi_{\boldsymbol{k}}(\omega) \rangle$$

---

[22] Strictly, the function $\chi_{\boldsymbol{k}}(\omega)$ is not a susceptibility because a $\boldsymbol{k}$-integration over the Brillouin zone still has to be performed. Nevertheless we call this object a susceptibility.

and at the position of the phonon $\omega_{p,0}$, this becomes the definition of the effective electron-phonon vertex $V$, namely

$$\langle g_{\boldsymbol{k}}^2 \chi_{\boldsymbol{k}}(\omega_{p,0})\rangle = \left(\alpha^2 T_e^2 + \beta^2\right) \rho(\omega_{p,0}) \equiv V^2 \rho(\omega_{p,0}) \ ,$$

where $\beta^2 = \langle(\delta g_{\boldsymbol{k}})^2 \chi_{\boldsymbol{k}}(\omega)\rangle / \rho(\omega_{p,0})$. It has already been shown that the coefficient $\alpha$ depends on temperature. This is also true for the coefficient $\beta$, because if $\chi_{\boldsymbol{k}}(\omega_{p,0})$ changes its $\boldsymbol{k}$-dependence, different $\boldsymbol{k}$-space regions of $\delta g_{\boldsymbol{k}}$ will be weighted differently in the average than before and the average in the definition of $\beta$ changes.

It is safe to assume that $V$ is constant (as a function of temperature) in the normal phase as well as in the superconducting phase and does change only at the phase transition. This justifies the assumption of having two different matrix elements $V$, one for the normal state, and one for the superconducting state.

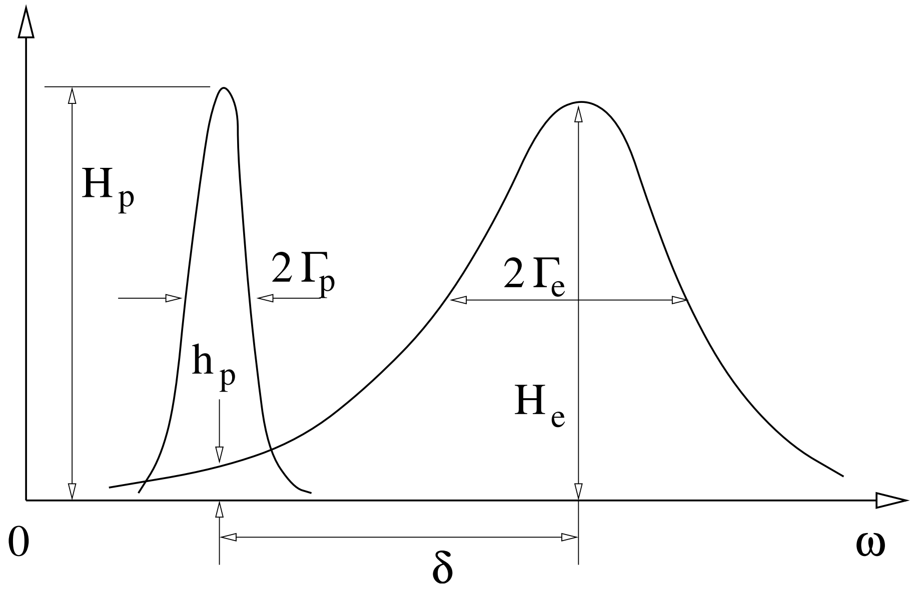

Figure 3.26: Definition of quantities used in the text for the electronic and phonon spectra of Hg-1234.

**A theoretical model.** We consider next the large frequency shifts $\delta\omega_p$ and the increase in the phonon intensity observed when lowering $T$ below $T_c$. In view of the many uncertainties involved in detailed microscopic theories we propose a simple treatment which is physically transparent and yields results in reasonable agreement with the observations. The calculations are based on the schematic representation of the electronic scattering spectra shown in Fig. 3.26. Instead of performing the Kramers-Kronig integrations required for the calculation of $\delta\omega_p$ directly from the electronic spectrum, we replace the electronic spectrum of Fig. 3.26 by a Lorentzian function at its maximum $\omega = \omega_a$ and having a width of $\Gamma_e$.

The Lorentzian function and its Kramers-Kronig transform are the real and imaginary part, respectively, of a retarded susceptibility of the form $\Pi(\omega) = N_e(\omega - \omega_e + i\Gamma_e)^{-1}$ , namely

$$R(\omega) = N_e \operatorname{Re}[(\omega - \omega_e) + i\Gamma_e]^{-1} \quad \text{and}$$
$$\pi\rho(\omega) = N_e \operatorname{Im}[(\omega - \omega_e) + i\Gamma_e]^{-1} \ .$$

Here, the quantity $N_e$ corresponds to the number of excitations involved in the electronic continuum.

Recalling the equations $\delta\omega_p = -V^2 R(\omega_p)$ and $\Gamma_p^{el} = \pi V^2 \rho(\omega_p)$ it is obvious that each of these relations separately is not of much use to us, because the matrix element $V$ as well as the excitation number $N_e$ are unknown. Both equations together, however, yield

$$\frac{\delta\omega_p}{\Gamma_p^{el}} = -\frac{R(\omega_p)}{\pi\rho(\omega_p)} \ ,$$

where $\Gamma_p^{el} = \Gamma_p^{tot} - \Gamma_p^{anh}$ is the electronic contribution to the phonon linewidth. If we make use of the model susceptibility defined above, the relation

$$\delta\omega_p = -\Gamma_p^{el} \frac{\delta}{\Gamma_e} \tag{3.44}$$

using $\delta = \omega_e - \omega_p$ results. The quantities on the right side of (3.44) can be taken from experiment, that is (3.44) allows for the calculation of the phonon lineshift.

For the phonons at 240 and 390 cm$^{-1}$ we use this relation to calculate "theoretical" lineshifts $\delta\omega_p^{theo}$ and compare these to the experimentally determined lineshifts $\delta\omega_p^{exp}$. The results are given in Tab. 3.2. In the case of the 487 and 575 cm$^{-1}$ phonons, the lineshift cannot be meaningfully determined from the experiment.

A similar expression can be derived for the height of the phonon peak $H_p$. We start with Eq. (3.37) and use $q\Gamma_p = \delta\omega_p$ as well as $q = R(\omega_p)/(\pi\rho(\omega_p))$. This yields

$$I_p = \frac{I_c}{\pi T_e^2 \rho(\omega_p)} \cdot \pi T_e^2 R(\omega_p) \cdot \delta\omega_p \ . \tag{3.45}$$

The quotient on the right side of this relation is one, and the factor $\pi T_e^2 R(\omega_p)$ is the Kramers-Kronig transform of the electronic Raman intensity at $\omega = \omega_p$. In suitable units we write $I_p = \pi H_p \Gamma_p$ and $\pi T_e^2 R(\omega_p) = \pi H_e \Gamma_e / \delta$ and obtain for the ratio of the phonon height to the height of the electronic peak the relation

$$\frac{H_p}{H_e} = \frac{\Gamma_e}{\Gamma_p} \cdot \frac{\delta\omega}{\delta} \ . \tag{3.46}$$

We use this relation to calculate "theoretical" phonon heights $H_p^{theo}$ of the 240 and 390 cm$^{-1}$ phonons and compare them to the experimentally determined phonon heights $H_p^{exp}$ in Tab. 3.2. For the 487 and 575 cm$^{-1}$ phonons we use Eq. (3.46) to calculate the lineshift which is experimentally not accessible.

The agreement of the "theoretical" values for the phonon lineshifts $\delta\omega_p^{theo}$ and phonon heights $H_p^{theo}$ and its experimentally determined counterparts $\delta\omega_p^{exp}$ and $H_p^{exp}$, is quite satisfactory, especially when one considers the simplicity of the theory.

For the purpose of extracting the coupling constant $V$ from the experimental spectra, the Raman vertex $T_e$ has to be known. Although it could be determined from experiment [3.37],

| $\frac{\omega_p}{\mathrm{cm}^{-1}}$ | $\frac{\Gamma_p}{\mathrm{cm}^{-1}}$ | $\frac{\Gamma^0_{anh}}{\mathrm{cm}^{-1}}$ | $\frac{\delta}{\mathrm{cm}^{-1}}$ | $\frac{h_p}{\mathrm{a.u.}}$ | $\frac{\delta\omega_p^{theo}}{\mathrm{cm}^{-1}}$ |
|---|---|---|---|---|---|
| 240 | 9 | 3 | 380 | 20 | 16 |
| 390 | 22 | 7.3 | 230 | 35 | 37 |
| 487 | 23 | - | 133 | - | 6.1 |
| 574 | 30 | - | 45 | - | 2.2 |

| $\frac{\omega_p}{\mathrm{cm}^{-1}}$ | $\frac{\delta\omega_p^{exp}}{\mathrm{cm}^{-1}}$ | $\frac{H_p^{theo}}{a.u.\cdot\mathrm{cm}^{-1}}$ | $\frac{H_p^{exp}}{a.u.\cdot\mathrm{cm}^{-1}}$ | $\frac{N_eV^2}{\mathrm{cm}^{-2}}$ | $\lambda_\nu$ |
|---|---|---|---|---|---|
| 240 | 15 | 87 | 120 | 5700 | 0.08 |
| 390 | 40 | 158 | 110 | 9200 | 0.08 |
| 487 | - | - | 40 | 810 | $5 \times 10^{-3}$ |
| 574 | - | - | 32 | 99 | $6 \times 10^{-4}$ |

Table 3.2: The *per-phonon* quantities at $T = 0$ used in the text. The *electronic peak* is characterized by its center frequency $\omega_e = 620\,\mathrm{cm}^{-1}$, its linewidth $\Gamma_e = 250\,\mathrm{cm}^{-1}$ and its peak intensity $H_e = 80\,\mathrm{a.u.}$ Here, the symbol "a.u." denotes the arbitrary units for the peak intensities taken from Fig. 3.22. The lineshift $\delta\omega_p^{theo}$ and the phonon height $H_p^{theo}$ are calculated using Eqs. (3.44) and (3.46), respectively, for the 240 and $390\,\mathrm{cm}^{-1}$ phonons. The lineshift $\delta\omega_p^{theo}$ of the 487 and $574\,\mathrm{cm}^{-1}$ phonons is as predicted by Eq. (3.46). The coupling strength $N_eV^2$ and electron-phonon coupling parameter $\lambda_\nu$ have been determined using Eq. (3.47) and Eq. (3.51), respectively, for all four phonons.

we will use here another approach to characterize the electron-phonon coupling strength. We define the number of electronic excitations $N_e$ involved in the electronic peak around $\omega = \omega_e$ by $\rho(\omega) = N_e\delta(\omega - \omega_e)$. Then, $\delta\omega_p = V^2R(\omega_p)$ becomes

$$N_eV^2 = \delta\omega_p \cdot \delta \tag{3.47}$$

and can be used to determine the values of the combination $N_eV^2$ from the experiment (see Tab. 3.2).

**Estimates of McMillan's $\lambda$.** It is of interest to express the electron-phonon coupling strength by means of McMillan's dimensionless electron-phonon interaction parameter $\lambda$ which in Eliashberg's theory plays the role of the combination "$N(0)V$" in the BCS theory and also represents the mass enhancement of electrons $(1+\lambda)$ induced by their coupling to the phonon system. This parameter, already discussed in Subsect. 3.4.6, is defined by [3.40]

$$\lambda = 2\int_0^\infty d\omega\,\frac{\alpha^2F(\omega)}{\omega} \tag{3.48}$$

where the spectral function $\alpha^2F(\omega)$ determines the transition temperature $T_c$ in Eliashberg's theory. Using the electronic density of states at the Fermi level $N_0 = 2\sum_{\boldsymbol{k}}\delta(\epsilon_{\boldsymbol{k}})$ in the normal state, $\alpha^2F(\omega)$ is given by the expression [3.40]

$$\alpha^2F(\omega) = N_0^{-1}\sum_{\nu,\boldsymbol{k}\sigma,\boldsymbol{k}'\sigma'}|V_{\nu,\boldsymbol{k}\sigma,\boldsymbol{k}'\sigma'}|^2\delta(\omega - \omega_{\nu,\boldsymbol{k}-\boldsymbol{k}'})\delta(\epsilon_{\boldsymbol{k}})\delta(\epsilon_{\boldsymbol{k}'}) \tag{3.49}$$

where $V_{\nu,\boldsymbol{k}\sigma,\boldsymbol{k}'\sigma'}$ is the electron-phonon matrix element for phonon branch $\nu$, $\omega_{\nu,\boldsymbol{k}}$ is the frequency of the phonon of branch $\nu$ with momentum $\boldsymbol{k}$, and the sum over $\nu$ includes all optical phonons. Because of the fact that Raman scattering only gives information about phonons at the center of the BZ (Γ-point), we approximate the optical phonons by dispersionless phonons with the frequency of the corresponding Γ-point phonon, that is $\omega_{\nu,\boldsymbol{q}} = \omega_{\nu,\boldsymbol{q}=0} \equiv \omega_{p,\nu}$ and also take $V_{\nu,\boldsymbol{k}\sigma,\boldsymbol{k}'\sigma'} = V_\nu \delta_{\sigma\sigma'}$. Replacing (3.49) into (3.48) yields

$$\lambda = N_0 \sum_\nu \frac{V_\nu^2}{\omega_{p,\nu}} \; . \tag{3.50}$$

The $\lambda$ represented by Eq. (3.50) is to be regarded as the contribution to $\lambda$ which one would have if all phonons of a given branch would couple as much as that at the Γ-point. We have determined above for several phonons values of $V^2 N_e$ where $N_e$ is the total number of interacting excitations induced by the superconductivity. To a reasonable approximation we can write $N_e \approx \Delta_0 N_0$ and, therefore,

$$\lambda = \sum_\nu \lambda_\nu \; , \qquad \lambda_\nu = \frac{1}{\Delta_0} \cdot \frac{N_e V_\nu^2}{\omega_{p,\nu}} . \tag{3.51}$$

Using $\Delta_0 = 310\,\mathrm{cm}^{-1}$, the values of $\lambda_\nu$ are given by 0.08, 0.08, $5 \times 10^{-3}$, and $6 \times 10^{-4}$ for the phonons at $240\,\mathrm{cm}^{-1}$, $390\,\mathrm{cm}^{-1}$, $487\,\mathrm{cm}^{-1}$, and $575\,\mathrm{cm}^{-1}$ respectively. In order to get a feeling for the magnitude of these electron-phonon coupling constants we note that if all phonons had the same value of $\lambda_\nu$ as that determined for the $390\,\mathrm{cm}^{-1}$ phonon ($\approx 0.1$ per branch), the total $\lambda$ would be $0.1 \cdot 60 = 6$, a large value indeed which would lead to a very high $T_c$ if taken literally in the BCS theory.

### 3.5.4 Refinements

The analysis of the experimental data presented above was guided by the quest for simplicity and clearness. Following this spirit some effects which should be taken into account in the theory have been neglected. The purpose of this subsection is to dicuss some of the effects that could be included in a simple manner in the theory presented above.

**Symmetry of the polarizability.** The first caveat when going through the theory above concerns the symmetry of the polarizability. A polarizability $\Pi(\omega)$ describes a bosonic excitation, therefore has the property $\Pi(\omega) = \Pi^*(-\omega)$. Consequently the symmetry relations

$$\begin{aligned} \rho(\omega) &= -\rho(-\omega) \\ R(\omega) &= R(-\omega) \end{aligned}$$

for the imaginary and the real part of the polarizability, respectively, have to be fulfilled. In Fig. 3.27, we have plotted the polarizability of a system possessing of a single Lorentzian excitation with an energy of $\omega_e = 620\,\mathrm{cm}^{-1}$ and a width of $\Gamma_e = 250\,\mathrm{cm}^{-1}$ as was used as a model for the electron-hole excitations in the theory presented in the preceding sections. The different curves in the figure under consideration are the spectral density $\rho_0(\omega)$ and the corresponding real part $R_0(\omega)$ of the polarizability $\Pi_0(\omega) = (\omega - \omega_e + i\Gamma_e)^{-1}$. Denoted by $\Pi_1(\omega)$ is the result of symmetrizing $\Pi_0(\omega)$, that is $\Pi_1(\omega) = \Pi_0(\omega) + \Pi_0^*(-\omega)$; the quantities $\rho_1(\omega)$ and $R_1(\omega)$ refer to the imaginary and real part of $\Pi_1(\omega)$, respectively. Finally, $R_\delta(\omega)$ is the real part of $(\omega - \omega_e)^{-1}$, the polarizability of a discrete $\delta$-function-like excitation at $\omega = \omega_e$.

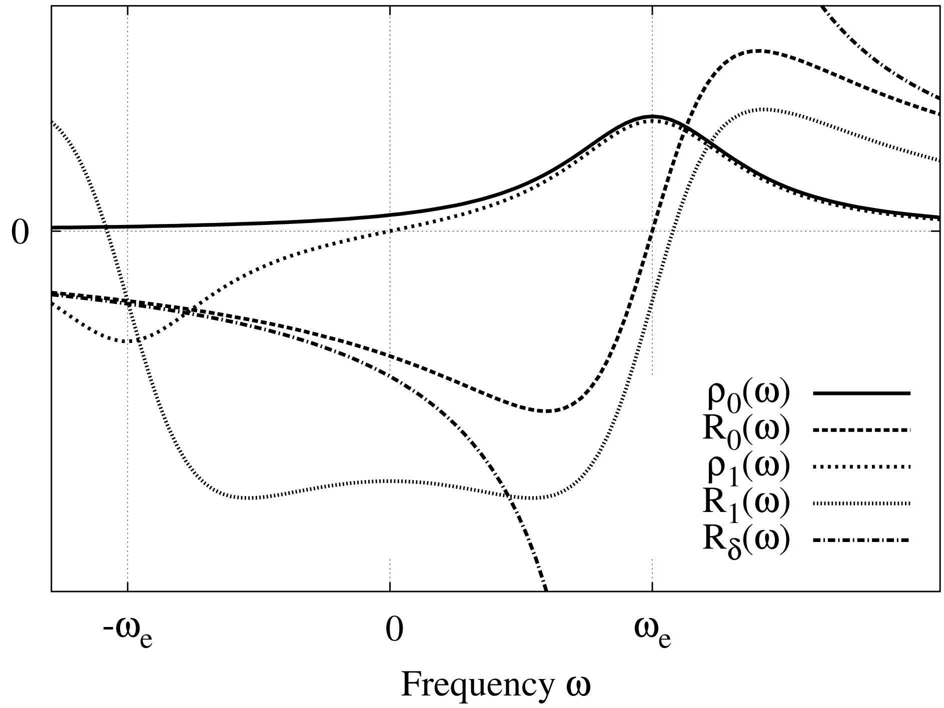

Figure 3.27: The real- and imaginary part $R_0(\omega)$ and $\pi\rho_0(\omega)$, respectively, of a discrete excitation at $\omega_e = 620\,\mathrm{cm}^{-1}$ having a width (HWHM) of $250\,\mathrm{cm}^{-1}$. The corresponding curves $R_1(\omega)$ and $\pi\rho_1(\omega)$ additionally have the correct parity. The curve $R_\delta(\omega)$ is the Kramers-Kronig transform of a $\delta$-function at $\omega_e$.

The spectral functions $\rho_0(\omega)$ and $\rho_1(\omega)$ are almost indistinguishable for $\omega > 0$. If we take either one of them and perform a Kramers-Kronig transformation (not taking the symmetry of the polarizability into account), the real part $R_0(\omega)$ will result. If we perform it the correct way, the real part $R_1(\omega)$ results. In contrast to the imaginary parts of the polarizability, the real parts are quite different, especially in the region up to $\approx \omega_e/2$. If a phonon is located there the lineshift predicted by the theory, being due to the coupling to the electronic continuum, may be off by up to a factor of two!

**Effective phonon-phonon interaction.** Another effect which should be considered in the present case of a rather strong coupling of the phonons to the electronic continuum is the effective phonon-phonon coupling mechanism described in Subsect. 3.4.4. In Fig. 3.28, we show the actual spectrum measured in the experiment (noisy solid line), and the efficiency predicted by the elementary Fano theory using the parameters determined by our theory. The long-dashed curve corresponds to the Fano efficiency when coupling the phonon at $\omega_p = 260\,\mathrm{cm}^{-1}$ to the electronic continuum, and the short-dashed curve is the result when coupling the phonon at $\omega_p = 390\,\mathrm{cm}^{-1}$ to the continuum. The structure around the two phonons is magnified in Fig. 3.29, where, in addition to the curves already mentioned, the result of the two-phonon theory with *the same coupling-parameters* as used in the other two curves is plotted. The figure shows clearly, that in the parameter regime under consideration, the phonon-phonon coupling mechanism mentioned maybe important; it may change the coupling constants resulting from our theory by up to a factor of two.

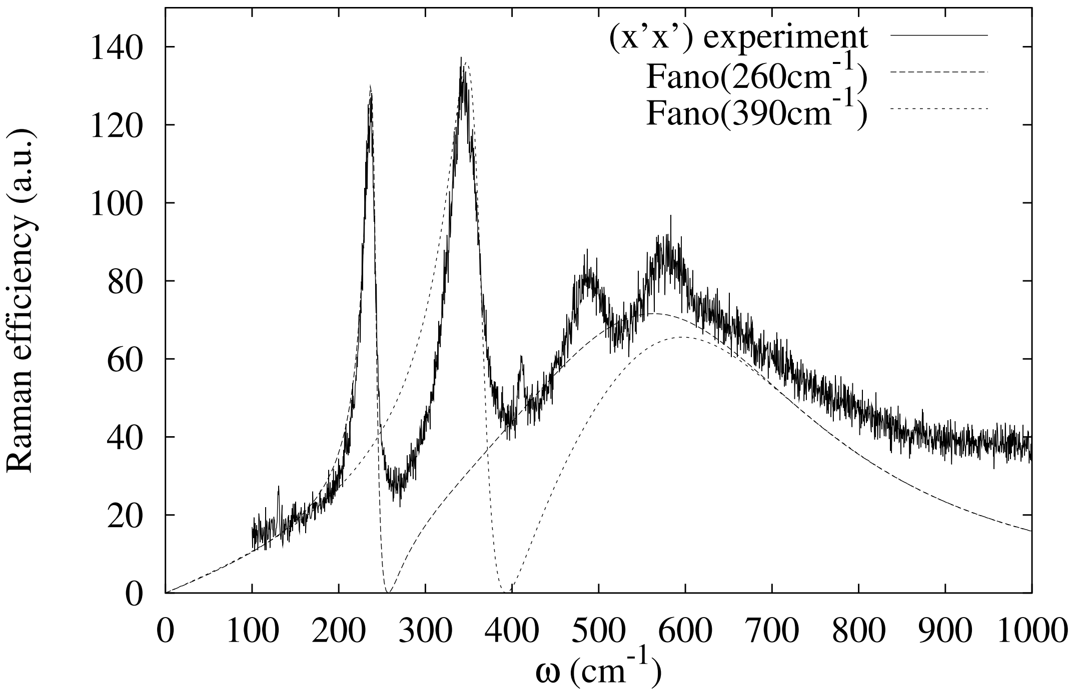

Figure 3.28: The Hg-1234 spectrum at $T = 5\,K$ (solid line), the Fano-fit involving the phonon at $\omega_p = 260\,\mathrm{cm}^{-1}$ (long-dashed line), and the Fano-fit involving the phonon at $\omega_p = 390\,\mathrm{cm}^{-1}$ (medium-dashed line).

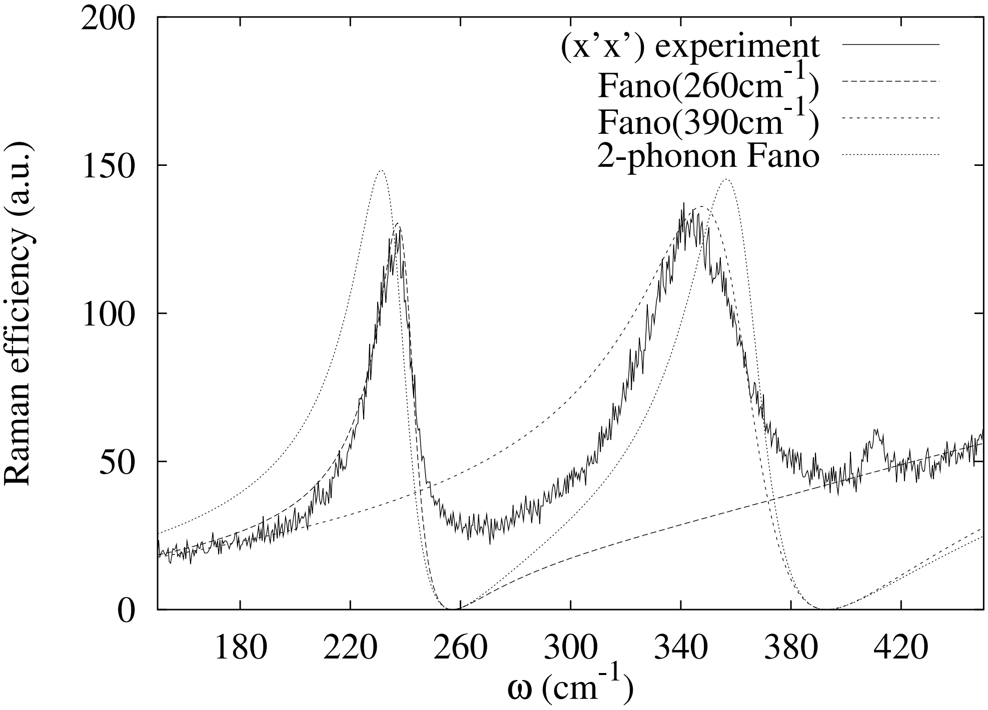

Figure 3.29: The solid, long-dashed, and medium-dashed lines are as in Fig. 3.28, with the exception that the frequency-range is different from the one there. The short-dashed line is the result from the 2-phonon Fano theory with the same parameters as in the simple Fano theory fits.

### 3.5.5 Conclusions

We have observed strong superconductivity-induced phonon self-energy effects for the $A_{1g}$ phonons in Hg-1234 which show a strength exceeding that found in any other cuprate superconductors so far. The dramatic softening of the 240 and 390 $\mathrm{cm}^{-1}$ phonons below $T_c$ is similar to that required to interpret the change in vibrational amplitude which has been observed in nearly optimally doped $\mathrm{YBa_2Cu_3O_{7-\delta}}$ at $T_c$ in ion channeling experiments [3.41] (see also the results from resonant neutron absorption spectroscopy in $\mathrm{Bi_2Sr_2CaCa_2O_8}$ by Mook and coworkers [3.42]). The phonon self-energy effects, in combination with a clear development of the superconductivity-induced electronic Raman peaks, offers a unique opportunity for a detailed theoretical modeling of electron-phonon coupling processes in superconducting cuprates. In spite of the large values of $\lambda$ associated with the large electron-phonon coupling effects discussed here, the question of a possible connection between the observed strong electron-phonon coupling and the remarkably high $T_c$ of the Hg-based superconducting cuprates must remain open.

# Chapter 4

# Summary and outlook

## 4.1 Electronic Raman scattering in high-temperature superconducting cuprates

In Chap. 2, devoted to electronic Raman scattering in high-temperature superconducting cuprates (see also [4.1]), we presented a numerical calculation of the electronic Raman efficiency for the high-temperature superconductors $YBa_2Cu_3O_7$ (Y-123) and $YBa_2Cu_4O_8$ (Y-124). The calculations are based on a BCS-like description of the superconducting state with a $\boldsymbol{k}$-dependent (but band-independent) gap function on the one hand, and on the result for the electronic band structure as predicted by the linear muffin-tin orbital (LMTO) method in combination with the atomic-spheres approximation (ASA), on the other. The electronic Raman efficiency has been calculated in *absolute units* (by making use of the Eqs. (2.31) and (2.52)), taking both, the real and imaginary parts of the Tsuneto-function into consideration. The effect of electronic screening on the Raman efficiency has been taken into account as well. The Raman vertex was derived from the electronic band structure using the effective mass approximation (hence, neglecting possible resonance effects), and for the gap function, the $d_{x^2-y^2}$-symmetric expression $\Delta_{\boldsymbol{k}} = \Delta_0 \cos\varphi_{\boldsymbol{k}}$, where $\Delta_0$ is the only free adjustable parameter in the calculation, has been adopted.

To the best of our knowledge, the calculations described are the first ones based on LMTO results, describing the superconducting state, and taking correctly (according to Eq. (2.52)) electronic screening into account. It seems that the work at hand also presents the first calculation of electronic Raman scattering in high-temperature superconducting cuprates providing results in absolute units. The conclusions from this calculation, and its comparison to experimental results, are presented in detail in Sect. 2.7.

The general observations are that the line shapes of the spectra are reproduced quite well by the calculations. Also the peak intensities, measured in absolute units, correspond to the experimentally determined ones within a factor of about two. The relative peak positions, as predicted by the calculations, coincide almost for the cases of $A_{1g}$ and $B_{1g}$ polarization (symmetry properties are given in tetragonal notation). This finding, however, is not reflected in the results of the experiment. In (optimally doped) Y-123 [4.2], it was found that the $B_{1g}$ spectrum peaks at approximately twice the Raman shift of the peak in the $A_{1g}$ spectrum. The experimental $B_{1g}$ peak is also much broader than the $A_{1g}$ peak.

A possible explanation of this fact already has been suggested by Devereaux *et al.* [4.3]. They observed that the electronic screening may affect the position of the $A_{1g}$ peak, while for the $B_{1g}$ Raman efficiency (in tetragonal systems) the screening vanishes by symmetry. Their conclusion was that the position of the $B_{1g}$ peak reflects the value of $2\Delta_0$, and that the $A_{1g}$ peak is shifted to lower values of the Raman shift by the influence of electronic screening.

Our calculations, however, have shown that this conjecture is incorrect. Neither in the calculated electronic Raman efficiency for Y-123, nor for Y-124, there is a significant shift of the $A_{1g}$ peak due to the presence of electronic screening. Moreover, we have proven (in Subsect. 2.3.10) that a significant shift of the $A_{1g}$ peak can only be achieved if the band structure shows rather peculiar properties. For this case, however, we have pointed out that even the $B_{1g}$ peak can shift its position [4.4], this time not by the influence of electronic screening, but by the properties of the band structure itself. All these observations led us to conjecture [4.1] that the $A_{1g}$ peak reflects the gap amplitude and that the $B_{1g}$ peak is shifted and broadened by additional excitations which are not contained in the model on which our calculation is based. In [4.1], we tentatively attributed these additional excitations to possess magnetic origin.

A further attempt to shed light onto the problem of the $A_{1g}$ and $B_{1g}$ relative peak positions was made by Manske *et al.* [4.5]. They have shown that the inclusion of a particular (exciton-like) kind of vertex renormalizations into the theory of electronic Raman scattering in superconductors leads to a nonvanishing electronic screening of the $B_{1g}$ component even in systems with tetragonal symmetry (this fact actually was discovered already earlier by Devereaux *et al.* [4.3]). Their theory and the model calculation they presented, however, was seriously flawed by algebraic errors, a fact that we have pointed out in [4.6].

Another conclusion concerns the form of the gap function. While electronic Raman scattering (in a system without impurities) is not sensitive to the phase of the gap function (and therefore cannot distinguish between a $d$-like and a $|d|$-like anisotropic $s$-wave gap function), due to its dependence on the polarization of the incoming and scattered light, it is able to provide more information on the gap function than most other experimental methods.

In tetragonal systems, a $d_{x^2-y^2}$-like gap function implies a linear dependence of the electronic Raman efficiency (at $T = 0$, or divided by the Bose factor) on the Raman shift in the low-frequency regime for the case of the $A_{1g}$ and $B_{2g}$ polarizations. Besides, it gives rise to a cubic dependence of the $B_{1g}$ component of the Raman efficiency on the Raman shift (the reason for this is that the gap function possesses $B_{1g}$ symmetry and, therefore, the gap function and the $B_{1g}$ component of the Raman vertex vanish along the $x \pm y$ diagonals of the Brillouin zone). These facts have already been shown by Devereaux *et al.* [4.7, 4.3].

Most of the high-temperature superconducting cuprates, however, do not possess tetragonal symmetry, but are slightly orthorhombically distorted. Two types of such distortion exist, they are present in Y-123 and $Bi_2Sr_2CaCu_2O_8$ (Bi-2212) and are depicted in Fig. 2.25. The distortion renders the $A_{1g}$ and $B_{1g}$ ($A_{1g}$ and $B_{2g}$) tetragonal representations of the point symmetry group of the Y-123 (Bi-2212) crystal degenerate. An implication of this is that the $B_{1g}$ Raman efficiency (divided by the Bose factor) of Y-123 acquires an additional linear, while the corresponding $B_{1g}$ spectrum of Bi-2212 does not. This was shown theoretically and also found when analyzing experimental data (Sect. 2.9). The additional linear component is related to the shift of the nodes of the gap function with respect to the position of the nodes of the $B_{1g}$ component of the Raman vertex (inverse effective mass). These features have been demonstrated in Sect. 2.9 and in [4.8], and a method for the determination of the mutual shift of the node positions for nontetragonal high-temperature superconducting cuprates, based on the inverse effective masses obtained from the LMTO band structure and the experimentally determined Raman efficiencies at low values of the Raman shift, has been developed. The method has been applied to the case of Y-123, for which a result has been given.

One problem posed by the interpretation of the linear component in the low-energy component of the $B_{1g}$ spectrum of Y-123-like orthorhombically distorted high-temperature superconductors, however, remains. It concerns the effect of impurities, which may also contribute a linear component to the $B_{1g}$ spectra. While the effect of the orthorhombic distortion on the linear component of the low-energy spectra is basically understood, we know very little about the effect of the impurities. Together with the fact that the low-energy part of the Raman spectra of high-temperature superconductors is quite delicate from an experimental point of view (among the complications involved we mention the proximity of the laser line to the frequency regime under interest and the presence of strongly coupled phonons, especially in Y-123), this renders the interpretation of the low-energy part of the Raman spectra rather difficult.

## 4.2 Raman scattering by phonons in high-temperature superconducting cuprates

In the field of Raman scattering by optical phonons, we investigated mainly the superconductivity-induced changes of the phonon self-energy and their implications, namely the variation of the widths and the frequencies of phonons. These changes arise from the corresponding modifications of the electronic susceptibility (which in essence plays the role of the phonon self-energy) when crossing the superconducting phase transition. They are therefore particularly important for phonons (we consider only Γ-point phonons because only these lead to inelastic light scattering) with frequencies in regimes where the transition from the normal to the superconducting state implies drastic changes of the real or the imaginary part of the electronic susceptibility. This is the case for frequencies up to approximately $2\Delta_0$.

We discovered [4.9] extremely strong superconductivity-induced phonon self-energy effects for two $A_{1g}$ phonons in $HgBa_2Ca_3Cu_4O_{10+\delta}$ (Hg-1234), which called for an explanation by means of a theoretical model. Such theoretical model should be based on the calculated electronic susceptibility for the normal and the superconducting states. This procedure, however, is problematic, because there is little known about the normal state effects of high-temperature superconducting cuprates. To circumvent this problem, we just assume that the influence of the normal state on the phonons under consideration is small (see Subsect. 3.5.3). The analysis of the experimentally determined spectra in the framework of this model then leads to an estimate of the strength of the electron-phonon coupling. Making use of the spectral function $\alpha^2F(\omega)$ from Eliashberg's theory, we determined the value of McMillan's electron-phonon interaction parameter $\lambda$. This parameter characterizes the electron-phonon coupling strength in Eliashberg's theory and determines the transition temperature $T_c$. Our theory in connection with parameters taken from the experimental spectra leads to an estimate of $\lambda = 0.08$ for the two phonons under consideration.

## 4.3 Outlook

- In view of the suggested contribution of *magnetic excitations* to the position and the width of the pair-breaking peak in the $B_{1g}$ electronic Raman spectra of the high-temperature superconducting cuprate Y-123, an attempt should be made to incorporate these excitations together with the coupling to the electronic excitations into the theory of electronic Raman scattering.
- In this context, there is little known about the *influence of the laser wavelength* on the Raman spectra. The application of the effective mass approximation neglects a possible dependence of the Raman spectra on the laser frequency. From the point of view of theory, this is hard to justify. Additional theoretical and experimental work should be carried out to ascertain possible resonance effects.
- Another very important topic which was basically left out of consideration in this work is the *dependence of the Raman spectra on doping.* It is already known for some years that the positions of the $A_{1g}$ and $B_{1g}$ pair breaking peaks in the Raman spectra depend strongly on the doping of the superconductor. For overdoped superconductors, the gap amplitude is small and so is the Raman shift of the pair-breaking peaks. The $A_{1g}$ and $B_{1g}$ peak-positions shift to larger frequencies as optimum doping is approached and the transition temperature $T_c$ approaches its maximum. When the doping is decreased below the optimum value, the $B_{1g}$ peak continues to increase its frequency, but, at the same time, it becomes very weak in intensity. For the $A_{1g}$ peak the situation is different. It seems to resemble the behavior of the gap amplitude (which, according to BCS-theory, is expected to be proportional to $T_c$), but also becomes smaller in terms of intensity. A description of this phenomenon seems to be out of the scope of the theory which we use for the deduction of the Raman efficiency.
- Another interesting path to take is the *quantitative determination of the electron-phonon coupling* in high-temperature superconducting cuprates by describing it with a deformation potential in the framework of a band-structure calculation based on the LMTO-method. Such calculations have already been performed in the group of O. K. Andersen [4.10], and the results should be linked to the experimentally determined (e.g., by a fit of a measured phonon spectrum to the Fano lineshape) parameters.
- When modelling the Raman efficiency for Raman scattering by phonons which are coupled to electron-hole excitations and which cause inelastic light scattering, the *Fano-Breit-Wigner equation* (3.10) is usually applied. This formula, however, is based on the strict $\boldsymbol{k}$-independence of the relevant vertices. This is an assumption which could be violated in the strongly anisotropic high-temperature superconducting cuprates. For this reason it should be investigated whether and under which circumstances the influence of the $\boldsymbol{k}$-dependence of vertices on the lineshape is important.

# Appendix A

# The theory of electron-phonon coupling

## A.1 Introduction

### A.1.1 Hamiltonian

In this appendix, we develop a formalism for the description of electron-phonon coupling. The Hamiltonian of a system consisting of electrons and ions (i.e., cores and core electrons) can be written in the form

$$H = H_{\mathrm{el}} + H_{\mathrm{el-ion}} + H_{\mathrm{ion}} \ .$$

We focus on the last part, the *ionic Hamiltonian* $H_{\mathrm{ion}}$, first. This is composed of the kinetic energy of the ions plus an ion-ion interaction part. Under the assumption, that the interaction can be written as a sum over pair interactions,[1] the ion Hamiltonian is given by

$$H_{\mathrm{ion}} = T + W = \sum_{(\boldsymbol{n},\alpha)} \frac{1}{2M_\alpha} \boldsymbol{P}_{\boldsymbol{n}\alpha}^2 + \frac{1}{2} \sum_{(\boldsymbol{n},\alpha)\neq(\boldsymbol{n}',\alpha')} W(\boldsymbol{R}_{\boldsymbol{n}\alpha}, \boldsymbol{R}_{\boldsymbol{n}'\alpha'}) \tag{A.1}$$

where $\boldsymbol{P}_{\boldsymbol{n}\alpha}$ and $\boldsymbol{R}_{\boldsymbol{n}\alpha}$ are the momentum and location of the ion $\alpha$ in the unit cell denoted by $\boldsymbol{n}$, respectively. The location $\boldsymbol{R}_{\boldsymbol{n}\alpha}$ is given by the location of the corresponding unit cell $\boldsymbol{R}_{\boldsymbol{n}}$, plus the relative position $\vec{\tau}_\alpha$ of the ion $\alpha$ in the unit cell, plus the displacement $\boldsymbol{Q}_{\boldsymbol{n}\alpha}$ of the ion $\alpha$ in cell $\boldsymbol{n}$ from its equilibrium position. Therefore,

$$\boldsymbol{R}_{\boldsymbol{n}\alpha} = \boldsymbol{R}_{\boldsymbol{n}\alpha}^0 + \boldsymbol{Q}_{\boldsymbol{n}\alpha} = \boldsymbol{R}_{\boldsymbol{n}} + \vec{\tau}_\alpha + \boldsymbol{Q}_{\boldsymbol{n}\alpha} \ , \tag{A.2}$$

where $\boldsymbol{R}_{\boldsymbol{n}\alpha}^0$ denotes the equilibrium position of the ion $\alpha$ in cell $\boldsymbol{n}$.

The *electron-ion interaction* between the electronic system and the ions, represented by $H_{\mathrm{el-ion}}$, will be described by a pair potential[2] $V_\alpha(\boldsymbol{R}_{\boldsymbol{n}\alpha}, \boldsymbol{r}_\nu)$, thus

$$H_{\mathrm{el-ion}} \equiv V = \sum_{\nu,(\boldsymbol{n},\alpha)} V_\alpha(\boldsymbol{R}_{\boldsymbol{n}\alpha}, \boldsymbol{r}_\nu) \ , \tag{A.3}$$

---

[1] i.e., there are no core electron excitations and no overlap of the core electron ground states of two different ions.

[2] We neglect exchange effects between core and conduction electrons.

where $\nu$ numbers the electrons in the system. The potential $V_\alpha$ depends on the ion type $\alpha$ to allow for differently charged ions.

The *electronic Hamiltonian* $H_{el}$ will be considered in App. B. In this context, we will also discuss the Born-Oppenheimer approximation.

### A.1.2 The Hamiltonian $H_{\text{ion}}$ in the harmonic approximation

The interactions $W$ in (A.3) and $V$ in (A.1) will be written as power series in the displacements $\boldsymbol{Q}_{n\alpha}$, and discussed in the lowest nontrivial order in $\boldsymbol{Q}_{n\alpha}$:

$$\begin{aligned} W(\boldsymbol{R}_{n\alpha}, \boldsymbol{R}_{n'\alpha'}) &= W^{(0)}_{n\alpha;n'\alpha'} + \boldsymbol{Q}_{n\alpha}\vec{W}^{(0)}_{1;n\alpha} + \boldsymbol{Q}_{n'\alpha'}\vec{W}^{(0)}_{2;n'\alpha'} \\ &+ \frac{1}{2}\boldsymbol{Q}_{n\alpha}\left(\hat{W}^{(0)}_{11;n\alpha;n'\alpha'} + 2\hat{W}^{(0)}_{12;n\alpha;n'\alpha'} + \hat{W}^{(0)}_{22;n\alpha;n'\alpha'}\right)\boldsymbol{Q}_{n'\alpha'} + O(Q^3)\ , \end{aligned}$$

where

$$\begin{aligned} W^{(0)}_{n\alpha;n'\alpha'} &= W(\boldsymbol{R}^0_{n\alpha}, \boldsymbol{R}^0_{n'\alpha'}) \\ \vec{W}^{(0)}_{i;n\alpha;n'\alpha'} &= \left.\frac{\partial W(\boldsymbol{R}_1, \boldsymbol{R}_2)}{\partial \boldsymbol{R}_i}\right|_{\boldsymbol{R}_1=\boldsymbol{R}^0_{n\alpha};\boldsymbol{R}_2=\boldsymbol{R}^0_{n'\alpha'}} \\ \hat{W}^{(0)}_{ij;n\alpha;n'\alpha'} &= \left.\frac{\partial W(\boldsymbol{R}_1, \boldsymbol{R}_2)}{\partial \boldsymbol{R}_i\partial \boldsymbol{R}_j}\right|_{\boldsymbol{R}_1=\boldsymbol{R}^0_{n\alpha};\boldsymbol{R}_2=\boldsymbol{R}^0_{n'\alpha'}} \end{aligned}$$

The first term in zeroth order in the displacement $\boldsymbol{Q}_{n\alpha}$, when summed over all ions, gives the Madelung energy of the crystal. This is a constant, so we do not consider it any longer. The terms linear in $\boldsymbol{Q}_{n\alpha}$ vanish, because $\vec{W}^{(0)}_{i;n\alpha}$ vanishes in the equilibrium position. The term in second order of $\boldsymbol{Q}_{n\alpha}$ is the first nontrivial one. It is clear that, when summed up over all the ion sites, this term can be written as a quadratic form

$$W = \frac{1}{2}\sum_{n\alpha;n'\alpha'} \boldsymbol{Q}_{n\alpha}\hat{\Phi}_{n\alpha;n'\alpha'}\boldsymbol{Q}_{n'\alpha'}\ . \tag{A.4}$$

The terms $O(Q^3)$ are neglected in the harmonic approximation. The matrix $\hat{\Phi}_{n\alpha;n'\alpha'}$ is called *dynamical matrix.*

### A.1.3 The electron-ion interaction $H_{\text{el}-\text{ion}}$ in linear approximation

We write (A.3) in the form $V = \sum_\nu \tilde{V}(\boldsymbol{r}_\nu)$ and perform the linear approximation in $\boldsymbol{Q}_{n\alpha}$,

$$\tilde{V}(\boldsymbol{r}) = \sum_{n\alpha} V_\alpha(\boldsymbol{R}_{n\alpha}, \boldsymbol{r}) = \sum_{n\alpha} V_\alpha(\boldsymbol{R}^0_{n\alpha}, \boldsymbol{r}) + \sum_{n\alpha}\boldsymbol{Q}_{n\alpha}\left.\frac{\partial V_\alpha(\boldsymbol{R}, \boldsymbol{r})}{\partial \boldsymbol{R}}\right|_{\boldsymbol{R}=\boldsymbol{R}^0_{n\alpha}} + O(Q^2)\ . \tag{A.5}$$

The first term in the series is the lattice-periodic potential for the electrons. This potential is supposed to be contained in the electronic part $H_{el}$ of the Hamiltonian, and therefore not considered here. The second part then gives the linear electron-ion interaction

$$V = \sum_\nu \tilde{V}(\boldsymbol{r}_\nu)\ ; \quad \tilde{V}(\boldsymbol{r}) = \sum_{n\alpha}\boldsymbol{Q}_{n\alpha}\left.\frac{\partial V_\alpha(\boldsymbol{R}, \boldsymbol{r})}{\partial \boldsymbol{R}}\right|_{\boldsymbol{R}=\boldsymbol{R}^0_{n\alpha}}\ . \tag{A.6}$$

The potential $\tilde{V}(\boldsymbol{r})$ is generated by the displacement of the ions from their equilibrium positions and acts on the electrons.

After having established the ion-ion Hamiltonian in the harmonic approximation, as well as the electron-ion interaction in linear approximation, we investigate these in the next two sections in detail.

## A.2 The bare phonon system

### A.2.1 Hamiltonian

In this section we are discussing the pure phonon system in harmonic approximation, which according to (A.1) and (A.4) is given by the Hamiltonian

$$H_{\text{ion}} = \sum_{\boldsymbol{n}\alpha} \frac{1}{2M_\alpha} \boldsymbol{P}_{\boldsymbol{n}\alpha}^2 + \frac{1}{2} \sum_{\boldsymbol{n}\alpha;\boldsymbol{n}'\alpha'} \boldsymbol{Q}_{\boldsymbol{n}\alpha} \hat{\Phi}_{\boldsymbol{n}\alpha;\boldsymbol{n}'\alpha'} \boldsymbol{Q}_{\boldsymbol{n}'\alpha'} \ , \tag{A.7}$$

where $\boldsymbol{P}_{\boldsymbol{n}\alpha}$ and $\boldsymbol{Q}_{\boldsymbol{n}\alpha}$ are hermitian operators satisfying the commutation relations

$$[\boldsymbol{P}_{\boldsymbol{n}\alpha}, \boldsymbol{Q}_{\boldsymbol{n}'\alpha'}] = -i\hbar\delta_{\boldsymbol{n}\boldsymbol{n}'}\delta_{\alpha\alpha'}\hat{1} \ , \quad [\boldsymbol{P}_{\boldsymbol{n}\alpha}, \boldsymbol{P}_{\boldsymbol{n}'\alpha'}] = 0 \ , \quad [\boldsymbol{Q}_{\boldsymbol{n}\alpha}, \boldsymbol{Q}_{\boldsymbol{n}'\alpha'}] = 0 \ . \tag{A.8}$$

The summations are over $N = N_1 \cdot N_2 \cdot N_3$ points in real space ($N$ is a finite number because we use periodic boundary conditions (PBC)) and over the different ions $\alpha = 1, \ldots, N_\alpha$ per unit cell, respectively. We now seek to decouple the $3 \cdot N \cdot N_\alpha$ degrees of freedom in (A.7).

### A.2.2 Symmetries of the dynamical matrix

Later on, we will have to diagonalize the dynamical matrix. As a preparative step, its symmetry properties in real and Fourier space are discussed here. The symmetries which are important for the diagonalization of the dynamical matrix are:

1. The translational symmetry of the crystal lattice implies that $\Phi_{i\alpha;i'\alpha'}(\boldsymbol{R}_{\boldsymbol{n}}, \boldsymbol{R}_{\boldsymbol{n}'})$ depends on space positions only through the difference $\boldsymbol{R}_{\boldsymbol{n}} - \boldsymbol{R}_{\boldsymbol{n}'}$, in other words, $\hat{\Phi}_{\boldsymbol{n}\alpha;\boldsymbol{n}'\alpha'} = \hat{\Phi}_{\boldsymbol{n}-\boldsymbol{n}',\alpha;0\alpha'}$. Consequently, the Fourier transform of the dynamical matrix

   $$\hat{\Phi}_{\boldsymbol{q};\alpha\alpha'} = \sum_{\boldsymbol{n}} \hat{\Phi}_{\boldsymbol{n}\alpha;0\alpha'} e^{i\boldsymbol{q}\boldsymbol{R}_{\boldsymbol{n}}} \tag{A.9}$$

   depends only on one quasimomentum variable $\boldsymbol{q}$. This is a discrete Fourier transformation, the sum involves $N$ terms.

2. The fact that $\hat{\Phi}_{\boldsymbol{n}\alpha;\boldsymbol{n}'\alpha'}$ appears in a quadratic form in (A.7) implies the hermiticity of $\hat{\Phi}$, that is,

   $$\begin{aligned} \hat{\Phi}_{\boldsymbol{n}\alpha;\boldsymbol{n}'\alpha'} &= \hat{\Phi}^{T*}_{\boldsymbol{n}'\alpha';\boldsymbol{n}\alpha} \\ \text{or} \quad \hat{\Phi}_{\boldsymbol{q};\alpha\alpha'} &= \hat{\Phi}^{T*}_{-\boldsymbol{q};\alpha\alpha'} \ . \end{aligned} \tag{A.10}$$

3. Take all displacements as equal, $\boldsymbol{Q}_{n\alpha} = \boldsymbol{Q}$. This corresponds to a translation of the lattice as a whole and does not change the energy of the lattice. Consequently,

   $$\sum_{n,\alpha;n',\alpha'} \hat{\Phi}_{n\alpha;n'\alpha'} = 0 \ ,$$

   and $\boldsymbol{Q}_{n\alpha} = \boldsymbol{Q}$ represents three linear independent eigenvectors of the dynamical matrix; the corresponding eigenvalues are zero.

   With respect to other displacements $\{\boldsymbol{Q}_{n\alpha}\}$, the lattice is stable in its equilibrium position (given by $\boldsymbol{Q}_{n\alpha} = 0$), that is,

   $$\sum_{n,\alpha;n',\alpha'} \boldsymbol{Q}_{n\alpha} \hat{\Phi}_{n\alpha;n'\alpha'} \boldsymbol{Q}_{n'\alpha'} > 0$$

   for all $\{\boldsymbol{Q}_{n\alpha}\}$, saved the case corresponding to the translation. We conclude that the $3 \cdot N_\alpha \cdot N$-dimensional dynamical matrix can be diagonalized and possesses 3 vanishing eigenvalues. All other eigenvalues are positive.

4. If the lattice possesses an inversion symmetry, then the dynamical matrix is real and its eigenvectors are real as well (see [A.1], Chap. 22).

### A.2.3 Site-site decoupling

As a first step in the diagonalization of the Hamiltonian (A.7), we introduce the Fourier representation of the operators in (A.8) by defining

$$\begin{aligned} \boldsymbol{P}_{q\alpha} &= \frac{1}{\sqrt{N}} \sum_{n} \boldsymbol{P}_{n\alpha} e^{+i\boldsymbol{q}\boldsymbol{R}_n} \ , & \boldsymbol{P}_{n\alpha} &= \frac{1}{\sqrt{N}} \sum_{q} \boldsymbol{P}_{q\alpha} e^{-i\boldsymbol{q}\boldsymbol{R}_n} \ , \\ \boldsymbol{Q}_{q\alpha} &= \frac{1}{\sqrt{N}} \sum_{n} \boldsymbol{Q}_{n\alpha} e^{-i\boldsymbol{q}\boldsymbol{R}_n} \ , & \boldsymbol{Q}_{n\alpha} &= \frac{1}{\sqrt{N}} \sum_{q} \boldsymbol{Q}_{q\alpha} e^{+i\boldsymbol{q}\boldsymbol{R}_n} \ . \end{aligned} \tag{A.11}$$

This is a canonical transformation, it leaves the commutation relations invariant, that is, the commutation relations (A.8) are valid for the operators $\boldsymbol{P}_{q\alpha}$ and $\boldsymbol{Q}_{q\alpha}$ as well. Note that for this reason, the different signs in the exponent of the exponential functions in the transformations for $\boldsymbol{Q}_{q\alpha}$ and $\boldsymbol{P}_{q\alpha}$ are necessary. The operators $\boldsymbol{Q}_{n\alpha}$ and $\boldsymbol{P}_{n\alpha}$ are hermitian, whereas the operators $\boldsymbol{Q}_{q\alpha}$ and $\boldsymbol{P}_{q\alpha}$ are not. Instead, the relations $\boldsymbol{Q}^+_{q\alpha} = \boldsymbol{Q}_{-q\alpha}$ and $\boldsymbol{P}^+_{q\alpha} = \boldsymbol{P}_{-q\alpha}$ hold. We apply the transformation (A.11) to the Hamiltonian (A.7). This yields

$$\sum_{n} \boldsymbol{P}^2_{n\alpha} = \sum_{q} \boldsymbol{P}^+_{q\alpha} \boldsymbol{P}_{q\alpha} \ ,$$

note that $\boldsymbol{P}^+_{q\alpha}\boldsymbol{P}_{q\alpha} = \boldsymbol{P}_{-q\alpha}\boldsymbol{P}^+_{-q\alpha}$. Transforming the second part of the Hamiltonian is more difficult. By a short calculation, we can show that

$$\sum_{n\alpha;n'\alpha'} \boldsymbol{Q}_{n\alpha} \hat{\Phi}_{n\alpha;n'\alpha'} \boldsymbol{Q}_{n'\alpha'} = \sum_{q} \boldsymbol{Q}^+_{q\alpha} \hat{\Phi}_{q;\alpha\alpha'} \boldsymbol{Q}_{q\alpha'}$$

and the Hamiltonian (A.7) becomes

$$\begin{aligned}
&H_{\text{ion}} = \sum_{\boldsymbol{q}} h_{\boldsymbol{q}} \ , \qquad h_{\boldsymbol{q}} = \sum_{\alpha} \frac{1}{2M_\alpha} \boldsymbol{P}^+_{\boldsymbol{q}\alpha} \boldsymbol{P}_{\boldsymbol{q}\alpha} + \frac{1}{2} \sum_{\alpha\alpha'} \boldsymbol{Q}^+_{\boldsymbol{q}\alpha} \hat{\Phi}_{\boldsymbol{q};\alpha\alpha'} \boldsymbol{Q}_{\boldsymbol{q}\alpha'} \\
&\text{with} \quad [\boldsymbol{P}^+_{\boldsymbol{q}\alpha}, \boldsymbol{Q}_{\boldsymbol{q}'\alpha'}] = -i\hbar \delta_{\boldsymbol{q}\boldsymbol{q}'} \delta_{\alpha\alpha'} \hat{1} \ , \quad [\boldsymbol{P}^+_{\boldsymbol{q}\alpha}, \boldsymbol{P}_{\boldsymbol{q}'\alpha'}] = 0 \ , \quad [\boldsymbol{Q}^+_{\boldsymbol{q}\alpha}, \boldsymbol{Q}_{\boldsymbol{q}'\alpha'}] = 0 \\
&\text{and} \quad \boldsymbol{Q}^+_{\boldsymbol{q}\alpha} = \boldsymbol{Q}_{-\boldsymbol{q}\alpha} \ , \quad \boldsymbol{P}^+_{\boldsymbol{q}\alpha} = \boldsymbol{P}_{-\boldsymbol{q}\alpha} \ .
\end{aligned} \tag{A.12}$$

The Hamiltonian (A.7) which describes a system of $3 \cdot N_\alpha \cdot N$ coupled degrees of freedom is therefore reduced to $N$ uncoupled systems of $3 \cdot N_\alpha$ degrees of freedom each.[3]

## A.2.4 Decoupling the remaining degrees of freedom for fixed $\boldsymbol{q}$

The next step is to decouple the degrees of freedom in $h_{\boldsymbol{q}}$. We suppress the index $\boldsymbol{q}$ from now on, introduce the index $i$ to denote the cartesian components of vectors, and define the non-singular transformation

$$\begin{aligned}
P_{i\alpha} &= \sqrt{M_\alpha} \sum_\lambda u^*_{i\alpha;\lambda} p_\lambda \\
Q_{i\alpha} &= \frac{1}{\sqrt{M_\alpha}} \sum_\lambda v_{i\alpha;\lambda} q_\lambda
\end{aligned} \tag{A.13}$$

with $i = 1, \ldots, 3$, $\alpha = 1, \ldots, N_\alpha$, and consequently $\lambda = 1, \ldots 3N_\alpha$. There are 3 conditions which determine the form of the matrices $(u_{i\alpha;\lambda})$ and $(v_{i\alpha;\lambda})$, they are

(1) the transformation has to be a canonical one, that is, the commutation relations must become
$$[p^+_\lambda, q_{\lambda'}] = -i\hbar\delta_{\lambda\lambda'} \ , \quad [p^+_\lambda, p_{\lambda'}] = 0 \ , \quad [q^+_\lambda, q_{\lambda'}] = 0 \ ,$$

(2) the sum $\sum_\alpha (1/2M_\alpha) \boldsymbol{P}^+_\alpha \boldsymbol{P}_\alpha$ has to transform to $\sum_\lambda p^+_\lambda p_\lambda$, that is, the masses all become 1 in the Hamiltonian, and

(3) the Hamiltonians $h_{\boldsymbol{q}}$ and $-h_{\boldsymbol{q}}$ have to become decoupled from each other by the transformation.

Condition (1) can be shown in a short calculation to be equivalent to

$$\sum_{i\alpha} u_{i\alpha;\lambda} v^*_{i\alpha;\lambda'} = \delta_{\lambda\lambda'} \tag{A.14}$$

which is a *orthonormality relation* for the matrices $(u_{i\alpha;\lambda})$ and $(v_{i\alpha;\lambda})$. Another straightforward calculation shows that the second condition is fulfilled if and only if the *closure relation*

$$\sum_\lambda u^*_{i\alpha;\lambda} u_{i'\alpha';\lambda} = \delta_{ii'} \delta_{\alpha\alpha'} \tag{A.15}$$

is valid. Using the orthogonality and closure relations, it is easily shown that

$$v_{i\alpha;\lambda} = u_{i\alpha;\lambda} \ .$$

---

[3] Actually this is not true. Because of $\boldsymbol{P}^+_{\boldsymbol{q}\alpha} = \boldsymbol{P}_{-\boldsymbol{q}\alpha}$, the parts $h_{\boldsymbol{q}}$ and $h_{-\boldsymbol{q}}$ are coupled still and we have $N/2$ uncoupled systems of $2 \cdot 3 \cdot N_\alpha$ degrees of freedom each.

If we consider the $u_{i\alpha;\lambda}$ as elements of a square matrix $U$, then the relations under consideration imply that $U$ is unitary.

Still the condition (3) has not been taken into account. This is our next step. We look for a unitary matrix $U$ with the property that the transformation (A.13) diagonalizes the $\boldsymbol{Q}^{+}\hat{\Phi}\boldsymbol{Q}$ term in (A.12). This term becomes

$$\frac{1}{2}\sum_{\lambda\lambda'}\left(\sum_{i\alpha;i'\alpha'}\frac{1}{\sqrt{M_\alpha M_{\alpha'}}}\Phi_{i\alpha;i'\alpha'}u^{*}_{i\alpha;\lambda}u_{i'\alpha';\lambda'}\right)q^{+}_{\lambda}q_{\lambda} \tag{A.16}$$

where $\Phi_{i\alpha;i'\alpha'}=\left(\hat{\Phi}_{\alpha;\alpha'}\right)_{ii'}$, and the expression in parentheses has to be proportional to $\delta_{\lambda\lambda'}$ for the condition (3) to hold.

### A.2.5 Eigenvalue equation

To find a unitary matrix $U$ which has the property that the expression in parenthesis in (A.16) becomes proportional to $\delta_{\lambda\lambda'}$, we solve the eigenvalue equation

$$\sum_{\alpha'}\frac{1}{\sqrt{M_\alpha M_{\alpha'}}}\hat{\Phi}_{\alpha\alpha'}\boldsymbol{e}_{\alpha'}=\omega^2\boldsymbol{e}_{\alpha}\ . \tag{A.17}$$

Because in general $\Phi_{i\alpha;i'\alpha'}$ is a hermitian matrix, the eigenvalue equation yields a set of eigenvectors $\boldsymbol{e}_{\alpha';\lambda}$ and real eigenvalues $\omega^2_\lambda$. As already discussed, the stability of the lattice in the equilibrium state forces the quadratic form (A.4) to be positive definite with the exception of the three acoustic Γ-point modes for which they are zero. Therefore, (with this exception) the eigenvalues of $\Phi$ are positive. The eigenvectors are complex in general. The vectors $\boldsymbol{e}_{\alpha'}$ will be orthogonal[4] We normalize these by

$$\sum_{\alpha}\boldsymbol{e}^{*}_{\alpha;\lambda}\boldsymbol{e}_{\alpha;\lambda'}=\delta_{\lambda\lambda'}\ .$$

Then, as a consequence of the eigenvalue problem, the closure relation (A.15) reads

$$\sum_{\lambda}(\boldsymbol{e}^{*}_{\alpha;\lambda})_i(\boldsymbol{e}_{\alpha';\lambda})_{i'}=\delta_{\alpha\alpha'}\delta_{ii'}$$

and is satisfied automatically. Now we choose[5]

$$u_{i\alpha;\lambda}=(\boldsymbol{e}_{\alpha;\lambda})_i \tag{A.18}$$

for the matrix $U$. Then the unitarity of $U$ is fulfilled, and (A.16) simplifies to $\sum_\lambda \omega^2_\lambda q^{+}_\lambda q_\lambda$. As a result, the Hamiltonian (A.12) is reduced to

$$H=\sum_{\boldsymbol{q}}h_{\boldsymbol{q}\lambda}\ ,\qquad h_{\boldsymbol{q}\lambda}=\sum_{\alpha}\frac{1}{2}\left(p^{+}_{\boldsymbol{q}\lambda}p_{\boldsymbol{q}\lambda}+\omega^2_{\boldsymbol{q}\lambda}q^{+}_{\boldsymbol{q}\lambda}q_{\boldsymbol{q}\lambda}\right)\ . \tag{A.19}$$

Note that the modes defined by the pairs of quantum numbers $(\boldsymbol{q},\lambda)$ and $(-\boldsymbol{q},\lambda)$ are still coupled because $q^{+}_{\boldsymbol{q}}=q_{-\boldsymbol{q}}$.

---

[4] except for cases with degeneracy, in which the vectors can be orthogonalized.

[5] By $(\boldsymbol{v})_i$ we denote the $i$th cartesian component of the vector $\boldsymbol{v}$.

### A.2.6 Creation and destruction operators

The introduction of creation and destruction operators for phonon modes is performed now in close analogy to the case of the one-dimensional harmonic oscillator (1DHO). Notice again that the difference of the 1DHO system and the system under consideration here is that the two modes described by $h_{\boldsymbol{q}\lambda}$ and $h_{-\boldsymbol{q}\lambda}$ are coupled. Nevertheless, the form of the creation and destruction operators is similar, they are given by

$$\begin{aligned} a^+_{\boldsymbol{q}\lambda} &= \frac{1}{\sqrt{2\hbar\omega_{\boldsymbol{q}\lambda}}}\left(\omega_{\boldsymbol{q}\lambda} q^+_{\boldsymbol{q}\lambda} - i p^+_{\boldsymbol{q}\lambda}\right) & \qquad q_{\boldsymbol{q}\lambda} &= \sqrt{\frac{\hbar}{2\omega}}\left(a_{\boldsymbol{q}\lambda} + a^+_{-\boldsymbol{q}\lambda}\right) \\ a_{\boldsymbol{q}\lambda} &= \frac{1}{\sqrt{2\hbar\omega_{\boldsymbol{q}\lambda}}}\left(\omega_{\boldsymbol{q}\lambda} q_{\boldsymbol{q}\lambda} + i p^+_{\boldsymbol{q}\lambda}\right) & p_{\boldsymbol{q}\lambda} &= -i\sqrt{\frac{\hbar\omega}{2}}\left(a_{\boldsymbol{q}\lambda} - a^+_{-\boldsymbol{q}\lambda}\right) \ . \end{aligned} \tag{A.20}$$

Using the commutation relation of the operators $q_{\boldsymbol{q}\lambda}$ and $p_{\boldsymbol{q}\lambda}$, Eq. (A.20) and the relations $p^+_{\boldsymbol{q}\lambda} = p_{-\boldsymbol{q}\lambda}$, and analogous for $q_{\boldsymbol{q}\lambda}$, we can show that

$$\hbar\omega_{\boldsymbol{q}\lambda}\left(a^+_{\boldsymbol{q}\lambda}a_{\boldsymbol{q}\lambda} + \frac{1}{2}\right) = \frac{1}{2}\left(p^+_{-\boldsymbol{q}\lambda}p_{-\boldsymbol{q}\lambda} + \omega^2_{\boldsymbol{q}\lambda}q^+_{\boldsymbol{q}\lambda}q_{\boldsymbol{q}\lambda}\right) + \frac{1}{2}\left(q_{\boldsymbol{q}\lambda}p_{\boldsymbol{q}\lambda} - q_{-\boldsymbol{q}\lambda}p_{-\boldsymbol{q}\lambda}\right) \ .$$

and, therefore,

$$h_{\boldsymbol{q}\lambda} + h_{-\boldsymbol{q}\lambda} = \hbar\omega_{\boldsymbol{q}\lambda}\left(a^+_{\boldsymbol{q}\lambda}a_{\boldsymbol{q}\lambda} + \frac{1}{2}\right) + (\boldsymbol{q} \leftrightarrow -\boldsymbol{q}) \ .$$

As a result, the diagonalized ion-ion Hamiltonian in the harmonic approximation can be written in the form[6]

$$H_{\text{ion}} = \sum_{\boldsymbol{q}\lambda}\hbar\omega_{\boldsymbol{q}\lambda}\left(a^+_{\boldsymbol{q}\lambda}a_{\boldsymbol{q}\lambda} + \frac{1}{2}\right) \ , \tag{A.21}$$

where the operators $a^+_{\boldsymbol{q}\lambda}$ and $a_{\boldsymbol{q}\lambda}$ fulfill the commutation relation

$$[a_{\boldsymbol{q}\lambda}, a^+_{\boldsymbol{q}\lambda}] = \delta_{\boldsymbol{q}\boldsymbol{q}'}\delta_{\lambda\lambda'} \ . \tag{A.22}$$

The pair $(\boldsymbol{q}, \lambda)$ denotes one single phonon mode with the energy $\hbar\omega_{\boldsymbol{q}\lambda}$, the frequencies $\omega_{\boldsymbol{q}\lambda}$ are obtained by solving the eigenvalue problem (A.17). In an occupation number representation, the operators $a^+_{\boldsymbol{q}\lambda}$ and $a_{\boldsymbol{q}\lambda}$ create and annihilate a phonon, respectively.

## A.3 The electron-phonon interaction

### A.3.1 Hamiltonian

After having discussed in length the phonon system, we are ready to attack the electron-phonon interaction. The electron-phonon interaction is given in linear approximation by the expression (A.6),

$$H_{\text{el-ion}} = V = \sum_{\nu}\tilde{V}(\boldsymbol{r}_\nu) \ ; \quad \tilde{V}(\boldsymbol{r}) = \sum_{n\alpha}\boldsymbol{Q}_{n\alpha}\,\nabla_{\boldsymbol{R}}V_\alpha(\boldsymbol{R}, \boldsymbol{r})|_{\boldsymbol{R}=\boldsymbol{R}^0_{n\alpha}} \ . \tag{A.23}$$

---

[6] The $\boldsymbol{q}$-sum runs over all $\boldsymbol{q}$ in the first BZ, because the operators $\boldsymbol{P}_{n\alpha}$ and $\boldsymbol{R}_{n\alpha}$ are defined only at lattice sites.

where the $\nu$-sum runs over all electrons, and the other sum over all ions. Note that in general, $\tilde{V}(\boldsymbol{r})$ is *not* lattice-periodic.

We use the translational invariance in the form $V_\alpha(\boldsymbol{R},\boldsymbol{r}) = V_\alpha(\boldsymbol{R}-\boldsymbol{r})$, note that $V_\alpha(\boldsymbol{r})$ has to obey periodic boundary conditions, and introduce its Fourier transform[7]

$$V_\alpha(\boldsymbol{r}) = \frac{1}{V}\sum_{\boldsymbol{k}}^{\infty} e^{i\boldsymbol{k}\boldsymbol{r}} V_{\alpha\boldsymbol{k}} \ ,$$

where the crystal volume is denoted by $V$. Introducing also the Fourier transform $\tilde{V}_{\boldsymbol{k}}$ of $\tilde{V}(\boldsymbol{r})$, we can rewrite Eq. (A.23) as

$$\tilde{V}_{\boldsymbol{k}} = i\boldsymbol{k}\sum_{n\alpha} V_{\alpha\boldsymbol{k}}\,\boldsymbol{Q}_{n\alpha} e^{-i\boldsymbol{k}\boldsymbol{R}^0_{n\alpha}} \ , \tag{A.24}$$

the inverse lattice vector $\boldsymbol{k}$ is *not* restricted to the first Brillouin zone. The sum in (A.24) is invariant upon the substitution $\boldsymbol{k} \to \boldsymbol{k} + \boldsymbol{G}$ ($\boldsymbol{G}$ is a reciprocal lattice vector), but $V_{\boldsymbol{k}\alpha}$ is not. Writing $\boldsymbol{R}^0_{n\alpha} = \boldsymbol{R}_n + \vec{\tau}_\alpha$ and using the definition of $\boldsymbol{Q}_{\boldsymbol{q}\alpha}$ in (A.11), we obtain

$$\sum_{n\alpha} V_{\alpha\boldsymbol{k}}\,\boldsymbol{Q}_{n\alpha} e^{-i\boldsymbol{k}\boldsymbol{R}^0_{n\alpha}} = \sqrt{N}\sum_{\alpha} V_{\alpha\boldsymbol{k}}\,\boldsymbol{Q}_{\bar{\boldsymbol{k}}\alpha} e^{-i\boldsymbol{k}\vec{\tau}_\alpha}$$

where we utilized the symbol $\bar{\boldsymbol{k}}$ to denote the mapping of $\boldsymbol{k}$ into the first Brillouin zone by adding an appropriate reciprocal lattice vector.

Using (A.13) and (A.18), the coupling (A.24) can be expressed in the form

$$\tilde{V}_{\boldsymbol{k}} = i\sqrt{N}\sum_{\alpha\lambda}\frac{1}{\sqrt{M_\alpha}} V_{\alpha\boldsymbol{k}} e^{-i\boldsymbol{k}\vec{\tau}_\alpha}\left(\boldsymbol{k}\cdot\boldsymbol{e}_{\alpha;\bar{\boldsymbol{k}}\lambda}\right) q_{\bar{\boldsymbol{k}}\lambda} \tag{A.25}$$

and two properties of this coupling becomes obvious:

- A phonon with quasimomentum $\boldsymbol{q}$ couples to all the Fourier components $V_{\alpha\boldsymbol{k}}$ of the electron-ion potential whose wave vectors $\boldsymbol{k}$ map to $\boldsymbol{q}$ in the first Brillouin zone (i.e., to all $V_{\alpha,\boldsymbol{q}+\boldsymbol{G}}$, where $\boldsymbol{G}$ is a reciprocal lattice vector).
- If we neglect the "Umklapp coupling" (i.e., assume $\boldsymbol{k} = \bar{\boldsymbol{k}}$), the product $\boldsymbol{k}\cdot\boldsymbol{e}_{\alpha;\bar{\boldsymbol{k}}\lambda}$ shows that "pure" transverse phonons do not couple to the electron system.

As a final step, we carry out the second quantization of $V \equiv H_{\text{el}-\text{ion}}$. The second quantized electron-ion interaction is given by

$$V = \sum_{n\boldsymbol{k};n'\boldsymbol{k}'} \langle n'\boldsymbol{k}'|\tilde{V}(\boldsymbol{r})|n\boldsymbol{k}\rangle c^+_{n'\boldsymbol{k}'} c_{n\boldsymbol{k}} \tag{A.26}$$

where the state $|n\boldsymbol{k}\rangle$ corresponds to a Bloch state $\psi_{n\boldsymbol{k}}(\boldsymbol{r}) = u_{n\boldsymbol{k}}(\boldsymbol{r})\exp(i\boldsymbol{k}\boldsymbol{r})$, and $c_{n\boldsymbol{k}}$ annihilates a Bloch electron with wavenumber $\boldsymbol{k}$ from band $n$.

---

[7] The $\boldsymbol{k}$-sum run over *all* values of $\boldsymbol{k}$ which are compatible with the PBC, not only those in the first BZ. We indicate this by putting the $\infty$ sign on top of the sum symbol.

The matrix element in (A.26) can be written in the form

$$\begin{aligned}\langle n'\boldsymbol{k}'|\tilde{V}(\boldsymbol{r})|n\boldsymbol{k}\rangle &= \frac{1}{V}\sum_{\boldsymbol{q}}^{\infty}\tilde{V}_{\boldsymbol{q}}\cdot\frac{1}{V}\int_{\text{crystal}} d^3r\, e^{i(\boldsymbol{k}-\boldsymbol{k}')\boldsymbol{r}} u^*_{n'\boldsymbol{k}'}(\boldsymbol{r}) u_{n\boldsymbol{k}}(\boldsymbol{r}) e^{i\boldsymbol{q}\boldsymbol{r}} \\ &\equiv \frac{1}{V}\sum_{\boldsymbol{q}}^{\infty}\tilde{V}_{\boldsymbol{q}}\cdot\alpha_{n'\boldsymbol{k}';n\boldsymbol{k}}\,\delta_{\boldsymbol{k}',\boldsymbol{k}+\boldsymbol{q}+\boldsymbol{G}}\ .\end{aligned}$$

This equation demostrates that a nonvanishing $\boldsymbol{q}$-component in the potential $\tilde{V}(\boldsymbol{r})$, which the electrons experience, induces electronic transitions from $|n\boldsymbol{k}\rangle$ to $|n'\boldsymbol{k}'\rangle$, where $\boldsymbol{k}' = \boldsymbol{k}+\boldsymbol{q}+\boldsymbol{G}$, and $\boldsymbol{G}$ is chosen in such a way that both, $\boldsymbol{k}$ and $\boldsymbol{k}'$ lie in the first Brillouin zone.

Making use of (A.25), the matrix element becomes

$$\begin{aligned}&\langle n'\boldsymbol{k}'|\tilde{V}(\boldsymbol{r})|n\boldsymbol{k}\rangle \\ &= \sum_{\boldsymbol{q}}^{\infty}\frac{i}{V_c\sqrt{N}}\sum_{\alpha\lambda}\frac{1}{\sqrt{M_\alpha}}V_{\alpha\boldsymbol{q}}e^{-i\boldsymbol{q}\vec{\tau}_\alpha}\left(\boldsymbol{q}\cdot\boldsymbol{e}_{\alpha;\boldsymbol{q}\lambda}\right)\cdot\sqrt{\frac{\hbar}{2\omega_{\boldsymbol{q}\lambda}}}\left(a^+_{-\boldsymbol{q}\lambda}+a_{\boldsymbol{q}\lambda}\right) \\ &\quad \alpha_{n'\boldsymbol{k}';n\boldsymbol{k}}\delta_{\boldsymbol{k}',\boldsymbol{k}+\boldsymbol{q}+\boldsymbol{G}} \\ &= \frac{i}{V_c\sqrt{N}}\sum_{\boldsymbol{q}\lambda}\sqrt{\frac{\hbar}{2\omega_{\boldsymbol{q}\lambda}}}\alpha_{n'\boldsymbol{k}';n\boldsymbol{k}}\left[\sum_{\alpha,\boldsymbol{G}}\frac{1}{\sqrt{M_\alpha}}V_{\alpha\boldsymbol{q}+\boldsymbol{G}}e^{-i(\boldsymbol{q}+Gvec)\vec{\tau}_\alpha}\left((\boldsymbol{q}+\boldsymbol{G})\cdot\boldsymbol{e}_{\alpha;\boldsymbol{q}\lambda}\right)\right] \\ &\quad \cdot\,\delta_{\boldsymbol{k}',\boldsymbol{k}+\boldsymbol{q}+\boldsymbol{G}}\left(a^+_{-\boldsymbol{q}\lambda}+a_{\boldsymbol{q}\lambda}\right) \\ &\equiv \sum_{\boldsymbol{q}\lambda} g^{\boldsymbol{q}\lambda}_{n'n\boldsymbol{k}}\delta_{\boldsymbol{k}',\boldsymbol{k}+\boldsymbol{q}+\boldsymbol{G}}\left(a^+_{-\boldsymbol{q}\lambda}+a_{\boldsymbol{q}\lambda}\right)\end{aligned}\tag{A.27}$$

where the unit cell volume $V/N = V_c$ has been introduced. Equation (A.27) defines the *electron-phonon vertex* $g^{\boldsymbol{q}\lambda}_{n'n\boldsymbol{k}}$ and relates it to the electron-ion potential $V_\alpha$. The electron-ion vertex $g^{\boldsymbol{q}\lambda}_{n'n\boldsymbol{k}}$ corresponds to the amplitude for the electron performing a transition from state $|n\boldsymbol{k}\rangle$ to state $|n,\boldsymbol{k}-\boldsymbol{q}\rangle$ while creating a phonon with quantum numbers $(\boldsymbol{q},\lambda)$ (or annihilating a phonon with quantum numbers $(-\boldsymbol{q},\lambda)$).

The second quantized electron-ion interaction finally becomes

$$H_{\text{el}-\text{ion}} = \sum_{n',n,\boldsymbol{k};\boldsymbol{q}\lambda} g^{\boldsymbol{q}\lambda}_{n'n\boldsymbol{k}}\, c^+_{n',\boldsymbol{k}+\boldsymbol{q}}c_{n,\boldsymbol{k}}\,\left(a^+_{-\boldsymbol{q}\lambda}+a_{\boldsymbol{q}\lambda}\right)\ ,$$

the electron-phonon vertex is denoted by $g^{\boldsymbol{q}\lambda}_{n'n\boldsymbol{k}}$; the operators $c$ ($c^+$) annihilate (create) an electron, whereas the operators $a$ ($a^+$) annihilate (create) a phonon.

## A.3.2 Different mechanisms

Equation (A.27) allows the calculation of the electron-phonon vertex for a known electron-ion potential $V_\alpha$. Usually, however, the electron-ion potential is not known, and one has to rely on certain approximation schemes, the so-called *electron-phonon coupling mechanisms.* The most important of these are the *deformation potential coupling*, the *piezoelectric interaction*, and the *polar coupling (Fröhlich interaction).*

The *deformation potential coupling* involves the coupling of long-wavelength longitudinal acoustic or optical phonons to the electrons. For the case of acoustic phonons, the corresponding displacements of the ions are closely related to a macroscopic deformation of the crystal. Deformations change the band structure; the amount of deformation of the band structure for a given static lattice distortion is known as *deformation potential* (see [A.2], Subsect. 3.3.1, and [A.3], Chap. 1.3C). In the case of optical phonons, the corresponding static displacements are called *frozen phonons*. These configurations are often used in conjunction with ab initio LDA- or semiempirical methods to calculate the electron-phonon coupling.

In piezoelectric crystals, stress induces a macroscopic polarization field. This is possible, however, only for crystals which lack an inversion center. Acoustic phonons are related to stress and therefore produce a macroscopic electric field in the crystal. This macroscopic electric field is equivalent to a potential that acts on the electrons (see [A.2], Subsect. 3.3.3, and [A.3], Chap. 1.3D). This type of interaction is known as *piezoelectric interaction*.

In *polar crystals* with at least 2 atoms per unit cell, long-wavelength longitudinal optical phonons can induce a macroscopic polarization. The macroscopic electric field which is related to the polarization couples the phonon to the electronic system. This effect is known as *polar coupling* or *Fröhlich interaction*.

# Appendix B

# The electronic structure of crystals

## B.1 The Hamiltonian of crystals

### B.1.1 Electrons and phonons

The Hamiltonian of the electron-ion system was already presented in Sect. A.1, where the discussion of the electronic part was postponed. This discussion is our concern here.

The electrons in an electron-ion system interact with other electrons and with the ions also. Therefore, the electronic part $H_{\mathrm{el}}$ of the Hamiltonian $H$ of the electron-ion system depends on the locations[1] $\{\boldsymbol{R}_{\boldsymbol{n}\alpha}\}$ of the ions, which correspond to lattice sites $\boldsymbol{R}^0_{\boldsymbol{n}\alpha}$ plus small[2] time-dependent displacements $\boldsymbol{Q}_{\boldsymbol{n}\alpha}(t)$. This dependence couples the electronic system to the ionic part of the Hamiltonian $H$, and renders a solution of the electronic Hamiltonian (e.g. the calculation of the electronic band structure) without solving at the same time the other parts of $H$ impossible. Therefore, an approximation is in order. This is the *Born-Oppenheimer-* or *adiabatic approximation*, which *for the electronic part $H_{\mathrm{el}}$ of the Hamiltonian* fixes the ions to their corresponding lattice sites,[3] that is, takes $\boldsymbol{Q}_{\boldsymbol{n}\alpha} = 0$. The electron-ion interaction (as described in Eq. (A.3)) corresponds to a lattice-periodic static potential (the first term in the sum of (A.5)) and will be considered as a part of $H_{\mathrm{el}}$. If we use second quantization and electron field operators $\Psi(\boldsymbol{r})$, the electronic Hamiltonian can be rewritten as

$$\begin{aligned} H_{\mathrm{el}} &= T + U + V \qquad \text{with} \\ T &= \frac{1}{2}\int \nabla\Psi^\dagger(\boldsymbol{r})\nabla\Psi(\boldsymbol{r})\,d^3r \\ U &= \frac{1}{2}\int \Psi^\dagger(\boldsymbol{r})\Psi^\dagger(\boldsymbol{r}')u(\boldsymbol{r}-\boldsymbol{r}')\Psi(\boldsymbol{r}')\Psi(\boldsymbol{r})\,d^3r\,d^3r' \\ V &= \int v(\boldsymbol{r})\Psi^\dagger(\boldsymbol{r})\Psi(\boldsymbol{r})\,d^3r \end{aligned} \tag{B.1}$$

where $U$ corresponds to the electron-electron interaction and $V$ to the lattice-periodic potential caused by the presence of the charged ions.

---

[1] For the notation refer to Sect. A.1.

[2] The displacements are small with respect to the lattice constant.

[3] Note again that this is only performed for the electronic part of the Hamiltonian!

Equation (B.1) is the starting point for the calculation of the electronic band structure.

## B.2 Density functional theory and the local density approximation

The LMTO calculations are performed to solve a one-electron self-consistent Schrödinger equation called the Kohn-Sham equation, which follows from the Hohenberg-Kohn density functional theory. In this section we give a short overview of the derivation.

### B.2.1 Density functional theory

The *density functional theory* (DFT), pioneered by Hohenberg and Kohn [B.1], establishes a relation between the ground state density $n_0(\boldsymbol{r})$ of the (electronic) Hamiltonian (B.1) and a potential[4] $v(\boldsymbol{r})$ needed to realize this ground state density, and sets up a variational principle for the calculation of the ground state density $n_0(\boldsymbol{r})$ of (B.1) for a given potential $v(\boldsymbol{r})$.

We start with the Hamiltonian $H_{\text{el}}$ in (B.1) and denote its ground state by $|0\rangle$. The electron density *in the ground state* is given by

$$n_0(\boldsymbol{r}) = \langle 0|\Psi^\dagger(\boldsymbol{r})\Psi(\boldsymbol{r})|0\rangle \ .$$

The Hamiltonian (B.1) is a functional of the external potential $v(\boldsymbol{r})$, therefore the ground state $|0\rangle$, and also the ground state density $n_0(\boldsymbol{r})$, are functionals of the external potential $v(\boldsymbol{r})$. So far, this is trivial.

Hohenberg and Kohn show now that the reverse is also true, that is, that $v(\boldsymbol{r})$ is a functional of the ground state density $n_0(\boldsymbol{r})$ (up to an additive constant in the external potential). If we fix the ground state density $n_0(\boldsymbol{r})$, the potential $v(\boldsymbol{r})$ needed to realize this density is fixed as well.[5] Therefore, there is a one-to-one correspondence between the external potential $v(\boldsymbol{r})$ (up to a constant) in the Hamiltonian (B.1) and the related ground state density $n_0(\boldsymbol{r})$.

*DFT I:* Between the potential $v(\boldsymbol{r})$ in the Hamiltonian (B.1) and the related ground state density $n_0(\boldsymbol{r})$ there is a one-to-one correspondence (up to an additive constant in $v(\boldsymbol{r})$).

As a consequence, *a given ground state density* $n_0(\boldsymbol{r})$ *fixes the Hamiltonian* $H_{\text{el}}$ in (B.1) by determining the potential $v(\boldsymbol{r})$. The Hamiltonian then can be solved for the ground state $|0\rangle$. Hence, the ground state $|0\rangle$ is also a functional of $n_0(\boldsymbol{r})$. This is by no means a trivial statement! An electron density $n(\boldsymbol{r})$ does not determine the state $|\psi\rangle$ of an electron system such that $n(\boldsymbol{r}) = \langle\psi|\Psi^\dagger(\boldsymbol{r})\Psi(\boldsymbol{r})|\psi\rangle$. But it does so, if the density is known to be the ground state density.

---

[4] The potential $v(\boldsymbol{r})$ defines the operator $V$ in (B.1). It has to be thought of as the potential arising from the interaction of the electrons with the static ions. The potential $v(\boldsymbol{r})$ an "*external*" potential because it arises from the interaction with particles or fields which are *not contained* in the Hamiltonian (B.1).

[5] In an ironic way, Hohenberg and Kohn [B.1] state in their footnote 12: *"We cannot prove whether an arbitrary positive density* $n'(\boldsymbol{r})$*,…, can be realized by some potential* $v'(\boldsymbol{r})$*. …and we believe that in fact all, except some pathological distributions, can be realized".*

The fact that the ground state $|0\rangle$ and the Hamiltonian are functionals of the ground state density allows us to define the kinetic and interaction energies as functionals of the ground state density

$$F[n(\boldsymbol{r})] = \langle 0|T + U|0\rangle \tag{B.2}$$

and $V[n(\boldsymbol{r})] = \langle 0|V|0\rangle$, which evaluates to

$$V[n(\boldsymbol{r})] = \int v(\boldsymbol{r})n(\boldsymbol{r})\, d^3r \ .$$

Note that the potential $v(\boldsymbol{r})$ by itself is also a functional of the ground state density (*DFT I*). The total energy is given by

$$E[n(\boldsymbol{r})] = F[n(\boldsymbol{r})] + \int v(\boldsymbol{r})n(\boldsymbol{r})\, d^3r \ . \tag{B.3}$$

Now, Hohenberg and Kohn define another functional[6] $E_v[n(\boldsymbol{r})]$ by

$$E_v[n(\boldsymbol{r})] = F[n(\boldsymbol{r})] + \int v(\boldsymbol{r})n(\boldsymbol{r})\, d^3r \ , \tag{B.4}$$

for a *fixed* potential $v(\boldsymbol{r})$. This functional is defined for any density $n(\boldsymbol{r})$, it does not have to be related to the potential $v(\boldsymbol{r})$. Is is clear that for the ground state density $n_0(\boldsymbol{r})$ which corresponds to the fixed potential $v(\boldsymbol{r})$, the energy $E_v[n_0(\boldsymbol{r})]$ is equal to the energy $E[n_0(\boldsymbol{r})]$ which is the ground state energy. Then they show that the minimization of the functional $E_v[n(\boldsymbol{r})]$ yields the ground state density related to $v(\boldsymbol{r})$, provided that the minimization is done in the subspace given by

$$\int n(\boldsymbol{r})\, d^3r = N = \text{fixed} \ , \tag{B.5}$$

that is, for a fixed number of particles.

*DFT II:* The functional $E_v[n(\boldsymbol{r})]$ in (B.4) assumes its minimum value for the correct ground state density $n = n_0[v(\boldsymbol{r})]$.

The two theorems (*DFT I*) and (*DFT II*) are the basic statements of density functional theory.

If the functional $F[n]$ were known, the problem of determining the ground state energy and density for a given potential would be relatively easy because we just would have to minimize the functional (B.4). The complexity of the many-body problem within density functional theory is hidden in the determination of $F[n]$ in (B.2).

---

[6] It is very important to understand the difference of the functionals $E[n]$ and $E_v[n]$. The first is only a functional of $n(\boldsymbol{r})$. The quantity $v(\boldsymbol{r})$ in (B.3) is determined by $v = v[n]$. In the functional $E_v[n]$, however, the quantity $v$ is a parameter.

### B.2.2 Kohn-Sham equations

The starting point for the derivation of the Kohn-Sham equations [B.2] is the Hohenberg-Kohn energy functional (B.4). We shall now try to specify the free energy $F[n]$ further. First of all the Coulomb energy of the electrons is included in $F[n]$. We separate this contribution by writing

$$F[n(\boldsymbol{r})] = \frac{1}{2}\int \frac{n(\boldsymbol{r})n(\boldsymbol{r}')}{|\boldsymbol{r}-\boldsymbol{r}'|}\, d^3r\, d^3r' + G[n(\boldsymbol{r})]$$

and call the term $F[n] - G[n]$ containing the integral the *Hartree term*.

The functional $G[n(\boldsymbol{r})]$ still contains the kinetic energy, the parts of the correlation energy which are not contained in the Hartree term, and also the exchange energy which is approximated by the Fock term in the Hartree-Fock equations.

We will also extract an approximation for the kinetic energy, namely the kinetic energy $T_{\mathrm{ni}}$ of a *system of non-interacting electrons* of density $n(\boldsymbol{r})$, out of $F[n(\boldsymbol{r})]$, and will see later why this is useful. The rest, that is, the functional $F[n]$ minus the Hartree term minus the kinetic energy $T_{\mathrm{ni}}$ of a non-interacting system, will be called the *exchange and correlation energy* and be denoted by $E_{\mathrm{xc}}$. The kinetic energy $T_{\mathrm{ni}}$ and the energy $E_{\mathrm{xc}}$ are both functionals of the density $n(\boldsymbol{r})$ Therefore, we write

$$G[n] = T_{\mathrm{ni}}[n] + E_{\mathrm{xc}}[n] \ .$$

Using this form for the energy functional (B.4) we perform the minimization by introducing a variation to the density $n(\boldsymbol{r}) \to n(\boldsymbol{r})+\delta n(\boldsymbol{r})$ taking into consideration the conservation of particles which is expressed by the condition

$$\int \delta n(\boldsymbol{r})\, d^3r = 0 \ .$$

In this way we arrive at the equation

$$\int \delta n(\boldsymbol{r}) \left\{ v(\boldsymbol{r}) + \int \frac{n(\boldsymbol{r}')}{|\boldsymbol{r}-\boldsymbol{r}'|}\, d^3r' + \frac{\delta T_{\mathrm{ni}}[n(\boldsymbol{r})]}{\delta n(\boldsymbol{r})} + \frac{\delta E_{\mathrm{xc}}[n(\boldsymbol{r})]}{\delta n(\boldsymbol{r})} \right\} d^3r = 0 \ , \tag{B.6}$$

which requires the expression in the curly brackets to vanish identically, because the variation $\delta n(\boldsymbol{r})$ is arbitrary (just the particle conservation (B.5) has to be fulfilled, this can be accomplished by the introduction of a Lagrangian multiplier $\mu$).

Consider now a system of non-interacting particles. For such system, the Hartree term as well as the exchange and correlation energy $E_{\mathrm{xc}}[n]$ vanish. Just the kinetic energy $T_{\mathrm{ni}}$, which now corresponds to the exact kinetic energy, and the external potential $v(\boldsymbol{r})$ are left in (B.6). Equation (B.6) now requires

$$\frac{\delta T_{\mathrm{ni}}[n(\boldsymbol{r})]}{\delta n(\boldsymbol{r})} + v(\boldsymbol{r}) = 0 \ .$$

The solution $n(\boldsymbol{r})$ of this equation corresponds to the ground state density of a system of non-interacting particles in the external potential $v(\boldsymbol{r})$. Still we do not know the explicit form of the kinetic energy $T_{ni}[n]$, but in the case of the non-interacting electrons we can calculate the ground state density $n_0(\boldsymbol{r})$ also by solving the Schrödinger equation

$$\left[-\frac{1}{2}\nabla^2 + v(\boldsymbol{r})\right]\psi_i(\boldsymbol{r}) = \epsilon_i\psi_i(\boldsymbol{r}) \ , \tag{B.7}$$

and the density to be determined is given by

$$n_0(\boldsymbol{r}) = \sum_{i=1}^{N} |\psi_i(\boldsymbol{r})|^2 \tag{B.8}$$

where the sum comprises all single-particle states which are occupied in the ground state of the $N$-particle system. To solve (B.6) we just perform the replacement

$$v(\boldsymbol{r}) \rightarrow v_{\text{eff}}(\boldsymbol{r}) = v(\boldsymbol{r}) + \int \frac{n(\boldsymbol{r}')}{|\boldsymbol{r}-\boldsymbol{r}'|}\, d^3r' + \frac{\delta E_{\text{xc}}[n(\boldsymbol{r})]}{\delta n(\boldsymbol{r})} \equiv v(\boldsymbol{r}) + v_{\text{H}}(\boldsymbol{r}) + v_{\text{xc}}(\boldsymbol{r}) \tag{B.9}$$

in (B.7) and consider the interacting system to be a non-interacting system in an effective potential $v_{\text{eff}}(\boldsymbol{r})$. The resulting equation is called *Kohn-Sham equation.* The fact that the effective potential $v_{\text{eff}}(\boldsymbol{r})$ is a functional of the ground state density $n_0(\boldsymbol{r})$ requires us to carry out the calculation self-consistently. This self-consistent calculation is performed in the following steps:

1. Choose an initial potential $v_{\text{in}}(\boldsymbol{r})$ to be used as an approximation to the effective potential $v_{\text{eff}}(\boldsymbol{r})$ instead of $v(\boldsymbol{r})$ in the Schrödinger equation (B.7).
2. Solve the Schrödinger equation (B.7).
3. Calculate the ground state density given by (B.8).
4. Determine the Hartree-part of the new potential by solving the Poisson equation $\nabla^2 v_{\text{H}}(\boldsymbol{r}) = -4\pi e \cdot n_0(\boldsymbol{r})$ *or* by using the integral in (B.9).
5. Compute the exchange-correlation potential $v_{\text{xc}}(\boldsymbol{r})$ (how this is performed is discussed in Subsect. B.2.3).
6. Then, according to (B.9), a new approximation to the potential $v_{\text{eff}}(\boldsymbol{r})$ is obtained by $v_{\text{new}}(\boldsymbol{r}) = v_{\text{in}}(\boldsymbol{r}) + v_{\text{H}}(\boldsymbol{r}) + v_{\text{xc}}(\boldsymbol{r})$. If the new potential $v_{\text{new}}(\boldsymbol{r})$ is equal to the old one $v_{\text{in}}(\boldsymbol{r})$ to within some specified accuracy, self-consistency has been achieved. Otherwise use $v_{\text{new}}(\boldsymbol{r})$ as the new potential $v_{\text{eff}}(\boldsymbol{r})$ for the Schrödinger equation. Proceed with step 2.

In essence, (B.9) and (B.7) specify a fixed-point problem of the form

$$v_{\text{eff}}(\boldsymbol{r}) = \Phi[v_{\text{eff}}(\boldsymbol{r})] \ . \tag{B.10}$$

We assume that this problem possesses a unique solution[7] (called fixed-point), and that the iterative solution starting with $v_{\text{eff}} = v_{\text{in}}$ converges to the fixed-point, which is the

---

[7] Up to a constant.

self-consistent periodic potential $v_{\text{eff}}(\boldsymbol{r})$. This potential must be used in the Schrödinger equation (B.7) in order to get single-particle wavefunctions and energies which are appropriate for the description of *the ground state* of the many-body problem (B.1).

Note that the two conclusions (*DFT I*) and (*DFT II*) of density functional theory apply to ground state properties only. In order to develop a theory of the optical properties of a solid, we need to know the excited states in addition to the ground state. Interpreting the eigenvalues of the Kohn-Sham equation as excitation energies, however, is problematic. The ground state energy is not given by the sum of all $\epsilon_i$ over all occupied states, there are also contributions from the Hartree term and the exchange and correlation term. In the Hartree-Fock theory, the situation is similar. There, however, Koopman's theorem allows for an interpretation of the $\epsilon_i$ as excitations energies of the system. But the requirements for the validity of Koopman's theorem are not given in density functional theory. Under certain circumstances, however, we may interpret the $\epsilon_i$ as excitation energies in density functional theory also (see [B.3], Sect. VI).

### B.2.3 The local density approximation (LDA)

Step 5 in the algorithm for solving the Kohn-Sham equation discussed above requires further elaboration. The exchange and correlation energy functional $E_{\text{xc}}[n(\boldsymbol{r})]$ is still unknown.

We will assume that the contribution of an infinitesimal volume element $d^3r$ at $\boldsymbol{r}$ to the exchange and correlation energy just depends on the density at $\boldsymbol{r}$. This is called the *local density approximation* (LDA). The exchange and correlation energy functional $E_{\text{xc}}[n(\boldsymbol{r})]$ then assumes the form

$$E_{\text{xc}}[n(\boldsymbol{r})] = \int \epsilon_{\text{xc}}(n(\boldsymbol{r}))\, d^3r \ ,$$

the *exchange-correlation density* $\epsilon_{\text{xc}}(n)$ has to be obtained, for instance, from calculations based on a homogeneous electron gas (interacting electrons without periodic potential, also known as jellium model). Estimations for $\epsilon_{\text{xc}}(n)$ can be found in [B.4].

## B.3 Traditional methods for solving the Schrödinger equation

In the last sections we reduced the calculation of the ground state of the full electron-ion problem of a crystalline solid to a Schrödinger equation (B.7) for one electron moving in a lattice-periodic potential $v(\boldsymbol{r})$ (this potential corresponds to the solution $v_{\text{eff}}(\boldsymbol{r})$ of the fixed-point problem (B.10)). This equation is used for the determination of the electronic band structure. The solution of this equation is the problem which we are tackling now.

A short description of the traditional methods [B.5, B.6] for solving the problem of an electron moving in a lattice-periodic potential, that is, for the calculation of the electronic band structure enables us to put the LMTO-method into the appropriate framework. Emphasising the advantages and disadvantages of the traditional methods also allows for the specification of the properties that a better method should show.

The traditional methods can roughly be divided into methods with *fixed basis functions* and methods which work by *matching partial waves*. The first group is constituted by the plane wave method and the method of linear combination of atomic orbitals (LCAO), also called the tight-binding method. In the second group, the most important members are the cellular method, the augmented plane wave (APW) method and the Korringa-Kohn-Rostocker (KKR) method.

### B.3.1 Plane wave method

In the *plane wave method* [B.7], the wave function which is to be determined is expressed as a Fourier series (i.e., as an expansion into plane waves) which takes into account the translational symmetry of the crystal lattice. The boundary condition is the *periodic boundary condition* for the crystal. The discrete nature of the translation symmetry has the consequence that the Schrödinger equation for the wave function $\psi(\boldsymbol{r}) = \sum_{\boldsymbol{q}} c_{\boldsymbol{q}} \exp(i\boldsymbol{qr})$ couples a coefficient $c_{\boldsymbol{q}}$ to all coefficients $c_{\boldsymbol{q}+\boldsymbol{K}}$ (where $\boldsymbol{K}$ is a reciprocal lattice vector) via the Fourier component $v_{\boldsymbol{K}}$ of the periodic potential $v(\boldsymbol{r})$ in which the electron moves.

The wave functions for energies in the interesting range oscillate strongly in a region close to the ion cores and oscillate very weakly (or even decay) in the region between the ions (called *interstitial region*). Consequently, a large amount of plane waves is needed in order to get quantitatively good results.

To find a solution to this problem, we explicitly distinguish between *core electrons*, which are well localized at the lattice sites, and *valence electrons*, which also may be located in the interstitial region.

In the *orthogonalized plane wave (OPW) method* [B.7], the core electrons are described by the corresponding wave functions $\varphi_{nlm}(\boldsymbol{r})$ of the *free* atom. Taking these wave functions at each of the lattice sites $\boldsymbol{R}$, $\varphi_{nlm}(\boldsymbol{r}-\boldsymbol{R})$, wave functions which obey Bloch's theorem (i.e., transform according to an irreducible representation $\boldsymbol{k}$ of the translation group of the crystal) can be constructed. This is accomplished by the *Bloch sum* $\varphi^{\boldsymbol{k}}_{nlm}(\boldsymbol{r}) = \sum_{\boldsymbol{k}} \exp(i\boldsymbol{kR})\varphi_{nlm}(\boldsymbol{r}-\boldsymbol{R})$.

Then the plane waves which are used in the expansion of the wave functions $\psi(\boldsymbol{r})$ are orthogonalized to the core states $\psi^{\boldsymbol{k}}_{nlm}(\boldsymbol{r})$. The resulting wave functions are called *orthogonalized* plane waves and are used as a basis set of functions for solving Schrödinger's equation. By virtue of the orthogonalization to the core states, the OPWs oscillate rapidly in the core region. As a result, the OPWs are much better suited for expanding $\psi(\boldsymbol{r})$ than plane waves are. The OPW method therefore diminishes the problem with the different behavior of $\psi(\boldsymbol{r})$ close to the ion cores and in the interstitial region.

The *pseudopotential* method is based on ideas of the OPW method. The plane waves in the OPW method are replaced by the exact valence wave functions $\psi^{\mathrm{v}}_{\boldsymbol{k}}(\boldsymbol{r})$ which are written as a superposition $\phi_{\boldsymbol{k}}(\boldsymbol{r})$ of plane waves and subsequently orthogonalized to the exact core states $\psi^{\mathrm{c}}_{\boldsymbol{k}}(\boldsymbol{r})$. The superposition $\phi_{\boldsymbol{k}}(\boldsymbol{r})$ of plane waves can be determined from a Schrödinger equation with a modified potential, the *pseudopotential.* The pseudopotential is the sum of the actual periodic potential $v(\boldsymbol{r})$ and a potential $V^{\mathrm{R}}$ (see [B.5], Eq. (11.34)) which takes the difference between $\phi_{\boldsymbol{k}}(\boldsymbol{r})$ and $\psi^{\mathrm{v}}_{\boldsymbol{k}}(\boldsymbol{r})$ into account. Strictly, $V^{\mathrm{R}}$ is an operator (i.e., nonlocal), but can be approximated by a function $V^{\mathrm{R}}(\boldsymbol{r})$ (i.e., a local operator) under certain circumstances.

The method relies on the assumption that the pseudopotential does not vary as strongly as the potential $v(\boldsymbol{r})$ and, as a consequence, expanding $\phi_{\boldsymbol{k}}(\boldsymbol{r})$ into a series of plane waves should be less problematic than doing so with $\psi^{\mathrm{v}}_{\boldsymbol{k}}(\boldsymbol{r})$. To get the exact valence wave functions $\psi^{\mathrm{v}}_{\boldsymbol{k}}(\boldsymbol{r})$, the wave functions $\phi_{\boldsymbol{k}}(\boldsymbol{r})$ have to be orthogonalized to the core wave functions $\psi^{\mathrm{c}}_{\boldsymbol{k}}(\boldsymbol{r})$.

### B.3.2 Tight-binding method

The *LCAO* or *tight-binding method* is suited for the description of well localized states. It considers the periodic potential as the atomic potential of a single atom plus a perturbation which corresponds to the periodic potential minus the single atom potential. Consequently, it uses the eigenfunctions $\psi_{nlm}(\boldsymbol{r})$ of atomic orbitals (bound states) with an energy $E_{nlm}$ of the *free atom* as the fixed basis and expresses the wave function for an electron in the crystal in the form of a *Bloch sum*

$$\psi_{\boldsymbol{k}}(\boldsymbol{r}) = \sum_{\boldsymbol{R}} e^{i\boldsymbol{k}\boldsymbol{R}} \sum_{nlm} a^{\boldsymbol{k}}_{nlm} \psi_{nlm}(\boldsymbol{r} - \boldsymbol{R}) \tag{B.11}$$

To determine the coefficients $a^{\boldsymbol{k}}_{nlm}$ one either substitutes $\psi_{\boldsymbol{k}}(\boldsymbol{r})$ into the Schrödinger equation, or uses a variational technique to eventually end up with a linear eigenvalue problem of the form

$$(\hat{H}_{\boldsymbol{k}} - E_{\boldsymbol{k}} \hat{O}_{\boldsymbol{k}}) \boldsymbol{a}^{\boldsymbol{k}} = 0 \ .$$

The matrix elements of the matrices $\hat{H}_{\boldsymbol{k}}$ and $\hat{O}_{\boldsymbol{k}}$ carry indices $(nlm; n'l'm')$ of the *atomic orbitals* $\psi_{nlm}$. The matrix $\hat{H}_{\boldsymbol{k}}$ contains matrix elements of the Hamiltonian (B.7) with bound state wave functions from the same lattice site, and $\hat{O}_{\boldsymbol{k}}$ such elements with bound state wave functions from different lattice sites (*overlap integrals*).

The energies $E_{j\boldsymbol{k}}$ of the electronic states $\psi_{j\boldsymbol{k}}(\boldsymbol{r})$ (*Bloch states*) are given by the *secular equation*

$$\det(\hat{H}_{\boldsymbol{k}} - E_{j\boldsymbol{k}} \hat{O}_{\boldsymbol{k}}) = 0$$

in the form of eigenvalues of a linear eigenvalue equation.

### B.3.3 Cellular method

Instead of treating the whole crystal with the Schrödinger equation, it is also possible to just consider the potential in one primitive lattice cell and to take into account the translational invariance of the potential by a boundary condition such as, for instance, the *Bloch relation*

$$\psi_{\boldsymbol{k}}(\boldsymbol{r} + \boldsymbol{R}) = e^{i\boldsymbol{k}\boldsymbol{R}} \psi_{\boldsymbol{k}}(\boldsymbol{r}) \ . \tag{B.12}$$

Such methods are called *cellular methods*.

The *partial wave approach* of Wigner and Seitz [B.8] is a cellular method. It extends the spherical symmetry of the one-atom potential up to the boundaries of the Wigner-Seitz cell (WSc)[8] and approximates the wave functions for the problem of one isolated muffin-tin potential by

$$\psi_{lm}(E, \boldsymbol{r}) = \Theta(\boldsymbol{r}) \cdot i^l Y_{lm}(\boldsymbol{e}_{\boldsymbol{r}}) \psi_l(E, |\boldsymbol{r}|) \ .$$

---

[8] This implies that the potential is not differentiable anymore at the boundary of the WSc!

The wave functions $\psi_{\boldsymbol{k}}(\boldsymbol{r})$ of the crystal are approximated by a linear combination of partial spherical waves

$$\psi_{\boldsymbol{k}}(\boldsymbol{r}) = \sum_{\boldsymbol{R}} e^{i\boldsymbol{k}\boldsymbol{R}} \sum_{lm} b^{\boldsymbol{k}}_{lm} \psi_{lm}(E, \boldsymbol{r} - \boldsymbol{R}) \ ,$$

where $\psi_l(E, r)$ is the solution of the radial Schrödinger equation for the given potential and $\Theta(\boldsymbol{r})$ is a function which is 1 inside the WSc and vanishes outside. For a given value of $\boldsymbol{k}$, the band energies $E_j(\boldsymbol{k})$ then are the energies for which coefficients $b^{\boldsymbol{k}}_{lm}$ exist such that the wave function $\psi_{\boldsymbol{k}}(\boldsymbol{r})$ is continuous and differentiable at the WSc boundary and obeys the boundary condition (B.12). The main disadvantage of the method at hand is the difficulty to fulfill the boundary condition.

### B.3.4 Augmented plane wave (APW) method

The disadvantage of the Wigner-Seitz partial wave method is circumvented in Slater's [B.9] *augmented plane wave* (APW) method. This is also a cellular method but it uses *muffin-tin spheres.* A muffin-tin (MT) sphere is a sphere centered around a lattice atom which is completely contained in the WSc. Inside the MT sphere, the potential is approximated to have spherical symmetry, and the wave function is expanded into partial spherical waves as in the Wigner-Seitz method. Outside the MT sphere, in the *interstitial region*, the potential is approximated to be constant or only slowly varying, and the wave function is expanded into plane waves. The boundary conditions are formulated on the MT sphere, not on the boundary of the WSc. Due to the fact that the MT sphere as well as the potential inside the MT sphere are spherically symmetric, the boundary conditions are much easier to apply than in the case of the Wigner-Seitz cellular method.

### B.3.5 Korringa, Kohn, and Rostocker (KKR)

The *method of Korringa, Kohn, and Rostocker* [B.10, B.11] (KKR) requires the potential in the interstitial region to be constant. Then the Schrödinger equation can be solved exactly with phase-shifted spherical waves in this region. The boundary condition (B.12) can be formulated as complete destructive interference of the tails of all the other atoms (at $\boldsymbol{R} \neq 0$) in the MT cell of a given atom at $\boldsymbol{R} = 0$ ("*tail cancellation*").

Due to the fact that partial waves are energy-dependent, the boundary conditions for all the partial wave methods correspond to eigenvalue equations which are nonlinear in the energy, and therefore very complicated. This is the main disadvantage of the Wigner-Seitz-, the APW-, and the KKR method.

## B.4 The LMTO-method

### B.4.1 Outline

The LMTO-method [B.12] combines some of the most advantageous features of the methods presented above.

Like the KKR-method, the *LMTO-method* uses a muffin-tin potential which is constant in the region outside the muffin-tin sphere. The solutions to the Schrödinger equation for the single-muffin-tin problem, which are *partial waves*, then can be given exactly in the interstitial region, and the boundary conditions (formulated on the MT sphere) are relatively simple.

The LMTO-method uses a variational principle to finally end up with a secular equation which is used to determine the wave functions corresponding to Bloch states and the band energies of the crystal. As a basis set of functions, the states constructed with a Bloch sum (B.11) of partial waves could be used. This choice, however, has two important disadvantages.

We take a spherically symmetric potential $v(r)$ with $v(r) \to 0$ for $r \to 0$. Then the normalization of the partial waves is different (a) for bound states with $E < 0$, (b) for nonbound states with $E < 0$, and (c) for states with $E > 0$ (*scattering states*). Note that all these states have to be included in the calculation in order to be able to calculate the band structure of the crystal for arbitrary energy regimes.

The other disadvantage is related to the energy-dependence of the partial waves. The consequence of this is that the eigenvalue problem which corresponds to the secular equation is nonlinear.

The definition of the *energy-independent muffin-tin orbitals (MTO)* and their application in constructing the Bloch sum overcomes all these problems. In particular, the eigenvalue problem becomes linear (this property is the origin of the 'L' in 'LMTO').

### B.4.2 The LMTO muffin-tin potential

The construction of the energy-independent muffin-tin orbitals which are used as a basis set in the LMTO-method starts with the definition of a muffin-tin potential. The MT potential is spherically symmetric, $v_{MT}(\boldsymbol{r}) = v_{MT}(r)$. Outside of the *muffin-tin sphere*, which is centered around the ion and possesses a radius $R_{MT}$, the MT potential is constant. Therefore,

$$v(r) = \begin{cases} v_{MT}(r) + v_{MTZ} & \text{for } r \le R_{MT} \\ v_{MTZ} & \text{for } r \ge R_{MT} \end{cases}$$

with $v_{MT}(R_{MT}) = 0$. We write $\kappa^2 = E - v_{MTZ}$ for the energy (with respect to $v_{MTZ}$) of waves propagating outside the MT sphere.

### B.4.3 The partial-wave solution

Now we look for the solutions of the Schrödinger equation for an electron moving in an isolated muffin-tin potential $v_{MT}(r)$. These are given by the *partial waves*

$$\psi_{lm}(E, \boldsymbol{r}) = i^l Y_{lm}(\boldsymbol{e}_r) \cdot \psi_l(E, r) \ ,$$

where the radial wave function $\psi_l(E, r)$ is a solution of the radial Schrödinger equation

$$\left[ -\frac{d^2}{dr^2} + \frac{l(l+1)}{r^2} + v_{MT}(r) - \kappa^2 \right] r\psi_l(E, r) = 0 \ . \tag{B.13}$$

If the potential $v_{MT}(r)$ increases slower for $r \to 0$ than the term proportional to $r^{-2}$ does, then the two linearly independent solutions of (B.13) are proportional to $r^l$ and $r^{-(l+1)}$, respectively. As we are not interested in the non-analytical solution, a boundary condition for $\psi_l(E,r)$ is specified herewith: $\psi_l(E,r)$ has to be analytic at $r=0$. For an arbitrary muffin-tin potential, the radial wave function inside the muffin-tin sphere has to be determined numerically. Outside the sphere, the muffin-tin potential vanishes and (B.13) becomes the Helmholtz equation which for the case $\kappa^2>0$ (the scattering case) possesses the spherical Bessel $j_l(\kappa r)$ and Neumann $n_l(\kappa r)$ functions as linearly independent solutions. The Bessel function is $\sim r^l$ for $r\to 0$ and the Neumann function is $\sim r^{-(l+1)}$ in the same limit. Both functions are regular for $r\neq 0$. Consequently, the solution for the radial wave function outside the sphere is a linear combination of the spherical Bessel and Neumann functions, and the coefficients have to be chosen as to guarantee continuity and differentiability of the radial wave function at the MT sphere at $r=R_{MT}$. Eventually, the partial wave is given by

$$\psi_{lm}(E,\boldsymbol{r}) = i^l Y_{lm}(\boldsymbol{e}_r)\cdot\begin{cases}\psi_l(E,r) & \text{if } r\le R_{MT}\\ \kappa[n_l(\kappa r)-\cot(\eta_l)j_l(\kappa r)] & \text{if } r\ge R_{MT}\end{cases} \tag{B.14}$$

where the phase $\eta_l$ is specified by the requirement of continuity and differentiability at the muffin-tin sphere boundary. The necessary match of the values of the function at the sphere and the match of the first derivatives is usually replaced by the demand for the matching of the logarithmic derivatives (see [B.6], Eq. (5.11)).

For the case of $\kappa^2<0$ (the bound case), the solutions to the Helmholtz equation are the Hankel functions $h_l^{(1)}$ and $h_l^{(2)}$ of the first and second kind. In (B.14), the Neumann function $n_l$ has to be replaced by the Hankel function $h^{(1)}$, and the Bessel function $j_l$ has to be replaced by the Hankel function $h^{(2)}$. Clearly, these functions have the asymptotic form $\sim\exp(-|\kappa|r)/|\kappa|r$ for the first kind, and $\sim\exp(|\kappa|r)/|\kappa|r$ for the second kind, respectively. As usual, bound states are defined by the vanishing of the coefficient of the diverging function $h_l^{(2)}$ outside the muffin-tin sphere.

The scattering states ($\kappa^2>0$) given by (B.14) are normalizable to a $\delta$-function, similarly to the case of plane waves. The partial waves for $\kappa^2<0$ which are nonbound states are not normalizable due to the asymptotics of the Hankel function of second kind for $r\to\infty$, and the bound states are normalizable to unity. This diversity of normalization situations is clearly not acceptable for basis functions of a method for the determination of electronic band structures. Therefore one tries to circumvent this problem by a suitable modification of the partial waves.

### B.4.4 Muffin-tin orbitals

Let us first treat the case of states with $\kappa^2<0$ which are nonbound states. The radial wave functions diverge exponentially for $r\to\infty$ because the Bessel function $j_l(\kappa r)$ in (B.14) has to be replaced by the second kind Hankel function $h_l^{(2)}$. Therefore, a normalization is impossible. To circumvent this problem, we add the term $\kappa\cot(\eta_l)j_l(\kappa r)$ to the radial function, this yields as a result the *muffin-tin orbital* (MTO)

$$\psi_{lm}(E,\boldsymbol{r}) = i^l Y_{lm}(\boldsymbol{e}_r)\cdot\begin{cases}\psi_l(E,r)+\kappa\cot(\eta_l)j_l(\kappa r) & \text{if } r\le R_{MT}\\ \kappa n_l(\kappa r) & \text{if } r\ge R_{MT}\end{cases} \tag{B.15}$$

We call the MTO for $r<R_{MT}$ the *head* and for $r>R_{MT}$ the *tail* of the MT orbital.

The continuous and differentiable MT orbital (B.15) is still regular at the origin but decays exponentially for $r \to \infty$ in the case $\kappa^2 < 0$ for both, bound states and nonbound states. For $\kappa^2 > 0$, the muffin-tin orbital is normalizable to a $\delta$-function.

As a caveat, we stress that the muffin-tin orbital (B.15) is no longer a solution of the Schrödinger equation for the muffin-tin potential. This does not matter insofar as we are constructing eigenfunctions to the translation operators of the crystal lattice by forming *Bloch sums* according to (B.11). And the partial wave (B.14) has the same Bloch sum as the muffin-tin orbital (B.15), because the Bloch sum of spherical Bessel functions (i.e., of the difference of (B.14) and (B.15)) vanishes.[9]

The Bloch sum

$$\psi_{lm}^{\boldsymbol{k}}(\boldsymbol{r}) = \sum_{\boldsymbol{R}} e^{i\boldsymbol{k}\boldsymbol{R}} \psi_{lm}(\boldsymbol{r} - \boldsymbol{R})$$

for a point $\boldsymbol{r}$ inside an MT sphere contered at $\boldsymbol{R} = 0$ consists of an MT head (for $\boldsymbol{R} = 0$), and an infinite number of MT tails (for $\boldsymbol{R} \neq 0$). By making use of the expansion theorem[10]

$$n_L(\kappa, \boldsymbol{r} - \boldsymbol{R}) = 4\pi \sum_{L', L''} C_{LL'L''} j_{L'}(\kappa, \boldsymbol{r} - \boldsymbol{R}') n_{L''}^*(\kappa, \boldsymbol{R} - \boldsymbol{R}') \ , \tag{B.16}$$

the sum of the MT tails can be written as a sum over Bessel functions $j_l(\kappa r)$. Note that $L$ is an abbreviation for the quantum numbers $l$ and $m$.

Still the MT orbitals (B.15) are energy-dependent. The energy-dependence is removed by defining the *energy-independent muffin-tin orbitals.* This is performed in two steps. First, the relation $\kappa^2 = E - v_{MTZ}$ is ignored and $\kappa$ is regarded as a free and constant parameter. This renders the tail of the MT orbital energy-independent. The energy-dependence of the head of the MT orbital is given by its first energy derivative (denoted by a dot on top of the function)

$$\dot{\psi}_{lm}(E, \boldsymbol{r}) = i^l Y_{lm}(\boldsymbol{e}_r) \cdot \left[ \dot{\psi}_l(E, r) + \kappa \dot{\cot}(\eta_l(E)) j_l(\kappa r) \right] \ . \tag{B.17}$$

For a fixed energy $E_\nu$, the head of the muffin-tin orbital can be made energy-independent in first order of $E - E_\nu$ in the following way. The Bessel function $j_l(\kappa r)$ in the MT orbital is replaced by the *augmented Bessel function* $J_l(\kappa r)$, which is chosen such that the derivative (B.17) (with $j_l$ replaced by $J_l$) vanishes. This yields

$$J_l(\kappa r) = \begin{cases} - \left. \dfrac{\dot{\psi}_l(E, r)}{\kappa \dot{\cot}(\eta_l(E))} \right|_{E = E_\nu} & \text{for } r \leq R_{MT} \\ j_l(\kappa r) & \text{for } r \geq R_{MT} \ . \end{cases}$$

We also replace the Neumann function $n_l(\kappa r)$ by the *augmented Neumann function* $N_l(\kappa r)$ which is chosen in such a way that the expansion theorem (B.16) remains valid in the form

$$N_L(\kappa, \boldsymbol{r} - \boldsymbol{R}) = 4\pi \sum_{L', L''} C_{LL'L''} J_{L'}(\kappa, \boldsymbol{r} - \boldsymbol{R}') n_{L''}^*(\kappa, \boldsymbol{R} - \boldsymbol{R}') \ . \tag{B.18}$$

---

[9] except for $\boldsymbol{k}^2 = \kappa^2$.

[10] The coefficients $C_{LL'L''}$ are the *Gaunt coefficients* (see [B.6], (5.14)) which are closely related to the Clebsch-Gordan coefficients. The function $j_L(\kappa, \boldsymbol{r})$ is defined by $j_L(\kappa, \boldsymbol{r}) = i^l Y_{lm}(\boldsymbol{e}_r) j_l(\kappa \boldsymbol{r})$, and the function $n_L(\kappa, \boldsymbol{r})$ in a similar way.

### B.4.5 The basis set and structure constants

As in the Wigner-Seitz method, the muffin-tin orbitals and the Bloch sum are used to construct wave functions $\psi^{\boldsymbol{k}}$ from the muffin-tin orbitals such that the $\psi^{\boldsymbol{k}}$ obey Bloch's theorem:

$$\psi^{\boldsymbol{k}}_{lm}(\boldsymbol{r}) = \sum_{\boldsymbol{R}} e^{i\boldsymbol{k}\boldsymbol{R}} \psi_{lm}(\boldsymbol{r} - \boldsymbol{R}) \ . \tag{B.19}$$

The expansion theorem for the augmented Neumann functions (B.18) simplifies the Bloch sum considerably. For $\boldsymbol{r}$ inside an MT sphere, we obtain

$$\psi^{\boldsymbol{k}}_{lm}(\boldsymbol{r}) = \psi_{lm}(\boldsymbol{r}) + \sum_{l'm'} B^{\boldsymbol{k}}_{ln;l'm'} i^{l'} Y_{l'm'}(\boldsymbol{e}_{\boldsymbol{r}}) J_{l'}(\kappa \boldsymbol{r}) \ ,$$

where the *structure constants* $B^{\boldsymbol{k}}_{ln;l'm'}$ are independent of the potential $v(\boldsymbol{r})$.

The functions (B.19) are used as a basis set in a variational principle which is based on the Kohn-Sham equation. Consequently, we write the solutions of the Schrödinger equation (B.7) as linear combinations of the basis set, that is,

$$\psi^{\boldsymbol{k}}(\boldsymbol{r}) = \sum_{lm} \alpha^{\boldsymbol{k}}_{lm} \psi^{\boldsymbol{k}}_{lm}(\boldsymbol{r}) \ . \tag{B.20}$$

### B.4.6 The eigenvalue problem

In the KKR method, tail cancellation is used to determine the coefficients $\alpha^{\boldsymbol{k}}_{lm}$ in (B.20). This is different in the LMTO method, where the Rayleigh-Ritz variational principle is made use of. The Hamiltonian $H_{\mathrm{el}}$ is given by (B.7), the wave functions $|\psi\rangle$ by (B.20), and the variational principle reads

$$\delta \langle \psi | H - E | \psi \rangle = 0 \ . \tag{B.21}$$

The necessary condition for a solution of (B.21) is

$$\det \langle \psi^{\boldsymbol{k}}_{lm} | H - E | \psi^{\boldsymbol{k}}_{l'm'} \rangle 0 \ , \tag{B.22}$$

where the wavevector $\boldsymbol{k}$ is fixed: due to the translational symmetry there is no mixing of wave functions (B.20) with different $\boldsymbol{k}$. By making use of the Bloch relation (B.12), the crystal integration in (B.22) can be expressed as an integration over a single Wigner-Seitz cell. Equation (B.20) corresponds to a *linear* eigenvalue problem, the eigenvalues $E^{\boldsymbol{k}}_j$ are the band energies and the eigenvectors $\alpha^{\boldsymbol{k}}_{lm,j}$ correspond to the Bloch functions $\psi^{\boldsymbol{k}}_j(\boldsymbol{r})$ of the system.

### B.4.7 The atomic spheres approximation (ASA)

The atomic spheres approximation (ASA) comprises two different approximations. First, the energy $\kappa^2$ is set to zero in the MTO (B.15). As a consequence, the oscillating Bessel and Neumann functions in (B.15) become simple power functions.

Depending on the energy, putting $\kappa$ to zero may be a bad approximation. We can compensate partly for this by diminishing the volume of the interstitial region. In this context, the *atomic sphere* is defined as a sphere centered around an atom and possessing the same volume as the WS cell. In the ASA, the MT sphere is replaced by the atomic sphere.

The ASA increases considerably the computational speed, but also introduces errors. These can be partly overcome by introducing a perturbation potential (see [B.6], Sect. 6.2).

# Appendix C

# Group theory and the classification of elementary excitations

## C.1 Motivation. The "why?" of group theory

In solid state physics there are a lot of complicated measurable quantities (observables) which depend crucially on the symmetry of the crystal under investigation. The $3 \times 3$ *dielectric tensor* $\varepsilon_{ij}$ provides examples of such quantities. It is a symmetrical tensor and therefore consists of 6 complex independent components. Symmetries of the crystal further reduce the number of independent quantities in the dielectric tensor. To figure out the exact number of independent components in case of crystals with complicated structure is by no means a simple task.

Another interesting quantity is the 4th rank tensor $c_{\mu\nu\rho\sigma}$ representing the *elastic constants*. In triclinic systems this tensor has 21 independent real components which are reduced to only 3 in cubic materials. Group theory[1] provides the means to investigate these questions systematically.

Group theory is also used to classify and characterize the various crystal structure and plays a very important role in the classification of electronic and vibrational states in crystals. In doing so it detects and explains symmetry-caused degeneracies of states. Last but not least, group theory is used to eludicate selections rules for light absorption and Raman scattering among other things.

## C.2 Definition of a group. Basic properties

**Groups.** A *group* $\mathcal{G}$ is a set of elements $\mathcal{G} = \{G_1, \ldots, G_g\}$ together with a mapping $\circ \colon \mathcal{G} \times \mathcal{G} \to \mathcal{G}$ called *group multiplication*. The latter satisfies the following *group axioms*:

*(A) Associativity:* For all $A, B, C \in \mathcal{G}$:

$$A \circ (B \circ C) = (A \circ B) \circ C$$

---

[1] Introductions to group theory are given in [C.1, C.2, C.3, C.4, C.5].

| $\boldsymbol{C}_{3v}$ | $E$ | $C_3$ | $C_3^{-1}$ | $\sigma_1$ | $\sigma_2$ | $\sigma_3$ |
|---|---|---|---|---|---|---|
| $E$ | $E$ | $C_3$ | $C_3^{-1}$ | $\sigma_1$ | $\sigma_2$ | $\sigma_3$ |
| $C_3$ | $C_3$ | $C_3^{-1}$ | $E$ | $\sigma_3$ | $\sigma_1$ | $\sigma_2$ |
| $C_3^{-1}$ | $C_3^{-1}$ | $E$ | $C_3$ | $\sigma_2$ | $\sigma_3$ | $\sigma_1$ |
| $\sigma_1$ | $\sigma_1$ | $\sigma_2$ | $\sigma_3$ | $E$ | $C_3$ | $C_3^{-1}$ |
| $\sigma_2$ | $\sigma_2$ | $\sigma_3$ | $\sigma_1$ | $C_3^{-1}$ | $E$ | $C_3$ |
| $\sigma_3$ | $\sigma_3$ | $\sigma_1$ | $\sigma_2$ | $C_3$ | $C_3^{-1}$ | $E$ |

Table C.1: Multiplication table of the group $\boldsymbol{C}_{3v}$. The table entries are $a \circ b$, where $a$ is given in the first row, and $b$ is given in the first column of the table.

*(N)* *Existence of a neutral element* (also *unit element* or *identity element*): There is an element $E \in \mathcal{G}$ such that for each $G \in \mathcal{G}$:

$$E \circ G = G \circ E = G$$

*(I)* *Existence of an inverse element*: For each $G \in \mathcal{G}$ there is an element $G^{-1} \in \mathcal{G}$ such that

$$G \circ G^{-1} = G^{-1} \circ G = E$$

If in addition to these three axioms[2] also the commutativity holds, then the group is called a *commutative* or *Abelian group*:

*(C)* *Commutativity:* For all $A, B \in \mathcal{G}$:

$$A \circ B = B \circ A$$

If a group has a finite number of elements it is called a *finite group*, otherwise it is an *infinite group*. The number of elements $g$ of a finite group $\mathcal{G}$ is called the *order of the group.*

**Example: $\boldsymbol{C}_{3v}$.** A very instructive example of a group is the group of symmetry operations of an equilateral triangle (see Fig. C.1). These symmetry operations are rotations by 0°, 120°, and 240° (denoted by $E$, $C_3$ and $C_3^{-1}$, latter is the inverse element of $C_3$) with rotation axis perpendicular to the triangle through its center $C$. The reflections at planes perpendicular to the triangle and passing through an edge and the center of the side opposite to it are also symmetry operations, we denote these by $\sigma_1$, $\sigma_2$, and $\sigma_3$ (see Fig. C.1). These symmetry operations of the triangle form the group $\boldsymbol{C}_{3v} = \{E, C_3, C_3^{-1}, \sigma_1, \sigma_2, \sigma_3\}$, the multiplication is defined by means of successive application of the symmetry operations; it is tabulated in the *multiplication table* of the group $\boldsymbol{C}_{3v}$ in Tab. C.1.

The multiplication table maps each pair of group elements to another group element and therefore represents the mapping $\circ\colon \mathcal{G} \times \mathcal{G} \to \mathcal{G}$. Associativity holds. The group element $E$ is the unit element and the fact that $E$ appears exactly once in every column and row of the multiplication table shows that every element of the group has one and only one inverse

---

[2] Actually, in $(N)$ only $E \circ G = G$ is an axiom. The property $G \circ E = G$ is a consequence of this is the other axioms. This is similar for $(I)$. See [C.1].

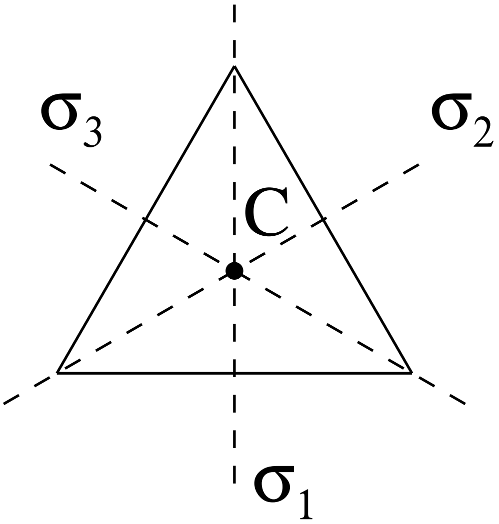

Figure C.1: Mirror planes of an equilateral triangle.

element. Furthermore note that $\sigma_1\sigma_2 = C_3$, but $\sigma_2\sigma_1 = C_3^{-1}$, that is, the group is not commutative (not Abelian).

**Subgroups.** By inspecting the multiplication table, it can be seen that the subset

$$\boldsymbol{C}_3 = \{E, C_3, C_3^{-1}\}$$

of the group $\boldsymbol{C}_{3v}$ is a group of its own. (Note that the group itself and one of its elements both are denoted by the symbol $C_3$ in the literature. Usually it is clear from the context, whether the group or the symmetry operation is meant. To remove any ambiguity we denote the groups using boldface letters). A subset $\mathcal{H}$ of a group $\mathcal{G}$ which is also a group with respect to the multiplication in $\mathcal{G}$ is called a *subgroup* of $\mathcal{G}$. The subsets $\{E\}$ containing just the unit element of $\mathcal{G}$, and the "subset" $\mathcal{G}$ consisting of the full group $\mathcal{G}$ are the *trivial subgroups* of $\mathcal{G}$, all other subgroups are called *proper subgroups*. The group $\boldsymbol{C}_3$ has an interesting property. By applying $C_3$ repeatedly, all the group elements of $\boldsymbol{C}_3$ can be generated: $C_3 \circ C_3 = C_3^{-1}$ and $C_3 \circ C_3 \circ C_3 = E$ (Tab. C.2, left panel). Therefore, $\boldsymbol{C}_3$ is called a *cyclic group* and the symmetry operation $C_3$ its *generating element*. Obviously, cyclic groups are always commutative (Abelian).

**Isomorphism.** Consider now the set $\mathbb{C}_3$ consisting of the three third roots of one, 1, $\alpha \equiv \exp(\frac{2\pi}{3}i)$, and $\alpha^2 \equiv \exp(\frac{4\pi}{3}i)$ with the complex multiplication as mapping (Tab. C.2, right panel). This set forms a group. It is cyclic and of order 3 just as the group $\boldsymbol{C}_3$. Furthermore its multiplication table shows exactly the same structure as that of the $\boldsymbol{C}_3$ group (Table C.2). The groups $\boldsymbol{C}_3$ and $\mathbb{C}_3$ are therefore called *isomorphic groups*. If a mapping $f\colon \mathcal{G} \to \mathcal{G}'$ exists between two groups $\mathcal{G}$ and $\mathcal{G}'$ that maps the elements $G \in \mathcal{G}$ to the elements $G' \in \mathcal{G}'$, that is, $G' = f(G)$, and has the property

$$f(G_iG_j) = f(G_i)f(G_j)$$

for arbitrary elements $G_i, G_j \in \mathcal{G}$, then the mapping $f$ is called a *homomorphism* and the groups $\mathcal{G}$ and $\mathcal{G}'$ are called *homomorphic*, $\mathcal{G} \sim \mathcal{G}'$. The mapping $f\colon \boldsymbol{C}_3 \to \mathbb{C}_3$ given by

| $\boldsymbol{C}_3$ | $E$ | $C_3$ | $C_3^{-1}$ |
|---|---|---|---|
| $E$ | $E$ | $C_3$ | $C_3^{-1}$ |
| $C_3$ | $C_3$ | $C_3^{-1}$ | $E$ |
| $C_3^{-1}$ | $C_3^{-1}$ | $E$ | $C_3$ |

| $\mathbb{C}_3$ | $1$ | $\alpha$ | $\alpha^2$ |
|---|---|---|---|
| $1$ | $1$ | $\alpha$ | $\alpha^2$ |
| $\alpha$ | $\alpha$ | $\alpha^2$ | $1$ |
| $\alpha^2$ | $\alpha^2$ | $1$ | $\alpha$ |

Table C.2: Multiplication tables of the groups $\boldsymbol{C}_3$ and $\mathbb{C}_3$.

$f(E) = 1$, $f(C_3) = \alpha$, and $f(C_3^{-1}) = \alpha^2$ has these properties but, in addition, the mapping is a one-to-one correspondence between the elements of the groups $\mathcal{G}$ and $\mathcal{G}'$. This is why such mapping is usually called an *isomorphism* and the groups are called *isomorphic*. Isomorphic groups can be considered equal, mathematically they have the same structure.

The definitions introduced so far are sufficient for an understanding of most of the theory of representations of *point groups*. In order to discuss the symmetry properties of *space groups* we need to introduce the following additional definitions and properties of groups.

**Cosets.** Let us come back to the $\boldsymbol{C}_{3v}$ group. The subset $\mathcal{H} = \{E, \sigma_1\}$ of $\boldsymbol{C}_{3v}$ is a subgroup of $\boldsymbol{C}_{3v}$, called $\boldsymbol{C}_s$. We can construct other subsets of $\boldsymbol{C}_{3v}$, the so-called *right cosets* by multiplying all elements of the subgroup $\mathcal{H}$ of $\mathcal{G}$ with a fixed element $G \in \mathcal{G}$ on the right,

$$\mathcal{H}G \equiv \{HG \mid H \in \mathcal{H}\} \ .$$

The element $G \in \mathcal{G}$ is called the *coset representative* of the coset $\mathcal{H}$.

The right cosets of $\boldsymbol{C}_{3v}$ are $\mathcal{H}\sigma_2 = \{\sigma_2, C_3\}$ and $\mathcal{H}\sigma_3 = \{\sigma_3, C_3^{-1}\}$ (note that $\mathcal{H}C_3 = \{C_3\sigma_2\} = \mathcal{H}\sigma_2$ etc.). The conjunction of the elements of the three cosets $\mathcal{H}$, $\mathcal{H}\sigma_2$, and $\mathcal{H}\sigma_3$ together contains all the elements of the group $\boldsymbol{C}_{3v}$. The relation

$$\boldsymbol{C}_{3v} = \mathcal{H} + \mathcal{H}\sigma_2 + \mathcal{H}\sigma_3 \ , \quad \mathcal{H} = \{E, \sigma_1\}$$

is called the *decomposition of* $\boldsymbol{C}_{3v}$ *into right cosets* with respect to the subgroup $\mathcal{H}$. Another right coset decomposition of $\boldsymbol{C}_{3v}$ is the one with respect to the subgroup $\boldsymbol{C}_3$, given by

$$\boldsymbol{C}_{3v} = \boldsymbol{C}_3 + \boldsymbol{C}_3\sigma_1 \ , \quad \boldsymbol{C}_3 = \{E, C_3, C_3^{-1}\} \ .$$

The definition of *left cosets* and the *decomposition into left cosets* is analogous to the one given above for right cosets. Note that two cosets $\mathcal{H}A$ and $\mathcal{H}B$ for $A, B \in \mathcal{G}$ are either identical or do not contain any common elements (they are *disjunct sets*).

Let $g$ and $h$ denote the order of the group $\mathcal{G}$ and its subgroup $\mathcal{H}$, respectively, and $l$ the number of cosets in the coset decomposition of $\mathcal{G}$ with respect to $\mathcal{H}$, called the *index* of $\mathcal{H}$ in $\mathcal{G}$. Then the relation $g = hl$ holds. An interesting consequence of this relationship is that a group with prime order does not have proper subgroups.

**Conjugate classes.** For the theory of representations of a group, the central part of this chapter, the notion of the *conjugate classes* is important. We define a relation on the group $\mathcal{G}$. Two elements $A$ and $B$ of $\mathcal{G}$ are called *conjugate*, if there exists an element $G$ of $\mathcal{G}$ such that $B = GAG^{-1}$. We represent conjugation of two elements as $A \sim B$, explicitly

$$A \sim B \quad \text{if and only if there is a } G \in \mathcal{G} \text{ such that} \quad A = GBG^{-1} \ . \tag{C.1}$$

| $G\mathcal{H}G^{-1}$ | $\mathcal{H}=\{E\}$ | $\mathcal{H}=\{E,\sigma_1\}$ | $\mathcal{H}=\{E,C_3,C_3^{-1}\}$ |
|---|---|---|---|
| $E$ | $\{E\}$ | $\{E,\sigma_1\}$ | $\{E,C_3,C_3^{-1}\}$ |
| $C_3$ | $\{E\}$ | $\{E,\sigma_2\}$ | $\{E,C_3,C_3^{-1}\}$ |
| $C_3^{-1}$ | $\{E\}$ | $\{E,\sigma_3\}$ | $\{E,C_3,C_3^{-1}\}$ |
| $\sigma_1$ | $\{E\}$ | $\{E,\sigma_1\}$ | $\{E,C_3,C_3^{-1}\}$ |
| $\sigma_2$ | $\{E\}$ | $\{E,\sigma_3\}$ | $\{E,C_3,C_3^{-1}\}$ |
| $\sigma_3$ | $\{E\}$ | $\{E,\sigma_2\}$ | $\{E,C_3,C_3^{-1}\}$ |

Table C.3: Conjugate classes of some subgroups of $\boldsymbol{C}_{3v}$.

The properties of the conjugation are the *reflectivity (r)* which states that $A \sim A$, then the *symmetry (s)* implying $A \sim B$ if $B \sim A$, and the *transitivity (t)* which expresses the fact that if $A \sim B$ and $B \sim C$ ($C \in \mathcal{G}$), then $A \sim C$ holds. These are the axioms of a *relation*. Relations decompose sets into *disjunct subsets* called *classes*. The decomposition of sets into classes is called *classification* of the set with respect to the given relation. The group $\boldsymbol{C}_{3v}$ decomposes into the three classes

$$\mathcal{C}_1 = \{E\}\ , \quad \mathcal{C}_2 = \{C_3, C_3^{-1}\}\ , \quad \text{and} \quad \mathcal{C}_3 = \{\sigma_1, \sigma_2, \sigma_3\}$$

containing the unit element, the rotations, and the reflections, respectively.

The coset decomposition and the classification of groups are two methods to decompose groups into disjunct subsets the composition of which covers the whole group.

Now we construct the sets

$$G\mathcal{H}G^{-1} = \{GHG^{-1}\colon H \in \mathcal{H}\}$$

for a *fixed* element $G \in \mathcal{G}$. These sets turn out to be subgroups of $\mathcal{G}$, and are called *conjugate subgroups* of $\mathcal{H}$. The conjugate subgroups of the trivial subgroup $\{E\}$ as well as the proper subgroup $\boldsymbol{C}_s = \{E, \sigma_1\}$, and $\boldsymbol{C}_3 = \{E, C_3, C_3^{-1}\}$ of $\boldsymbol{C}_{3v}$ with respect to a element $G \in \mathcal{G}$ are given in Tab. C.3. The conjugate subgroups of the trivial subgroup $\{E\}$ and $\boldsymbol{C}_3$ are the subgroups themself. This leads to the definition of the invariant subgroups.

**Invariant subgroups.** If all the conjugate elements to each element of the subgroup $\mathcal{H}$ of $\mathcal{G}$ are contained in $\mathcal{H}$, that is, if $G\mathcal{H}G^{-1} \in \mathcal{H}$ is fulfilled for *all* $G \in \mathcal{G}$, we call $\mathcal{H}$ an *invariant subgroup* of $\mathcal{G}$, also *normal divisor* (“Normalteiler” in German) or *normal subgroup*. In this case, $\mathcal{H}$ is composed out of classes of $\mathcal{G}$. The invariant subgroups of $\boldsymbol{C}_{3v}$ are the trivial ones, $\{E\}$ and $\mathcal{G}$, as well as the proper subgroup $\boldsymbol{C}_3 = \mathcal{C}_1 \cup \mathcal{C}_2$ (see Tab. C.3). Note that $G\mathcal{H}G^{-1} \in \mathcal{H}$ implies $G\mathcal{H}G^{-1} = \mathcal{H}$ which also can be written in the form $G\mathcal{H} = \mathcal{H}G$ and expresses the fact that for invariant subgroups $\mathcal{H}$ left and right cosets are identical and therefore the left and right coset decompositions are equivalent.

Using the notation of invariant subgroups, we can define new groups, the *factor groups*. Consider a group $\mathcal{G}$ of order $g$ and an invariant subgroup $\mathcal{N}$ of $\mathcal{G}$ of order $n$. The coset decomposition is

$$\mathcal{G} = \mathcal{N}E + \mathcal{N}G_2 + \cdots + \mathcal{N}G_l\ , \quad G_i \in \mathcal{G}$$

| $\boldsymbol{C}_{3v}/\boldsymbol{C}_3$ | $\boldsymbol{C}_3$ | $\boldsymbol{C}_3\sigma_1$ |
|---|---|---|
| $\boldsymbol{C}_3$ | $\boldsymbol{C}_3$ | $\boldsymbol{C}_3\sigma_1$ |
| $\boldsymbol{C}_3\sigma_1$ | $\boldsymbol{C}_3\sigma_1$ | $\boldsymbol{C}_3$ |

Table C.4: Multiplication table of the factor group $\boldsymbol{C}_{3v}/\boldsymbol{C}_3$.

with $l = g/n$. For two cosets $\mathcal{N}A$ and $\mathcal{N}B$ with $A, B \in \mathcal{G}$ a multiplication can be defined by[3]

$$\mathcal{N}A \cdot \mathcal{N}B \equiv \{NANB\colon M, N \in \mathcal{N}\} \ .$$

It can easily be seen that this set is the coset represented by $AB$, that is,

$$\mathcal{N}A \cdot \mathcal{N}B = \mathcal{N}(AB)$$

and, consequently, the product of two cosets is also a coset. The cosets of a coset decomposition with respect to an invariant subgroup form a group under the multiplication defined above. This group is called the *factor group* (or *quotient group*) of $\mathcal{G}$ with respect to the invariant subgroup $\mathcal{N}$, denoted by $\mathcal{G}/\mathcal{N}$. (This notation motivates the name *normal divisor* for an invariant subgroup).

As an example we mention the coset decomposition of the group $\boldsymbol{C}_{3v}$ with respect to its invariant subgroup $\boldsymbol{C}_3$,

$$\boldsymbol{C}_{3v} = \boldsymbol{C}_3 + \boldsymbol{C}_3\sigma_1$$

which defines the factor group $\boldsymbol{C}_{3v}/\boldsymbol{C}_3$. This is a group of order 2 (and therefore cyclic, commutative and isomorphic to the group $\{1, -1\}$ with real number multiplication). The multiplication table is given in Tab. C.4.

**Direct product.** We can do the other way around and construct "larger" groups by using the *direct product*. Given two groups $\mathcal{G} = \{G\}$ and $\mathcal{G}' = \{G'\}$ of order $g$ and $g'$ and a commutative multiplication $GG' = G'G$. Then the $gg'$ pairs $GG'$ form a group called the *direct product group* $\mathcal{G} \times \mathcal{G}'$.

## C.3 An important example for HTCS's: The tetragonal $\boldsymbol{D}_{4h}$ group

We start by describing the tetragonal $\boldsymbol{D}_4$ group which turns out to be a subgroup of $\boldsymbol{D}_{4h}$, namely the group of all *proper* rotations of $\boldsymbol{D}_{4h}$. This group contains a four-fold rotation axis $(E, C_4, C_2, C_4^{-1})$ and perpendicular to it four two-fold axes $(C_{2x}, C_{2x'}, C_{2y}, C_{2y'})$ which are the symmetry operations of the object in Fig. C.2, left panel and is of order 8. The multiplication table is given in Tab. C.5.

Next the classes are determined. The symmetry operation $E$ forms its own class as the operation $C_2$ does. The $C_4$ and $C_4^{-1}$ operations form the class called $2C_4$. The $C_{2x}$ and $C_{2y}$ operations constitute the class $2C_2'$ and the $C_{2x'}$ and $C_{2y'}$ operations constitute the class $2C_2''$. Therefore the $\boldsymbol{D}_4$ group has a total number of $n_c = 5$ classes.

---

[3] repeated elements in $\{NANB\colon M, N \in \mathcal{N}\}$ are considered to be removed.

| $\boldsymbol{D}_4$ | $E$ | $C_4$ | $C_2$ | $C_4^{-1}$ | $C_{2x}$ | $C_{2y}$ | $C_{2x'}$ | $C_{2y'}$ |
|---|---|---|---|---|---|---|---|---|
| $E$ | $E$ | $C_4$ | $C_2$ | $C_4^{-1}$ | $C_{2x}$ | $C_{2y}$ | $C_{2x'}$ | $C_{2y'}$ |
| $C_4$ | $C_4$ | $C_2$ | $C_4^{-1}$ | $E$ | $C_{2x'}$ | $C_{2y'}$ | $C_{2y}$ | $C_{2x}$ |
| $C_2$ | $C_2$ | $C_4^{-1}$ | $E$ | $C_4$ | $C_{2y}$ | $C_{2x}$ | $C_{2y'}$ | $C_{2x'}$ |
| $C_4^{-1}$ | $C_4^{-1}$ | $E$ | $C_4$ | $C_2$ | $C_{2y'}$ | $C_{2x'}$ | $C_{2x}$ | $C_{2y}$ |
| $C_{2x}$ | $C_{2x}$ | $C_{2y'}$ | $C_{2y}$ | $C_{2x'}$ | $E$ | $C_2$ | $C_4^{-1}$ | $C_4$ |
| $C_{2y}$ | $C_{2y}$ | $C_{2x'}$ | $C_{2x}$ | $C_{2y'}$ | $C_2$ | $E$ | $C_4$ | $C_4^{-1}$ |
| $C_{2x'}$ | $C_{2x'}$ | $C_{2x}$ | $C_{2y'}$ | $C_{2y}$ | $C_4$ | $C_4^{-1}$ | $E$ | $C_2$ |
| $C_{2y'}$ | $C_{2y'}$ | $C_{2y}$ | $C_{2x'}$ | $C_{2x}$ | $C_4^{-1}$ | $C_4$ | $C_2$ | $E$ |

Table C.5: Multiplication table of the group $\boldsymbol{D}_4$.

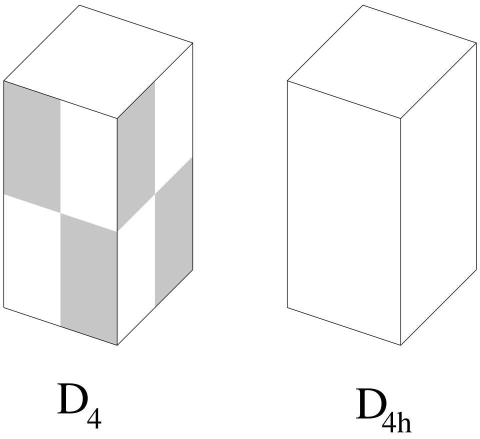

Figure C.2: The tetragonal $\boldsymbol{D}_4$ and $\boldsymbol{D}_{4h}$ point groups.

Each of the 5 two-fold rotations forms together with the identity $E$ a subgroup of order 2 of the $\boldsymbol{D}_4$ group. All these 5 subgroups are isomorphic to the group $\boldsymbol{C}_2 = \{E, C_2\}$. Furthermore, there are three subgroups of order 4. These are the groups $\boldsymbol{D}_2 = \{E, C_2, C_{2x}, C_{2y}\}$, the group $\{E, C_2, C_{2x'}, C_{2y'}\}$ which is isomorphic to $\boldsymbol{D}_2$, and the cyclic group $\boldsymbol{C}_4 = \{E, C_4, C_2, C_4^{-1}\}$. The five subgroups of order 2 and the latter 3 subgroups of order 4 exhaust the number of proper subgroups of $\boldsymbol{D}_4$. Invariant subgroups are subgroups which consist of classes. The subgroups $\boldsymbol{C}_2$, $\boldsymbol{C}_4$ and $\boldsymbol{D}_2$ are the invariant (proper) subgroups of $\boldsymbol{D}_4$, their decomposition in classes is given by

$$\begin{aligned}
\boldsymbol{C}_2 &= E \cup 2C_2 \\
\boldsymbol{C}_4 &= E \cup 2C_4 \cup C_2 \\
\boldsymbol{D}_2 &= E \cup C_2 \cup 2C_2' \; .
\end{aligned}$$

Using these 3 classes to perform a coset decomposition of $\boldsymbol{D}_4$, we get

$$\begin{aligned}
\boldsymbol{D}_4 &= \boldsymbol{C}_4 + \boldsymbol{C}_4 C_{2x} \\
\boldsymbol{D}_4 &= \boldsymbol{D}_2 + \boldsymbol{D}_2 C_4 \\
\boldsymbol{D}_4 &= \boldsymbol{C}_2 + \boldsymbol{C}_2 C_4 + \boldsymbol{C}_2 C_{2x} + \boldsymbol{C}_2 C_{2x'}
\end{aligned}$$

and the factor groups $\boldsymbol{D}_4/\boldsymbol{C}_4$, $\boldsymbol{D}_4/\boldsymbol{D}_2$, and $\boldsymbol{D}_4/\boldsymbol{C}_2$. The first two are isomorphic to the group $\boldsymbol{C}_2$, the last one is isomorphic to the group $\boldsymbol{C}_4$.

## C.4 Representations of a group

With respect to applications, especially calculations with a computer, it is very handy to have a one-to-one correspondence between an abstract group under consideration, and a group of matrices, consisting of real or complex numbers, which "shares some properties" with the former group. These correspondences are investigated in the theory of group representations.

**Representations.** Let $\mathcal{G}$ be a finite group of order $g$ and $\mathcal{M}$ the set of non-singular complex $n \times n$ square matrices, which, taking the matrix multiplication as the group multiplication, constitute a group called the *complex general linear group of order* $n$, denoted $GL(n, \mathbb{C})$. Furthermore let $D\colon \mathcal{G} \to \mathcal{M}$ be a mapping with the property of being *homomorphic*, that is,

$$AB = C \quad \Rightarrow \quad \hat{D}(A)\hat{D}(B) = \hat{D}(C) \tag{C.2}$$

for $A, B, C \in \mathcal{G}$. Then, the set $\mathcal{M} = \{\hat{D}(G)\colon G \in \mathcal{G}\}$ of matrices is called a *representation* of the group $\mathcal{G}$. The *dimension* $d_\alpha$ of a representation $\alpha$ is the size $n$ of the matrices.

Putting $A = E$ or $C = E$, respectively, in the former equation, we immediately see that $\hat{D}(E) = \hat{1}$, the unit element of $\mathcal{G}$ is represented by the unit matrix. Moreover, $\hat{D}(A^{-1}) = \hat{D}(A)^{-1}$, that is, the matrix representing the inverse of a group element is the inverse of the matrix representing the group element itself.

If the mapping $\hat{D}$ is *isomorphic*, that is, homomorphic but one-to-one in both directions, then the representation is called *faithful.* Each group has a trivial representation, the *identity representation* given by the "$1 \times 1$ matrix" $\hat{D}(G) = 1$ for all $G \in \mathcal{G}$. If the order of $\mathcal{G}$ is larger than 1, then this representation is obviously a homomorphism, not an isomorphism.

**Example.** To clarify the definitions and properties given, the point group $\boldsymbol{C}_4$ consisting of a single 4-fold rotation axis will serve. This is a cyclic group (and therefore Abelian) of order 4 with the elements $E$, $C_4$, $C_2$, and $C_4^{-1}$ and is a subgroup of $\boldsymbol{D}_4$ (see Tab. C.5). It is easy to see, that the $2 \times 2$ rotation matrices with rotations by 0, $\pi/2$, $\pi$, and $3\pi/2$ constitute a representation of the group $\boldsymbol{C}_4$:

$$\begin{aligned} \hat{D}(E) &= \begin{pmatrix} 1 & 0 \\ 0 & 1 \end{pmatrix} , & \hat{D}(C_4) &= \begin{pmatrix} 0 & -1 \\ 1 & 0 \end{pmatrix} , \\ \hat{D}(C_2) &= \begin{pmatrix} -1 & 0 \\ 0 & -1 \end{pmatrix} , & \hat{D}(C_4^{-1}) &= \begin{pmatrix} 0 & 1 \\ -1 & 0 \end{pmatrix} . \end{aligned} \tag{C.3}$$

This representation is faithful and also a *unitary representation*, because all constituent matrices are unitary. Instead of doing calculations using the elements $G$ of the group $\mathcal{G}$, we can use, for many purposes, the representation matrices $\hat{D}(G)$.

**Equivalent representations.** Given a representation $D_1$, we can easily construct others. One method is to take the matrices $\hat{D}_2(G) = \hat{M}^{-1}\hat{D}_1(G)\hat{M}$ for all $G$ in $\mathcal{G}$ and for a given non-singular matrix $\hat{M}$. It is easy to show that this set $\{\hat{D}_2(G)\colon G \in \mathcal{G}\}$ is also a representation of the group $\mathcal{G}$ isomorphic to $D_1$. As a consequence, a group has an infinite number of representations, most of them generated in a trivial way from others. To get rid of the seeming redundancy, we define an *equivalence relation* which relates representations which can be generated from each other in a trivial way. This relation decomposes the set of all representations into equivalence classes. Afterwards, we only consider these equivalence classes.

Two representation $\hat{D}_1$ and $\hat{D}_2$ are called *equivalent*, if there is a non-singular matrix $\hat{M}$ such that

$$\hat{D}_1(G) = \hat{M}^{-1}\hat{D}_2(G)\hat{M} , \qquad \text{for all } G \in \mathcal{G}. \tag{C.4}$$

Two representations which are not equivalent are called *inequivalent.*

**Direct sum.** Another method to construct new representation from existing ones is to form the set of diagonal matrices $\hat{D}(G) = \mathrm{diag}(\hat{D}_1(G), \hat{D}_2(G))$ from two representations $D_1$ and $D_2$ which also is a representation and called the *direct sum* $D = D_1 + D_2$ of the representation $D_1$ and $D_2$. For a representation to be used in a calculation, is should be as simple as possible, so we will investigate whether it is possible to decompose a given representation into the direct sum of two or more representations. This is the central aim of the theory of group representations.

A representation which has the property that all of its representation matrices $\hat{D}$ can be written in the block form

$$\hat{D} = \begin{pmatrix} \hat{A} & \hat{0} & \hat{0} & \cdots \\ \hat{0} & \hat{B} & \hat{0} & \cdots \\ \hat{0} & \hat{0} & \hat{C} & \cdots \\ \vdots & \vdots & \vdots & \ddots \end{pmatrix}$$

with blocks of the same size for all matrices of the representation is called a *reducible representation.* The reduction of a given reducible representation into irreducible representations is assisted by a number of important theorems stated in the next section.

## C.5 Theorems about representations

If a crystal possesses a certain point group symmetry $\mathcal{G}$, then the Hamiltonian of the crystal (in absence of external fields and strong spin-orbit coupling) is invariant with respect to this group. Two electronic wave functions (with quasimomentum $\boldsymbol{k} = 0$) which are related by the transformation given by a group element therefore have the same energy eigenvalue, they are degenerate. The same is true for $\boldsymbol{k} = 0$ vibrational patterns. If there is no accidental degeneracy, the wave functions (or vibrational patterns) which belong to a given energy eigenvalues can be classified according to irreducible representations of the point group $\mathcal{G}$. Irreducible representations on the other hand are classified using their characters. This classification is contained in character tables, which are constructed by applying the theorems to be presented in this section. Proofs in general will be omitted, in this case references will be given.

*Unitarization of a representation:* Every representation of a finite group is equivalent to a unitary representation.

This is a very important theorem, with many consequences. As an example consider a 1-dimensional representation. The latter theorem implies that the $1 \times 1$ matrices of the representation can all be taken to have absolute value 1, that is, can be written in the form $\exp(i\varphi)$. In addition, this theorem allows us to consider only unitary representations. From now on, we only consider *unitary, inequivalent, and irreducible representations (IRs).*[4]

**Characters.** The *character* $\chi^{(D)}(G)$ of a group element $G \in \mathcal{G}$ with respect to an IR $D$ is given by the trace of the representation matrix $\hat{D}(G)$,

$$\chi(G) = \mathrm{Tr}\, \hat{D}(G) = \sum_{i=1}^{d_D} D_{ii}(G) \ ,$$

where $d_D$ is the dimension of the representation $D$. Because of the property $\chi(\hat{M}\hat{D}\hat{M}^{-1}) = \chi(\hat{D})$, the character of a group element $G$ is the same for all equivalent representations. The set of characters $\{\chi^{(D)}(G)\colon G \in \mathcal{G}\}$ is called the *character of the representation* $D$ (and all equivalent ones).

The characters of the representation (C.3) of $\boldsymbol{C}_4$ are

$$\chi(E) = 2 \ , \quad \chi(C_4) = 0 \ , \quad \chi(C_4^2) = -2 \ , \quad \chi(C_4^{-1}) = 0 \ .$$

Note that the character of the unit element $E$ with respect to an IR $D$ is the dimension $d_D$ of the IR. It gives the essential degeneracy of states belonging to $D$.

We have seen that two elements $A, B \in \mathcal{G}$ are conjugated if an element $G \in \mathcal{G}$ exists, such that $A = GBG^{-1}$. For the IR $D$ then $\hat{D}(A) = \hat{D}(G)\hat{D}(B)\hat{D}(G^{-1})$ is valid and because of $\hat{D}(G^{-1}) = \hat{D}(G)^{-1}$ and the property $\mathrm{Tr}(ABC) = \mathrm{Tr}(CAB)$ of the trace of matrices, the character of $A$ is equal to that of $B$. Consequently the character of all group elements belonging to the same class is the same.

The character of an IR is its characteristic feature and can be used to identify the (inequivalent) IRs of a group. To determine the characters of the IRs of a group, some theorems are useful.

---

[4] In the literature, unitary, inequivalent, and irreducible representations are usually abbreviated by "REP." We use the abbreviation "IR" to stress the property of *irreducibility*.

*Dimensions of the IRs:* The dimensions $d_D$ of the IRs of a group $\mathcal{G}$ of order $g$ obey the relation

$$\sum_D d_D^2 = g \; . \tag{C.5}$$

This is a very useful theorem; for groups with small $g$ the dimensions $d_D$ of all IRs can often be determined already by inspection of (C.5). The $\boldsymbol{C}_4$ group is of order $g = 4$. One IR is the trivial one of dimension $d = 1$. Only $1^2 + 1^2 + 1^2 + 1^2 = 4$ satisfies (C.5) and, consequently, the $\boldsymbol{C}_4$ group has 4 IRs of dimension 1 each. The representation given in (C.3) is therefore reducible.

*First Orthogonality of Characters:* The characters of an irreducible representation of a finite group satisfy the orthogonality relation

$$\sum_{i=1}^{n_c} h_i \chi^{(\alpha)}(\mathcal{C}_i)^* \chi^{(\beta)}(\mathcal{C}_i) = g\delta_{\alpha\beta} \; , \tag{C.6}$$

the summation runs over all $n_c$ classes $\mathcal{C}_i$ of group elements, $\chi^{(\alpha)}(\mathcal{C})$ denotes the character of a group element $G$ of class $\mathcal{C}$ in the representation $D^{(a)}$.

*Second Orthogonality of Characters:* The characters of an irreducible representation of a finite group satisfy the orthogonality relation

$$\sum_{\alpha=1}^{n_r} \chi^{(\alpha)}(\mathcal{C}_i)^* \chi^{(\beta)}(\mathcal{C}_j) = \frac{g}{h_i}\delta_{ij} \; , \tag{C.7}$$

the summation runs over all $n_r$ IRs of the group and $h_i$ is the number of group elements contained in the same class as $G_i$.

Characters $\chi^{(\alpha)}(\mathcal{C})$ of irreducible representations are functions of the representations $D^{(\alpha)}$, $\alpha = 1 \ldots n_r$ and the class $\mathcal{C}_i$ of elements of the group, $i = 1 \ldots n_c$.

*Number of IRs:* The number $N_r$ of inequivalent irreducible representations of a finite group $\mathcal{G}$ is equal to the number of classes $n_c$ of group elements.

The characters of the $n_c$ classes of group elements with respect to the $n_r$ IRs are usually arranged in the *character table* of the group $\mathcal{G}$.

If we regard $(h_i/g)\chi^{(\alpha)}(\mathcal{C}_i)$ as components of $n_c$-dimensional vectors $\boldsymbol{v}^{(\alpha)} = ((h_i/g)\chi^{(\alpha)}(\mathcal{C}_i))$ with $i = 1 \ldots n_c$ or $\boldsymbol{v}_i = ((h_i/g)\chi^{(\alpha)}(\mathcal{C}_i)$ with $\alpha = 1 \ldots n_r$, the orthogonality theorems state that $\boldsymbol{v}^{(\alpha)}\boldsymbol{v}^{(\beta)} = \delta_{\alpha\beta}$ and $\boldsymbol{v}_i\vec{v}_j = \delta_{ij}$, that is, considered as rows or columns, they are orthonormal.

## C.6 Example: Character table of the $\boldsymbol{C}_{4v}$ group

To give an example for the construction of character tables using the rules stated in the last section, we focus on the $\boldsymbol{C}_{4v}$ group. This group is both, simple enough to be suitable as an example to illustrate the structure and construction of character tables, and important for this work, because $\boldsymbol{C}_{4v}$ is an invariant subgroup of the tetragonal group $\boldsymbol{D}_{4h}$ which is the symmetry group of many high-temperature superconductors.

The point group $\boldsymbol{C}_{4v}$ consists of 4 vertical mirror planes, denoted by $\sigma_x$, $\sigma_{x'}$, $\sigma_y$, and $\sigma_{y'}$ (see Fig. C.3), and an additional 4-fold rotation axis $C_4$. The other symmetry operations of the group are the identity $E$ and the rotations $C_4^2$ and $C_4^3 \equiv C_4^{-1}$. This makes a total of 8 symmetry operations, the group is of order $g = 8$.

Because of $\sigma_x C_4 \sigma_{x'} = C_4^{-1}$, the symmetry operations $C_4$ and $C_4^{-1}$ belong to the same class which we call $2C_4$. Furthermore, because of $C_4^{-1}\sigma_x C_4 = \sigma_y$, the reflections $\sigma_x$ and $\sigma_y$ constitute a class $2\sigma_v$. Similarly, $\sigma_{x'}$ and $\sigma_{y'}$ belong to a class $2\sigma_d$. Therefore, $\boldsymbol{C}_{4v}$ decomposes into the $n_c = 5$ classes $E$, $2C_4$, $C_4^2$, $2\sigma_v$, and $2\sigma_d$. The number of inequivalent irreducible representations (IRs) $n_r$ of a group is equal to the number $n_c$ of its classes, consequently, $n_r = 5$ for $\boldsymbol{C}_{4v}$.

Now we use the fact expressed by (C.5) that the sum of the squares of the dimensions of all IRs of a group is equal to its order $g$. The only possibility to fulfill this is $1^2+1^2+1^2+1^2+2^2 = 8$, that is, the group $\boldsymbol{C}_{4v}$ has four one-dimensional and one two-dimensional (inequivalent) irreducible representations.

We start constructing the character table of $\boldsymbol{C}_{4v}$. The character of the identity $E$ for any representation is equal to the dimension of the representation. This gives us the first column of Tab. C.6. The first row is also easy, because for the unit representation the character is 1 for every symmetry operation in the group.

According to the unitarity law (Sect. C.5), all representation matrices can be chosen to be unitary. Therefore, for one-dimensional representations, the magnitude of all characters is 1. On the other hand, the second orthogonality law (C.7) with $i = j$ states that for every class of symmetry operations, the sum of the magnitudes of the characters of all the IRs is equal to the order $g$ of the group divided by the number $h$ of symmetry operations in the class, $g/h$. In the case of the classes $2C_4$, $2\sigma_v$, and $2\sigma_d$, this is $g/h = 4$. The sum of the absolute squares of the 4 one-dimensional representations is already 4, consequently the character of the latter three classes is zero in the two-dimensional representation.

Now we use the fact that for *1-dimensional* representations the relation $\chi(G^n) = \chi(G)^n$ for $G \in \mathcal{G}$ holds. Therefore the characters of all the classes in the 1-dimensional representations of the $\boldsymbol{C}_{4v}$ group are $\pm 1$. Since the reflection at a mirror plane is its own inverse, the character of a reflection has the property $\chi(\sigma_v)^2 = 1$ (and analogous for $\sigma_d$), therefore, $\chi(\sigma_v) = \pm 1$. This is also true for the rotation $C_4$. From the fact that $C_4$ and $C_4^{-1}$ are in the same class, it follows that $\chi(C_4) = \chi(C_4^3)$, and therefore $\chi(C_4) = \pm 1$.

Let us compare this to the situation in the point group $\boldsymbol{C}_4$ which is the cyclic group generated by the 4-fold rotation $C_4$ and therefore of order 4. Each symmetry operations is a class of its own. Therefore, we only have $C_4^4 = E$ and $\chi(C_4)^4 = 1$ with the consequence that $\pm 1$ and $\pm i$ are all possible values of $\chi(C_4)$. A look into a group theory book shows that indeed there are IRs of the $\boldsymbol{C}_4$ group with the character of the $C_4$ 4-fold rotation assuming the values $\pm i$. The additional mirror planes in $\boldsymbol{C}_{4v}$ prevent the characters of the 4-fold rotation to become imaginary.

The second orthogonality theorem of characters states that for two different classes, the characters of the different IRs, considered as vectors, are orthogonal. Using this and the property proved in the last paragraph that all the characters of the 1-dimensional representations are $\pm 1$ in the case of the $\boldsymbol{C}_{4v}$ groups, the characters of the classes $2C_4$, $2\sigma_v$, and $2\sigma_d$ for all the IRs are determined. Now only the characters of the class $C_4^2$ are left.

These characters—considered as vectors—also have to be orthogonal to the characters of the other classes. This leaves only two possibilities, the first is the one in the character table in Tab. C.6, and the second which differs only in an overall sign from the first. This

| $\boldsymbol{C}_{4v}$ | $E$ | $2C_4$ | $C_4^2$ | $2\sigma_v$ | $2\sigma_d$ |
|---|---|---|---|---|---|
| $A_1$ | 1 | 1 | 1 | 1 | 1 |
| $A_2$ | 1 | 1 | 1 | $-1$ | $-1$ |
| $B_1$ | 1 | $-1$ | 1 | 1 | $-1$ |
| $B_2$ | 1 | $-1$ | 1 | $-1$ | 1 |
| $E$ | 2 | 0 | $-2$ | 0 | 0 |
| $\Gamma(\boldsymbol{r})$ | 3 | 1 | -1 | 1 | 1 |
| $\Gamma(\boldsymbol{r}) \times \Gamma(\boldsymbol{r})$ | 9 | 1 | 1 | 1 | 1 |

Table C.6: Character Table of $\boldsymbol{C}_{4v}$. The characters of the 5 irreducible representations, of the reducible representation of a vector and the representation of a 2nd rank tensor are given.

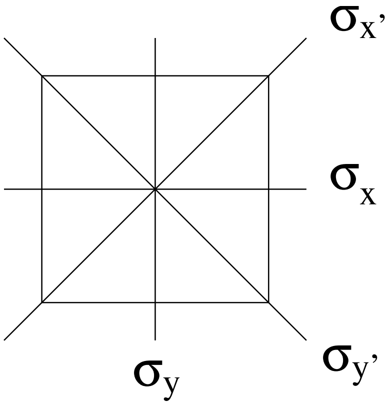

Figure C.3: Mirror planes of $\boldsymbol{C}_{4v}$.

sign is determined by the character of the trivial representation, $\chi^{(A_1)}(C_4^2) = 1$.

## C.7 Lattices and translational symmetry

**Point groups.** We already introduced a considerable number of point of groups, namely the groups $\boldsymbol{C}_3$, $\boldsymbol{C}_{3v}$, $\boldsymbol{D}_{4h}$, and $\boldsymbol{D}_4$. All these groups are *point groups*, groups of transformations which leave a particular point fixed. Another one of these point groups is the cyclic group $\boldsymbol{C}_5$, consisting of the 5 rotations by $n \cdot 72°$, $n = 0, \ldots, 4$ which leave the pentagon invariant.

**Bravais lattice.** The characteristic symmetry of a crystal is the translational symmetry which is described by 3 vectors $\boldsymbol{a}_i$ called the *primitive vectors.* Such three vectors $\boldsymbol{a}_i$ generate a set of points $\boldsymbol{t}_n = \sum n_i \boldsymbol{a}_i$ called *lattice vectors* or *lattice points* (and sometimes *lattice sites*), $\boldsymbol{n} = (n_i)$ with integer numbers $n_i$. The set $\{\boldsymbol{t}_n\}$ is called a *Bravais lattice*[5]

In this section, we determine the possible point group symmetries which are compatible with the translational symmetry of a Bravais lattice given by three primitive vectors $\boldsymbol{a}_i$. But before doing this, we introduce some terms and constructions which are in use when

---

[5] note that for a given Bravais lattice the choice of primitive vectors is not unique.

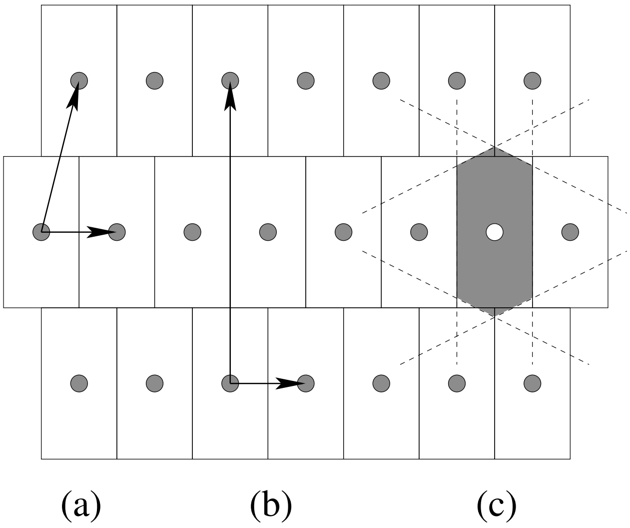

Figure C.4: (a) Two different primitive vectors and the primitive cell they span, (b) non-primitive translations vectors spanning a conventional unit cell, and (c) the Wigner-Seitz cell of $YBa_2Cu_4O_8$ (Y-124).

discussing properties of crystal lattices.

**Primitive cell.** A region of space which contains exactly one *lattice point* $\boldsymbol{t}_n$ and which fills (without overlapping) the whole space if translating it through the lattice vectors, is called a *primitive cell.* One obvious choice for the primitive cell is the parallelepiped spanned by the three primitive vectors $\boldsymbol{a}_i$ (see Fig. C.4(a)). Usually this choice has the disadvantage of not having the full symmetry of the Bravais lattice. Two ways to circumvent this problem are common.

**Conventional cell and Wigner-Seitz-cell.** The first is the *conventional (or crystallographic) unit cell* which is chosen to be larger than the primitive cell in order to have the full point group symmetry (see Fig. C.4(b)). The second choice is the *Wigner-Seitz cell* which is a primitive cell. Given a lattice point, the Wigner-Seitz cell contains all points which are closer to the lattice point under consideration than to any other equivalent (upon translations) point of the crystal (see Fig. C.4(c)). This cell by construction has the full symmetry of the lattice.

Figure C.4 shows the $b - c$ plane of the lattice of $YBa_2Cu_4O_8$ (Y-124), the points show the position of a particular atom, for instance the Y atom, in the lattice. On the left side $(a)$ a certain choice for the primitive vectors is shown. The perpendicular vectors in $(b)$ are the basis vectors of a suitable choice of a conventional unit cell. On the right side $(c)$ of the figure the construction of the Wigner-Seitz cell (grey area) is illustrated.

Let us return to the question of the compatibility of translational and point group symmetries and the classification of Bravais lattices. We look for the rotations which are compatible with the translational symmetry of a Bravais lattice. The origin of the rotation is considered to be a lattice point. Due to the discrete nature of the lattice, $n$ successive rotations have to be equal to the identity operation, that is, we consider $n$-fold rotation axes ($n \neq \infty$). First we show that the rotation axis of a rotation compatible with the translational symmetry

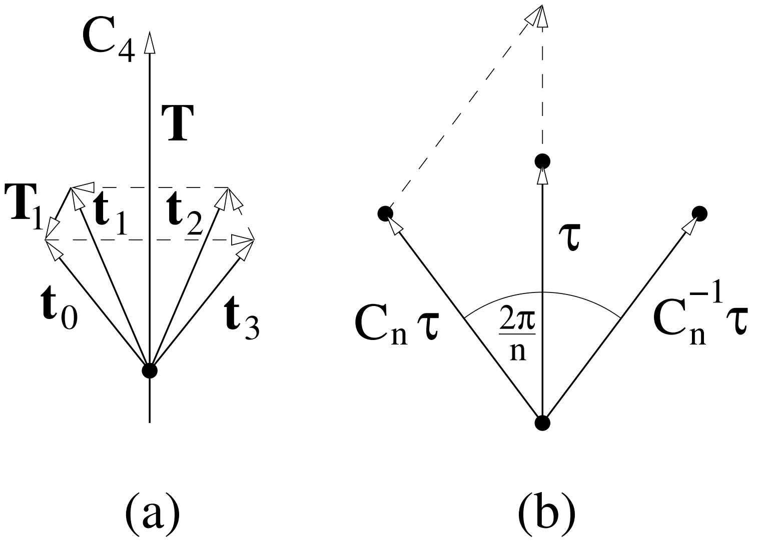

Figure C.5: The proof (see text) that only the rotations $C_2$, $C_3$, $C_4$, and $C_6$ are compatible with translational symmetry.

necessarily is parallel to a lattice vector. Take a lattice vector $\boldsymbol{t}_0$ and generate the vectors $\boldsymbol{t}_i = (C_n)^i \boldsymbol{t}_0$ for $i = 1, \ldots, n$. The lattice vector $\boldsymbol{T} \equiv \sum_{i=0}^{n-1} \boldsymbol{t}_i$ (see Fig. C.5(a)) is invariant with respect to the rotation $C_n$, and therefore parallel to the rotation axis (if it vanishes accidentally, we choose another lattice vector $\boldsymbol{t}_0$). The lattice vectors $\boldsymbol{T}_i = \boldsymbol{t}_i - \boldsymbol{t}_{i-1}$ (Fig. C.5(a)) are perpendicular to $\boldsymbol{T}$ because $\boldsymbol{T}_i \boldsymbol{T}$ is invariant upon rotation and $\sum_i \boldsymbol{T}_i \boldsymbol{T} = 0$. We have thus proved that if $C_n$ is a rotation leaving the Bravais lattice invariant, there are lattice vectors perpendicular to the rotation axis of $C_n$. The problem now is reduced to a two-dimensional one. For the shortest $\vec{\tau}$ of the lattice vectors perpendicular to the rotation axis, then $C_n\vec{\tau} + C_n^{-1}\vec{\tau} = 2\cos(2\pi/n)\vec{\tau}$ must be a primitive vector (Fig. C.5(b)). This is only possible for $n = 1$, 2, 3, 4, and 6 (the case $n = 1$ is trivial). Therefore, only rotations by $\pi$, $2\pi/3$, $\pi/2$, and $\pi/3$ are possible candidates for point group symmetry operations leaving a given Bravais lattice invariant. Other rotations can be excluded.

Taking these rotations and also the inversion, 32 different groups can be constructed. They are called the *32 crystallographic point groups*. All these groups are possible point symmetry groups of a given Bravais lattice. Two of the 32 point groups are the tetragonal $\boldsymbol{D}_{4h}$ and $\boldsymbol{D}_4$ groups. Only the former of these groups is important when classifying the Bravais lattices, because if a Bravais lattice has $\boldsymbol{D}_4$ symmetry, it automatically also has $\boldsymbol{D}_{4h}$ symmetry. This observation decomposes the set of 32 point groups into 7 subsets. The 7 symmetry groups with maximum symmetry in each of these 7 subsets are the *7 crystal systems* which are cubic ($\boldsymbol{O}_h$), hexagonal ($\boldsymbol{D}_{6h}$), tetragonal ($\boldsymbol{D}_{4h}$), trigonal ($\boldsymbol{D}_{3d}$), orthorhombic ($\boldsymbol{D}_{2h}$), monoclinic ($\boldsymbol{C}_{2h}$), and triclinic ($\boldsymbol{S}_2$).

**Lattice with a basis.** More complex crystals, as for instance crystals consisting of different kinds of atoms, do not have the property that all the atoms are located on a site of a Bravais lattice. This is also the case for some apparently simple structures as for instance the honeycomb net, which cannot be described by using just three primitive vectors $\boldsymbol{a}_i$. In such crystals, however, it is possible to group together few atoms and describe the position of these groups by means of a Bravais lattice. This construction is called a *lattice with a basis.* A simple example for the first case is sodium chloride (NaCl) which is cubic, with Cl atoms as nearest neighbors of the Na atoms and vice versa. This lattice is described by a face centered cubic lattice with a basis consisting of a sodium and a chloride atom. In the system $YBa_2Cu_4O_8$, for instance, each primitive cell of the Bravais lattice contains 15 atoms. Sometimes a lattice with a basis is used also to describe the body-centered cubic (bcc) and face-centered cubic (fcc) Bravais lattices to make more explicit their cubic symmetry.

The simple Bravais lattice can be considered as a Bravais lattice with a basis having the full symmetry of the simple Bravais lattice. A basis which does not have (at least) the full symmetry of the Bravais lattice breaks this symmetry. This symmetry breaking is possible in different ways which generate the 32 crystal systems. Consider a orthorhombic Bravais lattice which has $\boldsymbol{D}_{2h}$ symmetry. A basis can destroy this symmetry in two ways, either it destroys the horizontal mirror plane and the symmetry becomes $\boldsymbol{C}_{2v}$ or it destroys the vertical mirror planes and the symmetry becomes $\boldsymbol{D}_2$.

We summarize. Bravais lattices are the set of points generated in three dimensions by three non-collinear primitive vectors. Symmetry operations leaving a point invariant have to be compatible with the Bravais lattice. This is fulfilled just by the $C_2$, $C_3$, $C_4$, and $C_6$ operations out of all possible rotations. The point groups compatible with the Bravais lattice turn out to be 32, this is the number of different crystallographic point groups describing the different types of Bravais lattices with a basis. Selecting the groups with maximum symmetry, the Bravais lattices without a basis are found. These can be grouped into 7 types, corresponding to the number of crystal systems.

## C.8 Vectors, tensors, and their transformation behavior

The derivation of selection rules for light absorption, Raman scattering, and other forms of spectroscopy, is intimately related to the decomposition of the representations that correspond to the transformation laws for the appropriate vectors and tensors, into irreducible representations of the point group of the crystal under consideration.

**Vectors and representation matrices.** When rotating by an angle of $\varphi$ about an axis $\boldsymbol{n}$, a vector $\boldsymbol{v} = (v_i)$ transforms according to the law

$$\boldsymbol{v} \to R_{ij}(\boldsymbol{n},\varphi)\, v_j$$

where $\hat{R}(\boldsymbol{n},\varphi) = (R_{ij}(\boldsymbol{n},\varphi))$ is a *rotation matrix*, which in the special case of $\boldsymbol{n} = \boldsymbol{e}_z$ has the form

$$\hat{R}(\boldsymbol{e}_z,\varphi) = \begin{pmatrix} \cos\varphi & -\sin\varphi & 0 \\ \sin\varphi & \cos\varphi & 0 \\ 0 & 0 & 1 \end{pmatrix} . \tag{C.8}$$

Rotations about another axis $\boldsymbol{n}'$ can be written in the form

$$\hat{R}^{-1}\hat{R}(\boldsymbol{e}_z,\varphi)\hat{R}$$

with another rotation matrix $\hat{R}$, rotating first the axis $\boldsymbol{n}'$ to $\boldsymbol{e}_z$, then performing a rotation about the axis $\boldsymbol{e}_z$, and rotating back to $\boldsymbol{n}'$: All rotations by a given angle $\varphi$ are equivalent.

| $n$ | 1 | 2 | 3 | 4 | 6 |
|---|---|---|---|---|---|
| $\chi^{(\Gamma(\boldsymbol{r}))}(C_n)$ | 3 | -1 | 0 | 1 | 2 |

Table C.7: Characters of the $n$-fold rotation in the vector representation.

Particularly,

$$\mathrm{Sp}\,\hat{R}(\boldsymbol{n}', \varphi) = \mathrm{Sp}\,\hat{R}(\boldsymbol{e}_z, \varphi)$$

holds for any rotation axis $\boldsymbol{n}'$.

Consider now a point group $\mathcal{G}$. The proper rotations of the point group correspond to rotation matrices $\hat{R}$ and yield a 3-dimensional representation of the point group $\mathcal{G}$. Vectors transform according to this representation, therefore it is called the *vector representation* $\Gamma(\boldsymbol{r})$. The character of the rotation $C_n$ by an angle of $2\pi/n$ in the vector representation is given by the trace of $\hat{R}(\boldsymbol{n}, \varphi)$, that is,

$$\chi^{(\Gamma(\boldsymbol{r}))}(C_n) = \mathrm{Sp}\,\hat{R}(\boldsymbol{n}, 2\pi/n) = 1 + 2\cos\frac{2\pi}{n}$$

and is tabulated in Tab. C.7 for the rotations which are consistent with the translational symmetry of Bravais lattices. The character of rotatory inversions is the one of the corresponding proper rotation times $-1$ for the inversion. Mirror planes have the character $+1$.

Let us focus on the $\boldsymbol{C}_{4v}$ group (Tab. C.6) and reduce $\Gamma(\boldsymbol{r})$ into irreducible representations. The characters of the vector representation $\Gamma(\boldsymbol{r})$ in the group $\boldsymbol{C}_{4v}$ are given by Tab. C.6. From this, the decomposition

$$\Gamma(\boldsymbol{r}) = A_1 + E \qquad (\text{in } \boldsymbol{C}_{4v}) \tag{C.9}$$

follows easily.

As an illustration of the reduction of the representation associated with tensors of rank $r$, we treat the special case $r = 2$. Extension to the general case is straightforward. A tensor of rank 2 consists of $3 \times 3 = 9$ quantities $T_{ij}$ which transform under rotation according to

$$(T_{ij}) \rightarrow R_{ik} R_{jl} T_{kl} \ ,$$

that is, like a product of two vectors. The multiplication of rotation matrices $\hat{R}$ is related to the *product of representations* that must be defined next.

**Product representation.** Given two representations $A$ and $B$ of a group $\mathcal{G}$ with the representation matrices $D^{(A)}(G)$ and $D^{(B)}(G)$ for $G \in \mathcal{G}$, respectively, we define the *product representation* $A \times B$ by the representation matrix

$$D^{(A\times B)}_{ij,kl}(G) \equiv D^{(A)}_{ik}(G) D^{(B)}_{jl}(G) \ . \tag{C.10}$$

The character $\chi^{(A\times B)}(G) = \sum_{ij} D^{(A\times B)}_{ij,ij}(G)$ of the product group is given by the relation

$$\chi^{(A\times B)}(G) = \chi^{(A)}(G) \cdot \chi^{(B)}(G) \ , \tag{C.11}$$

that is, by the product of the character of the representations $A$ and $B$.

Using this, we see that a tensor of second rank gives raise to a IR corresponding to the product representation of two vector representations $\Gamma(\boldsymbol{r}) \times \Gamma(\boldsymbol{r})$. The characters of these representations are also tabulated in Tab. C.6.

In order to be specific, we once again consider the example of the $\boldsymbol{C}_{4v}$ group. After playing around a little bit with the character table, it turns out that

$$\Gamma(\boldsymbol{r}) \times \Gamma(\boldsymbol{r}) = 2A_1 + A_2 + B_1 + B_2 + 2E \tag{C.12}$$

is the decomposition we looked for.

**Decomposition of a $n$th rank tensor.** For tensors of rank $r > 2$ the decomposition works in a similar way, but it becomes difficult to carry it out just by inspection. Fortunately, there is a systematic way to perform the decomposition. We write the reducible representation $D$ as a direct sum

$$D = \sum_\alpha q_\alpha D^{(\alpha)} \tag{C.13}$$

of irreducible representations $D^{(\alpha)}$, and look for a way to determine the coefficients in (C.13). Calculating the trace of the representation matrices which are related to (C.13) yields the equation

$$\chi^{(D)}(G) = \sum_\alpha q_\alpha \chi^{(\alpha)}(G) \qquad \text{for all } G \in \mathcal{G}, \tag{C.14}$$

which decomposes the characters of the representation $D$ into those of the irreducible representations. Multiplying (C.14) by $\chi^{(\beta)\,*}(G)$, summing over all group elements, and applying the First Orthogonality of Characters, we find

$$q_\beta = \frac{1}{g} \sum_{G \in \mathcal{G}} \chi^{(\beta)\,*}(G) \chi^{(D)}(G) \tag{C.15}$$

where $g$ is the order of $\mathcal{G}$.

This is a very important result which leads to the decompositions of a reducible representation into irreducible ones by using (C.13), provided the character table of the group $\mathcal{G}$ is known.

The decomposition of an $n$th rank tensor is now straightforward. Because of (C.10), the $n$th rank tensor transforms according to the representation

$$D^{[n]} \equiv \underbrace{D^{\Gamma(\boldsymbol{r})} \times D^{\Gamma(\boldsymbol{r})} \times \cdots \times D^{\Gamma(\boldsymbol{r})}}_{n \text{ factors}} \tag{C.16}$$

whose character is (see C.11)

$$\chi^{[n]}(G) = \left(\chi^{\Gamma(\boldsymbol{r})}\right)^n \tag{C.17}$$

and the decomposition into irreducible representations is given by

$$D^{[n]} = \sum_\alpha q_\alpha D^{(\alpha)} \ ; \quad q_\alpha = \frac{1}{g} \sum_{G \in \mathcal{G}} \chi^{(\beta)\,*}(G) \left(\chi^{\Gamma(\boldsymbol{r})}(G)\right)^n \ . \tag{C.18}$$

We determined so far the irreducible representations which are contained in the representations of a $n$th rank tensor. But we did not yet decompose the tensor into parts which transform according to those irreducible representations. Such a decomposition is possible for all objects $f$ for which the transformation behavior with respect to the operation of the point symmetry group $\mathcal{G}$ is defined. We write

$$f = \sum_\alpha f^{(\alpha)} \quad \text{with} \qquad Gf^{(\alpha)} = D^{(\alpha)}(G) f^{(\alpha)} \quad \text{for all} \qquad G \in \mathcal{G} \; .$$

The quantity $D^{(\alpha)}(G)$ is the representation matrix of the group element $G$ in the irreducible representation $\alpha$.

The decomposition can be performed using *projection operators*. For each irreducible representation of a group $\mathcal{G}$, projection operator is given by

$$P^{(\alpha)} = \frac{d_\alpha}{g} \sum_{G \in \mathcal{G}} \chi^{(\alpha)\,*}(G)\, G \; , \tag{C.19}$$

where $D_\alpha$ is the dimension of the irreducible representation $\alpha$, and $g$ is the order of $\mathcal{G}$.

We apply this to the real 2nd rank tensor $\hat{T}$, choose the point group $\boldsymbol{C}_{4v}$ as symmetry group, and work in 2 dimensions. The $2 \times 2$ representation matrices of the vector representation have the form

$$\hat{D}(G) = \pm \begin{pmatrix} \cos\varphi & -\sin\varphi \\ \sin\varphi & \cos\varphi \end{pmatrix}$$

for $\varphi = n\pi/4$, and the application of the group elements of $\boldsymbol{C}_{4v}$ to the tensor is defined by

$$G\hat{T} = \hat{D}(G)\hat{T}\hat{D}^T(G) \; .$$

Therefore, the decomposition yields

$$\hat{T} = \sum_\alpha \hat{T}^{(\alpha)} \; , \quad \hat{T}^{(\alpha)} = \frac{1}{8} \sum_{G \in \boldsymbol{C}_{4v}} \chi^{(\alpha)}(G) \hat{D}(G) \hat{T} \hat{D}^T(G) \; ,$$

which evaluates to $\hat{T} = \hat{T}^{A_1} + \hat{T}^{A_2} + \hat{T}^{B_1} + \hat{T}^{B_2}$ with

$$\hat{T}^{A_1} = \begin{pmatrix} T_{xx} + T_{yy} & \\ & T_{xx} + T_{yy} \end{pmatrix} \; , \quad \hat{T}^{A_2} = \begin{pmatrix} & T_{xy} - T_{yx} \\ -(T_{xy} - T_{yx}) & \end{pmatrix} \; ,$$
$$\hat{T}^{B_1} = \begin{pmatrix} T_{xx} - T_{yy} & \\ & T_{xx} - T_{yy} \end{pmatrix} \; , \quad \hat{T}^{B_2} = \begin{pmatrix} & T_{xy} + T_{yx} \\ T_{xy} + T_{yx} & \end{pmatrix} \; .$$

The $E_{1g}$ representation does not appear in the decomposition. A table which shows the results of the decomposition of the 2nd rank Raman tensor for different point groups can be found in [C.6].

**Independent components of a tensor.** One of the important topics of this chapter is to answer the question concerning the number of independent components of a tensor (see [C.2], Sect. 8.5) for a particular point group symmetry of a crystal under consideration.

The tensor components corresponding to the irreducible representations which are different from the identity representation are not invariant when applying the symmetry operations on the lattice, and therefore have to vanish. Only the components which transform according to the identity representation are non-vanishing. Consequently, we are interested in the number of times the identity representation occurs in the tensor representation. Putting $\gamma = 1$ into (C.18), we find the answer that

$$n_{\text{ind}} = \frac{1}{g} \sum_{G \in \mathcal{G}} \left( \chi^{\Gamma(\boldsymbol{r})}(G) \right)^n \tag{C.20}$$

for a $n$th rank tensor. For the $\boldsymbol{C}_{4v}$ group a (non-symmetric) tensor of 2nd rank therefore has

$$n_{\text{ind}} = \frac{1}{8}[9 + 2 \cdot 1 + 2 + 2 \cdot 1 + 2 \cdot 1] = 2$$

independent components. In the $\boldsymbol{D}_{4h}$ group, a 4th rank tensor has

$$n_{\text{ind}} = \frac{2}{16}[81 + 2 \cdot 1 + 1 + 2 \cdot 1 + 2 \cdot 1] = 11$$

independent components.

**Tensors with additional symmetries.** When calculating the Raman efficiency for electronic Raman scattering in superconductors, 4th rank tensors like

$$\mu_{ijkl} = \langle \mu_{ij}^{-1} \mu_{kl}^{-1} \rangle \tag{C.21}$$

have to be discussed. The 4th rank tensor $c_{\mu\nu\rho\sigma}$ of elastic constants is analogous to $\mu_{ijkl}$ with respect to the symmetries. These tensors clearly are symmetric when interchanging $(i \leftrightarrow j)$, or $(k \leftrightarrow l)$, or $((i,j) \leftrightarrow (k,l))$.[6] The question arises as to how many independent components a tensor with this permutation symmetry in a crystal of a given point group symmetry has.

This question can be answered using (C.18), but the quantity $(\chi^{\Gamma(\boldsymbol{r})}(G))^n$ has to be replaced by the character of the accordingly symmetrized tensor.

The symmetry of a tensor is described by a subgroup of the group $\mathcal{P}_n$ of permutations of $n$ objects (refer to [C.3], Chap. 15). A permutation of $n$ objects is denoted by the symbol

$$p = \begin{pmatrix} 1 & 2 & \cdots & n \\ p_1 & p_2 & & p_n \end{pmatrix}$$

and describes the replacement of the object $i$ by $p_i$. Permutations often produce cyclic replacements. For instance, in the permutation

$$p = \begin{pmatrix} 1\,2\,3\,4 \\ 3\,2\,4\,1 \end{pmatrix} ,$$

the object 1 is replaced by 3, 3 by 4, and 4 by 1. Object 2 is replaced by itself, which is also some kind of cyclic replacement. In the *cycle notation* the permutation $p$ is denoted by $p = (1\,3\,4)(2)$, it is said to consist of two cycles of length $\nu_1 = 3$, and $\nu_2 = 1$. The equation $\sum_m \nu_m = n$ is always fulfilled.

---

[6] Recall that $\hat{\mu}^{-1}$ is the inverse effective mass tensor which has the property $\mu_{ij}^{-1}(\boldsymbol{k}) = \mu_{ji}^{-1}(\boldsymbol{k})$.

| Point group of crystal | independent components of $\mu_{ijkl}$ |
|---|---|
| $\{E\}$ | 21 |
| $\boldsymbol{D}_{2h}$ | 9 |
| $\boldsymbol{D}_{4h}$ | 6 |
| $\boldsymbol{O}_h$ | 3 |

Table C.8: Independent components of the tensor $\boldsymbol{k}$-independent tensor $\mu_{ijkl}$ defined in (C.21).

But let us go back to the 4th rank tensor $\mu_{ijkl}$. We denote the $m$th index of $\mu_{ijkl}$ by $m$. Then the permutations which are symmetry operations of $\mu_{ijkl}$, are

$$\begin{array}{rcll} (i \leftrightarrow j) & \to & p = (1\,2)(3)(4) & \text{with } \nu_1 = 2,\ \nu_2 = \nu_3 = 1 \\ (k \leftrightarrow l) & \to & p = (1)(2)(3\,4) & \text{with } \nu_1 = 2,\ \nu_2 = \nu_3 = 1 \\ ((i,j) \leftrightarrow (k,l)) & \to & p = (1\,3)(2\,4) & \text{with } \nu_1 = \nu_2 = 2. \end{array}$$

These three permutations generate a subgroup $\mathcal{P}$ of $\mathcal{P}_n$. This subgroup consists of 12 elements, all of which leave the tensor $\mu_{ijkl}$ invariant.

The character of a tensor which is invariant under the subgroup $\mathcal{P}$ is given by the sum

$$\chi_{\mathcal{P}}(a) = \frac{1}{\operatorname{ord}\mathcal{P}} \sum_{p\in\mathcal{P}} \{\chi(a)\}^{\nu_1}\{\chi(a^2)\}^{\nu_2}\cdots\{\chi(a^m)\}^{\nu_m} \ , \tag{C.22}$$

(see [C.2], Eq. (8.5.13)) where $\chi(a)$ is the character of $a \in \mathcal{G}$ in the vector representation and $\nu_i$ is the length of the cycles in the permutation $p$. The number of independent elements $n_{\text{ind}}$ then is given by (C.18), that is,

$$n_{\text{ind}} = \frac{1}{\operatorname{ord}\mathcal{G}} \sum_{a\in\mathcal{G}} \chi_{\mathcal{P}}(a) \ ,$$

where $\operatorname{ord}\mathcal{G}$ denotes the order of the point group $\mathcal{G}$.

For a given group $\mathcal{G}$, we consider (C.22) for the special case of a symmetric second rank tensor. The permutation group is given by $\mathcal{P} = \{E, (1\,2)\}$ where $\nu_1 = 2$ for $p = E$ and $\nu_2 = 1$ for $p = (1\,2)$. This yields

$$\chi^{\text{sy}}(a) = \frac{1}{2}\left[\chi(a)^2 + \chi(a^2)\right]$$

which is the character of the symmetric product representation.

In Tab. C.8 we have tabulated the number of independent elements of $\mu_{ijkl}$ for some given crystal point groups. If the crystal has no point symmetry at all (or is triclinic) then only the symmetry with respect to the permutation of the tensor indices reduces the number of independent components of the tensor, in our case from $3^4 = 81$ to 21. Additional point group symmetries further reduce the number of independent components of the tensor down to 3 for the cubic case.

## C.9 Classification of Γ-point phonons according to point group symmetry

The irreducible representations of a point group of a crystal are an indispensable tool for the classification of the normal vibration modes of the crystal. For one-phonon (dipole) Raman scattering, only phonons with the full *translational symmetry* of the crystal, that is, $k = 0$ or Γ-point phonons are of importance, and will be under consideration exclusively in this section.

The restriction to $k = 0$ phonons, and its consequence that the vibrational displacement patterns have the same translational symmetry as the crystal, allows us to focus on just one unit cell. When performing the group-theoretical treatment of the phonons, we also have to identify atoms which are related by a translation of the Bravais lattice. In the case of a system of two CuO planes, there are 6 independent sites. In the upper plane, there is one Cu (Cu(2)) site and two O sites (O(2) and O(3)). In the lower plane, there are also three independent sites, one Cu site and two O sites. The point symmetry group is $\boldsymbol{D}_{4h}$ (see Fig. C.6).

An important observation is the fact that *normal modes transform according to irreducible representations* of the point group $\mathcal{G}$ of the crystal. If we label the inequivalent atoms in the primitive unit cells with $k = 1, \ldots, N$, then the relation between the displacement $\boldsymbol{u}_k$ of a certain atom $k$, and the phonon normal coordinate $Q_s$ of the phonon labeled by $s = 1, \ldots, 3N$ is given by

$$\boldsymbol{u}_k = \frac{1}{\sqrt{m_k}} \sum_s Q_s \boldsymbol{e}_k^{(s)} \ . \tag{C.23}$$

The mass of atom $k$ is denoted by $m_k$, and $\boldsymbol{e}_k^{(s)}$ are the eigenvectors of the phonon $s$. The Hamiltonian is given by

$$E = \frac{1}{2} \sum_s \left[ \dot{Q}_s^2 + \omega_s^2 Q_s^2 \right]$$

where $\omega_s$ denotes the frequency of the phonon $s$. From this equation it becomes clear that the normal coordinates which belong to a given energy $\omega$, transform according to a certain representation of the point group $\mathcal{G}$. For cases of no accidental degeneracy, which are the only ones being considered here, this implies that the normal coordinates transform according to an *irreducible* representation of $\mathcal{G}$, and we write

$$G Q_s = \sum_{s'} Q_{s'} D_{s's}(G)$$

for all $G \in \mathcal{G}$. According to C.23, the normal coordinates $Q_s$ and the displacements $\boldsymbol{u}_k$ are related linearly. Therefore, we will perform a group-theoretical investigation of the displacements.

We consider the effect of symmetry operations on the equilibrium position $\boldsymbol{r}_k$ and displacement $\boldsymbol{u}_k$ of the atom $k$ in the primitive unit cell. The vectors $\boldsymbol{r}_k$ transform according to the vector representation, that is,

$$G \boldsymbol{r}_k = \hat{R}(G) \boldsymbol{r}_k = \boldsymbol{r}_{k'} \ ,$$

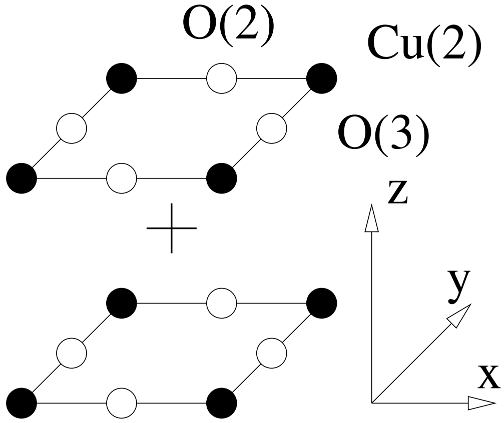

Figure C.6: The two CuO planes in two-plane high-$T_c$ superconductors.

the transformation takes the atom from the position $k$ to position $k'$. For the case of the displacements, the transformation law is more difficult, because the displacements transform like vectors, but at the same time, the atoms to which they refer, change place. When the transformation takes an atom from site $k$ to site $k'$, then displacement vector of the atom at site $k'$ becomes that one of the atom at site $k$ rotated by a rotation matrix,

$$G\boldsymbol{u}_{k'} = \hat{R}(G)\boldsymbol{u}_{\hat{R}^{-1}(G)\boldsymbol{r}_{k'}} = \hat{R}(G)\boldsymbol{u}_k \ .$$

The $N$ displacement vectors $\boldsymbol{U} = (\boldsymbol{u}_1, \ldots \boldsymbol{u}_N)^T$ transform according to a $3N$-dimensional representation $\hat{R}_{3N}$ like

$$G\boldsymbol{U} = \hat{R}_{3N}(G)\boldsymbol{U} \ .$$

The decomposition of the representation $\hat{R}_{3N}$ gives the different irreducible representations of the normal modes. For the decomposition we only need the character of the representation, that is, the trace of $\hat{R}_{3N}$. Only atoms that do *not move* in the transformation contribute non-vanishing *diagonal* elements to $\hat{R}_{3N}$. For an atom $k$ that does not move, $G\boldsymbol{u}_k = \hat{R}\boldsymbol{u}_k$, where $\hat{R}$ is a $3 \times 3$ rotation matrix. The character of $\hat{R}$ was already calculated in Sect. C.8 and tabulated in Tab. C.7. As a consequence, the character of the representation $\hat{R}_{3N}$ is given by

$$\chi^{(3N)}(G) = N_R \chi^{(\Gamma(\boldsymbol{r}))}(G) \ ,$$

where $N_R$ is the number of atoms which are not moved in the transformation represented by $G$.

The system shown in Fig. C.6 is composed of 6 independent sites and possesses tetragonal $\boldsymbol{D}_{4h}$ symmetry. In Tab. C.9, the number $N_R$ of atoms which are not moved by the transformation represented by $G \in \mathcal{G}$, the character $G$ in the vector representation, and its product, the character of the representation $\hat{R}_{3N}$ is given for each of the classes of $\boldsymbol{D}_{4h}$.

The decomposition of the representation $\hat{R}_{3N}$ by using (C.14) and (C.15) is easy now, and yields the result

$$2A_{1g} + B_{1g} + 3E_g + 2A_{1u} + B_{1u} + 3E_u \ .$$

The displacement patterns which belong to the particular normal modes are determined by applying the projection operators to the displacement vectors $\boldsymbol{U}$.

| | $E$ | $2C_4$ | $C_4^2$ | $2C_2'$ | $2C_2''$ | $I$ | $2IC_4$ | $\sigma_h$ | $2\sigma_v$ | $2\sigma_d$ |
|---|---|---|---|---|---|---|---|---|---|---|
| $N_R$ | 6 | 2 | 6 | 0 | 0 | 0 | 0 | 0 | 6 | 2 |
| $\chi^{(\Gamma(\boldsymbol{r}))}$ | 3 | 1 | -1 | 0 | 0 | 0 | 0 | 0 | 1 | 1 |
| $\chi^{(3N)}$ | 18 | 2 | -6 | 0 | 0 | 0 | 0 | 0 | 6 | 2 |

Table C.9: For each class of the tetragonal point group $\boldsymbol{D}_{4h}$, the number $N_R$ of invariant atoms of Fig. C.6, the character of the class in the vector representation and in the representation $\hat{R}_{3N}$ is given.

The modes carrying an index "g" (gerade) are even with respect to the inversion operation. Therefore they carry no dipole momentum and are forbidden in absorption. The "u" (ungerade) modes are odd with respect to inversion and are forbidden in Raman scattering (see next section). The even modes turn out to be Raman active. The odd modes are active in infrared absorption saved one exception: the $A_{1u}$ and $B_{1u}$ modes. The $B_{1u}$ modes possesses an odd parity symmetry pattern, but due to the fact that $\chi^{(B_{1u})}(C_4) = -1$, the dipole momentum vanishes (O(2) and O(3) carry the same ionic charge) and so does the coupling. This can also be seen in a more formal way. The Raman vertex (in effective mass approximation, i.e. far from resonance) corresponds to a symmetric 2nd rank tensor and decomposes in $\boldsymbol{D}_{4h}$ into

$$\text{symmetric 2nd rank tensor} \rightarrow 2A_{1g} + B_{1g} + B_{2g} + E_g \ ,$$

and the vector decomposes into

$$\text{vector} \rightarrow A_{2u} + E_u \ .$$

Therefore, the $A_{1u}$, $B_{1u}$, and $E_u$ phonons are Raman active and the $E_u$ phonons are infrared active. The $A_{1u}$ and $B_{1u}$ phonon, however, are neither Raman- nor infrared-active. They are called *silent* modes.

## C.10 Selection rules for Raman scattering by phonons

When talking about *selection rules* for Raman scattering, one usually refers to the fact that for different *polarization configurations* ($\boldsymbol{e}_L$, $\boldsymbol{e}_S$) of the incoming and scattered light, different excitations can be detected using Raman spectroscopy.

The Raman efficiency $S$ is related to a 2nd rank tensor, the *Raman tensor* $\hat{T}$ via the light polarization unit vectors $\boldsymbol{e}_S$ and $\boldsymbol{e}_L$ by the relation

$$S \sim \left| \boldsymbol{e}_S^* \cdot \hat{T} \cdot \boldsymbol{e}_L \right|^2 \ .$$

Certain excitations cause certain non-vanishing matrix elements of the Raman tensor $\hat{T}$ and allows for selecting them by an appropriate choice of the light polarization.

We focus on phonon Raman scattering (restricted to Stokes scattering) and discuss its microscopic mechanism. The basic process leading to phonon Raman scattering is shown

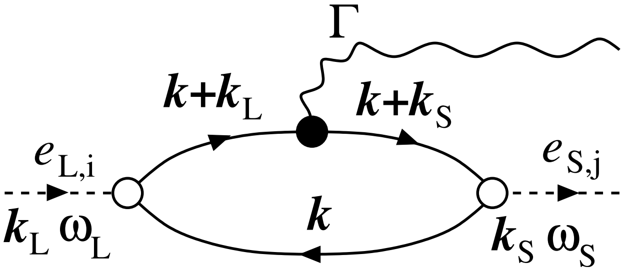

Figure C.7: The photon-phonon vertex involving an electronic pair-excitation. Note that there is also another diagram contributing in which the phonon is created by scattering with the hole.

in Fig. C.7. The incoming photon is annihilated and creates an electron-hole pair. Then either the electron or the hole scatter and create a phonon. The electron-hole pair finally recombines and creates the scattered photon. Due to the fact that the velocity of light is much larger than the Fermi velocity, the transition leading to the electron-hole pair can be considered to be direct. The transition corresponding to the recombination of the electron-hole pair has to be direct as well, and therefore the created phonon is a Γ-point phonon.

The vertices related to the creation and the annihilation of the electron-hole pair are matrix elements of the operators $\boldsymbol{e}_L \cdot \boldsymbol{p}$ and $\boldsymbol{e}_S^* \cdot \boldsymbol{p}$, respectively. We use cartesian components and take the unit vectors out of the expression for the transition amplitude of the process described by the diagram in Fig. C.7. Then the matrix elements are $\langle n_1 \boldsymbol{k} | p_i | n_i \boldsymbol{k} \rangle$ and $\langle n_i \boldsymbol{k} | p_j | n_2 \boldsymbol{k} \rangle$. They transform like vectors and thus their product like a 2nd rank tensor.

We assume now that it is possible to consider only one phonon in our discussion. This is given for instance when the other phonons are not very close in frequency to the phonon under discussion.[7] Then, the phonon will not mix with other phonons, and it is enough to take into account one electron-phonon vertex $g$. The creation of a phonon is accompanied by the scattering of an electron (hole) with quasimomentum $\boldsymbol{k}$ from band $n_1$ to $n_2$, and therefore the vertex $g$ depends on $\boldsymbol{k}$, $n_1$, and $n_2$ only.

The expression corresponding to the diagram in Fig. C.7, which gives the amplitude for the process of creating a phonon by inelastic scattering of light (involving an electron-hole pair), is given by a product of the vertices and three electronic Green's functions, and involves a summation $\langle \cdot \rangle$ over the Brillouin zone. We write

$$\langle p_i(n_i \to n_1, \boldsymbol{k}) \cdot g_{n_1 n_2; \boldsymbol{k}} \cdot p_j(n_2 \to n_i, \boldsymbol{k}) \cdot \Lambda_{n_i n_1 n_2; \boldsymbol{k}}(\omega) \rangle \ , \tag{C.24}$$

where the product of the Green's functions has been denoted by $\Lambda_{n_i n_1 n_2; \boldsymbol{k}}(\omega)$. This treatment also shows that the quantity defined in (C.24) is proportional to the Raman tensor $\hat{T}$.

The displacement pattern of a Γ-point phonons can be classified[8] according to the irreducible representations of the point group of the crystal. We denote the IR which represents the transformation properties of the displacement pattern of the phonon by $\mu$. Then, the electron-phonon vertex belongs to the same IR, we write $g_{\boldsymbol{k}}^{\mu}$.

---

[7] Otherwise, a perturbation like anharmonic coupling may mix different modes which belong to the same IR, but have different energy eigenvalues.

[8] if there is no accidental degeneracy.

The matrix elements of the momentum operator in (C.24) transform according to the components of the vector representation. Hence, the product of both transforms like a 2nd rank tensor.

Green's functions transform only by virtue of their dependence on the dispersion relation of the excitations which they describe. The dispersion relation $\epsilon_{\boldsymbol{k}}$ of the electrons is fully symmetric. Therefore the quantity $\Lambda_{\boldsymbol{k}}(\omega)$ in (C.24) is a scalar.

The averaging of the second rank tensor formed by the two momentum matrix elements and the electron-phonon vertex projects the irreducible representation $\mu$ out of the 2nd rank tensor,[9] all other irreducible representations vanish. As a conclusion, the amplitude (C.24) (which is proportional to the Raman tensor) only yields a non-vanishing contribution to that component of a the Raman tensor which belongs to the IR $\mu$.

We give an example using the point group $\boldsymbol{C}_{4v}$. This group describes the point symmetry of a square. Its group table is given in Tab. C.6.

The representation to which the Raman tensor (as every second rank tensor) belongs is denoted by $\Gamma(\boldsymbol{r}) \times \Gamma(\boldsymbol{r})$ and is the product of two vector representations. Using the orthogonality relations for characters of representations, the decomposition

$$\Gamma(\boldsymbol{r}) \times \Gamma(\boldsymbol{r}) = 2 \cdot A_1 + A_2 + B_1 + B_2 + 2 \cdot E$$

can be given. The projection of the components of the Raman tensor to the different IRs is performed using projection operators and yields the result

$$\hat{T} = \hat{T}_1^{A_1} + \hat{T}_2^{A_1} + \hat{T}^{A_2} + \hat{T}^{B_1} + \hat{T}^{B_2} + \hat{T}_1^{E} + \hat{T}_2^{E} \ , \tag{C.25}$$

where the components $\hat{T}^{\mu}$ are given by

$$\begin{aligned}
&\hat{T}_1^{A_1} = \begin{pmatrix} a & & \\ & a & \\ & & \end{pmatrix} , \quad \hat{T}_2^{A_1} = \begin{pmatrix} & & \\ & & \\ & & b \end{pmatrix} , \quad \hat{T}^{A_2} = \begin{pmatrix} & c & \\ -c & & \\ & & \end{pmatrix} \\
&\hat{T}^{B_1} = \begin{pmatrix} d & & \\ & -d & \\ & & \end{pmatrix} , \quad \hat{T}^{B_2} = \begin{pmatrix} & e & \\ e & & \\ & & \end{pmatrix} , \quad \hat{T}_1^{E} = \begin{pmatrix} & & f \\ & & f \\ & & \end{pmatrix} \\
&\hat{T}_2^{E} = \begin{pmatrix} & & \\ & & \\ g & g & \end{pmatrix} .
\end{aligned} \tag{C.26}$$

From this result is becomes clear, that in parallel polarizations, only $A_1$- and $B_1$-phonons can be detected. Phonons belonging to other IRs will not appear in the Raman spectrum. On the other hand, $A_1$- and $B_1$-phonons will not be visible in crossed polarization configurations.

---

[9] This can be seen as follows. Denote the product of the momentum matrix elements by $T_{ij}$, and decompose it into irreducible representations $T_{ij} = \sum_{\alpha} T_{ij}^{(\alpha)}$. The product of the electron-phonon vertex $g_{\boldsymbol{k}}$ and the function $\Lambda_{\boldsymbol{k}}$ will be denoted by $h_{\boldsymbol{k}}$. If $g_{\boldsymbol{k}}$ transforms according to the irreducible representation $\mu$, then $h_{\boldsymbol{k}}$ does so as well, hence we write $H_{\boldsymbol{k}}^{(\mu)}$. Then the average $\langle T_{\boldsymbol{k};ij}^{(\alpha)} h_{\boldsymbol{k}}^{(\mu)} \rangle$ vanishes if $\alpha \neq \mu$. This is the same is we replace the average $\langle \cdot \rangle$ by a sum $\sum_{\boldsymbol{k} \in \mathrm{star}\{\boldsymbol{k}_0\}} \cdot$ over the star of a particular, but arbitrary quasimomentum $\boldsymbol{k}_0$. The product $T_{\boldsymbol{k};ij}^{(\alpha)} h_{\boldsymbol{k}}^{(\mu)}$, however, does not vanish necessarily (saved cases when the star of $\boldsymbol{k}$ consists of just one element).

One important final note is in order. The selection rules only involve the polarization vectors, but not the direction of the wavevectors of the incoming and scattered light and, therefore, are not depending on whether a Raman experiment is performed in backscattering or forward scattering geometry.

# Appendix D

# A short tutorial on Green's functions

## D.1 Introduction

> *"... It might be noted, for the benefit of those interested in exact solutions, that there is an alternative formulation of the many-body problem, i.e., how many bodies are required before we have a problem? G.E. Brown points out, that this can be answered by a look at history. In eighteenth-century Newtonian mechanics, the three-body problem was insoluble. With the birth of general relativity around 1910 and quantum electrodynamics in 1930, the two- and one-body problems became insoluble. And within modern quantum field theory, the problem of zero bodies (vacuum) is insoluble. So, if we are out after exact solutions, no bodies is already too many!"*
> (in: R.D. Mattuck, A Guide to Feynman Diagrams in the Many-Body Problem)[1]

Only a few problems in quantum mechanics can be solved exactly. Therefore, one is dependent upon approximation schemes. One of these is perturbation theory. In perturbation theory, the Hamiltonian $H$ of the system under investigation is split into a "trivial," that is, exactly solvable part $H_0$, and a perturbation $V$ and written as

$$H = H_0 + V \ .$$

Perturbation theory then uses the knowledge of the solution to $H_0$ (i.e., of its eigenfunctions $|n\rangle_0$ and eigenvalues $E_n^0$) together with the perturbation $V$ to give an approximation to the solution of the full Hamiltonian $H$. In its simplest form, for the case of a one-particle problem with a discrete non-degenerate spectrum, the eigenvalues $E_n$ of $H$ are approximated by $E_n \approx E_n^0 + {}_0\langle n|V|n\rangle_0$ to first order in $V$.

It is clear that in the case of a many-particle system, the things are getting much more complicated, but surprisingly, a very nice and physically transparent perturbation theory can be given. This perturbation theory is based on Green's functions which characterize a

---

[1] Despite of having taking this citation out of the many-particle book of Mattuck [D.1], most of the material here resembles quite close the introduction presented in the book of Mahan [D.2] with traces from the book of Abrikosov, Gorkov, and Dzyaloshinski [D.3]. Also very instructive is the book of Landau and Lifshitz [D.4]. For those who like to give an eye to applications in physics, the book of Schrieffer [D.5] is great.

quasi-particle in the sense of Landau's Fermi liquid theory (see [D.4]. Landau, however, did not make use of Green's functions in his theory). We are going to present this theory in the appendix at hand.

## D.2 Second quantization

The first forms of quantum mechanics given by Schrödinger's wave equation and Heisenberg's matrices though originally developed for the description of systems with single particles, can also be applied to a system with a fixed number $N$ of identical particles. Nevertheless this is very cumbersome, mainly because of the Pauli principle forcing the wave functions to be antisymmetric (fermions) or symmetric (bosons) when exchanging two particles. Antisymmetrizing wave functions (usually done by using a Slater determinants) is rather complicated and error-prone. Therefore, a different representation for quantum mechanics, the *second quantization*, has been developed to remove the problems just mentioned. Indeed, second quantization removes the problem of antisymmetrizing (or symmetrizing) wave functions—the formalism of second quantization automatically takes care of that. Additionally, it allows for the treatment of systems with a varying number of particles, such as phonon or photon systems, or for the treatment of the superconducting state as formulated in the BCS-theory.

Quantum mechanics, in its original formulation, deals with operators acting on wave functions. This is also the case in the formulation provided by second quantization. But the operators used in second quantization are rather different from those in the original formulation which we call the *first quantization.* In first quantization we have learned how to describe a given physical system by means of the Hamilton operator. The description of the physical system in second quantization is based as well on a Hamilton operator, but its form is completely different from that of the former. One of our goals here is to show how to construct the Hamiltonian used to describe a given physical system in second quantization when the corresponding Hamiltonian for first quantization is given.

Let us first summarize the treatment of a system of a fixed number $N$ of identical particles in first quantization. If one of the particles is described by the Hamiltonian

$$h_0(\boldsymbol{p}, \boldsymbol{r}) = \frac{1}{2m}\boldsymbol{p}^2 + U(\boldsymbol{r}) \ ,$$

the collection of $N$ identical and not interacting particles is represented by the $N$-particle Hamiltonian

$$H_0 = \sum_{i=1}^{N} h_0(\boldsymbol{p}_i, \boldsymbol{r}_i) \tag{D.1}$$

where the operators $\boldsymbol{p}_i$ and $\boldsymbol{r}_i$ are acting on the particle $i$. The wave functions of the $N$-particle system are

$$\psi(\boldsymbol{r}_1 \ldots, \boldsymbol{r}_N)$$

which can be written as a linear combination of the functions

$$\psi_{\boldsymbol{k}_1}(\boldsymbol{r}_1) \cdot \ldots \cdot \psi_{\boldsymbol{k}_N}(\boldsymbol{r}_N) \ ,$$

that is, products of single particle wave functions $\psi_{\boldsymbol{k}}(\boldsymbol{r})$ which are usually chosen to be eigenfunctions of the Hamiltonian $h_0$, and therefore given by

$$h_0\psi_{\boldsymbol{k}}(\boldsymbol{r}) = \epsilon_{\boldsymbol{k}}\psi_{\boldsymbol{k}}(\boldsymbol{r}) \ ,$$

where $\boldsymbol{k}$ is a quantum number denoting a stationary state of the single-particle Hamiltonian $h_0$. In a translationally invariant system or a crystal, this may be the momentum or quasimomentum, respectively, together with a spin index if the particles under discussion carry such property. Note that these $N$-particle wave functions have to be antisymmetrized (we focus on fermion systems; for bosonic systems, the wave function has to be symmetrized), and therefore, all the single particle states $\boldsymbol{k}_i$ have to be different. Otherwise the wave function vanishes, expressing the fact that a single-particle state can be occupied only once in fermionic systems.

A translationally invariant two-particle interaction as for instance the Coulomb interaction is represented in the $N$-particle system by the Hamiltonian

$$H_I = \frac{1}{2}\sum_{\substack{i,j=1\\ i\neq j}}^{N} V(\boldsymbol{r}_i - \boldsymbol{r}_j)$$

summing over all combinations of two particles. The factor 1/2 compensates for a double-counting in the sum over $i$ and $j$.

## D.2.1 Creation and destruction operators

In second quantization, new operators are introduced. These are the *creation* and *destruction* operators. Given a state $|\rangle$, the creation operator $c^+_\lambda$ adds a particle in the single-particle state $\psi_\lambda$ to $|\rangle$. If $|\rangle$ is an $N$-particle state, then $c^+_\lambda|\rangle$ is an $(N+1)$-particle state. If the state $|\rangle$ already contains a particle in state $\lambda$, the expression $c^+_\lambda|\rangle$ vanishes. The destruction[2] operator $c_\lambda$ works in a similar way. It removes a particle in the single-particle state $\lambda$ from the (many-body) state $|\rangle$, and destroys the entire many-body state, if such particle was not there. As the notation suggests, the creation and destruction operators are mutually hermitian conjugate.

For bosons, creation and destruction operators $b^+_\lambda$ and $b_\lambda$ are also defined. They work similarly to their fermion-colleagues, but allow for a multiple-occupancy of the single-particle states. That is, the creation operator $b^+_\lambda$ never annihilates a state $|\rangle$, whether it already contained particles in the single-particle state $\lambda$ or not.

These properties of the fermionic and bosonic creation and destruction operators are guaranteed by anticommutation and commutation rules, respectively. For fermions, the anticommutators

$$\begin{aligned} \{c_\lambda, c_\mu\} &= \{c^+_\lambda, c^+_\mu\} = 0 \\ \{c_\lambda, c^+_\mu\} &= \{c^+_\mu, c_\lambda\} = \delta_{\lambda\mu} \end{aligned} \tag{D.2}$$

guarantee antisymmetry, because $c_\lambda c_\mu = -c_\mu c_\lambda$, and prevent from double-occupancy because for $\mu = \lambda$, we have $c_\lambda c_\lambda = -c_\lambda c_\lambda = 0$. The second relation (D.2) taken for $\mu = \lambda$ determines

---

[2] We use the terms “destruction operator” and “annihilation operator” interchangeably.

the eigenvalues of the creation and destruction operators. Applied to a state $|\rangle$, it yields $c_\lambda c_\lambda^+|\rangle + c_\lambda^+ c_\lambda|\rangle = |\rangle$. If the single-particle state $\lambda$ is occupied in $|\rangle$, the first term in the sum will vanish whereas the second one reproduces $|\rangle$ with a factor of one. If the state is unoccupied, the first term yields a factor of one, while the second vanishes.

For the bosonic operators, which have to express the fact that many-particle states of a system composed of identical bosonic particles are symmetric upon exchange of two particles, the commutation relations

$$\begin{aligned} [b_\lambda, b_\mu] &= [b_\lambda^+, b_\mu^+] = 0 \\ [b_\lambda, b_\mu^+] &= -[b_\mu^+, b_\lambda] = \delta_{\lambda\mu} \end{aligned} \tag{D.3}$$

hold and describe the fact that single-particle boson states can be occupied multiply.

Note that because of their non-hermiticity, the creation and destruction operators are not observable. The importance of these operators lies in the fact that all other operators can be expressed as linear combinations of products of creation and destruction operators. An example are the particle number operator $N$, and the Hamiltonian $H_0$, which are given by

$$N = \sum_{\boldsymbol{k}} n_{\boldsymbol{k}} = \sum_{\boldsymbol{k}} c_{\boldsymbol{k}}^+ c_{\boldsymbol{k}} \qquad \text{and} \qquad H_0 = \sum_{\boldsymbol{k}} \epsilon_{\boldsymbol{k}} c_{\boldsymbol{k}}^+ c_{\boldsymbol{k}} \ . \tag{D.4}$$

where $n_{\boldsymbol{k}}$ is the number operator counting the number of particles in the single-particle state $\boldsymbol{k}$, and $\epsilon_{\boldsymbol{k}}$ is the single-particle dispersion relation. States which are eigenstates to the particle number operator $N$ contain a fixed number of particles.

We introduce next the rules for determining the form that an operator given in first quantization assumes the second quantization. One-particle operators of the form $O^{(1)} = \sum_i O^{(1)}(\boldsymbol{p}_i, \boldsymbol{r}_i)$ are expressed in second quantization as

$$\begin{aligned} O &= \sum_{\alpha\beta} c_\alpha^+ O_{\alpha\beta}^{(1)} c_\beta \qquad \text{with} \\ O_{\alpha\beta}^{(1)} &= \langle\alpha|O^{(1)}|\beta\rangle = \int d^3r\, \psi_\alpha^*(\boldsymbol{r}) O^{(1)}(\boldsymbol{p}, \boldsymbol{r}) \psi_\beta(r) \end{aligned} \tag{D.5}$$

For a two-particle operator

$$O^{(2)} = \sum_{i \neq j} O^{(2)}(\boldsymbol{p}_i, \boldsymbol{r}_i; \boldsymbol{p}_j, \boldsymbol{r}_j)$$

its corresponding second quantized operator $O$ becomes

$$\begin{aligned} O &= \sum_{\alpha\beta\gamma\delta} c_\alpha^+ c_\beta^+ O_{\alpha\beta\gamma\delta}^{(2)} c_\gamma c_\delta \qquad \text{with} \\ O_{\alpha\beta\gamma\delta}^{(2)} &= \langle\alpha\beta|O^{(2)}|\gamma\delta\rangle \\ &= \int d^3r\, d^3r'\, \psi_\alpha^*(\boldsymbol{r}) \psi_\beta^*(\boldsymbol{r}') O^{(2)}(\boldsymbol{p}, \boldsymbol{r}; \boldsymbol{p}', \boldsymbol{r}') \psi_\gamma(\boldsymbol{r}') \psi_\delta(\boldsymbol{r}) \end{aligned} \tag{D.6}$$

The application of these rules to $H_0$ is easy. Suppose the external potential $U(r)$ vanishes. Then plane waves are eigenstates of the single-particle Hamiltonian $h_0$ (for simplicity we disregard the spin), and because of the relationship

$$\int d^3r\, e^{-i\boldsymbol{k}_\alpha \boldsymbol{r}} \frac{\boldsymbol{p}^2}{2m} e^{-i\boldsymbol{k}_\beta \boldsymbol{r}} = \frac{\boldsymbol{k}_\alpha^2}{2m} \delta_{\alpha\beta} \ ,$$

the second quantized Hamiltonian for the non-interacting system is given by the equation

$$H_0 = \sum_{\boldsymbol{k}} \epsilon_{\boldsymbol{k}} c^+_{\boldsymbol{k}} c_{\boldsymbol{k}} \qquad \text{with} \qquad \epsilon_{\boldsymbol{k}} = \frac{\boldsymbol{k}^2}{2m} \,. \tag{D.7}$$

The translation of a two-particle operator like the Coulomb interaction to the second quantized form is more delicate. According to (D.6), for a system with continuous translational symmetry we have to evaluate the integral

$$V_{\boldsymbol{k}_\alpha \boldsymbol{k}_\beta \boldsymbol{k}_\gamma \boldsymbol{k}_\delta} \int d^3r\, d^3r'\, e^{i(\boldsymbol{k}_\alpha - \boldsymbol{k}_\delta)\boldsymbol{r}} e^{i(\boldsymbol{k}_\beta - \boldsymbol{k}_\gamma)\boldsymbol{r}'} \frac{4\pi e^2}{|\boldsymbol{r} - \boldsymbol{r}'|}$$

Using $\boldsymbol{k}_\alpha = \boldsymbol{k} + \boldsymbol{q}$, $\boldsymbol{k}_\beta = \boldsymbol{k}' - (\boldsymbol{q} + \vec{\delta})$, $\boldsymbol{k}_\gamma = \boldsymbol{k}'$, and $\boldsymbol{k}_\delta = \boldsymbol{k}$, the exponentials can be written as $\exp(i\boldsymbol{q}(\boldsymbol{r} - \boldsymbol{r}')) \cdot \exp(-i\vec{\delta}\boldsymbol{r}')$. The fact that the Coulomb interaction just depends on the difference $\boldsymbol{r} - \boldsymbol{r}'$, and not on $\boldsymbol{r}$ and $\boldsymbol{r}'$ individually, implies that $\vec{\delta} = 0$, otherwise the integral would vanish. We are then left with the expression

$$V_{\boldsymbol{k}+\boldsymbol{q}, \boldsymbol{k}'-(\boldsymbol{q}+\vec{\delta}), \boldsymbol{k}', \boldsymbol{k}} = \delta_{\vec{\delta},0} \int d^3r\, d^3r'\, \frac{e^{-i\boldsymbol{q}(\boldsymbol{r}-\boldsymbol{r}')}}{|\boldsymbol{r} - \boldsymbol{r}'|} = \Omega \cdot \frac{4\pi e^2}{q^2} \delta_{\vec{\delta},0}$$

where $\Omega$ is the integration volume. This matrix element only depends on the differences $\boldsymbol{k}_\alpha - \boldsymbol{k}_\delta$ and $\boldsymbol{k}_\beta - \boldsymbol{k}_\gamma$ of the momenta of the scattered and incoming electrons, respectively. This is a consequence of the continuous translational symmetry of the system. The fact that the interaction depends only on the coordinates through $|\boldsymbol{r} - \boldsymbol{r}'|$ implies that in the scattering process the two interacting electrons cannot exchange momentum nor angular momentum with the rest of the system (this is only valid for free electrons. In a crystal, the pseudopotential breaks the continuous translational symmetry as well as the rotational symmetry of the Hamiltonian). The scattering process conserves momentum. Putting the matrix element under discussion into the expression for the two-particle operator in second quantization leaves us with the expression

$$V = \frac{1}{2} \sum_{\boldsymbol{k}, \boldsymbol{k}', \boldsymbol{q}} \frac{4\pi e^2}{q^2} c^+_{\boldsymbol{k}+\boldsymbol{q}} c^+_{\boldsymbol{k}'-\boldsymbol{q}} c_{\boldsymbol{k}'} c_{\boldsymbol{k}} \tag{D.8}$$

which can be represented in an obvious way by the diagram in Fig. D.1. Two electrons with momenta $\boldsymbol{k}$ and $\boldsymbol{k}'$ are propagating. Then they interact and continue propagating with momenta $\boldsymbol{k} + \boldsymbol{q}$ and $\boldsymbol{k}' - \boldsymbol{q}$. The total momentum is conserved, the label $\boldsymbol{q}$ on the dashed line denotes the momentum transfer.

## D.2.2 Normalizations and Fourier transforms

A final word on the normalization of wave functions and, related to that, the use of Fourier transformations. The Fermion field operators are defined by $\Psi(\boldsymbol{r}) = \sum_\lambda a_\lambda \psi_\lambda(\boldsymbol{r})$ using the single particle wave functions $\psi_\lambda(\boldsymbol{r})$. We work in a box of volume $V$, therefore the normalization condition for the wave functions is $\int_V d^3r\, \psi_\lambda(\boldsymbol{r}) \psi_{\lambda'}(\boldsymbol{r}) = \delta_{\lambda\lambda'}$. In the case of free particles, the wave functions are plane waves $\psi_{\boldsymbol{k}}(\boldsymbol{r}) = V^{-1/2} \exp i\boldsymbol{k}\boldsymbol{r}$.

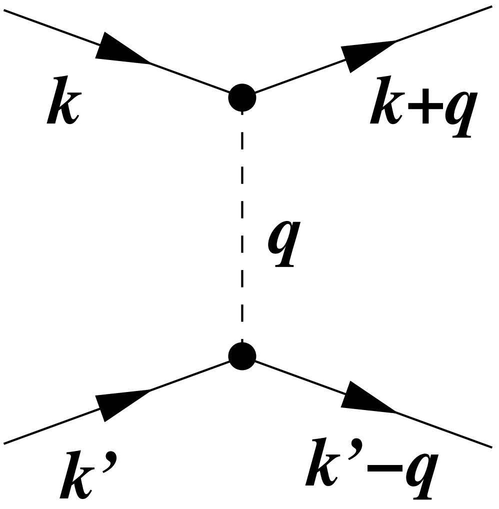

Figure D.1: The Coulomb interaction.

The Fourier transformation for functions of time is given by the expressions

$$f(\omega) = \int_{-\infty}^{\infty} dt\, e^{i\omega t} f(t) \qquad \text{and} \qquad f(t) = \int_{-\infty}^{\infty} \frac{d\omega}{2\pi}\, e^{-i\omega t} f(\omega)$$

where the frequency $\omega$ is a continuous variable. For functions of space, the Fourier transform is given by

$$f_{\boldsymbol{k}} = \int_V d^3r\, e^{-i\boldsymbol{k}\boldsymbol{r}} f(\boldsymbol{r}) \qquad \text{and} \qquad f(\boldsymbol{r}) = \frac{1}{V} \sum_{\boldsymbol{k}} e^{i\boldsymbol{k}\boldsymbol{r}} f_{\boldsymbol{k}}$$

whereas the variable $\boldsymbol{k}$ is discrete. The adjacent values of $\boldsymbol{k}$ have a distance of $2\pi/L$, where $V = L^3$. When having to perform $k$-space summations, we can convert them to integrals. This is possible for large $V$, and done by substituting

$$\frac{1}{V} \sum_{\boldsymbol{k}} \to \int \frac{d^3k}{(2\pi)^3} \qquad \text{and} \qquad \delta_{\boldsymbol{k}\boldsymbol{k}'} \to \frac{(2\pi)^3}{V} \delta(\boldsymbol{k} - \boldsymbol{k}') \ .$$

When manipulating expressions, we normally use the $k$-space summations and switch to integrals only if a $k$-space sum has to be calculated explicitly.

## D.3 The zero-temperature Green's function

In perturbation theory, the many-body Hamiltonian $H$ is split into a "simple" part $H_0$ (which is solvable exactly, that is, whose eigenfunctions and -energies are known), and a nontrivial part $V$, the particle-particle interaction treated as a *perturbation*. We denote the known ground state of the Hamiltonian $H_0$ by $|0\rangle$, and the ground state of the complete Hamiltonian $H$ by $|\mathrm{GS}\rangle$. The latter is often referred to as the *exact* ground state to distinguish it from the former. Furthermore, the Hamiltonian $H_0$ is assumed to describe a collection of systems of identical particles as in (D.1), such that single-particle excitations

| Schrödinger rep. | Heisenberg rep. | interaction rep. |
|---|---|---|
| $O_S$<br>$\psi_S(t) = e^{-iHt}\psi_S(0)$ | $O_H(t) = e^{iHt}O_S e^{-iHt}$<br>$\psi_H = \psi_S(0)$ | $O(t) = e^{iH_0 t}O_S e^{-iH_0 t}$<br>$\psi(t) = e^{iH_0 t}\psi_S(t)$ |

Table D.1: Definition of the representations under use.

are defined. Let us denote the wave functions describing these single-particle excitations by $\psi_\lambda$.

The first definition of the Green's function is given in the Heisenberg representation, in which the operators are time-dependent and the wave functions are not (see Tab. D.1). This allows for a very clear physical interpretation of the Green's function.

The *zero-temperature Green's function* $G$ for a system of electrons is given by the ground-state expectation value

$$G(\lambda, t - t') = -i\langle \mathrm{GS}|T\{c_{H,\lambda}(t)c^+_{H,\lambda}(t')\}|\mathrm{GS}\rangle \ . \tag{D.9}$$

In this definition, the Heisenberg operators[3] $c^+_{H,\lambda}(t)$ and $c_{H,\lambda}(t')$ create and destroy, respectively, an electron in the single-particle state $\psi_\lambda$, at the time $t$ and $t'$, respectively. The state $\psi_\lambda$ is an eigenstate of the *unperturbed* Hamiltonian $H_0$ for the case when the system contains exactly *one* particle. In the Heisenberg representation (see Tab. D.1), the time-dependence of the $c$-operators is given by $c^+_{H,\lambda}(t) = \exp(iHt)c^+_{H,\lambda}(0)\exp(-iHt)$. The "operator" $T$ is the time-ordering operator. Given two or more time-dependent operators, it orders these in such a way that the operators with later times are left ("the future is left"), and, additionally puts a minus sign for each interchange of two fermionic operators (i.e. anticommuting operators). The interchange of bosonic operators does not alter the sign. For the special case of two fermionic operators $A(t)$ and $B(t')$, this means

$$T\{A(t)B(t')\} = \begin{cases} A(t)B(t') & \text{for } t - t' > 0 \\ -B(t')A(t) & \text{for } t - t' < 0 \end{cases}$$

and leaves undetermined intentionally the case $t = t'$.

The *physical interpretation* of the Green's function (D.9) for the case $t > t'$ is as follows. At the time $t'$, an electron in the single-particle state $\psi_\lambda$ is added to the *exact* ground state $|\mathrm{GS}\rangle$. This electron then propagates in the system and interacts with other electrons as a consequence of not being in an eigenstate of the full Hamiltonian $H$. At a later time $t$, the electron is removed from the system. The quantity $G(\lambda, t - t')$ then describes the *amplitude* at the time of this removal. In the special case $V = 0$ of no present perturbation, the electron will stay in the state $\psi_\lambda$ and the *magnitude* of $G(\lambda, t - t')$ will be one for all values of $t - t' > 0$.

---

[3] We will use the Schrödinger-, Heisenberg-, and interaction-representation in this appendix. Operators or wave functions in the Schrödinger representation either will carry an index "S" or just no time-argument. The Heisenberg-representation is denoted by an index "H". In the interaction-representation, operators and wave functions just carry a time-argument.

## D.4 Interaction representation and $S$-matrix

Although the definition given in (D.9) is physically rather clear, it poses some problems. First of all, the exact ground state $|\mathrm{GS}\rangle$ needed to evaluate (D.9) is not known: its determination is *the* essential problem of many-body theory. Second, there is no clear separation of the implications of the free part $H_0$ and the interaction part $V$ of the Hamiltonian $H$ on the Green's function. This makes our goal of developing a perturbation theory for the determination of $G$ unnecessarily difficult. These deficiencies will be remedied by restating (D.9) in the *interaction representation* (see Tab. D.1) and introducing the $S$-matrix. The interaction representation makes the operators as well as the wave functions time-dependent. The trivial time-dependence generated by $H_0$ is put into the operators, and the nontrivial part, corresponding to $V$, is put into the wave functions by writing

$$\begin{aligned} O(t) &= e^{iH_0t} O_S e^{-iH_0t} \\ \psi(t) &= e^{iH_0t}\psi_S(t) = e^{iH_0t}e^{-iHt}\psi_S(0) = U(t)\psi_S(0) \ , \end{aligned}$$

where the unitary matrix $U(t) = e^{iH_0t}e^{-iHt}$ has been introduced. For vanishing perturbation $V = 0$, this matrix becomes the unit matrix, and therefore the interaction representation reverts to the Heisenberg representation. The $S$-matrix $S(t, t')$ can be defined by means of the $U$-matrix,

$$\psi(t) = S(t,t')\psi(t') = U(t)U^+(t')\psi(t') \ , \quad S(t,t') \equiv U(t)U^+(t') \tag{D.10}$$

it "takes $\psi$ from $t'$ to $t$." The $S$-matrix contains the time-evolution of the wave functions in the interaction representation. The properties of the $S$-matrix are the following:

1. $S(t,t') \equiv 1 \quad$ if $V = 0$
2. $S(t,t) = 1$
3. $S(t,t')S(t',t'') = S(t,t'') \quad$ (transitivity)
4. $S^+(t,t') = S(t',t) \quad$ (time reversal).

The most important of these properties is the third one, it allows for the connection of two subsequent time-evolutions.

Just by calculating the time-derivative of the definition of the $U$-matrix, we can give the differential equation

$$\frac{d}{dt}U(t) = -iV(t)U(t) \tag{D.11}$$

which together with the condition $U(0) = 1$ can be used to determine $U(t)$ and, therefore, by (D.10) the $S$-matrix $S(t, t')$. The solution for $U(t)$ is given by integrating (D.11) once and iterating this process. This yields the series

$$U(t) = 1 - i\int_0^t dt_1\, V(t_1) + (-i)^2 \int_0^t dt_1 \int_0^{t_1} dt_2\, V(t_1)V(t_2) + \cdots \tag{D.12}$$

which is an exact solution to (D.11). However, (D.12) is rather inconvenient because of the

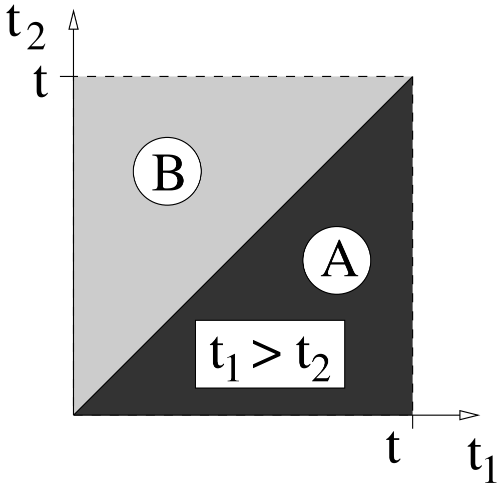

Figure D.2: The integration volume for the correction to the $S$-matrix in second order perturbation theory.

complicated integration limits, which, for the case of the term of second order in $V$ are given by region A in Fig. D.2. Exchanging $t_1$ and $t_2$ in the term of second order in $V$ changes the integration region from region A to region B, but leaves the integral (D.12) unchanged. In both cases A and B, the two operators $V(t)$ in the integral are ordered in such a way that the operator acting at the later time is to the left. Therefore, the integral under consideration is equivalent to

$$\frac{(-i)^2}{2}\int_0^t dt_1 \int_0^t dt_2 \, T\{V(t_1)V(t_2)\} \; ,$$

where the integration region is now a square. Arguing along the same lines for the other terms in the series (D.12), it can be shown that this series can be written in the form

$$U(t) = 1 + \sum_{n=1}^{\infty} \frac{(-i)^n}{n!} \int_0^t dt_1 \cdots \int_0^t dt_n \, T\{V(t_1)\cdots V(t_n)\} \; . \tag{D.13}$$

If we use the definition of the exponential function and the convention that the time-ordering operator $T$ operating on the exponential function is equivalent to operating on every term in the corresponding series expansion individually, the $S$-matrix (D.10) is given by the expression

$$\begin{aligned} S(t,t') &= 1 + \sum_{n=1}^{\infty} \frac{(-i)^n}{n!} \int_{t'}^t dt_1 \cdots \int_{t'}^t dt_n \, T\{V(t_1)\cdots V(t_n)\} \\ &= T \exp\left(-i \int_{t'}^t dt_0 \, V(t_0)\right) \end{aligned} \tag{D.14}$$

with the perturbation Hamiltonian $V$ in the *interaction representation*.

By just introducing the interaction representation, our main problem that the exact ground state $|\mathrm{GS}\rangle$ is unknown, remains unsolved. But the $S$-matrix is the key to solve it. Gell-Mann and Low [D.6] have proven a theorem which states that the exact ground state $|\mathrm{GS}\rangle$ (which is time-independent in the Heisenberg representation) is given by

$$|\mathrm{GS}\rangle = S(0,-\infty)|0\rangle \ .$$

The exact ground state can thus be generated by applying the evolution generated by the $S$-matrix from $t=-\infty$ till $t=0$ to the known ground state $|0\rangle$ of the unperturbed part of the Hamiltonian $H_0$.

Because of time reversal symmetry, it is clear that by applying the operator $S(\infty,0)$ to the exact ground state $|\mathrm{GS}\rangle$, we will recover the ground state $|0\rangle$ of $H_0$ up to a phase.[4] That is,

$$S(\infty,0)|\mathrm{GS}\rangle = e^{i\varphi}|0\rangle \qquad \text{or} \qquad \langle 0|S(\infty,-\infty)|0\rangle = e^{i\varphi} \ ,$$

which is a very important relation allowing us to write the bra-vector $\langle\mathrm{GS}|$ as

$$\langle\mathrm{GS}| = \langle 0|S(-\infty,0) = \frac{\langle 0|S(\infty,0)}{\langle 0|S(\infty,-\infty)|0\rangle} \ .$$

We apply the results derived in the discussion above and especially the relation $c_{H,\lambda}(t) = S(0,t)c_\lambda(t)S(t,0)$ to the Green's function (D.9). This yields

$$\begin{aligned}&\langle\mathrm{GS}|c_{H,\lambda}(t)c^+_{H,\lambda}(t')|\mathrm{GS}\rangle \\ &\quad = \frac{\langle 0|S(\infty,t)c_\lambda(t)S(t,t')c^+_\lambda(t')S(t',-\infty)|0\rangle}{\langle 0|S(\infty,-\infty)|0\rangle}\end{aligned} \tag{D.15}$$

for $t>t'$ and an analogous expression for $t<t'$. The numerator of (D.15) is written now in a very transparent form. At the right, one starts with the (known!) ground state $|0\rangle$, which evolves in time from $-\infty$ to $t'$, then an electron in state $\lambda$ is added. The resulting many-particle state evolves in time till $t$, where an electron in the same state $\lambda$ is removed. The new many-particle state then evolves in time until $\infty$ and is eventually projected onto the ground state $|0\rangle$. The denominator just represents a phase making the right hand side of (D.15) equal to the left hand side if the $c$-operators on both sides of the equation are removed.

Condensing again the notation by introducing the time-ordering operator, we can collect the 3 $S$-matrices in the expression above (note that $S(t,t')$ is a bosonic operator) and eventually arrive at

$$G(\lambda,t-t') = -i\frac{\langle 0|T\{c_\lambda(t)c^+_\lambda(t')S(\infty,-\infty)|0\rangle}{\langle 0|S(\infty,-\infty)|0\rangle} \tag{D.16}$$

which is the form of the Green's function used as the starting point for the perturbation theory. We note again that the operators in (D.16) are understood to be in the interaction representation. The state $|0\rangle$ is the ground state of $H_0$.

In the form (D.16), all the nontrivialities are hidden in the $S$-matrix, which can be written easily as a power series in the perturbation $V$ as was done with $U(t)$ in (D.13).

---

[4] We suppose that the ground state is a non-degenerate state. This is not the case in the strict sense for isotropic systems with a magnetic low-temperature phase or for gauge invariant systems with a superconducting low-temperature phase. These systems possess a continuous symmetry which is not a symmetry of the ground state, but commutes with the Hamiltonian. This effect is called spontaneous symmetry breaking.

All other elements of (D.16), the single-particle wave functions used in the definition of the $c$-operators, the ground state $|0\rangle$ of $H_0$, and the dynamics of the $c$-operators is given by the nonperturbed part $H_0$ of the Hamiltonian.

The only difficulty in (D.16) is the $S$-matrix in the denominator, which can be written as a power series in the perturbation $V$. We will see later, that the expectation value in the denominator of the Green's function will cancel some terms arising in the series expansion of the $S$-matrix in the numerator, and therefore poses no problem.

## D.5 The bare electron Green's function

As an example for a Green's function, we calculate the *bare electron Green's function*, which is the Green's function for the case of a vanishing perturbation $V = 0$. This case is particularly important, because the perturbation theory will eventually give rise to a rule for the calculation of the Green's function for the nontrivial case $V = 0$ from the bare Green's function $G^{(0)}(\lambda, t - t')$ and the perturbation $V$.

We use Eq. (D.16) as a starting point for the calculation and note that a vanishing perturbation $V$ implies that the $S$-matrix becomes the unit matrix. The bare Green's function, then, is given by the expression

$$G(\lambda, t - t') = -i\langle 0|T\{c_\lambda(t)c_\lambda^+(t')\}|0\rangle \equiv G^{(0)}(\lambda, t - t') \ . \tag{D.17}$$

We distinguish now two main cases for the ground state of the many-electron system. The first is given by a system allowing for a varying number of particles, or, resulting in the same bare Green's function, one electron in an otherwise *empty band*. Then the ground state is the vacuum containing no particles at all. The other—and more frequent—case is the one of a *degenerate electron gas* which is a model for a metal or a heavily doped semiconductor.[5] These systems contain a large but fixed number of electrons, and therefore the ground state, called *Fermi sea* $|\mathrm{FS}\rangle$, is the state with the lowest energy for a fixed number of $N$ particles and may be represented by the Fermi surface which separates the occupied from unoccupied states in $k$-space. We are talking here about the ground state $|0\rangle$ of the unperturbed system $H_0$. A Fermi surface, though, also exists in many systems exhibiting particle-particle interactions. In spherical systems, the Fermi surface is a sphere of radius $k_F$ in $k$-space. The Fermi sea plays the role of the vacuum state for a degenerate electron gas.

### D.5.1 An empty band

For the case of a system with a varying number of particles, the bare Green's function is particularly simple. The electron destruction operator $c_\lambda(t)$ applied to the ground state $|0\rangle$ (which corresponds to the particle vacuum) always gives zero. As a consequence, the bare Green's function (D.17) vanishes identically for the case $t < t'$. For $t > t'$, the creation operator is applied to the ground state resulting in the state $c_\lambda^+|0\rangle$ which has an energy of $\epsilon_\lambda$. The expectation value $\langle 0|c_\lambda c_\lambda^+|0\rangle$ turns out to be one, and hence the bare Green's function is given by

$$G^{(0)}(\lambda, t - t') = -i \cdot \theta(t - t') \cdot e^{-i\epsilon_\lambda(t-t')} \ . \tag{D.18}$$

---

[5] Doped in such a way that at least the dopant wave functions overlap, and therefore create a band rather that isolated levels.

Perturbation theory usually is formulated in $k$-space rather that in real space, so we also will give the Fourier transform of the bare Green's function defined by

$$G(\lambda, \omega) = \int_{-\infty}^{\infty} dt\, e^{i\omega t} G(\lambda, t) \ . \tag{D.19}$$

This integral, however, does not converge for the bare Green's function $G^{(0)}$ defined in (D.18). Hence, we are forced to introduce a convergence factor $\exp(-\delta t)$ with $\delta = 0^+$ to the exponential function in the integrand of (D.19). Because of the fact that the bare Green's function vanishes for negative times, this guarantees the existence of the Fourier transform, which becomes

$$G^{(0)}(\lambda, \omega) = \frac{1}{\omega - \epsilon_\lambda + i\delta}$$

and is just a simple pole in the lower half of the complex frequency plane at $\omega = \epsilon_\lambda$. *The poles of the Green's function corresponds to the excitation energies of the system.*

### D.5.2 The degenerate electron gas

We already mentioned that the filled Fermi sea $|\mathrm{FS}\rangle$ plays the role of the vacuum state for a degenerate electron gas. When working with this ground state, it is important to consider that an electron $\boldsymbol{k}$ can only be added to the ground state, if $|\boldsymbol{k}| > k_F$. In the other case $|\boldsymbol{k}| < k_F$, an electron can only be removed from the Fermi sea. This removal can be considered as the creation of a *hole*. The removal of an electron $\boldsymbol{k}\sigma$ removes a momentum $\boldsymbol{k}$ and a spin $\sigma$ as well as the energy $\epsilon_{\boldsymbol{k}}$ from the system. The creation of the hole has to have the same effect with respect to these quantities, therefore we conclude that the hole has a momentum, spin, and energy $-\boldsymbol{k}$, $-\sigma$, and $-\epsilon$, respectively.

Let us focus now the evaluation of the Green's function (D.17). We consider the case $t > t'$, call the energy of the Fermi sea $E_0$, and conclude from

$$\langle 0|e^{iH_0 t} c_{\boldsymbol{k}} e^{-iH_0(t-t')} c^+_{\boldsymbol{k}} e^{-iH_0 t'}|0\rangle = \langle 0|e^{iE_0 t} c_{\boldsymbol{k}} e^{-i(E_0+\epsilon_{\boldsymbol{k}})(t-t')} c^+_{\boldsymbol{k}} e^{-iE_0 t'}|0\rangle$$

and the fact that the operator $c^+_{\boldsymbol{k}}$ can create an electron only above the Fermi surface, that

$$G^{(0)}(\boldsymbol{k}, t-t') = -ie^{-i\epsilon_{\boldsymbol{k}}(t-t')}\Theta(k - k_F) \ .$$

For the case $t < t'$, we can carry out a similar calculation or simply infer the Green's function from that for $t > t'$ while taking into account that we have to (1) exchange $t$ and $t'$, (2) put an overall minus sign for the exchange of the operators, (3) exchange $\epsilon_{\boldsymbol{k}}$ by $-\epsilon_{\boldsymbol{k}}$, because an electron is removed now, and (4) replace $\Theta(k - k_F)$ by $\Theta(k_F - k)$, because electrons can only be removed below the Fermi surface. Combining the result obtained in this manner with that obtained above, the Green's function for the degenerate electron gas becomes

$$G^{(0)}(\boldsymbol{k}, t-t') = -i[\Theta(t-t')\Theta(k-k_F) - \Theta(t'-t)\Theta(k_F-k)]e^{-i\epsilon_{\boldsymbol{k}}(t-t')} \ ,$$

and performing the Fourier transformation of the function in time-space yields the expression

$$G^{(0)}(\boldsymbol{k}, \omega) = \frac{1}{\omega - \epsilon_{\boldsymbol{k}} + i\delta\,\mathrm{sign}(k - k_F)} \tag{D.20}$$

which has a pole in the lower frequency planes for energies above the Fermi surface and pole in the upper half plane for energies below the Fermi surface.

It is often very practical to measure the energy of the electrons in the degenerate electron gas with respect to the Fermi surface. We therefore try to modify the formalism used so far in such a way that instead of the energy $\epsilon_{\boldsymbol{k}}$ the energy $\xi_{\boldsymbol{k}} = \epsilon_{\boldsymbol{k}} - \mu$ measured with respect to the chemical potential $\mu$ (which depends on the particle number $N$) appears. A simple redefinition of the energy scale, however, is only possible if we restrict ourselves to particle-number conserving excitations. In the more general case, we use a new representation of many-body theory, in which not anymore the particle number $N$, but the chemical potential $\mu$ is given. Then, the exact ground state is no longer determined by minimizing $\langle \mathrm{GS}|H|\mathrm{GS}\rangle$ while keeping $\langle \mathrm{GS}|N|\mathrm{GS}\rangle$ constant. Instead, the expression $\langle \mathrm{GS}|H-\mu N|\mathrm{GS}\rangle$, when minimized, gives a $\mu$-dependent state $|\mu\rangle$ which corresponds to the exact ground state, if we put the chemical potential $\mu$ determined by the condition $\langle\mu|N|\mu\rangle = N_0$.

Then, in the definition of the Green's function $G(t)$ the operator $H_0$ giving the time-dependence of the $c$-operators is replaced by the combination $H_0 - \mu N$. Taking into consideration that the particle number commutes with the Hamiltonian $H_0$, it can be seen that the Green's function $G_{(\mu)}(t)$ defined for a fixed chemical potential is connected to the one defined for a fixed number of particles by the relation $G_{(\mu)}(t) = G(t)\cdot \exp i\mu t$. In the Fourier representation, therefore, the frequency $\omega$ in the expression for $G(\omega)$ has to be replaced by $\omega + \mu$ in order to get $G_{(\mu)}(\omega)$. Then, using the energy $\xi_{\boldsymbol{k}} = \epsilon_{\boldsymbol{k}} - \mu$ measured relatively to the Fermi energy, the expression

$$G^{(0)}_{(\mu)}(\boldsymbol{k},\omega) = \frac{1}{\omega - \xi_{\boldsymbol{k}} + i\delta\,\mathrm{sign}\,\xi_{\boldsymbol{k}}} \tag{D.21}$$

results for the bare Green's function of a degenerate electron gas for a fixed chemical potential $\mu$.

We see that the Green's function in frequency-space has a particularly simple form: for a given momentum $\boldsymbol{k}$ it consists of a simple pole (of residue 1) at the single-particle excitation energy $\xi_{\boldsymbol{k}}$. In order to describe electrons ($\xi_{\boldsymbol{k}} > 0$) and holes ($\xi_{\boldsymbol{k}} < 0$) with one single Green's function, the pole, if related to an electron, is located in the lower frequency half plane. If related to a hole, the pole is in the upper half of the complex frequency plane.

## D.6 Perturbative evaluation of the Green's function

### D.6.1 Expansion of the $S$-matrix

For the purpose of evaluating the Green's function, we are going to focus on its numerator of (D.16). We expand the $S$-matrix in a series in the perturbation $V$ using (D.14). Then, a typical term in the expansion looks like

$$\frac{(-i)^n}{n!}\int_{-\infty}^{\infty} dt_1 \cdots \int_{-\infty}^{\infty} dt_n\, \langle 0|T\{c_\lambda(t)c^+_\lambda(t')V(t_1)\cdots V(t_n)\}|0\rangle\ . \tag{D.22}$$

The perturbation $V$ in general will always consist of a number of electron creation and annihilation operators, and also of operators creating and annihilating other elementary excitations. We give two examples. In the first example, the *Coulomb interaction* only involves electronic excitations. Two electrons take part in the Coulomb interaction, therefore, two creation and two annihilation operators will come into the game. In the Schrödinger representation, the interaction is given by (D.8). In the interaction representation all four operators in the Coulomb interaction are taken at the same time.

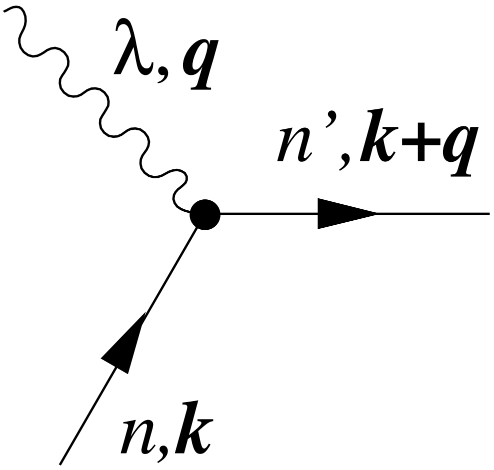

Figure D.3: The electron-phonon interaction.

The second example is the *electron-phonon interaction* which is represented by the equation

$$V = \sum_{\boldsymbol{q},\boldsymbol{k}} M_{\boldsymbol{q},\boldsymbol{k}}^{\lambda,n,n'} c_{n',\boldsymbol{k}+\boldsymbol{q}}^{+} c_{n,\boldsymbol{k}} (a_{\boldsymbol{q}\lambda} + a_{-\boldsymbol{q}\lambda}^{+}) \tag{D.23}$$

which describes the annihilation of a phonon of momentum $\boldsymbol{q}$ and branch index $\lambda$ (by the operator $a_{\boldsymbol{q}\lambda}$) while scattering an electron from band $n$ and momentum $\boldsymbol{k}$ to band $n'$ and momentum $\boldsymbol{k}+\boldsymbol{q}$ (see Fig. D.3). This electron scattering process may also be related to the creation of a phonon with momentum $-\boldsymbol{q}$ and branch index $\lambda$ (given by the operator $a_{-\boldsymbol{q}\lambda}^{+}$). Both processes have the same amplitude which is given by $M_{\boldsymbol{q},\boldsymbol{k}}^{\lambda,n,n'}$. Therefore, the two phonons under discussion are usually considered to be one phonon excitation by introducing the operator $A_{\boldsymbol{q}\lambda} = a_{\boldsymbol{q}\lambda} + a_{-\boldsymbol{q}\lambda}^{+}$. The transition to the interaction representation is performed again by writing the three operators in former equation in the interaction representation individually.

From the discussion given above, we conclude that the ground state expectation value in (D.22) can be considered for all practical purposes as consisting of an equal number of electron creation and destruction operators, taken at particular times, in the interaction representation and creation and destruction operators of other excitations, for instance phonon excitations. As a matter of fact, operators to different excitation types commute. Therefore the time-ordered product of a collection of, say, electron creation and destruction operators and phonon operators is equal to the time-ordered product of the electron operators times the time-ordered product of the phonon operators. The expectation value of this product can be separated into an expectation value of electron operators times an expectation value of phonon operators, respectively. Hence, we are going to discuss the ground state expectation value of the time-ordered product of a collection of $m$ electron creation and $m$ electron annihilation operators.

### D.6.2 Time-ordering, pairing, and Wick's theorem

The expectation values of time-ordered products of creation and destruction operators like the one in (D.22) with $V$ from (D.23) involve considerable complexity due to the presence of the time-ordering operator. A number of $2m$ operators, taken at different times, allows for up to $(2m)!$ different time-orderings. Fortunately, most of these ordered products vanish, and the time-ordering can be reformulated in a relatively simple manner. This reformulation is based on Wick's theorem. Before stating the theorem, we introduce some concepts which are important for its application.

Consider the expectation value

$$\langle 0|T\{c_\alpha(t_\alpha)c_\beta^+(t_\beta)c_\gamma(t_\gamma)c_\delta^+(t_\delta)\}|0\rangle \ . \tag{D.24}$$

We assume a certain relation for the time arguments, say $t_\delta > t_\alpha > t_\gamma > t_\beta$, and perform the time-ordering. This leads to

$$+\langle 0|c_\delta^+ c_\alpha c_\gamma c_\beta^+|0\rangle$$

(we suppress the time arguments from now on). The term has a positive sign because an even number of 4 transpositions is needed for the reordering of the operators.

The concept of *pairing* is based on the following observation. The operator $c_\beta^+$ adds an electron in state $\beta$ to the ground state. If this electron is not removed later on, the expectation value above will vanish. In other words, either $\alpha$ has to be equal to $\beta$, or $\gamma$ has to be equal to $\beta$. For all other cases, the expectation value vanishes. This yields

$$\langle 0|c_\gamma^+ c_\alpha c_\gamma c_\alpha^+|0\rangle\delta_{\alpha\beta}\delta_{\gamma\delta} + \langle 0|c_\alpha^+ c_\alpha c_\beta c_\beta^+|0\rangle\delta_{\alpha\delta}\delta_{\beta\gamma} \ , \tag{D.25}$$

and the number of two terms in this expression reflects the fact that there are two possibilities to pair two creation operators with two destruction operators. A product of $m$ creation and $m$ annihilation operators allows for $m!$ different pairings.

The operators in expression (D.25) may be regrouped. This *regrouping* is done in such a way that the ordering of operators to the same states is not altered because this would produce an extra term according to $\{c, c^+\} = 1$. Again we take into account that an odd number of transpositions of the operators yields a minus sign, and arrive at the expression

$$-\langle 0|c_\gamma^+ c_\gamma c_\alpha c_\alpha^+|0\rangle\delta_{\alpha\beta}\delta_{\gamma\delta} + \langle 0|c_\alpha^+ c_\alpha c_\beta c_\beta^+|0\rangle\delta_{\alpha\delta}\delta_{\beta\gamma} \ .$$

Note that in the first term of this expression, first an electron in state $\alpha$ is created, and subsequently removed. After the removal of this electron, we are back in the ground state, because the creation and destruction operators are creating and annihilating electrons in the eigenstates of $H_0$, and the ground state is meant to be the ground state of $H_0$. The dynamics added when introducing the interaction representation is the dynamics which is caused by the Hamiltonian $H_0$ also. Therefore, the electron created in state $\alpha$ will stay in this state. Hence, the expectation values in the equation above can be split into expectation values of products of one creation and one destruction operator,

$$\langle 0|c_\gamma^+ c_\gamma|0\rangle\langle 0|c_\alpha c_\alpha^+|0\rangle\delta_{\alpha\beta}\delta_{\gamma\delta} - \langle 0|c_\alpha^+ c_\alpha|0\rangle\langle 0|c_\beta c_\beta^+|0\rangle\delta_{\alpha\delta}\delta_{\beta\gamma} \ .$$

This is equivalent to (D.24) for the given time relation. The ground state expectation values only contain products of a creation and a destruction operator and, therefore, are very similar to the known bare Green's function. *Wick's theorem expresses expectation values of the form (D.24) as sums of products of bare Green's functions.*

*Wick's theorem* can be stated in the form of a handy rule:

- To calculate an expectation value of a time-ordered product of $m$ creation and $m$ annihilation operators, add all possible different pairings of creation and annihilation operators which amount to $m!$.
- To *pair* a creation and a annihilation operators means to bring them together (the annihilation operator to the left of the creation operator) by repeated transpositions while taking care of the sign. Then replace the pair by the time-ordered ground state expectation value of the pair.

For a proof of Wick's theorem, refer to [D.3], Sect. 8.2.

After having applied Wick's theorem, the expectation value under consideration is expressed as a sum of products made up of the factors

$$\begin{aligned} &\langle 0|T\{c_\lambda(t)c^+_{\lambda'}(t')\}|0\rangle = \\ &= \delta_{\lambda\lambda'} \times \begin{cases} iG^{(0)}(\lambda, t-t') & \text{for } t \neq t' \\ -\langle 0|c^+_\lambda(t)c_\lambda(t)|0\rangle = -\theta(\xi_\lambda - \xi_F) & \text{for } t = t'\ . \end{cases} \end{aligned} \tag{D.26}$$

Sometimes, the Fermi function $n_F(\xi_\lambda) = n_F(\epsilon_\lambda - \mu)$ is used instead of the factor $\theta(-\xi_\lambda)$. For $T = 0$ formalism, this is exactly the same.

### D.6.3 Feynman diagrams

As an example we calculate the numerator of the Green's function for the system $H = H_0 + V$ where $H_0$ is the Hamiltonian of the free Fermi gas (D.7), and $V$ is the electron-phonon coupling mentioned above. We shall consider only one phonon branch, one electronic band, and a electron-phonon matrix element independent of the electron momentum $\boldsymbol{k}$, that is

$$V = \sum_{\boldsymbol{q}} M_{\boldsymbol{q}} c^+_{\boldsymbol{k}+\boldsymbol{q}} c_{\boldsymbol{k}} A_{\boldsymbol{q}} \tag{D.27}$$

with $A_{\boldsymbol{q}} = a_{\boldsymbol{q}} + a^+_{-\boldsymbol{q}}$. The contribution of $n$th order in the perturbation $V$ to the numerator of the Green's function is given by (D.22). It is obvious that the contribution of zeroth order in $V$ leads to the bare Green's function $G^{(0)}$. Furthermore, the contribution to the Green's function of first order in the perturbation $V$ vanishes, because the expectation values of one phonon operator $\langle 0|A_{\boldsymbol{q}\lambda}|0\rangle$ are equal to zero. Hence we focus on the contribution of second order in $V$. Taking care on the prefactor, this reads

$$(-i) \cdot \frac{(-i)^2}{2!} \int_{-\infty}^{\infty} dt_1 \int_{-\infty}^{\infty} dt_2\, \langle 0|T\{c_{\boldsymbol{k}}(t)V(t_1)V(t_2)c^+_{\boldsymbol{k}}(t')\}|0\rangle\ . \tag{D.28}$$

By replacing the perturbation $V$ in the interaction representation into (D.28), and separating phonon operators from electron operators we find

$$\begin{aligned}&\frac{(-i)^3}{2!}\int_{-\infty}^{\infty}dt_1\int_{-\infty}^{\infty}dt_2\sum_{\boldsymbol{q}_1,\boldsymbol{q}_2}M_{\boldsymbol{q}_1}M_{\boldsymbol{q}_2}\langle 0|T\{A_{\boldsymbol{q}_1}(t_1)A_{\boldsymbol{q}_2}(t_2)\}|0\rangle\times\\ &\quad\times\sum_{\boldsymbol{k}_1,\boldsymbol{k}_2}\langle 0|T\{c_{\boldsymbol{k}}(t)c^+_{\boldsymbol{k}_1+\boldsymbol{q}_1}(t_1)c_{\boldsymbol{k}_1}(t_1)c^+_{\boldsymbol{k}_2+\boldsymbol{q}_2}(t_2)c_{\boldsymbol{k}_2}(t_2)c^+_{\boldsymbol{k}}(t')\}|0\rangle\ .\end{aligned}\tag{D.29}$$

The first expectation value in this expression can be written in terms of the (bare) phonon Green's function $D^{(0)}(\boldsymbol{q},t_1-t_2)$

$$i\delta_{\boldsymbol{q}_1+\boldsymbol{q}_2,0}D^{(0)}(\boldsymbol{q}_1,t_1-t_2)\ ,$$

where $D^{(0)}(\boldsymbol{q},t_1-t_2)$ is defined as

$$D^{(0)}(\boldsymbol{q},t_1-t_2)=-i\langle 0|T\{A_{\boldsymbol{q}}(t_1)A_{-\boldsymbol{q}}(t_2)\}|0\rangle\ .\tag{D.30}$$

The phonon Green's function will be discussed later in this appendix. The second expectation value has to be decomposed into combinations of the bare electron Green's function by making use of Wick's theorem. We find the $3!=6$ different pairings[6]

$$\begin{aligned}&\langle T\{c_{\boldsymbol{k}}(t)c^+_{\boldsymbol{k}_1+\boldsymbol{q}_1}(t_1)c_{\boldsymbol{k}_1}(t_1)c^+_{\boldsymbol{k}_2+\boldsymbol{q}_2}(t_2)c_{\boldsymbol{k}_2}(t_2)c^+_{\boldsymbol{k}}(t')\}\rangle\\ &=\langle T\{c_{\boldsymbol{k}}(t)c^+_{\boldsymbol{k}_1+\boldsymbol{q}_1}(t_1)\}\rangle\cdot\langle T\{c_{\boldsymbol{k}_1}(t_1)c^+_{\boldsymbol{k}_2+\boldsymbol{q}_2}(t_2)\}\rangle\cdot\langle T\{c_{\boldsymbol{k}_2}(t_2)c^+_{\boldsymbol{k}}(t')\}\rangle\\ &+\langle T\{c_{\boldsymbol{k}}(t)c^+_{\boldsymbol{k}_2+\boldsymbol{q}_2}(t_2)\}\rangle\cdot\langle T\{c_{\boldsymbol{k}_2}(t_2)c^+_{\boldsymbol{k}_1+\boldsymbol{q}_1}(t_1)\}\rangle\cdot\langle T\{c_{\boldsymbol{k}_1}(t_1)c^+_{\boldsymbol{k}}(t')\}\rangle\\ &-\langle T\{c_{\boldsymbol{k}}(t)c^+_{\boldsymbol{k}_1+\boldsymbol{q}_1}(t_1)\}\rangle\cdot\langle T\{c_{\boldsymbol{k}_1}(t_1)c^+_{\boldsymbol{k}}(t')\}\rangle\cdot\langle T\{c_{\boldsymbol{k}_2}(t_2)c^+_{\boldsymbol{k}_2+\boldsymbol{q}_2}(t_2)\}\rangle\\ &+\langle T\{c_{\boldsymbol{k}}(t)c^+_{\boldsymbol{k}}(t')\}\rangle\cdot\langle T\{c_{\boldsymbol{k}_1}(t_1)c^+_{\boldsymbol{k}_1+\boldsymbol{q}_1}(t_1)\}\rangle\cdot\langle T\{c_{\boldsymbol{k}_2}(t_2)c^+_{\boldsymbol{k}_2+\boldsymbol{q}_2}(t_2)\}\rangle\\ &+\langle T\{c_{\boldsymbol{k}}(t)c^+_{\boldsymbol{k}_2+\boldsymbol{q}_2}(t_2)\}\rangle\cdot\langle T\{c_{\boldsymbol{k}_1}(t_1)c^+_{\boldsymbol{k}_1+\boldsymbol{q}_1}(t_1)\}\rangle\cdot\langle T\{c_{\boldsymbol{k}_2}(t_2)c^+_{\boldsymbol{k}}(t')\}\rangle\\ &-\langle T\{c_{\boldsymbol{k}}(t)c^+_{\boldsymbol{k}}(t')\}\rangle\cdot\langle T\{c_{\boldsymbol{k}_1}(t_1)c^+_{\boldsymbol{k}_2+\boldsymbol{q}_2}(t_2)\}\rangle\cdot\langle T\{c_{\boldsymbol{k}_2}(t_2)c^+_{\boldsymbol{k}_1+\boldsymbol{q}_1}(t_1)\}\rangle\ .\end{aligned}\tag{D.31}$$

Note again that expectation values have been ordered such that the creation operator is placed to the right of the destruction operator, and in addition, a time ordering operator has been added. The expectation values in (D.31) can be expressed as bare Green's functions or as a Fermi function $n_F$ according to (D.26). Performing this step and noting that the factor $\delta_{\boldsymbol{q}_1+\boldsymbol{q}_2,0}=0$ is already present in (D.29), we obtain

$$\begin{aligned}&(\mathrm{a})=i^3\delta_{\boldsymbol{k},\boldsymbol{k}_1+\boldsymbol{q}_1}\delta_{\boldsymbol{k}\boldsymbol{k}_2}G^{(0)}(\boldsymbol{k},t-t_1)G^{(0)}(\boldsymbol{k}-\boldsymbol{q}_1,t_1-t_2)G^{(0)}(\boldsymbol{k},t_2-t')\\ &(\mathrm{b})=i^3\delta_{\boldsymbol{k}\boldsymbol{k}_1}\delta_{\boldsymbol{k},\boldsymbol{k}_2-\boldsymbol{q}_1}G^{(0)}(\boldsymbol{k},t-t_2)G^{(0)}(\boldsymbol{k}+\boldsymbol{q}_1,t_2-t_1)G^{(0)}(\boldsymbol{k},t_1-t')\\ &(\mathrm{c})=i^2\delta_{\boldsymbol{k}\boldsymbol{k}_1}\delta_{\boldsymbol{q}_1,0}n_F(\xi_{\boldsymbol{k}_2})G^{(0)}(\boldsymbol{k},t-t_1)G^{(0)}(\boldsymbol{k},t_1-t')\\ &(\mathrm{d})=i\delta_{\boldsymbol{q}_1,0}n_F(\xi_{\boldsymbol{k}_1})n_F(\xi_{\boldsymbol{k}_2})G^{(0)}(\boldsymbol{k},t-t')\\ &(\mathrm{e})=i^2\delta_{\boldsymbol{q}_1,0}\delta_{\boldsymbol{k}\boldsymbol{k}_2}n_F(\xi_{\boldsymbol{k}_1})G^{(0)}(\boldsymbol{k},t-t_2)G^{(0)}(\boldsymbol{k},t_2-t')\\ &(\mathrm{f})=-i^3\delta_{\boldsymbol{k}_1,\boldsymbol{k}_2-\boldsymbol{q}_1}G^{(0)}(\boldsymbol{k},t-t')G^{(0)}(\boldsymbol{k}_1,t_1-t_2)G^{(0)}(\boldsymbol{k}_1+\boldsymbol{q}_1,t_2-t_1)\end{aligned}\tag{D.32}$$

The terms have been written in the same order as in the equation above. Some of the Kronecker $\delta$-functions in (D.32) drop out, because they identically vanish.

---

[6] we have shortened a bit the notation writing $\langle\cdots\rangle$ as an abbreviation for $\langle 0|\cdots|0\rangle$.

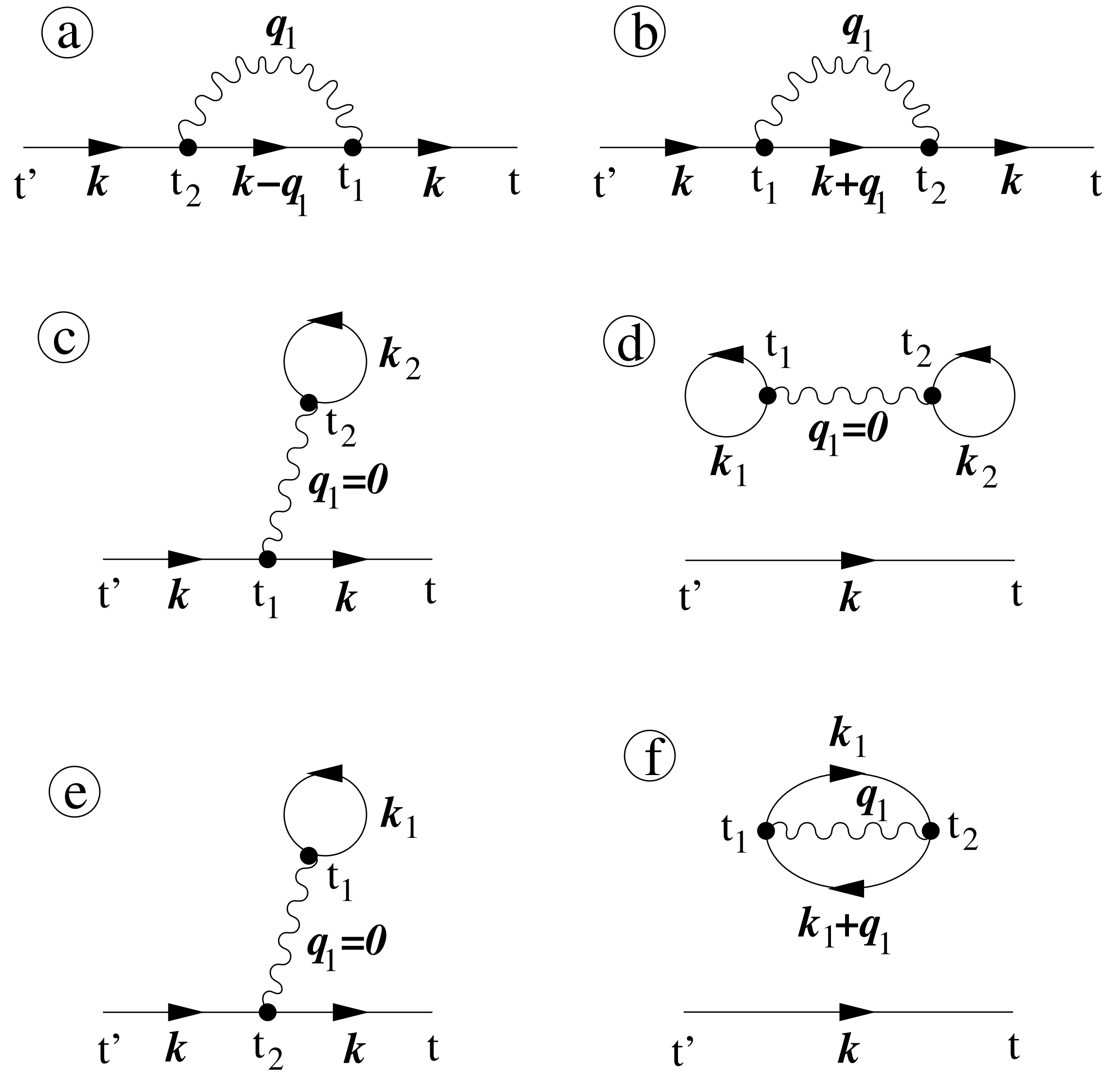

Figure D.4: Feynman diagrams for the renormalization of the electron Green's function by phonons to second order in the electron-phonon coupling matrix element.

This expression is still rather cumbersome but fortunately it can be expressed by physically very intuitive diagrams, the *Feynman diagrams*. In the time domain the rules for associating a Feynman diagram to an expression like one of the six above are as follows. Each bare Green's function $G^{(0)}(\boldsymbol{k}, t-t')$ is represented by a small straight line carrying a quasimomentum $\boldsymbol{k}$ and reaching from the time $t'$ to $t$. The line also includes an arrow denoting a direction. The meaning of this arrow will be explained later. It does *not* imply that $t' < t$. Nor does it imply that the line represents an electron if the arrow points from left to right and a hole, if it points from right to left. A Green's function with $t = t'$, that is, a factor $n_F$, is represented by a small circle. The direction of the line forming the circle is arbitrary and has no consequences.

A phonon is represented by a wavy line. It does not carry an arrow because the phonon Green's function is even in the time argument. The representations of the Coulomb interaction and also of photons will be given later. We can already surmise that the representation of photons (also other bosons) will be isomorphic to that of phonons.

We discuss now the 6 diagrams of Fig. D.4), starting with the one denoted by (a) and construct its associated Feynman diagram. The third Green's function from the left in expression (a) of (D.32) represents an electron propagating from $t'$ to $t_2$ and having a quasimomentum of $\boldsymbol{k}$. We denote it by a line from $t'$ to $t_2$ with a label $\boldsymbol{k}$. At the time $T_2$ two things happen. First, the electrons continues propagating, from $t_2$ to $t_1$, with a momentum of $\boldsymbol{k} - \boldsymbol{q}_1$. Second, a phonon carrying the missing $\boldsymbol{q}_1$ is created. We draw an electron line to $t_1$ and start a new wavy phonon line at $t_2$. At $t_1$, the phonon is destroyed, and the electron continues to propagate with its initial momentum $\boldsymbol{k}$ to $t$. The contribution of this diagram to the numerator of the Green's function (the term (D.29)) is given by the term

$$\begin{aligned} \frac{i}{2!}\int_{-\infty}^{\infty} dt_1 \int_{-\infty}^{\infty} dt_2 \sum_{\boldsymbol{q}} |M_{\boldsymbol{q}}|^2 D^{(0)}(\boldsymbol{q}, t_1 - t_2) \times \\ \times G^{(0)}(\boldsymbol{k}, t - t_1) G^{(0)}(\boldsymbol{k} - \boldsymbol{q}, t_1 - t_2) G^{(0)}(\boldsymbol{k}, t_2 - t') \ , \end{aligned} \tag{D.33}$$

it has to be taken into account that $M_{-\boldsymbol{q}} = M^*_{\boldsymbol{q}}$. The nodes at $t_1$ and $t_2$ in the diagram in Fig. D.4(a) are called *vertices* and are related to the electron-phonon matrix element $M_{\boldsymbol{q}}$. One of the vertices represents the creation of a phonon, the other the destruction of a phonon. Therefore, the matrix element $M_{\boldsymbol{q}}$ appears as a complex conjugated pair: the matrix element for a time reversed process is the complex conjugate of that for the direct process.

In the diagram, the quasimomentum $\boldsymbol{q}$ is summed over. In this way all possible phonons are included. The time integrations show that the way a diagram is drawn or the arrows are put on the electron lines does not imply any time ordering. The arrows denote *particle number conservation* at the vertices.

The diagram in Fig. D.4(b) is very similar to that in Fig. D.4(a). The only difference is the labeling of some of the variables. It can be shown that there are always $n!$ diagrams in the $n$th order perturbation contribution which are equal in the sense that their contribution to the Green's function is the same. The related diagrams then are called *topologically equal*, which means that by relabeling internal variables, the diagrams become identical. When using perturbation theory one only draws one representative of these $n!$ topologically identical diagrams, and removes the factor $1/n!$ in the corresponding perturbation term.

Let us proceed with the diagram Fig. D.4(c). This time we have an electron propagating from $t'$ to $t_1$, and then from $t_1$ to $t$. In both cases it carries a quasimomentum $\boldsymbol{k}$. At the time $t_1$, a phonon is created. Because of the factor $\delta_{\boldsymbol{q}_1,0}$ in the expression for the diagram (c), this must be a $\Gamma$-point phonon. At $t_2$ this phonon is destroyed. Correspondingly, the factor $n_F(\xi_{\boldsymbol{k}_2})$ appears. We recall the fact that this is a Green's function with the time argument $t_1 - t_1$. Therefore we draw this factor as a loop formed by an electron line. The loop is attached to the time $t_1$ (and similarly to $t_2$).

The diagrams (d) and (e) are constructed in a similar manner, and also contain a $\Gamma$-point phonon. This phonon has no dynamics,[7] it corresponds to static strain which is meant to be not included in the Hamiltonian $H$. Therefore, they vanish.

The last expression is represented by diagram (f). We start with its first Green's function which denotes an electron traveling from $t'$ to $t$. At $t_1$, an electron with momentum $\boldsymbol{k}_1$ and a phonon with quasimomentum $\boldsymbol{q}_1$ are created. Furthermore, an electron with quasimomentum $\boldsymbol{k}_1 + \boldsymbol{q}_1$ is destroyed. This is necessary to conserve particle number and the quasimomentum. At time $t_2$ a similar annihilation happens.

Note that the diagrams (d) and (f) have a very particular property: they decay into separable, independent parts. Diagram (f), for instance, is just given by a bare Green's function $G^{(0)}(\boldsymbol{k}, t - t')$ times some factor. It can be shown that the contributions arising from these separable parts, whose related diagrams are called *disconnected* diagrams, exactly cancel the factor $\langle 0|S(\infty, -\infty)|0\rangle$ in the denominator of the Green's function.

### D.6.4 Reformulation in the frequency-domain

Before concluding this section and stating the Feynman rules, which tell how to determine the contributions of $n$th order perturbation theory to the Green's function, we write the diagrams and their corresponding mathematical expressions in the frequency domain by performing a Fourier transformation of the Green's function. It will turn out that this introduces a further simplification in the perturbation series for the Green's function. We have seen in the paragraphs above (refer, e.g., to (D.33)) that the time integrals over the products of Green's function have the form of a convolution; the individual Green's functions in the integrand depend on time via differences $t_i - t_{i+1}$. By expressing the calculations in the frequency domain, these convolutions become simply products.

How this Fourier transformation is performed, and what implications it has, will be explained using as an example the contribution shown in Fig. D.4(a) to the Green's function, or, respectively, Eq. (D.33). In this expression, we replace the Green's functions by the corresponding frequency-dependent Green's functions

$$G(\boldsymbol{k}, t - t') = \int \frac{d\omega}{2\pi}\, e^{-i\omega(t-t')} G(\boldsymbol{k}, \omega) \ ,$$

and similarly for the phonon Green's function. This introduces the four factors $\exp -i\nu(t_1 - t_2)$, $\exp -i\omega(t - t_1)$, $\exp -i\omega'(t_1 - t_2)$, and $\exp -i\omega''(t_2 - t')$ for the bare phonon and the first, second, and third bare electron, respectively. Collecting all these terms together, the time dependent part of (D.33) becomes

$$\int dt_1 \int dt_2\, e^{-i\omega t} e^{-i(\omega'+\nu-\omega)t_1} e^{-i(\omega''-\nu-\omega')t_2} e^{i\omega'' t'}$$

---

[7] This is only true for acoustic phonons, but not for optical phonons.

which, when integrated, gives rise to the two $\delta$-functions $2\pi\delta(\omega'+\nu-\omega)$ and $2\pi\delta(\omega''-\nu-\omega')$ which guarantee the conservation of energy at the *vertices* (the vertices correspond to the nodes in the Feynman diagram, places where 2 or more lines are joined) and remove the integrals over the internal frequencies $\omega'$ and $\omega''$ introduced by the Fourier transformation. Then, only the factor $exp(-i\omega(t-t'))$ is left which resembles the one in the Fourier transformation of the whole expression (D.33). The diagram given in Fig. D.4(a) corresponds consequently to the diagram in Fig. D.5 when working in frequency space, whereas the corresponding contribution to the frequency-dependent Green's function becomes

$$\frac{i}{2!}\sum_{\boldsymbol{q}}|M_{\boldsymbol{q}}|^2 G^{(0)}(\boldsymbol{k},\omega)\left[\int\frac{d\omega}{2\pi}D^{(0)}(\boldsymbol{q},\nu)G^{(0)}(\boldsymbol{k}-\boldsymbol{q},\omega-\nu)\right]G^{(0)}(\boldsymbol{k},\omega)\;. \tag{D.34}$$

Comparing this expression to the diagram in Fig. D.5, we notice some important points related to Feynman diagrams. (i) the *incoming* and the *outgoing* bare Green's functions which carry the same indices as the Green's function $G(\boldsymbol{k},\omega)$ to which they contribute. This is clearly related to (ii), the conservation of quasimomentum and energy (i.e. frequency) at each of the vertices of the diagram. For the case of the two quasimomenta, this conservation was already introduced when building pairs according Wick's theorem, and ultimatively are a consequence of the translational invariance of the system under consideration (here it does not matter whether there is a "full" continuous translation like the translation group of space, or "only" discrete translations like those imposed by a Bravais lattice). The conservation of energy was introduced when performing the Fourier transformation, and relates to the fact that the Green's function is a function of time *differences* only.

(iii) All internal lines (i.e. all lines but the incoming and outgoing ones) are given *internal* quantum numbers (i.e. $\boldsymbol{q}$), which only have to satisfy the momentum and frequency conservation at each vertex. If many possibilities are compatible with this constraint, they are summed over as in the case of (D.34) for the variables $\boldsymbol{q}$ and $\omega$.

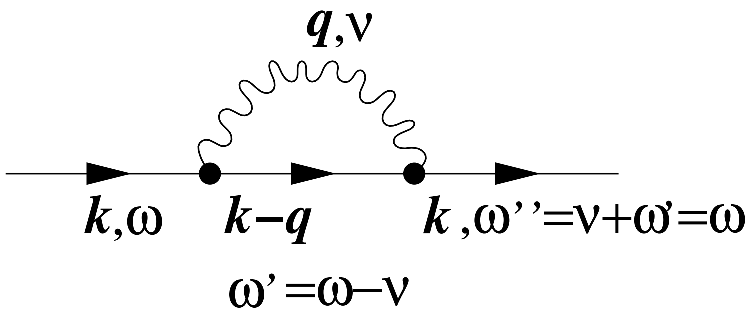

Figure D.5: A Feynman diagram in frequency space.

## D.6.5 A conclusion: the Feynman rules

In addition to introducing the Feynman diagrams, the example above has demonstrated some basic principles. The first is the cancellation of the ground state expectation value of the $S$-matrix. Those terms in the numerator of the Green's function (D.16) which correspond to *nonconnected* diagrams exactly cancel the denominator in (D.16). The second one deals with the *topologically equivalent* Feynman diagrams. The $n$th order (in $V$) term in the numerator of the Green's function yields $n!$ Feynman diagrams which are topologically equivalent, that is just differ by a different labeling of integration (or sum) variables.

Taking these principles into account, we can state that the Green's function is given by a formula much simpler than that in (D.16):

$$G(\boldsymbol{k}, t-t') = -i\langle 0|T\{c_{\boldsymbol{k}}(t)c^{+}_{\boldsymbol{k}}(t')S(\infty,-\infty)\}|0\rangle_{\text{diff, con}}$$

where the index "diff, con" indicates that only *topologically different* and *connected* (i.e. not disconnected) contributions are considered.

Reformulating this statement, and including the rules for drawing diagrams, we arrive at *Feynman's rules* for the calculation of the contribution to the Green's function arising as an $n$th order perturbation in $V$.

*Feynman rules:* When intending to calculate the contribution to the electron Green's function[8] $iG(\boldsymbol{k}, \omega)$ arising in $n$th order perturbation theory from electron-phonon coupling (here, $n = 2m$, all other contributions vanish), we

- draw all topologically different, connected diagrams which consist of an incoming and an outgoing bare Green's function, and contain $n/2$ internal phonon lines and $n-1$ electron lines. To the electron lines, arrows are added which represent particle conservation at the vertices of the diagram. Then,

- the incoming and outgoing electron Green's functions are labeled with momentum $\boldsymbol{k}$ and frequency $\omega$, and the internal lines are all also labeled with internal momentum and frequency variables taking into consideration the conservation of momentum and frequency at each of the vertices (This depends on the direction of the arrow in the case of electron lines).

- When translating the Feynman diagram to an analytic expression, we write $G^{(0)}(\boldsymbol{k}, \omega)$ for each of the electron lines carrying labels $\boldsymbol{k}, \omega$. The direction in which the arrow on the electron line points does not matter. We write $D^{(0)}(\boldsymbol{q}, \nu)$ for a phonon line with labels $\boldsymbol{q}, \nu$.

- Then each pair of vertices terminating phonon lines is represented by the squared electron-phonon matrix element $|M_{\boldsymbol{q}}|^2/\Omega$ ($\Omega$ is the integration volume).

- As a next step, all the internal quasimomenta are summed over and all the internal frequencies are integrated over by inserting the appropriate sums and integrals $\sum_{\boldsymbol{q}}$ and $\int d\omega/(2\pi)$.

- Finally, we put a factor $i^n(-1)^F(2S+1)^F$ where $F$ is the number of *closed* fermion loops, and $S$ denotes the spin quantum number of the electrons.

---

[8] Note the factor $i$ in front of the Green's function. The rules presented here are valid for the calculation of $iG$, not for $G$.

The last rule comes from the fact that the Green's functions actually correspond to second rank tensors in spin space and, in the simplest case of no external magnetic field and no spin-spin interactions, have the form $G_{\alpha\beta}(\boldsymbol{k},\omega) = \delta_{\alpha\beta}G(\boldsymbol{k},\omega)$. When evaluating the diagram obviously a sum over the spin indices has to be carried out. And in Fermion loops, combinations like $\delta_{\alpha\alpha}G$ or $\delta_{\beta\gamma}G\delta_{\gamma\beta}G$ yield a factor of $2S+1$ when the spin sum is performed.

### D.6.6 The bare phonon Green's function

We close this section by calculating explicitly the bare phonon Green's function defined in (D.30). The phonon operators $A_{\boldsymbol{q}}$ are given by $A_{\boldsymbol{q}} = a_{\boldsymbol{q}} + a^+_{-\boldsymbol{q}}$ (when suppressing the branch index $\lambda$). When evaluating the product $A_{\boldsymbol{q}}(t_1)A_{-\boldsymbol{q}}(t_2)$ we first restrict to the case $t_1 > t_2$ to circumvent the difficulty presented by the time-ordering operator. The other case works similarly and has to be taken into account when formulating the result of the calculation given here. The evaluation of the product above consisting of two $A$-operators, yields four combinations of two $a$-operators each. The expectation value of the combinations consisting of creation or destruction operators only vanishes, and the terms left contain the combinations $a^+_{-\boldsymbol{q}}a_{-\boldsymbol{q}}$ and $a_{\boldsymbol{q}}a^+_{\boldsymbol{q}}$. The state $|0\rangle$ here corresponds to the vacuum state of the phonon field, and therefore contains no phonon at all. Hence, the expectation value of $a^+_{-\boldsymbol{q}}a_{-\boldsymbol{q}}$ also vanishes. The time dependence of the remaining term is given by $a_{\boldsymbol{q}}(t_1)a^+_{\boldsymbol{q}}(t_2) = \exp -i\omega_{\boldsymbol{q}}(t_1 - t_2) \times a_{\boldsymbol{q}}a^+_{\boldsymbol{q}}$ and recalling the quantum theory of the harmonic oscillator then leaves us with the result

$$\begin{aligned} D^{(0)}(\boldsymbol{q}, t_1 - t_2) &= -i\langle 0|T\{A_{\boldsymbol{q}}(t_1)A_{-\boldsymbol{q}}(t_2)\}|0\rangle \\ &= -i \times \begin{cases} e^{-i\omega_{\boldsymbol{q}}(t_1-t_2)} & \text{for } t_1 > t_2 \\ e^{i\omega_{\boldsymbol{q}}(t_1-t_2)} & \text{for } t_1 < t_2 \end{cases} \end{aligned} \tag{D.35}$$

where the case $t_1 < t_2$ was taken into account already. The Fourier transformation of the bare phonon Green's function gives

$$\begin{aligned} D^{(0)}(\boldsymbol{q},\omega) &= \frac{1}{\omega - \omega_{\boldsymbol{q}} + i\delta} - \frac{1}{\omega + \omega_{\boldsymbol{q}} - i\delta} \\ &= \frac{2\omega_{\boldsymbol{q}}}{\omega^2 - \omega_{\boldsymbol{q}}^2 + i\delta} \end{aligned} \tag{D.36}$$

which has two poles, one at the frequency $\omega = \omega_{\boldsymbol{q}}$, slightly shifted to the lower frequency plane, and the second at $\omega = -\omega_{\boldsymbol{q}}$, slightly shifted to the upper frequency plane.

## D.7 Self-energy contributions and the Dyson equation

In the last section, we have come to the conclusion that the contribution to the Green's function in $n$th order of the perturbation $V$ in (D.27) is given by all topologically different and connected Feynman diagrams containing $n/2$ phonon lines. For most of the applications of Green's function theory it is still not sufficient to approximate the Green's function by its bare counterpart plus the terms given by perturbation theory up to, say, order $N$. Instead, important contributions to the Green's function have to be included to *all orders*.

It is important to stress that only the certain terms have to be included to infinite order. Taking all diagrams to all orders would be an insurmountable task. But the inclusion of certain important contributions[9] to all orders is relatively easy to manage by applying the *Dyson equation*.

Let us look at a simple example. The diagrams contributing to the electronic Green's function in 4th order of the electron-phonon matrix element are show in Fig. D.6.

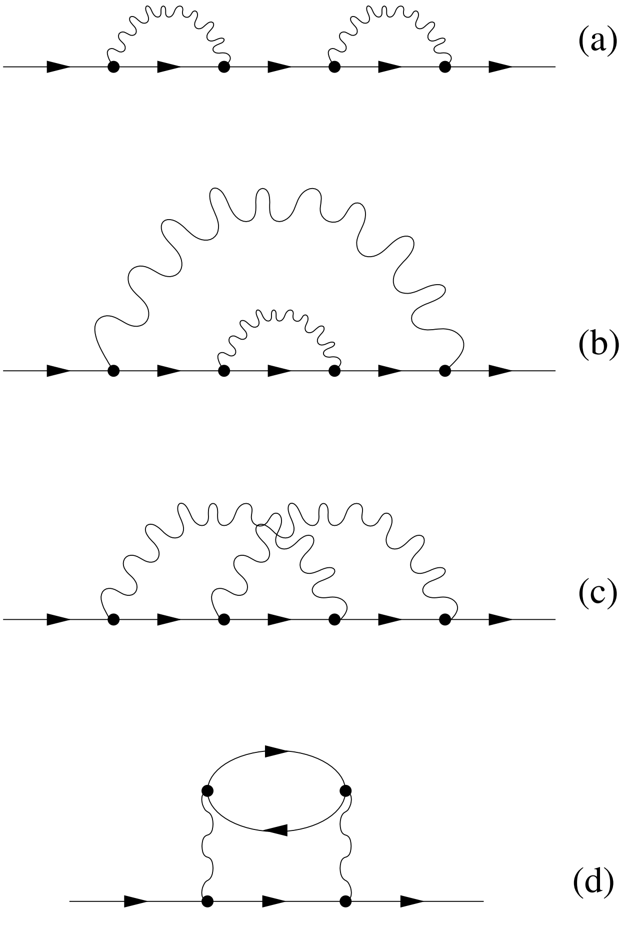

Figure D.6: Feynman diagrams for the renormalization of the electron Green's function by phonons in fourth order of the electron-phonon coupling matrix element.

We focus on the diagram of Fig. D.6(a). It is simply twice the diagram in Fig. D.5. In sixth order perturbation theory it will occur again, then being three times the diagram in Fig. D.5. Considering this class of diagrams up to infinite order is equivalent to summing a geometrical series and can be performed easily, provided it converges.

The diagram in Fig. D.5 translates according to the Feynman rules into the expression

$$
\begin{aligned}
& iG^{(0)}(\boldsymbol{k},\omega)\Sigma_1(\boldsymbol{k},\omega)G^{(0)}(\boldsymbol{k},\omega) \\
\text{with} \qquad & \Sigma_1(\boldsymbol{k},\omega) = -\sum_{\boldsymbol{q}} |M_{\boldsymbol{q}}|^2 \int \frac{d\omega}{2\pi} D^{(0)}(\boldsymbol{q},\nu)G^{(0)}(\boldsymbol{k}-\boldsymbol{q},\omega-\nu)\ .
\end{aligned}
$$

---

[9] Which contributions are important is shown by "experience."

It is clear that the diagram in Fig. D.6(a) then is represented by the expression

$$iG^{(0)}(\boldsymbol{k},\omega)\left[\Sigma_1(\boldsymbol{k},\omega)G^{(0)}(\boldsymbol{k},\omega)\right]^m$$

for $m = 2$. For $m = 2n > 2$ it corresponds to an $m$-fold repetition of Fig. D.5. Summing up the contributions for all $m = 2n$ $(n = 0\ldots\infty)$ yields

$$\begin{aligned} G_1(\boldsymbol{k},\omega) &= G^{(0)}(\boldsymbol{k},\omega) + \sum_m G^{(0)}(\boldsymbol{k},\omega)\left[\Sigma_1(\boldsymbol{k},\omega)G^{(0)}(\boldsymbol{k},\omega)\right]^m \\ &= G^{(0)}(\boldsymbol{k},\omega) + G^{(0)}(\boldsymbol{k},\omega)\Sigma_1(\boldsymbol{k},\omega)G_1(\boldsymbol{k},\omega)\ . \end{aligned} \tag{D.37}$$

We have denoted by $G_1(\boldsymbol{k},\omega)$ the Green's function that results from summing all the diagrams consisting of a sequence of that in Fig. D.5. A graphical representation of (D.37) is shown in Fig. D.7.

Clearly, the Green's function $G_1$ defined in the last paragraph is only an approximation to the exact Green's function $G$. But the method above can be extended to give the exact Green's function as well (at least in principle). This extension is based upon the observation that the function $\Sigma_1(\boldsymbol{k},\omega)$ can be replaced by a function $\Sigma(\boldsymbol{k},\omega)$, such that the function $G_1$ becomes the exact Green's function. The resulting *Dyson equation* is

$$G(\boldsymbol{k},\omega) = G^{(0)}(\boldsymbol{k},\omega) + G^{(0)}(\boldsymbol{k},\omega)\Sigma(\boldsymbol{k},\omega)G(\boldsymbol{k},\omega)\ , \tag{D.38}$$

where the *self energy* $\Sigma(\boldsymbol{k},\omega)$ is the sum of all *irreducible self-energy parts* $\Sigma_i(\boldsymbol{k},\omega)$. As irreducible self-energy parts we designate diagrams which can be put between two electron lines and cannot be separated into two nonconnected parts by just cutting one electron line. Equation (D.38) generates the whole series of diagrams contributing to the Green's function by iteration and in this manner generates all different sequences of self-energy parts $\Sigma_i$ to form diagrams of higher order in the perturbation. The diagram in Fig. D.6(a) is generated in the second iteration of the Dyson equation as

$$G^{(0)}(\boldsymbol{k},\omega)\Sigma_1(\boldsymbol{k},\omega)G^{(0)}(\boldsymbol{k},\omega)\Sigma_1(\boldsymbol{k},\omega)G^{(0)}(\boldsymbol{k},\omega)$$

and if the diagram related to the expression $\Sigma_1(\boldsymbol{k},\omega)G^{(0)}(\boldsymbol{k},\omega)\Sigma_1(\boldsymbol{k},\omega)$ would be included as a self-energy part $\Sigma_2$ in the self energy, the diagram in Fig. D.6(a) also would be generated in the first iteration of the Dyson equation as $G^{(0)}(\boldsymbol{k},\omega)\Sigma_2(\boldsymbol{k},\omega)G^{(0)}(\boldsymbol{k},\omega)$ and would be incorrectly counted twice.

The recipe usually employed to calculate the Green function is to calculate the self energy first, and then replace it into Dyson's equation. It is clear, however, that the self energy cannot be calculated exactly, because it consists of an infinite number of very different diagrams. But at this point, a rather systematic way of approximating the Green's function can be given: the one to approximate the self energy. This procedure is illustrated in Fig. D.7: the self energy is approximated by one self-energy part, which for some reason is considered to be the most important one, and is being used in conjunction with the Dyson equation the calculate an approximation of the Green's function.

Let us look again at the bare Green's function

$$G^{(0)}(\boldsymbol{k},\omega) = \frac{1}{\omega - \xi_{\boldsymbol{k}} + i\delta_{\boldsymbol{k}}}$$

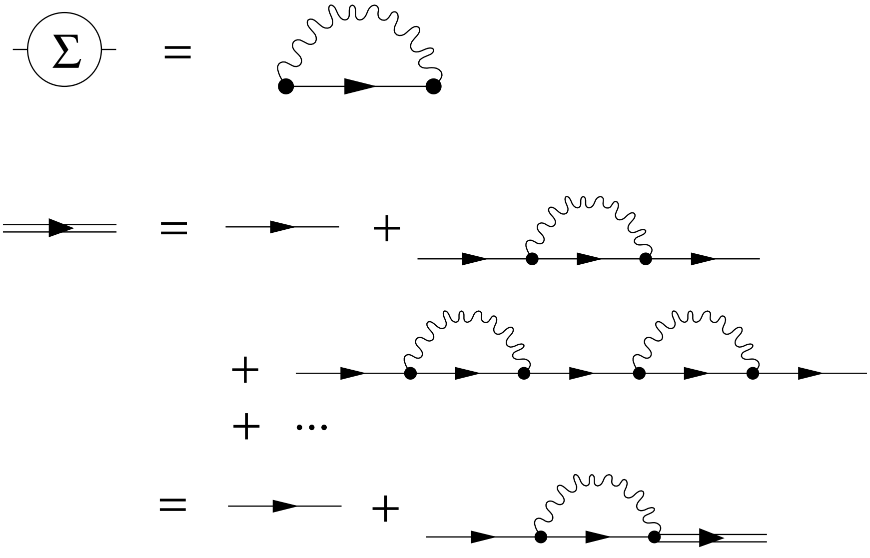

Figure D.7: Self energy and Dyson equation.

which is closely related to the excitation spectrum of the noninteracting system because it has poles at the unperturbed excitation energies. This property is shared by the full Green's function with respect to the interacting system:

$$G(\boldsymbol{k},\omega) = \frac{1}{\omega - \xi_{\boldsymbol{k}} - \Sigma(\boldsymbol{k},\omega) + i\delta_{\boldsymbol{k}}} \ . \tag{D.39}$$

The excitation energies of the perturbed system as obtained from (D.39) are

$$\begin{aligned} &\omega - \xi_{\boldsymbol{k}} - \Sigma(\boldsymbol{k},\omega) = 0 \\ \text{or} \quad &\omega = \xi_{\boldsymbol{k}} + \operatorname{Re}\Sigma(\boldsymbol{k},\omega) + i \operatorname{Im}\Sigma(\boldsymbol{k},\omega) \ . \end{aligned} \tag{D.40}$$

Note that due to the dependence of the self energy on the frequency, (D.40) is in general non-linear.

### D.7.1 The self-energy of a phonon

The formalism presented so far is also applicable to calculating the phonon Green's function $D(\boldsymbol{q},\nu)$ in a perturbational approach from the bare phonon Green's function $D^{(0)}(\boldsymbol{q},\nu)$. The following Dyson equation defines the phonon self-energy $\Pi(\boldsymbol{q},\nu)$:

$$D(\boldsymbol{q},\nu) = D^{(0)}(\boldsymbol{q},\nu) + D^{(0)}(\boldsymbol{q},\nu)\Pi(\boldsymbol{q},\nu)D(\boldsymbol{q},\nu) \ . \tag{D.41}$$

As in the case of the electron self-energy, the phonon self-energy is given by all diagrams, which can be inserted between two phonon lines representing $D^{(0)}(\boldsymbol{q},\nu)$, but cannot be separated into independent parts by just cutting one phonon line.

An important contribution to the phonon self-energy is the decay of the phonon into an electron-hole pair with a subsequent recombination of the electron-hole pair and creation

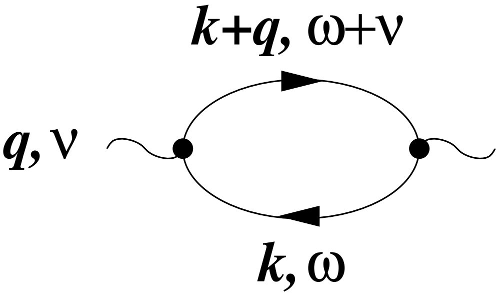

Figure D.8: A irreducible contribution to the phonon self-energy.

of a phonon. This process is depicted in Fig. D.8, and, using the Feynman rules, can be translated into the expression

$$\Pi(\boldsymbol{q},\nu) = -2i|M_{\boldsymbol{q}}|^2 \int \frac{d^3k\,d\omega}{(2\pi)^4} G^{(0)}(\boldsymbol{k}+\boldsymbol{q},\nu+\omega)G^{(0)}(\boldsymbol{k},\omega) \ .$$

As we will see later, this expression is very similar to the one for the longitudinal dielectric function.

We now evaluate the frequency integral in the expression above for a degenerate electron gas

$$\int \frac{d\omega}{2\pi} G^{(0)}(\boldsymbol{k}+\boldsymbol{q},\nu+\omega)G^{(0)}(\boldsymbol{k},\omega) = \int \frac{d\omega}{2\pi} \frac{1}{\omega+\nu-\xi_{\boldsymbol{k}+\boldsymbol{q}}+i\delta_{\boldsymbol{k}+\boldsymbol{q}}} \frac{1}{\omega+\nu-\xi_{\boldsymbol{k}}+i\delta_{\boldsymbol{k}}} \ .$$

We encounter four cases. The first is the case with $\xi_{\boldsymbol{k}+\boldsymbol{q}}$ above the Fermi surface and $\xi_{\boldsymbol{k}}$ below the Fermi surface, that is, the former corresponds to an electron and the latter to a hole. We close the integration contour in the upper frequency half plane and take the residue of the pole at $\omega = \xi_{\boldsymbol{k}} + i\delta$. The integral $\int d\omega$ equals to $2\pi i$ times the sum over all residues,

$$\int \frac{d\omega}{2\pi} \frac{1}{\omega+\nu-\xi_{\boldsymbol{k}+\boldsymbol{q}}+i\delta_{\boldsymbol{k}+\boldsymbol{q}}} \frac{1}{\omega+\nu-\xi_{\boldsymbol{k}}+i\delta_{\boldsymbol{k}}} = \frac{i}{\nu-(\xi_{\boldsymbol{k}+\boldsymbol{q}}-\xi_{\boldsymbol{k}})+i\delta} \ .$$

The second case deals with $\xi_{\boldsymbol{k}+\boldsymbol{q}}$ below the Fermi surface and $\xi_{\boldsymbol{k}}$ above the Fermi surface and results in the complex conjugate of the expression above. In the last two cases, either both poles are in the upper half plane or both are in the lower half plane. The contour can be closed in the half plane which does not contain a pole and the integral vanishes. Therefore, there are only contributions to the phonon self-energy from an electron and a hole, not from two electrons or two holes.

Adding all the contributions, from the different cases above, the resulting phonon self-energy becomes

$$\Pi(\boldsymbol{q},\nu) = 2|M_{\boldsymbol{q}}|^2 \int \frac{d^3k}{(2\pi)^3} \left[ \frac{1}{\nu-(\xi_{\boldsymbol{k}+\boldsymbol{q}}-\xi_{\boldsymbol{k}})+i\delta} + \text{c.c.} \right] \ .$$

This expression has poles at the energies $\xi_{\boldsymbol{k}+\boldsymbol{q}} - \xi_{\boldsymbol{k}}$ which are the excitation energies for pair excitations in which an electron from the state $\boldsymbol{k}$ is excited to the state $\boldsymbol{k} + \boldsymbol{q}$. Another very important property of the equation above is that its real part is even in frequency $\nu$ and its imaginary part is odd in frequency. This is a general rule for Green's functions and self-energies describing bosonic excitations. The excitation of fermion-pairs shares these properties.

## D.8 Analytic properties of Green's function

In this section, we will take a closer look to the analytic properties of Green's functions and define retarded Green's functions.

The analytic properties of the Green's function are of central importance for the interpretation of many-particle effects. We will investigate these properties for the Green's function $G(\boldsymbol{k}, \omega)$ in frequency space. We recall that $G(\boldsymbol{k}, t)$ is defined only for real times although the Fourier transform defines $G(\boldsymbol{k}, \omega)$ in the whole complex frequency plane.

### D.8.1 The spectral functions

The analytic properties of $G(\boldsymbol{k}, \omega)$ are brought clearly to light by introducing the *Lehmann representation*. We start with the definition of the Green's function (D.9) (the state $|\mathrm{GS}\rangle$ is the exact ground state of the system an we denote by $N$ its particle number) and treat the case $t > t'$. By inserting the complete sum $\sum_n |n\rangle\langle n| = 1$ of eigenstates of $H$ between the $c$-operators and using $E_0$ and $E_n$ to denote the eigenenergies of the exact ground state $|\mathrm{GS}\rangle$ and the states $|n\rangle$, respectively, the expression

$$G(\boldsymbol{k}, t - t') = -i \sum_n \left|\langle n|c_{\boldsymbol{k}}^+|\mathrm{GS}\rangle\right|^2 e^{-i(E_n - E_0)(t-t')}$$

can be derived. The states $\langle n|$ must contain $N + 1$ particles. Therefore, the energy $E_n$ is the energy of an eigenstate of the $(N + 1)$-particle system. If we denote by $\omega_n$ the energy difference between $E_n$ and the ground state energy $E_0$ of the $(N+1)$-particle system, and take into consideration that the difference of the ground state energies for the $(N+1)$-particle and the $N$-particle systems, respectively, equals the chemical potential $\mu$, the relation $E_n - E_0 = \omega_n + \mu$ holds. We consider the case for $t < t'$ and obtain an expression similar to the one above. Performing a Fourier transformation then yields the expression

$$\begin{aligned} G(\boldsymbol{k}, \omega) = & -i \sum_n \left|\langle n|c_{\boldsymbol{k}}^+|\mathrm{GS}\rangle\right|^2 \frac{i}{\omega - \omega_n - \mu + i\delta} \\ & + i \sum_n \left|\langle \mathrm{GS}|c_{\boldsymbol{k}}^+|n\rangle\right|^2 \frac{-i}{\omega + \omega_n - \mu - i\delta} \ . \end{aligned}$$

We further simplify this expression by introducing the *spectral functions*

$$\begin{aligned} A(\boldsymbol{k}, \omega') &= \sum_n \left|\langle n|c_{\boldsymbol{k}}^+|\mathrm{GS}\rangle\right|^2 \delta(\omega' - \omega_n) \\ B(\boldsymbol{k}, \omega') &= \sum_n \left|\langle \mathrm{GS}|c_{\boldsymbol{k}}^+|n\rangle\right|^2 \delta(\omega' - \omega_n) \end{aligned}$$

which vanish for negative frequencies $\omega'$, because $\omega_n$ is non-negative. These functions have a useful physical interpretation. The expression $A(\boldsymbol{k},\omega)\,d\omega'$ $[B(\boldsymbol{k},\omega)\,d\omega']$ gives the probability that an electron [hole] with momentum $\boldsymbol{k}$ has an energy (measured from the Fermi energy) in the interval from $\omega'$ to $\omega'+d\omega'$. Consequently, the sum rule

$$\int_0^\infty A(\boldsymbol{k},\omega')\,d\omega' = 1 - n_{\boldsymbol{k}} \qquad \left[\int_0^\infty B(\boldsymbol{k},\omega')\,d\omega' = n_{\boldsymbol{k}}\right]$$

expresses the fact that the electron [hole] with quasimomentum $\boldsymbol{k}$ has a positive energy (we use $n_{\boldsymbol{k}} = \Theta(|\boldsymbol{k}| - k_F)$). Note also the sum rule $\int (A+B)\,d\omega' = 1$.

Using the spectral functions, the Green's function can be written in the form

$$G(\boldsymbol{k},\omega) = \int_0^\infty d\omega' \left[\frac{A(\boldsymbol{k},\omega')}{\omega-\omega'-\mu+i\delta} + \frac{B(\boldsymbol{k},\omega')}{\omega+\omega'-\mu-i\delta}\right]$$

called the Lehmann representation. Taking the real and imaginary part, respectively, of this equation, it is easy to prove the relations

$$\begin{aligned}
\operatorname{Im} G(\boldsymbol{k},\omega) &= \begin{cases} -\pi A(\boldsymbol{k},\omega-\mu) & \text{for } \omega > \mu \\ \pi B(\boldsymbol{k},\mu-\omega) & \text{for } \omega < \mu \end{cases} \\
\operatorname{Re} G(\boldsymbol{k},\omega) &= \frac{1}{\pi}\int_{-\infty}^\infty \frac{\operatorname{Im} G(\boldsymbol{k},\omega')\operatorname{sign}(\omega'-\mu)}{\omega'-\omega}\,d\omega'
\end{aligned}$$

connecting the imaginary part of the Green's function $G(\boldsymbol{k},\omega)$ to the spectral functions $A(\boldsymbol{k},\omega)$ and $B(\boldsymbol{k},\omega)$, and relating the imaginary part of the Green's function to its real part by an equation similar to a Kramers-Kronig relation.

For a degenerate (noninteracting) electron gas, the spectral functions become $\delta$-functions, that is

$$A(\boldsymbol{k},\omega) = (1-n_{\boldsymbol{k}})\delta(\omega-\epsilon_{\boldsymbol{k}}) \qquad A(\boldsymbol{k},\omega) = n_{\boldsymbol{k}}\delta(\omega-\epsilon_{\boldsymbol{k}})\ .$$

Putting this into the Lehmann representation of the Green's function, Eq. (D.20) is easily recovered.

### D.8.2 The retarded Green's functions

When calculating measurable quantities, as for instance the density of states, or the conductivity, or lifetime broadenings, it is convenient to utilize the retarded Green's functions. On the other hand, the retarded Green's function cannot be calculated directly, there is no diagrammatic expansion for retarded Green's functions. But the retarded Green's function is related in a simple way to the time-ordered Green's function used so far. Hence, the usual approach in calculating measurable quantities is to first determine the time-ordered Green's function by diagram techniques. Then the relation given below is used to find the retarded Green's function. The *retarded Green's function* $G_{\mathrm{R}}(\boldsymbol{k},t-t')$ is defined in the Heisenberg representation by

$$G_{\mathrm{R}}(\boldsymbol{k},t-t') = -i\Theta(t-t')\langle \mathrm{GS}|[c_{H,\boldsymbol{k}}(t), c^+_{H,\boldsymbol{k}}(t')]|\mathrm{GS}\rangle \tag{D.42}$$

with the commutator $[A, B]$. Because of the theta function $\Theta(t-t')$ the $\omega$-$t$ Fouriertransform of (D.42) only has poles in the lower half frequency plane. It is now easy to see that the relation between the time-ordered and the retarded Green's function is

$$\begin{aligned}\operatorname{Im} G_{\mathrm{R}}(\boldsymbol{k}, \omega) &= \operatorname{Im} G(\boldsymbol{k}, \omega) \cdot \operatorname{sign}(\omega - \mu) \\ \operatorname{Re} G_{\mathrm{R}}(\boldsymbol{k}, \omega) &= \operatorname{Re} G(\boldsymbol{k}, \omega)\end{aligned}$$

Due to the fact that the retarded Green's function is analytical in the upper frequency half plane, the following Kramers-Kronig relations hold:

$$\begin{aligned}\operatorname{Re} G_{\mathrm{R}}(\boldsymbol{k}, \omega) &= \frac{1}{\pi} \int_{-\infty}^{\infty} \frac{\operatorname{Im} G_{\mathrm{R}}(\boldsymbol{k}, \omega')}{\omega' - \omega} \\ \operatorname{Im} G_{\mathrm{R}}(\boldsymbol{k}, \omega) &= -\frac{1}{\pi} \int_{-\infty}^{\infty} \frac{\operatorname{Re} G_{\mathrm{R}}(\boldsymbol{k}, \omega')}{\omega' - \omega} \ .\end{aligned} \tag{D.43}$$

# Appendix E

# BCS-theory and the gap function

## E.1 Introduction

This short appendix has two purposes. First it gives a short review of the one-band BCS-theory and defines some terms used in the main part of the thesis. Second it discusses the implications of crystal symmetry on the form of the gap function and tries to classify the possible gap functions in tetragonal high-$T_c$ superconductors using the formalism of point group representations.

## E.2 One-band BCS-theory

The first successful microscopic theory for the description of superconductors was given by Bardeen, Cooper, and Schrieffer in their pioneering paper *Theory of Superconductivity* which appeared December, 1st, 1957 [E.1]. This is the theory still used for the so-called weak-coupling conventional superconductors[1] and is also used often as a starting point for a theoretical model for high-$T_c$ superconductors.

The BCS-theory starts with a system of independent electrons described by the Hamiltonian

$$H_0 = \sum_{\boldsymbol{k}\sigma} \xi_{\boldsymbol{k}\sigma} c^+_{\boldsymbol{k}\sigma} c_{\boldsymbol{k}\sigma} \ ,$$

where $\xi_{\boldsymbol{k}} = \epsilon_{\boldsymbol{k}} - \mu$ represents the dispersion relation (measured with respect to the chemical potential) of the normal electron. A two-particle interaction[2] $V_{\boldsymbol{k}_1\sigma_1,\boldsymbol{k}_2\sigma_2;\boldsymbol{k}_3\sigma_3,\boldsymbol{k}_4\sigma_4}$ is then added. It has the following properties:

---

[1] Strong-coupling conventional superconductors are described by the Eliashberg-theory [E.2]. For the unconventional superconductors, of which the high-$T_c$ compounds are part, there is not yet a satisfactory theory.

[2] This interaction is caused by the exchange of a virtual phonon between two electrons (in other words, a moving electron polarizes the lattice of ions, and the polarized lattice then influences a second electron). The typical energy scale for which the interaction is attractive extends from zero to the Debye frequency. This attractive interaction is very small, and therefore it is surprising that it can form bound pairs. Usually when trying to bind an electron in a shallow potential in 3 dimensions, a certain strength of the potential is needed such that the electron can be bound. This minimum potential can be estimated by the Sommerfeld quantization condition. The fact that bound states can be formed for an arbitrarily small attractive potential was shown by Cooper [E.3] and is a very important feature of the BCS-theory.

- Only two electrons with opposite quasimomentum $\boldsymbol{k}$ are allowed to interact through exchange of phonons, that is, the conserved total quasimomentum $\boldsymbol{K}$ is zero (if no external field is applied) in the scattering process. Umklapp processes are neglected.[3]
- The spin configuration of the scattering electrons is that of a singlet. The two electrons have opposite spin.[4]

These properties allow us to write the interaction as

$$V_{\boldsymbol{k}_1\sigma_1,\boldsymbol{k}_2\sigma_2;\boldsymbol{k}_3\sigma_3,\boldsymbol{k}_4\sigma_4} = V_{(\boldsymbol{k}\sigma),-(\boldsymbol{k}\sigma),(\boldsymbol{k}'\sigma'),-(\boldsymbol{k}'\sigma')} \equiv V_{\boldsymbol{k}\sigma;\boldsymbol{k}'\sigma'}$$

(we use the convention $-(\boldsymbol{k}\sigma) = -\boldsymbol{k}, -\sigma$) and finally to introduce the interaction Hamiltonian

$$H_{\text{int}} = \frac{1}{2} \sum_{\boldsymbol{k}\sigma;\boldsymbol{k}'\sigma'} V_{\boldsymbol{k}\sigma;\boldsymbol{k}'\sigma'} c^+_{(\boldsymbol{k}'\sigma')} c^+_{-(\boldsymbol{k}'\sigma')} c_{-(\boldsymbol{k}\sigma)} c_{(\boldsymbol{k}\sigma)} \ . \tag{E.1}$$

Bardeen, Cooper, and Schrieffer [E.1] calculated the ground state of

$$H_{\text{BCS}} = H_0 + H_{\text{int}}$$

using an Ansatz for the ground state and then minimizing its energy by applying a variational technique (see also [E.4], Chap. 2-4). Using a mean field approximation (MFA) ([E.5], Chap. 3.5) results in the same ground state energy and wave function, but is more transparent, so we will follow the latter way.

The key observation in the mean field approximation is that the operator $c_{-\boldsymbol{k}\downarrow}c_{\boldsymbol{k}\uparrow}$ is almost a c-number (with only small fluctuations) and therefore we write

$$c_{-\boldsymbol{k}\downarrow}c_{\boldsymbol{k}\uparrow} = \langle c_{-\boldsymbol{k}\downarrow}c_{\boldsymbol{k}\uparrow}\rangle + (c_{-\boldsymbol{k}\downarrow}c_{\boldsymbol{k}\uparrow} - \langle c_{-\boldsymbol{k}\downarrow}c_{\boldsymbol{k}\uparrow}\rangle) \equiv \langle c_{-\boldsymbol{k}\downarrow}c_{\boldsymbol{k}\uparrow}\rangle + \Phi_{\boldsymbol{k}} \ ,$$

the quantity $\Phi_{\boldsymbol{k}}$ is small compared to $\langle c_{-\boldsymbol{k}\downarrow}c_{\boldsymbol{k}\uparrow}\rangle$ and can be treated as a perturbation. Using (E.1) we thus write, to first order in $\Phi_{\boldsymbol{k}}$,

$$\begin{aligned} H_{\text{BCS}} &= H_{\text{M}} + O(\Phi_{\boldsymbol{k}})^2 \\ H_{\text{M}} &= \sum_{\boldsymbol{k}\sigma} \xi_{\boldsymbol{k}\sigma} c^+_{\boldsymbol{k}\sigma} c_{\boldsymbol{k}\sigma} - \sum_{\boldsymbol{k}} (\Delta_{\boldsymbol{k}} c^+_{\boldsymbol{k}\uparrow} c^+_{-\boldsymbol{k}\downarrow} - \Delta^*_{\boldsymbol{k}} c_{-\boldsymbol{k}\downarrow} c_{\boldsymbol{k}\uparrow}) \end{aligned} \tag{E.2}$$

---

[3] We are only considering pairs with total momentum $\boldsymbol{K} = 0$, mainly because of two reasons. The first involves phase space arguments: Scattering is possible for non-zero total momentum as well, but the sharp drop of the occupation number at the Fermi surface, together with the observation that the energy transferred in the scattering process is smaller than the Debye frequency $\omega_D$ and therefore the change of the magnitude of the quasimomentum of the electron ($\approx \omega_D/v_F$) in the scattering process is small, therefore electrons involved in the scattering process stay in regions very closed to the Fermi surface. This implies that the phase space for scattering processes with vanishing total momentum is much larger than for other situations. In a time-dependent formulation, one finds that the pairs with $\boldsymbol{K} = 0$ have the largest 'growth rate' (see [E.4], Chap. 7). This is the same result stated with different words. A second reason for only taking into account pairs with $\boldsymbol{K} = 0$ is the fact that the pair energy increases linearly with $\boldsymbol{K}$ (see [E.4], (2-15)) such that the state with $\boldsymbol{K} = 0$ has the lowest energy of all pair states.

[4] The total wave function of an electron pair is a product of the spin function and the orbital wave function and has to be antisymmetric with respect to the exchange of the electrons. The singlet spin function is antisymmetric, therefore the related orbital wave function is symmetric and favors the situation where the "paired" electrons are closed to each other. The triplet spin function, however, is symmetric, therefore the orbital wave function must be antisymmetric and as a consequence the electrons are pushed away from each other. For an attractive interaction which decreases in strength with the electron distance, the singlet state will be of lower energy than the triplet state.

where the definition of the *gap function*

$$\Delta_{\boldsymbol{k}} = -\sum_{\boldsymbol{k}'} V_{\boldsymbol{k}\boldsymbol{k}'} \langle c_{-\boldsymbol{k}'\downarrow} c_{\boldsymbol{k}\uparrow} \rangle \tag{E.3}$$

has been used. The Hamiltonian (E.2) is bilinear in the $c$-operators and can be diagonalized by means of a canonical transformation. So far, the gap function $\Delta_{\boldsymbol{k}}$ remains unknown. The gap equation (E.3), however, provides a relation between the $c$-operators and the gap function. Therefore, the diagonalization of the Hamiltonian and the solution of the gap equation must be performed self-consistently. In practice this is done by first diagonalizing the Hamiltonian while treating the gap function as a freely adjustable. Then the average $\langle c_{-\boldsymbol{k}\downarrow} c_{\boldsymbol{k}\uparrow} \rangle$ can be evaluated and the gap function is given by the gap equation.

The Ansatz for the canonical transformation—which is called the *Bogoliubov-Valatin transformation*—is (see [E.5], Eq. (3.42))

$$\begin{aligned} c_{\boldsymbol{k}\uparrow} &= u^*_{\boldsymbol{k}} \gamma_{\boldsymbol{k}0} + v_{\boldsymbol{k}} \gamma^+_{\boldsymbol{k}1} \\ c^+_{-\boldsymbol{k}\downarrow} &= -v^+_{\boldsymbol{k}} \gamma_{\boldsymbol{k}0} + u_{\boldsymbol{k}} \gamma^+_{\boldsymbol{k}1} \; . \end{aligned} \tag{E.4}$$

The operator $\gamma_{\boldsymbol{k}0}$ possesses a certain probability amplitude for destroying an electron with quantum numbers ($\boldsymbol{k} \uparrow$) and for creating one with quantum numbers ($-\boldsymbol{k} \downarrow$). It removes a quasimomentum $\boldsymbol{k}$ from the system and lowers the quantum number $m_z$ related to the component of the angular momentum in direction of the quantization axis by 1/2. The operator $\gamma^+_{\boldsymbol{k}1}$ performs a similar change: It adds the quasimomentum $\boldsymbol{k}$ to the system and increases $m_z$ by 1/2. These amplitudes are given by the *coherence factors* $u_{\boldsymbol{k}}$ and $v_{\boldsymbol{k}}$ which are determined by demanding that the $\gamma$-operators obey the standard anticommutation relations for fermions and that the transformation (E.4) diagonalizes the Hamiltonian $H_{\mathrm{M}}$ in (E.2). The diagonalized Hamiltonian becomes

$$H_{\mathrm{M}} = \sum_{\boldsymbol{k}} E_{\boldsymbol{k}} (\gamma^+_{\boldsymbol{k}0} \gamma_{\boldsymbol{k}0} + \gamma^+_{\boldsymbol{k}1} \gamma_{\boldsymbol{k}1} + \text{const.}) \tag{E.5}$$

and introduces quasiparticles called *bogolons* which possess the energy $E_{\boldsymbol{k}}$ above or below the "ground state" with the *dispersion relation*

$$E_{\boldsymbol{k}} = \pm \sqrt{\xi^2_{\boldsymbol{k}} + |\Delta_{\boldsymbol{k}}|^2} \; . \tag{E.6}$$

The coherence factors which have to be used in the Bogoliubov-Valatin transformation are

$$|v_{\boldsymbol{k}}|^2 = 1 - |u_{\boldsymbol{k}}|^2 = \frac{1}{2} \left( 1 - \frac{\xi_{\boldsymbol{k}}}{E_{\boldsymbol{k}}} \right) \; . \tag{E.7}$$

Note that the diagonalization becomes a simple eigenvalue problem in this formulation.

Our main goal of determining the energy spectrum of $H_{\mathrm{BCS}}$ is almost reached. Just the calculation of the gap function is left. We perform this by using the canonical transformation to express the average $\langle c_{-\boldsymbol{k}\downarrow} c_{\boldsymbol{k}\uparrow} \rangle$ by means of the $\gamma$-operators. The result is

$$\langle c_{-\boldsymbol{k}\downarrow} c_{\boldsymbol{k}\uparrow} \rangle = u^*_{\boldsymbol{k}} v_{\boldsymbol{k}} \langle 1 - \gamma^+_{\boldsymbol{k}0} \gamma_{\boldsymbol{k}0} - \gamma^+_{\boldsymbol{k}1} \gamma_{\boldsymbol{k}1} \rangle = u^*_{\boldsymbol{k}} v_{\boldsymbol{k}} (1 - 2f(E_{\boldsymbol{k}})) \; ,$$

the second equation arises from the observation that the $\gamma$-operators $\gamma_{\boldsymbol{k}0}$ and $\gamma_{\boldsymbol{k}1}$ annihilate the ground state. The function $f(E)$ is the Fermi-function and $\beta = 1/(k_B T)$. Using the expression (E.7) for the coherence factors, the gap equation becomes

$$\Delta_{\boldsymbol{k}} = -\sum_{\boldsymbol{k}'} V_{\boldsymbol{k}\boldsymbol{k}'} \frac{\Delta_{\boldsymbol{k}'}}{2E_{\boldsymbol{k}'}} \tanh \frac{\beta E_{\boldsymbol{k}'}}{2} \ . \tag{E.8}$$

In this form, the gap equation (E.8) determines the gap function $\Delta_{\boldsymbol{k}}$ for a given interaction $V_{\boldsymbol{k}\boldsymbol{k}'}$, a given dispersion relation $\xi_{\boldsymbol{k}}$, and for a given temperature $T = 1/(k_B\beta)$. Note that (E.8) is *not* a homogeneous equation in the gap function, because $\Delta_{\boldsymbol{k}}$ appears also in the dispersion relation $E_{\boldsymbol{k}}$, and consequently, Eq. (E.8) is not an eigenvalue equation. Solving (E.8) is a non-trivial task. In the BCS formulation the simplification $V_{\boldsymbol{k}\boldsymbol{k}'} = -V_0$, independent of $\boldsymbol{k}$ and $\boldsymbol{k}'$, makes the analytic solution of the gap equation possible.

## E.3 Symmetries of the gap function

We can draw some general properties [E.6, E.7, E.8] of the gap function $\Delta_{\boldsymbol{k}}$ from the Hamiltonian $H_{\mathrm{M}}$ in (E.2), the dispersion relation (E.6) and the gap equation (E.8).

We focus once again on the interaction, this time taking closer attention to the spin. The interaction

$$V_{\sigma_1\sigma_2\sigma_3\sigma_4}(\boldsymbol{k}, \boldsymbol{k}') \equiv V_{-\boldsymbol{k}\sigma_1, \boldsymbol{k}\sigma_2; -\boldsymbol{k}'\sigma_3, \boldsymbol{k}'\sigma_4} \equiv \langle -\boldsymbol{k}\sigma_1, \boldsymbol{k}\sigma_2 | \hat{V} | -\boldsymbol{k}'\sigma_3, \boldsymbol{k}'\sigma_4 \rangle \tag{E.9}$$

has the property (refer to [E.7], Sect. IIA)

$$V_{\sigma_1\sigma_2\sigma_3\sigma_4}(\boldsymbol{k}, -\boldsymbol{k}') = +V_{\sigma_2\sigma_1\sigma_4\sigma_3}(-\boldsymbol{k}, \boldsymbol{k}') \tag{E.10}$$

which becomes clear from the operator product $c^+_{-\boldsymbol{k}\sigma_1} c^+_{\boldsymbol{k}\sigma_2} c_{-\boldsymbol{k}'\sigma_3} c_{\boldsymbol{k}'\sigma_4}$. The definition (E.3) of the gap function reads (see [E.7])

$$\Delta_{\sigma\sigma'}(\boldsymbol{k}) = -\sum_{\boldsymbol{k}', \sigma_3, \sigma_4} V_{\sigma'\sigma\sigma_3\sigma_4}(\boldsymbol{k}, \boldsymbol{k}') \langle c_{\boldsymbol{k}'\sigma_3} c_{-\boldsymbol{k}'\sigma_4} \rangle \tag{E.11}$$

and implies

$$\Delta_{\sigma\sigma'}(\boldsymbol{k}) = -\Delta_{\sigma'\sigma}(-\boldsymbol{k}) \tag{E.12}$$

when taking into account (E.10).

We assume now that the interaction $V$ vanishes for spin flip processes. Furthermore we restrict to *singlet pairing*. Then, $\langle c_{\boldsymbol{k}\sigma} c_{-\boldsymbol{k}\sigma'} \rangle \sim \delta_{\sigma,-\sigma'}$, and the gap function (E.11) becomes proportional to $\delta_{\sigma,-\sigma'}$. Equation (E.12) is fulfilled in this case by

$$(\Delta_{\sigma\sigma'}(\boldsymbol{k})) = \begin{pmatrix} 0 & \Delta_{\boldsymbol{k}} \\ -\Delta_{\boldsymbol{k}} & 0 \end{pmatrix} \ ; \quad \Delta_{\boldsymbol{k}} = \Delta_{-\boldsymbol{k}} \ , \tag{E.13}$$

where the complex scalar function $\Delta_{\boldsymbol{k}}$ corresponds to the gap function used in Eqs. (E.3) and (E.8) and must be an even function of $\boldsymbol{k}$.

The gap function is determined by the gap equation (E.8). Close to the critical temperature $T_c \equiv 1/(k_B\beta_c)$, the gap function becomes very small, and $E_{\boldsymbol{k}} \approx \xi_{\boldsymbol{k}}$ linearizes (E.8). In the weak-coupling limit, the $\boldsymbol{k}'$-sum of the linearized gap equation

$$\Delta_{\boldsymbol{k}} = -\sum_{\boldsymbol{k}'} V_{\boldsymbol{k}\boldsymbol{k}'}\Delta_{\boldsymbol{k}'} \cdot \frac{1}{2\xi_{\boldsymbol{k}'}} \tanh\frac{\beta_c\xi_{\boldsymbol{k}'}}{2}$$

is written as a product of two sums (we denote the interaction (E.9) for the singlet case by $V_{\boldsymbol{k}\boldsymbol{k}'}$, it corresponds to the interaction in (E.8)),

$$\Delta_{\boldsymbol{k}} = -\sum_{\boldsymbol{k}'} V_{\boldsymbol{k}\boldsymbol{k}'}\Delta_{\boldsymbol{k}'} \cdot \sum_{\boldsymbol{k}''} \frac{1}{2\xi_{\boldsymbol{k}''}} \tanh\frac{\beta_c\xi_{\boldsymbol{k}''}}{2} \ , \tag{E.14}$$

this is possible if $V_{\boldsymbol{k}\boldsymbol{k}'}$ depends only weakly on $\boldsymbol{k}$ and $\boldsymbol{k}'$ (see [E.7], Eq. (2.18)). The second sum in (E.14) can be evaluated and yields

$$-\sum_{\boldsymbol{k}'} V_{\boldsymbol{k}\boldsymbol{k}'}\Delta_{\boldsymbol{k}'} = v\Delta_{\boldsymbol{k}} \tag{E.15}$$

with $v^{-1} = \ln(1.14\beta_c\epsilon_c)$, where $\epsilon_c$ is an energy cutoff, which is of the order of the Debye energy. Eq. (E.15) has the following properties:

- It is an eigenvalue equation for the determination of the gap function $\Delta_{\boldsymbol{k}}$.
- The eigenvalues $v$ correspond to a critical temperature $T_c$.
- Because of $V_{\boldsymbol{k}\boldsymbol{k}'} < 0$, all eigenvalues are positive.
- The larger the eigenvalue $v$, the larger the corresponding critical temperature $T_c$.

The largest of the eigenvalues of (E.15) therefore gives the $T_c$ at which the system becomes superconducting. The corresponding eigenfunction $\Delta_{\boldsymbol{k}}$ is the gap function.

The fact that the dispersion relation (E.6) is invariant with respect to the symmetry transformations $G$ of the point symmetry group $\mathcal{G}$ of the crystal requires

$$|\Delta_{\boldsymbol{k}}| = |\Delta_{G\boldsymbol{k}}| \ . \tag{E.16}$$

The symbol $G\boldsymbol{k}$ denotes the application of the transformation $G$ to $\boldsymbol{k}$.

The gap function $\Delta_{\boldsymbol{k}}$ can be decomposed into parts $\Delta^{\mu}_{\boldsymbol{k}}$ transforming according to irreducible representation (IRs)[5] $\mu$ of the group $\mathcal{G}$. The decomposition is given by

$$\begin{aligned} \Delta_{\boldsymbol{k}} &= \sum_{\mu} \Delta^{\mu}_{\boldsymbol{k}} \ , \\ \Delta^{\mu}_{\boldsymbol{k}} &= \frac{1}{n_{\mathcal{G}}} \sum_{G\in\mathcal{G}} \chi^{\mu}(G)\Delta_{G\boldsymbol{k}} \end{aligned} \tag{E.17}$$

---

[5] In the literature, irreducible representations are called *reps*. We call them *IRs* and use the term *reps* to denote *representations* which may be reducible.

| IR name | Alternative name | Eigenfunction |
|---|---|---|
| $A_{1g}$ | $s^+$, $s$ | $1$ |
| $A_{2g}$ | $s^-$ | $xy(x^2-y^2)$ |
| $B_{1g}$ | $d^+$, $d_{x^2-y^2}$ | $x^2-y^2$ |
| $B_{2g}$ | $d^-$, $d_{xy}$ | $xy$ |
| $E_g$ | $e$ | $z(x \pm iy)$ |

Table E.1: Even-parity irreducible representations (IRs) of the tetragonal $D_{4h}$ point group.

where $\chi^\mu(G)$ is the character of the group element $G$ in the representation $\mu$, and $n_\mathcal{G}$ is the order of the group $\mathcal{G}$ (refer to App. C on group theory). We will assume that there is no accidental degeneracy, the largest $T_c$ of (E.15) corresponds to exactly one gap function $\Delta_{\boldsymbol{k}}$.

Now we ask for the IR which can occur in the decomposition (E.17) such that the gap function is consistent with the conditions (E.13) and (E.16). From (E.13) it is obvious that only even-parity IRs are allowed.

We specialize now to the tetragonal $D_{4h}$ group to give more concrete results. This group possesses five even-parity IRs, four out of these are one-dimensional (1D) IRs and the fifth is a two-dimensional (2D) IR (see Tab. E.1).

It is clear that the gap function $\Delta_{\boldsymbol{k}}$ may be composed out of exactly one of the four 1D IRs.

Due to the fact that the gap function is a complex function, 2D representations (reps) are also possible candidates. Indeed, a gap function transforming according to the $E_{1g}$ IR fulfills condition (E.16) perfectly.

We call the 5 IRs discussed so far the *pure phases* [E.6], they are

$$\Delta_{\boldsymbol{k}} = \Delta_{\boldsymbol{k}}^{s^+} \;, \quad \Delta_{\boldsymbol{k}} = \Delta_{\boldsymbol{k}}^{s^-} \;, \quad \Delta_{\boldsymbol{k}} = \Delta_{\boldsymbol{k}}^{d^+} \;, \quad \Delta_{\boldsymbol{k}} = \Delta_{\boldsymbol{k}}^{d^-} \;, \text{ and } \quad \Delta_{\boldsymbol{k}} = \Delta_{\boldsymbol{k}}^{e} \;. \tag{E.18}$$

For the notation of the IRs $\mu$, refer to Tab. E.1.

The reducible 2D reps are the next choice: the real part may transfer according to one 1D IR, and the imaginary part according to another. The four 1D IRs allow for the six *mixed phases* [E.6]

$$\begin{aligned} &\Delta_{\boldsymbol{k}}^{s^+} + i\Delta_{\boldsymbol{k}}^{s^-} \;, \quad \Delta_{\boldsymbol{k}}^{s^+} + i\Delta_{\boldsymbol{k}}^{d^+} \;, \quad \Delta_{\boldsymbol{k}}^{s^+} + i\Delta_{\boldsymbol{k}}^{d^-} \;, \quad \Delta_{\boldsymbol{k}}^{d^+} + i\Delta_{\boldsymbol{k}}^{d^-} \;, \\ &\Delta_{\boldsymbol{k}}^{s^-} + i\Delta_{\boldsymbol{k}}^{d^+} \;, \text{ and } \quad \Delta_{\boldsymbol{k}}^{s^-} + i\Delta_{\boldsymbol{k}}^{d^-} \end{aligned} \tag{E.19}$$

in this way.

The lists (E.18) and (E.19) exhausts the possible forms of the gap functions. Pure real mixtures of different reps, as for instance $\Delta_{\boldsymbol{k}}^{s^+} + \Delta_{\boldsymbol{k}}^{d^+}$ are not allowed in the $D_{4h}$ group.

They, however, become possible when the symmetry is lowered to, for instance, the one of the orthorhombic $D_{2h}$ group. The tetragonal IRs $A_{1g}$ and $B_{1g}$ then degenerate into the $A_g$ ($D_{2h}$) IR and therefore $\Delta_{\boldsymbol{k}}^{s^+} + \Delta_{\boldsymbol{k}}^{d^+}$ is allowed.

# Bibliography

## References for Chapter 1

[1.1] H. Kamerlingh Onnes, Leiden Comm., **120b**, **122b**, **124c** (1911).

[1.2] W. Meissner and R. Ochsenfeld, Naturwissenschaften **21**, 787 (1933).

[1.3] F. and H. London, Proc. Roy. Soc. (London) **A149**, 71 (1935).

[1.4] J. G. Daunt and K. Mendelssohn, Proc. Roy. Soc. (London) **A185**, 225 (1946).

[1.5] W. S. Corak, B. B. Goodman, C. B. Satterthwaite, and A. Wexler, Phys. Rev. **96**, 1442 (1954); **102**, 656 (1956).

[1.6] H. Fröhlich, Phys. Rev. **79**, 845 (1950).

[1.7] E. Maxwell, Phys. Rev. **78**, 477 (1950); C. A. Reynolds, B. Serin, W. H. Wright, and L. B. Nesbitt, Phys. Rev. **78**, 487 (1950).

[1.8] J. Bardeen, L. N. Cooper, and J. R. Schrieffer, *Theory of Superconductivity*, Phys. Rev. **108**, 1175 (1957).

[1.9] L. N. Cooper, *Bound Electron Pairs in a Degenerate Fermi Gas*, Phys. Rev. **104**, 1189 (1956).

[1.10] G. M. Eliashberg, *Interactions between electrons and lattice vibrations in a superconductor*, Sov. Phys. JETP **11**, 696 (1960).

[1.11] F. Steglich, J. Aarts, C. D. Bredll, W. Lieke, D. Meschede, W. Franz, and J. Schäfer, Phys. Rev. Lett. **43**, 1892 (1979).

[1.12] J. G. Bednorz and K. A. Müller, *Possible High $T_c$ Superconductivity in the Ba-La-Cu-O System*, Z. Phys. B **64**, 189 (1986).

[1.13] M. K. Wu *et al.*, Phys. Rev. Lett. **58**, 908 (1987).

[1.14] C. C. Tsuei, J. R. Kirtley, C. C. Chi, L. S. Yu-Jahnes, A. Gupta, T. Shaw, J. Z. Sun, and M. B. Ketchen, Phys. Rev. Lett. **73**, 593 (1994).

[1.15] A. G. Loeser *et al.*, Science **273**, 325 (1996); H. Ding *et al.*, Nature (London) **382**, 51 (1996).

[1.16] C. C. Homes *et al.*, Phys. Rev. Lett. **71**, 1645 (1993); C. Bernhard, D. Munzar, A. Wittlin, W. König, A. Golnik, C. T. Lin, M. Kläser, Th. Wolf, G. Müller-Vogt, and M. Cardona, *Far-infrared ellipsometric study of the spectral gap in the c-axis conductivity of* $\mathrm{Y_{1-x}Ca_xBa_2Cu_3O_{7-\delta}}$ *crystals*, Phys. Rev. B **59**, R6631 (1999).

[1.17] K. B. Lyons, S. H. Liou, M. Hong, H. S. Chen, J. Kwo, and T. J. Negron, *Raman detection of the superconducting gap in Ba-Y-Cu-O superconductors*, Phys. Rev. B **36**, 5592 (1987).

[1.18] R. C. Dynes, *The order parameter of high* $T_c$ *superconductors: experimental probes*, Solid State Commun. **92**, 53 (1994).

[1.19] J. R. Schrieffer, *Symmetry of the order parameter in high temperature superconductors*, Solid State Commun. **92**, 129 (1994).

[1.20] M. E. Reeves, T. A. Friedmann, and D. M. Ginsberg, Phys. Rev. B **35**, 7207 (1987).

[1.21] W. N. Hardy *et al.*, Phys. Rev. Lett. **70**, 3999 (1993); D. A. Bonn *et al.*, Phys. Rev. B **47**, 11314 (1993).

[1.22] Y. Iye, in: *Physical Properties of High Temperature Superconductors III*, ed. D. M. Ginsberg (World Scientific, Singapore, 1992).

[1.23] C. M. Varma, P. B. Littlewood, S. Schmitt-Rink, E. Abrahams, and A. E. Ruckenstein, *Phenomenology of the Normal State of Cu-O High-Temperature Superconductors*, Phys. Rev. Lett. **63**, 1996 (1989).

[1.24] C. M. Varma, *Theory of Copper-oxide Metals*, Phys. Rev. Lett. **75**, 898 (1995).

[1.25] C. Thomsen and M. Cardona, *Raman Scattering in High-*$T_c$ *Superconductors*, in: *Phys. Prop. of High Temp. Superconductors I*, ed. D. M. Ginsberg, p. 409.

[1.26] A. A. Abrikosov and L. A. Fal'kovskiĭ, *Raman scattering of light in superconductors*, Sov. Phys. JETP **13**, 179 (1961).

[1.27] A. A. Abrikosov and V. M. Genkin, *On the theory of Raman scattering of light in superconductors*, Sov. Phys. JETP **38**, 417 (1974).

[1.28] M. V. Klein and S. B. Dierker, *Theory of Raman scattering in superconductors*, Phys. Rev. B **29**, 4976 (1984).

[1.29] P. B. Allen, *Fermi-surface Harmonics: A general method for nonspherical problems. Application to Boltzmann and Eliashberg equations*, Phys. Rev. B **13**, 1416 (1976).

[1.30] T. P. Devereaux, D. Einzel, B. Stadlober, R. Hackl, D. H. Leach, and J. J. Neumeier, *Electronic Raman Scattering in High-*$T_c$ *Superconductors: A Probe of* $d_{x^2-y^2}$ *Pairing*, Phys. Rev. Lett. **72**, 396 (1994).

[1.31] T. P. Devereaux, D. Einzel, B. Stadlober, and R. Hackl, *Reply*, Phys. Rev. Lett. **72**, 3291 (1995).

[1.32] T. P. Devereaux and D. Einzel, *Electronic Raman scattering in superconductors as a probe of anisotropic electron pairing*, Phys. Rev. B **51**, 16336 (1995).

[1.33] M. Krantz, I. I. Mazin, D. H. Leach, W. Y. Lee, and M. Cardona, *Normal-state electronic Raman-scattering efficiencies of* $YBa_2Cu_3O_{7-\delta}$, $Bi_2Sr_2CaCu_2O_8$, *and* $Tl_2Ba_2Ca_2Cu_3O_{10}$*: Effects of local-density-approximation Fermi-surface mass fluctuations*, Phys. Rev. B **51**, 5949 (1995).

[1.34] W. Kohn and L. J. Sham, *Self-Consistent Equations Including Exchange and Correlation Effects*, Phys. Rev. **140**, A1133 (1965).

[1.35] O. K. Andersen, O. Jepsen, A. I. Liechtenstein, and I. I. Mazin, *Plane dimpling and saddle-point bifurcation in the band structures of optimally doped high-temperature superconductors: A tight-binding model*, Phys. Rev. B **49**, 4145 (1994).

[1.36] O. K. Andersen, A. I. Liechtenstein, C. O. Rodriguez, I. I. Mazin, O. Jepsen, V. P. Antropov, O. Gunnarson, and S. Gopalan, *Electrons, phonons and their interaction in* $YBa_2Cu_3O_7$, Physica C **185-189**, 147 (1991).

[1.37] T. Tsuneto, *Transverse Collective Excitations in Superconductors and Electromagnetic Absorption*, Phys. Rev. **118**, 1029 (1960).

[1.38] M. Krantz and M. Cardona, *Raman Scattering by Electronic Excitations in Semiconductors and in High* $T_c$ *Superconductors*, J. Low Temp. Phys. **99**, 205 (1995).

[1.39] T. P. Devereaux, *Theory of Electronic Raman Scattering in Disordered Unconventional Superconductors*, Phys. Rev. Lett. **21**, 4313 (1995).

[1.40] S. L. Cooper, M. V. Klein, B. G. Pazol, J. P. Rice, and D. M. Ginsberg, *Raman scattering from superconducting gap excitations in single-crystal* $YBa_2Cu_3O_{7-\delta}$, Phys. Rev. B **37**, 5920 (1988).

[1.41] C. Thomsen, M. Cardona, B. Friedl, I. I. Mazin, O. Jepsen, O. K. Andersen, and M. Methfessel, Solid State Commun. **75**, 219 (1990).

[1.42] B. Friedl, C. Thomsen, and M. Cardona, *Determination of the Superconducting Gap in* $RBa_2Cu_3O_{7-\delta}$, Phys. Rev. Lett. **65**, 915 (1990).

[1.43] E. Altendorf, X. K. Chen, J. C. Irwin, R. Liang, and W. N. Hardy, Phys. Rev. B **47**, 8140 (1993).

[1.44] D. H. Leach, C. Thomsen, and M. Cardona, Solid State Commun. **88**, 457 (1993).

[1.45] X. J. Zhou, M. Cardona, D. Colson, and V. Viallet, *Plane oxygen vibrations and their temperature dependence in* $HgBa_2Ca_2Cu_3O_{8+\delta}$ *single crystals*, Phys. Rev. B **55**, 12 770 (1997).

[1.46] R. Zeyher and G. Zwicknagl, *Superconductivity-induced phonon self-energy effects in high-*$T_c$ *superconductors*, Z. Phys. B **78**, 175 (1990).

[1.47] E. J. Nicol, C. Jiang, and J. P. Carbotte, *Effect of d-wave energy-gap symmetry on Raman shifts*, Phys. Rev. B **47**, 8131 (1993).

[1.48] C. Jiang and J. P. Carbotte, Phys. Rev. B **50**, 9449 (1994).

[1.49] B. Friedl, C. Thomsen, H.-U. Habermeier, and M. Cardona, Solid State Commun. **81**, 989 (1992).

[1.50] E. T. Heyen, M. Cardona, J. Karpinski, E. Kaldis, and S. Rusiecki, Phys. Rev. B **43**, 12958 (1991).

[1.51] T. Strohm and M. Cardona, *Electronic Raman scattering in* $YBa_2Cu_3O_7$ *and other superconducting cuprates*, Phys. Rev. B **55**, 12 725 (1997).

[1.52] M. Cardona and I. P. Ipatova, in: *Elementary excitations in Solids*, ed. by J. L. Birman, C. Sébenne, and R. F. Wallis (Elsevier, Amsterdam, 1992), p. 237.

[1.53] T. P. Devereaux, Phys. Rev. B **50**, 10287 (1994); see Erratum: T. P. Devereaux and D. Einzel, Phys. Rev. B **54**, 15547–8 (1996).

[1.54] T. Strohm and M. Cardona, *Determination of the s-wave/d-wave gap ratio in* $YBa_2Cu_3O_7$ *from electronic Raman scattering and the LMTO band structure*, Solid State Comm. **104**, 233 (1997).

## References for Chapter 2

[2.1] Mahan, G., *Many-Particle Physics*, New York 1981.

[2.2] M. V. Klein, J. A. Holy, and W. S. Williams, *Raman scattering induced by carbon vacancies in* $TiC_x$, Phys. Rev. B **17**, 1546 (1978).

[2.3] A. A. Abrikosov and L. A. Fal'kovskiĭ, *Raman scattering of light in superconductors*, Sov. Phys. JETP **13**, 179 (1961).

[2.4] A. A. Abrikosov and V. M. Genkin, *On the theory of Raman scattering of light in superconductors*, Sov. Phys. JETP **38**, 417 (1974).

[2.5] M. V. Klein and S. B. Dierker, *Theory of Raman scattering in superconductors*, Phys. Rev. B **29**, 4976 (1984).

[2.6] V. N. Kostur, *Electron Raman scattering in metals with strong electron-phonon coupling*, Z. Phys. B **89**, 149 (1992).

[2.7] P. Wölfle, *Kinetic Theory of Anisotropic Fermi Superfluids*, J. Low Temp. Phys. **22**, 157 (1976).

[2.8] T. P. Devereaux, D. Einzel, B. Stadlober, R. Hackl, D. H. Leach, and J. J. Neumeier, *Electronic Raman Scattering in High-*$T_c$ *Superconductors: A Probe of* $d_{x^2-y^2}$ *Pairing*, Phys. Rev. Lett. **72**, 396 (1994).

[2.9] Ashcroft, N. W. and N. D. Mermin, *Solid State Physics*, Philadelphia 1976.

[2.10] P. B. Allen, *Fermi-surface Harmonics: A general method for nonspherical problems. Application to Boltzmann and Eliashberg equations*, Phys. Rev. B **13**, 1416 (1976).

[2.11] O. K. Andersen, O. Jepsen, A. I. Liechtenstein, and I. I. Mazin, *Plane dimpling and saddle-point bifurcation in the band structures of optimally doped high-temperature superconductors: A tight-binding model*, Phys. Rev. B **49**, 4145 (1994).

[2.12] M. Cardona, *Resonance Phenomena*, in: *Light Scattering in Solids II*, eds. M. Cardona and G. Güntherodt, Berlin and New York, 1982.

[2.13] G. Rickayzen, *Green's functions and condensed matter*, London, 1980.

[2.14] J. Zaanen, G. A. Sawatzky, and J. W. Allen, *Band Gaps and Electron Structure of Transition-Metal Compounds*, Phys. Rev. Lett. **55**, 418 (1985).

[2.15] P. Horsch and W. Stephan, in: *Electronic Properties of High-$T_c$ Superconductors*, eds: H. Kuzmany, M. Mehring, and J. Fink, Springer 1993.

[2.16] W. Brenig, *Aspects of electron correlation in the cuprate superconductors*, Phys. Rpts. **251**, 153 (1995).

[2.17] T. Matsubara, *A New Approach to Quantum-Statistical Mechanics*, Progr. Theoret. Phys. (Kyoto) **14**, 351 (1955).

[2.18] Schrieffer, J. R., *Theory of Superconductivity*, New York 1964.

[2.19] Y. Nambu, *Quasi-Particles and Gauge Invariance in the Theory of Superconductivity*, Phys. Rev. **117**, 648 (1960).

[2.20] T. Tsuneto, *Transverse Collective Excitations in Superconductors and Electromagnetic Absorption*, Phys. Rev. **118**, 1029 (1960).

[2.21] D. Manske, C. T. Rieck, R. Das Sharma, A. Bock, and D. Fay, *Screening of the $B_{1g}$ Raman response in d-wave superconductors*, Phys. Rev. B **56**, R2940 (1997).

[2.22] G. Baym and L. P. Kadanoff, *Conservation Laws and Correlation Functions*, Phys. Ref. **124**, 287 (1961).

[2.23] P. W. Anderson, *Random-Phase Approximation in the Theory of Superconductivity*, Phys. Rev. **112**, 1900 (1958).

[2.24] D. Branch and J. P. Carbotte, *Raman electronic continuum in a spin-fluctuation model for superconductivity*, Phys. Rev. B **52**, 603 (1995).

[2.25] T. P. Devereaux and D. Einzel, *Electronic Raman scattering in superconductors as a probe of anisotropic electron pairing*, Phys. Rev. B **51**, 16336 (1995).

[2.26] P. W. Anderson, *Knight shift in superconductors*, Phys. Rev. Lett. **3**, 328 (1959).

[2.27] T. Strohm and M. Cardona, *Electronic Raman scattering in* $YBa_2Cu_3O_7$ *and other superconducting cuprates*, Phys. Rev. B **55**, 12725 (1997).

[2.28] T. Strohm and M. Cardona, *Determination of the s-wave/d-wave gap ratio in* $YBa_2Cu_3O_7$ *from electronic Raman scattering and the LMTO band structure*, Solid State Comm. **104**, 233 (1997).

[2.29] P. J. Hirschfeld, D. Vollhardt and P. Wölfle, *Resonant Impurity Scattering in Heavy Fermion Superconductors*, Solid State Commun. **59**, 111 (1986).

[2.30] P. J. Hirschfeld, P. Wölfle, and D. Einzel, *Consequences of resonant impurity scattering in anisotropic superconductors: Thermal and spin relaxation properties*, Phys. Rev. B **37**, 83 (1988).

[2.31] P. J. Hirschfeld and N. Goldenfeld, *Effect of strong scattering on the low-temperature penetration depth of a d-wave superconductor*, Phys. Rev. B **48**, 4219 (1993).

[2.32] L. S. Borkowski and P. J. Hirschfeld, *Distinguishing d-wave superconductors from highly anisotropic s-wave superconductors*, Phys. Rev. B **49**, 15404 (1994).

[2.33] T. P. Devereaux, *Theory of Electronic Raman Scattering in Disordered Unconventional Superconductors*, Phys. Rev. Lett. **74**, 4313 (1995).

[2.34] C. M. Varma, P. B. Littlewood, S. Schmitt-Rink, E. Abrahams, and A. E. Ruckenstein, *Phenomenology of the Normal State of Cu-O High-Temperature Superconductors*, Phys. Rev. Lett. **63**, 1996 (1989).

[2.35] S. M. Quinlan, P. J. Hirschfeld, and D. J. Scalapino, *Infrared conductivity of a* $d_{x^2-y^2}$*-wave superconductor with impurity and spin-fluctuation scattering*, Phys. Rev. B **53**, 8575 (1996).

[2.36] M. Cardona and I. P. Ipatova, in: *Elementary Excitations in Solids*, Amsterdam, 1992.

[2.37] A. Zawadowski and M. Cardona, *Theory of Raman scattering on normal metals with impurities*, Phys. Rev. B **42**, 10732 (1990).

[2.38] C. M. Varma, *Theory of Copper-oxide Metals*, Phys. Rev. Lett. **75**, 898 (1995).

[2.39] A. J. Millis, H. Monien, and D. Pines, *Phenmenological model of nuclear relaxation in the normal state of* $YBa_2Cu_3O_7$, Phys. Rev. B **42**, 167 (1990).

[2.40] V. Barzykin and D. Pines, *Magnetic scaling in cuprate superconductors*, Phys. Rev. B **52**, 13585 (1995).

[2.41] J. Ruvalds and A. Virosztek, *Optical properties and Fermi-surface nesting in superconducting oxides*, Phys. Rev. B **43**, 5498 (1991).

[2.42] M. Cardona, T. Strohm, and J. Kircher, *Raman scattering in high-*$T_c$ *superconductors: Electronic excitations*, in: *Spectroscopic Studies of Superconductors*, ed. I. Bozovic, Proc. SPIE **2696**, 182 (1996).

[2.43] S. Donovan, J. Kircher, J. Karpinski, E. Kaldis, and M. Cardona, *Electronic Raman Scattering in* $YBa_2Cu_4O_8$, J. Supercond. **8**, 417 (1995).

[2.44] T. Zhou, K. Syassen, M. Cardona, J. Karpinski, and E. Kaldis, *Electronic Raman scattering in* $YBa_2Cu_4O_8$ *at high pressure*, Solid State Comm. **99**, 669 (1996).

[2.45] M. Krantz, I. I. Mazin, D. H. Leach, W. Y. Lee, and M. Cardona, *Normal-state electronic Raman-scattering efficiencies of* $YBa_2Cu_3O_{7-\delta}$, $Bi_2Sr_2CaCu_2O_8$*, and* $Tl_2Ba_2Ca_2Cu_3O_{10}$*: Effects of local-density-approximation Fermi-surface mass fluctuations*, Phys. Rev. B **51**, 5949 (1995).

[2.46] R. Hackl, G. Krug, R. Nemetschek, M. Opel, and B. Stadlober, *Electronic Raman scattering in copper-oxide superconductors and related compounds*, in: *Spectroscopic Studies of Superconductors*, ed. I. Bozovic, Proc. SPIE **2696**, 194 (1996).

[2.47] T. Inui, Y. Tanabe, and Y. Onodera, *Group Theory and Its Applications in Physics*, Berlin, Heidelberg 1990.

[2.48] Krier, G., O. Jepsen, A. Burkhardt, and O. K. Andersen, *The TB-LMTO-ASA program.*

[2.49] B. W. Kernighan and D. M. Ritchie, *Programmieren in C*, München 1990.

[2.50] M. Krantz and M. Cardona, *Raman Scattering by Electronic Excitations in Semiconductors and in High* $T_c$ *Superconductors*, J. Low Temp. Phys. **99**, 205 (1995).

[2.51] G. Lehmann and M. Tant, *On the Numerical Calculation of the Density of States and Related Properties*, Phys. Status Solidi B **54**, 469 (1972).

[2.52] O. Jepsen and O. K. Andersen, *???*, Solid State Commun. **9**, 1793 (1971).

[2.53] M. Krantz and M. Cardona, *Comment on "Electronic Raman Scattering in High-*$T_c$ *Superconductors: A Probe of* $d_{x^2-y^2}$ *Pairing"*, Phys. Rev. Lett. **72**, 3290 (1995).

[2.54] T. P. Devereaux, D. Einzel, B. Stadlober, and R. Hackl, *Reply*, Phys. Rev. Lett. **72**, 3291 (1995).

[2.55] B. Friedl, C. Thomsen, and M. Cardona, *Determination of the Superconducting Gap in* $RBa_2Cu_3O_{7-\delta}$, Phys. Rev. Lett. **65**, 915 (1990).

[2.56] R. Hackl, W. Gläser, P. Müller, D. Einzel, and K. Andres, *Light-scattering study of the superconducting energy gap in* $YBa_2Cu_3O_7$ *single crystals*, Phys. Rev. B **38**, 7133 (1988).

[2.57] T. Staufer, R. Nemetschek, R. Hackl, P. Müller, and H. Veith, *Investigation of the Superconducting Order Parameter in* $Bi_2Sr_2CaCu_2O_8$ *Single Crysta'¡ls*, Phys. Rev. Lett. **68**, 1069 (1992).

[2.58] B. Brandow, *private communication.*

[2.59] M. Sigrist and T. M. Rice, *Unusual paramagnetic phenomena in granular high-temperature superconductors—A consequence of d-wave pairing?* Rev. Mod. Phys. **67**, 503 (1995).

[2.60] D. J. van Harlingen, *Phase-sensitive tests of the symmetry of the pairing state in the high-temperature superconductors—Evidence for $d_{x^2-y^2}$ symmetry*, Rev. Mod. Phys. **67**, 515 (1995).

[2.61] C. O'Donovan and J. P. Carbotte, *In Plane Anisotropy in Optimally Doped* $YBa_2Cu_3O_{6.95}$, J. Low Temp. Phys. **105**, 495 (1996).

[2.62] M. T. Beal-Monod and K. Maki, *Low temperature thermal conductivity in $d+s$ wave superconductivity*, Physica C **265**, 309 (1996).

[2.63] M. Cardona, T. Strohm, and X. Zhou, *Raman Scattering by Electronic Excitations in High-$T_c$ Superconductors*, Proceedings of the $M^2$S-HTSC-V Conference, 1997, Beijing, China. Also to be published in Physica C.

[2.64] O. K. Andersen, O. Jepsen, A. I. Liechtenstein, and I. I. Mazin, *Plane dimpling and saddle-point bifurcation in the band structures of optimally doped high-temperature superconductors: A tight-binding model*, Phys. Rev. B **49**, 4145 (1994).

[2.65] T. P.Devereaux and D. Einzel *Electronic Raman scattering in superconductors as a probe of anisotropic electron pairing*, Phys. Rev. B **51**, 16336 (1995).

[2.66] T. P. Devereaux, *Theory of Electronic Raman Scattering in Disordered Unconventional Superconductors*, Phys. Rev. Lett. **74**, 4313 (1995).

[2.67] A. A. Martin, ??.

[2.68] M. V. Klein and S. B. Dierker, *Theory of Raman scattering in superconductors*, Phys. Rev. B **29**, 4976 (1984).

[2.69] T. P. Devereaux, A. Virosztek, and A. Zawadowski, *Multiband electronic Raman scattering in bilayer superconductors*, Phys. Rev. B **54**, 12523 (1996).

[2.70] R. Hackl, W. Gläser, P. Müller, D. Einzel, and K. Andres, *Light-scattering study of the superconducting energy gap in* $YBa_2Cu_3O_7$ *single crystals*, Phys. Rev. Lett. **68**, 7133 (1988).

[2.71] M. Krantz, I. I. Mazin, D. H. Leach, W. Y. Lee, and M. Cardona, *Normal-state electronic Raman-scattering efficiencies of* $YBa_2Cu_3O_{7-\delta}$, $Bi_2Sr_2CaCu_2O_8$, *and* $Tl_2Ba_2Ca_2Cu_3O_{10}$*: Effects of local-density-approximation Fermi-surface mass fluctuations*, Phys. Rev. B **51**, 5949 (1995).

[2.72] J. C. Campuzano, G. Jennings, M. Faiz, L. Beaulaigue, B. W. Veal, J. Z. Liu, A. P. Paulikas, K. Vandervoort, and H. Claus, *Fermi Surfaces of* $YBa_2Cu_3O_{6.9}$ *as Seen by Angle-Resolved Photoemission*, Phys. Rev. Lett. **64**, 2308 (1990).

## References for Chapter 3

[3.1] U. Fano, *Effects of Configuration Interaction on Intensities and Phase Shifts*, Phys. Rev. **124**, 1866 (1961).

[3.2] P. W. Anderson, *Localized Magnetic States in Metals*, Phys. Rev. **124**, 41 (1996).

[3.3] G. Mahan, *Many-Particle Physics*, New York 1981.

[3.4] R. Enderlein, K. Peuker, and F. Bechstedt, *General Theory of Light Scattering in Solids*, Phys. stat. sol. (b) **92**, 149 (1979).

[3.5] D. L. Mills and E. Burnstein, *Theory of First-Order Raman Scattering in Insulators*, Phys. Rev. **188**, 1465 (1969).

[3.6] A. Kawabata, *Green Function Theory of Raman Scattering*, J. Phys. Soc. Jap. **30**, 68 (1971).

[3.7] M. V. Klein and S. B. Dierker, *Theory of Raman scattering in superconductors*, Phys. Rev. B **29**, 4976 (1984).

[3.8] V. I. Belitsky, A. Cantarero, M. Cardona, C. Trallero-Giner, and S. T. Pavlov, *Feynman diagrams and Fano interference in light scattering from doped semiconductors*, J. Phys.: Condens. Matter **9**, 5965 (1997).

[3.9] K. Itai, *Theory of Raman scattering in coupled electron-phonon systems*, Phys. Rev. B **45**, 707 (1992).

[3.10] V. G. Hadjiev, X. Zhou, T. Strohm, and M. Cardona, *Strong superconductivity-induced phonon self-energy effects in* $HgBa_2Ca_3Cu_4O_{10+\delta}$, Phys. Rev. B **58**, 1043 (1998).

[3.11] M. V. Klein, *Electronic Raman Scattering*, in: *Light Scattering in Solids I*, ed. M. Cardona (Springer, Berlin, 1983).

[3.12] G. Abstreiter, M. Cardona, and A. Pinczuk, *Light Scattering by Free Carrier Excitations in Semiconductors*, in: *Light Scattering in Solids IV*, ed. M. Cardona (Springer, Berlin, 1983).

[3.13] R. A. Cowley, *Anharmonic Interactions*, in: *Phonons in perfect lattices and in lattices with point imperfections*, ed. R. W. H. Stevenson (Oliver&Boyd, Edinburgh and London, 1966).

[3.14] M. Balkanski, R. F. Wallis, and E. Harom, *Anharmonic effects in light scattering due to optical phonons in silicon*, Phys. Rev. B **28**, 1928 (1983).

[3.15] J. Kosztin and A. Zawadowski, *Violation of the f-sum rule for Raman scattering in metals*, Solid State Commun. **78**, 1029 (1991).

[3.16] P. B. Allen and B. Mitrović, *Theory of the Superconducting* $T_c$, Solid State Phys. **37**, 1 (19??).

[3.17] R. M. Macfarlane, H. .J. Rosen, and H. Seki, *Temperature Dependence of the Raman Spectrum of the High $T_c$ Superconductor* $YBa_2Cu_3O_7$, Solid State Commun. **63**, 831 (1987).

[3.18] C. Thomsen, M. Cardona, B. Gegenheimer, R. Liu, and A. Simon, *Untwinned single crystals of* $YBa_2Cu_3O_{7-\delta}$*: An optical investigation of the a-b anisotropy*, Phys. Rev. B **37**, 9860 (1988).

[3.19] P. M. Horn, D. T. Keane, G. A. Held, J. L. Jordon-Sweet, D. L. Kaiser, F. Holtzberg, and T. M. Rice, *Orthorhombic Distortion at the Superconducting Transition in* $YBa_2Cu_3O_7$*: Evidence for Anisotropic Pairing*, Phys. Rev. B **59**, 2272 (1987).

[3.20] S. L. Cooper, M. V. Klein, B. G. Pazol, J. P. Rice, and D. M. Ginsberg, *Raman scattering from superconducting gap excitations in single-crystal* $YBa_2Cu_3O_{7-\delta}$, Phys. Rev. B **37**, 5920 (1988).

[3.21] B. Friedl, C. Thomsen, and M. Cardona, *Determination of the Superconducting Gap in* $RBa_2Cu_3O_{7-\delta}$, Phys. Rev. Lett. **65**, 915 (1990).

[3.22] X. J. Zhou, M. Cardona, C. W. Chu, Q. M. Lin, S. M. Loureiro, and M. Marezio, *Raman study of* $HgBa_2Ca_{n-1}Cu_nO_{2n+2+\delta}$ ($n = 1, 2, 3, 4$ *and* 5) *superconductors*, Physica C **270**, 193 (1996).

[3.23] X. J. Zhou, M. Cardona, D. Colson, and V. Viallet, *Plane oxygen vibrations and their temperature dependence in* $HgBa_2Ca_2Cu_3O_{8+\delta}$ *single crystals*, Phys. Rev. B **55**, 12 770 (1997).

[3.24] R. Zeyher and G. Zwicknagl, *Superconductivity-induced phonon self-energy effects in high-$T_c$ superconductors*, Z. Phys. B **78**, 175 (1990).

[3.25] E. J. Nicol, C. Jiang, and J. P. Carbotte, *Effect of d-wave energy-gap symmetry on Raman shifts*, Phys. Rev. B **47**, 8131 (1993).

[3.26] E. J. Nicol, C. Jiang, and J. P. Carbotte, *Phonon-self-energy effects due to an electronic mechanism in high-$T_c$ superconductors*, Phys. Rev. B **47**, 8205 (1993).

[3.27] T. P. Devereaux, *Symmetry dependence of phonon line shapes in superconductors with anisotropic gaps*, Phys. Rev. B **50**, 10 287 (1994).

[3.28] T. P. Devereaux, A. Virosztek, and A. Zawadowski, *Charge-transfer fluctuation, d-wave superconductivity, and the $B_{1g}$ Raman phonon in cuprates*, Phys. Rev. B **51**, 505 (1995).

[3.29] Q. M. Lin, Z. H. He, Y. Y. Sun, L. Gao, Y. Y. Xue, and C. W. Chu, *Precursor effects on* $HgBa_2Ca_2Cu_3O_8$ *formation under high pressure*, Physica C **254**, 207 (1996).

[3.30] H. Schwer, K. Conder, E. Kopnin, G. I. Meijer, R. Molinski and J. Karpinski, *X-ray single crystal structure analysis of* $Sr_{0.73}CuO_2$ *and* $Hg_{1-x}Pb_xBa_2Ca_{n-1}Cu_nO_{2n+2+\delta}$ *compounds ($n = 1-5$, $x = 0-0.5$)*, Proceedings of the $M^2$S-HTSC-V Conference, 1997, Beijing, China. Also to be published in Physica C.

[3.31] A. D. Kulkarni, F. W. de Wette, J. Prade, U. Schröder, and W. Kress, *Lattice dynamics of high-$T_c$ superconductors: Optical modes of the thallium-based compounds*, Phys. Rev. B **41**, 6409 (1990).

[3.32] R. Henn, T. Strach, E. Schönherr, and M. Cardona, *Isotope effects on the optical phonons of* $YBa_2Cu_3O_7$*: Eigenvector and infrared charge determination*, Phys. Rev. B **55**, 3285 (1997).

[3.33] C. O. Rodriguez, A. I. Liechtenstein, I. I. Mazin, O. Jepsen, O. K. Andersen, and M. Methfessel, *Optical near-zone-center phonons and their interaction with electrons in* $YBa_2Cu_3O_7$*: Results of the local-density approximation*, Phys. Rev. B **42**, 2692 (1990).

[3.34] W. E. Pickett, R. E. Cohen, and H. Krakauer, *Precise band structure and Fermi-surface calculation for* $YBa_2Cu_3O_7$*: Importance of three-dimensional dispersion*, Phys. Rev. B **42**, 8764 (1990).

[3.35] M. Chandrasekhar, H. R. Chandrasekhar, M. Grimsditch, and M. Cardona, *Study of the localized vibrations of boron in heavily doped Si*, Phys. Rev. B **22**, 4825 (1980).

[3.36] M. Krantz, *Superconducting gap symmetries in* $YBa_2Cu_3O_{7-\delta}$ *compatible with electronic Raman efficiencies and the local-density-approximation band structure*, Phys. Rev. B **54**, 1334 (1996).

[3.37] T. Strohm and M. Cardona, *Electronic Raman scattering in* $YBa_2Cu_3O_7$ *and other superconducting cuprates*, Phys. Rev. B **55**, 12 725 (1997).

[3.38] S. Donovan, J. Kircher, J. Karpinski, E. Kaldis, and M. Cardona, *Electronic Raman Scattering in* $YBa_2Cu_3O_8$, J. Supercond. **8**, 417 (1995).

[3.39] T. P. Devereaux, *Symmetry dependence of phonon line shapes in superconductors with anisotropic gaps*, Phys. Rev. B **50**, 10 287 (1994); see Erratum: T. P. Devereaux and D. Einzel, Phys. Rev. B **54**, 15 547 (1996).

[3.40] P. B. Allen, *Neutron Spectroscopy of Superconductors*, Phys. Rev. B **6**, 2577 (1972).

[3.41] R. P. Sharma, T. Venkatesan, Z. H. Zhang, J. R. Liu, R. Chu, and W. K. Chu, *Evidence for Large Static and Dynamic Distortions in High $T_c$ Superconducting* $YBa_2Cu_3O_{7-\delta}$ *Crystals over a Wide Temperature Range*, Phys. Rev. Lett. **77**, 4624 (1996).

[3.42] H. A. Mook, M. Mostoller, J. A. Harvey, N. W. Hill, B. C. Chakoumakos, and B. C. Sales, *Observation of Phonon Softening at the Superconducting Transition in* $BiSr_2CaCu_2O_8$, Phys. Rev. Lett. **65**, 2712 (1990).

# References for Chapter 4

[4.1] T. Strohm and M. Cardona, *Electronic Raman scattering in* $YBa_2Cu_3O_7$ *and other superconducting cuprates*, Phys. Rev. B **55**, 12725 (1997).

[4.2] M. Krantz and M. Cardona, *Raman Scattering by Electronic Excitations in Semiconductors and in High* $T_c$ *Superconductors*, J. Low Temp. Phys. **99**, 205 (1995).

[4.3] T. P. Devereaux and D. Einzel, *Electronic Raman scattering in superconductors as a probe of anisotropic electron pairing*, Phys. Rev. B **51**, 16336 (1995).

[4.4] M. Cardona, T. Strohm, and X. Zhou, *Raman scattering by Electronic Excitations in High-*$T_c$ *Superconductors*, Physica C **282–287**, 2001 (1997).

[4.5] D. Manske, C. T. Rieck, R. Das Sharma, A. Bock, and D. Fay, *Screening of the* $B_{1g}$ *Raman response in d-wave superconductors*, Phys. Rev. B **56**, R2940 (1997).

[4.6] T. Strohm, D. Munzar, and M. Cardona, *Comment on "Screening of the* $B_{1g}$ *Raman response in d-wave superconductors"*, Phys. Rev. B **58**, 8839 (1998).

[4.7] T. P. Devereaux, D. Einzel, B. Stadlober, R. Hackl, D. H. Leach, and J. J. Neumeier, *Electronic Raman Scattering in High-*$T_c$ *Superconductors: A Probe of* $d_{x^2-y^2}$ *Pairing*, Phys. Rev. Lett. **72**, 396 (1994).

[4.8] T. Strohm and M. Cardona, *Determination of the d-wave/s-wave gap ratio in* $YBa_2Cu_3O_7$ *from electronic Raman scattering and the LMTO band structure*, Solid State Comm. **104**, 223 (1997).

[4.9] V. G. Hadjiev, X. Zhou, T. Strohm, and M. Cardona, *Strong superconductivity-induced phonon self-energy effects in* $HgBa_2Ca_3Cu_4O_{10+\delta}$, Phys. Rev. B **58**, 1043 (1998).

[4.10] S. Y. Savrasov, D. Y. Savrasov, and O. K. Andersen, *Linear-Response Calculations of Electron-Phonon Interactions*, Phys. Rev. Lett. **72**, 372 (1994).

# References for Appendix A

[A.1] N. W. Ashcroft and N. D. Mermin, *Solid State Physics*, Philadelphia 1976.

[A.2] P. Y. Yu and M. Cardona, *Fundamentals of Semiconductors*, Berlin Heidelberg 1996.

[A.3] G. Mahan, *Many-Particle Physics*, New York 1981.

# References for Appendix B

[B.1] P. Hohenberg and W. Kohn, *Inhomogeneous Electron Gas*, Phys. Rev. **136**, B864 (1964).

[B.2] W. Kohn and L. J. Sham, *Self-Consistent Equations Including Exchange and Correlation Effects*, Phys. Rev. **140**, A1133 (1965).

[B.3] R. O. Jones and O. Gunnarson, *The density functional formalism, its applications and prospects*, Rev. Mod. Phys. **61**, 689 (1989).

[B.4] L. Hedin and B. I. Lundqvist, *Explicit local exchange-correlation potentials*, J. Phys. C **4**, 2064 (1971).

[B.5] N. W. Ashcroft and N. D. Mermin, *Solid State Physics*, Philadelphia 1976.

[B.6] H. L. Skriver, *The LMTO Method*, Springer Series in Solid-State Sciences 41.

[B.7] C. Herring, *A New Method for Calculating Wave Functions in Crystals*, Phys. Rev. **57**, 1169 (1940).

[B.8] E. Wigner and F. Seitz, *On the Constitution of Metallic Sodium*, Phys. Rev. **43**, 804 (1933); E. Wigner and F. Seitz, *On the Constitution of Metallic Sodium. II*, Phys. Rev. **46**, 509 (1934).

[B.9] J. C. Slater, *Wave Function in a Periodic Potential*, Phys. Rev. **51**, 846 (1937).

[B.10] J. Korringa, *??*, Physica **13**, 392 (1947).

[B.11] W. Kohn and N. Rostocker, *Solution of the Schrödinger Equation in Periodic Lattices with an Application to Metallic Lithium*, Phys. Rev. **94**, 111 (1954).

[B.12] O. K. Andersen, *Linear methods in band theory*, Phys. Rev. B **12**, 3060 (1975).

# References for Appendix C

[C.1] L. M. Falicov, *Group Theory and Its Physical Applications*, Chicago & London 1969.

[C.2] W. Ludwig and C. Falter, *Symmetries in Physics*, Springer Series in Solid-State Sciences 64.

[C.3] T. Inui, Y. Tanabe, and Y. Onodera, *Group Theory and Its Applications in Physics*, Springer Series in Solid-State Sciences 78.

[C.4] P. Y. Yu and M. Cardona, *Fundamentals of Semiconductors*, Springer 1996.

[C.5] E. P. Wigner, *Group Theory and Its Application to the Quantum Mechanics of Atomic Spectra*, New York and London 1959.

[C.6] M. Cardona, *Resonance Phenomena*, in: *Light Scattering in Solids II*, ed. M. Cardona and G. Güntherodt.

## References for Appendix D

[D.1] R. D. Mattuck, *A Guide to Feynman Diagrams in the Many-Body Problem*, 2nd ed., Dover, New York 1992.

[D.2] G. Mahan, *Many-Particle Physics*, New York 1981.

[D.3] A. A. Abrikosov, L. P. Gorkov, and I. E. Dzyaloshinski, *Methods of quatum field theory in statistical physics*, Dover, New York 1963.

[D.4] L. D. Landau and E. M. Lifschitz, *Lehrbuch der theoretischen Physik IX, Statistische Physik Teil 2*, 3. Aufl., Akademie, Berlin 1989.

[D.5] J. R. Schrieffer, *Theory of Superconductivity*, Benjamin, New York 1964.

[D.6] M. Gell-Mann and F. Low, *Bound states in quantum field theory*, Phys. Rev. **84**, 350 (1951).

## References for Appendix E

[E.1] J. Bardeen, L. N. Cooper, and J. R. Schrieffer, *Theory of Superconductivity*, Phys. Ref. **108**, 1175 (1957).

[E.2] G. M. Eliashberg, *Interactions between electrons and lattice vibrations in a superconductor*, Sov. Phys. JETP **11**, 696 (1960).

[E.3] L. N. Cooper, *Bound Electron Pairs in a Degenerate Fermi Gas*, Phys. Rev. **104**, 1189 (1956).

[E.4] J. R. Schrieffer, *Theory of Superconductivity*, New York 1964.

[E.5] M. Tinkham, *Introduction to Superconductivity*, New York 1996.

[E.6] F. Wenger and S. Östlund, *d-wave pairing in tetragonal superconductors*, Phys. Rev. B **47**, 5977 (1993).

[E.7] M. Sigrist and K. Ueda, *Phenomenological theory of unconventional superconductivity*, Rev. Mod. Phys. **63**, 239 (1991).

[E.8] J. R. Schrieffer, *Symmetry of the order parameter in high temperature superconductors*, Solid State Comm. **92**, 129 (1994).